

Proceedings of the
**10th Virtual International Conference on
Science, Technology and
Management in Energy**

Editor:
Velimirović, L. Z.

Publishers:
Complex System Research Centre, Niš, Serbia
Mathematical Institute of the Serbian Academy of
Sciences and Arts, Belgrade, Serbia

Serbia, Belgrade, November 25-26, 2024

Editor
Velimirović, L. Z.

eNergetics 2024

10th Virtual International Conference on Science,
Technology and Management in Energy

Proceedings

Publishers

Complex System Research Centre, Niš, Serbia

Mathematical Institute of the Serbian Academy of Sciences and
Arts, Belgrade, Serbia

Serbia, Belgrade, November 25-26, 2024



Proceedings of the
**10th Virtual International Conference
on Science Technology and Management in Energy**

Serbia, Belgrade, November 25-26, 2024

Editors:

Dr. Lazar Z. Velimirović

Technical Editor:

Dr. Petar Vranić

Published by:

Complex System Research Centre, Niš, Serbia

Mathematical Institute of the Serbian Academy of Sciences and Arts, Belgrade, Serbia

Printed by:

Blue Copy, Niš, Serbia

Number of copies printed: 100

The publishing year: 2025

Printing of this edition has been financially supported by

The Ministry of Science, Technological Development and Innovation of the Republic of Serbia

ISBN-978-86-82602-05-7

CIP - Каталогизacija u publikaciji
Nародна библиотека Србије, Београд

620.9(082)(0.034.2)

VIRTUAL International Conference on Science Technology and Management in Energy
(10 ; 2024 ; Beograd)

Energetics 2025 [Elektronski izvor] : proceedings / 10th Virtual International Conference on Science Technology and Management in Energy, Serbia, Belgrade, November 25-26, 2024 ; editor Velimirović, L.[Lazar] Z. - Niš : Complex System Research Centre ; Belgrade : Mathematical Institute of the SASA, 2025 (Niš : Blue Copy). - 1 elektronski optički disk (CD-ROM) ; 12 cm

Sistemska zahtevi: Nisu navedeni. - Nasl. sa naslovne strane dokumenta. - Tiraž 100.
- Bibliografija uz svaki rad.

ISBN 978-86-82602-05-7 (CSRC)

a) Енергетика -- Зборници

COBISS.SR-ID 163344137

eNergetics 2024

10th Virtual International Conference on Science Technology and Management in Energy

Organizer:

Mathematical Institute of the Serbian Academy of Sciences and Arts,
Belgrade, Serbia

Co-organizers:

- Academy of Sciences and Arts of the Republika Srpska
- Faculty of Mining and Geology, University of Belgrade
- Faculty of Technical Sciences, University St. Climent Ohridski
- Complex System Research Centre COSREC

Supported by:

The Ministry of Science, Technological Development and Innovation of the
Republic of Serbia



Program Committee

Chair:

Dr. Lazar Z. Velimrović, Mathematical Institute of the Serbian Academy of Sciences and Arts, Belgrade, Serbia

Members:

Prof. Dr. Aleksandar Janjić, Faculty of Electronic Engineering, Serbia

Prof. Dr. Detelin Markov, Faculty of Power Engineering and Power Machines, Bulgaria

Prof. Dr. Marko Serafimov, Faculty of Mechanical Engineering, Macedonia

Prof. Dr. Mileta Janjić, Faculty of Mechanical Engineering, Montenegro

Prof. Dr. Zoran Stajić, Faculty of Electronic Engineering, Serbia

Prof. Dr. Miomir Stanković, Mathematical Institute of the Serbian Academy of Sciences and Arts, Serbia

Prof. Dr. Tomislav Sekara, School of Electrical Engineering, Serbia

Prof. Dr. Enver Agić, Public Enterprise Electric Utility of Bosnia and Herzegovina, Bosnia and Herzegovina

Prof. Dr. Niko Majdandžić, Faculty of Mechanical Engineering, Croatia

Prof. Dr. Serkan Abbasoglu, Cyprus International University, Turkey

Prof. Dr. Bojan Srđević, Faculty of Agriculture, Serbia

Dr. Lenin Kanagasabai, PVP Siddhartha Institute of Technology, India

Prof. Dr. Abdelhak Djoudi, National Polytechnic School, Algeria

Dr. Elson Avallone, Federal Institute of Education, Science and Technology of São Paulo, Brazil

Prof. Dr. Zdravko Milovanović, Faculty of Mechanical Engineering, Bosnia and Herzegovina

Prof. Dr. Miloš Jelić, Research and Development Center Alfatec, Serbia

Prof. Dr. Zoran Markov, Faculty of Mechanical Engineering, Macedonia

Dr. Jovan Mikulović, School of Electrical Engineering, Serbia

Dr. Sasa Milić, Institute Nikola Tesla, Serbia

Prof. Dr. Krsto Miljanović, Agromediterranean Faculty, Bosnia and Herzegovina
Prof. Dr. Lana Pantić-Randjelović, Faculty of Sciences and Mathematics, Serbia
Prof. Dr. Krum Todorov, Faculty of Power Engineering and Power Machines,
Bulgaria
Prof. Dr. Dragoljub Mirjanić, Academy of Sciences and Arts of Republic of Srpska,
Bosnia and Herzegovina
Prof. Dr. Tomislav Pavlović, Faculty of Sciences and Mathematics, Serbia
Dr. Howard Njoku, University of Nigeria, Nigeria
Prof. Dr. Zoran Gligorić, Faculty of Mining and Geology, Serbia
Dr. Reza Hamidi, Arkansas Tech University, USA
Prof. Dr. Danijel M. Dankovic, Faculty of Electronic Engineering, Serbia
Dr. Wassila Issaadi, Faculty of Technology, University of Bejaia, Algeria
Dr. Monica Carvalho, Federal University of Paraíba, Brazil
Dr. Prahaladh Paniyil, Clemson University, USA
Prof. Dr. Milan Rapajić, Faculty of Technical Sciences, Serbia
Dr. Sandra Patricia Castaño Solis, ETS Universidad Politécnica de Madrid, Spain
Dr. Arunava Chatterjee, Meghnad Saha Institute of Technology, India
Prof. Dr. Vesna Karović Maričić, Faculty of mining and geology, Serbia
Dr. Ivana Radonjić Mitić, Faculty of Sciences and Mathematics, Serbia

Organizing Committee

Chair:

Dr. Petar Vranić, Mathematical Institute of the Serbian Academy of Sciences and Arts, Serbia

Members:

Prof. Dr. Miomir Stanković, Mathematical Institute of the Serbian Academy of Sciences and Arts, Serbia

Prof. Dr. Zoran Stajić, Faculty of Electronic Engineering, Serbia

Dr. Lazar Velimirović, Mathematical Institute of the Serbian Academy of Sciences and Arts, Serbia

Dr. Dusan Tatić, Mathematical Institute of the Serbian Academy of Science and Arts, Serbia

Dr. Radmila Janković, Mathematical Institute of the Serbian Academy of Science and Arts, Serbia

Dr. Danijela Protić, Serbian Armed Force, Serbia

Dr. Jelena Velimirović, Mathematical Institute of the Serbian Academy of Sciences and Arts, Serbia

Dr. Ivana Petkovski, Mathematical Institute of the Serbian Academy of Sciences and Arts, Serbia

M.Sc. Vladimir Antic, Serbian Armed Force, Serbia

Table of Contents

A Decade of eNergetics - Shaping the Future of Energy	i
Editorial	
Nonlinear Control of a Photovoltaic Water Pumping System	3
Ali Berboucha, Kamel Djermouni, Said Aissou, Kaci Ghedamsi, Elyazid Amirouche, Djamal Aouzellag	
A More Sustainable Society through Electric Mobility: Analysis of the Operational Emissions of the Renault Kwid E-Tech	9
João Marcelo Fernandes Gualberto de Galiza, Daniel de Paula Diniz, Monica Carvalho	
Solar Salt Recycling: Cost-opportunity Ratio	17
Manuel Botejara-Antúnez, Jaime González-Domínguez, Pavlos Zalimidis, Justo García-Sanz-Calcedo	
An Experimental Investigation of Falling Film Evaporation on a Vertical Plate	23
Hayat El Baamrani, Abdelaaziz Yagour, Aicha Eddemani, Ahmed Aharoune, Abdallah Boukhris	
Anaerobic Biodigesters and their By-products: A Systematic Literature Review	29
João Pedro Cruz de Almeida, Adriano da Silva Marques, Cristiani Viegas Brandão Grisi, Rita de Cassia Andrade da Silva, Marllon Costa Lira, Miriane Moreira Fernandes Santo	
Effect of Damping Coefficient and Inertia Constant on Performance of Virtual Synchronous Machine Control	37
Souhil Drias, Abderrahmane Berkani, Mohamed Bey	
Enhancement of Microchannel Heat Sink by Introducing Double-layer Microchannel, Truncated Microchannel and Multi-layer Microchannel Heat Sinks having Various Flow Channel Structures: An Overview	45
Dipak Debbarma, K.M Pandey, Abhishek Paul, Sunita Debbarma	

Exergy Analysis Applied to Cogeneration Systems: A Strategy for Energy Sustainability	53
Marcos Oliveira Lima, Alexandre Magno Vieira Gonçalves de Brito, Fazal Um Min Allah, Daniel de Paula Diniz, Antônio Carlos Cabral dos Santos, Monica Carvalho	
Experimental Study for the Improvement of Savonius Wind Turbine by Wind Flow Direction Control	61
Pinku Debnath, M. D. Raiesh, Abhishek Kumar Singh, Krishna Murari Pandey	
Energetic and Exergetic Investigation of Transcritical Heat Pump System using an Expander Device Substituted for Throttle Valve	69
Youcef Maalem, Hakim Madani	
Experimental Study on Concentration of Milk in an Electric Still	77
Mahesh Kumar, Om Prakash, Rahul Grewal, Shimpy	
Analysis of the Effect of Ethyl Acetate on the Crystallization of MAPbI₃ and its Impact on the Efficiency of the Perovskite Solar Cells	85
Erro Quiñonez José Eulalio, García Gutiérrez Rafael, Arias-Ramos Carlos Fabián, Cancino-Gordillo Francisco Enrique, Rangel Segura Ricardo	
Biodiesel Synthesis using Animal Fat and Ethyl Route	91
Alânia Kallyne Graciliano Teixeira, Jhonatas Wagner Barbosa da Costa Gouveia, José Luiz Francisco Alves, Marta Célia Dantas Silva, Silvia Layara Floriani Andersen	
The Effect of Gas Bubble Diameter at the Inlet of Two-phase Centrifugal Pumps on the Formation of Gas Pockets Obstructing Flow	97
Toumi Bessam, Atif Abdelmadjid, Hazem Meharzi	
Control of Open-end Winding Induction Generator for Supporting Various Grid-isolated Loads	103
Arunava Chatterjee, Soumyajit Ghosh	
Development of an Energy Map of Available Biomass Raw Materials in the Geographic Information System (GIS)	109
Srećko Čurčić, Aleksandar Peulić	

Ferroelectricity-driven Photovoltaic Effect under Visible Light in the Absence of an External Electric Field for CsGeI(3-t)Br_t (t=1,2): A First-principles Study	115
Naouel Chelil, Mohammed Sahnoun	
Numerical Simulation and Optimization of Stable CH₃NH₃PbI₃-based 2D/3D Mixed Dimensional Perovskite Solar Cell	121
Walagedara Gamage Ayomi Pabasara, Galhenage Asha Sewvandi	
Influence of Different Recommendations for Walls Pressure Coefficients in a Pavilion under Natural Ventilation	129
Paulo Cesar Mioralli, Ricardo Nunes Pereira Junior, Elson Avallone	
Modeling the Effects of Wall Orientations on Indoor Temperature During the Autumn Season: A Case Study of Ouled Sidi Brahim (Algeria)	135
Nabila Ihaddadene, Mohamed Chouidira, Razika Ihaddadene	
Implementation of an Automatic Feedback Control Unit for a Double-pass Thermoelectric-assisted Solar Air Heater	143
Chinemerem Jerry Chukwu, Izuchukwu Kenneth Onyenwe, Chibundu Ogbonnia	
Exploring Organic Photovoltaic Systems: A Sustainable Solution for Energy-efficient Building Facades in Northeastern Brazil	151
Dafne Negrão Cordeiro e Silva, Taynara G. S. Lago	
Numerical Study on the Performance Comparison of Classical and Elliptical Savonius Turbines with Various Parameters at Different Wind Variations ...	159
Sri Kurniati, Sudirman Syam, Nursa Lim, Wellem F. Galla	
Numerical Study of Nanofluid Forced Convection in a Channel with Flexible Vortex Generators	167
Khaoula Dedouh, Brahim Fersadou, Henda Kahalerras	
Conversion of Castor Oil Plant through a Biorefinery Scheme for Sustainable Aviation Fuel and Succinic Acid Production	175
Carlos Eduardo Guzmán-Martínez, Claudia Gutiérrez-Antonio	
Energy Management based on a Systems Approach to the Analysis of Energy Indicators, Strategies and Policies	183
Jelena Malenović-Nikolić	

Effect of Solar Radiation Intensity on the Drying of Tomatoes	189
Razika Ihaddadene, Nabila Ihaddadene, Réda Khama, Hachemi Benouadah	
Experimental Study of Fouling Effect on Feed Water Heaters: A CFD Modeling Approach in Steam Power Plants	195
Mkpamdi N. Eke, Emmanuel E. Duke, Imole A. Agunbiade	
Exergetic Performance Analysis of a CPV/T-TEG System	201
Khaled Mouaici, Henda Kahalerras, Kamil Arslan, Brahim Fersadou, Selahattin Çelik	
Obtaining Optical Radiation Splitters for Hybrid Photovoltaic and Thermal Systems	207
Philippe Pereira Moreira, Lucas Medeiros de França, Lucas Vinicius Borges Pereira, José Felix da Silva Neto, Pollyana Caetano Ribeiro Fernandes	
Performance Optimization of Solar Air Heater with Impinging Jet Technique	213
Siddhita Yadav, K. M. Pandey	
Performance Analysis of Maximum Power Point Tracking based on Perturb & Observe Algorithm and Fuzzy Logic Control	219
Yacine Bouali, Khoukha Imarazene, El Madjid Berkouk	
Substitution of Calcium at A-site in LaCaMnNiO₆ for Optimized Electrochemical Energy Storage Application	227
Dinesh, Mukul Gupta, Parasmani Rajput, Ashok Kumar	
Simplified Nusselt Correlations for Easier Estimation of Heat Exchange in Natural Convection in Vertical Cavities	231
Paulo Cesar Mioralli, Marcos Vinicius dos Santos, Elson Avallone	
Prioritization of Measures for Achieving Energy and Climate Goals in Serbia	239
Gabrijela Popović, Aleksandra Fedajev, Petar Mitić	
The Impact of Varying the Frequency and Amplitude of Porous Wavy Strip Inserts on the Hydrothermal Performance of a Nanofluid-filled Tube	247
Benelhaoues Mohamed, Fersadou Brahim, Nessab Walid, Djeddou Hessem	

Estimating the Potentials for Indoor Comfort in Smart Green Buildings with BIPV	253
Nnabuike Ngwu, Michael Ahanonu, Ken Chen, Yongjun Sang, Howard Njoku, Gang Pei	
Systematic Literature Review for Recycling Cooperatives from the Perspective of Life Cycle Assessment: Interrelations and Gaps	261
Murilo dos Santos Oliveira, Julio Cesar Sales Bezerra, Andreza da Silva Santana Peruchi, Emerson Ribeiro Machado, Raphael Abrahao	
Modeling and Simulation of the Light Water Nuclear Small Modular Reactor CAREM-25 with OpenMC Code	269
Karima Ziche, Amira Guessoum, Salah Eddine Bentriddi, Naima Amrani	
Red Deer Vocalizations based Optimization and Unique Football Player Skills inspired Algorithm for Active Power Loss Dwindling in Electrical Transmission System	277
Lenin Kanagasabai	
Solar Distiller for Machining Cutting Fluid: An Alternative to Reduce Costs	285
Wesley Mateus Basso, Vinicius Souza Cardozo, Paulo César Mioralli, Francine Martins Molinari, Pablo Sampaio Gomes Natividade, Paulo Henrique Palota, Rodrigo Garcia da Silva, Sílvio Aparecido Verdério Junior, José Ferreira da Costa, Jonas Rafael Antonio, Elson Avallone	
Selection of Viable Areas for Geothermal Installations with Helical Probes using 3D Geophysical Modeling of the Subsoil	293
V́ctor Ṕrez Ferńndez, Cristina Śez Blázquez, Ignacio Mart́n Nieto	
Numerical Study of Heat Transfer from a Nanofluid in a Waved Channel Equipped with a Rotating Cylinder in the Presence of a Magnetic Field	301
Nawal Guerroudj, Brahim Fersadou, Henda Kahalerras	
Xylitol Production from Sugar and Alcohol Industry Waste	307
Lucas Vinicius Borges Pereira, Laís Campos Teixeira de Carvalho Gonçalves, Joelda Dantas	

Selection of Electric Vehicle Charging Station using PROMETHEE II and Shannon Entropy: A Case Study from Niš, Serbia	315
Petar Vranić, Ivana Petkovski	
The Promise of Indium Gallium Nitride Solar Modules for Sustainable Energy	323
Sabira Nour, Abdelhak Merabti, Houcine Aissani, Rachid Abdeldjebbar, Abdelkader Benslimane, Ahmed Djatout	
Photovoltaic Solar Energy to Mitigate Emissions Associated with Public Buildings: A Bibliometric Study	329
Ana Paula Freire de Araújo, Andrezza Pereira de Matos, Joelda Dantas, Monica Carvalho	
The Importance of Implementing Artificial Neural Networks in Boiler Automation Systems	337
Stefan Popović, Dejan Djukić, Nebojsa Denić, Sonja Djukić Popović, Jelena Stojanović	
Theoretical Studies on the Hydrogen Adsorption Properties of Transition Metal Decorated Covalent Organic Framework	343
Valarmani M. Vasanthakannan, Kittusamy Senthilkumar	
Valorizing the Invasive Macrophyte <i>Eichhornia crassipes</i> as a Potential Bionergy Feedstock: Preliminary Assessment from Thermochemical Characterization	351
Maxwell de Arandas Pimentel, Fernando Mateus de Oliveira Santos, Gabriela Aurora Alexandre de Vasconcellos, Jhonatas Wagner Barbosa de Costa Gouveia, José Luiz Francisco Alves, Silvia Layara Floriani Andersen	
Attack Evaluation of Cyber Security Analysis in Cyber-physical Power Systems: A Review Concept	359
Erdem Koca, Musa Terkes, Alpaslan Demirci	
Sustainability: A Bibliometric Review of Cassava in Flour and Starch Processing from an Environmental Perspective	369
Julio Cesar Sales Bezerra, Murilo dos Santos Oliveira, Emanuely Alves Pelogio, Emerson Ribeiro Machado, Raphael Abrahao	

Power System Stability Analysis in Presence of Renewable Energies377

Nour El Yakine Kouba, Amel Brik

**A Review on Cyber Attack Detection and Defense Strategies in Cyber-physical
Power Systems385**

Erdem Koca, Musa Terkes, Alpaslan Demirci

A Decade of eNergetics - Shaping the Future of Energy

I. INTRODUCTION

On the tenth anniversary of the Virtual International Conference on Science, Technology, and Management in Energy - eNergetics, we reflect on conference growth since its introduction in 2015, when it was established with aim to become an international platform for research exchange on contemporary challenges in energy domain. Over a past ten years we, as a society, witnessed impressive developments in energy technologies. Through this conference, researchers have emphasized some of them like the integration of IoT in energy management, increased use of renewable energy sources, integration with smart grid technologies, and the increasing need for new technologies for energy storage systems. In addition, the conference held talks concerning the continued relevance of conventional power generation and its optimization, energy policies and administration elaborating some of the global issues posed by accessibility problems, control systems, and social-economic consequences of energy transitions. Over the years, the eNergetics has remained an important agent in promoting our collective understanding of how to manage energy in an efficient, sustainable, and fair manner.

The success of this conference is a testament to the dedication of many researchers who have contributed their insights, expertise, and above all time to develop the conference either as organizers, reviewers, or authors. Among them, some deserve particular attention.

Professor Dr. Miomir Stanković, without a doubt, was the visionary leader behind this conference, having outlined its scope, selected themes, and formed program boards to ensure its success. His hard effort established the

ISBN: 978-86-82602-05-7

foundation of the conference that supports its decadal growth. At this point, we should also recognize the contributions of Professor Dr. Zoran Stajić, who significantly supported the conference during the inception years both through the Alfatec Research and Innovation Centre and as an editor maintaining excellent publication standards. He is still an active member of our program committee.

Furthermore, we would like to thank Professor Dr. Aleksandar Janjić, who has been on our program committee from its start and editor in the foundation years of the conference. His professional skills and consistent assistance have contributed significantly to the conference's continued success. Their collaborative work will be recognized as one that sparked a decade of scientific collaboration at eNergetics.

Moreover, heartfelt gratitude goes to Dr. Lazar Velimirović for his incredible input as the present editorial head of this conference. While taking over this role from previous editors, he has kept up with and even improved upon those standards that were set earlier, maintaining the spirit of excellence as part of his professors' legacy. Next gratitude goes to Dr. Petar Vranić who serves as technical editor and always puts much care into all our documents. His efforts combined with correctness make the entire editing process run smoothly. Last but not least is an amazing group of researchers, members of the organizing committee, the conference's success is greatly indebted to: Dr. Dušan Tatić, Dr. Jelena Velimirović, Dr. Radmila Janković Babić, Dr. Ivana Petkovski, M.Sc. Biserka Mijucić, and M.Sc. Ljubiša Stajić. They are real doers behind organizers: logistics, communication, moderation etc. The appreciation goes to their remarkable efforts of the conference marketing and correspondence

i



team, especially for their tireless work in managing a contact database of over 300,000 contacts. A dedication to ensuring seamless communication, from the initial calls to authors and reviewers to the countless follow-up correspondences, has been truly outstanding. Handling between 35000 and 50000 emails annually is no small feat, and ability to do so with precision, professionalism, and care has been instrumental in the success of this conference.

Since we can't mention everyone's names here, the collective effort is presented in numbers on the following pages.

II. CONFERENCE TRENDS

A. Reviewers

The Reviewers play a significant role in preserving the scholarly value and academic integrity of this conference. The rigorous assessments, constructive criticisms, and perceptive suggestions that they provide have helped to maintain the quality of accepted papers. From 2015 forward there has been a remarkable rise in the number of reviewers for the conference. It started with 30 reviewers in 2015 and increased consistently to reach its peak of 300 in 2021 (Fig. 1). During the last ten years, the total number of reviewers reached 1495 i.e., an average of 150 every year; this indicates both growth in size and significance for this conference as well as strong and increasing involvement by academic and professional communities in facilitating its peer review process.

B. Acceptance Rate and Number of Papers Published

The analysis of the data from 2015 to 2024 shows a changing acceptance rate of manuscripts based on number of papers received and accepted (Fig. 2). Over a decade the conference organizing team received a 1799, while only 413 were accepted for publication. This results in an average acceptance rate of 22.9%. The acceptance rate was 39% in 2015. The acceptance rate declined over the years to 19% in 2024. These figures indicate the increasing selectivity trend. The most significant number of submissions, with 396 papers, occurred in 2021. Presented trend suggests the conference is becoming more competitive by attracting more submissions while maintaining rigorous standards for publication.

C. Analysis of Authorship

Looking at the authorship between 2015 and 2024 conference witnessed a growing number of international authors. In the following lines overall and specific trends are presented.

Overall Participation Trends. During the observed period, the conference has received contributions from more than 40 countries, and from all continents. This fact points to the conference growing international recognition (Fig. 3). There has been also a significant increase in the total number of authors per year. The year 2024 witnessed a prominent rise in contributions, particularly from countries like Algeria and Brazi.

Top Contributing Countries. Serbia, as a host country, has remained throughout the decade a contributor with the highest number of authorships counting from 43 in 2015 to a peak of 66 in 2018, with a total of 361 over the observed period. These numbers reflect a growing research community within Serbia dedicated to the topics of the conference. The second most prominent contributor is the research community from Brazil which showed consistent growth, with authorships rising from 24 in 2018 to 66 in 2024, with a total number of

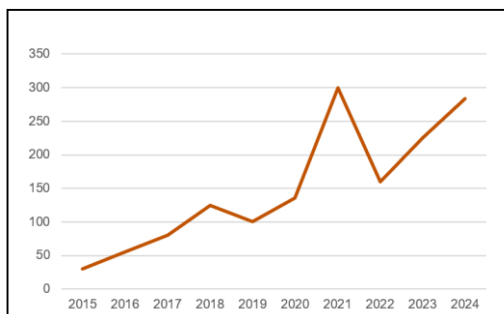


Figure 1. Number of reviewers per year.

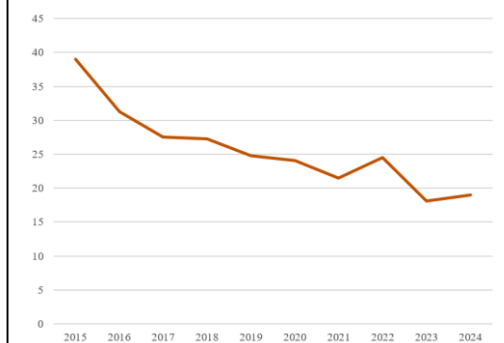


Figure 2. Acceptance rate.

authorships of 233 over ten years. Besides Brazil, the Algerian authorship expanded from 4 in 2019 to 55 in 2022, and 53 in 2024 with a total of 184 authorships in the observed period. Also, a significant number of contributors comes from India, Bosnia and Herzegovina, Iran, and Morocco with a total of 69, 40, 41, and 49 authorships respectively.

Regional distribution of authorships. When it comes to Europe, countries like Serbia, Bosnia and Herzegovina, and Spain have been continuous contributors, while Poland, Slovenia, Greece, Croatia, Russia, Hungary, Belgium, North Macedonia, Moldova, Montenegro, Romania, Turkey, UK and Ukraine, participated during selected years, adding to the overall European representation. Besides Algeria, Nigeria, Ghana, Mauritania, Mauritius, Morocco, South Africa, and Togo are the African countries represented. Many Asian and Middle East countries have also increased their participation over the years like India, Iraq, Iran, Lebanon, China, Malaysia, the Kingdom of Saudi Arabia, United Arab Emirates, Sri Lanka, Nepal, Uzbekistan, and Pakistan, underlining the growing contribution of the Asia researchers. North and South America are represented, notably by Brazil and the USA and sporadic participation from Mexico. Oceania had very limited participation, coming in only from Australia in 2020 and 2018, thus creating an opportunity to improve the participation rate from this region.

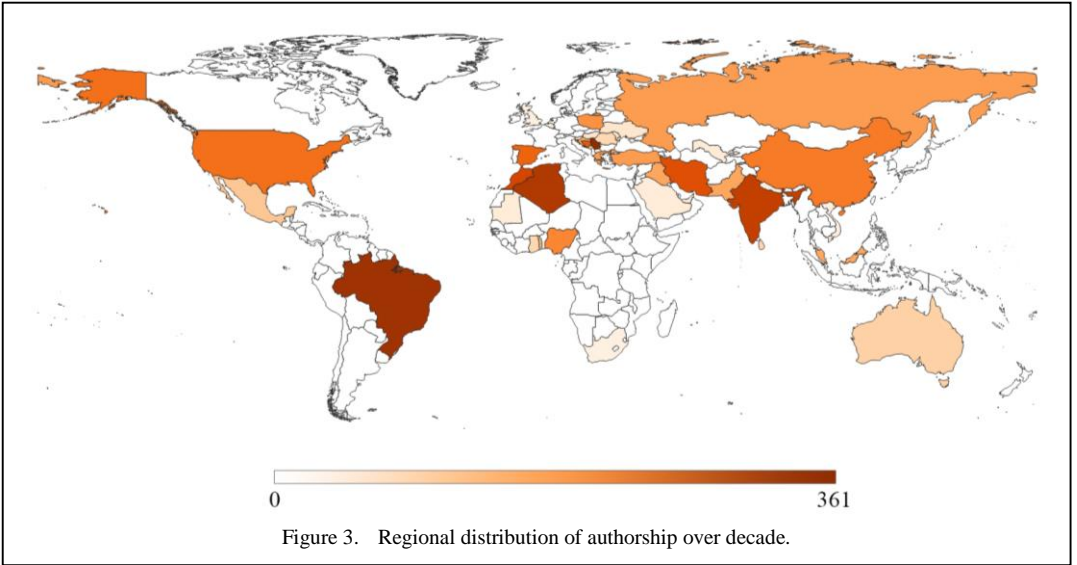
Year-wise Highlights. Considering inception years 2015-2017, participation was more concentrated, with fewer countries involved and lower authorships counts, from 11 countries in total, starting with 47 authorships in 2015 up to 70 in 2017. Between 2018 to 2020 conference expanded with a prominent increase both in the number of countries (20) and authorships (349). From 2021-2024, the conference became even more diversified with contribution from new countries like Indonesia. It enlarged in terms of the international scope, with a total of 30 countries and 765 authorships. These facts point to the conference's established prominence.

D. Analysis of International Collaboration

Only 8.2% of papers are part of the joint international collaboration. However, looking at that segment the data shows a diverse range of international collaborations. Among the top collaborators are author teams from Poland and Iraq with 9 joint papers. Serbian researchers collaborated with colleagues from Slovenia (2 papers), Italy (2 papers), and UAE, KSA, and Iran. Neighboring countries like Bosnia and Herzegovina, and Croatia co-authored 3 papers, emphasizing regional academic cooperation. In the cross-continent collaborations include Turkey and Australia, USA and Nigeria, and Brazil with both Spain and Belgium. Among emerging collaborations are Algeria, Nigeria, and Iran.

E. Analysis of Funded Research

Financial support is a key element in research academically-both in terms of resources



and in the sense that it represents a founding confidence about the potential impact and value of a particular research domain. Examining the number of papers that received funding for the research presented at the conference, top countries are Serbia with 81 funded studies out of 129 (62%), and Brazil with 35 out of 54 (65%), which demonstrates a good commitment to research in the energy field. After them comes Spain with 5 studies, Algeria with 6 studies, and Turkey with 3 studies. Several studies are jointly funded across borders, such as Iran-Serbia, Serbia-Italy, Serbia-UAE-KSA, and Spain-Pakistan. However, a majority of papers presented received no funding.

F. Analysis of Scientific Fields

To achieve comprehensive and holistic research results in one field it is critical to include researchers from diverse scientific backgrounds. When it comes to eNergetics diverse disciplines are present, with Electronics as a dominant field with a 25.4% share in a combined number of papers, indicating a significant incline of the conference objectives towards technological innovation and development (Fig. 4). Combined disciplines count for 24.7%, reflecting the interdisciplinary nature of research issues presented in the conference. Mechanical engineering and Environmental studies have a share of 13.1%, and 10.2% respectively, highlighting the sustainability and engineering perspective in the current conference research. Other significant fields include Planning studies (7.7%), Chemistry (4.1%), emphasize the role of strategic development and fundamental sciences, Mining and metallurgy (3.1%), Economics (2.4%), Physics (2.4%), Technology (6.5%), and Mathematics (0.2%), contributing to a well-rounded conference’s research portfolio.

G. Analysis of Conference Topics

The conference eNergetics considers papers on 10 different topics of research. Below are shares of papers by topic. Energy Management is the most numerous themes with 136 papers, thus comprising 32.9% of all papers. This suggests a concentrated focus on management practices in energy systems, reflecting among others the growing importance of optimizing energy use, modeling of energy systems and prediction, distribution systems monitoring, operation and control, and integrating various energy sources within distribution systems. After Energy Management, Energy Efficiency and Conservation and Renewable Energy and

Alternative Fuels have the largest share in total number of papers, 74 (17.9%) and 73 papers (17.7%), respectively. New Technologies for Energy Saving and Sustainable Energy Technologies have contributed with 21 (5.1%) and 18 papers (4.4%), respectively. Energy and Climate Change and Energy Economics contributed only with 10 (2.4%) and 5 (1.2%) papers, respectively. The significant share of papers in fields of management, efficiency, and renewable energy reflects topical global discourse in the energy sector related to the necessary efficiency, sustainability, and alternatives to traditional sources of energy. This fact alone testifies to the fact that eNergetics positions itself in the cross-over area between traditional approaches to energy management and innovative forward-looking energy solution approaches.

H. Analysis of Energy Sources Considered

Energy sources are central to contemporary energy discourse due to their profound impact on energy security, environmental impact, economic growth, energy transition, sustainability and social justice. Looking at the overall dedication of the conference papers to problems related to the diverse energy sources solar energy emerges as the most prominent energy source discussed, with 65 papers (15.7%). 41 papers (9.3%) consider combined energy sources. Biofuels are also well-represented, with 37 papers (8.9%). 26 papers (6.3%) explicitly discuss fossil fuels indicating an ongoing discussion about its role during the energy transition to cleaner alternatives. Wind energy and hydro energy have moderate representation,

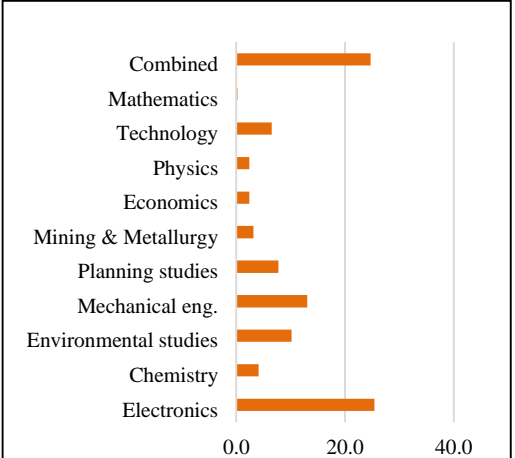


Figure 4. Scientific field distribution.

with 17 papers (4.1%) and 14 papers (3.4%), respectively. Geothermal energy is presented in 7 papers (1.7%), while nuclear energy is represented through 6 papers (1.5%). The minimal presence of hydrogen energy and fusion energy, with only 7 papers each (1.7%), reflects the current status of these technologies. Another topic that received fewer papers was waste-to-energy with only 2 papers or 0.5%. Many papers did not specify an energy source, that is 191 papers, which is 46.2% of the whole. Such papers probably discuss more general energy issues like policy, economic models, sustainability assessments, predictions, optimization or general technology discussion that does not specify a particular energy source. The facts indicate that eNERgetics is prominently focused on renewable energy sources and integrated systems, reflecting the current global trends toward renewables.

I. Analysis of Paper Types and Novelty

The originality of research is a significant indicator of the quality of the conference. In the case of eNERgetics distribution of papers demonstrates a considerable emphasis on the original, novel research with a share of 80.6% (333 papers). Although review papers have a smaller share 19.4%, they offer a synthesis of the current research trends and identify research gaps pointing out directions for future research.

Nearly half of the papers (45,3%) applied existing research methods. This reflects the fact that a significant portion of the presented studies is directed toward the implementation of existing methods for solving actual optimization problems. The almost equal share (45,1%) goes to papers that develop new methods. This suggests that eNERgetics is a platform for the presentation of new scientific methods. The originality of research is a significant indicator of the quality of the conference. In the case of eNERgetics distribution of papers demonstrates a considerable emphasis on the original, novel research with a share of 80.6% (333 papers). Although review papers have a smaller share 19.4%, they offer a synthesis of the current research trends and identify research gaps pointing out directions for future research.

J. Analysis of Methodological Approaches

The most frequent methodological approach adopted at eNERgetics is mathematical modeling, used in 28.3% of the papers. The second-best represented approach is review, taken in its general sense, covering 17.5%. The use of virtual experiments and computation

simulation methods follows, applied in 16.7% of the papers. Finally, experimental design is used in 15.6% of the papers. Combined approaches are applied in 11.7% of the papers and contribute to studies that integrate more than one methodology intending to overcome energy challenges that are multidimensional and may require a blend of theoretical, empirical, and computational methods. Other methods account for 10.3% of the papers and cover qualitative approaches, case studies, policy analysis, or other less frequent methodologies that still play an essential role in developing a comprehensive view of energy problems. In keeping with the orientation of eNERgetics on quantitative methods - mathematical modeling, among others - in the distribution of methodological approaches, it indicates that the venue is for showing the latest front research that involves a sophisticated analytical approach (Fig. 5).

K. Analysis of Data Sources

41.4% of the papers rely on primary data sources. That indicates a strong focus of the presented papers on original research and empirical data collection. Primary data sources typically involve first-hand data collection, such as experiments, surveys, field studies, or direct measurements, which are crucial for advancing new insights in the domain. 31.9% of the papers rely on secondary data, including existing data sets, previously published research, statistical databases, or government reports. The use of secondary data is essential for conducting comparative studies, trend analysis, or validating new theories with existing information. In 26.6% of the papers, authors did not mention explicitly data sources.

L. Analysis of Spatial Level Considered

The fact that nearly 70 percent of the papers analyzed fail to specify any particular level of spatial resolution indicates that a number of the

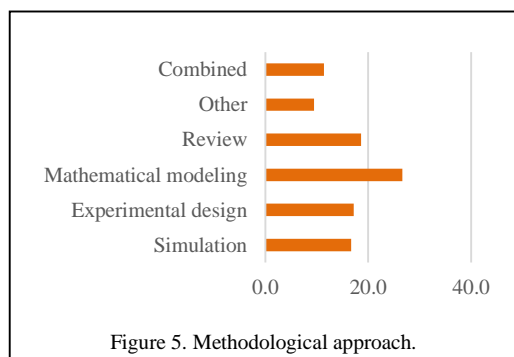


Figure 5. Methodological approach.







studies really might tend to treat the aspects of energy research without reference to geography: for example, research on energy policies or their global environmental impacts or on technologies that would be applied everywhere as opposed to a single location. However, the remaining studies that reported spatial aspects have the following distribution: (1) Local-level research, accounts for 14.1% of the papers; (2) National-level studies account for 7.1% of the papers, indicating interest in country-specific energy policies; (3) Regional level research, which comprises 4.1% of the papers, involve studies focusing on broader geographic areas that encompass several cities or counties; (4) Papers focusing on the city/municipality level (3.6%) and county level (1.6%): this indicates that part of the research is

devoted to urban and sub-national governance issues related to energy.

III. OUTLOOK

Considering the ongoing climate change challenges, depletion of resources, and need for sustainable development, the 10th edition of eNegetics is not only about celebrating past accomplishments but also reaffirming this conference's dedication to leading discussions about current energy topics. As we embark on the next decade eNegetics will keep inspiring and influencing the growth of fundamental energy research, policies, and practices related to the future where energy is abundant, sustainable, and accessible to all.

Nonlinear Control of a Photovoltaic Water Pumping System

Ali Berboucha¹, Kamel Djermouni², Said Aissou³, Kaci Ghedamsi⁴,
Elyazid Amirouche⁵, Djamel Aouzellag⁶

^{1,2,3,4,5,6}Université de Bejaia, Faculté de Technologie, Laboratoire de Maitrise des Energies
Renouvelables, Bejaia, Algeria

¹ali.berboucha@univ-bejaia.dz

Abstract—The objective of this study was to evaluate the operational efficiency and performance characteristics of a photovoltaic water pumping system. The proposed photovoltaic water pumping system comprises a photovoltaic array, a DC-DC boost converter equipped with a fuzzy logic-based maximum power point tracking controller, a three-level neutral point clamped inverter controlled by a simplified space vector pulse width modulation technique, a motor-pump unit based on an induction motor and a water storage tank. Sliding mode control-based regulators are used to adjust the field-oriented control's speed, rotor flux, and d-q axis currents. To assess the performance of the proposed control approach, simulations were carried out on the Matlab/Simulink platform with different levels of irradiation and temperature. The results of the simulation clearly show that the suggested system control performs well in terms of power quality, control robustness, and dynamic reactions, confirming its efficacy.

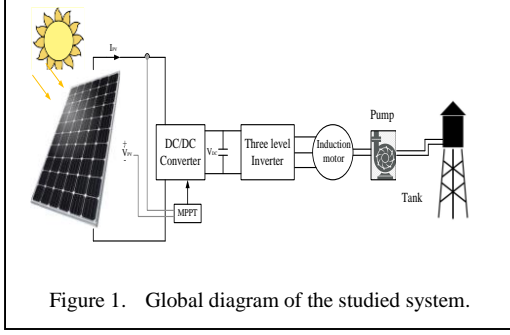
Keywords - sliding mode control, fuzzy logic MPPT, Three-level Neutral Point Clamped (NPC) inverter, simplified space vector modulation, photovoltaic water pumping system

I. INTRODUCTION

Photovoltaic (PV) solar energy has become a highly promising energy source due to its numerous benefits. These include its eco-friendly characteristics, lack of pollution, inherent safety, quiet operation, straightforward installation, and relatively quick setup time. As a result, PV solar technology is widely utilized in various

applications such as grid-connected systems, photovoltaic pumps, and stand-alone systems [1,2]. To optimize the efficiency of photovoltaic (PV) systems, incorporating a maximum power point tracking (MPPT) controller is essential. The primary goal of MPPT is to consistently maximize power output from PV panels, even as environmental conditions fluctuate. This is accomplished by adjusting the operating point of the PV module (current-voltage, $I-V$) to match the load characteristics [3,4]. The MPPT achieves this by adjusting the PV panel's voltage or current outputs, which enables the converter to function at or close to the MPP on the $P-V$ characteristic curve. The fuzzy logic MPPT approach is applied in this work. Since their invention, multilevel inverters received a lot of interest and are frequently used in medium and high voltage/power applications. They have been the subject of an extensive amount of research and are used in many different areas of the power industry, including: renewable energy systems, industrial drives, and power system applications like high voltage DC transmission (HVDC) and flexible AC transmission systems (FACTS) [5-9]. Multilevel inverters emerge as one of the greatest options for high power and large-scale grid-connected renewable energy systems due to their many benefits. Among these benefits are a decrease in harmonic distortion (THD), which calls for fewer filters; modularity; a reduction in the voltage stress placed on power semiconductor devices; and a general increase in efficiency [10]. These systems operate better and are more reliable when multilevel inverters are





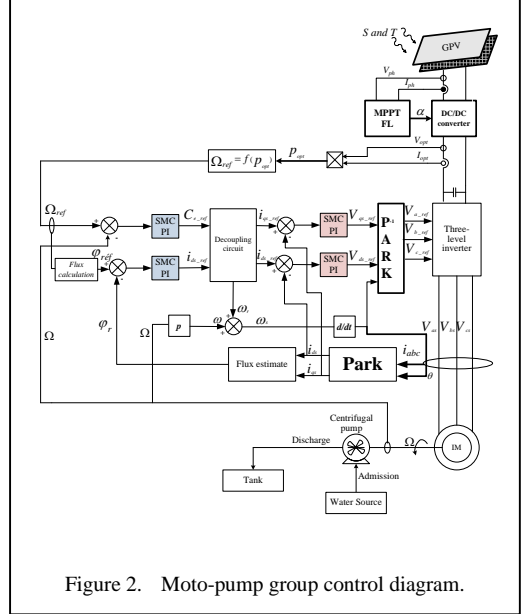
used. This study uses a simplified space vector modulation control for a three-level Neutral Point Clamped inverter topology. The induction motor stands out due to its affordability, reliability, and robustness. The induction motor's mathematical model in the Park configuration is nonlinear and highly coupled, making it difficult to control. This is why field-oriented control, replacing classical PI regulators with PI regulator-based sliding mode control, is used to control the induction motor. Sliding mode control is a popular method for controlling uncertain and non-linear systems, which can deal with uncertainties and unmodeled dynamics, stability and a fast dynamic response due to its simplicity and robustness against external disturbances [11,12]. A typical PV water pumping system is shown in Fig. 1.

II. MATERIALS AND METHODS

Fig. 1 illustrates a typical PV water pumping system. The system under consideration comprises of a $DC-DC$ converter coupled to a PV array, this study uses the fuzzy logic based $MPPT$ approach, a three-phase, three-level NPC inverter controlled by a simplified space vector modulation, the inverter feeds a moto-pump group which in turn feeds water tank.

Numerous mathematical models have been proposed to explain how photovoltaic cells behave and operate. These models differ in terms of the calculation methodology, the number of parameters involved, and the accuracy of the model. The PV panel in this study is represented by the two diodes model described in [13], this model includes a current source to imitate sunlight flux, and series and shunt resistors are used to characterize the losses.

Voltage variation happen in photovoltaic panels in response to solar irradiation levels. The incorporation of a $DC-DC$ converter becomes essential to enhance the control over the energy produced by these panels. In order to achieve



maximum power extraction from the PV panel and increase voltage, a boost $DC-DC$ converter proposed in [14] has been used in this paper. The $DC-DC$ converter is placed between the PV panels and the inverter. To extract the maximum power from the PV panels the fuzzy logic based technique presented in [15] is used in this paper.

To supply the induction motor from PV panels, $DC-AC$ converter must be used, in this paper a three level inverter based on the Neutral-Point-Clamped topology is chosen, the structure of the converter and its operating principle is described in [16]. To control the inverter a Simplified Space Vector Modulation is applied, the principle of this technique is detailed in [6].

The mathematical model of the Induction Motor and the pump are widely developed in the literature, the model of the Induction motor and the pump, including the electrical and mechanical part and the control are detailed in [17]. To control the moto-pump group the field-oriented control with space vector modulation is used, the classical PI regulators are replaced by Sliding Mode Control PI as detailed in Fig. 2.

The speed Ω and rotor flux ϕ_r are controlled by the first's regulators, and the stator current components (i_{ds} , i_{qs}) are controlled by the seconds regulators. Each regulator's sliding surface is determined as follows:

$$T_r : \text{the rotor time constant } (T_r = L_r / R_r),$$

$$M : \text{the mutual inductance,}$$

J : the total inertia of the machine,

k_f : the coefficient of friction,

C_r : the load torque,

Ω : the mechanical speed of the machine,

p : the number of pole pairs,

R_s and R_r : the stator and rotor resistances,

L_s and L_r : the stator and rotor inductances,

$R_{sm} = R_s + R_r M^2 / L_r^2$,

ω_s : the stator angular frequency,

ω_r : the rotor speed,

σ is the total leakage coefficient.

$$\begin{cases} S(\varphi_r) = \varphi_{r-ref} - \varphi_r \\ S(\Omega) = \Omega_{ref} - \Omega \\ S(i_{ds}) = i_{ds-ref} - i_{ds} \\ S(i_{qs}) = i_{qs-ref} - i_{qs} \end{cases} \quad (1)$$

For the rotor flux regulation:

$$\begin{aligned} \dot{S}(\varphi_r) &= 0 \Rightarrow \\ (i_{ds-eq}) &= \left(\varphi_r + T_r \dot{\varphi}_{r-ref} \right) / M \quad , \quad (2) \end{aligned}$$

$$\begin{aligned} \dot{S}(\varphi_r) S(\varphi_r) &< 0 \Rightarrow \\ (i_{ds-n}) &= \begin{cases} \left(\frac{k_\varphi}{\varepsilon_\varphi} \right) S(\varphi_r) \text{ if } |S(\varphi_r)| < \varepsilon_\varphi \\ k_\varphi \text{sgn}(S(\varphi_r)) \text{ if } |S(\varphi_r)| > \varepsilon_\varphi \end{cases} \quad , \quad (3) \end{aligned}$$

$$i_{ds-ref} = i_{ds-eq} + i_{ds-n} \quad . \quad (4)$$

For the speed regulation:

$$\begin{aligned} \dot{S}(\Omega) &= 0 \Rightarrow \\ (i_{qs-eq}) &= \left(J \dot{\Omega}_{ref} + k_f \Omega + C_r \right) / (pM \varphi_r / L_r) \quad , \quad (5) \end{aligned}$$

$$\dot{S}(\Omega) S(\Omega) < 0 \Rightarrow$$

$$(i_{qs-n}) = \begin{cases} \left(\frac{k_\Omega}{\varepsilon_\Omega} \right) S(\Omega) \text{ if } |S(\Omega)| < \varepsilon_\Omega \\ k_\Omega \text{sgn}(S(\Omega)) \text{ if } |S(\Omega)| > \varepsilon_\Omega \end{cases} \quad , \quad (6)$$

$$i_{qs-ref} = i_{qs-eq} + i_{qs-n} \quad . \quad (7)$$

For the direct current regulation:

$$\begin{aligned} \dot{S}(i_{ds}) &= 0 \Rightarrow \\ (V_{ds-eq}) &= \sigma L_s (i_{ds-ref}) + R_{sm} i_{ds} - \\ &\quad - \sigma L_s \omega_s i_{qs} - \left(\frac{M}{L_r T_r} \right) \varphi_r \quad , \quad (8) \end{aligned}$$

$$\dot{S}(i_{ds}) S(i_{ds}) < 0 \Rightarrow$$

$$(V_{ds-n}) = \begin{cases} \left(\frac{k_d}{\varepsilon_d} \right) S(i_{ds}) \text{ if } |S(i_{ds})| < \varepsilon_d \\ k_d \text{sgn}(S(i_{ds})) \text{ if } |S(i_{ds})| > \varepsilon_d \end{cases} \quad , \quad (9)$$

$$V_{ds-ref} = V_{ds-eq} + V_{ds-n} \quad . \quad (10)$$

For the quadrature current regulation:

$$\begin{aligned} \dot{S}(i_{qs}) &= 0 \Rightarrow \\ (V_{qs-eq}) &= \sigma L_s (i_{qs-ref}) + R_{sm} i_{qs} - \\ &\quad - \sigma L_s \omega_s i_{ds} - \left(\frac{M}{L_r} \right) \omega_r \varphi_r \quad , \quad (11) \end{aligned}$$

$$\dot{S}(i_{qs}) S(i_{qs}) < 0 \Rightarrow$$

$$(V_{qs-n}) = \begin{cases} \left(\frac{k_q}{\varepsilon_q} \right) S(i_{qs}) \text{ if } |S(i_{qs})| < \varepsilon_q \\ k_q \text{sgn}(S(i_{qs})) \text{ if } |S(i_{qs})| > \varepsilon_q \end{cases} \quad , \quad (12)$$

$$V_{qs-ref} = V_{qs-eq} + V_{qs-n} \quad . \quad (13)$$

For the stability condition of the system, the gains: k_d , k_q , k_φ and k_Ω should be chosen positive.

III. RESULTS AND DISCUSSION

Global photovoltaic water pumping system of Fig. 1 is simulated using MATLAB-SIMULINK. Variable temperature and sunshine for a day are taken as shown in Fig. 3.

The data was taken in the form of a table and a linear interpolation is used to have the curves of the Fig. 3.

Fig. 4 depicts the power generated by photovoltaic panels; it has the same look as irradiance which demonstrates the effectiveness of our *MPPT* controller.

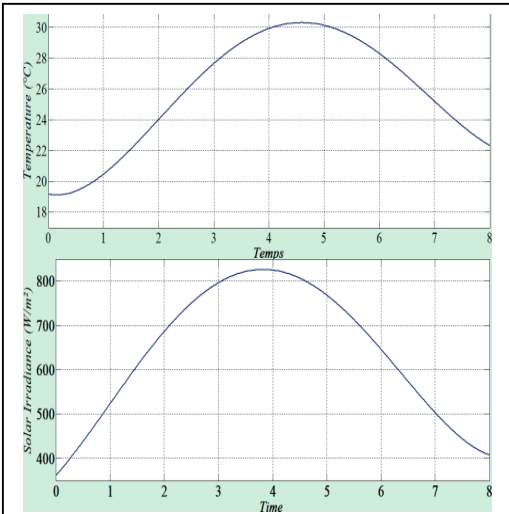


Figure 3. Variations of solar irradiance and temperature.

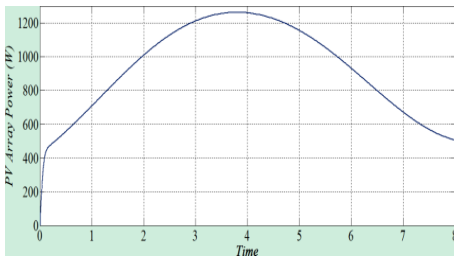


Figure 4. Power generated by photovoltaic panels.

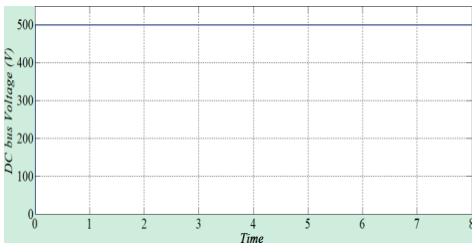


Figure 5. DC bus voltage.

Fig. 5 shows the *DC* bus voltage, which is kept at $500V$, it corresponds to the input voltage of our three-level *NPC* inverter.

The *NPC* inverter output voltage and its spectral analysis are displayed in Fig. 6; compared to a traditional two-level inverter, the output voltage has a staircase shape with multiple levels that resembles a sinusoid. The voltage's *THD* has an acceptable value of 34.78% .

The pump's rotational speed and its reference are shown in Fig. 7. We see that the pump's speed closely matches its reference, indicating how

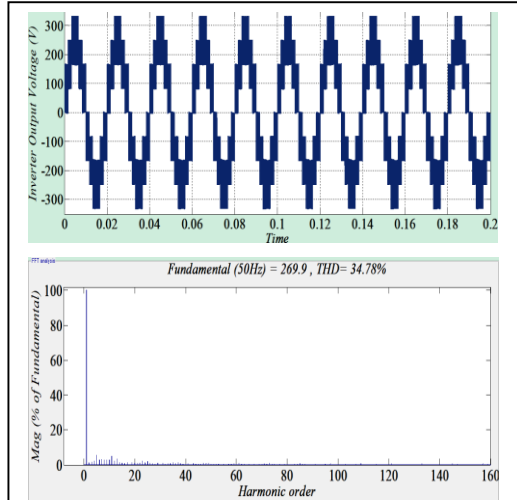


Figure 6. Output voltage of the *NPC* inverter and its spectral analysis.

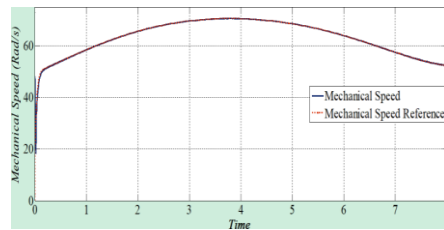


Figure 7. Rotation speed of the pump and its reference.

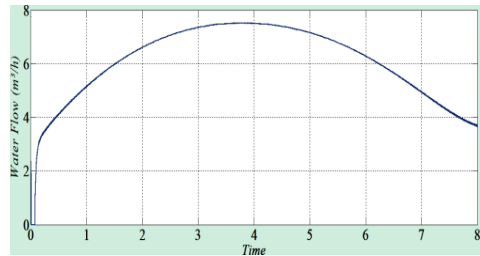


Figure 8. Flow of water pumped.

roughly is the induction machine control based on *SMC*.

Fig. 8 show the pumped water's flow; since the flow is dependent on the power supplied to the pump, it shares the same form as the power produced by the *PV* panels.

IV. CONCLUSION

This work describes a three-phase photovoltaic water pumping system with sliding mode control. MATLAB/Simulink was used to simulate the configuration of the suggested system. The simulation's results demonstrate the efficacy and robustness of the suggested control methods.

REFERENCES

- [1] Djermouni, K., Berboucha, A., Ghedamsi, K., & Aouzellag, D. (2015). Optimization of a photovoltaic field during faulty and normal operation. *Solar Energy*, 113, 171-180.
- [2] Amirouche, E., Benyahia, N., Aissou, S., Belkaid, A., Colak, I., & Berboucha, A. (2024, May). Energy management strategy for nano-grid in isolated areas. In *2024 12th International Conference on Smart Grid (icSmartGrid)* (pp. 265-269). IEEE.
- [3] Kumar, N., Hussain, I., Singh, B., & Panigrahi, B. K. (2017). Framework of maximum power extraction from solar PV panel using self predictive perturb and observe algorithm. *IEEE Transactions on sustainable energy*, 9(2), 895-903.
- [4] Djermouni, K., Berboucha, A., Tamalouzt, S., & Ziane, D. (2024). Voltage and current balancing of a faulty photovoltaic system connected to cascaded H - bridge multilevel inverter. *International Transactions on Electrical Energy Systems*, 2024(1), 6585584.
- [5] Uddin, M. H., Abid, A., Inam, U., Urooj, A., & Siddiqui, M. R. (2023). A comparative analysis of a multilevel inverter topology based on phase disposition sinusoidal pulse width modulation. *Engineering Proceedings*, 46(1), 30.
- [6] Berboucha, A., & Ghedamsi, K. (2018). Control of wind-battery energy systems connected to grid using nine-level inverter. *Electrotehnica, Electronica, Automatica*, 66(1), 17-24.
- [7] Colak, I., Kabalci, E., & Bayindir, R. (2011). Review of multilevel voltage source inverter topologies and control schemes. *Energy conversion and management*, 52(2), 1114-1128.
- [8] Berboucha, A., Djermouni, K., Ghedamsi, K., & Aouzellag, D. Fuzzy logic control of 5MW grid connected wind turbine. In *eNergetics 2023*, 227.
- [9] Veerendra, A. S., Chavali, P. S., Shivarudraswamy, R., Nagaraja Kumari, C. H., & Janamala, V. (2023). Total harmonic distortion analysis of a seven-level inverter for fuel cell applications. *Engineering Proceedings*, 59(1), 130.
- [10] Berboucha, A., Djermouni, K., Ghedamsi, K., & Aouzellag, D. (2017). Fuzzy logic control of wind turbine storage system connected to the grid using multilevel inverter. *International Journal of Energetica*, 2(1), 15-23.
- [11] Barrero, F., Gonzalez, A., Torralba, A., Galvan, E., & Franquelo, L. G. (2002). Speed control of induction motors using a novel fuzzy sliding-mode structure. *IEEE Transactions on Fuzzy Systems*, 10(3), 375-383.
- [12] Mourad, A., & Youcef, Z. (2022). Adaptive sliding mode control improved by fuzzy-Pi Controller: Applied to Magnetic Levitation System. *Engineering Proceedings*, 14(1), 14.
- [13] Djermouni, K., Berboucha, A., Ghedamsi, K., Aouzellag, D., & Tamalouzt, S. (2024). Energy management applied to non-autonomous photovoltaic station for hybrid vehicle loading. *Journal of Renewable Energies*, 1(1), 33-45.
- [14] Roy, T. K., Oo, A. M. T., & Ghosh, S. K. (2024). Designing a high-order sliding mode controller for photovoltaic-and battery energy storage system-based DC microgrids with ANN-MPPT. *Energies*, 17(2),532.
- [15] Berboucha, A., Hamoudi, Y., Djermouni, K., Ghedamsi, K., & Aouzellag, D. (2024). Fuzzy logic control of two-stage grid-connected photovoltaic system. *Algerian Journal of Signals and Systems*, 9(2), 91-97.
- [16] Ghennam, T., Belhadji, L., Rizoug, N., Francois, B., & Bacha, S. (2024). A three-level neutral-point-clamped converter based standalone wind energy conversion system controlled with a new simplified line-to-line space vector modulation. *Energies*, 17(9), 2214.
- [17] Rawat, R., Kaushik, S. C., & Lamba, R. (2016). A review on modeling, design methodology and size optimization of photovoltaic based water pumping, standalone and grid connected system. *Renewable and Sustainable Energy Reviews*, 57, 1506-1519.

A More Sustainable Society through Electric Mobility: Analysis of the Operational Emissions of the Renault Kwid E-Tech

João Marcelo Fernandes Gualberto de Galiza¹, Daniel de Paula Diniz², Monica Carvalho³

^{1,2}Graduate Program in Mechanical Engineering, Federal University of Paraiba, João Pessoa, Brazil

³Department of Renewable Energy Engineering, Federal University of Paraiba, Joao Pessoa, Brazil

¹joaomarcelofgg@gmail.com, ²danieldiniz@alumni.cear.ufpb.br, ³monica@cear.ufpb.br

Abstract—This study conducts an environmental analysis of the Renault Kwid E-Tech over 100,000 km, quantifying the carbon footprint associated with the use and maintenance of the electric vehicle in Brazil. The assessment was based on the Life Cycle Assessment (LCA) methodology, using the SimaPro v.9.6.0.1 software and the IPCC 2021 GWP 100y method. The supply of electricity from the national grid and maintenance and replacement of components were considered. The carbon footprint associated with electricity consumption is 0.136 CO₂-eq/kWh, which yields 1,999.26 kg CO₂-eq throughout the lifetime of the vehicle. The carbon footprint associated with the maintenance and replacements of components represented 6.85% of the total footprint (2146.89 kg CO₂-eq). This study contributes to the discussion of sustainability of electric mobility and the need for more sustainable production and maintenance practices.

Keywords – electric vehicle, renewable energy, Life Cycle Assessment (LCA)

I. INTRODUCTION

The transportation sector is a significant producer of greenhouse gases (GHGs), accounting for more than 16% of worldwide emissions [1]. This percentage is second only to the electricity and heating production sector, which accounts for 31%. In Brazil, the transportation sector emitted about 216.9 MtCO₂ in 2022, which is 9.43% of the country's total greenhouse gas emissions, based on estimates

from the Greenhouse Gas Emissions and Removals Estimating System [2].

Road transportation contributes significantly and progressively to the world's anthropogenic carbon dioxide (CO₂) emissions [2]. Its almost total dependence on energy derived from petroleum exposes it to changes in oil prices and causes interruptions in the flow of products and services. Furthermore, the use of fuel produced from petroleum in internal combustion engines produces exhaust emissions of pollutants such as suspended particles, CO₂, nitrogen oxides (NO_x), and others, all of which are harmful to human health and the environment [3].

Vehicle electrification has brought about a shift in our current system, being a more aligned option with the goals of energy transition than fossil fuel cars [4]. This aligns with public policies for cleaner energy but requires a stronger and more flexible electrical infrastructure, thus stimulating innovation in energy storage, distribution, and more efficient and sustainable technologies.

Concern about car pollution is rising worldwide, seen in both developed nations and the actions taken by big car companies. Mayors in Paris, Madrid, Athens, and Mexico City have pledged to phase out all diesel automobiles and trucks in their cities by 2025 to improve air quality [5]. Norway and Sweden are global leaders in the adoption of hybrid and electric vehicles. In 2022, electric vehicles (EVs) or hybrids accounted for approximately 80% of the

ISBN: 978-86-82602-05-7



Creative Commons Non Commercial CC BY-NC: This article is distributed under the terms of the Creative Commons Attribution-Non Commercial 4.0 License (<https://creativecommons.org/licenses/by-nc/4.0/>) which permits non-commercial use, reproduction and distribution of the work without further permission.

newly registered car fleet in Norway [6]. Likewise, Norway plans to outlaw the sale of all fossil-fueled vehicles by 2025 [7].

Life Cycle Assessment (LCA) is an established method for conducting environmental evaluations, estimating the potential environmental implications of a product, process, or activity [8]. LCA is regulated by ISO standards and is frequently used to assess the environmental impact of various products, processes, or activities. In the context of energy transition, LCA can aid in decision-making by indicating options with fewer environmental impacts.

The objective of this study is to quantify the GHG emissions associated with the operation and maintenance of an EV, the Renault Kwid E-Tech, in Brazil.

II. THEORETICAL FOUNDATION

A. Sustainable Mobility

Sustainable development is an essential concept for contemporary growth, aiming to meet the demands of the present without compromising the ability of future generations to meet their own needs [9]. This development is based on three equally important pillars: social, economic, and environmental. The United Nations (UN) established the 17 Sustainable Development Goals (SDGs) to promote inclusive and sustainable economic growth, reduce poverty, reduce inequalities, and combat climate action [10].

Within this context, sustainable mobility appears to be a crucial aspect, influencing both land use and transportation management. Sustainable mobility involves more than just efficient urban transportation with a low carbon footprint. It also promotes a higher quality of life, encouraging people to live healthier and more sustainable lifestyles [11].

According to [11], reducing GHGs is one of the pillars of sustainable urban mobility. An effective strategy to achieve this goal is the adoption of cleaner transportation modes. Encouraging new urban mobility technologies (electric scooters, shared bicycles, and carpooling), active mobility (walking or cycling), public transportation, advanced fuels (second-generation ethanol (E2G), biodiesel, aviation bio-kerosene, biofuels), sustainable logistics (route optimization, smart roads, electrification of truck fleets, rail transport, for

example), the use of autonomous vehicles, etc. [12].

However, adopting EVs shifts the environmental burden to the energy generation required to charge and maintain this new infrastructure. The sustainability of these energy sources is determined by a comprehensive analysis of the entire life cycle, from raw material extraction and processing to power plant installation, energy generation processes, and waste disposal [13].

B. Life Cycle Assessment

LCA is a methodology that emerged in the 1970s with the aim of analyzing the environmental load associated with products, processes, and services throughout all stages of their life cycle [14]. According to Lalau et al. [15], any system seeking to improve environmental performance, resource utilization, and reduce impacts in its production chain should be evaluated by an LCA. Therefore, it is a methodology that assesses the production chain, aiming to present and measure the environmental impacts caused during the entire process, enabling the search for the most effective options to achieve the desired sustainable development.

LCA is internationally standardized by the International Organization for Standardization (ISO) in its ISO 14040 [16] and ISO 14044 [17] standards. There are four main stages of LCA: (1) the definition of the objective and scope involves the clear specification of the study's objectives, (2) the inventory analysis quantifies the inputs and outputs of the analyzed system, (3) the impact assessment consists of choosing appropriate methods to evaluate the collected data, and (4) the interpretation of results relates and integrates the results of the previous stages, providing an understanding of the impacts associated with the system under study. The impact assessment methods adopted in stage 3 can evaluate the impact in various areas, such as ecosystem quality, human health, resource allocation, and climate change. The stages of LCA are interdependent, allowing flexibility to return to any of them during the course of the study, as shown in Fig. 1.

As [18] noted, globally present companies often strive to pursue certain sustainability agendas regarding value addition to their products, efficiency in production, and conformance with the locally-set environmental standard by local governments. This

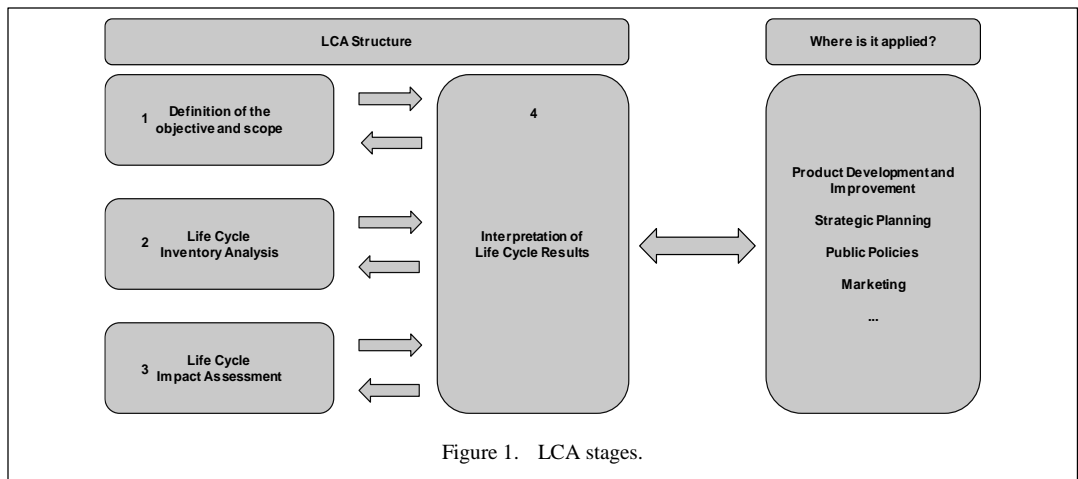


Figure 1. LCA stages.

demonstrates the advantages of LCA not only as an environmental assessment tool, but also as a way to promote sustainable and competitive business practices in the global market.

LCA plays an important role in the analysis of EVs considering that it covers all phases of their life cycle, from raw material extraction to production, transportation, and use to disposal [19]. Fig. 2 illustrates the main stages evaluated in an LCA during the vehicle use and maintenance phase.

III. METHODOLOGY

The case study presented here refers to the Renault Kwid E-Tech, which was the second most affordable electric car until the end of 2023, consolidating its significant presence in the EV fleet in Brazil [20]. The Kwid E-Tech has an average range of 185 km, a 26.8 kWh lithium-ion battery, and a maximum power of 65 hp. Due to the lack of data on the degradation of the Kwid E-Tech battery over time, we considered data from the Renault Kangoo, which has the same type of battery, showing a performance loss of

0.85% per year or every 20,000 kilometers, considering an average annual mileage [21].

The LCA was developed with the help of SimaPro software version 9.6.0.1 [22], using the Ecoinvent 3.8 database [23]. Due to concerns about climate change, the IPCC 2021 GWP 100y environmental impact assessment method was selected, which aggregates GHG emissions into a common metric (CO₂-eq) over 100 years [24].

The inventory for the use and maintenance phase, using a Well-to-Wheel approach, was established as shown in Table I, considering a functional unit of 100,000 kilometers, and the material consumption items list was stipulated through Renault's maintenance program, carried out every 10,000 kilometers. The weight values

TABLE I. INVENTORY OF RESOURCES USED DURING THE LIFE OF THE VEHICLE.

Inflows	Functional Unit (100000 km)	Unit	Material
Energy Consumption			
Electricity	14732.76	kWh	National electricity mix
Material Consumption			
Lubricants	7.20	kg	Synthetic oil
Interior filter	4.00	kg	Cellulose paper
Brake fluid	3.09	kg	Glycols + additives
Coolant	1.68	kg	Ethylene glycol + additives
12 V Battery	26.00	kg	69% Pb + 8% H ₂ SO ₄
Tires	26.00	kg	Rubber

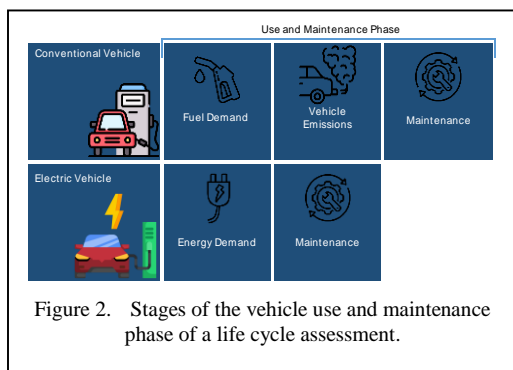


Figure 2. Stages of the vehicle use and maintenance phase of a life cycle assessment.

of items used in the vehicle's life cycle take into account market averages for products.

Data on power generation in Brazil was obtained from the National System Operator (ONS) and made available at www.ons.org.br [25]. For this study, the "national electricity mix" was used, which is the sum of all the Brazilian energy subsystems. Data was collected on the type of energy and fuel used to obtain electricity to analyze and quantify the composition of each subsystem for the year 2023. Table II shows the composition of Brazil's electricity mix in 2023.

TABLE II. COMPOSITION OF THE ELECTRICITY MIX FOR 2023, BRAZIL - ABSOLUTE VALUES AND PERCENTAGE SHARE OF EACH FUEL.

Fuel Source	Power Generation (GWh)	Share (%)
Hydraulic	374049.26	67.76
Wind	80069.33	14.42
Solar	43377.86	7.84
Biomass	20671.52	3.75
Gas	14596.50	2.65
Nuclear	13001.70	2.36
Coal	6266.65	1.12
Oil	517.07	0.09
Total	552549.89	100.00

TABLE III. INVENTORY ANALYSIS RESULTS MATERIALS CONSUMPTION.

Outflows	Carbon Footprint (kg CO ₂ -eq/kg)	Carbon Footprint in 100,000 km (kg CO ₂ -eq)
Material Consumption		
Lubricants	1.37	9.75
Interior filter	2.92	11.70
Brake fluid	2.30	7.11
Coolant	2.02	3.40
12 V Battery	1.73	44.95
Tires	2.72	70.73

IV. RESULTS

Regarding the consumption of materials associated with the operation of the EV (Table I), the results shown in Table III are obtained.

It is observed that tire replacement contributes 47.91% and battery replacement 30.44% to the total emissions associated with material consumption during the use period. It is interesting to note that lead-acid batteries, due to their intensive manufacturing process and the use of materials such as lead, demonstrate a relatively high carbon footprint compared to other battery technologies. On the other hand, in the case of tires, their production requires a considerable amount of energy and results in GHG emissions, especially during the production of rubber compounds and the vulcanization process.

Table IV presents the carbon footprint associated with each energy source of the electricity mix. Nuclear, wind, hydro, and solar energies stand out with significantly low emission factors. On the other hand, coal and oil have much higher emission factors.

Using the percentages from Table II and the emission factors of Table IV, the carbon footprint associated with electricity consumption is 0.136 kg CO₂-eq/kWh, which equates to approximately 0.01999 kg CO₂-eq/km. When analyzing the emissions from different energy sources, a significant variation in the carbon footprint

TABLE IV. CARBON FOOTPRINT OF DIFFERENT ELECTRICITY SOURCES WITHIN THE BRAZILIAN ELECTRIC MIX.

Emission Factors	Carbon Footprint (kg CO ₂ -eq/kWh)
Hydraulic	0.098
Wind	0.020
Solar	0.106
Biomass	0.161
Gas	0.756
Nuclear	0.016
Coal	2.697
Oil	1.434

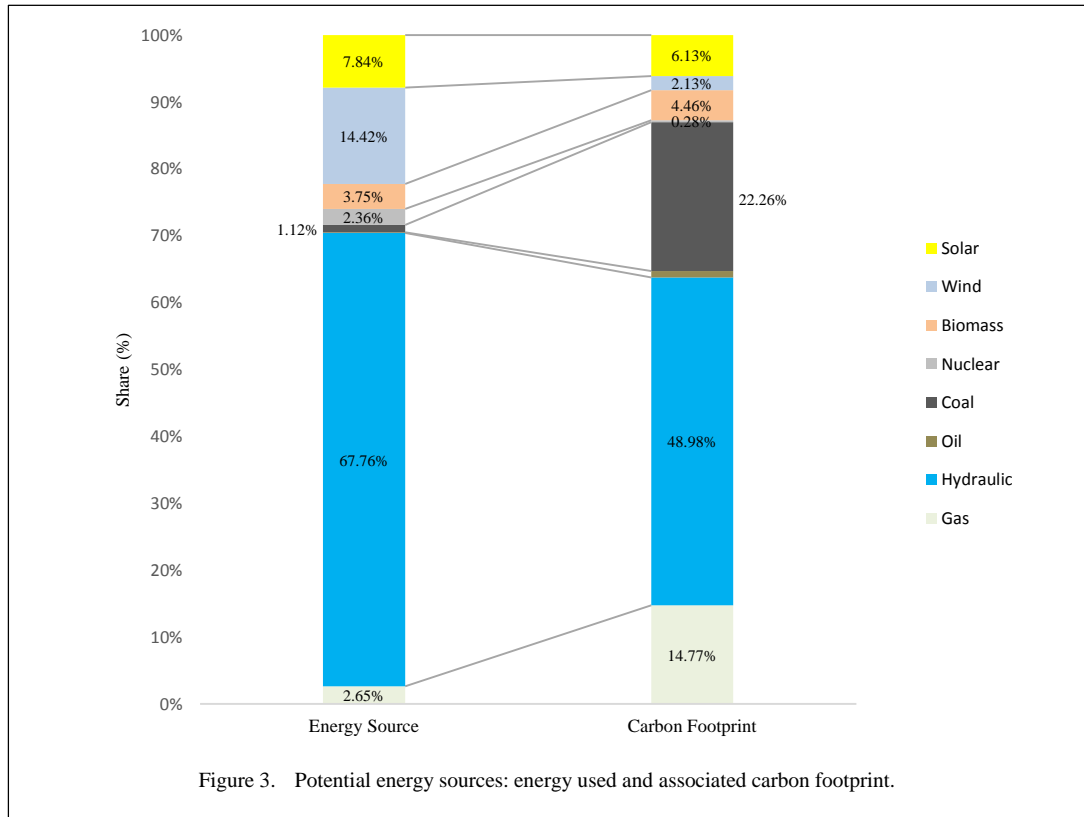


Figure 3. Potential energy sources: energy used and associated carbon footprint.

associated with each fuel was observed. Although hydropower makes up 67.76% of the electricity matrix, it contributes 48.98% of the total carbon footprint. In contrast, even though only 1.21% of energy comes from coal, this source is responsible for 22.26% of the carbon footprint. Similarly, natural gas, which accounts for 2.65% of energy generation, is responsible for 14.77% of the GHG emissions associated with the vehicle. Fig. 3 compares the share of different energy sources with their contribution to the carbon footprint.

Table V summarizes the carbon footprint of the EV, for the use and maintenance phase.

Total emissions during this period amount to 2146.89 kg CO₂-eq. The high contribution of the use phase, specifically vehicle charging, highlights the importance of the electricity source used to charge the vehicle. In regions where the energy matrix has a higher share of hydro or renewable energy, the carbon footprint of vehicle use can be significantly reduced. Although maintenance contributes relatively little to the total carbon footprint, it is important

TABLE V. CARBON FOOTPRINT OF THE ELECTRIC VEHICLE OVER 100000 KM.

Phase	Carbon Footprint	Share (%)
Use	1999.26	93.15
Maintenance	147.63	6.85
Total	2146.89	100.00

to consider sustainable practices and the choice of replacement parts with lower environmental impact to further reduce this contribution.

V. CONCLUSION

This study was based on an environmental assessment of the use of the Renault Kwid E-Tech 2024 in Brazil. To this end, the Life Cycle Assessment (LCA) methodology was used, where the functional unit was defined as 100000 km, and the emission sources for the vehicle were in refueling, travel, and maintenance and part replacements carried out during the period. The analysis revealed that the carbon footprint of different electricity generation sources in Brazil, such as coal, has a significant impact on global warming potential.

In Brazil, studies show that battery electric vehicles (BEVs) have significantly lower life-cycle greenhouse gas emissions than internal combustion engine vehicles, with potential reductions of 65% to 67% across several vehicle types [26,27]. The main type of battery used is the lithium-ion battery, which is favored for its higher efficiency and lower environmental risk. However, more research is needed to reduce reliance on specific chemical elements, such as cobalt, as well as to lower battery costs [28].

GHG emissions from maintenance and part replacement accounted for a relatively small portion of total emissions, only 6.85%. The main contribution of this work was to calculate the carbon footprint associated with the operation of the Kwid E-Tech in Brazil, highlighting the importance of life cycle assessment as part of efforts to reduce GHG emissions and promote the sustainable use of electric vehicles.

ACKNOWLEDGMENTS

The authors wish to acknowledge the support of the Laboratory of Environmental and Energy Assessment (LAvAE) at the Federal University of Paraíba, and National Council for Scientific and Technological Development (CNPq Productivity Grant 309452/2021-0, PhD scholarship 141303/2021-2, and project 424173/2021-2).

REFERENCES

- [1] Ritchie, H. (2020). *Sector by sector: Where do global greenhouse gas emissions come from? Our World in Data*. Available at: <https://ourworldindata.org/ghg-emissions-by-sector>.
- [2] SEEG. (2023). *Análise das emissões de gases de efeito estufa e suas implicações para as metas climáticas do Brasil 1970 - 2022*. Available at: <https://www.oc.eco.br/wp-content/uploads/2023/03/SEEG-10-anos-v4.pdf>.
- [3] Offer, G., Howey, D., Contestabile, M., Clague, R., & Brandon, N. (2010). Comparative analysis of battery electric, hydrogen fuel cell and hybrid vehicles in a future sustainable road transport system. *Energy Policy*, 38(1), 24–29.
- [4] Elzinga, D., Simón, M., Taylor, P., Ward, K., & Wanner, B. (2014). *Energy technology perspectives 2014: Harnessing electricity's potential*. International Energy Agency.
- [5] Prins. (2016). *Four major cities move to ban diesel vehicles by 2025*. Available at: <https://www.prinsautogas.com/en/news/four-major-cities-move-ban-diesel-vehicles-2025>.
- [6] NeoCharge. (2022). *Confirma alguns países que já prometem o fim dos carros a combustão*. Available at: <https://www.neocharge.com.br/blogs/post/fim-carros-combustao>.
- [7] International Environmental Technology. (2023). *By 2025, no Norwegian will drive a car with a combustion engine*. *Petro Online*. Available at: <https://www.petro-online.com/news/fuel-for-thought/13/international-environmental-technology/by-2025-no-norwegian-will-drive-a-car-with-a-combustion-engine/60647>.
- [8] Guinée, J. B., Heijungs, R., Huppes, G., Zamagni, A., Masoni, P., & Buonamici, R. (2011). *Life cycle assessment: Past, present, and future*. ACS Publications.
- [9] Brundtland, G. H., Khalid, M., Agnelli, S., Al-Athel, S., Chidzero, B., Fadika, L., ... & Moreira, A. (1987). *Our common future: By World Commission on Environment and Development*. Oxford University Press.
- [10] United Nations, Department of Economic and Social Affairs - Sustainable Development. (2015). *Transforming our world: The 2030 agenda for sustainable development*. Available at: <https://sdgs.un.org/2030agenda>.
- [11] Campos, V. B. G. (2006). Uma visão da mobilidade urbana sustentável. *Revista dos Transportes Públicos*, 2, 99–106.
- [12] Borba, B. (2020). *Big Push para a Mobilidade Sustentável: Cenários para acelerar a penetração de veículos elétricos leves no Brasil*. Economic Commission for Latin America and the Caribbean (ECLAC).
- [13] Tian, J., Kang, J., Song, S., & Chen, H. (2024). Is renewable energy sustainable? Potential relationships between renewable energy production and the Sustainable Development Goals. *NPJ Climate Action*, 3(1), 1–7.
- [14] Guinée, J. B. (2002). *Handbook on life cycle assessment: Operational guide to the ISO standards (Vol. 7)*. Springer Science & Business Media.
- [15] Lalau, Y., Meyer, L., Kurowski, M., & Hegger, J. (2022). Energy analysis and life cycle assessment of a thermal energy storage unit involving conventional or recycled storage materials and devoted to industrial waste heat valorisation. *Journal of Cleaner Production*, 330, 129950.
- [16] International Organization for Standardization. (2006). *ISO 14040: Environmental management – Life cycle assessment – Principles and framework*. Geneva, Switzerland: ISO.
- [17] International Organization for Standardization. (2006). *ISO 14044: Environmental management – Life cycle assessment – Requirements and guidelines*. Geneva, Switzerland: ISO.
- [18] Coelho Filho, O., Saccaro Junior, N. L., & Luedemann, G. (2015). O uso da análise de ciclo de vida (ACV) nas políticas públicas: Condicionantes e estratégias de implementação da ACV no Brasil.
- [19] Schelte, N., Hertwich, E. G., & Knobloch, F. (2021). Life cycle assessment on electric moped scooter sharing. *Sustainability*, 13(15), 8297.
- [20] Revista Quatro Rodas. (2023). Quanto custa manter um Renault Kwid E-Tech. Available at: <https://www.quatrorodas.abril.com.br/auto-servico/qu-anto-custa-manter-um-renault-kwid-e-tech-r-139-990>.
- [21] Geotab. (2024). EV battery health: What impacts it and how to maximize it. Available at: <https://www.geotab.com/blog/ev-battery-health/>.

- [22] PRé Sustainability. (2019). Simapro. Available at: <https://simapro.com/>.
- [23] Ecoinvent Centre. (2023). Ecoinvent database version 3.8. Swiss Centre for Life Cycle Inventories.
- [24] Intergovernmental Panel on Climate Change. (2021). Climate change 2021: The physical science basis. Agenda.
- [25] National Operator System. (2024). *Histórico da operação - Geração de energia*. Available at: https://www.ons.org.br/Paginas/resultados-da-operacao/historico-da-operacao/geracao_energia.aspx.
- [26] Mera, Z., Bieker, G., Rebouças, A. B., & Cieplinski, A. (2023). *Comparison of the Life-Cycle Greenhouse Gas Emissions of Combustion Engine and Electric Passenger Cars in Brazil*. International Council on Clean Transportation. Available at: <https://theiccct.org/publication/comparison-of-life-cycle-ghg-emissions-of-combustion-engines-and-electric-pv-brazil-oct23/>.
- [27] Lavrador, R. B., & Teles, B. A. de S. (2022). Life cycle assessment of battery electric vehicles and internal combustion vehicles using sugarcane ethanol in Brazil: A critical review. *Cleaner Energy Systems*, 2, 100008.
- [28] Zubi, G., Dufo-López, R., Carvalho, M., & Pasaoglu, G. (2018). The lithium-ion battery: State of the art and future perspectives. *Renewable and Sustainable Energy Reviews*, 89, 292–308.

Solar Salt Recycling: Cost-opportunity Ratio

Manuel Botejara-Antúnez¹, Jaime González-Domínguez², Pavlos Zalimidis³,
Justo García-Sanz-Calcedo⁴

^{1,2,4}Department of Graphical Expression, School of Industrial Engineering, University of Extremadura, Badajoz, Spain

³Department of Educational Mechanical Engineering, Anotati Scholi Pedagogikis & Technologikis Ekpedefsis, Athens, Greece

¹manuelba@unex.es, ²jaimegd@unex.es, ³pzalimidis@aspete.gr, ⁴jgsanz@unex.es

Abstract—Concentrated solar power (CSP) plants stand out within the renewable energy sector by directly harnessing solar radiation to generate electricity from thermal energy. However, these facilities encounter the disadvantage of relying on weather conditions and the absence of sunlight during the night. To address this issue, CSP plants employ energy storage systems that retain excess energy produced during periods of peak radiation, allowing its use during cloudy periods and overnight. Molten salt, specifically Solar Salt, is used as the storage medium. Given the large quantity of Solar Salt utilised, concerns arise regarding its disposal at the end of the plant's operational life or when replacements are needed. The research focuses on the development of recycling strategies to make use of this raw material. The most relevant applications of sodium nitrate and potassium nitrate, the main components of Solar Salt, have been analysed. The strategies identified include the production of fertilisers for the agricultural sector, the production of gunpowder, and the development of food additives. A comparative analysis of the feasibility of these strategies was carried out, ranking them according to their application potential. The results obtained show a high potential at regional, national and international level. In addition, they will allow CSP plant managers to reduce the environmental impact of their activity by recycling a key component, generating economic benefits that can be used to cover operation and maintenance costs or for future investments, thus increasing the profitability of the plant.

Keywords - solar salt, CSP, recycling strategies, recycling scenarios

I. INTRODUCTION

According to estimates by the International Energy Agency, energy consumption will rise by up to 33% by 2040, which implies a significant increase in CO₂ emissions [1]. This scenario highlights the urgent need to move towards a low-carbon energy mix that provides for different energy storage scenarios [2,3].

In this context, large-scale sustainable energy storage has become one of the major challenges in fulfilling the ambitious targets set for a significant increase in the penetration of renewable energies [4]. Within renewable technologies, concentrating solar power (CSP) plants have great potential for the integration of sustainable energy storage, which makes them highly scalable compared to other technologies such as photovoltaic or wind power [5].

Spain and the United States are currently the two leading countries in the deployment of this type of energy [6]. Other regions, such as Australia and North Africa, also have great potential for deployment (see Fig. 1) [7,8], with a significant number of CSP projects recently planned in these regions. The International Energy Agency's Technology Roadmap foresees CSP covering 7% of global electricity demand by 2030 and 15% by 2050 [6]. Fig. 2 illustrates the current global landscape of CSP technology.



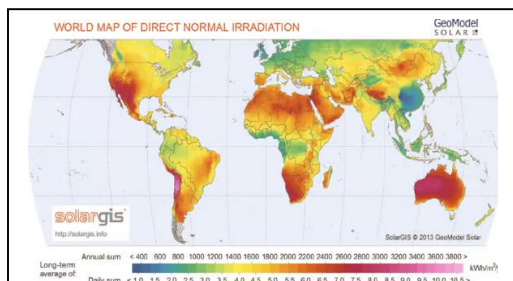


Figure 1. Direct Normal Irradiation World Map [9].

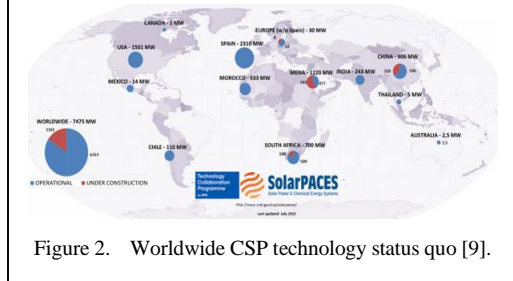


Figure 2. Worldwide CSP technology status quo [9].

Within the energy storage market, the technology based on sensible heat exchange from molten salts (MS) leads the projects share linked/associated to CSP plants [9], having experienced significant growth over the last decade. However, molten salts have a number of drawbacks, such as corrosion [10], the need to maintain them at temperatures above ~ 220 °C to avoid solidification (which involves significant energy consumption) [11], and limiting the maximum temperature to ~ 550 °C to avoid degradation of the salts [12], which limits the efficiency of the power block [13].

The growth in the use of molten salt technologies also implies an increase in the by-products derived from the energy production process, causing different problems related to their management and/or disposal [14]. In this context, the different engineers and/or managers of CSP plants must address this challenge by defining a series of strategies that enable the treatment of these by-products, either through recycling or disposal.

In the scientific field, numerous authors have supported and endorsed the potential of this technology, investigating its performance and applicability [15]. Scientific production in this field has focused more on their thermo-physical characterisation, developing new salt solutions (binary and tertiary) that maximise the energy efficiency of the heat transfer fluid and minimise costs and corrosive effects [16]. Thus, the authors [17] carried out a comparative analysis of

the thermophysical properties of the four most commonly used molten salt types in the CSP field (carbonate, chloride, nitrate and polybasic salt), highlighting their main advantages and disadvantages. Others, such as [8] evaluated the potential of the molten chloride salt typology 60% $MgCl_2$ + 20% KCl + 20% $NaCl$ in the fight against the corrosiveness of metallic elements and the reduction of costs derived from the energy production process. In the same line, Villada et al. (2021), corroborated the potential of the tertiary mixture 60% $MgCl_2$ + 20% KCl + 20% $NaCl$ in the fight against corrosion, also developing methods and models for monitoring corrosive phenomena. Finally, [18] evaluated the potential improvement in thermal conductivity obtained by incorporating silicon oxide (SiO_2), aluminium oxide (Al_2O_3) and graphite nanoparticles into traditional Solar Salt.

Nevertheless, until now, there is no evidence of any research that evaluates the recyclability or reusability potential of the aforementioned salts. Therefore, it is necessary to carry out a specific study on this potential, defining and characterising different scenarios and/or recycling strategies for molten salts and analysing their technical and economic feasibility.

II. MATERIALS AND METHODS

In this study, the feasibility of different strategies and scenarios for the recycling of molten salts used in CSP plants has been defined and analysed. Fig. 3 illustrates the workflow followed.

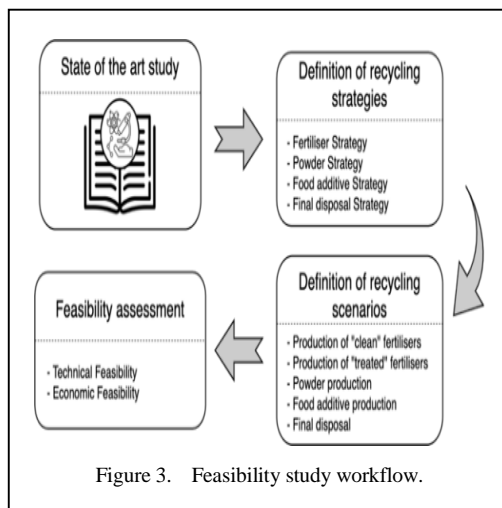


Figure 3. Feasibility study workflow.

A. Definition of Recycling Strategies

After an exhaustive analysis of the state of the technique, we proceeded with the identification of recycling strategies for the “Solar Salt” molten salt typology (Balf-Haifa 60%-40%), the most widely used salt solution in CSP technology plants. For this purpose, an international expert panel of researchers with more than 150 years of combined experience in energy storage engineering was used to document the following set of strategies:

- **Fertiliser strategy:** strategy based on the reuse of sodium and potassium nitrates present in the Balf-Haifa 60%-40%) saline solution as fertilisers for agro-industrial use. Here, it is essential to verify the levels of metals released in the salt solutions as dictated by Regulation (EU) 2019/1009 of the European Parliament and of the European Council [19]. This strategy comprises drying, milling, pressing and cooling processes.
- **Powder strategy:** strategy based on the re-use of potassium nitrate in combination with specific proportions of carbon and sulphur to produce black powder. This strategy comprises the separation of nitrates, milling, mixing, pressing, granulation and polishing.
- **Food additive strategy:** a strategy based on the re-use of sodium and potassium nitrates to produce E-251 and E-252 preservatives. This strategy comprises the separation of nitrates.
- **Final disposal strategy:** strategy based on the extraction of the salts from the CSP plant and their subsequent disposal process.

B. Definition of Recycling Scenarios

Once the recycling strategies were identified, different scenarios were projected for each of them. Fig. 4 illustrates all the strategies and scenarios proposed for the Solar Salt recycling.

In the case of the Fertiliser strategy, it can be seen how this recycling strategy presents up to two scenarios based on the potential results to be obtained from the metal contamination analysis process (verification of the level of metals released).

- **Production of “clean” fertilisers:** scenario with nickel and chromium

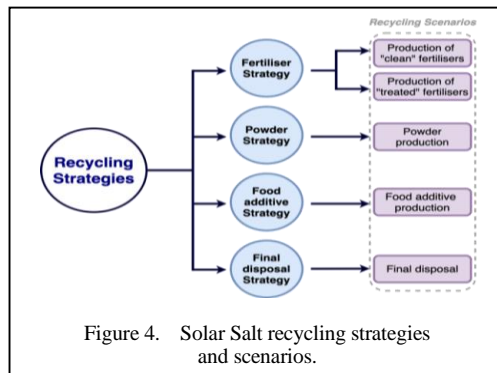


Figure 4. Solar Salt recycling strategies and scenarios.

values lower than those set by Regulation (EU) 2019/1009 of the European Parliament and of the European Council [17].

- **Production of “treated” fertilisers:** scenario with nickel and chromium values higher than those set out in Regulation (EU) 2019/1009 of the European Parliament and of the European Council [19].

III. RESULTS AND DISCUSSION

According to the recycling scenarios defined for Solar Salt by the panel of experts, the technical-economic feasibility study was carried out.

A. Fertiliser Strategy Feasibility Study

The proposal to reuse molten salts from CSP plants as fertiliser proved to be technically feasible. After extraction, the salts could be dried, ground, pressed and cooled for agricultural application. In particular, sodium, potassium and calcium nitrates present an attractive economic alternative in the manufacture of nitrogen fertilisers, a market valued at 9.13 billion euros in 2021 [20]. The economic feasibility study for the present strategy is presented in Table I.

TABLE I. ECONOMIC FEASIBILITY STUDY – FERTILISER STRATEGY.

Scenario	Nitrate Cost (€/kg)	Energy process		Total Cost (€/kg)
		Energy (kWh)	^a Cost (€/kg)	
“Clean” Fertiliser	-	0.135	0.024	0.024
“Treated” Fertiliser	-	0.335	0.061	0.061
Traditional	0.820	0.135	0.024	0.844

^a Considering a value of 0.1823 €/kWh

From the results of the feasibility study in Table I, it can be seen that for both proposed recycling scenarios, “Clean” Fertiliser and “Treated” Fertiliser, the costs associated with fertiliser production would be much cheaper than for the traditional procedure, with values between 13.8 and 35.2 times cheaper, respectively. Furthermore, it can be seen that the “Clean” Fertiliser scenario would be the optimal scenario with an associated cost of 0.024 €/kg. Likewise, as a result of corroborated feasibility, the sale of the CSP by-products would enable the option of a reduction in the cost of energy derived from the profits obtained from the sale.

B. Powder Strategy Feasibility Study

Due to the simplicity of the process, the strategy of producing black powder from sodium nitrate from molten salts was identified as technically feasible. It also proved to be economically feasible, as gunpowder is widely used in fireworks, mining and weaponry. The economic feasibility study of the Powder strategy is presented in Table II.

From the results of the feasibility study in Table II, it can be seen that the costs associated with the production of gunpowder by recycling sodium nitrate would be much cheaper than for the traditional process, with values up to 7 times cheaper. This represents a significant savings opportunity, reducing costs by 85.75%. Likewise, as a result of corroborated feasibility, the sale of the CSP by-products would enable the option of a reduction in the cost of energy derived from the profits obtained from the sale.

TABLE II. ECONOMIC FEASIBILITY STUDY – POWDER STRATEGY.

Scenario	Components Cost (€/kg)	Energy process		Total Cost (€/kg)
		Energy (kWh)	^a Cost (€/kg)	
Powder Production	0.014	0.839	0.153	0.167
Traditional	1.104	0.373	0.068	1.172
^a Considering a value of 0.1823 €/kWh				

C. Food Additive Strategy Feasibility Study

The food additive production strategy did not prove to be technically feasible due to the required high purity of the nitrate, which is difficult to achieve due to impurities present in the molten salts from steel corrosion. However, although the production of the E-251 and E-252 preservatives was economically feasible due to their simple chemical synthesis, the production strategy for these preservatives was not recommended. Finally, it should be noted that as a result of the transformation of nitrates to nitrites, this strategy could lead to carcinogenic side effects, as well as increase the occurrence of cardiovascular diseases after ingestion [21]. In this context, the Consumers and Users Organisation suggested avoiding their consumption [22], which led to this option being discarded.

D. Final Disposal Strategy Feasibility Study

The final disposal of the salts did not require significant technical complexity. Although it did not generate direct income, it was considered a necessary process in the absence of viable alternatives. Thus, despite the cost associated with transport to landfill, estimated at 0.001 €/kg (considering a diesel price of 1.30 €/L), it was not considered a net loss from an economic perspective.

IV. CONCLUSIONS

The methodology used in this study has proven to be effective in assessing the technical and economic feasibility of various strategies for recycling solar salt used in CSP storage plants. The results obtained indicate that, of the four strategies evaluated, only the food additive strategy is unfeasible from both a technical and economic perspective. In contrast, the fertiliser and gunpowder production strategies present significant savings opportunities, with projected profit margins between 85.75% and 97.2%, depending on the recycling scenario considered. In particular, the gunpowder production strategy is particularly cost-effective, offering savings of up to €1.01/kg compared to conventional production methods.

Besides the economic benefits, the adoption of these strategies will allow CSP plant managers to reduce the environmental impact of their activity by recycling one of the main components, transforming by-products into a source of income. This improves CSP plant's overall profitability, generating benefits that can

be used to support operational and maintenance costs, reduce/offset the cost of energy or even for future strategic investments.

Together, these strategies contribute to climate neutrality through minimising waste generation and maximising the socio-economic value of CSP plants by making them more sustainable. In this way, the implementation of these recycling approaches optimises operating costs and strengthens the commitment to a more responsible and environmentally friendly energy transition.


ACKNOWLEDGMENT

Grant PCI2022-134993-2 funded by MCIN/AEI/10.13039/501100011033 and, by the “European Union Next Generation EU/PRTR”.

REFERENCES

- [1] International Energy Agency (IEA) (2023). *World Energy Outlook 2023*, International Energy Agency (IEA), Paris.
- [2] Batuecas, E., Mayo, C., Díaz, R., & Pérez, F.J. (2017). Life Cycle Assessment of heat transfer fluids in parabolic trough concentrating solar power technology. *Sol. Energy Mater. Sol. Cells*, 171, 91–97.
- [3] Lamnatou, C., & Chemisana, D. (2017). Concentrating solar systems: Life Cycle Assessment (LCA) and environmental issues. *Renew. Sustain. Energy Rev.*, 78, 916–932.
- [4] Nojavan, S., Pashaie-Didani, H., Saberi, K., & Zare, K. (2019). Risk assessment in a central concentrating solar power plant. *Sol. Energy*, 180, 293–300.
- [5] Kiefer, C.P., Caldés, N., & Del Río, P. (2021). Will dispatchability be a main driver to the European Union cooperation mechanisms for concentrated solar power?. *Energy Sources, Part B Econ. Planning, Policy*, 16, 42–54.
- [6] Dersch, J., Paucar, J., Polkas, T., Schweitzer, A., & Stryk, A. (2021). Blueprint for Molten Salt CSP Power Plant. *Final report of the project “CSP-Reference Power Plant” No. 0324253*.
- [7] Shah, R., Yan, R., & Saha, T.K. (2015). Chronological risk assessment approach of distribution system with concentrated solar power plant. *IET Renew. Power Gener.*, 9, 629–637.
- [8] Desideri, U., & Campana, P.E. (2014). Analysis and comparison between a concentrating solar and a photovoltaic power plant. *Appl. Energy*, 113, 422–433.
- [9] National Renewable Energy Laboratory (NREL), *Concentrating Solar Power Projects*, (2020). <https://solarpaces.nrel.gov/> (accessed October 5, 2023).
- [10] Encinas-Sánchez, V., Macías-García, A., de Miguel, M.T., Pérez, F.J., & Rodríguez-Rego, J.M. (2023). Electrochemical impedance analysis for corrosion rate monitoring of sol-gel protective coatings in contact with nitrate molten salts for CSP applications. *Materials (Basel)*, 16, 546.
- [11] Bhatnagar, P., Siddiqui, S., Sreedhar, I., & Parameshwaran, R. (2022). Molten salts: Potential candidates for thermal energy storage applications. *Int. J. Energy Res.*, 46, 17755–17785.
- [12] Palacios, A., Navarro, M.E., Jiang, Z., Avila, A., Qiao, G., Mura, E., & Ding, Y (2020). High-temperature corrosion behaviour of metal alloys in commercial molten salts. *Sol. Energy*, 201, 437–452.
- [13] Bauer, T., Odenthal, C., & Bonk, A. (2021). Molten salt storage for power generation. *Chemie Ing. Tech.*, 93, 534–546..
- [14] Encinas-Sánchez, V., Batuecas, V., Macías-García, A., Mayo, C., Díaz, R., & Pérez, F.J. (2018). Corrosion resistance of protective coatings against molten nitrate salts for thermal energy storage and their environmental impact in CSP technology. *Sol. Energy*, 176, 688–697.
- [15] Bilal Awan, A., Khan, M.N., Zubair, M., & Bellos, E. (2020). Commercial parabolic trough CSP plants: Research trends and technological advancements. *Sol. Energy*, 211, 1422–1458.
- [16] Roper, R., Harkema, M., Sabharwall, P., Riddle, C., Chisholm, B., Day, B., & Marotta, P. (2022). Molten salt for advanced energy applications: A review. *Ann. Nucl. Energy*, 169, 108924.
- [17] Song, X., Zhang, G., Tan, H., Chang, L., Cai, L., Xu, G., Deng, Z., & Han, Z. (2020). Review on thermophysical properties and corrosion performance of molten salt in high temperature thermal energy storage. *IOP Conference Series: Earth and Environmental Science*, 474(5), 052071
- [18] Abir, F. M., Altwarah, Q., Rana, M. T., & Shin, D. (2024). Recent advances in molten salt-based nanofluids as thermal energy storage in concentrated solar power: A comprehensive review. *Materials*, 17(4), 955. <https://doi.org/10.3390/ma17040955>
- [19] European Parliament and the Council of the European Union (2019). Regulation of the european parliament and of the council laying down rules on the making available on the market of EU fertilising products and amending Regulations (EC) No 1069/2009 and (EC) No 1107/2009 and repealing Regulation (EC) No 2003/2003, *Off. J. Eur. Union* 2019, 114.
- [20] Observatorio de complejidad económica (2022). *Fertilizantes con nitratos y fosfatos*. Available at: <https://oec.world/es/profile/hs/fertilizers-with-nitrates-and-phosphates-nes-10kg> (accessed May 7, 2024).
- [21] Mortensen, A., et al. (2017). Re- evaluation of sodium nitrate (E 251) and potassium nitrate (E 252) as food additives. *EFSA J.*, 15.
- [22] Organización de Consumidores y Usuarios (2023). *Nitratos y nitritos: nuevos límites de estos aditivos alimentarios*. Available at: <https://www.ocu.org/alimentacion/seguridad-alimentaria/noticias/aditivos-en-productos-camicos> (accessed May 7, 2024).

An Experimental Investigation of Falling Film Evaporation on a Vertical Plate

Hayat El Baamrani¹, Abdelaaziz Yagour², Aicha Eddemani³, Ahmed Aharoune⁴, Abdallah Boukhris⁵

^{1,3,4,5}Thermodynamics and Energetics Laboratory, Faculty of Science, Ibn Zohr University, BP8106, 80006 Agadir, Morocco

²Electronic, signal processing and physical modeling Laboratory, Faculty of Science, Ibn Zohr University, BP8106, 80006 Agadir, Morocco

¹hayatelbaamrani92@gmail.com

Abstract—In this paper, an experimental study of the evaporation of a water film is realized. The liquid film is falling down on the wall of a vertical channel and is subjected to a constant heat flux density. A metal plate with practical dimensions was chosen to obtain an easy-to-use system. A grid of 32 thermistors (NTC) was used to track the evolution of the temperature on the plate; the results show that increased liquid film evaporation is associated with a lower mass flow rate and a higher heat flux density.

Keywords - liquid film, heat and mass transfer, vertical plate, experimental study, evaporation

I. INTRODUCTION

Liquid film evaporation in flow contexts is a frequent occurrence seen in a variety of industrial and natural environments. This common occurrence has generated a great deal of research curiosity, which has resulted in the creation of multiple studies in this field. Notably, a wide range of industrial processes, including cooling, desalination, chemical solution concentration, cooling tower operations, and other industrial activities, heavily rely on liquid film evaporation. The literature currently in publication contains numerous numerical and experimental studies aimed at explaining this phenomenon. Conventional literature on heat and mass transfer has been well documented and discussed in the literature [1-7]. A study on heat and mass transfer in a distillation cell was conducted by [8,9] in the context of experimental investigations. Their

research showed that latent heat transfer dominated the distillation cell's overall heat transfer dynamics. Similar to this, [10] carried out experimental studies to investigate evaporation processes in a vertical channel where a thin liquid film falls among two parallel plates under the influence of forced and natural convection. Their investigation indicated a relationship between higher airflow velocity and heat flux density and improved thermal efficiency of evaporation. In addition, Experimental studies of evaporation processes in a vertical channel with a wet porous layer have been carried by [11]. Their research showed that using porous layers is effective, especially when there is a high heating flow and a low inlet flow. Also, they found that latent Nusselt number was more important than sensible Nusselt number, which is crucial knowledge for designing and improving passive confinement cooling systems. An experimental study by [12] studied the processes of evaporation of a falling film in a rectangular channel. Evaporation rates and the partial vapor pressure differential between the film surface and the surrounding air mass were analyzed in order to calculate the mass transfer coefficient controlling evaporation. According to experimental results, increasing the airflow rate seems to improve the evaporation transfer coefficient, whereas changes in film temperature and flow rate have little effect. Furthermore, the authors demonstrated the difficulties in adjusting the liquid film temperature, attributing these



difficulties to elements like feed tank thermal conditions and storage capacity. A brackish water desalination device was created by [13] using a vertical concentric multi-effect solar tube system. This device, which consists of four closely spaced concentric pipes, uses hot brine water to warm the input water in order to maximize evaporation efficiency. The study sought to clarify the effect of gas carrier-water vapor mixtures on increasing device productivity through experimental research and analytical analysis. The performance of several carrier gases, such as carbon dioxide, helium, nitrogen, oxygen, air, and argon, was assessed. Under various gas compositions, the study evaluated the device's condensing surface's upper and lower temperature profiles as well as water yield. The authors also suggested a theoretical yield prediction model based on 30.76% when helium was used instead of air as the carrier gas. The authors also suggested a theoretical yield prediction model based on internal mass and heat transfer mechanisms. The water productivity rate in experiments using helium as the carrier gas and heating at 80 °C was 1.19 kg/h, which was a significant increase of 30.76% when helium was used instead of air as the carrier gas.

II. MATERIALS AND METHOD

An aluminum plate with dimensions of $0.33m \times 0.5m \times 0.002m$ was selected due to its high thermal conductivity of $237 \text{ W.m}^{-1}\text{.K}^{-1}$, facilitating more uniform heating. Achieving a water film covering the entire surface necessitated modifying the surface tension of the

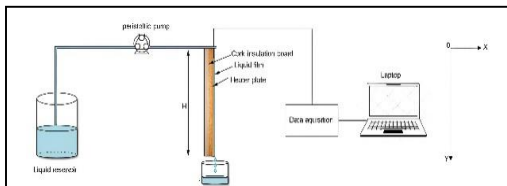


Figure 1. General presentation of the physical domain.

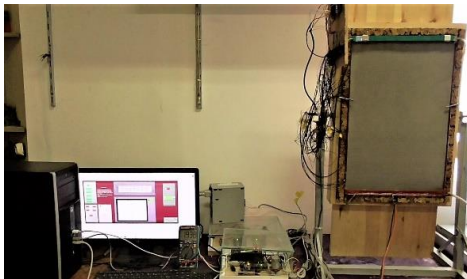


Figure 2. Picture of the experimental device.

aluminum. To improve wettability, sandblasting was employed to treat the plate's surface (Figs. 1 and 2).

A. Isolation

A 4 cm thick cork layer and 3 cm thick glass wool have been placed behind the heating plate to prevent thermal dissipation and ensure that the entire heat flow goes directly into the aluminum plate (Fig. 3).

B. Temperature Measurement

To calculate the aluminum plate's temperature, we employed a grid of NTC sensors assembled in a matrix format consisting of 8 rows and 4 columns, boasting an accuracy of $\Delta T = 0.01^\circ\text{C}$ (as depicted in Fig. 4). To retrieve temperature readings, two multiplexers with 16 inputs each were utilized. This configuration enabled the selection of the desired input by switching the pins S_0, S_1, S_2, S_3 , and the inputs A_0, A_1 of the Arduino, facilitating precise temperature data acquisition.



Figure 3. System isolation presentation.

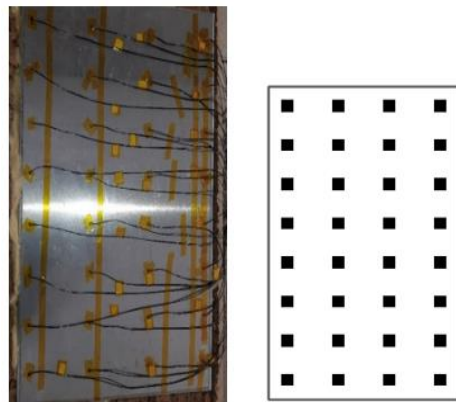


Figure 4. Placement of the thermistors on the plate.

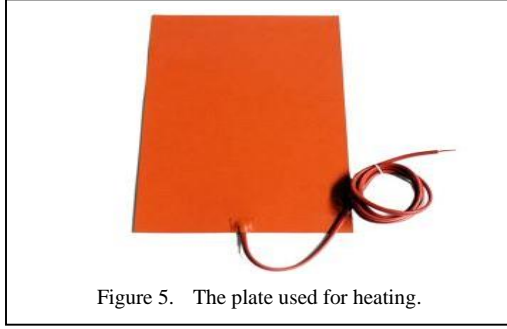


Figure 5. The plate used for heating.

C. Heating System

In this section, our attention will be directed towards regulating the power supplied to the hot plate (as illustrated in Fig. 5). To this end, we have designed an electronic control system to transmit commands to the current control unit, in order to obtain the desired power.

D. Film Forming System

The system in responsible for producing the film is an essential component of the hydraulic circuit. An aquarium air diffuser used to uniformly distribute the water across the plate's surface in order to produce a continuous film of water that cascaded over it (Fig. 6). In addition, to ensure uniformity of the water film, a 0.1 mm grid was used for homogenization purposes.

E. Film Feeding System

To ensure an even distribution of flow, a peristaltic pump was employed. An Arduino Uno board was utilized to produce a Pulse Width Modulation (PWM) signal to regulate a MOSFET, which in turn controls the motor speed of the pump. This arrangement creates a square wave signal with a frequency of 1Hz ($period = 1s$), maintaining the intended flow rate. The high state's duty cycle is modified within each period to match the intended flow rate. In order to accomplish this, a calibration

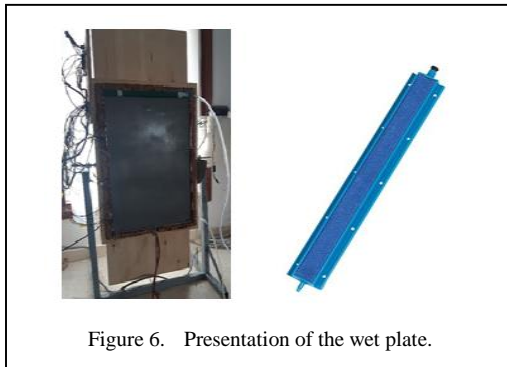


Figure 6. Presentation of the wet plate.

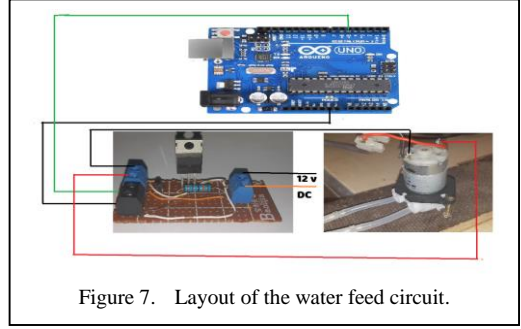


Figure 7. Layout of the water feed circuit.

procedure was carried out to determine the connection between the duty cycle and flow rate (Fig. 7).

In order to perform the various experimental tests, the following protocol is followed:

- put distilled water into the tank and set the mass flow to the appropriate rate.
- Start the LabVIEW application to control the required mass flow and power.
- Upon attainment of a steady-state condition and stabilization of the plate temperature, record the readings from the thermistors directly onto the computer.
- Measure the mass flow rate of the water at the outlet using the precision balance.
- Calculate the rate of evaporated water flow as the disparity between the inlet water flow rate and the outlet water flow rate.

III. RESULTS AND DISCUSSION

In this investigation, we elucidate the impact of heat flux density and mass flow rate on heat and mass transfer phenomena during the evaporation of the water film. The ranges encompassing the experimental parameters are delineated in Table I.

TABLE I. THE RANGES OF EXPERIMENTAL PARAMETERS.

Variables	Minimum	Maximum
q (W/m^2)	600	3200
Γ_0 ($Kg/h.m$)	1	6
T_0 ($^{\circ}C$)	20	25
T_{L0} ($^{\circ}C$)	20	25

Fig. 8 presents the temperature evolution along the plate for different heating densities. We can see that the plate's temperature increases linearly until it reaches its maximum. The water film receives a sensible heat flux in this part of the plate. We also notice that the plate's temperature becomes almost constant from this point to the bottom of the plate. In fact, in this second part, the latent flow uses all the heat flux received by the water film in the evaporation process. As expected, the temperature is increased for a higher applied heat flux favoring more the evaporation process of the water film, which is in accord with the results provided by [8,9]. Comparing cases in Figs. 8a, 8b, and 8c, a small variation of temperature is observed by the change in the mass flow rate.

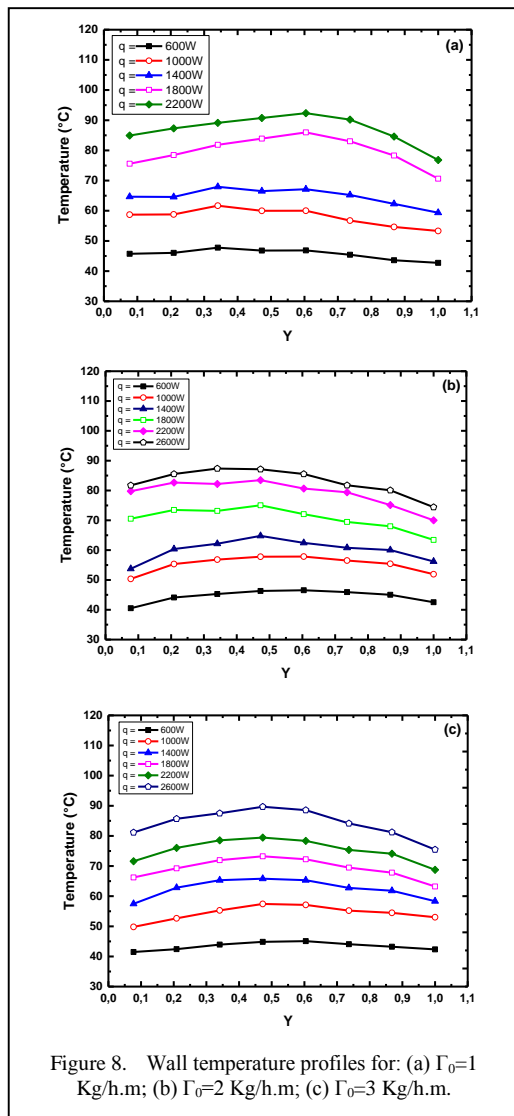
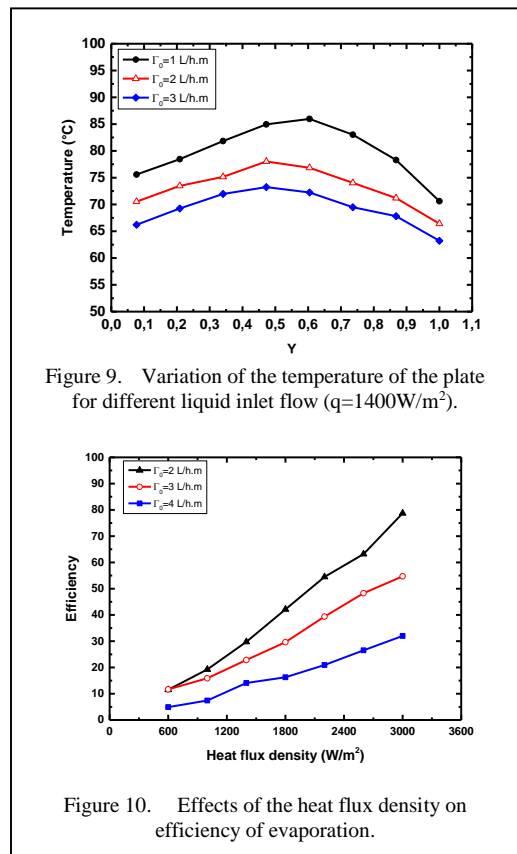


Fig. 9 shows the temperature distributions along the plate. As expected, the temperature is higher for a lower liquid mass flow rate. The thickness of the water film is less for low water flow rates, so the thermal resistance of the film is less, which favors vapor generation.

In order to quantify the efficiency of the system, it is interesting to define its efficiency as the ratio of the quantity of water evaporated to the initial amount of water.

The influence of heating flux density and water inlet flow rate on the evaporation of the film has been shown in Fig. 10. It can be seen that the evaporation process increases with heating flux and at a low water inlet flow rate. This effect can be explained by the fact that the film and heated plate have less contact time when the water flow rate is high. This is a result of the film covering the plate's height and flowing over it more quickly.

Fig. 11 shows the evaporated flow rate as a function of the water inlet flow rate, and it is clearly observed that the evaporated flow rate decreases in early with the increase of the water



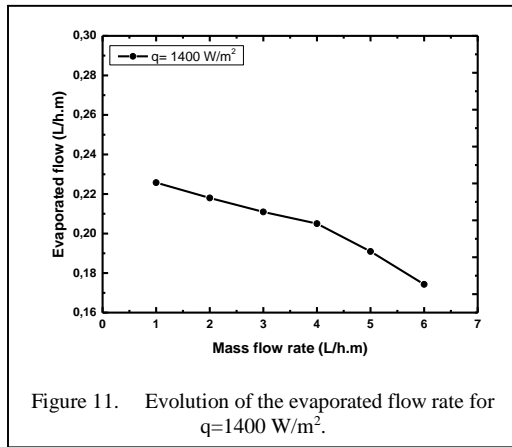


Figure 11. Evolution of the evaporated flow rate for $q=1400 \text{ W/m}^2$.

inlet flow rate until 5L, and then it goes down quickly. It is clear that the evaporated water flow rate increases with decreasing water inlet flow rate.

IV. CONCLUSION

In this work, we experimentally studied the dynamics of liquid film evaporation along a vertical channel. Along with measuring the evaporation flow rates, temperature readings were taken throughout the plate. The study looked into how mass and heat transfer phenomena were affected by the inlet liquid mass flow rate and the heat flux density applied to the wet wall. We concluded that higher heat flux densities and lower mass flow rates were associated with higher temperatures. Additionally, it was found that it is beneficial to operate the system with a lower mass flow rate in order to increase the evaporation rate.

REFERENCES

[1] Chow, L. C., & Chung, J. N. (1983). Evaporation of water into a laminar stream of air and superheated steam. *International Journal of Heat and Mass Transfer*, 26(3), 373- 380.

[2] Schröppel, J., & Thiele, F. (1983). On the calculation of momentum, heat, and mass transfer in laminar and turbulent boundary layer flows along a vaporizing liquid film. *Numerical Heat Transfer*, 6(4), 475- 496.

[3] Chang, C. J., Lin, T. F., & Yan, W. M. (1986). Natural convection flows in a vertical, open tube resulting from combined buoyancy effects of thermal and mass diffusion. *International Journal of Heat and Mass Transfer*, 29(10), 1543- 1552.

[4] Shembharkar, T. R., & Pai, B. R. (1986). Prediction of film cooling with a liquid coolant. *International Journal of Heat and Mass Transfer*, 29(6), 899- 908.

[5] Trevisan, O. V., & Bejan, A. (1987). Combined heat and mass transfer by natural convection in a vertical enclosure. *Journal of Heat Transfer*, 109(1), 104- 112.

[6] Nelson, D. J., & Wood, B. D. (1989). Fully developed combined heat and mass transfer natural convection between parallel plates with asymmetric boundary conditions. *International Journal of Heat and Mass Transfer*, 32(9), 1789- 1792.

[7] Wee, H. K., Keey, R. B., & Cunningham, M. J. (1989). Heat and moisture transfer by natural convection in a rectangular cavity. *International Journal of Heat and Mass Transfer*, 32(9), 1765- 1778.

[8] Jabrallah, S. B., Cherif, A. S., Dhifaoui, B., Belghith, A., & Corriou, J. P. (2005). Experimental study of the evaporation of a falling film in a closed cavity. *Desalination*, 180(1-3), 197-206.

[9] Ben Jabrallah, S., Belghith, A., & Corriou, J. P. (2006). Convective heat and mass transfer with evaporation of a falling film in a cavity. *International Journal of Thermal Sciences*, 45(1), 16- 28.

[10] Cherif, A. S., Kassim, M. A., Benhamou, B., Harmand, S., Corriou, J. P., & Ben Jabrallah, S. (2011). Experimental and numerical study of mixed convection heat and mass transfer in a vertical channel with film evaporation. *International Journal of Thermal Sciences*, 50(6), 942- 953.

[11] Terzi, A., Foudhil, W., Harmand, S., & Jabrallah, S. Ben. (2016). Experimental investigation on the evaporation of a wet porous layer inside a vertical channel with resolution of the heat equation by inverse method. *Energy Conversion and Management*, 126(November 2017), 158- 167.

[12] Huang, X. G., Yang, Y. H., & Hu, P. (2015). Experimental study of falling film evaporation in large scale rectangular channel. *Annals of Nuclear Energy*, 76, 237- 242.

[13] Hou, J., Yang, J., Chang, Z., Zheng, H., & Su, Y. (2018). Effect of different carrier gases on productivity enhancement of a novel multi-effect vertical concentric tubular solar brackish water desalination device. *Desalination*, 432(January), 72- 80.

Anaerobic Biodigesters and their By-products: A Systematic Literature Review

João Pedro Cruz de Almeida¹, Adriano da Silva Marques², Cristiani Viegas Brandão Grisi³, Rita de Cassia Andrade da Silva⁴, Marllon Costa Lira⁵, Miriane Moreira Fernandes Santos⁶

¹Postgraduate Program in Renewable Energy Engineering, Federal University of Paraíba, João Pessoa, Brazil

²Department of Renewable Energy Engineering, Federal University of Paraíba, João Pessoa, Brazil

³Postgraduate Program in Chemical Engineering, Federal University of Paraíba, João Pessoa, Paraíba, Brazil

⁴Postgraduate Program in Chemistry, Federal University of Paraíba, João Pessoa, Paraíba, Brazil

⁵Graduate Program in Renewable Energy Engineering, Federal University of Paraíba, João Pessoa, Paraíba, Brazil

⁶Technology Department, State University of Feira de Santana, Feira de Santana, Bahia, Brazil

¹joao.almeida@cear.ufpb.br, ²adriano@cear.ufpb.br

Abstract—Background. Anaerobic digestion and biodigesters offer a sustainable solution for waste management and renewable energy production, addressing global issues like waste disposal and energy scarcity. These systems convert waste into valuable resources such as bioenergy, supporting the circular economy and mitigating climate change. However, their full potential and by-products are still underexplored. **Methods.** This study reviews the current knowledge on anaerobic digesters, focusing on four key areas: biomass, types of digesters, digestate and biogas. **Results.** The studies indicate a growing trend in utilizing organic urban waste and agricultural substrates, alongside the development of low-cost biodigestion systems integrated with solar and photovoltaic energy. Additionally, biofertilizers show promise for sustainable soil nutrition, and future research on biogas purification for natural gas networks and thermal energy generation holds significant potential. **Conclusions.** A variety of studies on biomass, biogas and biofertilizers were identified by this review. Although biodigester technology is widely used in many regions, there are still gaps that prevent its widespread adoption.

Keywords - bioenergy, biodigester, anaerobic biodigestation, biofertilizer, biogas

I. INTRODUCTION

Bioenergy is the energy obtained from organic materials, known as biomass, which can be of plant, animal or industrial and urban waste origin. Solid biomass is one of the sources of bioenergy. The increasing demand for bioproducts has been driven by consumers and the replacement of fossil fuels with renewable energy sources [1] and many countries are interested in sustainable development goals [2]. In this context, biomass plays an important role in this transition. Today, biomass produces 5×10^{19} kJ of energy/year, which corresponds to 10% of the annual global energy consumption. Considering the variety of biomass resources, this value is predicted to reach 150×10^{19} kJ by 2050 [3].

In parallel, biodigestion is a chemical process in which organic matter, such as agricultural waste, urban waste and even sewage, is decomposed by a biological means. This metabolic process is complex and requires anaerobic conditions and depends on the joint activity of an association of microorganisms to transform organic material into carbon dioxide and methane [4]. The result is the production of biogas and a nutrient-rich material known as



digestate, which can be used as fertilizer. The metabolic process of microbes is regulated by their microbial activities in the digestion process, which are strongly affected by temperature, emphasizing that temperature is the most important parameter inside the digester [5]. The process can be divided into four phases: hydrolysis, acidogenesis, acetogenesis and methanogenesis. Each stage is carried out by different groups of microorganisms, in syntrophy, and may require different environmental conditions. These biochemical phases are directly linked in such a manner that the byproduct of one phase is the substrate of the next phase [6].

Anaerobic biodigestion (AD) and the energy transition are linked by their joint contribution to promoting a cleaner, renewable and sustainable energy matrix, mainly for its gaseous fraction, biogas. Therefore, it is reasonable to assume that gases produced from other sources (such as biomass) will continue to grow in importance as the need to replace fossil fuels as an energy source continues to grow [7]. Biogas is composed mainly of methane (CH_4) and carbon dioxide (CO_2). Raw biogas may also contain trace amounts of H_2S , water vapor, NH_3 , and siloxane, therefore biogas must undergo pretreatment to remove CO_2 and other trace gases in a process known as biogas upgrading to produce biomethane [8].

Moving ahead, it is well known that the main by-product of anaerobic digestion is biogas. However, it is also important to keep in mind the second product, i.e., digestate, which is a valuable fertilizer that acts comprehensively to accelerate plant growth [9]. The digestate has high nutrient concentrations that can potentially be used as fertilizer; it contains nutrients nitrogen, phosphorus and potassium [10]. The application of anaerobic digestate as a fertilizer can help reduce synthetic fertilizer usage and contribute to the circular economy [11]. Despite its qualities, the direct use of such a large quantity of digestate without proper treatment can potentially lead to the transmission of pathogenic microorganisms and the spread of diseases among animals, humans, and the environment, resulting in significant harm [12]. Notwithstanding the quantity of research that examines biodigestion process, factors, and operation for biodigester (BD) systems, it is indisputable that there is still more to be learned from the literature.

In order to clear the way for future researchers who hope to further contribute to the field, this article attempts to determine the areas that could still be explored by looking into studies that seek to identify the characteristics intrinsic to the biodigestion process and the products with the highest added value - the organic fertilizer and biogas - in a perspective of economic and energetic aspects found in the literature.

A systematic review was conducted in this study, and we also developed two research questions (RQ's) to direct the investigation throughout this work:

RQ 1: "What are the by-products main applications and obtaining characteristics?"

RQ 2: "How are emerging studies improving the efficiency of production and the use of biodigester organic by-products?"

Thus, this review aims to provide a summary of the state of knowledge on biodigesters, their byproducts and characteristics, aligning with our research questions for this review.

II. METHOD

To collect a sample of what has been researched in the recent past, we conducted a manual search process primordially in Google Scholar, Web of Science and Scopus platform. 40 articles were found in the search. We divided the literature into three broad categories: the different sources of biomass that can be used in the anaerobic biodigestion process, the physical and chemical characteristics of the biofertilizer and biogas generated, as well as the particularities of gas flow in the biodigester system. The search strings were as follows, with their respective boolean operators: "biomass", "anaerobic biodigestion", "anaerobic biodigester", "anaerobic biodigestion AND biomass", "digestate OR organic fertilizer", "biogas AND biomethane", "anaerobic biodigester AND organic waste" and "biogas purification". Furthermore, we searched for publications in English and Portuguese published during the period 2020-2024. The inclusion criteria adopted were studies that address the functioning of biodigesters and the production of their by-products. Theses and articles that had a focus restricted humanities or social aspects that did not include empirical data on biodigester by-products, without technical considerations about the biodigestion process,

were excluded. Duplicate studies between the databases were also removed. The selection of studies was carried out in three stages. Firstly, the titles and summaries of the articles identified in the searches were read to check their suitability for the topic. Secondly, the studies considered relevant underwent a complete reading. Finally, the extraction of data such as year of publication, type of biodigester studied, biomass used to feed the biodigester, biogas production and its composition, possible applications of biofertilizers and solid organic waste, and biodigesters computational modeling was carried out as well as the analysis of extracted data, focusing on identifying common patterns between studies.

III. RESULTS

A. *Main Types of Biomass and Their Specificities in Anaerobic Biodigestion*

Biomass can appear in many forms, including agricultural waste, forestry, agri-food, and human rubbish. Two studies have shown the potential use of food waste as a substrate for anaerobic digesters and its usage strategies. Pre-select microbiological groups and enzymes can optimize the process and production of a biodigester using organic waste, showing that enzyme selection has significant positive effects, highlighting the importance of choosing the right microbial groups for efficient anaerobic digestion (AD) [13]. The source of organic matter in this study was food waste from a restaurant. The study of [14] deals with the potential use of food waste in Porto Santo Island, largely due to the abundance in which it is generated and its richness in complex organic compounds, serving as a substrate for the bacteria that carry out biodigestion. According to the authors, the study aimed to evaluate bio-waste from municipal solid waste and its organic fraction - food waste -through anaerobic digestion and a combined heat and power (CHP) plant. As well as developing solutions for bio-waste separation, collection, and analysis, they are tailored to local resources and needs, demonstrating the potential of food residue. Furthermore, the self-consumption of the cogeneration unit is lower than the total electricity produced and the total thermal energy.

A further three studies have investigated the use of agricultural waste during AD. The effects of feedstock (agricultural organic wastes) characteristics, including particle size, carbon-

to-nitrogen ratio, and pretreatment options, can modify the performance of an anaerobic digestion process [15]. The researchers referenced above provided an overview of the effect of the main control parameters, including retention time, temperature, digestate, pH, volatile fatty acid content, total solids content and organic loading rate. The possibility of processing these wastes coming from rural areas through the technology of biomass biorefinery with anaerobic digestion as a central process has also been studied. Investigate and evaluating the feasibility of the full utilization of organic waste, particularly waste from agricultural and livestock units, together with the implementation of biorefineries has several great benefits as it provides environmental-friendly energy and, at the same time, exploits energy efficiency and contributes to the comprehensive and holistic waste management [16].

In addition, agro-crop residues can be used in multi-phase mixtures of different origins, such as singular, binary and ternary mixture, under bio-methane and combined heat and power pathways [17]. Following this, much of the biomass and biodigestion literature has been developed from an economic perspective and energetic valorization vision of residues. Four studies attempted to deal with the bio-economy framework: two focusing on the circular economy perspective - generating income through the sale of energy and the biodigestion products - by economic efficiency [15,16]. Another one adopting the energy security concept - which contributes to the energy autonomy of communities and regions nearby [17] and the last one optimizing the anaerobic digestion process for greater production in the biodigester by maximizing microbial activity, and consequently maximizing the plant's economy [13].

Another common topic found was the use of biomass as a fuel in cogeneration plants for electrical and thermal energy associated with biodigesters, as shown by [14] and [17]. They showed that the introduction of a CHP unit has considerably improved the economics of anaerobic biodigestion through the use of biogas produced from organic waste.

B. *Biodigesters Models and Their Singularities*

The classification of biodigesters can fall into several different fields, from their mode of operation, and construction material to their

geometric shape. The most often constructed type of semi-batch reactor is the fixed-dome biogas digester, also known as the hydraulic reactor model, which originated in China and is the most widely used type of reactor [18]. In this case, gas is produced under pressure. The volume of gas generated is proportional to the gas pressure and implies that, as the pressure increases, gas volume increases [19]. The floating drum biogas digester features an underground digester (cylindrical or dome-shaped) and a movable gas holder that floats on the fermentation slurry or in a water jacket in which the gas is collected in the drum, which rises or lowers based on the amount of gas stored [20]. The issue with existing floating drum biodigesters is that when biogas is produced, the floating gas holder rises, causing it to tilt and allowing gas to escape [21]. The third most common type is the tubular model. It consists of a tubular polyethylene or PVC bag (the digester), buried in a trench, and fed with diluted feedstock, which flows from the inlet to the outlet [22]. Moreover, this reactor's cost-effectiveness is a benefit, particularly during the early stages of development [23]. Continuous and batch systems are the two primary operational modes. In a batch AD, a digester is fed with fresh waste once and an inoculum is introduced on closure for a fixed duration to anaerobically degrade the substratum [24]. On the other hand, a continuous BD system is a type of anaerobic digestion process in which feedstock is continuously fed into the reactor, while the digested material is simultaneously removed.

When it comes to the economics of operation, operating and investment costs are evaluated according to the optimum design of the biodigester. To globally optimize methane bioreactor performance, it's essential to integrate substrate characteristics, process kinetics, and business parameters into the design, aiming to optimize profitability by incorporating stochastic optimization, mathematical geometry, and economics [25]. The implementation of a biomass plant requires a carefully conducted economic viability analysis, called risk analysis, mainly because of the volatility associated with technical and economic parameters, especially those associated with the energy market [26]. As presented by [27], the economic viability BD study can provide the design economically viable by minimum acceptable rates of return,

simple and discounted paybacks below the proposed horizon, and satisfactory benefit-cost ratios.

There is also a great opportunity to use BDs aligned with solar and photovoltaic energy, forming hybrid systems. In the developed system layout, the thermal energy required to control the temperature of the reactor is matched by a solar thermal source and the electrical demand is met by means of a photovoltaic field [28]. In Biogas-Solar Photovoltaic Hybrid Mini-grid, the power generation section is essentially composed of two major units: the biogas power unit and the solar power unit, where these units are usually connected to inverters or converters to effectively supply electricity to end-users [29]. This enables identifying operating conditions for systems that result in greater utilization of solar radiation, lower heat losses to the external environment, increased microbial activity rate, optimization of treatment, and selection of materials with more favorable thermal properties [30].

From the selected primary studies analysis, it is shown that current biodigesters studies research mostly focuses on two topics: optimal operation. Such an approach is based on the application of exergy concepts to the modeling of BDs. Through exergoeconomic analysis, the costs related to each exergy stream and component of the thermal system can be comprehensively analyzed [31]. The themes of system optimization, economic viability and exergetic analysis permeate the [21], Neba et al. [25-28,31] with a strong emphasis on maximizing energy efficiency and reducing costs. The importance of sustainability and reducing environmental impact are also argued by [26] and [31], as the first evaluates the environmental impacts of using biodigesters and the latter examines the emissions and environmental efficiency of their system. Another point in common is the emphasis on payback - return on investment - addressed by [25-27]. The second most common point in the studies analyzed was the use of other renewable energy sources alongside the biodigester, mainly solar and photovoltaic energies, as mentioned by [24,29,30], capable of maintaining the temperature for optimum microbial activity and supplying the electrical demands of biodigestion, such as pumps and mixers. Lastly, constructive aspects of comics were also identified as a point of convergence between the studies [18-20,22,23].

C. Digestate and its Use as Organic Fertilizer

Biofertilizers are natural inputs derived from biological processes that contain living microorganisms or organic compounds capable of stimulating plant growth, improving soil fertility and providing essential nutrients such as nitrogen, phosphorus and potassium. By interacting synergistically with soil organisms, biofertilizers facilitate the fixation and gradual release of nutrients, increasing their availability to plants and promoting more sustainable and productive agriculture [32]. This approach contributes to the continuous regeneration of soil fertility, creating a more balanced and resilient agricultural system. Unlike synthetic fertilizers, which are industrially produced, biofertilizers offer an ecological alternative, ensuring more sustainable and environmentally friendly nutrition. Although chemical fertilizers can provide nutrients immediately, their excessive use results in soil degradation and environmental contamination. In contrast, biofertilizers promote long-term soil enrichment, improving its structure, health and fertility without causing damage to the ecosystem, favoring a natural and lasting balance in agricultural production [33].

The production of biofertilizers involves various methods that use organic materials and microorganisms to improve soil fertility and increase agricultural productivity. Among the main approaches are the isolation of phosphate-solubilizing bacteria, such as species of the genus *Pseudomonas*, which make phosphorus more accessible to plants [34]. In addition, nitrogen-fixing and phosphate-solubilizing biofertilizers are produced by fermentation processes using specific microorganisms, which results in greater nutrient availability in an efficient manner [35]. Anaerobic digestion of organic waste combined with materials such as sawdust is another effective method for producing biofertilizers. This process generates a final product rich in essential nutrients [36]. Humic compounds present in the digestate stimulate root growth, while beneficial microorganisms such as nitrogen-fixing bacteria help promote long-term soil fertility. By providing nutrients gradually and encouraging biological activity in the soil, biofertilizers derived from biodigesters are an environmentally friendly and efficient alternative to chemical fertilizers [37].

Biofertilizers can be obtained from a wide variety of organic raw materials, each with its characteristics that influence the anaerobic digestion process. Among the main sources are vegetable sludge, which includes primary and secondary sludge from wastewater treatment, and waste from the agri-food industry, such as fruit and vegetable by-products, canteen waste and kitchen waste, which is part of municipal solid waste. Green waste, such as pruning waste, and animal waste, especially manure from dairy cows, also feature prominently. Food waste, from leftovers and household waste, completes the range of materials used to produce biofertilizers. Each of these raw material sources has characteristics that affect both the efficiency of the digestion process and the final composition. The right combination of these raw materials makes it possible to optimize the quality of biofertilizers, adjusting the balance of nutrients and maximizing the benefits for soil fertility and plant growth [38].

Nitrogen is essential for plant development and microbial activity in the soil, and is the most consumed nutrient. Its adequate availability is crucial for productivity and soil health. Biofertilizers, rich in ammoniacal nitrogen, improve this availability. Although nitrogen fertilizers increase agricultural productivity, it is essential to optimize nitrogen use efficiency for better agronomic and environmental results. High productivity and crop yields can be achieved when the right amount of nitrogen is introduced into the soil system. However, excessive application can result in several negative impacts, such as soil toxicity, nutrient leaching, ammonia volatilization and nitrous oxide emissions, which are harmful to the environment [39].

There are several barriers that hinder the use of biofertilizers on a large scale, such as issues related to efficacy, stability and adaptation to the environment. Even if laboratory tests show good results, biofertilizers often fail to maintain the same performance under field conditions, resulting in inconsistent yields. This is due to their sensitivity to environmental factors, such as temperature and pH, which affect their efficiency in the soil [40]. Another relevant challenge is the shelf life and storage of biofertilizers, which generally have a short shelf life, making it difficult to transport and maintain their viability for long periods. The lack of adequate infrastructure to store biofertilizers is a major obstacle for farmers. In addition, the

microbial diversity available is limited, restricting application in different soils and climates. High doses are often needed to cover large agricultural areas, which makes the practical use of biofertilizers unfeasible. However, ongoing research focused on developing more robust formulations with long shelf lives and biostimulants shows the potential to overcome the limitations and increase the adoption of biofertilizers in sustainable agriculture, offering higher yields and better long-term results [41].

D. Biogas and Biomethane

Biogas is the result of the anaerobic decomposition of organic matter and is mainly composed of methane (CH_4) and carbon dioxide (CO_2). This renewable energy resource is formed in anaerobic environments, where microorganisms break down organic materials such as agricultural waste, animal waste, sewage sludge and other organic compounds [42]. Methane is the main component of biogas, accounting for between 50% and 70% of its composition, and is particularly valued due to its high energy potential, which can be used to generate electricity, heat or as a vehicle fuel. Carbon dioxide, on the other hand, is the second largest component, generally representing between 30% and 50% of the mixture, although its energy value is lower than that of methane [43]. In addition to these, small amounts of gases such as hydrogen sulfide (H_2S), water vapor and traces of volatile organic compounds can be present in biogas, affecting its quality and viability as an energy source. Therefore, removing or reducing these unwanted components is crucial to improving biogas efficiency [44].

Biomethane is a renewable, high-purity gas obtained from the biogas purification process, where components such as carbon dioxide (CO_2), hydrogen sulfide (H_2S) and other unwanted gases are removed. Biomethane has a methane (CH_4) concentration of over 90%, making it chemically equivalent to natural gas [45].

Its main advantage over raw biogas is its versatility of use. It can be injected directly into natural gas distribution networks, as well as being used as a vehicle fuel to replace fossil natural gas [46]. This high purity makes it suitable for a wider range of applications, especially in contexts where untreated biogas would be less efficient or unsuitable.

Purification processes vary according to the technology used, including techniques such as chemical absorption, pressure adsorption and membrane filtration [47]. The result is a low-carbon fuel that is key to the energy transition and mitigating the impacts of climate change.

Another crucial point raised by the selected articles is the biogas production process. It is crucial to consider that the composition of biogas can vary significantly based on the raw material used, the type of biodigester and the operating conditions. Proper control of these factors is key to optimizing biogas production and ensuring its efficiency as a viable and sustainable energy source [48]. Biogas is produced mainly through anaerobic digestion in biodigesters, which break down organic matter in the absence of oxygen [49,50]. The biogas production process follows four phases: hydrolysis, acidogenesis, acetogenesis and methanogenesis, where organic matter is converted into biogas by microorganisms [51]. Efficiency depends on factors such as temperature, pH and retention time of the materials in the biodigester, which affect microbial activity and biogas production [52]. It is also important to note, in terms of political support, the existence of laws that promote the acceleration of the adoption of DBs and their by-products. At the end of 2017, Brazil passed Law No. 13.576, known as the National Biofuels Policy (RenovaBio), putting the advancement of biofuels, including biogas, including biogas [53]. This serves as a tool for reorienting the path of innovation in these systems.

IV. CONCLUSIONS

This review revealed a diverse range of studies, covering from biomass to the use of biofertilizers and biogas. Although biodigester technology is well established in various parts of the world, there are still gaps that limit its widespread adoption and optimization on larger scales. Future studies should focus on adapting biodigesters to different climates and types of biomasses, as well as investigating the long-term environmental impact of the by-products. It is also recommended to study the implementation of hybrid technologies that combine biodigesters with other renewable sources, which represent a promising research opportunity.

ACKNOWLEDGMENT


This research was financially supported by the National Council for Scientific and Technological Development (CNPq) through the Technological and Industrial Development scholarship to the first author and financial aid for research, in accordance with grant agreement N° 382978/2024-2. Paraíba State Research Foundation (Fapesq-PB) through a postdoctoral scholarship to the third author (2023/3390.18).

REFERENCES

- [1] Popp, J., Kovács, S., Oláh, J., Divéki, Z., & Balázs, E. (2021). Bioeconomy: Biomass and biomass-based energy supply and demand. *New biotechnology*, 60, 76-84.
- [2] Wang, Z., Bui, Q., Zhang, B., & Pham, T. L. H. (2020). Biomass energy production and its impacts on the ecological footprint: an investigation of the G7 countries. *Science of the Total Environment*, 743, 140741.
- [3] Alper, K., Tekin, K., Karagöz, S., & Ragauskas, A. J. (2020). Sustainable energy and fuels from biomass: a review focusing on hydrothermal biomass processing. *Sustainable Energy & Fuels*, 4(9), 4390-4414.
- [4] Kunz, A., Steinmetz, R. L. R., & do Amaral, A. C. (2022). *Fundamentals of anaerobic digestion, biogas purification, use and treatment of digestate*.
- [5] Shukla, R. K., Kumar Shrivastava, R., Singh Bhadauria, S., & Jain, S. (2022). Assessment of feasibility for biodigestion of cattle waste in gwalior city, India. *Advances in Civil Engineering*, 2022(1), 8675409.
- [6] Nwokolo, N., Mukumba, P., Obileke, K., & Enebe, M. (2020). Waste to energy: A focus on the impact of substrate type in biogas production. *Processes*, 8(10), 1224.
- [7] Mignogna, D., Ceci, P., Cafaro, C., Corazzi, G., & Avino, P. (2023). Production of Biogas and biomethane as renewable energy sources: A review. *Applied Sciences*, 13(18), 10219.
- [8] Francisco López, A., Lago Rodríguez, T., Faraji Abdolmaleki, S., Galera Martínez, M., & Bello Bugallo, P. M. (2024). From biogas to biomethane: an in-depth review of upgrading technologies that enhance sustainability and reduce greenhouse gas emissions. *Applied Sciences*, 14(6), 2342.
- [9] Czekala, W., Jasiński, T., Grzelak, M., Witaszek, K., & Dach, J. (2022). Biogas plant operation: Digestate as the valuable product. *Energies*, 15(21), 8275.
- [10] Unpaprom, Y., Pimpimol, T., Whangchai, K., & Ramaraj, R. (2021). Sustainability assessment of water hyacinth with swine dung for biogas production, methane enhancement, and biofertilizer. *Biomass Conversion and Biorefinery*, 11, 849-860.
- [11] Chojnacka, K., & Moustakas, K. (2024). Anaerobic digestate management for carbon neutrality and fertilizer use: A review of current practices and future opportunities. *Biomass and Bioenergy*, 180, 106991.
- [12] Guan, D., et al. (2024). A critical review on sustainable management and resource utilization of digestate. *Process Safety and Environmental Protection*.
- [13] Monteiro, P. I., et al. (2023). Optimizing food waste biodigestion: pre-selection of microbial groups and isolated enzymes using the plackett-burman experimental design. *Observatory of the Latin American Economy*, 21(3), 1718-1750.
- [14] Pereira, F., & Silva, C. (2023). Energetic valorization of bio-waste from municipal solid waste in Porto Santo Island. *Clean Technologies*, 5(1), 233-258.
- [15] Pan, S. Y., Tsai, C. Y., Liu, C. W., Wang, S. W., Kim, H., & Fan, C. (2021). Anaerobic co-digestion of agricultural wastes toward circular bioeconomy. *Iscience*, 24(7).
- [16] Rekleitis, G., Haralambous, K. J., Loizidou, M., & Aravossis, K. (2020). Utilization of agricultural and livestock waste in anaerobic digestion (AD): Applying the biorefinery concept in a circular economy. *Energies*, 13(17), 4428.
- [17] Li, Y., Han, Y., Zhang, Y., Luo, W., & Li, G. (2020). Anaerobic digestion of different agricultural wastes: A techno-economic assessment. *Bioresource technology*, 315, 123836.
- [18] Uche, A. M., et al. (2020). Design and construction of fixed dome digester for biogas production using cow dung and water hyacinth. *African Journal of Environmental Science and Technology*, 14(1), 15-25.
- [19] Abubakar, A. M. (2022). Biodigester and feedstock type: characteristic, selection, and global biogas production. *Journal of Engineering Research Science*, 1(2), 170-187.
- [20] Budiman, I. (2020). The role of fixed-dome and floating drum biogas digester for energy security in Indonesia. *Indonesian Journal of Energy*, 3(2), 83-93.
- [21] Alibe, A. M., Kallamu, U. M., & Hammajam, A. A. (2022). Improvement On the Design of An Anaerobic Floating Drum Biogas Digester. *Journal of Research in Mechanical Engineering*, 8(3), 09-16.
- [22] Cucina, M., Castro, L., Escalante, H., Ferrer, I., & Garfí, M. (2021). Benefits and risks of agricultural reuse of digestates from plastic tubular digesters in Colombia. *Waste Management*, 135, 220-228.
- [23] Souvannasouk, V., Singthong, O., Sayavongsa, P., Meas, S., Phaxaisithidit, T., & Fongsamouth, S. (2023). Revolutionizing biogas generation: polyethylene tubular digesters for household pig farms. *Maejo International Journal of Energy and Environmental Communication*, 5(1), 6-13.
- [24] Mahmudul, H. M., et al. (2021). A comprehensive review of the recent development and challenges of a solar-assisted biodigester system. *Science of The Total Environment*, 753, 141920.
- [25] Neba, F. A., Asiedu, N. Y., Addo, A., Morken, J., Østerhus, S. W., & Seidu, R. (2020). A coupled modeling of design and investment parameters for optimal operation of methane bioreactors: Attainable region concept approach. *Renewable Energy*, 148, 1054-1064.
- [26] Pinto, L. S., Neto, D. P., de Leles Ferreira Filho, A., & Domingues, E. G. (2020). An alternative methodology for analyzing the risk and sensitivity of the economic viability for generating electrical energy with biogas

- from the anaerobic bio-digestion of vinasse. *Renewable Energy*, 155, 1401-1410.
- [27] Demeu, F. A., et al. (2021). *Economic viability of a canadian biodigester for power generation in dairy farming*.
- [28] Calise, F., Cappiello, F. L., Cimmino, L., Napolitano, M., & Vicidomini, M. (2023). Dynamic simulation and thermo-economic analysis of a novel hybrid solar system for biomethane production by the organic fraction of municipal wastes. *Energies*, 16(6), 2716.
- [29] Bambokela, J. E., Belaid, M., Muzenda, E., & Nhubu, T. (2022). Developing a pilot biogas-solar PV system for farming communities in Botswana: case of Palapye. *Procedia Computer Science*, 200, 1593-1604.
- [30] de Paula Sousa, I., et al. (2022). Study of internal and external temperatures and their influence on covered lagoon digester performance. *Biomass and Bioenergy*, 159, 106380.
- [31] Wu, Z., et al. (2020). Combined biomass gasification, SOFC, IC engine, and waste heat recovery system for power and heat generation: Energy, exergy, exergoeconomic, environmental (4E) evaluations. *Applied Energy*, 279, 115794.
- [32] Sharma, H., et al. (2024). A Sustainable Agriculture Method Using Biofertilizers: An Eco-Friendly Approach. *Plant Science Today*.
- [33] Atieno, M., et al. (2020). Assessment of biofertilizer use for sustainable agriculture in the Great Mekong Region. *Journal of Environmental Management*, 275, 111300.
- [34] Isiya, S., & Salisu, B. (2024). Biofertilizer production using phosphate-solubilizing *Pseudomonas* spp. isolated from rhizosphere soil: Towards indigenous biofertilizer for enhanced crop productivity in Katsina, Nigeria. *UMYU Journal of Microbiology Research (UJMR)*, 9(1), 123-133.
- [35] Shamil, Z., & Tofike, R. (2021). Production of Nitrogen Fixing and Phosphorous Solubilizing Liquid Bio-fertilizer for the improves of the Crops Growth and Yield. *Modern Chemistry*, 9(3), 61.
- [36] Ezemagu, I. G., Ejimofor, M. I., Menkiti, M. C., & Diyoke, C. (2021). Biofertilizer production via composting of digestate obtained from anaerobic digestion of post biocoagulation sludge blended with saw dust: Physicochemical characterization and kinetic study. *Environmental Challenges*, 5, 100288.
- [37] Wang, P., Wang, H., Qiu, Y., Ren, L., & Jiang, B. (2018). Microbial characteristics in anaerobic digestion process of food waste for methane production—A review. *Bioresource Technology*, 248, 29-36.
- [38] Bhatt, A. H., & Tao, L. (2020). Economic Perspectives of Biogas Production via Anaerobic Digestion. *Bioengineering*, 7(3), 74.
- [39] Doyeni, M. O., Stulpinaite, U., Baksinskaite, A., Suproniene, S., & Tilvikiene, V. (2021). The Effectiveness of Digestate Use for Fertilization in an Agricultural Cropping System. *Plants*, 10(8), 1734.
- [40] Kumar, A., et al. (2024). Revolutionizing Indian agriculture: the imperative of advanced biofertilizer technologies for sustainability. *Discover Agriculture*, 2(1).
- [41] Mora, N. E., Simarmata, N. T., & N.Kamaluddin, N. N., (2024). A review: Revealing the important of bio stimulant coated microbeads biofertilizers for improving the effectiveness of inoculant for enhancing the agronomic traits and productivity of crops. *International Journal of Frontiers in Life Science Research*, 6(1), 039-044.
- [42] Obaideen, K., et al. (2022). Biogas role in achievement of the sustainable development goals: Evaluation, Challenges, and Guidelines. *Journal of the Taiwan Institute of Chemical Engineers*, 131, 104207.
- [43] Calbry-Muzyka, A., Madi, H., Rüsich-Pfund, F., Gandiglio, M., & Biollaz, S. (2022). Biogas composition from agricultural sources and organic fraction of municipal solid waste. *Renewable Energy*, 181, 1000-1007.
- [44] Rafiee, A., Khalilpour, K. R., Prest, J., & Skryabin, I. (2021). Biogas as an energy vector. *Biomass and Bioenergy*, 144, 105935.
- [45] de Albuquerque, S. M., & de Aviz Cardoso, S. (2020). Projeto de digester anaeróbio para produção de biometano auxiliado por computador. *Brazilian Journal of Animal and Environmental Research*, 3(4), 3395-3405.
- [46] Bezerra, F. E. C. (2020). Biogas as an energy source for internal combustion engines: A review. *Holos*, 7, 1-14.
- [47] Rizzioli, F., Magonara, C., Mengoli, G., Bolzonella, D., & Battista, F. (2024). Production, purification and recovery of caproic acid, Volatile fatty acids and methane from *Opuntia ficus indica*. *Renewable and Sustainable Energy Reviews*, 190, 114083.
- [48] Kabeyi, M. J. B., & Olanrewaju, O. A. (2022). Biogas production and applications in the sustainable energy transition. *Journal of Energy*, 2022(1), 8750221.
- [49] Devi, M. K., et al. (2022). Recent advances in biogas production using Agro-Industrial Waste: A comprehensive review outlook of Techno-Economic analysis. *Bioresource Technology*, 363, 127871.
- [50] Kunatsa, T., & Xia, X. (2022). A review on anaerobic digestion with focus on the role of biomass co-digestion, modelling and optimisation on biogas production and enhancement. *Bioresource technology*, 344, 126311.
- [51] Akcakaya, M., Tuncay, S., & Içgen, B. (2022). Two-stage anaerobic digestion of ozonated sewage sludge predominantly took over by acetotrophic methanogens with increased biogas and methane production. *Fuel*, 317, 123434.
- [52] Nuhu, S. K., Gyang, J. A., & Kwarbak, J. J. (2021). Production and optimization of biomethane from chicken, food, and sewage wastes: The domestic pilot biodigester performance. *Cleaner Engineering and Technology*, 5, 100298.
- [53] da Silva, E., da Cunha, S. K., & dos Santos, D. D. (2023). Direcionalidade do biogás no brasil para a política de inovação transformadora (pit): caso da renovabio. *Revista foco*, 16(1), e785-e785.

Effect of Damping Coefficient and Inertia Constant on Performance of Virtual Synchronous Machine Control

Souhil Drias¹, Abderrahmane Berkani², Mohamed Bey³

^{1,2,3}L2GEGI Laboratory, University of Tiaret, Tiaret, Algeria

¹souhil.drias@univ-tiaret.dz, ²abderrahmane.berkani@univ-tiaret.dz, ³mohamed.bey@univ-tiaret.dz

Abstract—In this paper, we investigate the consequences of the damping coefficient and the inertia constant on the performance of VSM control in power systems where renewable energy sources are widely present. The analysis highlights the crucial importance of these parameters to improve the system stability and dynamic response to disturbances. When active power references change, the damping coefficient shows a significant influence on the system's ability to eliminate oscillations and improve the response speed. The obtained results confirm fine tuning of damping and inertia parameters improves the performance of VSMs, positioning them as essential components in the transition towards more sustainable energy systems.

Keywords - VSM control, damping coefficient, inertia constant

I. INTRODUCTION

Grid-forming converters (GFC) exhibit the classical characteristics of traditional synchronous machines, such as inertia, damping, fault current, active power control, and reactive power control. The control strategies in a GFC system are developed to mimic the dynamic responses of conventional synchronous machines. It is crucial to implement this emulation to ensure the stability of power systems during various disturbances [1].

Grid-forming converters, especially those using virtual synchronous machine (VSM) control, are gaining attention as they can improve the stability and resilience of contemporary

power systems. In 2007, Beck and Hesse proposed the concept of a virtual synchronous machine (VSM), or VISMA.

In research and industry, virtual synchronous machine (VSM) control is gaining popularity for its ability to mimic the characteristics of synchronous generators, using parameters such as virtual inertia and virtual damping. It is crucial to implement this technology to improve grid stability, especially as the integration of renewable energy sources continues to grow [2,3]. VSMs are designed to operate in grid-connected mode, meaning that the VSM acts as a grid-forming inverter that generates a constant grid frequency and voltage. The control method is based on the idea of a “virtual synchronous machine” (VSM), a mathematical model that reproduces the operation of a classical synchronous machine [4].

The performance of synchronous virtual machines in network training applications mainly relies on their ability to effectively cope with load fluctuations. Synchronous virtual machines can significantly improve network stability and reliability under dynamic conditions by providing virtual inertia and using adequate control strategies [5].

The damping coefficient and the inertia constant are essential parameters that have a significant influence on the dynamic response of VSMs during instantaneous changes of active power references. Capturing these effects is crucial to preserve the stability and performance



of contemporary power systems, as renewable energy sources are increasingly present [6].

In this paper, we analyze the consequences of inertia constants and damping coefficients on the dynamic response of VSMs when there are instantaneous variations of active power references. The inertia constant corresponds to the resistance of the system to frequency variations, while the damping coefficient gives an indication of the efficiency with which oscillations are damped after disturbances. Understanding how these two parameters interact is crucial to improve the performance of VSMs in contemporary power systems.

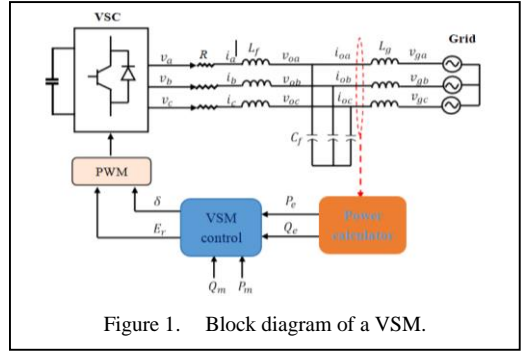
II. GRID-FORMING CONTROL METHOD

Grid-fed inverters (GFI) are increasingly considered as indispensable elements of contemporary power systems, especially with the emergence of renewable energy integration. Different approaches have been developed to improve system stability and performance. GFMs offer resources that use inverters (such as solar panels, wind turbines, and batteries) the ability to be used as voltage sources, mimicking the operation of conventional synchronous machines. Having this capability is essential to maintain grid stability, especially in low-inertia environments where traditional generators are less common.

III. VIRTUAL SYNCHRONOUS MACHINE (VSM) CONTROL

VSM is a contemporary method that aims to enhance the stability and reliability of power systems, especially when integrating renewable energy sources (Fig. 1). It has been introduced as a “network-forming” control method to improve converter behaviour from the grid perspective [7].

Using a mathematical model and incorporating equations for rotor dynamics and electromagnetic transients, a virtual synchronous machine is a control method that efficiently reproduces the internal and external characteristics of synchronous machines [7]. By reproducing the dynamics of synchronous machines, VSM control provides inertia and damping to the system. Frequency and voltage stability are improved with this method, which allows the inverter to react to disturbances in the same way as a traditional generator. In fact, thanks to the VSM control method, the inverters that make up a network can reproduce the



behavior of synchronous machines, which provides a solid framework for integrating renewable energy sources into AC systems [8,9]. The essential features of VSM control will be discussed below, with emphasis on its capabilities in active power frequency regulation, reactive power voltage regulation, virtual inertia control, and damping control (Table I). When the grid operating conditions are changed, the converter adapts according to the problems affecting grid operations [10].

It is crucial to have a dynamic response in order to preserve frequency stability and reduce fluctuations in power systems. Equation (1) that determines the dynamics of the VSG is presented below:

$$T_a \cdot s \cdot \omega_{vsm} = P_0 - P_{Ele} - P_d, \quad (1)$$

$$P_d = K_p (\omega_{vsm} - \omega_g), \quad (2)$$

$$T_a \cdot s \cdot \omega_{vsm} = P_0 - P_{Ele} - K_p (\omega_{vsm} - \omega_g). \quad (3)$$

With: T_a (2H) is the mechanical time constant of the emulated inertia (the inertia constant). The damping constant K_d provides the damping power P_d , while the difference between pu, P_o , represents the active power reference and P_{Eel} represents the electrical power provided by the V_{SM} . ω_{VSM} represents the rotation speed of the VSM, while ω_g corresponds to the angular speed of the grid. Thus, K_p can be calculated when the derivative of the reference frequency is zero.

$$K_d = \frac{P_{\max, vsm} - P_{Load}}{\omega_0 - \omega_{\min}}. \quad (4)$$

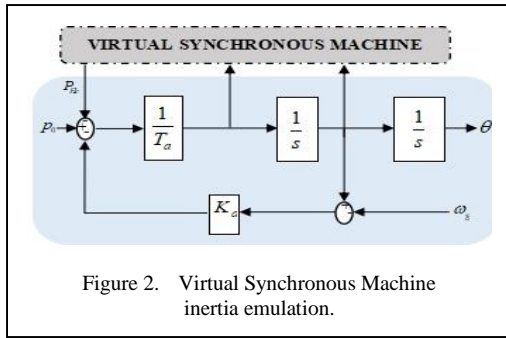


Figure 2. Virtual Synchronous Machine inertia emulation.

TABLE I. ADVANTAGES OF VSM CONTROL.

Advantage	Description
Emulation of Synchronous Behavior	VSM control techniques replicate the dynamic response of conventional synchronous machines, providing essential grid services such as inertia and damping (damping). This helps maintain stable frequency and voltage in the event of disturbances.
Autonomous Operation	The autonomous operation of VSM-controlled converters allows them to react to grid fluctuations without requiring external controls. Having this capability is crucial to make rapid adjustments in the face of unexpected events.
Fault Ride-Through	VSM converters have the ability to improve fault handling skills, allowing them to maintain operation during outages and recover more efficiently than conventional converters. This is of particular importance in weak networks where the voltage can be significantly fluctuating.
Voltage Source Behavior	Instead of relying on external voltage references for grid following converters, VSM converters produce their own voltage, allowing them to provide voltage support and improve the overall resilience of the power grid.

IV. VOLTAGE AND CURRENT CONTROLLERS

Internal control loops are used to control voltage and current. Cascaded PI controllers consist of two pairs and their purpose is to control the AC voltages and currents at the output of the converter filter. In a power converter, voltage and current can be regulated by clipping the reference voltage amplitudes for each direct-quadrature axis, namely Vd^* and Vq^* . It is essential to be able to autonomously control the d-axis (direct axis) and q-axis (quadrature axis) elements in order to efficiently regulate the output voltages and currents. It is essential to be able to autonomously control the d-axis (direct axis) and q-axis (quadrature axis) elements in order to efficiently regulate the output voltages and currents. A schematic of the implementation of the voltage and current controllers is shown in Fig. 3 [11].

The voltage control system in a power converter receives the reference voltage values in the direct quadrature axis, represented by $Vd^*, Vq^* = 0$. These references are compared with the actual values of the voltage magnitudes in the axile and q-axile axes (Vd, Vq) to generate the error signals that drive the voltage regulators. The voltage errors are fed to the voltage regulators, usually PI regulators, which generate the axis and Q-axis references id^*, iq^* . The actual references are then passed to the internal control loop to regulate the converter flows. The deviation between the reference values and the actual values of the converter currents in the direct-quadrature axis, in particular Id and Iq , is handled in the actual control system. This error is fed to two PI controllers, which are distinguished by their proportional gain K_{pi} and their integral gain k_{ij} .

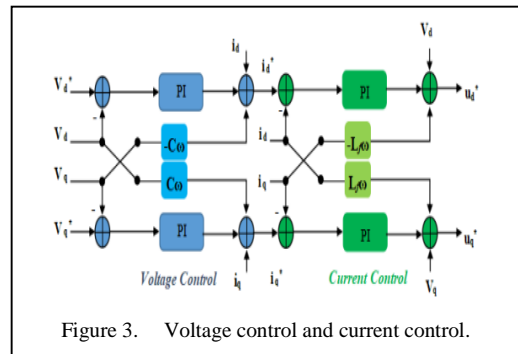


Figure 3. Voltage control and current control.

$$\begin{cases} \dot{i}_d^* = (v_d^* - v_d) \left[K_p + \frac{k_i}{s} \right] + i_d - C_f \cdot \omega \cdot v_q \\ \dot{i}_q^* = (v_q^* - v_q) \left[K_p + \frac{k_i}{s} \right] + i_q - C_f \cdot \omega \cdot v_d \end{cases}, \quad (5)$$

where K_{pv} and K_{iv} are the proportional and integral gains of the voltage PI controller, C_f represents the filter capacitance.

$$\begin{cases} \dot{u}_d^* = (i_d^* - i_d) \left[K_p + \frac{k_i}{s} \right] + v_d - L_f \cdot \omega \cdot i_q \\ \dot{u}_q^* = (i_q^* - i_q) \left[K_p + \frac{k_i}{s} \right] + v_q - L_f \cdot \omega \cdot i_d \end{cases}, \quad (6)$$

where K_{pi} and K_{ij} are the proportional and integral gains of the current PI controller, and L_f is the filter inductor.

Once feedback and feedforward words have been added, the modulation signals in the d-q frame are denoted md and mq. Once modulation is complete, the md and mq signals are created in the d-q frame and are translated to the “abc” reference. Control of the voltage-source converter (VSC) is crucial with this transformation, as it allows the modulation

signals to be applied in a three-phase system [12].

V. RESULTS AND ANALYSIS

In this section, we present the suggested results and the results obtained during the VSM grid formation control. The figure presents the basic control structures of the distributed generator that uses a voltage source converter (VSC) (Figs. 4 and 5). Three main elements compose this system: the hardware, which includes the VSC, the LC filter, and the grid; the measurement component; and the control algorithm, which includes power control, cascaded voltage and current control, and pulse width modulation (PWM). Table II presents the parameters of the test system as well as the grid formation control method.

In this part, our goal is to measure the efficiency of a well-trained VSM controller. A comparative analysis of its control performance will be performed in various scenarios.

- In the first case, we examine the VSM control reaction considering a load fluctuation.
- The next scenario Changed the active power reference
- The third case Changed the damping coefficient
- The fourth case Constant inertia. Change in Load

TABLE II. PARAMETERS OF THE VSM SIMULATION MODE.

Parameter	Value
Grid frequency f	50 Hz
Grid voltage Vg	1pu
DC voltage Vdc	1100V
Filter inductance Lf	8 mH
Damping coefficient	1.055pu/Hz
Active power reference	0.8 pu
Filter resistance	0.1Ω
Filter capacitance	28μF
Reactive power reference	0.38 pu
Virtual inertia constant Ta	1pu

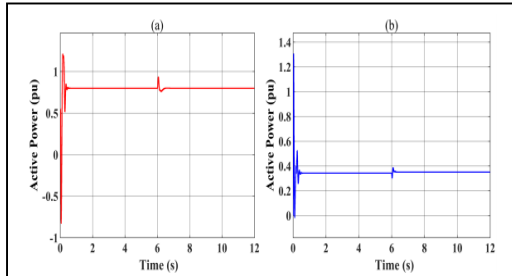


Figure 4. Dynamic response of VSM (a) Active power; (b) reactive power.

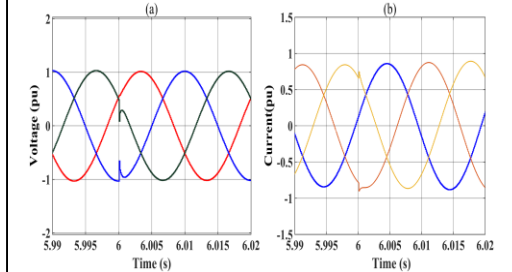
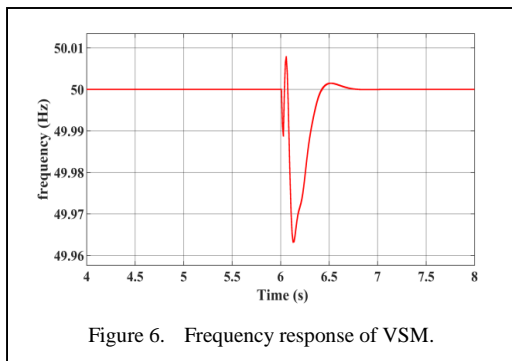


Figure 5. Dynamic response of VSM (a) Voltage, (b) Current.

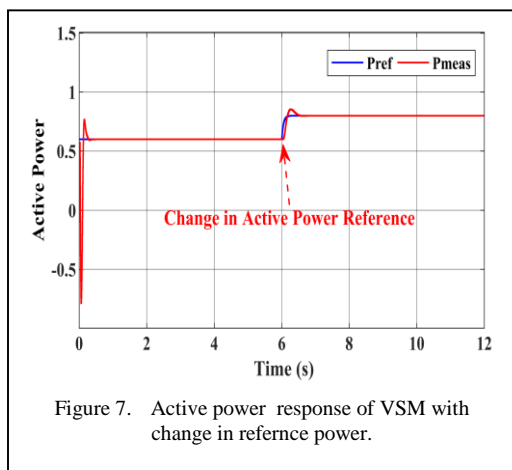


A. Load Fluctuation

The simulation scenarios are mainly carried out when the load power is disturbed (Fig. 6).

B. Change in Active Power Reference

The response of VSMs to changes in the power reference is determined by their assessment of inertial dynamics. The ability of the VSM to accommodate this change is influenced by its inertia constant and damping coefficient when the power reference changes. The tracking capabilities may be driven more slowly by higher emulated inertia, making effective control of the power flow more difficult. Fig. 7 shows the power response to a reference step change. At the beginning of the simulation, the active control power is 0.6 pu. When $t = 6$ s, the active control power increases from 0.6 pu to 0.8 pu. The results demonstrate that the system meets the established dynamic response specifications and that the grid converter is able to supply power almost immediately even if the active power reference is changed.



C. Effects of Changing the Damping Coefficient

The damping coefficient (K_p) plays a vital role in the stability of virtual synchronous machines (VSMs), as it evaluates their ability to ensure damping and improve grid stability.

According to research, it has been shown that increasing the damping coefficient has a negative impact on the dynamic response of the GFM converter, resulting in slower recovery after disturbances. From the simulation results, it is clear that the damping parameters and the output power stabilization speed after faults are related.

For a VM set with the same inertia constant ($T_a = 1pu$) but different damping coefficient (1.055, 2.03, 3.5), a comparison (Fig. 9) illustrates the different response

The response of the GFM converter is slower when the damping coefficient is higher (see Figs. 9 and 10).

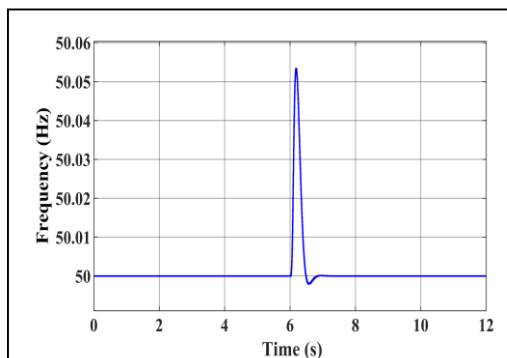


Figure 8. Frequency response of VSM with change in active power reference.

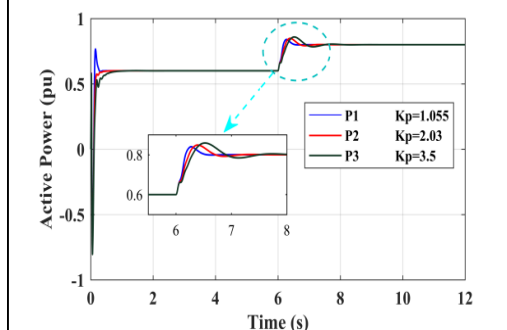


Figure 9. Active power response of VSM under different damping coefficients K_p .

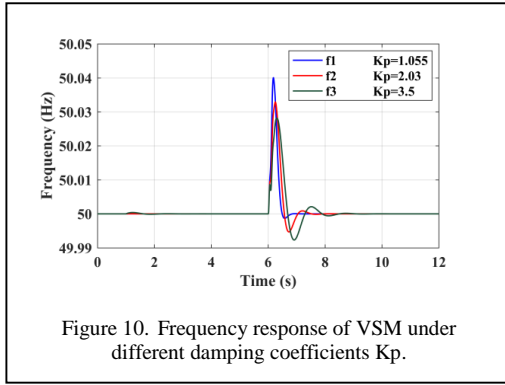


Figure 10. Frequency response of VSM under different damping coefficients K_p .

It is therefore possible to obtain a different damping by simply changing the design inputs. The consequences of the damping ratio when an active power reference changes immediately. The higher the damping coefficient, the slower the response of the GFM converter.

According to Figs. 9 and 10, using a fixed damping coefficient, the decrease in virtual inertia results in a reduction in active power overshoot and a short settling time. However, this decrease results in an increase in the frequency deviation.

However, this decrease is accompanied by an increase in the frequency difference. According to Fig. 3, when the virtual inertia is stable, an increase in the damping coefficient results in a reduction in the active power overshoot, a decrease in the adjustment time, and a reduction in the frequency deviation.

D. Effects of Changing the Inertia Constant

The study shows that virtual inertia is crucial to regulate the oscillation frequency during the dynamic response of virtual synchronous machines (VSMs). By modifying the imitated inertia in VSM control strategies, power systems have the potential to significantly improve their

TABLE III. SYSTEM ANALYSIS RESULT UNDER DIFFERENT DAMPING COEFFICIENT (FREQUENCY).

Damping Coefficient	Nadir (Hz)	Settling time(s)
1.055	50.04	0.78
2.03	50.032	1.52
3.5	50.027	1.92

transient behavior with respect to frequency stability. The response of a virtual synchronous machine (VSMs) to frequency disturbances and the oscillation frequency characteristic of its inertial dynamics are directly influenced by the inertia constant (T_a) (Figs. 11 and 12).

According to the results, it is possible to modify the dynamics of the regulator converters to adjust to the fluctuations of power conditions, which improves the transient response of the microgrid frequency. By modifying the inertia emulation in the control strategy, the frequency stability can be improved under various power scenarios.

TABLE IV. SYSTEM ANALYSIS RESULT UNDER DIFFERENT VIRTUAL INERTIA (FREQUENCY).

T_a (s)	Nadir (Hz)	Settling time (s)
1s	50.053 Hz	0.8
3s	50.058 Hz	1
5s	50.0585 Hz	2
8s	50.056 Hz	3

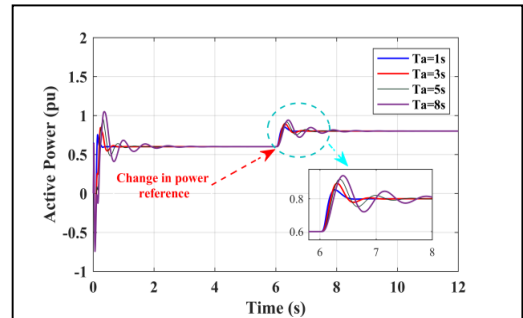


Figure 11. Active power response of VSM under different virtual inertia (T_a).

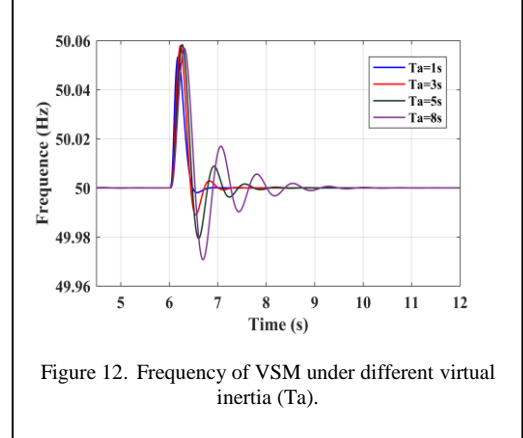


Figure 12. Frequency of VSM under different virtual inertia (T_a).

VI. CONCLUSION

Indeed, it is possible to impose the dynamics of the regulator converters of virtual synchronous machines (VSMs) according to the power conditions in order to improve the transient behavior of the microgrid frequency. This adaptability is mainly achieved by adjusting the imitated inertia in the control strategy. A change in the power reference of a VSM can have a significant impact on its damping effect and overall performance. The damping coefficient plays a crucial role in GFM converters, as it directly impacts their ability to maintain synchronization.

It is crucial to adopt an adequate tuning and adaptively control the damping coefficient in order to ensure stability and avoid any loss of synchronism, especially under variable grid conditions. The dynamic response of VSMs is influenced by the inertia constants and damping coefficients, which are essential parameters during instantaneous changes of the active power references. Oscillatory responses are caused by higher inertia constants, while damping coefficients impact the rate at which these oscillations attenuate. It is essential to properly manage the interaction between these factors in order to ensure reliable and stable operation of contemporary power grids.

According to the analysis, the oscillation frequency during the dynamic response of the VSM is regulated by the virtual inertia, while the damping coefficient defines the attenuation rate of the oscillation process.

REFERENCES

- [1] Amenedo, J. L. R., Gomez, S. A., Alonso-Martinez, J., & De Armas, M. G. (2021). Grid-forming converters control based on the reactive power synchronization method for renewable power plants. *IEEE Access*, 9, 67989–68007.
- [2] D'Arco, S., & Suul, J. A. (2013, June 1). Virtual synchronous machines—Classification of implementations and analysis of equivalence to droop controllers for microgrids. *PowerTech Conference Proceedings*.
- [3] Beck, H.-P., & Hesse, R. (2007, October 1). Virtual synchronous machine. In *Proceedings of the 9th International Conference on Electrical Power Quality and Utilisation*. <https://doi.org/10.1109/EPQU.2007.4424220>
- [4] Alassi, A., Feng, Z., Ahmed, K., Syed, M., Egea-Alvarez, A., & Foote, C. (2023). Grid-forming VSM control for black-start applications with experimental PHIL validation. *International Journal of Electrical Power & Energy Systems*, 151, 109119.
- [5] Gonzalez-Cajigas, A., Roldan-Perez, J., & Bueno, E. J. (2022). Design and analysis of parallel-connected grid-forming virtual synchronous machines for island and grid-connected applications. *IEEE Transactions on Power Electronics*, 37(5), 5107–5121.
- [6] Lu, C., & Zhuan, X. (2024). Adaptive control for virtual synchronous generator parameters based on soft actor critic. *Sensors*, 24(7), 2035–2035.
- [7] Miao, H., Mei, F., Yang, Y., Chen, H., & Zheng, J. (2019). A comprehensive VSM control strategy designed for unbalanced grids. *Energies*, 12(6), 1169.
- [8] Davenport, T. H., De Long, D. W., & Beers, M. C. (1998). Successful knowledge management projects. *MIT Sloan Management Review*, 39(2), 43.
- [9] Qoria, T., Gruson, F., Colas, F., Denis, G., Prevost, T., & Guillaud, X. (2020). Critical clearing time determination and enhancement of grid-forming converters embedding virtual impedance as current limitation algorithm. *IEEE Journal of Emerging and Selected Topics in Power Electronics*, 8(2), 1050–1061.
- [10] Barac, B., Krpan, M., Capuder, T., & Kuzle, I. (2021). Modeling and initialization of a virtual synchronous machine for power system fundamental frequency simulations. *IEEE Access*, 9, 160116–160134.
- [11] Tripathi, S. M. (n.d.). Real-time simulation and hardware-in-the-loop testing using Typhoon HIL. *Springer Nature*
- [12] D'Arco, S., Suul, J. A., & Fosso, O. B. (2013). Control system tuning and stability analysis of Virtual Synchronous Machines. *IEEE Xplore*, 2664–2671.

Enhancement of Microchannel Heat Sink by Introducing Double-layer Microchannel, Truncated Microchannel and Multi-layer Microchannel Heat Sinks having Various Flow Channel Structures: An Overview

Dipak Debbarma¹, K. M. Pandey², Abhishek Paul³, Sunita Debbarma⁴

¹Tripura Institute of Technology, Agartala, Tripura, India

^{2,3}National Institute of Technology, Silchar, Assam, India

⁴Women's Polytechnic, Agartala, Tripura, India

¹dipakdb.2003@gmail.com, ²kmpandey2001@yahoo.com

Abstract—The appropriate structure of micro heat sink and geometry of channel passage have significant role in increasing cooling rate in electronics compact components amongst the passive enhancement techniques. Enhancement of heat dissipation at considerable pumping power penalty is the challenge for the researchers. Attachment of rib, protrusion, porous section into flow-channel and subtraction by bringing in cavity, dimple, groove on channel wall should be performed by maintaining optimum parameters. Because in most cases of investigations, it is perceived that enhancement of performance of microchannels is possible by virtue of certain pumping loss. This paper is presenting the overview of the available literatures on such relevant research works. Intermixing of fluid layers, interception of boundary layer by introduction of rib, protrusion, porous section, cavity, dimple, groove, waviness in flow channel enhance performance deliberately in microchannel heat sink (MCHS). In one of such studies, maximum Nu/Nu_o of 2.12 was evaluated at $Re = 589$ by using fan cavity & circular rib. Researchers articulated that more cooling and better overall performance are possible by introducing double layer microchannel since top channel coolant cools the exit fluid of bottom channel. The appropriate channel structures in truncated and multilayer microchannel heat sinks

also provide better parameters such as low bottom wall temperature, low heat resistance etc.

Keywords - cavity, protrusion, secondary flow, thermal resistance, Nusselt number

I. INTRODUCTION

The ever-changing evolution of technology needs miniaturized and capable electronics devices in our present world in the context of domestic as well as industrial applications. Cooling of such micro-scale devices with suitable capacity rate is the real challenge today. After the novel experimental research work of [1] introducing the micro sink four decades ago, microchannel became the attractive means for the cooling of IC products and hence several investigations have been carried out by many researchers. Smaller the hydraulic diameter higher the heat transfer coefficient in a channel [2] is significant fundamental concept behind the use of microchannel. Small volume, but bigger surface area of micro-channels makes the micro heat sink advantageous, but more additional efficient features of parallel channels in the heat sink are required to meet present challenges. For the example, the temperature of laptop CPU, must be maintained below 90 °C in order to prevent it from damage [3]. Reference [4]



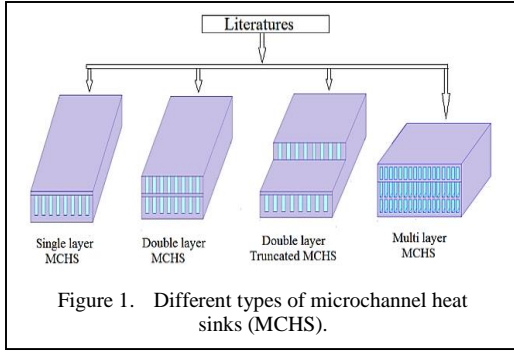


Figure 1. Different types of microchannel heat sinks (MCHS).

highlighted that heat dissipation by 177 mm^2 die of Intel core processor produced by Intel in 2014 was 88 W and the heat flux of future computers could reach 2 MW/m^2 by 2026.

Therefore, various mechanisms and techniques are predicted by the researchers for the purpose of enhancing micro sink. The researchers in the last four decades introduced innovative design and techniques to increase the removal of the heat generated in such devices. Numerous investigations were performed on the single layer micro sinks with the rectangular channel. Among the works, some were based on different channel shapes and others were on various channel wall structures, employment of cavity, rib, protrusions etc., into the channels. The effect estimation of substrate materials such as aluminum, copper, silicon, brass, steel was also part of few investigations. In many studies different nanofluids as coolant were used. After the new micro sink with double layer [5] came into existence in 1997, investigational works started on this kind of novel heat sink to a large extent.

Most of the studies have been performed on channel of rectangular cross-section comparing to circular, triangular, trapezium channel. In the various research investigations such as [6], it was concluded that rectangular microchannels have advantages over circular microchannels in context of thermal as well as hydro performances in the micro heat sink domain. Because larger surface area, higher surface to volume ratio of rectangular microchannel lead to better performance results. In contrary, [7] using genetic algorithm reported that for a minimized thermal resistance, the circular channel shows better performance than the square channel; it might be due to different design conditions applied for study.

This review work covers the investigational reports on rectangular micro sinks available in

the literatures based on single-phase and forced convective flow to assess the parameters such as Nu/Nu_o , f/f_o , thermal factor etc. and to find the efficient constructional design of microchannel. Literatures on single layer microchannel heat sink (S-MCHS) [1-19], double layer microchannel heat sink (D-MCHS) [5,20-52], double layer truncated microchannel heat sink (D-T-MCHS) [53-58], multilayer microchannel heat sink (M-MCHS) [59-64] are reviewed in this work and comprehensive comparisons among the different microchannel heat sinks are made. Performance evaluation of all heat sink designs as proposed by the researchers are carried out and the relevant data are also presented. Fig. 1 shows different types of such MCHS.

II. INVESTIGATIONAL PROCEDURE

Investigating the micro-scale devices is challenging and undertaking experiment is more challenging. In case of experimental study, accuracy during fabrication of microchannel, setting up of whole arrangement, measurement of data is to be maintained. Reference [8] addressed the experimental uncertainties which can become quite large due to complication in measurement in microchannel heat exchanger. Simulation i.e. numerical analysis is widely adopted by the researchers in this heat sink domain now-a-days due to high cost involved in experimental work. However, opting viable assumptions, mathematical equations along with suited numerical method are the factors which lead to the authentic results in Simulation. In some of the investigations, analytical method is utilized to evaluate the flow in channel. In experimental work, fabrication of micro sink is the key part. Both additive and subtractive i.e., etching fabrication technologies are widely available for the purpose [9]. Most of the investigations experimental or numerical on

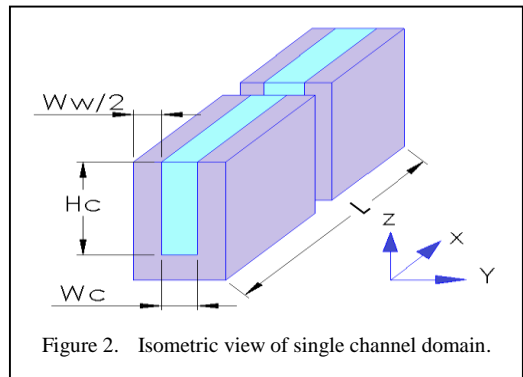


Figure 2. Isometric view of single channel domain.

micro heat sink are based on the conjugate heat transfer model. Like other researchers, [3] suggested that solid axial heat conduction should not be neglected for study of parallel channels of microchannels.

III. ASSOCIATED EQUATIONS

The conservation equations of momentum and energy do apply to microchannel study as the general equations. The associated equations along with general equations are applicable in microchannels similar to the conventional channels for Knudsen numbers below 0.001 as stated by [10]. Fig. 2 depicts isometric view of single channel domain. Channel height (H_c), channel width (W_c) and half of solid substrate thickness (W_w).

The Reynolds number (Re):

$$Re = \rho u_m d_h / \mu. \quad (1)$$

The hydraulic diameter (d_h):

$$d_h = 2W_c H_c / (W_c + H_c). \quad (2)$$

The average friction factor (f):

$$f = (2\Delta p d_h) / (\rho u_m^2 L). \quad (3)$$

Nusselt number (N_u):

$$N_u = h d_h / k. \quad (4)$$

The average heat coefficient (h) is written as:

$$h = q A_b / A_{con} (T_b - T_{int}). \quad (5)$$

The thermal enhancement factor (η) or performance evaluation criteria (PEC)

$$\eta = (N_u / N_{u_0}) / (f / f_0)^{(1/3)}. \quad (6)$$

Thermal resistance or heat resistance:

$$R_{th} = \Delta T_{max} / Q_{b,total}. \quad (7)$$

In the investigations, heat transfer coefficient R_{th} , bottom temperature was estimated and compared by the early researchers. Afterwards, investigators used more effective parameters for evaluation such as f, N_u friction factor ratio, Nusselt number ratio. Since 2010, investigators

emphasized on the parameter called thermal enhancement factor (η) which signifies the enhancement of N_u of the novel microchannel considering corresponding friction in comparison to that of simple straight microchannel.

IV. SINGLE-LAYERED MICRO CHANNEL HEAT SINKS

The extensive investigations on the single layer microchannel heat sink recommend various effective design structures with suitable parameters. Q_u and [11] performed experiment on micro-sink made of copper to determine the applicability of conservation equations in micro-channel heat sinks. Reference [12] varied the aspect ratio of the channel from 1 to 10 to calculate the local as well as average N_u with the applied heat flux on all external boundaries of channel. They proposed correlation of Nusselt number considering N_u as a function of aspect ratio and axial distance. Reference [13] simulated plain and U -shaped microchannels by varying the number of channels and some parameters of channel. Heat sinks with different channel cross sections were compared by Reference [14]. The geometrical parameters like height and width of these shapes of channel were evaluated. They revealed that the rectangular microchannel was the best, followed by trapezoidal and triangular shaped microchannels. Fig. 3 shows single layer sink (S-MCHS).

Single layer microchannel heat sink (S-MCHS) is shown by Fig. 3. Interception of fully developed flow throughout the channel passage and inter-mixing different layers of flowing fluid are the major contribution of using cavity, dimple, rib etc. [15,16] investigated numerically the effects of cavity parameters of different shapes on heat transfer and visualized the fluid flow. They could observe strong impacts of cavities by predicting the best configuration which exhibited heat transfer enhancement factor

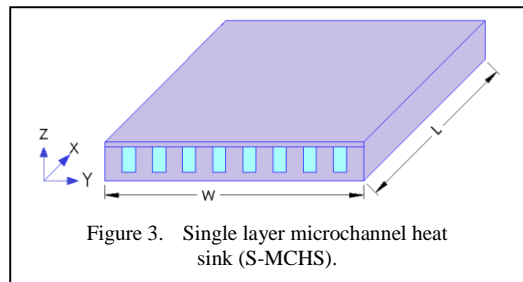


Figure 3. Single layer microchannel heat sink (S-MCHS).

(η) of 1.6. Reference [17] specially performed numerical analysis on heat sink with circular shaped cavity. Reference [18] in their experimental investigations assessed pressure drop, thermal characteristics for different cross sections of channel and received good agreement with numerical results. Reference [19] conducted study on triangular grooved channel.

V. DOUBLE-LAYERED MICRO CHANNEL HEAT SINKS

Up gradation of single layer heat sink towards double layer or stacked micro sink had been conceptualized by [5] in 1997. They described the unique feature of the double layered sink design and noted 5 °C as the maximum temperature rise. The new type of sink helped to lower temperature gradient by enabling the upstream coolant in top channel to cool downstream coolant in bottom channel [5]. Reference [20] compared the single and double layered micro sink numerically and analytically. Reference [21] applied the analytical method to study single and double layered microchannels with available correlations. They reported that the double layered microchannels exhibited low pressure drop which was the key finding of [5,20].

The Fig. 4 shows double layer heat sink (D-MHS). Works [22-25] suggested optimum parameters of stacked channel. Reference [26] like other investigators had reported the significant larger flow area in case of stacked layered sink. Reference [27] compared wavy single- and double-layer channels and estimated larger wave amplitude for maximum wall temperature reduction and higher N_u . In similar investigation, [28] studied the influence of counter and parallel flow for wavy channel. They interestingly noticed that superiority of counter flow or parallel flow was depending on the Re and volumetric flow ratio. They revealed that parallel flow shows higher N_u at low R_e and it was opposite at larger R_e . The counter flow had

superior N_u at higher volumetric flow ratio. Reference [29] studied parallel and counter flow for staggered arrangement. The counter flow of the staggered one having both inlets set on upper channel showed the highest heat transfer coefficient. In the slightly different work, [30] took novel structures having staggered flow alternation. They made flow alternation five times and lesser. The single alternated, staggered channel with counter stream showed better overall convective thermal performance. Reference [31] was an extension work of Reference [30]. Three models with single alteration were investigated to measure N_u , pressure drop and thermal performance factor and the best model was proposed. Reference [32] compared plain staggered and wavy staggered double layer channels. They ascertained that plain staggered channel contributed higher thermal performance considering pressure penalty than wavy one. Performance variation for different width ratio, aspect ratio, and flow rate was studied by [33-35] assessed 14 cases of single and stacked channels. From thermal resistance and temperature uniformity's point of view, D-MHS was found superior than S-MHS for same mass flow rate. Reference [36] performed experiments on rectangular and triangular heat sink of aluminum substrate using nanofluids.

Extensive comparisons were made between single- and double-layer heat sinks having different channel heights, wall-mounted cavity, ribs through the investigation of [37-39]. Reference [40] investigated heat sink by field synergy principle. Reference [41] conducted numerical study to evaluate impacts of flow pattern. In another investigation, [42] considered tapered and converging channel. The result suggested that taper channel had signified better thermal performance in comparison to simple straight channel at the cost of higher pumping power. Reference [43] employed optimization method to predict the best performance of heat sinks and noted an optimal channel with maximum bottom wall temperature change of 3.23 [44] optimized the geometry of channel for different values of power and coolant mass flow. The analysis suggested a lowest thermal resistance of 0.089 K/W. Transverse flow had been studied by [45]. The effects of flow direction were compared. Heat sink was simulated with large heat flux of 556W/cm² and optimized by [46].

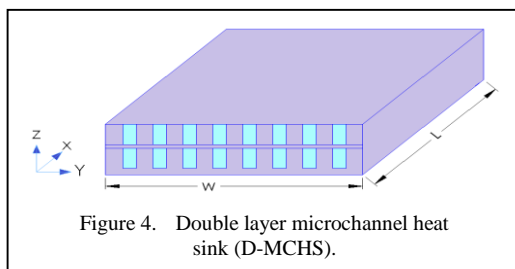


Figure 4. Double layer microchannel heat sink (D-MCHS).

In the investigation of [47] performances of the porous D-MHS had been improved for certain porous material. Reference [48] reported that the suitable combination of lower pressure drops of porous ribs and better conductivity of solid helped in improvement of performance for a double-layer sink. They recommended an improved model comprising lower channel of solid copper ribs and upper layer of porous ribs. Their analysis showed that thermal resistance was reduced by 11% whereas temperature uniformity was enhanced by 56%. It was opined by [49] that pumping power was reduced remarkably, for the porous heat sink. Reference [50] optimized design parameters of stacked channel. Reference [51] realized that pumping power was inversely proportional to the increase of heat flux. As they detailed, it had occurred since fluid viscosity decreases with increase of heat flux. Reference [52] introduced new concept of applying phase change material (PCM) slurries into double layer channel which found to be advantageous in improving cooling performance.

As per the articulation of researchers the pressure loss of D-MCHS is lesser than that of S-MHS for same volume flow rate, same channel size. Bottom temperature of D-MCHS is also lesser than that of S-MCHS for same volume flow rate as observed in the literatures.

VI. DOUBLE-LAYER MICRO HEAT SINKS WITH TRUNCATED TOP CHANNEL

The advantageous feature of truncated top channel was unveiled by [53]. The top channels were truncated at their outlet position so that fluid coolant at inlet of lower channel didn't get affected by the heat of coolant of upper channel in case of counter flow. Reference [54] applied the optimization technique on the same heat sink

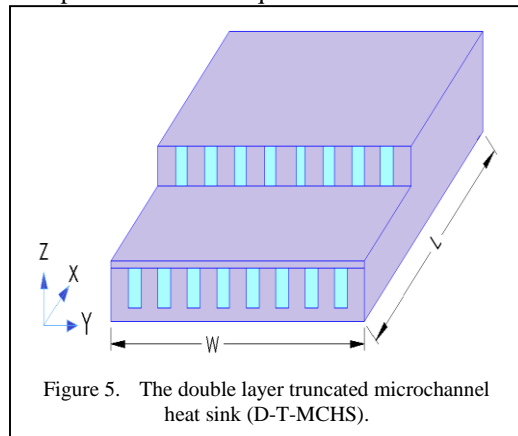


Figure 5. The double layer truncated microchannel heat sink (D-T-MCHS).

of [53]. To minimize the overall heat resistance, improved sink with converging channels was suggested by [55] where the temperature distribution, heat resistance and required power were obtained for different flow rates and convergence angles. The double-layer truncated micro sink is presented in Fig. 5.

Reference [56] proposed double layered truncated channel with new channel shape. They applied optimization algorithm to study the effects of few design variables. They noticed, optimum design was showing the PEC with 38 % hike. Reference [57] incorporated carbon nanofluids as coolant in truncated microchannel and unveiled good results. Reference [58] applied optimization scheme on truncated model and ascertained that the thermal performance as high as 1.38 could be obtained for the optimum design.

VII. MULTI-LAYERED MICRO CHANNEL HEAT SINKS

Advantages of DL-MCHS convinced the researchers to assess multilayer channel. The multilayer microchannels were studied by both numerical and analytical methods in the work of Reference [59]. Results showed that increase of the layer effectively reduced the overall resistance and increase of layers above four or five was not favorable. Reference [60] also verified the influence of layers. Their findings were identical to that of [59]. The reason is that conduction resistance increases with more layers. Reference [61] too performed work to predict the number of layers best suited for heat sink. They took same range of mass flow rates varying the layers of heat sinks. Not conflicting with other author's result, they concluded that the pressure drop had been reduced with more layers. Since more the layers, lesser the flow is for individual channel. For the three-layer case enhancement was reduced noticeably. They also added their view that parameters of multi-layer channel must be optimized to enhance their performance. Reference [62] studied the scale variation in multi-layered heat sink. They correlated the porosity scaling parameter with improvement of performance. Reference [63] optimized the size of multi-layer heat sink and validated their results by simulation. Reference [64] compiled the findings of various research works based on double-layer and multi-layer. They pointed out that multi-layer sink caused thermal resistance reduction from 6% to 97%.

TABLE I. RESULTS OF SOME STUDIES ON MICROCHANNEL HEAT SINKS AS OBTAINED IN DIFFERENT LITERATURES.

Author & Study details	Important parameters	Findings & Best Result
[30,15]	For fan shaped cavity: $R_e=132-931$ Silicon sink with water as coolant	Highest $\eta = 1.53$ Corresponding $N_u/N_{no} = 1.6$ & $f/f_o = 1.17$, $\Delta P=23\text{kPa}$ $R_e = 529$
[31,16]	For Triangular cavity: $R_e = 201-1015$ Silicon sink with water as coolant	Highest $\eta = 1.54$ Corresponding $N_u/N_{no} = 1.76$ $f/f_o = 1.43$, $R_e=1015$
[32,17]	For fan shaped cavity: Flow rate and heat flux : varied, $R_e=100-900$ Silicon sink with water as coolant	Highest $N_u/N_{no} = 1.39$ Corresponding $R_e = 841$
[33,18]	Fan-shaped cavity, triangular-shaped cavity: used, Mass flux of 832.17–5825.1 kg/(m ² s). $R_e=100-800$, Silicon sink with water as coolant	Highest $N_u = 13.81$ $N_u/N_{no} = 1.85$ Corresponding $R_e = 807$
[34,19]	For Triangular cavity: $R_e=266, 532$, and 798 Silicon sink with water, ethylene glycol, engine oil & nano particles	Highest $\eta = 1.63$ Corresponding $N_u/N_{no} = 2.13$ CuO ($\phi = 0.04$), $R_e = 798$
[42]	For fan shaped cavity: Flow rate: varied $R_e=230-650$ Silicon sink with water as coolant	1. Maximum thermal enhancement factor =1.24 at $R_e=611$ 2. Total thermal resistance is reduced by 18% at 0.44 K/W. 3. The pumping power is reduced 18.99%.

VIII. CONCLUSION

The beneficial impact of flow disturbance by the application of wavy, groove, cavity, dimple, rib and protrusions are subject to suitable fluid mixing and breaking up of boundary layer inside the flow passages of channel. The groove, cavity, dimple attribute towards flow expansion, recirculation whereas rib and protrusions implicate throttling mechanism i.e. constriction. Combination of such expansion and throttling passages into channel in view of developing performance augmentation has shown significant result.

The high temperature gradient hampers device reliability due to undesirable thermal stresses in chips materials [5] and double layered sink overcomes this demerit. Researchers articulated that pressure drop of D-MCHS is lower than that of S-MCHS for same volume flow rate, same channel size. Thermal resistance and bottom wall temperature of D-MCHS are also lower than that of S-MCHS for same volume flow rate as observed in the studies. The heat resistance as low as 0.017 K/W [27] and

maximum bottom wall temperature difference as small as 1.08 °C [40] could be achieved by D-MCHS. The growing interest in such heat sinks indicates that research in this area is still developing.

The double layer sink with truncated top channel is another impressive design due to the fact that fluid coolant at inlet of lower channel doesn't get affected by the heat of coolant of upper channel.





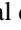

REFERENCES

- [1] Tuckerman, D. B., & Pease, R. F. W. (1981). High-Performance Heat Sinking for VLSI. *IEEE Electronic device letters*, 2(5), 126-129.
- [2] Collins L., Weibel, J. A., Pan, L., & Garimella, S. V. (2019). A permeable-membrane microchannel heat sink made by additive manufacturing. *International Journal of Heat and Mass Transfer*, 131, 1174–1183.
- [3] Rosa, P., Karayiannis T. G., & Collins, M. W. (2009). Single-phase heat transfer in microchannels: The importance of scaling effects. *Applied Thermal Engineering*, 29, 3447–3468.
- [4] Karayiannis, T. G., & Mahmoud, M. M. (2017). Flow boiling in microchannels: Fundamentals and applications. *Applied Thermal Engineering*, 115, 1372–1397.
- [5] Vafai, K., & Zhu, L. (1999). Analysis of two layered microchannel heat sink concept in electronic cooling. *International Journal of Heat and Mass Transfer*, 42, 2287-2297.
- [6] Liu N., Li J. M., Sun J., & Wang, H. S. (2013). Heat transfer and pressure drop during condensation of R152a in circular and square microchannels. *Experimental Thermal and Fluid Science*, 4760–67.
- [7] Ghazali-Mohd, N., Jong-Taek, O., Chien, N. B., Kwang-II, C., & Ahmad, R. (2015). Comparison of the optimized thermal performance of square and circular ammonia-cooled microchannel heat sink with genetic algorithm. *Energy Conversion and Management*.
- [8] Steinke M. E., & Kandlikar S. G. (2006). Single-phase liquid friction factors in microchannels. *International Journal of Thermal Sciences*, 45, 1073–1083.
- [9] Kandlikar, S. G., & Grande, W. J. (2003). Flow Passages-Thermohydraulic Performance and Fabrication Technology Evolution of Microchannel. *Heat Transfer Engineering*, 24(1), 3–17.
- [10] Kandlikar, S. G., & Grande, W. J. (2003). Evolution of Microchannel Flow Passages-Thermohydraulic Performance and Fabrication Technology. *Heat Transfer Engineering*, 24(1), 3–17.
- [11] Qu, W., & Mudawar, I. (2002). Experimental and numerical study of pressure drop and heat transfer in a single-phase micro-channel heat sink. *International Journal of Heat and Mass Transfer*, 45, 2549–2565.
- [12] Lee, P. S., & Garimella, S. V. (2006). Thermally developing flow and heat transfer in rectangular microchannels of different aspect ratios. *International Journal of Heat and Mass Transfer*, 49, 3060–3067.
- [13] Zhang, J., Lin, P. T., & Jaluria, Y. Design and Optimization of Multiple Microchannel Heat Transfer

- Systems. *Journal of Thermal Science and Engineering Applications*, 6 011004.
- [14] Gunnasegaran, P., et al. (2010). The effect of geometrical parameters on heat transfer characteristics of microchannels heat sink with different shapes. *International Communications in Heat and Mass Transfer*, 37, 1078–1086.
- [15] Xia, G. D., Chai, L., Zhou, M., & Wang, H. (2011). Effects of structural parameters on fluid flow and heat transfer in a microchannel with aligned fan-shaped reentrant cavities. *International Journal of Thermal Sciences*, 50, 411–419.
- [16] Xia, G. D., Chai, L., Wang, H., Zhou, M., & Cui, Z. (2011). Optimum thermal design of microchannel heat sink with triangular reentrant cavities. *Applied Thermal Engineering*, 31, 1208–1219.
- [17] Chai, L., Xia, G. D., Zhou, M., & Li, J. (2011). Numerical simulation of fluid flow and heat transfer in a microchannel heat sink with offset fan-shaped reentrant cavities in sidewall. *International Communications in Heat and Mass Transfer*, 38, 577–584.
- [18] Chai, L., Xia, G. D., Wang, L., Zhou, M., & Cui, Z. (2013). Heat transfer enhancement in microchannel heat sinks with periodic expansion–contraction cross-sections. *International Journal of Heat and Mass Transfer*, 62, 741–751.
- [19] Kuppusamy, N. R., Mohammed, H. A., & Lim, C. W. (2014). Thermal and hydraulic characteristics of nanofluid in a triangular grooved microchannel heat sink (TGMCHS). *Applied Mathematics and Computation*, 246, 168–183.
- [20] Vafai, K., & Khaled, A. R. A. (2005). Analysis of flexible microchannel heat sink systems. *International Journal of Heat and Mass Transfer*, 48, 1739–1746.
- [21] Chong, S. H., Ooi, K. T., & Wong, T. N. (2002). Optimisation of single and double layer counter flow microchannel heat sinks. *Applied Thermal Engineering*, 22, 1569–1585.
- [22] Hung, T. C., Yan, W. M., & Li, W. P. (2012). Analysis of heat transfer characteristics of double-layered microchannel heat sink. *International Journal of Heat and Mass Transfer*, 55, 3090–3099.
- [23] Hung, T. C., Sheu, T. S., & Yan, W. M. (2012). Optimal thermal design of microchannel heat sinks with different geometric configurations. *International Communications in Heat and Mass Transfer*, 39, 1572–1577.
- [24] Hung, T. C., Yan, W. M., Wang, X. D., & Huang, Y. X. (2012). Optimal design of geometric parameters of double-layered microchannel heat sinks. *International Journal of Heat and Mass Transfer*, 55, 3262–3272.
- [25] Hung, T. C., & Yan, W. M. (2012). Enhancement of thermal performance in double-layered microchannel heat sink with nanofluids. *International Journal of Heat and Mass Transfer*, 55, 3225–3238.
- [26] Xie, G., Liu, Y., Sunden, B., & Zhang, W. (2013). Computational Study and Optimization of Laminar Heat Transfer and Pressure Loss of Double-Layer Microchannels for Chip Liquid Cooling. *Journal of Thermal Science and Engineering Applications*, 5, 011004.
- [27] Xie, G., Chen, Z., Sunden, B., & Zhang, W. (2013). Predictions of the Flow and Thermal Performance of Water-Cooled Single-Layer and Double-Layer Wavy Microchannel Heat Sinks. *Numerical Heat Transfer, Part A*, 63, 201–225.
- [28] Xie, G., Chen, Z., Sunden, B., & Zhang, W. (2013). Comparative study of the flow and thermal performance of liquid-cooling parallel-flow and counter-flow double-layer wavy microchannel heat sinks. *Numerical Heat Transfer, Part A*, 64, 30–55.
- [29] Shen, H., Zhang, Y., & Yan, H. (2018). Convective heat transfer of parallel-flow and counter-flow double-layer microchannel heat sinks in staggered arrangement. In *Proceedings of the ASME 2017. International Mechanical Engineering Congress and Exposition*, USA.
- [30] Shen, H., Xie, G., & Wang, C. C. (2019). Heat transfer and thermodynamic analysis by introducing multiple alternation structures into double-layer microchannel heat sinks. *International Journal of Thermal Sciences*, 145, 105975.
- [31] Shen, H., Xie, G., & Wang, C. C. (2019). The numerical simulation with staggered alternation locations and multiflow directions on the thermal performance of double-layer microchannel heat sinks. *Applied Thermal Engineering*, 163, 114332.
- [32] Shen, H., Zhang, Y., Wang, C. C., & Xie, G. (2018). Comparative Study for Convective Heat Transfer of Counter-Flow Wavy Double-Layer Microchannel Heat Sinks in Staggered Arrangement. *Applied Thermal Engineering*.
- [33] Wu, J. M., Zhao, J. Y., & Tseng, K. J. (2014). Parametric study on the performance of double layered microchannels heat sink. *Energy Conversion and Management*, 80, 550–560.
- [34] Wei, X., Joshi, Y., & Patterson, M. K. (2007). Experimental and Numerical Study of a Stacked Microchannel Heat Sink for Liquid Cooling of Microelectronic Devices. *Journal of Heat Transfer*, 129, 1432–1444.
- [35] Levac, M. L. J., Soliman, H. M., & Ormiston, S. J. (2011). Three-dimensional analysis of fluid flow and heat transfer in single- and two-layered micro-channel heat sinks. *Heat Mass Transfer*, 47, 1375–1383.
- [36] Ahmed, H. E., Ahmed, M. I., Seder, I. M. F., & Salman, B.H. (2016). Experimental investigation for sequential triangular double-layered microchannel heat sink with nanofluids. *International Communications in Heat and Mass Transfer*.
- [37] Zhai, Y.L., Xia, G.D., Liu, X.F., & Wang, J. (2015). Characteristics of entropy generation and heat transfer in double-layered micro heat sinks with complex structure. *Energy Conversion and Management*, 103, 477–486.
- [38] Zhai, Y., Li, Z., Wang, H., & Xu, J. (2016). Analysis of field synergy principle and the relationship between secondary flow and heat transfer in double-layered microchannels with cavities and ribs. *International Journal of Heat and Mass Transfer*, 101, 190–197.
- [39] Zhai, Y., Xia, G. D., Li, Z., & Wang, H. (2016). A novel flow arrangement of staggered flow in double-layered microchannel heat sinks for microelectronic cooling. *International Communications in Heat and Mass Transfer*, 79, 98–104.

- [40] Zhai, Y., Li, Z., Wang, H., & Xu, J. (2017). Thermodynamic analysis of the effect of channel geometry on heat transfer in double-layered microchannel heat sinks. *Energy Conversion and Management*, 143, 431–439.
- [41] Wong, K. C., & Muezzin, F. N. A. (2013). Heat transfer of a parallel flow two-layered microchannel heat sink. *International Communications in Heat and Mass Transfer*.
- [42] Wong, K. C., & Ang, M. L. (2016). Thermal hydraulic performance of a double-layer microchannel heat sink with channel contraction. *International Communications in Heat and Mass Transfer*.
- [43] Leng, C., Wang, X. D., Wang, T.H., & Yan, W. M. (2015). Optimization of thermal resistance and bottom wall temperature uniformity for double-layered microchannel heat sink. *Energy Conversion and Management*, 93, 141–150.
- [44] Lin, L., Chen, Y. Y., Zhang, X. X., & Wang, X. D. (2014). Optimization of geometry and flow rate distribution for double-layer microchannel heat sink. *International Journal of Thermal Sciences*, 78, 158-168.
- [45] Ansari, D., & Kim, K. Y. (2016). Double-Layer Microchannel Heat Sinks with Transverse-Flow Configurations. *Journal of Electronic Packaging*, 138, 31005.
- [46] Shao, B. D., Wang, L., Cheng, H., & Li, J.(2012). Optimization and Numerical Simulation of Multi-layer Microchannel Heat Sink, *International Conference on Advances in Computational Modeling and Simulation. Procedia Engineering*, 31, 928–933.
- [47] Ghahremannezhad, A., Xu, H., Nazari, M. A., Ahmadi, M.H., & Vafai, K. (2019). Effect of porous substrates on thermohydraulic performance enhancement of double layer microchannel heat sinks. *International Journal of Heat and Mass Transfer*, 131, 52–63.
- [48] Li, X. Y., Wang, S. L., Wang, X. D., & Wang, T. H. (2019). Selected porous-ribs design for performance improvement in double-layered microchannel heat sinks. *International Journal of Thermal Sciences*, 137, 616–626.
- [49] Wang, S.L., Li, X.Y., Wang, X.D., & Lu, G. (2018). Flow and heat transfer characteristics in double-layered microchannel heat sinks with porous fins. *International Communications in Heat and Mass Transfer*, 93, 41–47.
- [50] Wang, T. H., Wu, H. C., Meng, J. H., & Yan, W. M. (2020). Optimization of a double-layered microchannel heat sink with semi-porous-ribs by multi-objective genetic algorithm. *International Journal of Heat and Mass Transfer*, 149, 119217.
- [51] Kulkarni, K., Afzal, A., & Kim, K. Y. (2016). Multi-objective optimization of a double-layered microchannel heat sink with temperature-dependent fluid properties. *Applied Thermal Engineering*.
- [52] Rajabifar, B. (2015). Enhancement of the performance of a double layered microchannel heat sink using PCM slurry and nanofluid coolants. *International Journal of Heat and Mass Transfer*, 88, 627–635.
- [53] Leng, C., Wang, X. D., & Wang, T. H. (2015). An improved design of double-layered microchannel heat sink with truncated top channels. *Applied Thermal Engineering*, 79, 54-62.
- [54] Leng, C., et al. (2015). Multi-parameter optimization of flow and heat transfer for a novel double-layered microchannel heat sink. *International Journal of Heat and Mass Transfer*, 84, 359–369.
- [55] Osanloo, B., Ahmar, A. M., Solati, A., & Baghani, M. (2016). Performance enhancement of the double-layered micro-channel heat sink by use of tapered channels. *Applied Thermal Engineering*, 102, 1345–1354.
- [56] Chamoli, Lu R., Chen, H., Cheng, Y., & Yu, P. (2019). Numerical optimization of design parameters for a modified double-layer microchannel heat sink. *International Journal of Heat and Mass Transfer*, 138, 373–389.
- [57] Arani, A. A. A., et al. (2017). Heat transfer improvement of water/single-wall carbon nanotubes (SWCNT) nanofluid in a novel design of a truncated double-layered microchannel heat sink. *International Journal of Heat and Mass Transfer*, 113, 780–795.
- [58] Shen H., Jin X., Zhang, Y., Xie, G., Sunden, B., & Yan, H. (2017). Computational optimization of counter-flow double-layered microchannel heat sinks subjected to thermal resistance and pumping power. *Applied Thermal Engineering*.
- [59] Saidi, M. H., & Khiabani, R. H. (2007). Forced Convective Heat Transfer in Parallel Flow Multilayer Microchannels. *Journal of Heat Transfer*, 128, 1230-1235
- [60] Wei, X., & Joshi, Y. (2004). Stacked microchannel heat sinks for liquid cooling of microelectronic components. *J. Electron. Packag.*, 126(1), 60-66.
- [61] Effat, M. B., Abdel Karim, M. S., Hassan, O., & Abdelgawad, M. (2016). Numerical investigations of the effect of flow arrangement and number of layers on the performance of multi-layer microchannel heat sinks. In *Proceedings of the ASME 2015. International Mechanical Engineering Congress and Exposition, IMECE2015, Texas*.
- [62] Hassell, B., & Ortega, A. (2016). An investigation of scale variation in multi-layer mini- and microchannel heat sinks in single phase flow using a two equation porous media model. In *Proceedings of the ASME. 2009, Heat Transfer Summer Conference, California USA*.
- [63] Shao, B., Wang, L., Cheng, H., & Li J. (2012). Optimization and Numerical Simulation of Multi-layer Microchannel Heat Sink. *International Conference on Advances in Computational Modeling and Simulation. Procedia Engineering*, 31, 928–933.
- [64] Lu, S., & Vafai, K. (2016). A comparative analysis of innovative microchannel heat sinks for electronic cooling. *International Communications in Heat and Mass Transfer*.

Exergy Analysis Applied to Cogeneration Systems: A Strategy for Energy Sustainability

Marcos Oliveira Lima¹, Alexandre Magno Vieira Gonçalves de Brito², Fazal Um Min Allah³
Daniel de Paula Diniz⁴, Antônio Carlos Cabral dos Santos⁵, Monica Carvalho⁶

^{1,2,3,4}Graduate Program in Mechanical Engineering, Federal University of Paraiba,
Joao Pessoa, Brazil

⁵Department of Mechanical Engineering, Federal University of Paraiba, Joao Pessoa, Brazil

⁶Department of Renewable Energy Engineering, Federal University of Paraiba, Joao Pessoa, Brazil

¹marcosoliveiralima0@gmail.com, ²alexandreh_magno@hotmail.com,
³fazaluminallah@cear.ufpb.br, ⁴danieldiniz@alumni.cear.ufpb.br,
⁵carloscabralsantos@yahoo.com.br, ⁶monica@cear.ufpb.br

Abstract—Population growth, coupled with economic and technological development, has contributed, over the years, to the increasing consumption of electrical energy needed to meet the demands of society. This study makes a Systematic Literature Review in order to comprehend the state of the art of the most recent discussions on exergetic analysis applied to cogeneration systems for industrial refrigeration. In 50% of the reviewed papers, an evaluation of a cogeneration system was present. In 30%, the usage of different coolant fluids is analyzed. In 20%, new configurations for cogeneration systems are proposed. Within the reviewed papers, it was observed that discussion focused on aspects related to improving operation, replacing low-efficiency components, substituting working fluids, and proposing/combining systems to achieve greater energetic, thermal, economic, and environmental efficiency.

Keywords – exergy analysis, cogeneration systems, energetic efficiency, environmental impact, energy efficiency, systematic review

I. INTRODUCTION

Population growth, coupled with economic and technological development, has been contributing, over the years, to the progressively ever-increasing consumption of electrical energy needed to meet the demands of human society [1].

Furthermore, the COVID-19 pandemic and the international instability regarding the Russo-Ukrainian war have further demonstrated the dependence *on* and increased usage *of* non-renewable energy sources in many nation-states. This situation puts pressure on their energy matrices, which struggle to meet the energy demands of their populations and industrial facilities [2].

Thus, there are implications related to environmental impacts associated with the heavy dependence on fossil fuels. Mitigation of such impacts pose a global challenge [3].

In this sense, the energy transition has brought technical solutions and technological improvements which have been applied to the efficient use of energy resources, enabling efficient and sustainable energy use alongside minimal environmental impacts [4]. To achieve this, the improvement of heat energy conversion systems, electrical energy systems, and refrigeration systems are among the advancements that stand out the most [5].

As highlighted by [6], in recent decades, the scarcity of fossil fuels and the environmental impact of their usage are leading researchers to explore alternative methods of efficient and environmentally sustainable energy conversion and utilization.



As a result, numerous studies feature cogeneration systems due to their favorable characteristics, such as: high thermodynamic performance, lower greenhouse gas emissions, and their cost-effective generation of thermal and electric energy [7].

According to [8], in various industrial settings, the application of exergy analysis of systems and their processes is considered important in the quest for higher energetic, economic, and environmental efficiency at industrial production operations. Thus, exergy analysis is a tool that can be used to evaluate the performance of refrigeration cycles by determining the magnitude and location of process irreversibilities, *i.e.*, losses of energy quality, and by assessing changes in operational process variables, with the aim of increasing efficiency and saving energy [9].

Thus, it is advantageous to make exergetic analyses as they enable greater scientific research possibilities. According to [10], exergetic analysis is recognized as the most effective method to assess the quality of energy flows, their conversion processes, and their rational usage. The same author suggests that exergy principles can also be employed to develop new methods that use energy resources more efficiently.

Indeed, cogeneration, also known as combined heat and power generation, is the simultaneous production of two forms of energy from a single fuel source. Furthermore, cogeneration plays a significant role in shaping the long-term prospects in global energy markets, mainly due to its numerous operational, environmental, and economic benefits [11]. Since the 1970s, cogeneration has been used to enhance the energetic efficiency of industrial production, including that of refrigeration systems [12].

The use of residual thermal energy may provide heat-related services, *e.g.*, heating rooms, providing hot water, as well as provide cold-related services, *e.g.*, cold storage rooms, refrigeration systems in automotive or pharmaceutical settings. Also, sugarcane and alcohol industries benefit from cogeneration systems [13].

Furthermore, there is also the issue of sustainability since there is worldwide concern about the environmental impacts of industrial production processes. The use of cogeneration,

as an efficient technology to reduce greenhouse gas emissions, benefits planet Earth. Hence, cogeneration, which relies on clean energy sources, is preferable [14].

According to [15], industrial refrigeration, specifically the cold chain, is responsible for significant energy demand, which then results in considerable environmental impact due to greenhouse gas (GHG) emissions. As a result, the investment in non-GHG-emitting energy sources grew substantially since the late 1980s, in the aftermath of the 1970s oil crisis. Such scenario led to a significant increase in the exploitation of energy sources from the wind, biomass, and solar energy matrices [16].

In light of the above, this study aims to conduct a Systematic Literature Review (SLR) in order to assess the state of the art regarding the most recent applications of exergetic analysis to cogeneration systems for industrial refrigeration. Thus, this SLR aims to map primary sources related to the following research question: “What is the state of the art regarding the application of exergetic analysis in electricity generation and industrial heating/refrigeration systems from 2017 to 2022?”.

For this purpose, this paper was organized as follows: Section II describes the methodology, including the inclusion/exclusion criteria for the selection of previous studies. Section III presents the main results and discusses the studies selected by the protocol defined at Section II. Finally, Section IV presents the conclusions of this SLR.

II. METHODOLOGY

To compile primary sources, it is necessary to establish a protocol for the systematic review process. This study uses the protocol established by [17]. Therefore, the scope of bibliographic search spanned publications from 2017 to 2022, with the aim of mapping the discussion on exergetic analysis applied to cogeneration systems for electricity generation, industrial heating, and refrigeration.

According to [18], the Systematic Review process is structured into the following stages: i) planning, ii) conducting, and iii) write-up and dissemination of the review results. This process should be followed with methodological rigor to ensure the alignment of several different papers being concatenated into a single systematic literature review work.

For the search for articles aligned with the research objective, the Scopus® database was used. Article selection was done exclusively in English. The search strings were: “cogeneration”, “exergy”, “industrial cooling”, “cold chambers”. Papers with only the abstract in English were disregarded.

For this SLR, only open access papers were considered. Only articles published from 2017 to 2022 were included were surveyed for contributions to the state-of-the-art exergetic analysis applied to cogeneration systems for industrial refrigeration.

The research also employed document type as a filter, including only scientific articles. Theses, dissertations, and other systematic review papers were not analyzed.

In addition, journals with an Impact Factor (JCR) less than 1 were removed from the analysis. In this way the SLR aims to map primary sources related to the research question: “What is the state of the art of exergetic analysis applied to cogeneration systems in electricity production and industrial refrigeration from 2017 to 2022?”.

III. RESULTS AND DISCUSSION

Results from queries to the Scopus® database, contained no duplicated papers. Papers with titles not aligned with the research question were not considered.

Subsequently, in a second stage of bibliographic selection, the papers’ abstracts were analyzed for indications of their relevance to the research question. The same procedure was further applied throughout the assessment of the introduction, methodology, and conclusion sections of each paper.

In the Scopus® database, a total of 75 documents were obtained by querying for the search strings at Section II and then applying the inclusion/exclusion criteria. From these 75, only 34 papers had, in their titles, key-words relevant to the research question. Subsequently, only open access papers were considered. Papers that could not be accessed were not considered. Then, there were 33 papers left.

Papers from journals with an Impact Factor (JCR) < 1 were, then, disregarded. Further, papers featuring second-hand research were disregarded, resulting in 29 primary sources. Subsequently, a review of the 29 abstracts found

9 studies that were not aligned with the research question. Their exclusion left 20 papers.

One paper featured only its abstract in English. It was disregarded. Thus 19 papers were further assessed throughout their introduction, methodology, and conclusion. Finally, at the last selection stage, after the full assessment, only 12 articles met the criteria established in this SLR.

Within the final selection, 3 studies were published in the “Applied Energy”, which has an Impact Factor (JCR) =11.30. The year with the most publications was 2020 with 5 papers, followed by 2022 and 2019 with 3 and 9 papers, respectively. Only 1 paper was published in 2018 and no papers were published in 2021.

In all of the 12 studies there are at least three authors or more. Only two studies feature an author in common. Thus, it is safe to assume that there is no saturation in the discussions regarding the topic. The final 12 papers encompass various methodologies related to the use of exergetic analysis as a tool to assess cogeneration systems and their potential from energetic, economic, and environmental perspectives.

Furthermore, out of the final 12 papers, only four were published in journals with an Impact Factor (JCR) < 3.

It is important to note that all of the studies featured in this SLR used exergetic analysis methodology as a tool for assessing the thermal and energy performance of cogeneration systems.

Within the final the 12 studies, the discussions were focused on three main branches: (i.) operational assessment of cogeneration systems; (ii.) efficiency assessment when using different cooling fluids; and (iii.) comparison between or proposals of new cogeneration systems for electricity generation and refrigeration.

As to the distribution of different perspectives of this SLR’s research question among each paper, the evaluation of cogeneration system operation was present in 50% of surveyed papers. Analyses of the usage of different refrigerants are present in 30%. The remaining 20% feature comparative studies and the proposal of new cogeneration system configurations.

These proportions are determined both quantitatively, through titles and keywords, and

qualitatively, by reading and fully analyzing the selected articles.

Each of the 12 papers is analyzed below in chronological order, according to its date of publication. Emphasis is given to every paper's research objective and result.

Reference [19] examines the potential of cogeneration for electricity generation and refrigeration, highlighting the importance of proposing a new type of cogeneration cycle. It introduces the usage of H_2O and NH_3 and compounds to analyze heat and mass transfer performance when the working fluid temperature is in the range between 200 °C and 360 °C. Further, the paper presents the usage of compound solvents for the cogeneration cycle implementation and analysis as a way of separating power generation and refrigeration performance. Results make it evident that, when compared to other sorption cycles for cogeneration of electricity and refrigeration, at similar heat source temperatures, the proposed reabsorption cycle exhibits exergetic efficiency $\approx 30\%$ higher than that of the H_2O/NH_3 sorption cogeneration cycle and twice as high as that of the basic reabsorption cogeneration cycle. The paper concludes that cogeneration systems can convert a primary energy source into different forms of energy, and, if such systems are well-designed and operated, they provide more electricity than in power plant architectures with separate electricity generation and heating systems. Thus, the paper establishes that cogeneration systems are more efficient than non-cogeneration systems.

Thermodynamic and exergetic analyses are introduced in [20] in the context of a cooling, heating, and electricity generation system that includes a solid oxide fuel cell and a single effect $LiBr$ (lithium bromide) absorption chiller. Results show that, as the airflow rate entering the system increases, the overall efficiency is reduced. This occurs due to an increase in the amount of work performed by the air compressor when cooling the fuel cell. Authors also noted that, with an increase in the airflow rates at the system's inlet, the exergy destruction rate is reduced, and the system's exergy loss rate is increased.

Energy and exergy analyses of a Steam Absorption Chiller (SAC), considered the main component of a cogeneration plant in the context of chilled water supply, are introduced in [21].

The cooling system's input is steam. The authors fitted the SAC within the PJ1 cogeneration plant, which features a double-effect $LiBr/H_2O$ cycle. Plant performance is monitored based on the Coefficient of Performance (COP), on the Exergetic Efficiency (ECOP), and on the Load Factor (LF) over a one-week period. The authors calculated system exergy destructions and the total exergy loss using an Excel® spreadsheet. Various operating conditions were analyzed, *i.e.*, several numeric values were tested for the steam inlet temperature, for the chilled water inlet temperature, and for the load factor. Results showed that the highest exergy destruction occurred in the high-temperature generator, followed by the absorber. An increase in the load factor, steam and chilled water inlet temperature raised the system's performance temperature.

Reference [22] discusses a scientific literature gap regarding configurations, reactants, and performance criteria for hybrid thermochemical cycles for cogeneration of electricity and refrigeration. Authors analyzed a solid/gas sorption refrigeration cycle coupled with a Rankine cycle. Three methods for coupling these cycles were devised. The combined cycle enables cogeneration of electricity and refrigeration with intrinsic energy storage. The methodology sought to investigate five performance criteria: required heat source temperature, energetic efficiency, exergetic efficiency, power production rate, and exergy storage density. Also, a large set of 103 reactant salts was analyzed. In conclusion, the authors compared each case of cycle coupling and usage of a reactant salt with respect to the performance criteria. Each case was characterized on the basis of how well it performs in several industrial applications.

Thermoeconomic analysis of a cogeneration cycle for was introduced in [23]. Authors used an H_2O/NH_3 solution as the working fluid and geothermal hot water as the heat source to achieve a combined electricity generation and refrigeration cycle. This system is a combines a modified Kalina Cycle (KC) for power generation and an Absorption Refrigeration Cycle (ARC) for cooling. Authors analyzed the system from both the thermodynamic and the economic perspectives using the Engineering Equation Solver® (EES) software package. Authors also conducted a parametric study to analyze the impact of changing the numeric values of certain decision parameters in the combined cycle performance. Results

demonstrate that, when comparing the combined cycle cogeneration system performance with that of its subsystems, the combination of the two subsystems resulted in less cost per energy unit. This holds even if the combined cycle energy output is compared to a situation where the same energy output is produced solely from the Kalina Cycle. Thermo-economic analyses show that the combined cycle features higher values for the total exergy destruction rate and for the total exergy destruction cost rate.

In the same research direction, [24] also introduces a cogeneration cycle for electricity generation combined with refrigeration. A double-effect organic Rankine cycle (ORC) is used to recover waste heat in a solid oxide fuel cell system connected to a gas turbine (SOFC-GT). Authors examine the proposed system from both the energy and from the exergy perspectives and apply economic cost balance equations to each component of the system to provide an economic/financial assessment of the SOFC-GT-ORC system. The plant's operation parameters are selected through a multi-objective optimization procedure based on an artificial neural network. The optimization algorithm assesses system performance for every given combination of two working fluids – one at each of the cycles being combined. Among 20 samples of different working fluid combinations, the combination of R601 (at the upper cycle) and ethane (at the lower cycle) is suggested as the optimum by the LINMAP algorithm. Thermo-economic analysis of the SOFC-GT-ORC system indicates that the cost of electricity production for the electric system results in \$33.2 per MWh. This is, respectively, 12.9% and 73.9% lower than the levelized cost of electricity for individual SOFC-GT and SOFC systems.

Reference [25] introduces the use of biomass in large-scale combined heat and power (CHP) plants urban heating and cooling. Focus lies on the thermodynamic design and performance assessment of large-scale biomass-fired USC CHP plant configurations. Authors assess system performance when supplying the heat demand of industrial processes at aluminum/pulp and paper production plants. The model considers the simultaneous influence of urban heating and cooling at the plant's surroundings. Results show that the electric (exergetic) efficiencies of the aluminum and pulp/paper plants are 43.45% (44.22%), and 38.93% (39.62%), respectively. For the CHP

cycle, when maximizing output heat, the electrical, exergetic electrical, CHP, and exergetic CHP efficiencies of the aluminum/pulp and paper production plants are, respectively: 21.81% and 34.32%; 19.54% and 31.70%; 92.50% and 86.76%; 39.43% and 39.01%.

A systematic review in [26] reports not finding a study where a compact electricity-cooling cogeneration system is assessed using the Specific Exergy Costing (SPECOC) method. Authors proceeded to an exergoeconomic evaluation, using SPECOC, of a compact electricity-cooling cogeneration system. The system consists of an internal combustion engine coupled with a single-effect H_2O/NH_3 absorption chiller. The authors divided the exergy analysis into two stages: (i.) internal combustion engine and (ii.) each component of the absorption refrigeration system. Cogeneration is done by using exhaust gases from a 126 hp Otto cycle internal combustion engine (ICE) to drive a 5 RT water-ammonia absorption cooling unit. Most of the exergy destruction occurs in the ICE (67.88%), followed by the steam generator (14.46%). Considering the cost of destroyed exergy plus the equipment cost rate, the highest costs are found in the ICE and then in the steam generator. Authors conclude that the SPECOC method is effective in identifying energy system inefficiencies. Furthermore, authors establish that exergoeconomic assessments adequately guide the design of more efficient electricity-cooling cogeneration systems.

Hybrid thermochemical cycles for heat storage and combined generation of energy and cooling are introduced by [27]. Thermodynamic balance equations were solved using EES@ software package. Such cycles have three main features: (i.) they can be powered by low-grade heat, such as industrial waste heat, at temperatures ranging from 100 to 250 °C; (ii.) they are capable of storing energy as chemical potential and (iii.) converting stored energy into refrigeration and/or electricity. The cycle output may consist mostly of refrigeration or electricity - depending on the mode of operation. For this, five operation modes were designed: some for predominant refrigeration, others for electricity generation. Authors, based on commercial systems, also designed alternative systems for producing the same outputs. The alternatives were compared to hybrid thermochemical cycles. Comparison results show that hybrid

cycles feature lower energy storage density. However, hybrid cycles feature higher net energy efficiency. Especially at the predominant refrigeration operation modes, where the hybrid system efficiency is 34% higher than that of the alternative commercial system.

Reference [28] introduces an energy, exergy, and environmental assessment of a new Photovoltaic/Thermal (PV/T) ejector-heat-pump system for simultaneous cooling of a data center with the waste heat redirected to room heating. The study compared system performance when circulating eleven refrigerants with lower global warming potential (GWP) from various ASHRAE safety groups (R450A, R513A, R515A, R515B, R516A, R152a, R444A, R1234ze(E), R1234yf, R290, and R1243zf) to the performance when circulating hydrofluorocarbon (HFC) R134a. Results show that, for all the refrigerants, the new system configuration performs better. In terms of an energy analysis, the enhancement in the cooling coefficient of performance (COPC) goes from 15% to 54% when compared to a traditional R134a heat pump. The exergy analysis demonstrates that fluid R515B exhibits the highest exergetic efficiency.

Reference [29] introduces a double-effect Vapor Absorption Refrigeration System (VARs) driven by the waste heat from a 210 MW thermal power plant located in Badarpur. System performance was analyzed using the Response Surface Methodology (RSM) by [29].

Results showed that the exergetic efficiency is most significantly influenced by the absorber temperature (F -value = 2,049.4), followed by the condenser temperature (F -value = 1,596.4), and is less impacted by the high-pressure generator temperature (F -value = 495.0).

Parallel flows with the aim of improving energy and refrigeration flows are introduced by [30]. For the cycle analysis, five key variables were investigated: 1) wet vapor temperature; 2) wet vapor dryness fraction; 3) concentration of the basic, *i.e.*, anti-acidic solution; 4) evaporator exit temperature; and 5) ambient water temperature. These 5 variables were studied in two cogeneration systems. The model proposed by the authors was fed with ammonia-water mixture thermodynamic properties evaluated using REFPROP® 9.1 and MATLAB® programming. The Goswami cycle is put forth as a solution to simultaneously generate electricity and refrigeration with less pollution.

The energy and refrigeration flows are connected in series, with the refrigeration output capped in a series arrangement. Results led to the conclusion that power generation increases as dryness fraction increases and as the concentration of the basic, solution decreases. The cooling effect is enhanced by a decrease in dryness fraction and an increase in the concentration of the basic solution.

IV. CONCLUSION

This study aimed to present results obtained through a systematic literature review that identified the main studies — and their spin-offs — regarding the use of exergetic analysis in cogeneration systems applied to industrial refrigeration from 2017 to 2022.

Through the studies identified in this SRL, it was observed that the discussions focused on aspects related to improving operation, replacing low-efficiency components, substituting working fluids, and either proposing or combining systems to promote greater energetic, thermal, economic, and environmental efficiency.

Thus, the studies identified in this RSL point to the diversity of research areas within the main theme, highlighting the potential of the exergy evaluation methodology applied to cogeneration systems. This methodology has the potential to identify techniques for enhancing electrical energy generation, energy and thermal optimization of heating and cooling systems for industrial processes, industrial refrigeration systems and large buildings. Thus, promoting, through technological development, cleaner, more sustainable and economically viable energy conversion processes.

ACKNOWLEDGMENT



The authors wish to acknowledge the support of the Laboratory of Environmental and Energy Assessment (LAvAE) at the Federal University of Paraíba. Also, the authors acknowledge the support of the National Council for Scientific and Technological Development (CNPq) for the PhD scholarship 141303/2021-2, productivity grant 309452/2021-0, and project 424173/2021-2. Thanks are extended to the Paraíba State Research Foundation (FAPESQ) due to the financial support of grants 77/2022 and 08/2023.

REFERENCES

- [1] Ibrahim, T. K., Mohammed, M. K., Awad, O. I., Abdalla, A. N., Basrawi, F., Mohammed, M. N., ... & Mamat, R. (2018). A comprehensive review on the exergy analysis of combined cycle power plants. *Renewable and Sustainable Energy Reviews*, *90*, 835-850.
- [2] Zakeri, B., Paulavets, K., Barreto-Gomez, L., Echeverri, L. G., Pachauri, S., Boza-Kiss, B., ... & Ürge-Vorsatz, D. (2022). Pandemic, War, and Global Energy Transitions. *Energies*, *15*, 6114.
- [3] Polyvianchuk, A., Semenenko, R., Kapustenko, P., Klemeš, J. J., & Arsenyeva, O. (2023). The efficiency of innovative technologies for transition to 4th generation of district heating systems in Ukraine. *Energy*, *263*, 125876.
- [4] Catrini, P., Cellura, M., Guarino, F., Panno, D., & Piacentino, A. (2018). An integrated approach based on Life Cycle Assessment and Thermoconomics: Application to a water-cooled chiller for an air conditioning plant. *Energy*, *160*, 72-86.
- [5] Moghimi, M., Emadi, M., Ahmadi, P., & Moghadasi, H. (2018). 4E analysis and multi-objective optimization of a CCHP cycle based on gas turbine and ejector refrigeration. *Applied Thermal Engineering*, *141*, 516-530.
- [6] Best, R., & Rivera, W. (2015). A review of thermal cooling systems. *Applied thermal engineering*, *75*, 1162-1175.
- [7] Catalano, F., Perone, C., Iannacci, V., Leone, A., Tamborrino, A., & Bianchi, B. (2020). Energetic analysis and optimal design of a CHP plant in a frozen food processing factory through a dynamical simulation model. *Energy Conversion and Management*, *225*, 113444.
- [8] Caglayan, H., & Caliskan, H. (2022). Assessment of a cogeneration system for ceramic industry by using various exergy based economic approaches. *Renewable and Sustainable Energy Reviews*, *167*, 112728.
- [9] Pereira, J. B., Araújo, C. C. S., de Rezende, T. T. G., Guimarães, L. G. M., da Silva, J. A., Teixeira, F. N., & dos Santos Guzella, M. (2022). Análise exergética em bancada de ciclo de refrigeração por compressão de vapor: Exergetic analysis in a refrigeration cycle bench by vapor compression. *Brazilian Journal of Development*, *56293-56308*.
- [10] Liu, Z., Liu, B., Guo, J., Xin, X., & Yang, X. (2019). Conventional and advanced exergy analysis of a novel transcritical compressed carbon dioxide energy storage system. *Energy conversion and management*, *198*, 111807.
- [11] Al Moussawi, H., Fardoun, F., & Louahlia-Gualous, H. (2016). Review of tri-generation technologies: Design evaluation, optimization, decision-making, and selection approach. *Energy Conversion and Management*, *120*, 157-196.
- [12] Branchini, L., Bignozzi, M. C., Ferrari, B., Mazzanti, B., Ottaviano, S., Salvio, M., ... & Canetti, A. (2021). Cogeneration supporting the energy transition in the Italian ceramic tile industry. *Sustainability*, *13*(7), 4006.
- [13] Man, S. S., Lee, W. K. H., Wong, K. P., & Chan, A. H. S. (2022). Policy Implications for Promoting the Adoption of Cogeneration Systems in the Hotel Industry: An Extension of the Technology Acceptance Mode. *Buildings*, *12*(8), 1247.
- [14] Brito, A.M.V.G. (2023) Cogeração na indústria cerâmica: uma revisão sistemática sobre a recuperação de calor em fornos cerâmicos e seus benefícios. In: Encontro Internacional sobre Gestão Empresarial e Meio Ambiente.
- [15] Peng, Z., Li, Z., Zeng, J., Yu, J., & Lv, S. (2022). Thermo-economic analysis of absorption-compression hybrid cooling systems with parallel subcooling and recooling for small scale low-grade heat source and low temperature application. *International Journal of Refrigeration*, *138*, 220-232.
- [16] da Silva Morais, P. H., Lodi, A., Aoki, A. C., & Modesto, M. (2020). Energy, exergetic and economic analyses of a combined solar-biomass-ORC cooling cogeneration systems for a Brazilian small plant. *Renewable Energy*, *157*, 1131-1147.
- [17] Kitchenham, B., & Brereton, P. (2013). A systematic review of systematic review process research in software engineering. *Information and software technology*, *55*(12), 2049-2075.
- [18] Tranfield, D., Denyer, D., & Smart, P. (2003). Towards a methodology for developing evidence-informed management knowledge by means of systematic review. *British journal of management*, *14*(3), 207-222.
- [19] Jiang, L., Roskilly, A. P., Wang, R. Z., & Wang, L. W. (2018). Analysis on innovative resorption cycle for power and refrigeration cogeneration. *Applied Energy*, *218*, 10-21.
- [20] Pirkandi, J., Joharchi, A. M., & Ommian, M. (2019). Thermodynamic and exergetic modelling of a combined cooling, heating and power system based on solid oxide fuel cell. *Journal of Mechanical Engineering and Sciences*, *13*(4), 6088-6111.
- [21] Bahsan, R., Sarudin, K. A. M., Ali, N. M., & Mohamad, S. N. A. (2019). Analysis on the performance of steam absorption chiller at various operating conditions. *International Journal of Engineering and Advanced Technology*, *9*(1), 5728-5735.
- [22] Godefroy, A., Perier-Muzet, M., & Mazet, N. (2019). Thermodynamic analyses on hybrid sorption cycles for low-grade heat storage and cogeneration of power and refrigeration. *Applied Energy*, *255*, 113751.
- [23] Javanshir, N., Mahmoudi SM, S., Kordlar, M. A., & A. Rosen, M. (2020). Energy and cost analysis and optimization of a geothermal-based cogeneration cycle using an ammonia-water solution: Thermodynamic and thermoeconomic viewpoints. *Sustainability*, *12*(2), 484.
- [24] Emadi, M. A., Chitgar, N., Oyewunmi, O. A., & Markides, C. N. (2020). Working-fluid selection and thermoeconomic optimisation of a combined cycle cogeneration dual-loop organic Rankine cycle (ORC) system for solid oxide fuel cell (SOFC) waste-heat recovery. *Applied Energy*, *261*, 114384.
- [25] Braimakis, K., Magiri-Skouloudi, D., Grimekis, D., & Karellas, S. (2020). Energy-exergy analysis of ultra-supercritical biomass-fuelled steam power plants for industrial CHP, district heating and cooling. *Renewable Energy*, *154*, 252-269.

- [26] Marques, A. D. S., Carvalho, M., Ochoa, Á. A., Souza, R. J., & Santos, C. A. D. (2020). Exergoeconomic assessment of a compact electricity-cooling cogeneration unit. *Energies*, 13(20), 5417.
- [27] Godefroy, A., Perier-Muzet, M., Neveu, P., & Mazet, N. (2020). Hybrid thermochemical cycles for low-grade heat storage and conversion into cold and/or power. *Energy Conversion and Management*, 225, 113347.
- [28] Al-Sayyab, A. K. S., Navarro-Esbrí, J., & Mota-Babiloni, A. (2022). Energy, exergy, and environmental (3E) analysis of a compound ejector-heat pump with low GWP refrigerants for simultaneous data center cooling and district heating. *International Journal of Refrigeration*, 133, 61-72.
- [29] Gambhir, D., Sherwani, A. F., & Arora, A. (2022). Parametric optimization of blowdown operated double-effect vapour absorption refrigeration system. *Journal of Thermal Engineering*, 8(1), 78-89.
- [30] Nath, R. R., Reddy, K. H., & Reddy, C. V. B. (2022). A cogeneration cycle comparative analysis with parallel arrangement. *Alexandria Engineering Journal*, 61(2), 1171-1181

Experimental Study for the Improvement of Savonius Wind Turbine by Wind Flow Direction Control

Pinku Debnath¹, M. D. Raiesh², Abhishek Kumar Singh³, Krishna Murari Pandey⁴

^{1,2,3}Department of Mechanical Engineering, National Institute of Technology Agartala, Tripura, India

⁴Department of Mechanical Engineering, National Institute of Technology Silchar, Assam, India

¹er.pinkunits@yahoo.com

Abstract—The Savonius rotor is a drag driven vertical axis wind rotor, having lesser power coefficients, as it makes negative torque in certain rotor angle. The various geometric and aerodynamic performance parameters have been designed to improve the performance of the convention S-type rotor. To reduce the negative drag force of the rotor and enhance the aerodynamic performance of the conventional Savonius wind rotor. So, a curtain has been placed in front of the rotor. The experimental analysis has been done in wind tunnel experimentation. So far the comparison has been performed for power versus RPM and torque versus RPM for Savonius rotor blades with and without curtain arrangement. The result indicates that torque and power generation is more from curtain arrangement with Savonius wind rotor. The peak torque magnitude of 1.42 N-m and power generation of 8.4 W from curtain-1 model configuration of Savonius wind rotor.

Keywords - Savonius wind rotor, curtain, power coefficient, torque coefficient, wind tunnel

I. INTRODUCTION

The energy plays a great role in economic development and industrialization of the nation. The fossil fuels have the major resources that supply the world's energy demand. However, fossil fuel reserves are limited and usage of fossil fuels to generate energy has negative environmental effects [1]. The wind energy is an important source of free and green energy. The

wind turbines are the machine for harnessing renewable energy from free wind from natural resources. The performance of the Savonius wind turbine is lower but it has a number of advantages in comparison to conventional horizontal axis wind turbines. Savonius wind rotor is a vertical-axis wind rotor invented by Finnish engineer, Savonius, S. J., on 1925 [2,3]. The design of Savonius wind rotor is comparatively simple. They also start to run on their own and independent of the direction of wind. They also have a high starting torque and despite of these considerable advantages Savonius wind turbine has less demand due to their low aerodynamic performance. To improve the aerodynamics performance curtain has been designed and installed in front of the rotor [4,5] experimentally studied on pressure distribution around the Savonius rotor to find the low and high-pressure region which is contributing to overall torque generation of Savonius turbine. The modified rotor arrangement has been experimentally performed to improve the power coefficient of the rotor. The power coefficient of the rotor has been explored through wind tunnel tests, which are affected by single and multiple stages. They found that the effect of Reynolds number, height to diameter ratio (h/d) and overlap ratio of Savonius rotor have been investigated experimentally. The experimental analysis shows the positive impact on power coefficient. Thus, changes made in the parameters such as number of rotor stage,



number of buckets, blade shape, aspect ratio, overlap ratio and wind flow guide have been found to significantly improve the aerodynamic performance of the rotor [6,7]. Reference [4,6] studied on Savonius wind rotor to increase the performance by using the modified curtain. This curtain has been placed in front of the rotor and the experiments have been carried out when the rotor positions are in front of with and without curtain. Reference [8] studied on parameter optimization of Savonius turbine using an obstacle shielding by returning blade. They introduce an obstacle plate that shields partly the returning blade of a Savonius turbine by using either two or three blades and optimized the wind direction toward the advance blade. The torque coefficient is even higher for larger values of Tip speed ratio. The obtained output power coefficient of the two-blade configuration is clearly better than the three-blade turbine. This optimal configuration leads to a peak power output coefficient of 0.258 at tip speed ratio of 0.8. Reference [9] found that two bladed rotor is more efficient compared to three bladed rotor. They also found that helical Savonius rotor has a positive torque coefficient at all the rotor angles. Reference [10] performance studied on Savonius wind turbine. Their comparison revealed that in the range of tip speed ratio between 0.2 and 0.4 the elliptical Savonius rotor performance has better than the Bach-type Savonius rotor. Reference [11] studied on Savonius rotor to enhance the aerodynamic performance of the wind rotor. For the development of air foil shaped blades named SR3345 and SR5050 rotor are used of a new curtain system, which is self-orienting relative to the wind flow direction. They found that curtain can enhance the performance of the rotor. Reference [12] studied on flow physics analysis of three bucket helical Savonius wind rotor at 90° twist angle. From the flow physics analysis they found that three bucket 90° twist angle helical Savonius rotor at 60° rotor angle has maximum lift force during power stroke and maximum positive static torque was evaluated at 150° rotor angle. Reference [13] studied on aerodynamics performance and wind flow analysis around the helical Savonius rotor. The physical model of helical Savonius rotor with helix angles of $\alpha = 0^\circ, 45^\circ, 90^\circ, 135^\circ$, for different rotor angle of $\gamma = 0^\circ$ to 180° have been studied numerically. They found that 45° helical rotor is better for power coefficient and torque coefficient, which is significantly higher

compared to conventional Savonius wind rotor. Reference [14] numerical studied on Savonius wind rotor for the improvement of the performance of the rotor. They found that form elliptical rotor blades, the peak power magnitude of 10 W and average power of 7 W are obtained. Whereas, from conventional S-rotor blades, the peak power magnitude of 8 W and average power of 4 W are achieved. Reference [15] studied on the performance of the 45° twisted Savonius wind rotor. They found that maximum power coefficient for the twisted rotor with the modified profile, with a performance gain of 75.3% compared to the conventional Savonius wind rotor. Reference [16] studied on aerodynamics performance improvement of modified Savonius wind turbine blade. The power coefficient of the modified blade has increased by 20% compared to conventional shape of Savonius blade. Reference [17] studied numerically and experimentally on some notable blade profiles of Savonius wind rotor. They found that elliptical-bladed rotors demonstrate the maximum power coefficient. Reference [8] studied considerably improve the design of Savonius wind rotor in order to increase the power output of the Savonius turbine with two or three blades. They found that the position of an obstacle in front of the returning blade possibly leading to better flow orientation toward the advancing bucket of the Savonius turbine. Reference [18] studied on modified Savonius wind rotor with different convex and concave sides of the rotor to maximize the power output. They found that the optimal C_p is 0.25 and this value is 4.41% higher than the traditional design. Reference [19] numerical studied on vent-augmented Savonius wind turbine. They found that maximum power coefficient (C_p) of 0.132 is obtained from modified elliptical blade. Reference [20] studied on the performance analysis of helical Savonius wind rotor. The performance of helical rotor with shaft between the end plates and without shaft between end plates at different overlap ratios of 0.0, 0.1 and 0.16 is studied. They found that helical Savonius wind turbine without shaft at an overlap ratio of 0.0 and an aspect ratio of 0.88 is found more coefficient of power generation compared to conventional Savonius rotor. Reference [21] studied on aerodynamic modelling of vertical axis wind turbines. They found that vertical axis wind turbines having curved blades has more susceptible to local dynamic stall compared to turbines with straight

blades. Reference [22] experimental studied on Savonius wind rotor with end plates. They found that Savonius wind rotor has more output than rotors without end plates. They also found that, the two blades rotor is more efficient than three and four blades. Reference [23] experimentally studied on the performance, drag, and horizontal mid plane wake characteristics of Savonius rotor. They found that the wake was found to be asymmetrical and deflected to the side where the blade moves opposite direction of the wind. Reference [15] studied on the performance of 45° twisted Savonius wind rotor with a modified blade profile. The maximum power coefficient is found from the twisted rotor with modified blade profile. Reference [24] studied on aerodynamics performance of Savonius wind rotor. They found that rotor required drag force for rotation but the torque and power performance are less compared to lift-based turbines. For the manufacture of wind turbine blade the glass fibers or epoxy matrix composites, natural composites are suitable for Savonius wind rotor [25,26].

The objective of this study is experimental analysis of curtain arrangement in front of the Savonius wind rotor to improve the aerodynamics performance of the rotor. This will make it possible to increase the usage fields of the Savonius wind rotor, which, despite their many advantages over the other vertical-axis wind rotors, have a restricted field of use due to their low aerodynamic performance, but orientation of curtain arrangement in front of the rotor is still in debate.

II. EXPERIMENTAL MODEL

A. End Plates Construction

The mild steel sheet has been used to make the Savonius wind rotor, cleaned it with sandpaper, marked a circle on it and cut it with sheet metal sniper, made a hole of size of shaft in the center of plate. The effectiveness of the end plates is measured and compared with the benchmark case, i.e., without endplate. The rotor with circular endplate generates positive power coefficient even at tip speed ratio (TSR) greater than 1.0. The circular shape endplate increases the power coefficient of the wind turbine, the TSR corresponding to the power coefficients of all the rotor angles. The rotor with circular endplate faces the greatest levels of the drag and lift forces exerting on the rotor shaft.

B. Shaft Construction

The shaft of the blades is constructed in such a way that it properly fitted to the blade. The shaft should be as thin as possible as less in thickness and light in weight for the two blades, the shaft used is very thin in size and it is all properly fitted. It is made up of iron pipe which is very light weight. The length of shaft and diameter of shaft are 40 cm and 1.54 cm respectively. The bearing's shaft of length 1.15 cm and diameter 2.6 cm are inserted at the top and bottom end of constructed blades to give contact between base and shaft. The shaft height is more long, so it can be cut with hacksaw blade by measuring with the length of blade of turbine and joined it again by arc welding and made thread on both sides.

C. Construction of Blade

In the analysis two blades with vertical shaft with height and breadth of 32 cm and 14.7 cm respectively are constructed. The angle between the two blades is 180°, if one blade moves the other blade comes in the position of the first blade. It is cleaned both the rectangular shape blade with sand paper, then bent it in semicircle form by heating and beating with hammer in smithy shop on a solid cylinder.

D. Assemble of the Parts

The shaft, blades and end plates are welded in the blades in opposite manner at 180° angle on end plates. The gas welding is used to weld the shaft and blade each together. The blades are fixed in shaft with end plates by arc welding. As the wind blows into the structure and comes into contact with the opposite faced surfaces i.e., one is convex and other one is concave, two different forces are drag and lift exerted on these two surfaces. The basic principle is based on the difference of the drag force between the convex and the concave parts of the rotor blades when they rotate around a vertical shaft. Thus, the drag force is the main driving force of the Savonius wind rotor.

E. Support Stand and Base Construction

For the smooth operation of the turbine shaft, a bearing mechanism with lubricant is used to reduce the rotational friction. The two ends of blade's shaft are pivoted into the same dimension bearing, so it reduces the frictional

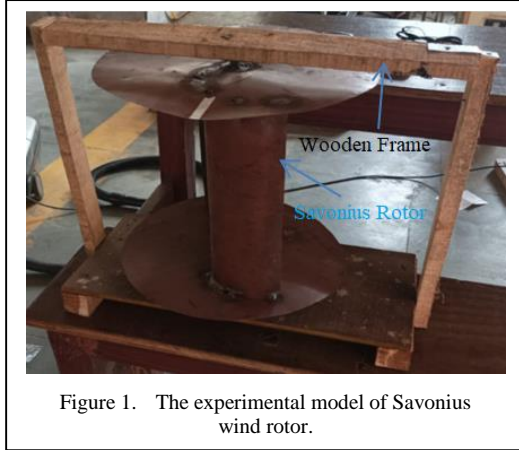


Figure 1. The experimental model of Savonius wind rotor.

loss of wind energy. The shaft bearing has diameter of 2.6 cm. These bearings are generally provided for supporting the shaft and smooth operation of shaft. The one side hole has been made on the surface of upper and lower support and pivoted the bearing into it with M-seal. The base is important for the construction of the wind turbine tower, because it supports the wind turbine. But it also is considered to their own weight and the drag force of the wind. In this model preparation it has been taken a flat piece of wood and joined another by two long wood bars of same shape and size on opposite side. To make a hole on upper and lower support bar to inserted the bearing. It has been taken another two long wood bars of same size and shape to connect upper and lower part by beating nail with hammer into it. The experimental model has been shown in Fig. 1.

F. Curtain Arrangement

The three curtain has been created the height of the all curtain are same. The height is 32 cm and length is 45 cm, 34 cm and 22 cm. The curtain deflection angle of $\alpha = 45^\circ$ in left side of in front of the rotor and $\beta = 15^\circ$ is right side of the rotor. The details dimension of the curtain arrangement as shown in Table I.

TABLE I. THE DETAILS DIMENSIONS OF THE CURTAIN ARRANGEMENT.

Curtain orientation	Length of curtain L_1 (cm)	Length of curtain L_2 (cm)	Height H (cm)	Thickness t (mm)
Curtain 1	45	52	32	2
Curtain 2	34	39	32	2
Curtain 3	22	26	32	2

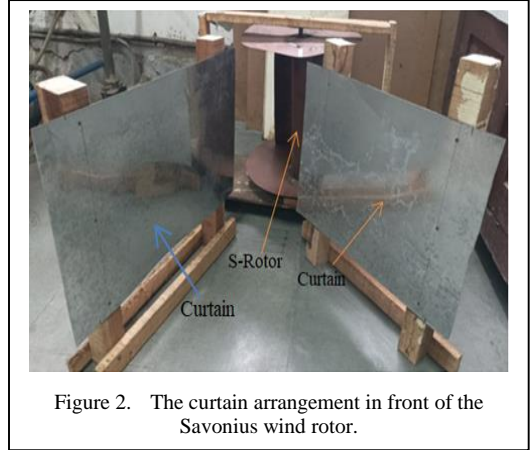


Figure 2. The curtain arrangement in front of the Savonius wind rotor.

It has been taken four wooden pillars and used two pillars to support each curtain sheet. The three thin wooden pieces are also used on the base of pillars to avoid the fall of sheet due to wind flow, as shown in Fig. 2. It is used iron nails by beating with hammer to join sheet with wood. After arranged the both curtains according to the measurement it has been performed the experiment by blowing the wind from blower.

III. DATA REDUCTION

The power coefficient and torque coefficient of wind turbine indicates the performance of the turbine. It is the ratio of actual electric power produced by a wind turbine divided by the total wind power flowing into the turbine blades at specific wind speed. The data reduction equations are as follows:

$$\lambda = \frac{\text{velocity of tip blade}}{\text{wind speed through blade}}, \quad (1)$$

$$v_{rotor} = \omega R = \frac{2nNR}{60}, \quad (2)$$

$$\lambda = \frac{v_{rotor}}{v}, \quad (3)$$

$$\lambda = \frac{C_p}{C_t}, \quad (4)$$

where, λ = tip speed ratio, R = rotor diameter, ω = angular velocity of rotor, T = torque developed by rotor, ρ is density of air = 1.225

kg/m^3 , A = swept area of blades, C_p = power coefficient.

$$A = \text{rotor height} \times \text{rotor diameter}, \quad (5)$$

$$C_p = \frac{\text{Maximum power obtained from wind}}{\text{Total power available from wind}}, \quad (6)$$

$$C_p = \frac{P_i}{P_a} = \frac{T\omega}{\frac{1}{2}\rho Av^3} = \frac{2T\omega}{\rho Av^3}, \quad (7)$$

$$C_p = \frac{2T\omega}{(\rho Av^3)}, \quad (8)$$

$$C_p = \frac{2T \frac{2\pi N}{60}}{\rho Av^3}. \quad (9)$$

The power is calculated by using the following formula:

$$P = 2\pi N_s T_y + 2\pi N_G T_z, \quad (10)$$

where, T_y and T_z are the torque near blade wall in y-axis and z-axis respectively. Also, we can get torque by using power, $P = T\omega$, where P is power, T is torque and ω is angular velocity.

IV. RESULTS AND DISCUSSION

The Fig. 3 shows the comparison of torque with and without curtain arrangement. The torque generation is more for Savonius rotor with curtain arrangement compared to without curtain in front of the rotor. When RPM is increased, the torque is reduced. The maximum torque of 0.6 N-m is obtained from Savonius

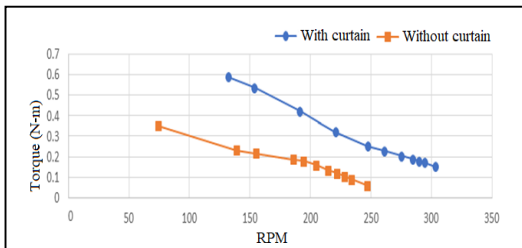


Figure 3. Comparison of the experimental torque changes at different RPM with curtain and without curtain.

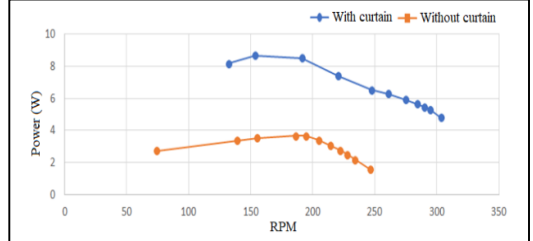


Figure 4. Comparison of power output from savonius wind rotor with and without curtain.

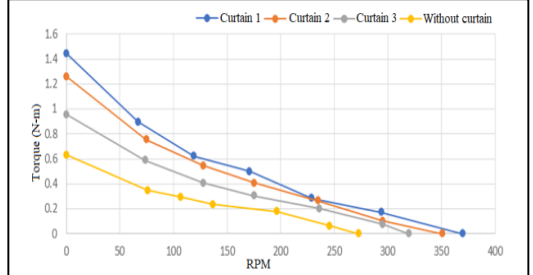


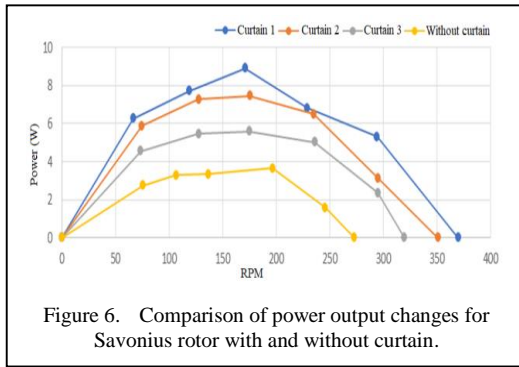
Figure 5. Comparison of torque output changes with RPM of the rotor with and without curtain.

rotor with curtain arrangement at RPM of 130. Whereas, 0.35 N-m torque is found from Savonius wind rotor without curtain arrangement at RPM of 75.

The Fig. 4 shows the comparison of power with and without curtain arrangement. The power generation is more with curtain arrangement compared to without curtain in front of the rotor. When RPM of the rotor is increased, the power is increased up to RPM of 151 then reduced. The maximum power 8.32 W is generated from Savonius wind rotor with curtain arrangement. The maximum power 3.8 W is generated from Savonius wind turbine without curtain arrangement at RPM of 190.

The Fig. 5 shows the comparison of torque with different curtain position and without curtain installation in front of the rotor. The curtain-1 has more torque (N-m) compared to curtain-2, curtain-3 and without curtain in front of the wind turbine. The torque generation is reduced with increased the RPM of the rotor up to RPM of 352. The maximum torque of 1.42 N-m is found at initial starting RPM from Savonius wind turbine with curtain 1 type model. Whereas, the torque of 0.6 N-m is obtained from without curtain arrangement at initial starting RPM.

The Fig. 6 shows the comparison of power with different curtain position and without curtain installation in front of the Savonius wind



turbine. The power generation is increased up to RPM of 175, and then reduced at RPM of 352. The curtain-1 can generate the more power as compared to curtain-2, curtain-3 and without curtain. The maximum power output of 8.4 W at RPM of 175 from curtain-1 model configuration of Savonius wind rotor. Whereas, maximum power of 3.9 W is obtained from RPM of 195 from Savonius wind rotor without curtain arrangement.

V. CONCLUSIONS

The Savonius wind rotor has simple geometry construction and less power generation. So curtain has been used in front of the rotor. This curtain acts like a wind deflector. It has been designed and placed in front of the rotor to prevent the negative torque affecting the convex surface of the rotor. The utilization of the curtain the upstream velocity of the wind will also increase. The purpose is to enhance the performance of the Savonius wind rotor. The curtain can prevent wind flow to the convex blade and increase the positive torque of the rotor. The following conclusions are drawn from the simulations:

- The optimum magnitude of torque and power from Savonius wind rotor with curtain is more compared to without curtain configuration of Savonius wind turbine.
- The best aerodynamics performance is obtained from geometry of the curtain 1 having length of $l_1=45$ cm and $l_2=52$ cm.
- The maximum power output of 8.4W from curtain-1 model configuration of Savonius wind rotor. Whereas, maximum power of 3.9W is obtained from Savonius wind rotor without curtain arrangement.

NOMENCLATURE

TSR	Tip speed ratio
RPM	Rotation per minute
C_p	Power coefficient
C_t	Torque coefficient
h	height of the rotor
d	diameter of the rotor
l	Curtain length
ω	Angular velocity
α	Helix angle
γ	Rotor angle

ACKNOWLEDGMENTS

The author would like to thanks the Mechanical Engineering Department, National Institute of Technology Agartala, Tripura, India for providing the wind tunnel research work and computer facilities.

REFERENCES

- [1] El-Askary, W. A., Nasef, M. H., Abdel-Hamid, A. A., & Gad, H. E. (2015). Harvesting wind energy for improving Performance of Savonius rotor. *Journal of Wind Engineering and Industrial Aerodynamics*, 139, 8-15.
- [2] Savonius, S. J. (1931). The S-rotor and its applications. *Mechanical Engineering*, 53(5), 333-8.
- [3] Debnath, P., & Gandhirajan, V. (2023). A comprehensive review on design and development analysis and blade material selection of helical Savonius rotor. *Wind Engineering*, 47(4), 883-893.
- [4] Altan, B. D. (2006). Performance investigation of Savonius wind rotor with curtaining method, PhD thesis in mechanical engineering. Denizli, Turkey: Graduate School of Natural and Applied Sciences. Pamukkale University, 147.
- [5] Altan, B. D., & Atilgan, M. (2008). An experimental study on improvement of a Savonius rotor performance with curtaining. *Experimental Thermal and Fluid Science*, 32, 1673-1678.
- [6] Altan, B. D., & Atilgan, M. (2010). The use of a curtain design to increase the performance level of a Savonius wind rotors. *Renewable Energy*, 35, 821-829.
- [7] Altan, B. D., & Atilgan, M. (2012). A study on increasing the performance of Savonius wind rotors, *Journal of Mechanical Science and Technology*, 26(5), 1493-1499,
- [8] Mohamed, M. H., Janiga, G., Pap, E., & Thévenin, D. (2010). Optimization of Savonius turbines using an obstacle shielding the returning blade. *Renewable Energy*, 35, 2618-2626.
- [9] Debnath, P., Gupta, R., & Pandey, K.M. (2014). Performance Analysis of the Helical Savonius Rotor Using Computational Fluid Dynamics. *ISESCO Journal of Science and Technology*, 10(18), 17-28.
- [10] Kacprzak, K., Liskiewicz, G., & Sobczak, K. (2013). Numerical investigation of conventional and modified Savonius wind Turbines. *Renewable Energy*, 60, 578-585.

- [11] Tartuferi, M., D'Alessandro, V., Montelpare, S., & Ricci, R. (2015). Enhancement of Savonius wind rotor aerodynamic performance: a computational study of new blade shapes and curtain systems. *Energy*, 79, 371-384.
- [12] Debnath, P., & Gupta, R. (2013). Flow Physics Analysis of Three-Bucket Helical Savonius Rotor at 90° Twist Angle Using CFD. *International Journal of Modern Engineering Research*, 3(2), 739-746.
- [13] Debnath, P., & Gandhirajan, V. (2023). Numerical investigation on performance and wind flow simulation around the helical savonius wind turbine. *AIP Conference Proceedings*, 2863, 020009.
- [14] Debnath, P., & Debbarma, R. (2024). Numerical study for the improvement of performance of Savonius wind turbine having elliptical blades. *E3S Web of Conferences*, 540, 03002.
- [15] El-Askary, W. A., Saad, A. S., AbdelSalam, A. M., & Sakr, I. M. (2020). Experimental and theoretical studies for improving the performance of a modified shape Savonius wind turbine. *Journal of Energy Resources Technology*, 142(12), 121303.
- [16] Ramarajan, J., & Jayavel, S. (2021). Performance improvement in Savonius wind turbine by modification of blade shape. *Journal of Applied Fluid Mechanics*, 15(1), 99-107.
- [17] Alom, N., & Saha, U. K. (2019). Influence of blade profiles on Savonius rotor performance: Numerical simulation and experimental validation. *Energy Conversion and Management*, 186, 267-277.
- [18] Tian, W., Mao, Z., Zhang, B., & Li, Y. (2018). Shape optimization of a Savonius wind rotor with different convex and concave sides. *Renewable energy*, 117, 287-299.
- [19] Alom N., (2022). Influence of curtain plates on the aerodynamic performance of an elliptical bladed Savonius rotor (S-rotor). *Energy Systems*, 13, 265-280.
- [20] Kamoji, M. A., Kedare, S. B., & Prabhu, S. V. (2009). Performance tests on helical Savonius rotors. *Renewable Energy*, 34(3), 521-529.
- [21] Scheurich F., Fletcher T. M. & Brown R. E. (2011). Effect of blade geometry on the aerodynamic loads produced by vertical-axis wind turbines. In *Proceedings of the Institution of Mechanical Engineers, Part A: Journal of Power and Energy*, 225(3), 327-341.
- [22] Mahmoud, N. H., El-Haroun, A. A., Wahba, E., & Nasef, M. H. (2012). An experimental study on improvement of Savonius rotor performance. *Alexandria Engineering Journal*, 51(1), 19-25.
- [23] Aliferis, A. D., Jessen, M. S., Bracchi, T., & Hearst, R. J. (2019). Performance and wake of a Savonius vertical- axis wind turbine under different incoming conditions. *Wind Energy*, 22(9), 1260-1273.
- [24] Thakre, A. A., & Durge, P. U. (2022, November). Improvement in Torque and Power Performance of an Elliptical Savonius Wind Turbine Using Numerical and Experimental Analysis. In *International Conference on Robotics, Control, Automation and Artificial Intelligence* (pp. 747-761). Singapore: Springer Nature Singapore.
- [25] Brøndsted, P., Lilholt, H., & Lystrup, A. (2005). Composite materials for wind power turbine blades. *Annual Review of Materials Research*, 35, 505-538.
- [26] Holmes, J. W., Sørensen B. F., & Brøndsted P., (2007). Reliability of Wind Turbine Blades: An Overview of Materials Testing. In *Proceedings of the Wind Power Shanghai 2007, Shanghai, China, 1-3 November*.

Energetic and Exergetic Investigation of Transcritical Heat Pump System using an Expander Device Substituted for Throttle Valve

Youcef Maalem¹ , Hakim Madani² 

¹National Polytechnic School of Constantine, BP75 A, Nouvelle Ville RP, 25000 Constantine, Algeria

²Laboratory of Studies of Industrial Energy Systems (LESEI), Department of Mechanical Engineering, Faculty of Technology, University of Batna 2, 05000 Batna, Algeria

¹youcef.maalem@cp.enp-constantine.dz, ²h.madani@univ-batna2.dz

Abstract—The present study investigation aims to contribute to the field of energy engineering by exploring the thermodynamic analysis and comparison between two configurations of heat pump system using expansion devices (throttling valve and expander) to assess the thermodynamic performances such as the coefficient of performance (COP) heating, optimum discharge pressure and exergy efficiency using carbon dioxide as working fluid. The thermodynamic analysis is performed with energy and exergy methods. Moreover, a parametric study is performed to examine the impact of the evaporator (t_{ev}) and gas cooler (t_{gc}) temperatures, on the performance indicators of configurations. Computer code was developed using MATLAB software for the numerical simulation. Overall, the results reveal that heat pump system, which operate with expander device, exhibited a higher COP heating and exergy efficiency, as well as lower optimum discharge pressure compared with heat pump system, which operate with throttling valve under the same operating temperatures.

Keywords - carbon dioxide, heat pump systems, expansion devices, energy analysis, exergy analysis

I. INTRODUCTION

Recently, one of the hot topics in energy engineering has been the search for environmentally friendly working fluids for

energy systems, where has gained international attention due to environment problems of the traditional fluids [1]. Due to the depletion of ozone caused by Chloro-Fluoro-Carbons (CFCs: R11, R12, R113, etc.), the first family of working fluoride substances for energy systems (such as domestic air-conditioning system, cooling system, heat pump system, automotive air conditioners, etc.) was banned in 1987 by the restrictive regulations of Montreal Protocol and is being replaced by the family of Hydro-Fluoro-Carbons (HFCs: R134a, R152a, R125, etc.) and Hydro-Chloro Fluoro Carbons (HCFCs: R22, R123, R142b, etc.) [2].

The phase-out of the family of CFCs widely used in the applications of the vapor compression cycles (VCCs), which mainly includes a compressor, a condenser and throttle valve was finished in 1996. Because family of HFCs and HCFCs have a lower Ozone Depletion Potential (ODP) than CFCs, they were recommended as an alternative for VCCs. However, it was discovered in 1990 that certain working fluids with low ODP were linked to the phenomenon of global warming. Thus, the Kyoto Protocol was established in 1997 with the aim of reducing greenhouse gas emissions and mitigating global warming. Part of this involves promoting the use of working fluids with low Global Warming



Potential (GWP) [3]. By 2030, the maximum GWP for authorized working fluids in energy systems will have dropped to 150 [4].

Nowadays, one of the energy systems applications (such as heat pump and cooling systems) most significant renewal processes is currently taking place as traditional working fluids (CFCs, HFCs and HCFCs), which have a significant negative impact on the environment, are replaced with more environmentally friendly working fluids, the majority of which come from the natural family owing to their zero-ozone depletion potential (ODP) and low global warming potential (GWP) [5]. The natural working fluids such as air, water, ammonia, propane, nitrous oxide and carbon dioxide have received increasing attention as future working fluids in the vapor compression cycles of energy systems [6]. In this context, carbon dioxide has been widely acknowledged its favorable qualities in engineering application such as excellent thermo physical properties, non-flammability, non-toxicity, environmental safety, easy availability, no recycling problem, low cost, etc., [7]. However, since of its low critical temperature (31.1 °C) which cause it to operate in trans-critical conditions, engineers have developed the trans-critical carbon dioxide cycle, in which the evaporation process stays subcritical and the heat rejection process uses supercritical vapor cooling with heat exchangers called gas coolers instead of condensation through condensers [8]. It is discovered that there are a number of unusual opportunities, including hot water heating [9-16], when using a gas cooler with heat rejection occurring over an exceptionally large temperature glide. In heat pump systems, which operate with the trans-critical cycle, expansion devices such as throttling valve and expander play a crucial role in the trans-critical cycle. Technology of expansion devices are responsible for reducing the pressure and temperature of the working fluid as it passes from the high-pressure side of the cycle to the low-pressure side. Expansion devices create a pressure drop that allows the working fluid to expand, which, in turn, enables it to absorb heat efficiently in the evaporator unit and repeat the trans-critical cycle.

To the best of the author’s knowledge, thermodynamic (energy-exergy) investigation of carbon dioxide heat pump system with throttling valve and expander are not performed. In order to cover the shortcomings existing in the literature, in this study, for the first time, author’s

purpose to evaluate and compare the energy and exergy performance of carbon dioxide heat pump cycle with a throttling valve and carbon dioxide heat pump cycle with an expander.

II. DESCRIPTION OF HEAT PUMP CYCLES

A. Carbon Dioxide Heat Pump Cycle with a Throttling Valve

Fig. 1, shows the schematic illustration of the configuration of the carbon dioxide heat pump cycle with a throttling valve. The configuration comprises four essential components, which are: a compressor, a gas cooler, a throttling valve and an evaporator.

The temperature–entropy (T–s) diagram of the configuration of the carbon dioxide heat pump cycle with a throttling valve (1-2-3-4h-1) is depicted in Fig. 2. The thermodynamic cycle of this configuration has four basic transformations.

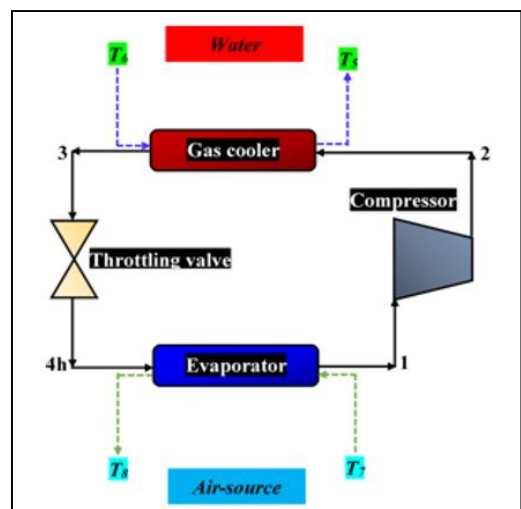


Figure 1. Schematic of heat pump cycle with a throttling valve.

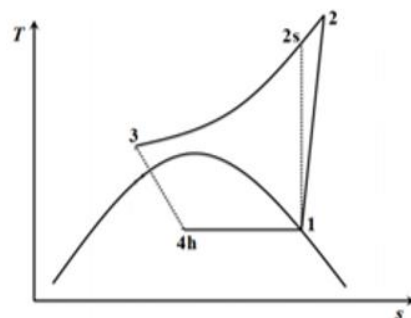


Figure 2. Temperature–entropy (T–s) diagram.

The different processes of carbon dioxide heat pump cycle with a throttling valve are presented as follows:

- **Process (4→1):** is a heat absorption in the evaporator;
- **Process (1→2s):** is isentropic compression;
- **Process (1→2):** is the actual compression;
- **Process (2→3):** is a heat rejection in the gas cooler;
- **Process (3→4h):** is the actual expansion of the throttling valve.

The following is the operating principle of the carbon dioxide heat pump cycle with a throttling valve: At first, in the evaporator, the carbon dioxide blend (liquid and vapor) (state 4h) at low-pressure evaporates as heat is received from air-source whose temperature drops from T_7 to T_8 . At the evaporator outlet, the carbon dioxide enters the compressor at state (1), then, it is compressed up to the supercritical high-pressure level at state (2), where the highest pressure and temperature are reached within the thermodynamic cycle. After the compression phase, the high-pressure carbon dioxide leaving the compressor flows through the gas cooler rejecting heat to the water whose temperature rises from T_5 to T_6 to give the useful heating at state (3). At last, by entering carbon dioxide flows in the throttling valve, the carbon dioxide is reduced down from supercritical pressure to the subcritical low-pressure level into the two-phase region (gas–liquid), until the initial conditions.

B. Carbon Dioxide Heat Pump Cycle with an Expander

The schematic of the carbon dioxide heat pump cycle with an expander is presented in Fig. 3. As the carbon dioxide heat pump cycle with a throttling valve, the configuration of carbon dioxide heat pump cycle with an expander comprises has four essential components, which are: a compressor, a gas cooler, an expander and an evaporator.

The operating principle of the carbon dioxide heat pump cycle with an expander is identical to carbon dioxide heat pump cycle with a throttling valve. The only difference between heat pump cycles is in the type of expansion device used.

The temperature–entropy (T – s) diagram of the configuration of the carbon dioxide heat pump cycle with an expander (1-2-3-4-1) is depicted in Fig. 4.

The different processes of the cycle are presented as follows:

- **Process (4→1):** is a heat absorption in the evaporator;
- **Process (1→2s):** is isentropic compression;
- **Process (1→2):** is the actual compression;
- **Process (2→3):** is a heat rejection in the gas cooler;
- **Process (3→4s):** is isentropic expansion;
- **Process (3→4s):** is the actual expansion of the expander.

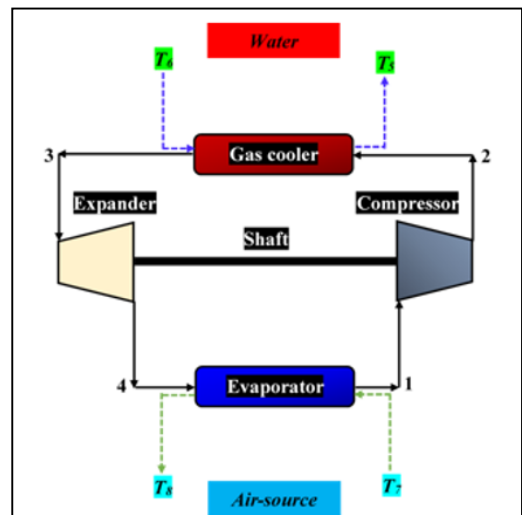


Figure 3. Schematic of heat pump cycle with an expander.

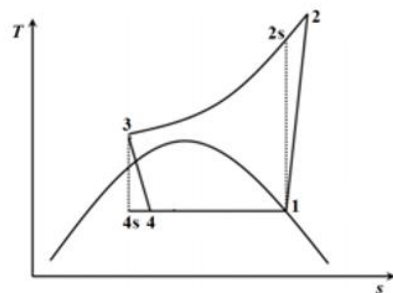


Figure 4. Temperature–entropy (T – s) diagram.

III. MATHEMATICAL MODELLING AND SIMULATION

A. Assumptions

In order to investigate the energy and exergy of the investigated carbon dioxide heat pump cycles (carbon dioxide heat pump cycle with a throttling valve and carbon dioxide heat pump cycle with an expander), the following assumptions are made to simplify the calculation:

- The heat pump cycles operate in a steady-state condition;
- The heat transfer with the ambient is negligible;
- The compression process is adiabatic but non-isentropic;
- There are no pressure losses in pipes and heat exchangers;
- The variations in kinetic and potential energy are not considerable;
- The flow across the throttling valve is isenthalpic ($h = cte$);
- The refrigerant condition is saturated vapor at the exit of the evaporator ($x = 1$);
- The evaporation and gas cooling processes are isobaric ($P = cte$).

Based on the assumptions above, thermodynamic models of the investigated carbon dioxide heat pump cycles are developed using basic energy and exergy relations.

B. Energetic Analysis for Carbon Dioxide Heat Pump Cycle with a Throttling Valve

For compressor (1-2):

The work input to the compressor is computed as:

$$W_{com,tvc} = (h_2 - h_1). \quad (1)$$

The isentropic efficiency of the compressor is calculated as follows:

$$\eta_{com,tvc} = \frac{(h_{2s} - h_1)}{(h_2 - h_1)}. \quad (2)$$

For gas cooler (2-3):

The heat rejected to the water can be using the following equation:

$$q_{gc,tvc} = (h_3 - h_2). \quad (3)$$

For throttling valve (3-4):

The throttling valve operate under an isenthalpic process:

$$h_3 = h_{4h}. \quad (4)$$

For evaporator (4h-1):

The air-source heat gain can be calculated by:

$$q_{eva,tvc} = (h_1 - h_{4h}). \quad (5)$$

The energy efficiency of carbon dioxide heat pump cycle with a throttling valve is evaluated by its heating coefficient of performance (COP_{tvc}), which is defined as the ratio of the useful output energy (heating capacity ($q_{gc,tvc}$)) to the input energy (work input to the compressor ($w_{com,tvc}$)):

$$COP_{tvc} = \frac{q_{gc,tvc}}{w_{com,tvc}}. \quad (6)$$

C. Energetic Analysis for Carbon Dioxide Heat Pump Cycle with an Expander

The same procedure as described in carbon dioxide heat pump cycle with a throttling valve is repeated for the heat pump cycle with an expander.

For compressor (1-2):

The work input to the compressor is calculated as:

$$W_{com,ec} = (h_2 - h_1). \quad (7)$$

The isentropic efficiency of the compressor is given by:

$$\eta_{com,ec} = \frac{(h_{2s} - h_1)}{(h_2 - h_1)}. \quad (8)$$

For gas cooler (2-3):

The heat rejected to the water can be obtained by:

$$q_{gc,ec} = (h_3 - h_2). \quad (9)$$

For expander (3-4):

The work generated by the expander is computed as:

$$W_{exp,ex} (h_3 - h_{4s}) \eta_{exp,ec}. \quad (10)$$

The isentropic efficiency of the expander is given by:

$$\eta_{exp,ec} = \frac{(h_3 - h_4)}{(h_3 - h_{4s})}. \quad (11)$$

For evaporator (4-1):

The air-source heat gain can be calculated by:

$$q_{eva,ec} = (h_1 - h_4). \quad (12)$$

To calculate the COP heating of carbon dioxide heat pump cycle with an expander, the following Eq. (13) can be used:

$$COP_{ec} = \frac{q_{eva,ec}}{W_{exp,ec} - W_{com,ec}}. \quad (13)$$

D. Exergetic Loss for Carbon Dioxide Heat Pump Cycle with a Throttling Valve

The exergy losses in each component (compressor, gas cooler, throttling valve and evaporator) of the carbon dioxide heat pump cycle with a throttling valve can be obtained with the following equations:

For compressor (1-2):

$$I_{com,tvc} = T_0 (s_2 - s_1). \quad (14)$$

For gas cooler (2-3):

$$I_{gc,tvc} = h_2 - h_3 - T_0 (s_2 - s_3). \quad (15)$$

For throttling valve (3-4h):

$$I_{tvc,tv} = T_0 (s_{4h} - s_3). \quad (16)$$

For evaporator (4h-1):

$$I_{eva,tv} = T_0 (s_1 - s_{4h}) + (h_{4h} - h_1) \times T_0 / T_r. \quad (17)$$

The total exergy destruction of the carbon dioxide heat pump cycle with a throttling valve is sum of individual component exergy destruction rates:

$$I_{tot,tvc} = \sum I_{components}, \quad (18)$$

$$I_{tot,tvc} = I_{com,tvc} + I_{gc,tvc} + I_{tvc,tvc} + I_{eva,tvc}. \quad (19)$$

The exergy efficiency for the carbon dioxide heat pump cycles can be defined as the ratio of the minimum work requirement to the actual work input.

The exergy efficiency of the carbon dioxide heat pump cycle with a throttling valve is:

$$\eta_{tvc} = 1 - \frac{I_{tot,tvc}}{W_{com,tvc}}. \quad (20)$$

E. Exergetic Loss for Carbon Dioxide Heat Pump Cycle with an Expander

The exergy losses for the components: compressor, gas cooler, expander and evaporator of the carbon dioxide heat pump cycle with an expander is calculated from the following relationships:

For compressor (1-2):

$$I_{com,ec} = T_0 (s_2 - s_1). \quad (21)$$

For gas cooler (2-3):

$$I_{gc,ec} = h_2 - h_3 - T_0 (s_2 - s_3). \quad (22)$$

For expander (3-4):

$$I_{exp,ec} = T_0 (s_4 - s_3). \quad (23)$$

For evaporator (4-1):

$$I_{eva,ec} = T_0 (s_1 - s_4) + (h_4 - h_1) \times T_0 / T_r. \quad (24)$$

The total exergy destruction of the carbon dioxide heat pump cycle with an expander is sum

of individual component exergy destruction rates:

$$I_{tot,ec} = \sum I_{components}, \quad (25)$$

$$I_{tot,ec} = I_{com,ec} + I_{gc,ec} + I_{exp,ec} + I_{eva,ec}. \quad (26)$$

The exergy efficiency of the carbon dioxide heat pump cycle with an expander is:

$$\eta_{ec} = 1 - \frac{I_{tot,ec}}{W_{exp,ec} - W_{com,ec}}. \quad (27)$$

Based on the above equations and assumptions, a computational model is developed in MATLAB software for carrying out the energy and exergy analysis of the investigated heat pump cycles at various operating conditions. The cycles are simulated under the following operating conditions:

- The temperature difference for water is equal to 5 K;
- The compressor has an isentropic efficiency of 75%;
- The expander has an isentropic efficiency of 65%;
- The outlet temperature of the gas cooler is $32\text{ }^{\circ}\text{C} \leq t_{gc} \leq 50\text{ }^{\circ}\text{C}$;
- The evaporating temperature is $-25\text{ }^{\circ}\text{C} \leq t_{eva} \leq 20\text{ }^{\circ}\text{C}$;
- The environment temperature: $T_0=303\text{K}$;
- The refrigerated object temperature: $-20\text{ }^{\circ}\text{C} \leq T_r \leq 25\text{ }^{\circ}\text{C}$.

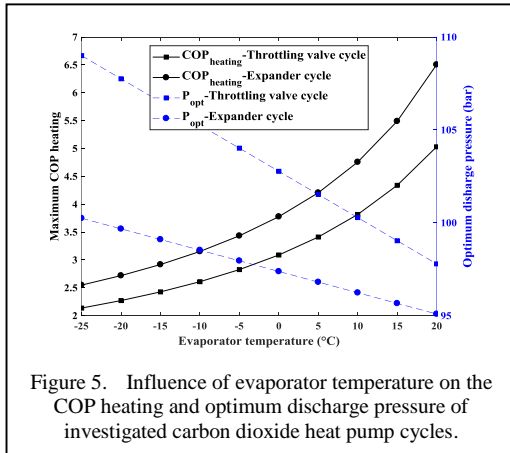


Figure 5. Influence of evaporator temperature on the COP heating and optimum discharge pressure of investigated carbon dioxide heat pump cycles.

IV. SIMULATION RESULTS AND DISCUSSIONS

A. Influence of Evaporator and Gas Cooler Temperature on the COP Heating and Optimum Discharge Pressure

Fig. 5 shows the influence of evaporation temperature on the maximum COP heating with corresponding optimum discharge pressure of the investigated carbon dioxide heat pump cycles (heat pump cycle with a throttling valve and heat pump cycle with an expander) using carbon dioxide as working fluid, while keeping the other operating conditions constant. In this case, carbon dioxide changes its phase from liquid to vapor in evaporator as heat is received from air-source whose temperature drops from T_7 to T_8 .

It can be found from the profiles of maximum COP heating of both carbon dioxide heat pump cycles that the performance of cycles depends largely on evaporator temperatures, where with an increase in evaporator temperature from $(-25\text{ }^{\circ}\text{C}$ to $20\text{ }^{\circ}\text{C})$, the performance of the heat pump systems increases. On other hand, it can be found from the profiles of variation optimum discharge pressure of both carbon dioxide heat pump cycles that the variation with evaporator temperature is much less significant, where with an increase in evaporator temperature from $(-25\text{ }^{\circ}\text{C}$ to $20\text{ }^{\circ}\text{C})$, the optimum pressure of the heat pump systems decreases linearly. In sum, a conclusion can easily be drawn that the COP heating of investigated cycles reaches a maximum at higher values of discharge pressure for lower evaporator temperatures as it is illustrated in the graph.

By comparing the simulation results of the maximum COP heating obtained for each carbon dioxide heat pump cycle, an important discovery on the results showed that the carbon dioxide

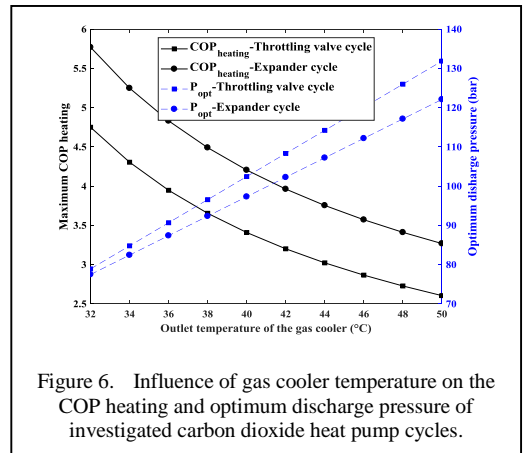


Figure 6. Influence of gas cooler temperature on the COP heating and optimum discharge pressure of investigated carbon dioxide heat pump cycles.

heat pump cycle with an expander has better maximum COP heating than carbon dioxide heat pump cycle with a throttling valve. Also, it can be found that the carbon dioxide heat pump cycle with a throttling valve has the higher optimum pressure than carbon dioxide heat pump cycle with an expander.

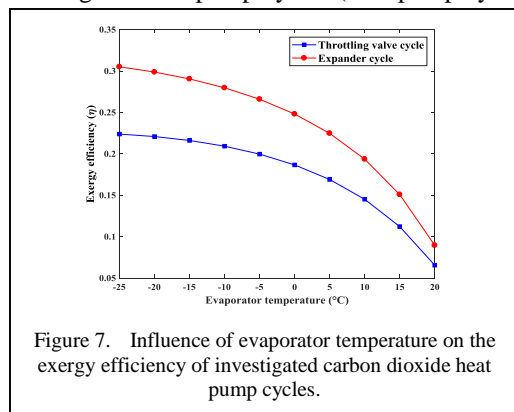
Fig. 6 illustrates the influence of gas cooler temperature on the maximum COP heating with corresponding optimum discharge pressure of the investigated heat pump cycles using carbon dioxide as working fluid while keeping the other operating conditions constant.

Examining the profiles of maximum COP heating of both carbon dioxide heat pump cycles in the figure, it can be found that with an increase in gas cooler temperature from (32 °C to 50 °C), the performance of the heat pump systems decreases linearly. However, the optimum pressure increases linearly. In sum, a conclusion can easily be drawn that the COP heating of investigated cycles increases sharply with a decrease in the cooler temperature as it is illustrated in the graph.

By comparing the simulation results of the maximum COP heating obtained for each carbon dioxide heat pump cycle, it can be seen that the carbon dioxide heat pump cycle with an expander has also better maximum COP heating than carbon dioxide heat pump cycle with a throttling valve. Also, it can be found that the carbon dioxide heat pump cycle with a throttling valve has the higher optimum pressure than heat pump cycle with an expander.

B. Influence of Evaporator and Gas Cooler Temperature on the Exergy

Fig. 7 show the effects of the of evaporation temperature on the exergy efficiency of the investigated heat pump cycles (heat pump cycle



with a throttling valve and heat pump cycle with an expander) using carbon dioxide as working fluid while keeping the other operating conditions constant.

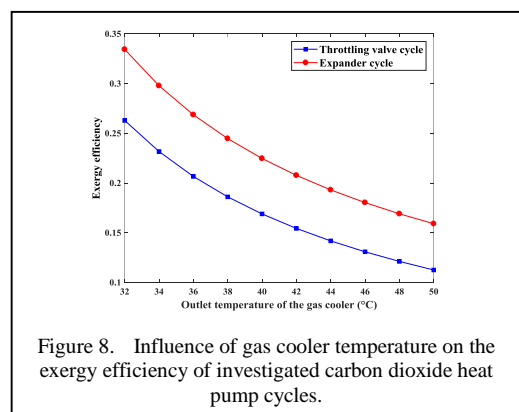
It is found that the exergy efficiencies of carbon dioxide heat pump cycles are decreased and tend to close with increasing evaporating temperature (-25 °C to 20 °C).

By comparing the simulation results of the exergy efficiency obtained for each carbon dioxide heat pump cycle, an important discovery on the results showed that the carbon dioxide heat pump cycle with an expander has better exergy efficiency than carbon dioxide heat pump cycle with a throttling valve. This is because, employing an expander device can efficiently recover work and move it to the compressor, which will significantly enhance the heat pump system.

Fig. 8 illustrates the effects of the of gas cooler temperature on the exergy efficiency of the investigated heat pump cycles using carbon dioxide as working fluid while keeping the other operating conditions constant.

Examining the profiles of both carbon dioxide heat pump cycles in the figure, it can be found that with an increase in gas cooler temperature from (32 °C to 50 °C), the exergy efficiencies of the heat pump systems also decreased.

By comparing the simulation results of the exergy efficiency obtained for each carbon dioxide heat pump cycle, it can be seen that the carbon dioxide heat pump cycle with an expander has better exergy efficiency than carbon dioxide heat pump cycle with a throttling valve.



V. CONCLUSION

A comparative analysis between two configurations of heat pump system using expansion devices (throttling valve and expander) was carried out to assess the thermodynamic performances such as the coefficient of performance (COP) heating, optimum discharge pressure and exergy efficiency using carbon dioxide as working fluid. The thermodynamic analysis is performed with energy and exergy methods. In addition, a parametric study is performed to examine the impact of the evaporator and gas cooler temperatures, on the performance indicators of configurations.

This led us to the following conclusions:

- The COP heating of the investigated heat pump cycles increases with the increase in the evaporator temperature;
- The optimum discharge pressure of the investigated heat pump cycles decreases with the increase in the evaporator temperature;
- The COP heating of the investigated heat pump cycles decreases with the increase in the gas cooler temperature;
- The optimum discharge pressure of the investigated heat pump cycles increases with the increase in the gas cooler temperature;
- The replacing of the throttling valve by an expander improves the maximum COP heating and the exergy efficiency;
- The replacing of the throttling valve by an expander reduces the optimal heat rejection pressure.

In future works, it would be very interesting to research about the optimization study of heat pump cycle with an expander.

REFERENCES

- [1] Maalem, Y., Fedali, S., Madani, H., & Tamene, Y. (2020). Performance analysis of ternary azeotropic mixtures in different vapor compression refrigeration cycles. *International Journal of Refrigeration*, 119 (1), 139-151.
- [2] Maalem, Y., Tamene, Y., & Madani, H. (2023). Performances Investigation of the Eco-friendly Refrigerant R131I used as Working Fluid in the Ejector-Expansion Refrigeration Cycle. *International Journal of Thermodynamics*, 26 (3), 025-035.
- [3] Yildirim, C., Ozkan, D.B., & Onan, C. (2018). Theoretical study of R32 to replace R410A in variable refrigerant flow systems. *International Journal of Ambient Energy*, 39, 87-92.
- [4] Maalem, Y., Tamene, Y., & Madani, H. (2021). Behavior of the thermo-physical properties and performance evaluation of the refrigerants blends of (fluorocarbon/hydrocarbon) for cooling cycle. *Recueil de mécanique*, 6(1), 544-559.
- [5] Calm, J. M. (2008). The next generation of refrigerants—Historical review, considerations, and outlook. *International Journal of Refrigeration*, 31(7), 1123-1133.
- [6] Sawalha, S., M, Karampour., J, & Rogstam. (2015). Field measurements of supermarket refrigeration systems. Part I: Analysis of CO₂ trans-critical refrigeration systems. *Applied Thermal Engineering*, 87(5), 633-647.
- [7] Megdouli, K., et al. (2019). Theoretical research of the performance of a novel enhanced transcritical CO₂ refrigeration cycle for power and cold generation. *Energy Conversion and Management*, 201, 112139.
- [8] Zhang, J., Qin, Y., & Wang, C. (2015). Review on CO₂ heat pump water heater for residential use in Japan. *Renewable and Sustainable Energy Reviews*, 50, 1383-1391.
- [9] Neksa, P. (2002). CO₂ heat pump systems. *International Journal of Refrigeration*, 25(4), 421-427.
- [10] Yin, X., Cao, F., & Wang, X. (2019). Investigation on the real-time control of the optimal discharge pressure in a transcritical CO₂ system with data-handling and neural network method. *Energy Procedia*, 160, 451-458.
- [11] Wang, S., He, Y., Tuo, H., Cao, F., & Xing, Z. (2013). Effect of heat transfer area and refrigerant mass flux in a gas cooler on heating performance of air-source transcritical CO₂ heat pump water heater system. *Energy and Buildings*, 67, 1-10.
- [12] Yin, X., Cao, F., & Wang, X. (2004). Optimization of a transcritical CO₂ heat pump cycle for simultaneous cooling and heating applications. *Energy Procedia*, 27 (8), 830-838.
- [13] Aprea, C., & Maiorino, A. (2009). Heat rejection pressure optimization for a carbon dioxide split system: An experimental study. *Applied Energy*, 86(11), 2373-2380.
- [14] Qi, P., He, Y., Wang, X., & Meng, X. (2013). Experimental investigation of the optimal heat rejection pressure for a transcritical CO₂ heat pump water heater. *Applied Thermal Engineering*, 56, (1-2), 120-125.
- [15] Cecchinato, L., et al. (2005). Carbon dioxide as refrigerant for tap water heat pumps: A comparison with the traditional solution. *International Journal of Refrigeration*, 28 (8), 1250-1258.
- [16] Richter, M. R., et al. (2003). Experimental results of transcritical CO₂ heat pump for residential application. *Energy*, 28 (10) 1005-1019.

Experimental Study on Concentration of Milk in an Electric Still

Mahesh Kumar¹, Om Prakash², Rahul Grewal³, Shimpy⁴

^{1,4}Department of Mechanical Engineering, Guru Jambheshwar University of Science & Technology, Hisar, India

²Department of Mechanical Engineering, National Institute of Technology, Patna, India

³Department of Mechanical Engineering, Chaudhary Ranbir Singh State Institute of Engineering and Technology, Jhajjar, India

¹maheshkumar@gjust.org, ²dromprakash67@gmail.com, ³rs180160080009@gjust.org,

⁴shimpymehra@mail.com

Abstract—In this paper, the values of fluid-surface constant (C_{sf}) in the Rohsenow pool boiling correlation for the concentration of milk in Al and SS pots of an electric still are evaluated. The electric still is consisting of an electric hot plate over which pots were fitted with a vertical cylinder covered by a hemi-spherical condensing cover. The rate of heat inputs were 240, 280, 320 and 360 W. The data gathered during the concentration of milk were analyzed and the values of C_{sf} were evaluated. The average values of C_{sf} for Al and SS pot surfaces during heating of milk in an electric still were found to be 0.011414 and 0.012461, respectively. The evaluated values of convective heat transfer coefficient (h_c) were observed to be a function of heat flux inputs.

Keywords - pool boiling, concentration of milk, Rohsenow correlation, fluid-surface constant, electric still

I. INTRODUCTION

In boiling process, fluid changes from liquid to vapor when the heating surface temperature (T_1) is maintained above the saturation temperature (T_{sat}) of the liquid. Many researches have been performed to know the pool boiling heat transfer mechanism but it has not yet been accurately understood. The boiling regimes namely, nucleate, transition and film boiling are categorized on the basis of excess temperature

(ΔT_{exc}), i.e., the difference between T_1 and T_{sat} . In nucleate boiling, the bubbles rise from the heating surface, whose temperature is in excess of the saturation temperature of liquid. When the heating surface temperature is more than 100 °C, film boiling occurs, in which a thin vapor layer is formed on the heating surface that acts as insulation, consequently, reduced heat transfer. Transition boiling takes place when the heating surface lies in between the maximum and minimum attainable temperatures for nucleate and film boiling, respectively [1,2].

Pool boiling occurs in a stationary liquid and it has been extensively investigated in last seven decades. Reference [3] proposed a correlation for pool boiling of liquids. A list of values for various surface-fluid combination constants (C_{sf}) has been suggested by [3,4]. The Rohsenow pool boiling correlation has been studied at various pressure conditions [4–9]. The convective heat and mass transfer coefficient was found to vary from 50.65 to 345.20 W/m² °C for heat inputs ranging from 160 to 340 W during boiling of sugarcane juice [10]. The effects of nanoparticles on sub-cooled nucleate pool boiling has been experimentally studied by [11]. Concentration of nanoparticle and surfactants effects on pool boiling heat transfer was studied by [12]. Nanoparticles deposition on the surface resulted in increased bubble nucleation and their



departure. In the sub-cooled pool boiling regime, the bubble dynamics and mechanisms for interactions of adjacently vapor bubbles were studied by [13]. Heat transfer in pool boiling of sugarcane juice was experimentally studied by [14].

Reference [13] studied the pool boiling behavior of milk during khoa (heat desiccated milk product) making in Al and SS pots under open conditions by varying the heat inputs ranging from 240 to 360 W [15,16]. The values of h_c were reported to be in the range of 334.48 - 837.78 W/m² °C and 283.02 - 783.97 W/m² °C for Al and SS pots, respectively. The pool boiling behavior of milk has also been reported for closed conditions under the given heat inputs for open conditions using Al and SS pots for which the values of h_c were reported to vary from 186.32 - 567.56 W/m² °C and from 160.51 - 374.52 W/m² °C, respectively [17,18]. The nucleate boiling heat flux was reported to increase exponentially with an increase in ΔT_{exc} . The fluid-surface constants (C_{sf}) for khoa making in Al and SS pots under open conditions were reported by [19] as 7.8815×10^{-3} and 9.4772×10^{-3} , respectively. The pool boiling heat transfer phenomenon have been reviewed by various researchers [20–25].

In this research paper, the values of C_{sf} for the concentration of milk in Al and SS pots of an electric still are evaluated. The experimental data were analyzed and equations similar to the Rohsenow correlation for the concentration of milk in an electric still is proposed. This research work would be helpful in the design of a better heating surface (heat exchanger) for the processing of milk.

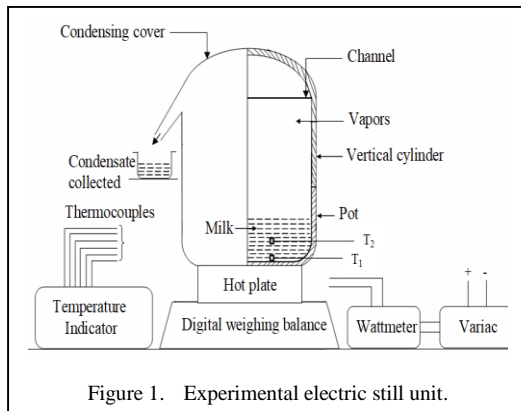


Figure 1. Experimental electric still unit.

II. EXPERIMENTAL DETAILS AND PROCEDURE

The experimental unit is schematically shown in Fig. 1 which is mainly consisting of an electric still, watt meter, variac, digital weighing balance and temperature indicator having copper-constantan thermocouples. Al and SS pots are taken since these are generally used for the heating of milk at Indian homes. The pot and hot plate have a perfect surface contact therefore, uniform heat distribution is assumed across the pot surfaces. The detailed specifications of these parts are given in Table I.

The condensate obtained due to evaporation of milk was made to come out using a channel fitted at the bottom of the condensing cover. The condensate collection was observed when the temperature of the milk was more than 90 °C (i.e., nucleate boiling condition). It is pertinent to mention here that milk heating at a temperature of <90 °C is considered as natural convective heating condition, i.e., free convection [26,27]. The following steps were followed for performing the experimentation on heating of milk in the electric still at varying heat inputs.

TABLE I. DETAILED SPECIFICATIONS OF EXPERIMENTAL UNIT.

Component		Specification
Electric still	Electric hot plate	Diameter (ϕ) : 0.178 m; Power capacity: 1000 W
	Pots	ϕ : 0.2 m; Depth: 0.102 m, Thickness: 0.0016 m; Capacity: 0.0032 m ³ ; Material: aluminium (Al) and stainless steel (SS)
	Vertical cylinder	ϕ : 0.2 m; Height: 0.192 m; Material: galvanized sheet; Thickness: 0.511 mm
	Spherical condensing cover	ϕ : 0.2 m; Height: 0.06 m; Material: galvanized sheet; Thickness: 0.511 mm
Watt meter		Accuracy: $\pm 0.5\%$, Least count (L_c) : 1 W; Range: 1-1500 W
Variac		Range: 50-60 Hz; L_c : 1 W
Weighing balance		L_c : 0.1g; Accuracy: $\pm 2\%$
Temperature indicator and thermocouples		Accuracy: $\pm 0.1\%$; Range: -50 to 200 °C; Thermocouples: Copper-constantan type

1. Fresh sample of cow milk was heated in an Al pot at heat inputs of 240, 280, 320 and 360 W.
2. Constant mass of 0.935 kg of milk was taken for the heat inputs of 240, 280 and 320 W while 0.735 kg was taken for 360 W to avoid the spillover of the milk from the electric still.
3. The data for pool boiling of milk was started to record when milk temperature (T_2) becomes 90 °C and were ended when solidification of concentrated milk was observed.
4. The values of mass evaporated (m_{ev}) and excess temperature (ΔT_{exc}) were recorded at a time interval of 10 minutes.
5. The values of ΔT_{exc} for the milk heating were obtained for the increasing heat inputs (i.e., 240, 280, 320 and 360 W).
6. The above-mentioned procedure has also been repeated for the concentration of milk in the SS pot.

III. RESULTS AND DISCUSSION

The experimental data for T_1 , ΔT_{exc} and m_{ev} during nucleate boiling condition of the milk in the Al and SS pots of an electric still for the heat inputs of 240, 280, 320 and 360 W are given in Table II and III, respectively.

The Rohsenow correlation for nucleate pool boiling is as below [3].

$$C_{pl} \left[\frac{\Delta T_{exc}}{h_{fg} \times Pr_l^n} \right] = C_{sf} \left[\frac{q_{nucleate}}{\mu_l \times h_{fg}} \sqrt{\frac{\sigma}{g(\rho_l - \rho_v)}} \right]^{\frac{1}{3}} \quad (1)$$

The thermo-physical properties of milk were evaluated at T_{sat} using expressions given in Table IV.

TABLE II. EXPERIMENTAL DATA FOR MILK HEATING IN AL POT OF AN ELECTRIC STILL.

Time interval (min)	T_1 (°C)				ΔT_{exc} (°C)				m_{ev} (g)			
	240 W	280 W	320 W	360 W	240 W	280 W	320 W	360 W	240 W	280 W	320 W	360 W
10	98.6	93.9	97.9	96.5	9.3	5.3	8.7	6.7	9.9	8.8	29.3	21.8
10	100.6	100.6	100.4	100.2	11.3	12.0	11.2	10.4	22.1	28.9	39.0	46.1
10	100.8	100.9	100.5	100.6	11.5	12.3	11.3	10.8	21.9	30.1	39.1	48.1
10	100.7	100.8	100.6	100.7	11.4	12.2	11.4	10.9	21.2	29.4	37.4	46.8
10	100.7	100.8	100.6	101.0	11.4	12.2	11.4	11.2	21.1	29.3	36.9	47.7
10	100.7	100.8	100.7	100.9	11.4	12.2	11.5	11.1	21.2	29.7	37.7	46.3
10	100.9	100.8	100.7	101.2	11.6	12.2	11.5	11.4	21.4	24.1	37.9	45.4
10	100.8	101.1	100.7	101.1	11.5	12.5	11.5	11.3	20.9	28.6	38.1	45.6
10	100.6	101.0	100.8	100.6	11.3	12.4	11.6	10.8	21.4	29.2	37.2	46.9
10	100.7	101.0	100.7	101.0	11.4	12.4	11.5	11.2	21.9	29.1	37.3	47.4
10	101.0	101.2	100.7	104.1	11.7	12.6	11.5	14.3	21.2	29.8	39.7	41.6
10	100.8	101.2	100.7	109.1	11.5	12.6	11.5	19.3	21.7	29.2	38.0	33.7
10	100.7	101.3	100.7		11.4	12.7	11.5		21.3	29.9	37.6	
10	100.7	101.2			11.4	12.6			21.2	30.2		
10	101.0	100.8			11.7	12.2			21.9	30.8		
10	100.7	100.9			11.4	12.3			20.9	29.4		
10	100.8	101.0			11.5	12.4			21.4	30.0		
10	100.7				11.4				21.5			
10	100.9				11.6				22.6			
10	101.0				11.7				20.7			
10	100.9				11.6				21.3			

TABLE III. EXPERIMENTAL DATA FOR MILK HEATING IN SS POT OF AN ELECTRIC STILL.

Time interval (min)	T_l (°C)				ΔT_{exc} (°C)				m_{ev} (g)			
	240 W	280 W	320 W	240 W	280 W	320 W	240 W	280 W	320 W	240 W	280 W	320 W
10	98.8	95.3	98.8	97.6	9.4	6.5	9.5	7.4	8.4	7.9	28.1	33.2
10	100.9	100.3	100.8	100.5	11.5	11.5	11.5	10.3	19.6	12.9	32.9	37.2
10	100.9	100.5	100.7	101.1	11.5	11.7	11.4	10.9	18.4	24.7	31.8	38.8
10	101.0	100.6	100.8	101.2	11.6	11.8	11.5	11.0	18.5	25.7	31.5	38.3
10	101.0	100.7	100.8	101.2	11.6	11.9	11.5	11.0	17.7	24.7	31.4	38.4
10	101.0	100.7	101.0	101.3	11.6	11.9	11.7	11.1	18.5	24.0	31.6	39.0
10	100.9	100.9	101.0	101.7	11.5	12.1	11.7	11.5	19.1	23.6	32.2	39.4
10	101.0	100.8	101.1	102.0	11.6	12.0	11.8	11.8	18.8	23.9	31.1	40.3
10	101.1	100.7	101.1	101.9	11.7	11.9	11.8	11.7	20.4	24.3	32.8	39.8
10	101.2	100.7	101.2	101.8	11.8	11.9	11.9	11.6	18.6	24.4	33.2	38.1
10	101.2	100.7	101.3	102.7	11.8	11.9	12.0	12.5	18.7	25.1	32.6	37.9
10	101.3	100.8	101.5	102.5	11.9	12.0	12.2	12.2	18.8	25.2	32.1	38.9
10	101.3	100.7	101.6		11.9	11.9	12.3		18.8	25.1	33.6	
10	101.3	100.7			11.9	11.9			18.9	25.6		
10	101.4	100.8			12.0	12.0			18.7	26.0		
10	101.3	100.9			11.9	12.1			19.0	25.3		
10	101.5	100.9			12.1	12.1			19.1	25.0		
10	101.2				11.8				19.2			
10	101.5				12.1				19.4			
10	101.8				12.4				19.3			
10	102.1				12.7				19.4			

Table V shows the values of thermo-physical properties of milk during pool boiling in Al and SS pots of an electric still which were evaluated using expressions given in Table IV.

The experimental data given in Tables II and III and thermo-physical properties of milk for nucleate boiling condition given in Table V were used to evaluate the average values of nucleate boiling heat flux ($q_{nucleate}$) by linear regression. The values of $q_{nucleate}$ so obtained at heat inputs of 240, 280, 320 and 360 W for Al pot were found to be 2132.14, 3078.84, 3901.39 and 7978.89 W/m², respectively, and corresponding values determined for SS pot were 1902.19, 2434.59, 3352.5 and 4324.46 W/m² respectively.

The value of Prandtl number (Pr_l) in Eq.(1) was evaluated using Eq. (2) [28].

$$Pr_l = \frac{\mu_l \times C_{pl}}{k_l} \quad (2)$$

The exponent for Pr_l in Eq. (1) was taken as 1.7. Equation (1) can also be rewritten by

considering $C_{pl} \left[\frac{\Delta T_{exc}}{h_{fg} \times Pr_l^n} \right] = x$ and

$$\left[\frac{q_{nucleate}}{\mu_l \times h_{fg}} \sqrt{\frac{\sigma}{g(\rho_l - \rho_v)}} \right]^{\frac{1}{3}} = y \text{ as follows.}$$

$$x = C_{sf} \times y. \quad (3)$$

Thus, the value of C_{sf} is calculated as, $C_{sf} = (x/y)$.

TABLE IV. EXPRESSIONS FOR THERMO-PHYSICAL PROPERTIES OF MILK.

Property	Expression	Reference
Specific heat (C_{pl}), J/kg °C	$C_{pl} = 2.976T + 3692.$	[29]
Surface tension (σ), N/m	$\sigma = 1.8 \times 10^{(-4)}T^2 - 0.163T + 55.6.$	[30]
Density of milk (ρ_l), kg/m ³	$\rho_l = -0.2307 \times 10^{-2}T^2 - 0.2655T + 1040.51$ $-F(-0.478 \times 10^{-4}T^2 + 0.969 \times 10^{-2}T + 0.967).$	[31]
Density of vapor (ρ_v), kg/m ³	$\rho_v = \frac{353.44}{(T + 273.15)}.$	[32]
Viscosity (μ_l), kg/m. s	$\ln \mu_l = 4.03 \times 10^{-5}T^2 - 2 \times 10^{-2}T + 0.827.$	[33]
Thermal conductivity (k_l), W/m ² °C	$k_l = 0.356439\bar{X}_w + 0.223544.$	[34]
Enthalpy of vaporization (h_{fg}), J/kg	$h_{fg} = (h_{fg \text{ of water}}) \times \bar{X}_w.$	[35]

Note: σ is in N.m⁻¹×10⁻³, F is % fat content, μ_l is in Pa.s ×10⁻³ and \bar{X}_w is average percentage of the water contents.

TABLE V. THERMO-PHYSICAL PROPERTIES OF MILK DURING POOL BOILING IN AN ELECTRIC STILL.

Heat input (W)	μ_l (kg/m. s)	C_{pl} (J/kg °C)	k_l (W/m ² °C)	σ (N/m)	ρ_l (kg/m ³)	ρ_v (kg/m ³)	h_{fg} (J/kg)
<i>Al pot</i>							
240	0.000529	3957.757	0.519253	0.042479	998.3384	0.97514	1895696
280	0.000533	3955.674	0.517145	0.042571	998.8116	0.97703	1883354
320	0.000529	3957.459	0.515742	0.042493	998.4061	0.97541	1873402
360	0.000525	3959.245	0.512675	0.042414	997.999	0.97379	1852478
<i>SS pot</i>							
240	0.000528	3958.054	0.519253	0.042466	998.2706	0.974872	1895480
280	0.000532	3956.269	0.517145	0.042545	998.6766	0.976488	1883255
320	0.000529	3957.757	0.515742	0.042479	998.3384	0.975141	1873189
360	0.000523	3960.435	0.512675	0.042363	997.7267	0.972726	1851634

TABLE VI. C_{sf} VALUES EVALUATED FOR AN ELECTRIC STILL.

Heat input (W)	x	y	C_{sf}
<i>Al pot</i>			
240	0.002222	0.164285	0.013524
280	0.002296	0.18559	0.012373
320	0.002189	0.201656	0.010856
360	0.002293	0.257524	0.008903
<i>SS pot</i>			
240	0.002295	0.15822	0.014505
280	0.002238	0.171757	0.013031
320	0.002265	0.191798	0.011807
360	0.002209	0.21032	0.010502

The values of fluid-surface constants (C_{sf}) in boiling correlation of milk in the Al and SS pots of an electric still were determined and are given in Table VI. This table shows that values of C_{sf} during concentration of milk in an

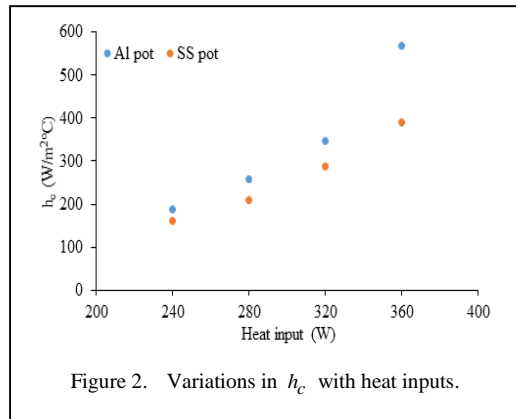


Figure 2. Variations in h_c with heat inputs.

electric still for the given rate of heat inputs for Al surface and milk combination varied from 0.008903 to 0.013524 while for SS surface and milk combination varied from 0.010502 to 0.014505. The average values of C_{sf} for the heating of milk in Al and SS pots were evaluated

to be 0.011414 and 0.012461, respectively. The values of some of the fluid heating surface combinations are 0.0130 (water-copper), 0.0060 (water-brass), 0.0094712 (Khoa-SS under open condition), 0.0078815 (Khoa-Al under open condition) and 0.0002557 (Ghee-SS) [8,16,35].

The values of h_c for the concentration of milk in Al and SS pots of an electric still were also evaluated which were found in the range of 187.36 – 567.56 W/m² °C and 162.18 - 389.88 W/m²°C, respectively. The average values of h_c during the concentration of milk in the Al pot of an electric still for the heat inputs of 240, 280, 320 and 360 W were evaluated to be 187.36, 257.71, 347.15 and 567.56 W/m² °C, respectively, while the corresponding values for the SS pot were found to be 162.18, 209.98, 289.01 and 389.88 W/m²°C. The variation of h_c with respect to change in heat inputs for Al and SS pots of an electric still is illustrated in Fig. 2.

From Fig. 2 it is observed that the values of h_c increases with an increase in rate of heat inputs which are found to be in accordance with the results reported in the literature [10,15,16,18,19]. The values of h_c for the concentration of milk in the Al pot of an electric still were observed to be 29.37% higher than the heating of milk in SS pot.

The errors measured in terms of uncertainty (U) for the collected experimental data were evaluated using least count of the instrument (L_c) and maximum value measure by the instrument (V_{max}) as $U = (L_c / V_{max}) \times 100$. [36]. The experimental error in the results were observed to be within the range of 1.01%.

IV. CONCLUSIONS

In this paper, the values of fluid-surface constants (C_{sf}) in the Rohsenow correlation for the concentration of milk in Al and SS pots of an electric still were evaluated. The values of C_{sf} for Al and SS pots for the concentration of milk were found to be 0.011414 and 0.012461, respectively. The values of h_c were found to increase with the increase in the rate of heat inputs. The values of h_c for the concentration of milk in the Al pot of an electric still were observed to be 29.37% higher than in the case of SS pot. This work would help in developing a better heating surface (heat exchanger) for




obtaining the concentrated milk and would also help in its preservation.

REFERENCES

- [1] Whiting, M. S., van den Bergh, W. J., Theodorakis, P. E., & Everts, M. (2024). Influence of cavity geometry on the bubble dynamics of nucleate pool boiling. *Physics of Fluids*, 36(8), 87102.
- [2] Zhao, C. Y., Zheng, C. M., Wang, X. S., Qi, D., Jiang, J. M., Ji, W. T., Jin, P. H., & Tao, W. Q. (2024). Correlations of falling film hydrodynamics and heat transfer on horizontal tubes: A review. *Renewable and Sustainable Energy Reviews*, 197, 114384.
- [3] Rohsenow, W. M. (1952). A method of correlating heat-transfer data for surface boiling of liquids. *Journal of Fluids Engineering*, 74(6), 969–975.
- [4] Vachon, R. I., Nix, G. H., & Tanger, G. E. (1968). Evaluation of constants for the rohsenow pool-boiling correlation. *Journal of Heat Transfer*, 90(2), 239–246.
- [5] Berenson, P. J. (1962). Experiments on pool-boiling heat transfer. *International Journal of Heat and Mass Transfer*, 5(10).
- [6] Labuntsov, D. A. (1972). Heat Transfer Problems with Nucleate Boiling of Liquids. *Thermal Engineering (English Translation of Teplotenergetika)*, 19(9).
- [7] Sinnarwalla, A. (1970). *Effect of surface conditions on nucleate pool boiling of refrigerant-11*. Masters Theses. Available at: https://scholarsmine.mst.edu/masters_theses/7223
- [8] Lal, G., & Verma, R. D. (1987). Evaluation of constants for Rohsenow pool boiling correlation for ghee. *Indian Journal of Dairy Science*, 40(4), 431–434.
- [9] Jabardo, J. M. S., Fockink Da Silva, E., Ribatski, G., & De Barros, S. F. (2004). Evaluation of the Rohsenow correlation through experimental pool boiling of halocarbon refrigerants on cylindrical surfaces. *Journal of the Brazilian Society of Mechanical Sciences and Engineering*, 26(2).
- [10] Tiwari, G. N., Prakash, O., & Kumar, S. (2004). Evaluation of convective heat and mass transfer for pool boiling of sugarcane juice. *Energy Conversion and Management*, 45(2), 171–179.
- [11] Kangude, P., Bhatt, D., & Srivastava, A. (2018). Experiments on the effects of nanoparticles on subcooled nucleate pool boiling. *Physics of Fluids*, 30(5), 57105.
- [12] Du, J., Wang, Y., Yang, W., Wang, J., Cao, Z., & Sundén, B. (2024). Effect of nanoparticle concentration and surfactants on nanofluid pool boiling. *International Journal of Heat and Mass Transfer*, 221, 125080.
- [13] Kumar, A., Kangude, P., & Srivastava, A. (2023). Coupled bubble dynamics and interaction mechanisms of adjacently nucleated vapor bubbles under subcooled pool boiling regime. *Physics of Fluids*, 35(8).
- [14] Villar, P., Marcelo, D., Saavedra, R., & La Madrid, R. (2016). An experimental study of heat transfer in pool boiling of sugarcane juice. *JP Journal of Heat and Mass Transfer*, 13(4), 445–464.
- [15] Kumar, M., Prakash, O., & Kasana, K. S. (2011). An experimental study on pool boiling of milk. *Heat Transfer - Asian Research*, 40(2), 159–170.

- [16] Kumar, M., Prakash, O., & Kasana, K. S. (2011). An experimental study on pool boiling heat transfer coefficient of milk. *Facta Universitatis, Series: Mechanical Engineering*, 9(1), 61–70.
- [17] Kumar, M., Kasana, K. S., Kumar, S., & Prakash, O. (2010). Evaluation of convective heat transfer coefficient for pool boiling of milk under closed condition. *SAMRIDDHI: A Journal of Physical Sciences, Engineering and Technology*, 1(02), 91–99.
- [18] Kumar, M., Kumar, S., Prakash, O., & Kasana, K. S. (2011). Pool boiling of milk in a stainless steel pot under closed condition. *International Journal of Current Research*, 3(8), 94–99.
- [19] Kumar, M., Kasana, K. S., Kumar, S., & Prakash, O. (2011). Experimental evaluation of constants for the Rohsenow pool boiling correlation for khoa. *SAMRIDDHI: A Journal of Physical Sciences, Engineering and Technology*, 2, 21–26.
- [20] Ali Adib, T., & Vasseur, J. (2008). Bibliographic analysis of predicting heat transfer coefficients in boiling for applications in designing liquid food evaporators. *Journal of Food Engineering*, 87(2), 149–161.
- [21] Kumar, M., Bhutani, V., & Khatak, P. (2015). Research progresses and future directions on pool boiling heat transfer. *Journal of Mechanical Engineering and Sciences*, 9(December), 1538–1555.
- [22] Li, W., Dai, R., Zeng, M., & Wang, Q. (2020). Review of two types of surface modification on pool boiling enhancement: Passive and active. *Renewable and Sustainable Energy Reviews*, 130.
- [23] Singh, S. K., & Sharma, D. (2021). Review of pool and flow boiling heat transfer enhancement through surface modification. *International Journal of Heat and Mass Transfer*, 181.
- [24] Liang, G., & Mudawar, I. (2019). Review of pool boiling enhancement by surface modification. *International Journal of Heat and Mass Transfer*, 128.
- [25] Pereira, J., Souza, R., Lima, R., Moreira, A., & Moita, A. (2024). An overview of the recent advances in pool boiling enhancement materials, structure, and devices. *Micromachines*, 15(2).
- [26] Kumar, M., Prakash, O., & Kasana, K. S. (2012). Experimental investigation on natural convective heating of milk. *Journal of Food Process Engineering*, 35(5), 715–726.
- [27] Kumar, M., Kasana, K. S., Kumar, S., & Prakash, O. (2011). Experimental study on heat and mass transfer for heating milk. *Journal of Energy in Southern Africa*, 22(3), 45–53.
- [28] Bertsch, A. J. (1982). The specific heat capacity of whole and skimmed milk between 50 and 140 °C. *Lait*, 62, 265–275.
- [29] Bertsch, A. J. (1983). Surface tension of whole and skim-milk between 18 and 135 C. *Journal of Dairy Research*, 50(3).
- [30] Bertsch, A. J., C. de J.-J. L. de M. L. et de G. A., Bimbenet, J. J., & Cerf, O. (1982). Density of milk and creams between 65 and 140 degrees C [physical properties]. *Lait (France)*, 62(615–616).
- [31] Grewal, R., & Kumar, M. (2023). Induction heating of sugarcane juice: thermo-enviro-economic analyses. *Journal of Thermal Analysis and Calorimetry*, 148(15), 7939–7950.
- [32] Bertsch, A. J., & Cerf, O. (1983). Dynamic viscosities of milk and cream from 70 to 135 C. *Journal of Dairy Research*, 50(2).
- [33] Murdia, L. K., & Verma, R. D. (1982). *Thermal conductivity of liquid dairy products by line heat sources method*. KrishiKosh. <http://krishikosh.egranth.ac.in/handle/1/49040>
- [34] Cengel, Y. A. (2004). *Heat transfer: A practical approach*. In MacGraw-Hill Education (India).
- [35] Kumar, M., Shimpy, Sahdev, R. K., Sansaniwal, S. K., & Bhutani, V. (2023). Experimental forced convection greenhouse and indirect cabinet drying of date fruits: A comparative study. *Journal of Thermal Analysis and Calorimetry*, 148, 5437–5454.
- [36] Shimpy, Kumar, M., & Kumar, A. (2024). Assessment of a beeswax-packed domestic solar dryer for sustainable bitter gourd drying: An experimental study. *Food and Bioproducts Processing*, 148, 72–87.

Analysis of the Effect of Ethyl Acetate on the Crystallization of MAPbI₃ and its Impact on the Efficiency of the Perovskite Solar Cells

Erro Quiñonez José Eulalio¹, García Gutiérrez Rafael², Arias-Ramos Carlos Fabián³,
Cancino-Gordillo Francisco Enrique⁴, Rangel Segura Ricardo⁵

^{1,2}Universidad de Sonora, Hermosillo Son., México

^{3,4}Instituto de Energías Renovables, Temixco Mor., México

⁵Universidad Michoacana de San Nicolás de Hidalgo: Morelia, Mich., México

¹a222230161@unison.mx, ²rgarcia@cifus.uson.mx, ³cafaar@ier.unam.mx,

⁴cancinogordillof@outlook.com, ⁵rrangel@umich.mx

Abstract—This research presents an experimental methodology for fabricating MAPbI₃ perovskite solar cells, focusing on optimizing the crystallization process. Ethyl acetate was used as a selective antisolvent during the perovskite deposition to enhance film quality. Film characterization was performed using profilometry, UV-Vis spectroscopy, scanning electron microscopy (SEM), and X-ray diffraction (XRD). The results revealed that the use of ethyl acetate significantly improved perovskite film properties owing to the larger, more uniform grains and a well-defined crystalline structure. These enhancements lead to increased light absorption in the visible spectrum, resulting in a marked improvement in solar cell efficiency, reaching 13.75%, compared to 5.46% for untreated cells.

Keywords - Perovskite, MAPbI₃, spin-coating, antisolvent, ethyl acetate

I. INTRODUCTION

The demand for energy increases every day, but traditional energy sources dominating the market are far from environmentally friendly.

Therefore, exist a significant interest in researching devices that harness renewable energy resources, such as MAPbI₃ (methyl ammonium lead iodide) perovskite solar cells. These cells present a promising alternative, with

their efficiency rising remarkably from 3% to 26.7% from 2009 to 2024 [1]. The present work focuses on optimizing the fabrication of organometallic perovskite solar cells with a direct architecture (N-i-P). The spin-coating technique was employed, using ethyl acetate as a selective antisolvent, which enhanced the perovskite crystallization [2]. Several characterization techniques were utilized, including profilometry to measure thicknesses, UV-Vis spectroscopy to evaluate optical properties, scanning electron microscopy (SEM) for morphology analysis, X-ray diffraction (XRD) to identify crystalline phases, and current-voltage (I-V) curves to evaluate electrical performance for the perovskite solar cells.

The methodology and the results have proven invaluable, enabling a deeper understanding of the fabrication processes. As a result, more efficient and stable perovskite solar cells were produced, which is a critical step toward the large-scale adoption of solar energy [3]. This progress underscores the potential of perovskite-based solar cells as a viable solution for future clean and sustainable energy generation [4].



II. EXPERIMENTAL METHODOLOGY

A. Perovskite Solution

The solution was composed of a 1:1:1 molar ratio of methylammonium iodide (MAI):lead iodide (PbI₂):dimethyl sulfoxide (DMSO) all dissolved in 1 mL of dimethylformamide (DMF) and stirred at 650 rpm for 12 hours prior to use.

B. Cell Fabrication

The first step involves preparing FTO-coated glass substrates in pieces of 25x25mm dimension. The substrates are then cleaned with alkaline soap solution and dried, subsequently they are sonicated (BRANSON 1800 ultrasonic bath) for 15min in acetone and isopropyl alcohol (IPA) for 15min also in ultrasonic bath, both procedures were without temperature. Finally, the substrates are dried and cleaned in UV-Ozone for 20min.

The second step is the formation of the electron transporting layer (ETL) on the device. The ETL is composed of a titanium oxide solution aimed at the formation of a compact morphology layer (c-TiO₂) on the solar cell. The c-TiO₂ solution is synthesized by SOL-GEL methodology from titanium isopropoxide, IPA and hydrochloric acid. The c-TiO₂ layer is deposited via spin-coating (Fig. 1) with 100μL over FTO layer at 2000rpm for 20s followed by heat treatment at 150 °C for 15min and a thermal treatment at 450 °C for 30min.



Figure 1. Compact TiO₂ deposit.



Figure 2. Mesoporous TiO₂ deposit.

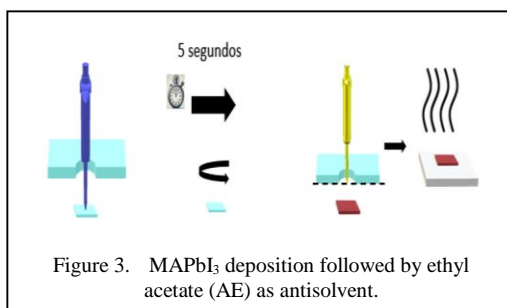


Figure 3. MAPbI₃ deposition followed by ethyl acetate (AE) as antisolvent.

The third step is the formation of the mesoporous layer as part of the ETL which allows us to increase the contact area with the absorber layer and improve the extraction of free charges. This layer composed of mesoporous TiO₂ (mp-TiO₂) is obtained from the TiO₂ paste dissolved (NR-30, Dysol) in ethanol in a weight ratio of 1:6 (TiO₂: Ethanol) and stirred 5h prior to use at 650rpm without temperature. The mp-TiO₂ solution (100μL) is deposited over the c-TiO₂ layer via spin-coating at 4000rpm for 30s followed by a thermal treatment at 500 °C for 30min (Fig. 2).

The fourth step is focused on the formation of the absorber layer in the device, which will be composed of methylammonium lead iodide perovskite (MAPbI₃). The perovskite solution is deposited on the mp-TiO₂ layer by spin-coating. In static mode, 70μL of the perovskite solution is placed at the center of the substrate, allowing it to disperse over the entire surface of the substrate prior to activating the spin at 5000rpm for 20s. Samples made with antisolvent, after 5s of rotation of the substrate, 140μL of the antisolvent ethyl acetate (EA) are deposited with a separation of 4 cm from the central surface of the substrate in a continuous and perpendicular manner to the substrate (Fig. 3). The amount of antisolvent was defined after performing tests ranging from 40μl to 400μl. For all samples, after the spin time the substrates are heat treated at 100 °C for 2 min in a hot-plate.

In the fifth step the hole transport layer (HTL) is fabricated by the SPIRO solution synthesized from the polymer SPIRO-OMeTAD dissolved in chlorobenzene (CB) at a concentration of 80mg/mL to which are added 13.4μL of a lithium salt solution and 22μL of 4-Tertbutyl-Pyridine (tBP). The lithium salt solution is obtained from the dissolution of the lithium salt in acetonitrile (ACN) at a concentration of 516mg/mL and stirred for 1h at 650rpm without temperature. To form this layer, 60μL of the SPIRO solution was deposited over the perovskite previously

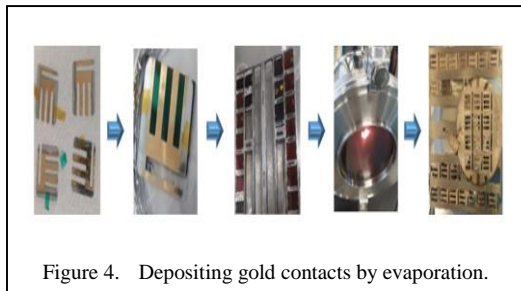


Figure 4. Depositing gold contacts by evaporation.

deposited via spin-coating at 4000rpm for 20s in a glovebox.

Finally, in the seventh step, a mask is applied on top of the HTL for the deposition of 80nm of gold contacts using cathodic evaporation in a high vacuum chamber of $\approx 2.6 \times 10^{-5}$ Torr (Fig. 4).

III. CHARACTERIZATION TECHNIQUES

Various characterization techniques were used for the perovskite films studies. To identify the crystalline phase, a Bruker D8 Advance X-ray diffractometer equipped with Dynamic Beam Optimization™ technology was used, with an incidence angle of 1.5° in a detection range from 10° to 70° . The optical absorbance (A) of perovskite films with and without antisolvent were measured in a spectrophotometer (Shimadzu UV-1800) in the wavelength range from 300 to 1000 nm. The film thickness of perovskites was measured by an AMBios XP-200 profilometer measured the film thickness, with a vertical resolution of up to 1\AA and a scanning range of 55mm. Surface morphology of the films were analyzed using a JEOL JSM-7800F high-resolution scanning electron microscopy (SEM), featuring a resolution of 0.8nm and a microanalysis system. Photocurrent density-voltage (J-V) curves of perovskite solar cells were measured in an Oriel 81.174 class AAA equipped solar simulator under AM 1.5G with a Keithley 2.400 source meter as a data acquirer. The light intensity was calibrated with a Newport Si reference cell to achieve $100\text{mW}/\text{cm}^2$ intensity (one-sun illumination). The device area was 0.104 cm^2 delimited through a mask. The voltage scan direction was setup from 1.1 to - 0.1 V.

IV. RESULTS AND DISCUSSION

The use of ethyl acetate as a selective antisolvent accelerated the crystallization process due to its miscibility with DMF and DMSO, while the perovskite precursors remain

insoluble in it. This feature facilitates the formation of larger, more uniformly distributed crystals, improves crystalline quality, and reduces charge carrier recombination. These enhancements significantly improved morphology, and crystallinity of the perovskite films, leading to increased efficiency and reproducibility of perovskite-based solar cells [5].

Fig. 5 presents the absorbance spectra of treated and untreated films. As can be seen, the absorbance spectra of the treated films with antisolvent are nearly identical, suggesting that ethyl acetate treatment produces consistent and reproducible results.

Treated films showed higher absorbance in the 300–550nm range compared to untreated films, indicating improved visible light absorption. This enhancement is critical for solar cells, as greater light absorption increases photon capture and charge carrier generation [6].

Additionally, treated films displayed a sharper absorption edge around 750–800nm. A more defined absorption edge suggests better crystallinity and fewer defects in the perovskite structure, which can lead to improved energy conversion efficiency [7].

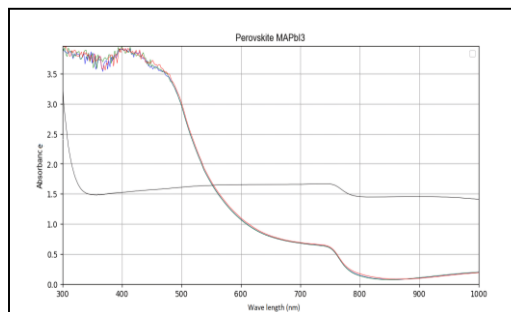


Figure 5. Absorbance graphs of MAPbI₃ films: A) Untreated, B) Antisolvent treated films.

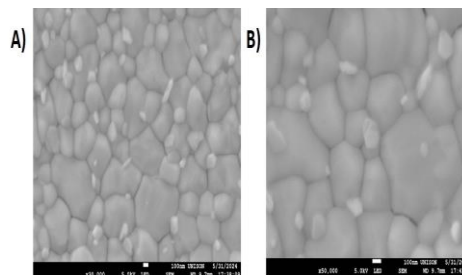
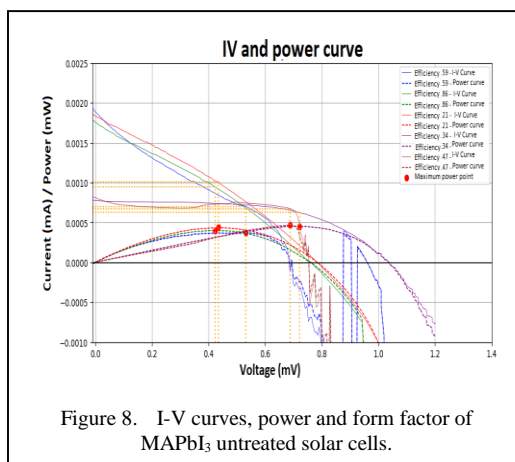
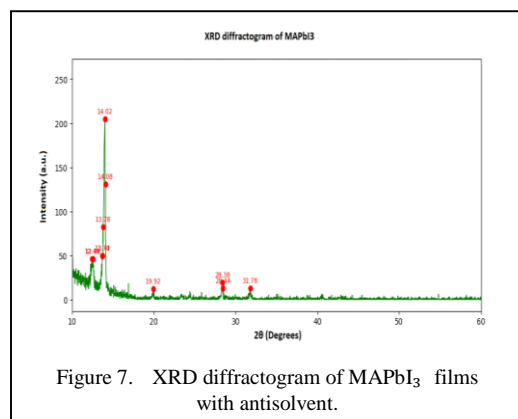


Figure 6. SEM view of the film surface: A) MAPbI₃ without antisolvent, B) MAPbI₃ with antisolvent.

Surface morphology was analyzed using scanning electron microscopy (SEM), as shown in Fig. 6. Untreated films exhibit smaller grains (average size: 66.72nm) and less uniform distribution, which can lead to increased charge carrier recombination and reduced efficiency of solar cells [8].

On the other hand, the treated films with ethyl acetate showed significantly larger and more uniformly distributed grains, with an average grain size of 279.64nm. The increment in the grain size indicates improved crystallization, reduced recombination, and enhanced charge carrier mobility, all of which are essential for efficient solar energy conversion [9]. Overall, ethyl acetate treatment enhances the quality of MAPbI₃ films by improving film morphology, reducing charge carrier recombination, and increasing the consistency of optoelectronic properties. These advancements contribute to higher efficiency, better stability, and improved control in the fabrication of perovskite solar cells [10].

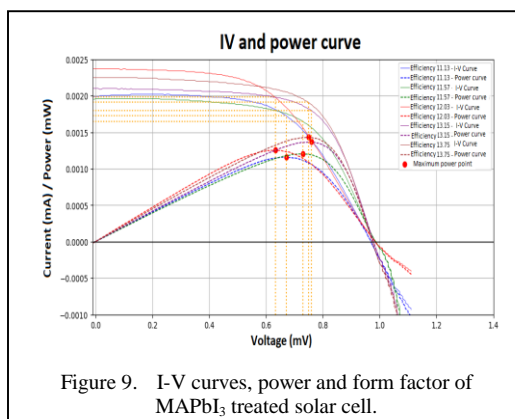
X-ray diffraction (XRD) was employed to assess the purity, crystal structure of the perovskite films. The XRD diffractogram present in Fig. 7 displays well-defined peaks which correspond to the tetragonal phase of the perovskite, and high crystalline quality, suggests that the MAPbI₃ material structure is optimal for solar cell applications. The peak at $2\theta = 14.02$ corresponds to the (110) plane, while the peak at $2\theta = 19.92$ is related to the (112) plane. Peaks at $2\theta = 28.38$ and $2\theta = 28.44$ are associated with the (220) plane, and the peaks at $2\theta = 31.78$ and $2\theta = 12.54$ may indicate the presence of PbI₂, in addition to corresponding to the (310) plane in the tetragonal structure of MAPbI₃. These peaks reflect the presence of Pb, I, and CH₃NH₃ in the crystalline structure [11].



This positively impacts efficiency by minimizing charge carrier recombination, improving charge mobility, and ensuring that the material is fully utilized in its photovoltaic function. All these factors combined can lead to a significant increase in the efficiency of converting sunlight into electricity [12].

When analyzing the I-V curves of MAPbI₃ solar cells, both untreated (Fig. 8) and treated (Fig. 9) with ethyl acetate as a selective antisolvent for DMF and DMSO via spin coating, it is evident that the ethyl acetate treatment positively impacts the electrical properties of the MAPbI₃-based solar cells [13].

The treated cells exhibit higher efficiency, an improved fill factor, and greater uniformity in their electrical behavior, making them more suitable for photovoltaic applications. In contrast, the untreated cells show greater variability and lower performance, highlighting the importance of the treatment in the fabrication of efficient solar cells [14].



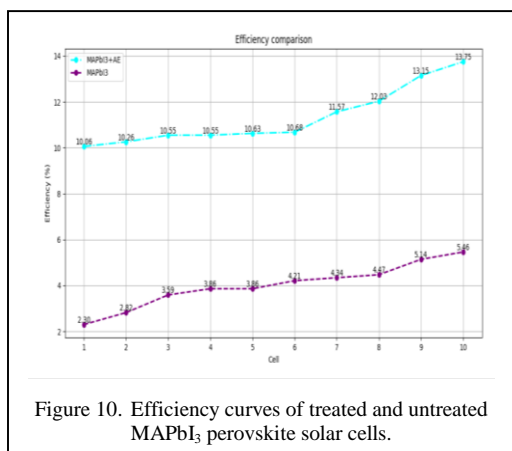


Figure 10. Efficiency curves of treated and untreated MAPbI₃ perovskite solar cells.

It is evident that the use of ethyl acetate as a selective antisolvent in the fabrication of MAPbI₃ solar cells significantly improves their efficiency. In Fig. 10, treated cells show an efficiency increase from 10.65% to 13.75%, while untreated cells reach a maximum of only 5.46%. This improvement is attributed to better crystallization, larger and more uniform grains, and a more homogeneous film. The ethyl acetate treatment nearly triples the efficiency, making these cells significantly more effective and consistent in their performance [15].

V. CONCLUSIONS

The use of ethyl acetate as a selective solvent in the fabrication of MAPbI₃ perovskite solar cells has proven to be an effective strategy to significantly improve their performance. Key findings of this study are:

- Morphological improvement: Ethyl acetate treatment results in larger and more uniform perovskite grains, with the mean grain size increasing from 66.72nm to 279.64nm.
- Optimized optical properties: Treated films show increased absorbance in the visible range and a sharper absorption edge, indicating improved crystalline quality.
- Improved crystal structure: XRD analysis reveals a pure tetragonal phase of MAPbI₃ with well-defined peaks, indicating high crystalline quality.
- Significant increase in efficiency: Ethyl acetate-treated solar cells achieve efficiencies of up to 13.75%, almost tripling the performance of untreated cells.

These results infer the importance of precise crystallization control in the fabrication of perovskite solar cells. The use of ethyl acetate as a selective solvent is a viable option to improve the quality of the perovskite film and, consequently, the performance of photovoltaic devices.

And as a final conclusion, in future solar cell manufacturing sessions the amount of antisolvent will be varied and the application window times will be improved.

ACKNOWLEDGMENT

The authors thank Ari Martín Vargas-Sotomayor for technical support and Hailin Hu for valuable discussions. JEEQ thank CONAHCYT-Mexico for the graduate scholarship. Financial support from PAPIIT-UNAM (IT102625) is acknowledged. CFAR and FECG acknowledges CONAHCYT, Mexico for the postdoctoral fellowship (CVU # 709010, and 784149, respectively).

REFERENCES

- [1] National Renewable Energy Laboratory. (2024). *Best research-cell efficiencies*. National Renewable Energy Laboratory. Available at: <https://www.nrel.gov/pv/cell-efficiency.html>
- [2] Jeon, N. J., Noh, J. H., Yang, W. S., Kim, Y. C., Ryu, S., Seo, J., & Seok, S. I. (2015). Compositional engineering of perovskite materials for high-performance solar cells. *Nature*, *517*(7535), 476-480.
- [3] Yang, W. S., Park, B. W., Jung, E. H., Jeon, N. J., Kim, Y. C., Lee, D. U., ... & Seok, S. I. (2017). Iodide management in formamidinium-lead-halide-based perovskite layers for efficient solar cells. *Science*, *356*(6345), 1376-1379.
- [4] Gonzalez Clavijo, A. (2020). *Materiales de interés en el campo de las energías limpias*. Available at: <http://riull.ull.es/xmlui/handle/915/19695>
- [5] Xiao, M., Huang, F., Huang, W., Dkhissi, Y., Zhu, Y., Etheridge, J., ... & Spiccia, L. (2014). A fast deposition-crystallization procedure for highly efficient lead iodide perovskite thin-film solar cells. *Angewandte Chemie International Edition*, *53*(37), 9898-9903.
- [6] Adjogri, S. J., & Meyer, E. L. (2020). A review on lead-free hybrid halide perovskites as light absorbers for photovoltaic applications based on their structural, optical, and morphological properties. *Molecules*, *25*(21), 5039.
- [7] Akel, S., Kulkarni, A., Rau, U., & Kirchartz, T. (2023). Relevance of long diffusion lengths for efficient halide perovskite solar cells. *Prx Energy*, *2*(1), 013004.
- [8] Montes, F. R., Rosiles-Perez, C., Ramos, C. F. A., Hu, H., Sánchez, J. L. S., & González, A. E. J. (2022). Study of DMSO concentration on the optical and structural properties of perovskite CH₃NH₃PbI₃ and its use in solar cells. *Journal of Solid State Chemistry*, *312*, 123158.

- [9] Bi, D., Tress, W., Dar, M. I., Gao, P., Luo, J., Renevier, C., ... & Hagfeldt, A. (2016). Efficient luminescent solar cells based on tailored mixed-cation perovskites. *Science advances*, 2(1), e1501170.
- [10] Cao, X., Hao, L., Liu, Z., Su, G., He, X., Zeng, Q., & Wei, J. (2022). All green solvent engineering of organic-inorganic hybrid perovskite layer for high-performance solar cells. *Chemical Engineering Journal*, 437, 135458.
- [11] Hossain, A., Bandyopadhyay, P., Karmakar, A., Ullah, A. A., Manavalan, R. K., Sakthipandi, K., ... & Ahmed, J. (2022). The hybrid halide perovskite: Synthesis strategies, fabrications, and modern applications. *Ceramics International*, 48(6), 7325-7343.
- [12] Stoumpos, C. C., Malliakas, C. D., & Kanatzidis, M. G. (2013). Semiconducting tin and lead iodide perovskites with organic cations: phase transitions, high mobilities, and near-infrared photoluminescent properties. *Inorganic chemistry*, 52(15), 9019-9038.
- [13] Chen, Y., Zhang, M., Li, F., & Yang, Z. (2023). Recent progress in perovskite solar cells: status and future. *Coatings*, 13(3), 644.
- [14] Yang, W. S., Noh, J. H., Jeon, N. J., Kim, Y. C., Ryu, S., Seo, J., & Seok, S. I. (2015). High-performance photovoltaic perovskite layers fabricated through intramolecular exchange. *Science*, 348(6240), 1234-1237.
- [15] De Los Santos, I. M., Cortina-Marrero, H. J., Ruíz-Sánchez, M. A., Hechavarría-Difur, L., Sánchez-Rodríguez, F. J., Courel, M., & Hu, H. (2020). Optimization of CH₃NH₃PbI₃ perovskite solar cells: A theoretical and experimental study. *Solar Energy*, 199, 198-205.

Biodiesel Synthesis using Animal Fat and Ethyl Route

Alânia Kallyne Graciliano Teixeira¹, Jhonatas Wagner Barbosa da Costa Gouveia², José Luiz Francisco Alves³, Marta Célia Dantas Silva⁴, Sílvia Layara Floriani Andersen⁵

^{1,2,3,4,5}Federal University of Paraíba (UFPB), João Pessoa, Brazil

¹alania.teixeira@estudante.cear.ufpb.br, ²jhonataswagner@yahoo.com.br, ³joseluiz@cear.ufpb.br, ⁴marta.cds@cear.ufpb.br, ⁵silvia@cear.ufpb.br

Abstract—The current energy scenario is marked by the growing search for renewable alternatives to the dependence on petroleum-derived fuels. In this context of sustainable alternatives, biomass emerges as a potential source for the production of biofuels, such as biodiesel, with Brazil being the great pillar for the implementation of this trend due to its solid agricultural and livestock infrastructure. Therefore, the objective of this article was to produce biodiesel using pork fat and ethanol. Thus, the process involved the use of a fat/alcohol ratio of 1:9, with the catalyst (KOH). The transesterification reaction was controlled at a temperature of 60 °C for a period of one hour. The process efficiency was 58% and the biodiesel properties were analyzed by FTIR spectroscopy in addition to thermogravimetric analysis (TG). The results demonstrated that pork fat is a viable raw material for biodiesel production.

Keywords - biodiesel, pork fat, ethanol transesterification

I. INTRODUCTION

The Industrial Revolution, which began at the end of the 18th century, marked a change in society, especially in terms of economic and technological development. However, one of the most pressing and profound issues of this era is the over-reliance on fossil fuels. These powerful and abundant energy resources formed the basis of the industrial economy and fueled global productivity growth [1].

In the 20th century, oil and natural gas began to replace coal in many areas, especially

transportation, consolidating the role of ancient oil as the backbone of the world economy [2].

Currently, the transportation sector is the one that contributes the most to the increase in energy consumption, according to the Energy Agency and the National Energy Balance report, with an increase rate of around 2% per year [3,4]. This is a worrying scenario for the future and the environment, since fossil fuels are finite resources that cause serious environmental impacts, since the method of extraction and use of these fuels can generate imbalances ranging from marine life to the generation of toxic gases, which contributes to global warming [5]. Therefore, more sustainable energy alternatives must be explored to achieve a balance in energy demand and environmental protection [6].

These efforts are aligned with Sustainable Development Goals (SDGs) 7 and 13 to promote sustainable and affordable energy and combat climate change. They also play an important role in the development of chemical processes and products, reducing the use of non-renewable materials, which supports the foundations of green chemistry. A transition to a sustainable transport system drives the reduction of CO₂ emissions, an urgent demand and, at the same time, an opportunity for sustainable development that must prioritize all other global agendas.

In this context, energy obtained from biomass appears to be a good alternative, especially in the transportation sector, due to its availability, biodegradability, and low cost [7,8].



In Brazil, in 2023, according to the country's energy index [9], the main fuel used in the automotive sector is diesel oil, leading to a 19.2% increase in the country's total energy consumption. According to this information, diesel is the most widely used fuel throughout the country, especially in transportation and passenger cars. With the development of business, in addition to the effects of international trade, the need for transportation arises, which directly affects the increase in the amount of fuel. Despite the pressure to move towards a clean environment and energy efficiency, current trends are directed towards the use of vehicles that use diesel [10].

In this context, biofuels are an alternative to petroleum and its derivatives, as their production plays an important role in reducing pollution [11,12]. In addition to making a renewable energy plan to replace fossil diesel.

In 2023, Brazilian biodiesel production increased by 20.3% compared to the previous year, reaching a total of 7,527,659 m³, due to the increase from 10.0% to 11.5% of the percentage of biodiesel in fossil diesel [13]. Biodiesel production in the country is expected to increase further, to 13% by the end of 2024, and then to 15% by 2025.

With the growing demand for this biofuel, it is increasingly necessary to diversify the raw materials used in biodiesel production, since soybean oil currently represents around 70% of the input used. To ensure sustainable growth and meet future blending targets, Brazil will need to explore new sources, such as animal industry waste and residual oils, thus expanding the supply of raw materials and ensuring greater stability for the sector in the long term.

In the global context, Brazil stands out in biodiesel production due to its solid agricultural and livestock infrastructure, achieving a leading position in this market. Thanks to continuous investment in agricultural research in recent decades, the country has become one of the largest producers and exporters of animal protein in the world [14]. This advance generates approximately 2.5 million tons of animal fat annually [15], which can be used as raw material for the production of soap and biodiesel [16]. This direction not only presents economic options, but also promotes more efficient management of industrial by-products [17].

Pork fat stands out as a promising alternative in the bioenergy sector due to its rich composition in fatty acids, making it a viable raw material for the production of biolubricants and also biofuels. This abundant byproduct of the pork production chain, yielding approximately 8 kg per animal, contributes significantly to the reduction of production costs [18]. This productive potential not only benefits the biofuel industry, but also promotes the valorization of byproducts, driving a more sustainable economy.

Furthermore, pork fat has chemical properties suitable for the transesterification process, which is the most commonly used method to convert triglycerides into biodiesel [19].

Transesterification or alcoholysis results from the change of the alkoxide group and the reaction of triglycerides with short-chain alcohols (usually methanol or ethanol) in the presence of a catalyst, producing a mixture of fatty acid alkyl esters (biodiesel) and glycerol [20].

The most commonly used alcohols in biofuel production are methanol and ethanol [21]. While they all work well, biomass ethanol is known to be less toxic, help reduce greenhouse gas emissions, and provide a sustainable method of converting triglycerides to esters [22,23].

To scale up biodiesel production processes using ethanol, homogeneous alkaline catalysts are often added. These materials have greater catalytic activity than acid catalysts, accelerating the transesterification reaction and promoting the efficient conversion of triglycerides into esters. Therefore, the use of original catalysts not only reduces the occurrence time but also increases the yield, which produces better biodiesel with better fuel characteristics and performance [24].

This work aims to synthesize biodiesel from pork fat via the ethyl route and evaluate its potential conversion through analysis.

II. METHODOLOGY

A. Biodiesel Synthesis

An alternative approach was investigated to improve biodiesel production, instead of the traditional chemicals used in the conversion reaction. In this study, pork fat was chosen as the lipid source, and anhydrous ethanol replaced

traditional methanol, aiming at better performance and lower toxicity.

For the reaction to occur, a fat/alcohol molar ratio of 1:9 was used, ensuring efficiency during the process, as well as the conversion of triglycerides present in the fat into esters and fatty acids, which make up the biodiesel. In order to accelerate the conversion process, the catalyst used in the concentration was potassium hydroxide (KOH), with a concentration of 0.5% in relation to the mass of the fat.

It was initially added to the alcohol for better solubility, then the pork fat was added to the occurrence where it was performed, keeping the temperature constant at 60 °C for a period of one hour, with continuous stirring to ensure the uniformity of the mixture. At the end of the process, it was possible to observe the separation into two phases: the upper layer, with lower density, corresponded to the raw biodiesel, while the lower layer, denser, was composed of glycerol, a byproduct of the process.

In order for the biodiesel to reach purity, it was necessary to go through the washing process. In this process, an equivalent volume of distilled water was used, twice in succession, in order to remove any catalyst residues and even other impurities. After this, the biodiesel drying process begins, where the sample is placed in an oven, with forced air circulation, at a temperature of 70 °C, for a period of three consecutive hours. The biodiesel drying process is carried out due to the extreme importance of removing any remaining moisture, which ensures that the final product obtains stability and the desired quality.

Right after the biodiesel drying process, the material was stored so that later analyses could be performed, considering its physical and chemical properties. Therefore, the calculation of the mass ratio of the biodiesel produced to the initial amount of pork fat at the beginning of the process was performed to obtain the biodiesel yield. This step is performed in order to evaluate how productive the transesterification reaction is under the experimental circumstances used.

B. Biodiesel Characterization

The FTIR spectra of the biodiesel and pork fat samples were obtained using a Shimadzu UV-2550 spectrometer equipped with an Attenuated Total Reflectance (ATR) sensor. The procedure involved applying a drop of the biodiesel and pork fat samples to the equipment crystal, where

a radiation source excites the molecules, providing information about the chemical bonds present. The results were obtained in a wavenumber range of 600 – 4000 cm^{-1} , with a resolution of 4 cm^{-1} and 32 scans.

For TG analysis, a Netzsch equipment, model STA449F5, was used under an atmosphere of N₂ (purity 99.99%), with an average flow rate of 50 mL/min. TG was used to study the thermal properties and composition of the samples. The analysis was performed with a heating rate of 10 °C/min.

III. RESULTS AND DISCUSSION

Given the process performed, the biodiesel had a yield of approximately 58% in relation to the mass of fat, in agreement with the literature. In this sense, pork fat appears as a potential alternative for biodiesel production, especially in regions where animal fat is abundant.

The FTIR spectra of pork fat and biodiesel synthesized from fat are shown in Fig. 1. Stretching can be observed at 3008 cm^{-1} , which may be associated with a specific bond vibration in carbon-hydrogen (C-H) or carbon-carbon (C = C) in biodiesel molecules from pork fat.

Absorption around the range of 2983 cm^{-1} to 2852 cm^{-1} in the spectrum is mainly associated with stretching vibrations of C-H (carbon-hydrogen) bonds in methyl groups (CH₃). Characterized by C-H bonds in aliphatic chains, common in organic compounds [25,26].

The stretching around 1737 cm^{-1} is related to the stretching vibrations of the C=O (carbon-oxygen) bond [27]. It is characteristic of ester groups, which are formed during the transesterification process in biodiesel production [28].

The stretching between the range of 1462 cm^{-1} to 1301 cm^{-1} in the spectrum are associated with the presence of functional groups related to deformations (bends) of C-H bonds, typical of alkyl esters [29].

The presence of stretching in the range between 1244 cm^{-1} and 858 cm^{-1} represents a specific region and is related to the vibrations of the ester bonds (C-O) and the stretching of the C-O-C group, which represents the existence of ester bonds in methyl or ethyl esters [29].

The stretching observed at 723 cm^{-1} is linked to the vibrations of the C-H (carbon-hydrogen) bond in aliphatic chains [30].

Finally, the spectroscopic analysis also reveals information about the moisture content of the synthesized biodiesel. The low water content is evidenced by the absence of bands in the region of $3100\text{-}3500\text{ cm}^{-1}$ [27].

The conversion into biodiesel is evidenced by the presence of three relevant spectral regions, located in the bands of 1170.16 cm^{-1} , 1366.39 cm^{-1} and 1458.19 cm^{-1} [31]. These specific regions reflect significant changes in the chemical structure of the analyzed compounds, serving as key indicators to confirm the transesterification process of the triglycerides present in the raw material. An important aspect observed in the present study is the decrease in the intensity of the methyl peak of the O-CH_3 functional group after the transesterification step.

In addition, the peaks associated with the methylene (O-CH_2) and methyl ($-\text{CH}_3$) groups, commonly found in intact fat molecules, show a reduction during the transesterification process.

This decrease is a relevant result and consistent with the expected changes in the chemical structure of the molecules, since these groups are progressively consumed and converted into esters during the reaction. The results obtained are in agreement with the literature data, reinforcing the validity of the experimental observations and the consistency of the method used.

However, although FTIR analysis made it possible to identify the functional groups in the samples, this technique alone is not sufficient to confirm the complete conversion of oil and/or fat into biodiesel. For a more comprehensive

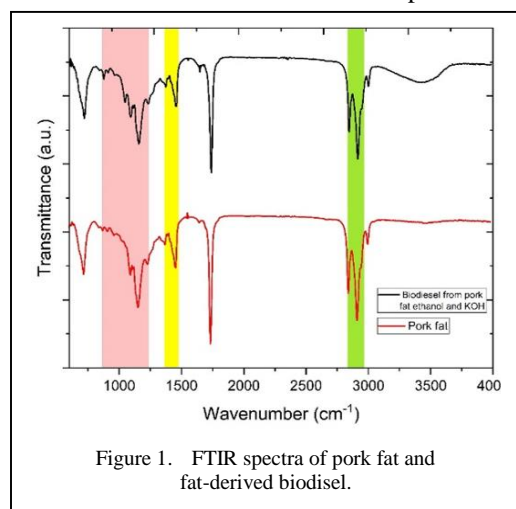


Figure 1. FTIR spectra of pork fat and fat-derived biodiesel.

validation, it is common to resort to other analytical techniques such as gas chromatography coupled to mass spectrometry (GC-MS) [32]. This technique is used in biodiesel analysis to determine the composition and quality of the final product. It allows the quantification of esters, glycerol and impurities present in biodiesel [33].

With the results obtained from the TG analysis of pork fat presented in Fig. 2, a significant mass loss rate can be observed starting at $394.27\text{ }^\circ\text{C}$, with the maximum decomposition rate occurring at $428.36\text{ }^\circ\text{C}$. At this temperature, the mass loss rate (DTG) was $-1.87853\%/^\circ\text{C}$, reflecting the breakdown of the main components, primarily triglycerides. The stabilization of the TG curve after $450\text{ }^\circ\text{C}$ indicates that the volatile components have already been released, leaving only carbon residues.

These results are in line with studies on the pyrolysis of animal fats, such as those of [34], which report similar behavior in beef tallow, and corroborate those of [35], who investigated the transesterification of fat to biodiesel. The thermal behavior of pork fat confirms its potential as a source for biofuels, being relevant for energy processes, as indicated by [36] in studies of animal fats for thermal energy storage.

In the TG analysis of biodiesel, as shown in Fig. 3, a thermal behavior characteristic of methyl esters of fatty acids resulting from the transesterification of animal fats is observed. This technique reveals that the thermal decomposition of biodiesel occurs in distinct

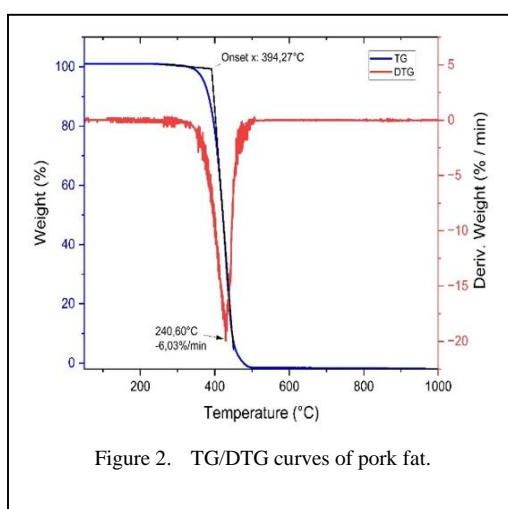


Figure 2. TG/DTG curves of pork fat.

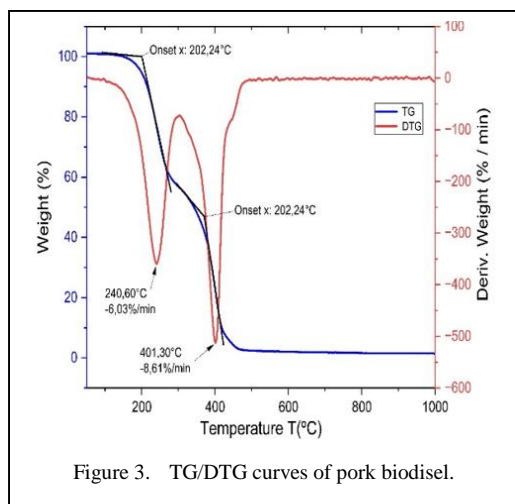


Figure 3. TG/DTG curves of pork biodiesel.

stages, reflecting the complexity of its chemical composition.

The first significant loss of mass occurs from 202 °C, due to the volatilization of lighter components, such as short and intermediate chain fatty acids. This behavior is also present in studies using animal fat for biodiesel production, where the volatilization of saturated and unsaturated fatty acids, such as palmitate and oleate, was observed [16,37].

The second stage of thermal decomposition, occurring at around 378 °C, reflects the degradation of more stable, long-chain molecules, such as stearic acid. This phase culminates in a more pronounced mass loss rate, evidenced by the Derivative of Thermogravimetry (DTG) peaks at 401.3 °C. This suggests that more complex chemical structures require higher temperatures to initiate decomposition, indicating their thermal stability.

Furthermore, the presence of a residue of around 1,45% at 1000 °C, attributed to impurities or non-volatile inorganic compounds, highlights the high thermal stability of biodiesel derived from animal fats. This stability is crucial to performance in internal combustion engines, especially at high temperatures.

IV. CONCLUSION

The conclusion of this study reinforces the viability of using pork fat as a raw material for biodiesel production, highlighting the potential of the ethyl route. This abundant byproduct of the pork production chain demonstrated high potential for conversion into fatty acid esters through the transesterification process with

ethanol. With a conversion rate of approximately 58%, the results are in line with previous studies that analyzed the use of animal fats for biofuel production.

TG and FTIR analyses confirmed the quality of the biodiesel produced, showing characteristic thermal decomposition of fatty acid esters and the presence of the expected functional groups after transesterification. These findings indicate that pork fat represents a viable and sustainable alternative for diversifying raw material sources in the biofuel sector, contributing to the valorization of byproducts from the agri-food industry.

However, it is crucial to further investigate the variables that directly influence biodiesel yield and quality, such as molar ratios, catalyst amounts, reaction time and temperature, as well as the interactions between these factors. Future research should explore both the individual impact of each variable and their combined relationships to optimize process efficiency, in addition to investigating economic aspects related to synthesis and process variables.

REFERENCES

- [1] Gani, A. (2021). Fossil fuel energy and environmental performance in an extended STIRPAT model. *Journal of Cleaner Production*, 297, 126526.
- [2] Johnstone, P., & McLeish, C. (2020). World wars and the age of oil: Exploring directionality in deep energy transitions. *Energy Research & Social Science*, 69, 101732-101732.
- [3] International Energy Agency. (2024). *World Energy Outlook 2024-Analysis*. Available at: <https://www.iea.org/reporth>
- [4] Balanço Energético Nacional. (2024). *EPE*. Available at: <https://www.epe.gov.br/pt/publicacoes-dados-abertos/publicacoes/balanco-energetico-nacional-2024>
- [5] Harfoot, M., et al. (2018). Present and future biodiversity risks from fossil fuel exploitation. *Conservation Letters*, 11.
- [6] Genc, T. S., & Kosempel, S. (2023). Energy transition and the economy: a review article. *Energies*, 16(7), 2965.
- [7] Bhatia, S. K., et al. (2019). Bioconversion of barley straw lignin into biodiesel using *Rhodococcus* sp. YHY01. *Bioresource Technology*, 289(121704), 121704.
- [8] Nguyen, H. C., Nguyen, M. L., Wang, F.-M., Juan, H.-Y., & Su, C.-H. (2020). Biodiesel production by direct transesterification of wet spent coffee grounds using switchable solvent as a catalyst and solvent. *Bioresource Technology*, 296(122334), 122334.
- [9] Balanço Energético Nacional. (2024). *EPE*. Available at: <https://www.epe.gov.br/pt/publicacoes-dados-abertos/publicacoes/balanco-energetico-nacional-2024>

- [10] Guo, T., Chen, J., & Liu, P. (2022). Impact of Emerging Transport Technologies on Freight Economic and Environmental Performance: A System Dynamics View. *International Journal of Environmental Research and Public Health*, 19.
- [11] Messias, G. (2020). Evaluation of the Behavior of the Kinetic Parameters of the Oxidation Reaction of Biodiesel in Contact with Metal Alloys During Storage. *Revista Virtual de Química*, 608-615.
- [12] Guedes, J. M., Santos, A. G. D., & Santos, H. S. dos. (2021). Use of biomass as an energy source for the production of biofuels. *Electronic Magazine Environment Management and Development*.
- [13] Balanço Energético Nacional. (2024). EPE. Available at: <https://www.epe.gov.br/pt/publicacoes-dados-abertos/publicacoes/balanco-energetico-nacional-2024>
- [14] Moretti, C. L. (2020). *Investing in agricultural research brings returns to Brazilian society*.
- [15] Empresa Brasileira de Pesquisa Agropecuária. Gordura animal. (2024). Available at: <https://www.embrapa.br/en/international>
- [16] Toldrá-Reig, F., Mora, L., & Toldrá, F. (2020). Trends in biodiesel production from animal fat waste. *Applied Sciences*, 10(10), 3644.
- [17] Friedrichsen, J. de S. A., et al. (2022). The appropriate use of residues from the sugar and alcohol agroindustry for the development of byproducts: a review. *Research, Society and Development*, 11(13), e597111336082.
- [18] Ramos, M., Dias, A., Puna, J., Gomes, J., & Bordado, J. (2019). Biodiesel Production Processes and Sustainable Raw Materials. *Energies*, 12, 1-30.
- [19] Chhandama, M. V. L., Ruatpuia, J. V. L., Ao, S., Chetia, A. C., Satyan, K. B., & Rokhum, S. L. (2023). Microalgae as a sustainable feedstock for biodiesel and other production industries: *Prospects and challenges*. *Energy Nexus*, 12(100255), 100255.
- [20] Mathew, G. M., et al. (2021). Recent advances in biodiesel production: Challenges and solutions. *The Science of the Total Environment*, 794(148751), 148751.
- [21] Mendonça, I. M., et al. (2019). New heterogeneous catalyst for biodiesel production from waste tucumã peels (*Astrocaryum aculeatum* Meyer): Parameters optimization study. *Renewable Energy*, 130, 103-110.
- [22] Stamenković, O. S., Veličković, A. V., & Veljković, V. B. (2011). The production of biodiesel from vegetable oils by ethanolysis: Current state and perspectives. *Fuel (London, England)*, 90(11), 3141-3155.
- [23] Liu, M., et al. (2019). Direct catalytic methanol-to-ethanol photo-conversion via methyl carbene. *Chem*, 5(4), 858-867.
- [24] Tacias-Pascacio, V. G., et al. (2019). Comparison of acid, basic and enzymatic catalysis on the production of biodiesel after RSM optimization. *Renewable Energy*, 135, 1-9.
- [25] Ruschel, C. F. C., Huang, C. T., Samios, D., & Ferrão, M. F. (2014). Exploratory analysis applied to attenuated total reflectance Fourier transform infrared (atr-ftir) of biodiesel/diesel blends. *Química Nova*, 37(5), 810-815.
- [26] Qiu, F., Li, Y., Yang, D., Li, X., & Sun, P. (2011). Biodiesel production from mixed soybean oil and rapeseed oil. *Applied Energy*, 88(6), 2050-2055.
- [27] Nisar, J., et al. (2017). Enhanced biodiesel production from *Jatropha* oil using calcined waste animal bones as catalyst. *Renewable Energy*, 101, 111-119.
- [28] Elango, R. K., Sathiasivan, K., Muthukumaran, C., Thangavelu, V., Rajesh, M., & Tamilarasan, K. (2019). Transesterification of castor oil for biodiesel production: process optimization and characterization. *Microchemical Journal*, 145, 1162-1168.
- [29] da Costa, J. M. (2022). *Applications of infrared spectrometry and chemometric techniques for evaluating the quality and susceptibility to mycodeterioration of biodiesel*. Federal University of Rio Grande do Sul.
- [30] Kamarozaman, M. F. F., Kahar, H., Hassan, N., Hanafi, M. F., & Sapawe, N. (2020). Analysis of biodiesel product derived from waste cooking oil using fourier transform infrared spectroscopy. *Materials Today: Proceedings*, 31, 329-332.
- [31] Goli, J., & Sahu, O. (2018). Development of heterogeneous alkali catalyst from waste chicken eggshell for biodiesel production. *Renewable Energy*, 128(PA), 142-154.
- [32] Kumar, R., Moorthy, I., Goswami, L., Pugazhenthii, G., Pakshirajan, K., Silva, A., & Morales-Torres, S. (2019). Analytical Methods in Biodiesel Production. *Energy, Environment, and Sustainability*.
- [33] Breshike, C., Furstenberg, R., Huffman, T., Kozak, D., Stievater, T., & McGill, R. (2020). In situ detection of gas chromatography analytes by active illumination with quantum cascade lasers. *Optical Engineering*, 59, 092004-092004.
- [34] Crnkovic, P. M., Koch, C., Ávila, I., Mortari, D. A., Cordoba, A. M., & Moreira dos Santos, A. (2012). Determination of the activation energies of beef tallow and crude glycerin combustion using thermogravimetry. *Biomass & Bioenergy*, 44, 8-16.
- [35] Ronchi, G. A., da Trindade, C. M., Fontoura, L. A. M., & Marques, M. V. (2019). Obtaining ethyl biodiesel from pork lard and residual frying oil by homogeneous catalysis with sodium glyceroxide. In *Proceedings of the National Interdisciplinary Scientific and Technological Initiation Exhibition (MICTI)*.
- [36] Fabiani, C., Pisello, A. L., Barbanera, M., Cabeza, L. F., & Cotana, F. (2019). Assessing the potentiality of animal fat based-bio phase change materials (PCM) for building applications: An innovative multipurpose thermal investigation. *Energies*, 12(6), 1111.
- [37] Ramalho, E. F. S. M., Santos, I. M. G., Maia, A. S., Souza, A. L., & Souza, A. G. (2011). Thermal characterization of the poultry fat biodiesel. *Journal of Thermal Analysis and Calorimetry*, 106(3), 825-829.

The Effect of Gas Bubble Diameter at the Inlet of Two-phase Centrifugal Pumps on the Formation of Gas Pockets Obstructing Flow

Toumi Bessam¹, Atif Abdelmadjid², Hazem Meharzi³

^{1,2,3}Laboratory of Energetic Mechanics and Conversion Systems, Faculty of Mechanical and Process Engineering, University of Sciences and Technologies Houari Boumediene, BP. 32, El-Alia, 16111 Bab-Ezaoaur, Algiers, Algeria

¹btoumi@usthb.dz, ²aatif@usthb.dz, ³hmeharzi@usthb.edu.dz

Abstract—The transportation of fluids of various types is an essential requirement in numerous human activities, including agriculture, industry, and many other fields. Centrifugal pumps are among the most widely used tools for fluid transportation due to their high efficiency, particularly for single-phase flows. However, centrifugal pumps experience a significant decline in performance when handling two-phase flows. A thorough understanding of the effects of two-phase flows on pump performance is a crucial step toward mitigating these adverse effects, CFD tools are among the most commonly used methods for studying the behavior of two-phase flows. Most of the CFD tools are based on the Euler-Lagrange model in the study of two-phase flows with low gas IGVF. This model is considered a non-continuous phase of gas, which is bubbles with a constant diameter. This study aims to understand the extent to which bubble diameter affects the performance of centrifugal pumps. The most suitable choice for bubble diameter ensures accurate simulation results.

Keywords - two-phase flows, gas bubble accumulation, centrifugal pump, Euler-Lagrange – Diameter of bubble

I. INTRODUCTION

The transport of liquid materials is essential for meeting human needs across various sectors, including, but not limited to, the electricity industry (such as thermal power plants, geothermal power plants, and nuclear power

plants) and the petroleum industry (both production and transportation) [1-3]. The centrifugal pump is an effective tool to achieve this for the simplicity of its installation, and maintenance, as well as its high efficiency. This type of pump is often set to transport single-phase flow, causing a deterioration in their efficiency when used to transport two-phase flow [3-6].

The reason for the performance deterioration of centrifugal pumps when transporting two-phase flows is due to the accumulation of gas bubbles that form large pockets that hinder the flow in the pump's impeller, which causes performance to deteriorate. Gas bubbles tend to accumulate in the pump's impeller as a result of the forces applied to it and the density difference between the two phases, causing them to move from areas of high pressure to areas of low pressure [6-9].

Improving the performance of centrifugal pumps, even by small margins, is crucial due to their high energy consumption. Hence, numerous studies have been carried out, either to thoroughly understand the causes of performance degradation as an initial step toward improvement or to propose new designs that enhance performance [10]. Most of these studies rely on computational tools, often employing the Euler-Lagrange model to investigate two-phase flows in centrifugal pumps. This model treats the liquid phase as a continuous medium governed



by Euler equations, while the gas phase is considered discontinuous, represented by bubbles with a constant diameter. Determining the bubble diameter is a particularly complex task due to its direct impact on the reliability of the results.

This work aims primarily to study the effect of air bubble diameter at the inlet of the pump on the performance of centrifugal pumps and on the formation of gas pockets in the pump impeller. The results highlighted a significant effect of bubble diameter on the centrifugal pumps performances, where the increase of the latter leads to a significant deterioration in performance with tendencies to stabilize at values $d = 0.5$ mm.

II. NUMERICAL METHOD

A. Geometric Model Pump

The pump used in this research is a single-stage centrifugal pump operating at high rotational speeds. This pump is a closed pump impeller .

These pumps are known for providing stable and efficient performance, particularly in handling single-phase flows. Table I represents the most important characteristics of the pump such as the optimal flow value, rotational speed, head, impeller dimensions and pump operational capacity.

TABLE I. ORIGINAL PUMP CHARACTERISTICS.

Parameter	Symbol	Unit	Value
Flow rate	Q_0	[m ³ /h]	18
Rotational speed	N	[r/min]	2950
Power	P_0	[kW]	1.2
Head	H	[m]	18
Impeller inlet diameter	D_1	[mm]	52
Impeller outlet diameter	D_2	[mm]	132
Blade number	z	-	6
Blade inlet width	b_1	[mm]	10
Blade outlet width	b_2	[mm]	6

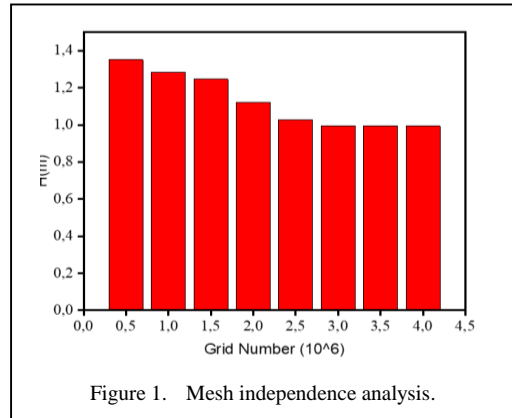


Figure 1. Mesh independence analysis.

B. Meshing

Mesh quality is an important factor in simulation ensure accurate results with less computation time. Fig. 1 presents a mesh dependency study, where the effect of mesh grid on the pump head was investigated. As shown in the figure, the appropriate mesh grid for this study is 3 million.

To ensure accurate results, the mesh was improved by refining the areas most exposed to large pressure or velocity differences. Fig. 2 illustrates the mesh used in the pump impeller.

III. GOVERNING EQUATIONS

Two-phase flows in centrifugal pumps are studied using the Euler-Lagrange model, which treats the liquid phase as a continuous medium

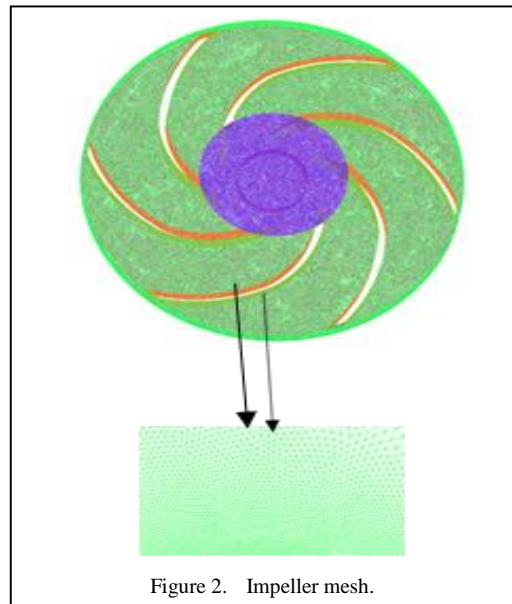


Figure 2. Impeller mesh.

and the gas phase as a discontinuous phase represented by bubbles of constant diameter. The governing equations for the liquid phase are the Euler equations, while the governing equations for the gas phase are the Lagrange equations, taking into account the interfacial forces exchanged between the liquid and gas phases. The governing equations for two-phase flow are.

Mass conservation equation for gas:

$$\frac{\partial((1-\alpha)\rho_l)}{\partial t} + \frac{\partial((1-\alpha)\rho_l u_{li})}{\partial x_i} = 0. \quad (1)$$

The gas volume fraction is defined by:

$$\alpha = \frac{Q_g}{(Q_g + Q_l)}. \quad (2)$$

Momentum equation for gas:

$$\begin{aligned} \frac{\partial(\rho_g U_{gi})}{\partial t} + \frac{\partial(\alpha \rho_g U_{gj} U_{gi})}{\partial x_i} = \\ = -\frac{\partial \rho_g}{\partial x_i} + \frac{\partial \tau_{gij}}{\partial x_i} \end{aligned} \quad (3)$$

Momentum equation for liquid:

$$\begin{aligned} \frac{\partial(\rho_l U_{li})}{\partial t} + \frac{\partial((1-\alpha)\rho_l U_{lj} U_{li})}{\partial x_i} = \\ = -\frac{\partial \rho_l}{\partial x_i} + \frac{\partial \tau_{lij}}{\partial x_i} \end{aligned} \quad (4)$$

ρ_g : density of gas,

ρ_l : density of a liquid,

τ : the shear stress tensor,

t : is time,

x : the spatial dimensions. Gravity is neglected.

Drag Force

The total pulling force F_{DI} acting on the spherical bubbles per unit volume is as follows:

$$F_{DI} = -F_{Dg} = \frac{3}{4} C_D \frac{\rho_l}{d} \alpha U_g - U_l (U_g - U_l). \quad (5)$$

The drag coefficient C_D is calculated by the equation Schiller Naumann:

$$C_{DFDL} = \frac{24}{Re} (1 + 0.15 Re^{0.687}), \quad (6)$$

$$C_D = 0.44$$

Re : the Reynolds number:

$$Re = \frac{\rho_l d |U_g - U_l|}{\mu_l}. \quad (7)$$

d : bubble diameter, $(U_g - U_l)$: slip velocity between two phases,

μ : the dynamic viscosity of the liquid,

ρ_l : density of liquid.

Pump head calculation formula:

$$\begin{aligned} H = (1-x) \left[\frac{(p_2 - p_1)}{\rho G} + \frac{(U_2^2 - U_1^2)}{2G} \right]_l + \\ + \gamma \left[\frac{(p_2 - p_1)}{\rho G} + \frac{(U_2^2 - U_1^2)}{2G} \right]_g \end{aligned} \quad (8)$$

This relation is based on calculating the pressure and velocity differences between the pump crayon and outlet for both gaseous and liquid states.

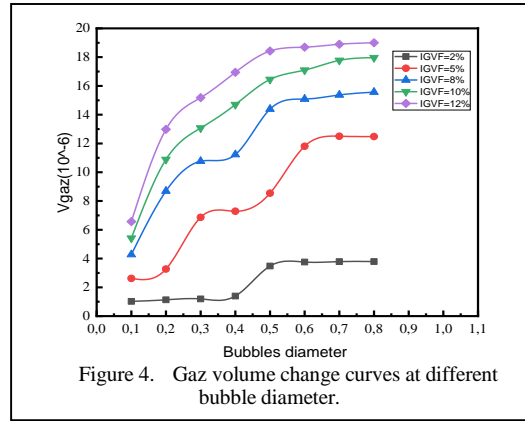
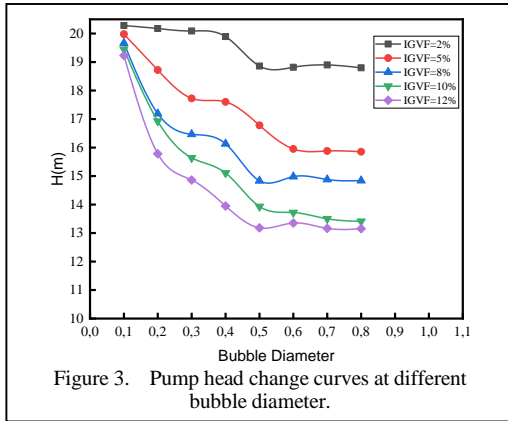
χ : quality of the mixture in mass defined as:

$$x = \left[\frac{\alpha \rho_g}{\alpha \rho_g + (1-\alpha) \rho_l} \right]. \quad (9)$$

IV. RESULTS

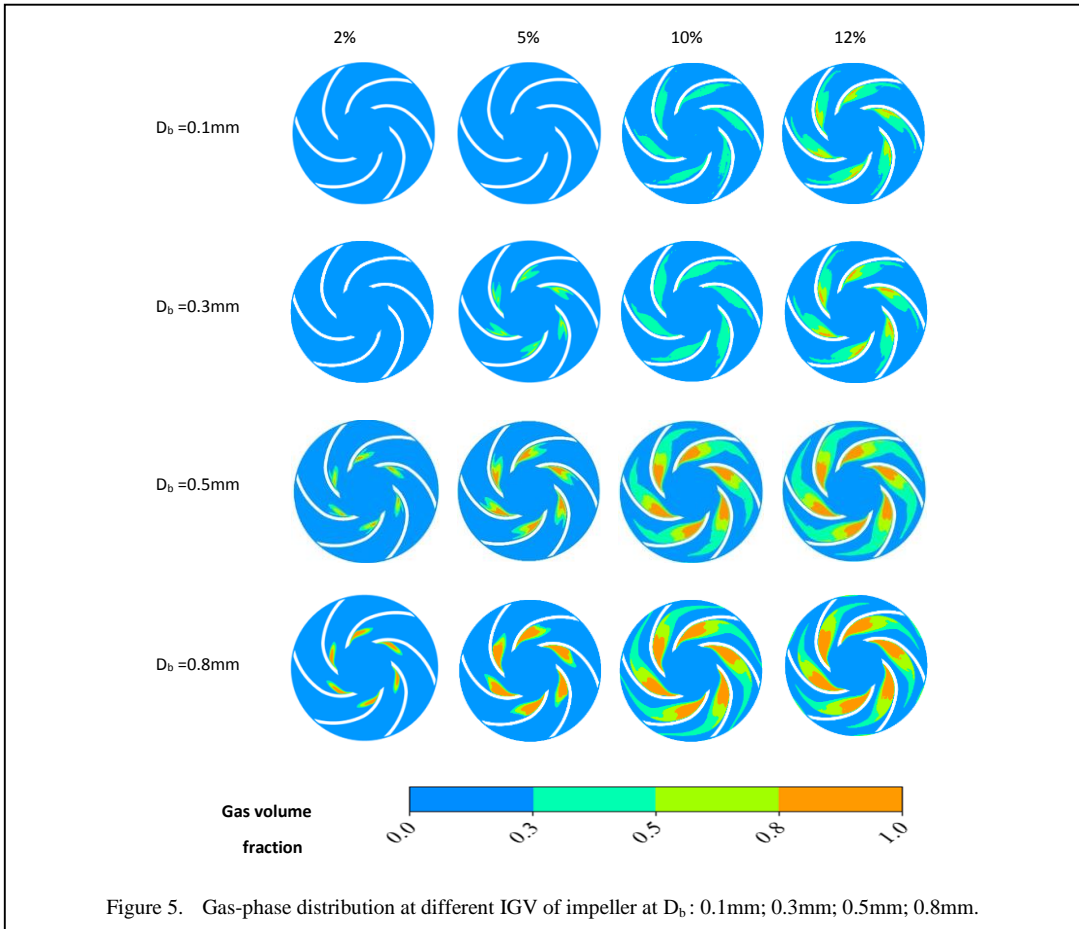
A. Head vs Bubble Diameter

Fig. 3 demonstrates the impact of bubble diameter on the pump head across a range of gas volume fractions. By examining the plotted curves, it becomes clear that the diameter of bubbles entering the pump plays a critical role in its overall performance, with this influence varying significantly depending on the bubble size. This effect can be classified into three distinct categories. First, for bubble diameters smaller than 0.4 mm, the pump head experiences a gradual and steady decline, which occurs consistently across all tested gas fractions,



indicating a minor initial impact on performance. However, as the bubble diameter approaches 0.4 mm, a sharp and noticeable drop in pump performance is observed. This rapid degradation tends to start at bubble diameters slightly below 0.4 mm, particularly in cases where the gas volume fractions are relatively high, making the effect more pronounced, the final stage, when

bubble diameters exceed 0.5 mm, the pump head stabilizes at constant values. This suggests that further increases in bubble size no longer have a significant impact on pump efficiency, as the system reaches a state of equilibrium. At this point, the pump operates with relatively consistent performance, regardless of additional changes in bubble diameter. The varying



response of pump efficiency to changes in bubble size can be attributed to the forces acting on the bubbles within the flow. These forces cause the gas phase to separate from the liquid phase, resulting in the formation of gas pockets. These gas pockets disrupt the smooth flow of liquid and are a primary cause of the observed performance degradation, particularly at specific bubble diameters and higher gas fractions.

B. Head vs Gas Volume

Fig. 4 illustrates the curves of volume of accumulated gas in the pump impeller as a function of bubble diameter across different gas fractions. These gas volume curves correspond to the head variation curves in Fig. 3. The effect is as follows: an increase in the accumulated gas fraction in the pump impeller leads to a reduction in pump head, confirming the direct impact of accumulated gas bubbles on pump efficiency. The bubble diameter at the pump inlet also has a varying effect on the accumulated gas volume. For bubble diameters less than 0.4 mm, the effect on pump efficiency is minimal, followed by a rapid decline in performance starting from bubble diameters greater than 0.4 mm. Gas volume tends to stabilize at bubble diameters of 0.5 mm or larger.

C. Gas Phase Distribution in Impeller

Fig. 5 illustrates the distribution of the gas phase within the pump impeller for various bubble diameters. It is evident that bubble accumulation is nearly absent at smaller diameters, particularly those less than 0.3 mm. This phenomenon is primarily attributed to the relatively weak drag forces exerted by the liquid on the bubble, resulting from its small size. Consequently, the gas phase achieves a more uniform distribution throughout the impeller, which enhances the homogeneity of the gas-liquid mixture.

Conversely, as the bubble diameter exceeds 0.5 mm, gas bubbles tend to accumulate, forming substantial gas pockets. This shift is mainly due to the increased drag forces acting on the larger bubbles. The stronger drag forces facilitate phase separation, leading to significant gas accumulation in lower-pressure regions within the pump impeller. Such dynamics underscore the critical role of bubble size in influencing flow behavior and performance in centrifugal pump.

V. CONCLUSION

CFD software is an effective tool for studying various types of flows. These programs rely on different models to achieve this. For studying two-phase flows in centrifugal pumps, most of these programs use the Euler-Lagrange model, which allows for the study of each bubble's movement individually, while assuming a constant bubble diameter.

This study provided a deeper understanding of how bubble diameter affects gas accumulation in the pump. As the bubble diameter increases, the liquid forces acting on the bubble also increase, leading to more significant gas bubble accumulation in the pump impeller and, consequently, performance deterioration.

Starting from a bubble diameter of 0.5 mm, any further increase in diameter has a minimal effect on pump performance, making it an appropriate diameter for the study the drag forces applied to the bubble have a direct impact on gas accumulation. This effect increases as the bubble diameter increases.

REFERENCES

- [1] Mansour, M., Kopparthy, S., & Thévenin, D. (2022). Investigations on the effect of rotational speed on the transport of air-water two-phase flows by centrifugal pumps. *International Journal of Heat and Fluid Flow*, 94, 108939.
- [2] Mansour, M., Wunderlich, B., & Thévenin, D. (2018). Effect of tip clearance gap and inducer on the transport of two-phase air-water flows by centrifugal pumps. *Experimental Thermal and Fluid Science*, 99, 487–509.
- [3] Abdelmadjid, A. (2014). Étude de la dégradation des performances d'une pompe centrifuge en écoulement diphasique. *Doctoral dissertation*.
- [4] Atif, A., & Senouci, S. (2019). Numerical analysis of performance deterioration of a centrifugal pump operating in two-phase flows. *Journal of Applied Fluid Mechanics*, 12(4), 1203–1211.
- [5] Bois, G. (2023). State of the art on two-phase non-miscible liquid/gas flow transport analysis in radial centrifugal pumps - Part A: General considerations on two-phase liquid/gas flows in centrifugal pumps. *International Journal of Turbomachinery, Propulsion and Power*, 8(2), 16.
- [6] Hundshagen, M., & Skoda, R. (2023). State of the art on two-phase non-miscible liquid/gas flow transport analysis in radial centrifugal pumps - Part C: CFD approaches with emphasis on improved models. *International Journal of Turbomachinery, Propulsion and Power*, 8(2), 15.
- [7] Mansour, M., & Thévenin, D. (2023). State of the art on two-phase non-miscible liquid/gas flow transport analysis in radial centrifugal pumps - Part B: Review of experimental investigations. *International Journal of Turbomachinery, Propulsion and Power*, 8(4), 42.

- [8] Li, S.-T., Li, R.-L., He, D.-H., Huang, R., & Sun, S.-H. (2024). The identification of gas–liquid two-phase flow patterns in a centrifugal pump with an imbalanced sample and variable rotational speeds. *Physics of Fluids*, 36(2).
- [9] Shahid, S., Dol, S. S., Hasan, A. Q., Kassem, O. M., Gadala, M. S., & Aris, M. S. (2021). A review on electrical submersible pump head losses and methods to analyze two-phase performance curve. *WSEAS Transactions on Fluid Mechanics*, 16, 1431.
- [10] Toumi, B., Atif, A., & Bennaceur, M. A. (2024). Enhanced impeller gas-liquid flow using ribs for high performance of centrifugal pump. *International Journal of Computational Fluid Dynamics*, 1–12.

Control of Open-end Winding Induction Generator for Supporting Various Grid-isolated Loads

Arunava Chatterjee¹, Soumyajit Ghosh²

¹Department of Electrical Engineering, Raghunathpur Government Polytechnic, Purulia 723121, India

²Center for Internet of Things, Madhav Institute of Technology & Science, Gwalior - 474005, India

¹arunava7.ju@gmail.com, ²soumyajit@mitsgwalior.in

Abstract—This paper provides control strategy and technical analysis of integrating an open-end winding induction generator for supplying various connected loads. The generator is series compensated with closed loop control based on constant voltage control. A voltage source inverter with a charged capacitor is employed to supply the required reactive power of both the generator and the loads. A photovoltaic panel and battery is used as backup. The generation and load characteristics are observed for the induction generator. The system is simple in its control and also quite flexible for supporting critical loads. The proposed control is validated using various simulation results.

Keywords - open-end winding, induction generator, grid-isolated, voltage regulation, wind power

I. INTRODUCTION

The majority of the energy required to create electricity nowadays is produced from burning fossil fuels like coal, oil, and natural gas. These fossil fuels are scarce, and when they are burned, a significant number of toxic gasses are released into the atmosphere. Thus, the search for clean, sustainable energy sources is ongoing. Wind is a clean, limitless renewable energy source. Although there are other options as well, a wind turbine is by far the most often used device for converting wind energy into electrical energy [1]. Any generator may theoretically be installed atop a wind turbine to produce electricity. By

connecting the required inverters, the need for grid-compatible electric current can now be met even if the generator only generates direct current or alternating current with variable amplitude and frequency. Because of its dependability, low maintenance requirements, and straightforward controls, the induction generator (IG) seems like a fantastic option for these applications [2]. IG is suggested for wind energy production due to its modest size per generated kilowatt, robustness, and ease of usage. Furthermore, independent generators (IGs) can produce the excitation magnetic field without external power assistance. They can thus be used in isolated locations [3-5].

The main disadvantages of IGs remain to be reactive power consumption and inadequate voltage regulation at varying speeds, despite the introduction of static power converters making it easier to control the output voltage of IGs [6]. Since it does not need an extra power source to produce the magnetic field, the self-excited induction generator (SEIG) is a suitable alternative for wind-driven electric generation applications, especially in places with variable wind speed and isolation. The SEIG scheme was created more than 80 years ago, but only recently have a significant number of research publications started focusing more on the analysis and uses of SEIGs [7,8]. This is because of better techniques for managing voltage and frequency as well as the considerable global focus that has been given to the development of renewable energy sources during the last thirty



years. The primary operational issue with the SEIG system is its incapacity to regulate frequency and voltage in the presence of varying loads. The machine excitation is immediately impacted by a change in the load impedance.

Poor voltage regulation results from the generator's voltage reduction as the load impedance increases. However, even if the prime mover's speed is constant, the induction generator's slip increases with increasing load, resulting in a frequency that is load-dependent. Numerous studies have been conducted in the past to manage the voltage and frequency of a SEIG system operating with variable loads. A sliding mode controller was demonstrated, according to [9], showing controlled dynamic reaction and behavior of the system in response to variations in the characteristics of the generator and the load. An electronic load controller was used to study how a SEIG regulates its voltage and frequency under various load conditions [10]. Static converters help to address the voltage control problem to some extent, but at a large cost increase to the system [11,12]. Maximum power point tracking (MPPT)-based control techniques are frequently employed. MPPT approaches can facilitate the operation of grid-connected generation [13], whereas standalone grid-secluded producing is often handled without MPPT to reduce system complexity [14]. However, maintaining a stable generation becomes crucial as separate generations are frequently utilized to complete important tasks [15]. However, because of the machine's extreme dynamic slip variations and the challenges associated with creating a smooth variable reactive power supply at a reasonable cost, the control of speed and voltage does not always produce a performance level that is always appropriate. Open-end winding induction generators (OEWIG) are a relatively new concept used in More Electric Aircrafts (MEA) which carries frequency insensitive loads [16-18]. This induction generator is a robust and dependable option for auxiliary load power generation because of its tough design. The same is used in this research for voltage generation with a new concept for control of generation.

Here, a three-phase OEWIG is proposed for isolated wind power generation. The reactive power requirement is provided by a voltage source inverter with its DC bus supplied by a photovoltaic (PV) panel. Essentially it is a hybrid generation system which can supply AC loads via the generator and optional connected DC

loads. The control of the generator is done using a simple yet novel voltage-based control loop. Emphasis is given on the continuity of the generated voltage for supplying critical isolated loads rather than proposing complex control techniques. The advantage of the proposed scheme is in its simplicity to provide power to both DC and AC loads at the same time maintaining IG winding current ratings. OEWIGs is suitable in applications where variable speed operation is needed, as it allows efficient energy capture over a wide range of speeds. They are particularly suitable for wind turbines, where flexible and efficient control of power generation is crucial.

II. DESCRIPTION OF THE PROPOSED SYSTEM

As seen in Fig. 1, the suggested system comprises of an induction generator with open-end stator windings, one end of which is linked to three-phase AC loads and the other end to a PV panel supplied voltage source inverter (VSI). The voltage source inverter's DC side is where the optional DC loads can be linked.

Since the VSI supplies the reactive power needed for the induction generator to be excited, its fundamental frequency of operation determines the frequency of the AC voltage that is generated. Now, suitable control schemes will be applied to maintain generation to support the different loads.

III. PROPOSED SYSTEM CONTROL

The OEWIG is used to generate power for most of the load demand. Additionally, a photovoltaic (PV) panel may also be connected to the VSI side. The proposed control scheme is shown in Fig. 2. In the control technique adopted, the DC link voltage of the VSI is used to generate the inverter q -axis reference current. The d -axis reference current is generated from the AC load side generated voltage reference and the unit vectors computed from the AC load side currents

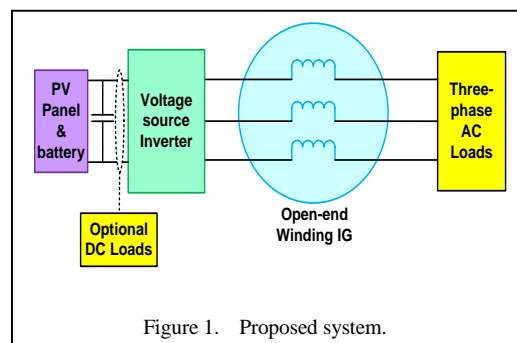


Figure 1. Proposed system.

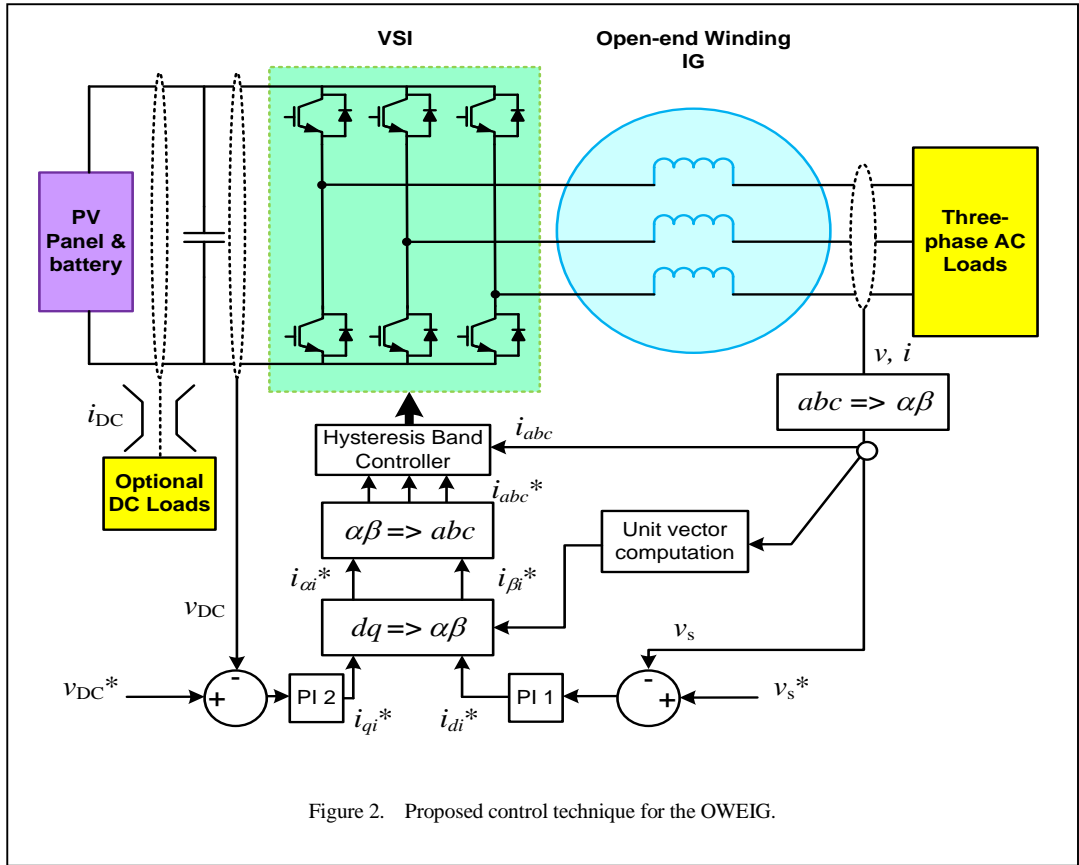


Figure 2. Proposed control technique for the OWEIG.

and voltages. These currents are then converted to phase currents to generate the pulses for VSI. Hysteresis band based current controller is used for generating the pulses. The errors from the compared values of sensed and reference quantities are passed through proportional-integral (PI) controllers to generate the said references. The PI controllers are tuned using Ziegler-Nichols method. The OEWIG is modelled using the stationary reference frame theory.

$$v_{\alpha s} = R_{\alpha s} i_{\alpha s} + \frac{d}{dt} \psi_{\alpha s}, \quad (1)$$

$$v_{\beta s} = R_{\beta s} i_{\beta s} + \frac{d}{dt} \psi_{\beta s}, \quad (2)$$

$$0 = R_{\alpha r} i_{\alpha r} + \frac{d}{dt} \psi_{\alpha r} + \omega_r \psi_{\beta r}, \quad (3)$$

$$0 = R_{\beta r} i_{\beta r} + \frac{d}{dt} \psi_{\beta r} + \omega_r \psi_{\alpha r}, \quad (4)$$

where, $R_{\alpha s}$, $R_{\beta s}$ are the α and β axes stator resistances, $v_{\alpha s}$, $v_{\beta s}$ are the $\alpha - \beta$ axes stator voltages, currents $i_{\alpha s}$, $i_{\beta s}$, $i_{\alpha r}$ and $i_{\beta r}$ are the stator and rotor $\alpha - \beta$ axes currents. ω_r is the speed of the rotor. The corresponding flux linkages are represented as ψ and are given as:

$$\psi_{\alpha s} = L_{l\alpha s} i_{\alpha s} + L_{\alpha m} (i_{\alpha s} + i_{\alpha r}), \quad (5)$$

$$\psi_{\beta s} = L_{l\beta s} i_{\beta s} + L_{\beta m} (i_{\beta s} + i_{\beta r}), \quad (6)$$

$$\psi_{\alpha r} = L_{l\alpha r} i_{\alpha r} + L_{\alpha m} (i_{\alpha s} + i_{\alpha r}), \quad (7)$$

$$\psi_{\beta r} = L_{l\beta r} i_{\beta r} + L_{\beta m} (i_{\beta s} + i_{\beta r}). \quad (8)$$

The stator flux ψ_s is calculated from the stator $d - q$ axes flux linkages from obtained stator voltages as:

$$\psi_s = \sqrt{\psi_{\alpha s}^2 + \psi_{\beta s}^2}. \quad (9)$$

The unit vectors for transformation are defined as:

$$\cos \theta_e = \frac{\psi_{\alpha s}}{\psi_s}, \quad (10)$$

$$\sin \theta_e = \frac{\psi_{\beta s}}{\psi_s}. \quad (11)$$

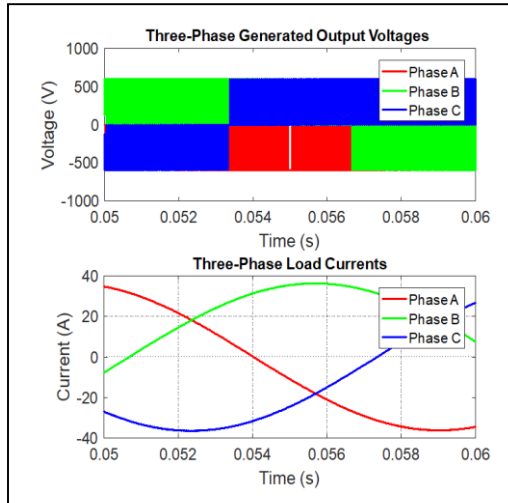


Figure 3. Output voltage and load current for three-phase R load.

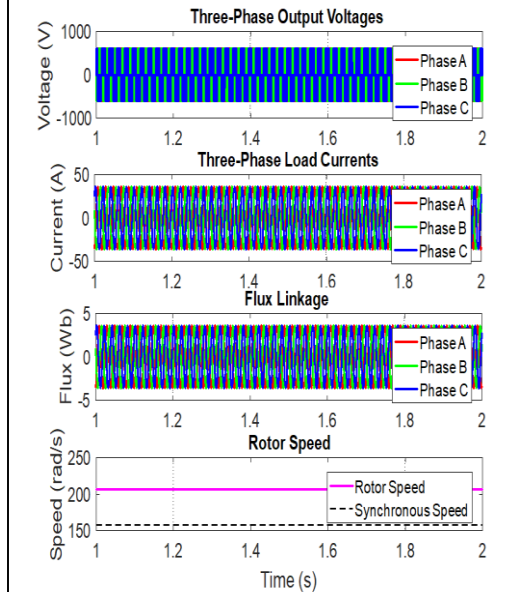


Figure 4. Condition of voltage, current, flux and rotor speed of the OWEIG with the control.

The PV panel is essentially connected to a Lead-acid storage battery via a charge controller. The control is open loop and thus it is not discussed here.

IV. RESULTS AND DISCUSSION

At first, the generator and its control are simulated in MATLAB. The three-phase open-end winding induction generator is considered with a rating of 2.2 kW at 415V, 50Hz, and is coiled for four stator poles. The PV panel is rated at 1kWp. Without the suggested control, the voltage generation starts at 1150 rpm with no load. But the frequency of the voltage generated at this speed is less than 50Hz. After the generator reaches a steady state, terminal loads can be connected across the primary windings.

At first, with the proposed control, the generated voltage output is shown with the set steady resistive inductive load. The Fig. 3 shows the output plot.

Fig. 4 shows the plots for the generated voltage, the load current, the generator flux waveform and the speed of the generator. The rotor speed is higher than the synchronous speed indicating the generating operation. Also, the generated voltage is shown to be at a stable value with the proposed control adopted. With step change in the terminal load, the generated voltage waveform condition is shown in Fig. 5.

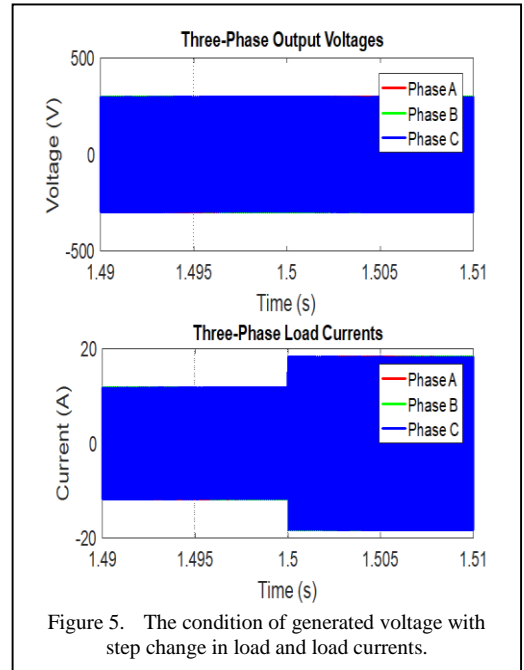


Figure 5. The condition of generated voltage with step change in load and load currents.

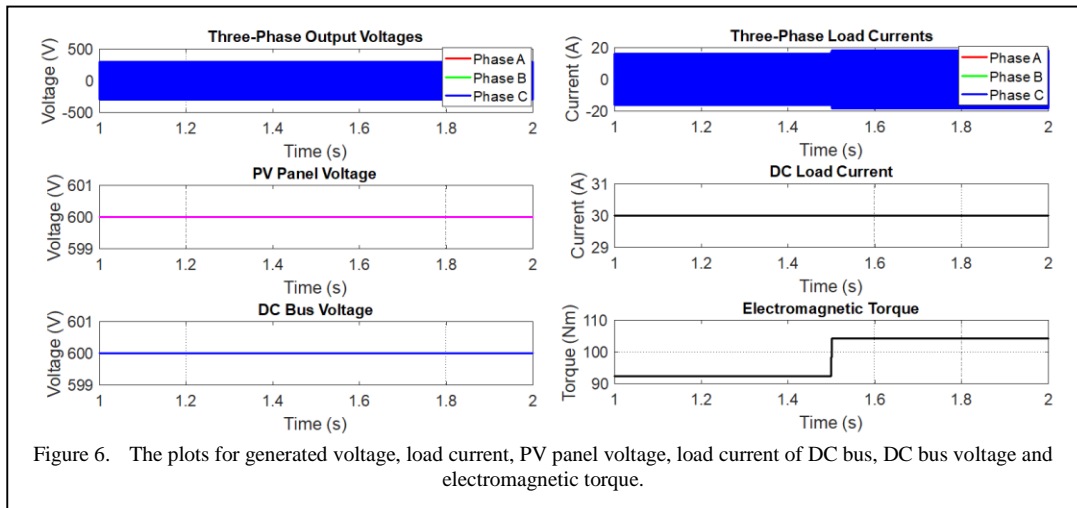


Figure 6. The plots for generated voltage, load current, PV panel voltage, load current of DC bus, DC bus voltage and electromagnetic torque.

As observed, the voltage is stable indicating valid control technique. The load current change is also shown in Fig. 5.

The plots for generated voltage, load current, PV panel voltage, load current of DC bus, DC bus voltage and electromagnetic torque are shown in Fig. 6.

The PV panel is simulated using standard PV panel model [19]. The proposed control is thus suitable for such a generation scheme as observed from the obtained results.

V. CONCLUSION

This study provides a technical study of OEIWG feeding three-phase AC loads and optional DC loads effectively. The voltage is maintained using a voltage control loop. Additionally, a PV panel is used across the voltage-source inverter to support the generation. The generated voltage is shown to be stable with step change in load. Further, with DC side load, the generation can also be sustained which validates the proposed control.

Future improvements will include improved design processes where more optimizations can be made to enhance its performance. An experimental prototype is being made to validate the proposed control with the results with varying loads and wind speed ranges. Further, optimization techniques [20] may be applied for its wide-speed range control [21] for maximizing wind power generation. Generated voltage harmonic optimization can also be done which can improve the generated voltage profile helping in providing better quality of generated voltage [4,22]. Also, strategies like model-based

predictive control (MPC), future system states can be predicted and optimized in real-time, allowing for better regulation of voltage, frequency, and rotor speed for better anticipation of transients and disturbances. The system is also at par with similar rated conventional wind generator systems as same three phase machine can be configured for OEIWG. However, regarding the generation and cost effectiveness of the same, it can be confirmed using an economic case study [23].

REFERENCES

- [1] Patel, M. R., & Beik, O. (2021). *Wind and solar power systems 3rd Ed.* CRC Press.
- [2] Chojaa, H., et al. (2023). A novel DPC approach for DFIG-based variable speed wind power systems using dspac. *IEEE Access*, 11, 9493-9510.
- [3] Faisal Khan, M., Khan, M., & Iqbal, A. (2022). Effects of induction machine parameters on its performance as a standalone self-excited induction generator. *Energy Reports*, 8, 2302.
- [4] Chatterjee, A., Roy, K., & Chatterjee, D. (2014). A Gravitational Search Algorithm (GSA) based Photo-Voltaic (PV) excitation control strategy for single phase operation of three phase wind-turbine coupled induction generator. *Energy*, 74, 707-718.
- [5] Islam, M., & Chatterjee, A. (2019). Analysis of a hybrid energy system for supplying a remote critical load in onshore coastal India. In *5th Jubilee Virtual International Conference on Science, Technology and Management in Energy, Republic of Serbia* (pp. 28-29).
- [6] Hamid, B., Hussain, I., Iqbal, S., Singh, B., Das, S., & Kumar, N. (2022). Optimal MPPT and BES control for grid-tied DFIG-based wind energy conversion system. *IEEE Transactions on Industry Application*, 58, 6, 7966-7977.
- [7] Ion, C. (2020). A comprehensive overview of single-phase self-excited induction generators. *IEEE Access*, 8, 197420-197430.

- [8] Chatterjee, A., & Chatterjee, D. (2017). PV- assisted microgeneration scheme with single- phase induction generator suitable for wide speed range application. *IET Power Electronics*, 10(14), 1859-1869.
- [9] Mi, Y., Song, Y., Fu, Y., & Wang, C. (2020). The adaptive sliding mode reactive power control strategy for wind-diesel power system based on sliding mode observer. *IEEE Transactions on Sustainable Energy*, 11(4), 2241-2251.
- [10] Chatterjee, A. (2024). Wind power generation for isolated loads with IoT-based smart load controller. *Journal of Fuzzy Systems and Control*, 2(2), 92-96.
- [11] Chatterjee, A. (2022). Analysis of a Wind-PV hybrid system with smart control for grid-secluded critical loads in onshore Indian area. In *Proceedings of the International Conference Industrial Instrumentation and Control. Lecture Notes in Electrical Engineering*, 815, Springer, Singapore.
- [12] Chatterjee, A., Ghosh, S., & Mitra, A. (2022, August). Wind-PV based isolated hybrid generation for smart irrigation management and supplying other critical loads. In *2022 IEEE 2nd International Conference on Sustainable Energy and Future Electric Transportation (SeFeT)* (pp. 1-6). IEEE.
- [13] Huynh, P., Tungare, S., & Banerjee, A. (2021). Maximum power point tracking for wind turbine using integrated generator-rectifier systems. *IEEE Transaction on Power Electronics*, 36(1), 504-512.
- [14] Roy, K., Chatterjee, A., Chatterjee, D., & Ganguli, A. (2015). A photovoltaic-based improved excitation control strategy of three-phase self-excited induction generator suitable for wind power generation. *Electric Power Components and System*, 43(17), 1912-1920.
- [15] Chatterjee, A. (2022). Wind-PV based generation with smart control suitable for grid-isolated critical loads in onshore India. *Journal of the Institution of Engineers (India) Series B*, 52, 1-11.
- [16] Gadipudi, S., Rajeevan, P., & Sudarshan Kaarthik R. (2022). A grid connected open-end winding induction generator system with series compensation. *IEEE Transactions on Industry Applications*, 58(1), 678-685.
- [17] Soares, E., et al. (2022). Half-controlled converters connecting open-end doubly fed induction generator to a dc-microgrid. *IEEE Transactions on Industry Applications*, 58(5), 6386-6396.
- [18] Soares, E., et al. (2022). Dual converter connecting open-end doubly fed induction generator to a dc-microgrid. *IEEE Transactions on Industry Applications*, 57(5), 5001-5012.
- [19] Villalva, M., Gazoli, J., & Filho, E. (2009). Comprehensive approach to modeling and simulation of photovoltaic arrays. *IEEE Transactions on Power Electronics*, 24(5), 1198-1208.
- [20] Chatterjee, A., & Banerjee, B. (2023). Grid-secluded induction generator with ann and interval type-2 fuzzy based controller for wind power generation with smart load control. *Qeios*, 1-8.
- [21] Chatterjee, A., Ghosh, S., & Mitra, A. (2023). Hybrid generation scheme for delivering irrigation loads and other critical loads with smart IoT based control. *IEEE Transactions on Industry Applications*, 60(1), 828-837.
- [22] Steczek, M., Chatterjee, A., & Chatterjee, D. (2018). Optimisation of current harmonics for three - level VSI based induction motor drive suitable for traction application. *IET Power Electronics*, 11(9), 1529-1536.
- [23] Chatterjee, A., & Chatterjee, D. (2015) A wind based micro-generation and storage scheme at low wind speeds using single-phase induction machine. In *Proceedings of the Michael Faraday IET International Summit*, Kolkata, India.

Development of an Energy Map of Available Biomass Raw Materials in the Geographic Information System (GIS)

Srećko Ćurčić¹, Aleksandar Peulić²

¹Faculty of Technical Sciences, Čačak, University of Kragujevac

²Faculty of Geography, University of Belgrade

¹srecko.curcic@ftn.kg.ac.rs, ²aleksandar.peulic@gef.bg.ac.rs

Abstract—For the rational utilization of available biomass resources for energy production, it is crucial to collect, process and transport them at times when the energy potential is highest. Obtaining information on the type, location and quantity of available energy sources is slow and unreliable without a developed ENERGY MAP. Therefore, the creation of an ENERGY MAP for a given area is of great importance and serves the needs of interested companies and local self-governments. In this paper, the GIS software QGIS and Geo Python are used to create a table that is constantly updated to create a GIS energy map of available biomass resources. The application of this methodology enables efficient analysis and management of biomass resources. The generated map provides important information about the availability and locations of biomass resources, allowing for better planning and decision making regarding their utilization for energy purposes. The paper describes the process of creating a form for users of available biomass feedstocks to determine the dependence of energy potential on the moisture content of the source resources, and the interpretation of the results by obtaining up-to-date data on the type and energy potential of waste biomass feedstocks at the source sites.

Keywords - biomass, energy map, GIS

I. INTRODUCTION

In today's world, where we are facing increasing challenges related to energy sustainability and environmental protection, finding efficient ways to use renewable energy

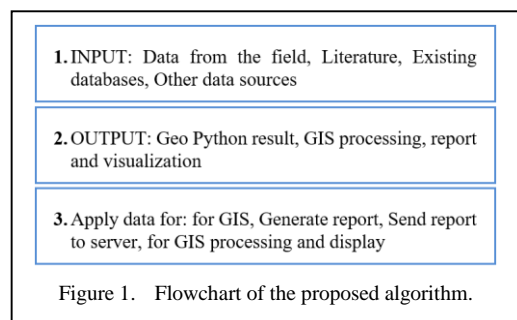
sources is becoming essential. One of the key resources that stands out for its potential role in the sustainable energy chain is biomass energy. Biomass energy, which is derived from organic materials such as plants, forest biomass and waste materials, is an important resource for electricity generation, heating and other energy needs [1]. However, making optimal use of these resources requires a thorough understanding of their availability, locations, and potential. In this project, we provide a methodology for creating a GIS energy map of available biomass raw materials as a key tool in optimizing the use of biomass energy. We focus on the process of collecting, analyzing and visualizing biomass data to enable efficient planning and management of these key energy sources. Through the implementation of free software such as QGIS and Geo Python, we provide a practical approach to creating a dynamic and up-to-date GIS energy map that will benefit interested companies, local governments and other relevant stakeholders. The project also explores ways to interpret the results, providing concrete guidelines for the efficient use of biomass resources in order to achieve energy sustainability and environmental protection. Through the integration of geospatial technologies and energy strategy, this work contributes to the understanding and promotion of sustainable energy solutions that are crucial for the future of our society. In the territory of



Northern Montenegro, there are various sources of waste biomass raw materials. Sources of waste biomass raw materials are created by: road maintenance, in primary and secondary agricultural production, in river watercourses, in economic and communal systems, in regular deforestation (stumps and branches), in the wood processing industry, in the slaughterhouse industry, etc. For the rational use of available resources, it is necessary to ensure: collection, preparation and transport when the energy potential for use is greatest. The problem in the region is the non-use or irrational use of waste biomass raw materials. The use of waste biomass raw materials would have a significant impact on raising the technological level in the energy sector, mechanical engineering and food industry. Also, the use of these resources can affect the promotion of the development of underdeveloped regions, which can be achieved through: investment realization, employment of local workforce, creation of new jobs, improvement of local infrastructure and income generation through various production jobs. The creation of a GIS energy map of available biomass raw materials should enable appropriate business entities to access up-to-date data on: available types, quantities and location of waste biomass raw materials. Based on the data obtained by the company at different levels, it will analyze the possibility of buying at the appropriate price and defined delivery time. Also, in direct communication with the owner of available resources, a model for the organization of the preparation and receipt of raw materials is defined. Today, biomass residues are very little or not used at all in Serbia, which directly reflects on significant environmental pollution. These residues can be used primarily as a source of energy, but also for some other purposes. By using these residues, emissions of CO₂ and other harmful gases would be significantly reduced, and we would also have energy sources whose price would be significantly lower compared to competitors. The implementation of project activities will require the definition of all locations where waste wood and agricultural raw materials occur in the defined territory, and they can be reached by working in the field and using appropriate literature and software sources for collecting data for appropriate raw materials. Based on the collected data and processing in Geo Python, a database will be created that is

available for analysis using a free GIS tool, Qgis. The created database will be the basis for expanding the new data. Once the locations, types and quantities of input raw materials are defined using the created Geo Python application and GIS tools, it will be possible to define a logistic connection for their appropriate rational use. Also, for the rational use of available resources, the creation of a database will enable the definition of preparatory technologies. Fig. 1 shows a flowchart of the defined procedure.

Algorithm: GIS Energy map of biomass raw materials.



A defined database can be used by appropriate companies that will analyze the possibility of purchase at the appropriate price and defined time of delivery of available energy products. Also, in direct communication with the owner of available resources, a model for the organization of the preparation and receipt of raw materials is defined. The implementation of the developed concept will reduce the cost of procurement for the respective company that is interested in purchasing the available raw materials. It is quite realistic that the justification for the use of appropriate waste biomass raw materials in the defined territory, for appropriate use, will show justification through the financial and economic analysis of the justification, the Ecological justification of use (reduction of carbon dioxide and other harmful gases into the atmosphere), it will enable the employment of the workforce for the implementation of the planned activities for the use of available resources. Biomass waste can be used for a variety of purposes.

II. RESULTS

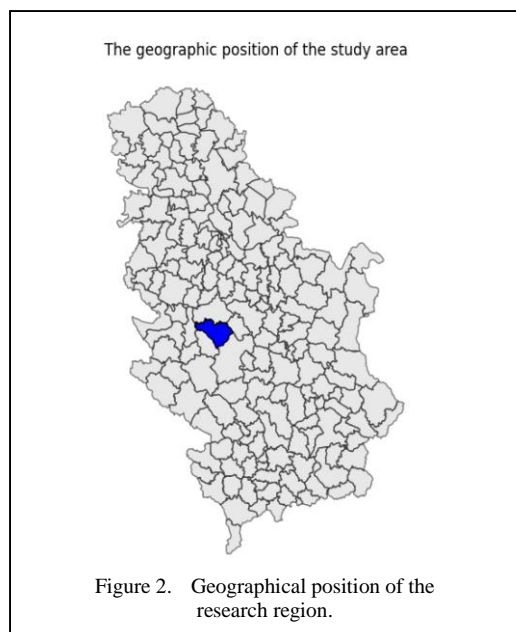
In the territories of local self-governments of Moravica, we have available energy potentials

from waste wood and plant biomass, as follows [2]:

- for Čačak about 10 TJ/year,
- for Ivanjica about 15 TJ/year,
- for Lucani about 10 TJ/year,
- for Gornji Milanovac about 10 TJ/year.

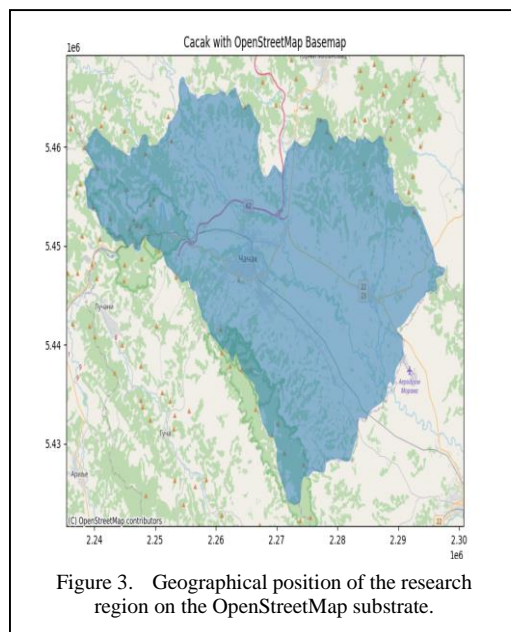
The above data were obtained by studying scientific papers and studies, without insight into where the sources of raw materials with quantities and types are produced [3]. For the purposes of this paper, data processing in the territory of the municipality of Čačak is presented. To load and process data, an application written using free software, Python and appropriate libraries is used. The Geopandas Library allows you to work with geothermal data and define the geographical area where the potentials of the bio mass are analyzed. Fig. 2 shows the loading of a defined geographical location, which in this paper is the area of the municipality of Čačak [4].

In this project, the emphasis is on the use of free software, so the OpenStreetMap background is used as the base, which is automatically loaded into the application, after defining the coordinate system for the defined territory, and therefore for the territory of northern Montenegro. Fig. 3 shows the territory of interest on the OpenStreetMap background.



Field research, using modern technological systems for defining the location, storing and transmitting data for processing, defined several test locations. To show the biomass locations in the municipality of Čačak on the map, the geospatial data containing the geometry of the municipality of Čačak is first loaded. Then, the coordinates of the points are defined that represent the locations of the biomass, such as sun and example, beech, cherry, raspberry, vineyard and slaughterhouse. After that, a GeoDataFrame was created that contains these locations. Ray-like colors are defined for each location, which allows for visual visibility. Then, a map was created showing the geometry of the municipality of Čačak with the data transformed into the appropriate coordinate reference system, with a transparency of 0.5. After that, points are added to the map for each defined biomass location, with the appropriate color and size of the marker, as well as a background map from the OpenStreetMap service and the title of the map, Fig. 4.

By implementing the defined algorithms for estimating and analyzing the biomass potential in the Geo Python application, it is possible to calculate the biomass energy potential for each defined location, which represent a test in order to demonstrate the proposed implementation, as the first result in Fig. 5 shows the bio mass potential on a representative sample for the purposes of this paper [4].



Visualizing the distance between regions for transport planning, for example, is another result of the analysis. This distance is represented by lines that connect points on the map and represents the distance in kilometers in a particular case. This distance representation provides a better understanding of the spatial relationships between biomass sites in the municipality of Čačak. A detailed overview of this aspect of the code can be seen in Fig. 6.

For the realization of the complete energy base, the appropriate GIS software, QGIS, is

used, which accesses the database of realized for each potential location in the territory of the Republic of Serbia using the described application realized using Geo Python resources [4,5]. Fig. 7 shows an example of uploaded and displayed bio mass resources on the territory of the Republic of Serbia, for the territory of the municipalities of Čačak, Jagodina, Vojvodina and Belgrade. In this way, the concept proposed in this paper in several regions in the Republic of Serbia is presented. The ultimate goal is to constantly fill in the data and update the energy map.

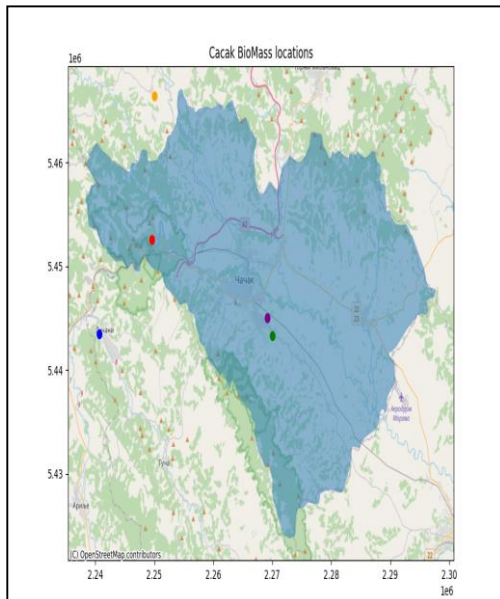


Figure 4. Geographical position of defined biomass locations on the OpenStreetMap substrate.

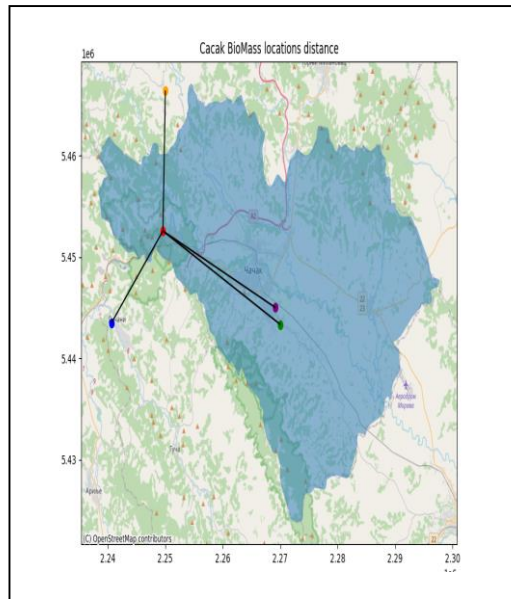


Figure 6. Display of spatial relationship and distance.

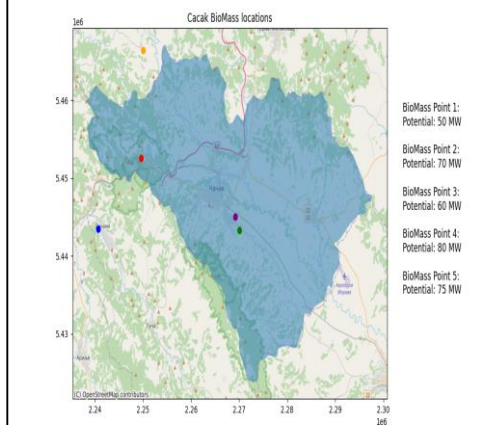


Figure 5. The potential of bio-mass resources at test sites.

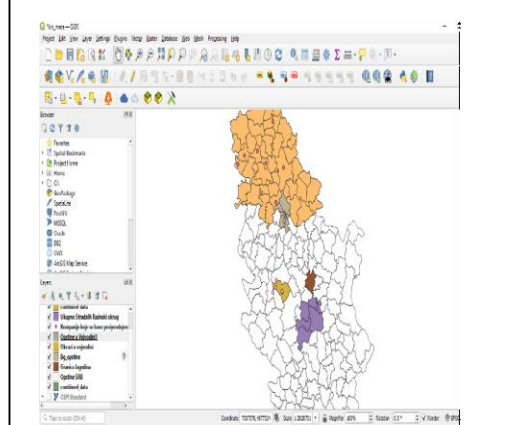


Figure 7. Display of the energy map at the test locations.

The results of the ENERGY MAP have not been compared with other methods or existing data to confirm its accuracy and reliability, due to the unavailability of appropriate data sources to be included in the GIZ energy map. The developed methodology is scalable for larger regions with more diverse biomass resources. The authors can quantify the potential economic or environmental benefits of implementing the ENERGY MAP in a defined territory. The developed system can process incomplete or outdated data, but this does not ensure the reliability of the ENERGY MAP. The authors believe that the ENERGY MAP can significantly contribute to the decentralization of energy production, due to the rational use of available resources in a defined territory that should be limited by minimal logistical costs. Finally, the proposed methodology is not aligned with national or regional energy policies. Also, the ENERGY MAP can be expanded to include considerations such as: preparation, transportation costs or seasonal variations in biomass availability.

III. CONCLUSION

For the rational use of available resources for appropriate energy purposes, the digitalization of the sector is an essential need to build a smart energy infrastructure in which the decentralization of production is one of the important principles, and it will enable locally produced green kWh of electricity not to burden the transmission networks. A sustainable growth strategy should not be tied to the exploitation of wasteful resources. This is especially important

for our country and for the region. The sustainability of the energy sector remains an enduring goal, along with the well-known concepts of security of supply and the development of competitiveness in the energy sector.

ACKNOWLEDGEMENT

Technological Development and Innovation of the Republic of Serbia, and these results are parts of the Grant No. 451-03-66 / 2024-03 / 200132 with University of Kragujevac - Faculty of Technical Sciences Čačak. Grant No. 451-03-65/2024-03/ 200122, Faculty of Science, University of Kragujevac.

REFERENCE

- [1] Zekić, V., Rodić, V., & Jovanović, M. (2010). Potentials and economic viability of small grain residue use as a source of energy in Serbia. *Biomass and bioenergy*, 34(12), 1789-1795.
- [2] Ćurčić, S., Gavrilović, R., Nikolić, D., & Trifunović, I. (2016). Available energy potentials from wood and plant biomass from the territory of the municipality of Čačak. *Journal of Energy, Ecology, Economy* (3-4), 331-339.
- [3] Ćurčić, S., & Blagojević, M (2018). Analysis of energy potentials from wood and biology by application of single neuron networks. *Journal of Energy, Ecology, Economy*, XIV (3-4), 171-176.
- [4] Rey, S. J., & Anselin, L. (2010). PySAL: A python library of spatial analytical methods. In *Handbook of applied spatial analysis* (pp. 175-193). Springer.
- [5] Kezurer, I., & Slatger, R. (2018). Using Python and GeoPandas in urban planning practice. *Planning Theory & Practice*, 19(3), 455-484.

Ferroelectricity-driven Photovoltaic Effect under Visible Light in the Absence of an External Electric Field for $\text{CsGeI}_{(3-t)}\text{Br}_t$ ($t = 1,2$): A First-principles Study

Naouel Chelil¹, Mohammed Sahnoun²

^{1,2}Laboratoire de Physique Quantique de la Modélisation Mathématique (LPQ3M),
Mascara, Algeria

¹n.chelil@univ-mascara.dz, ²sahnoun_cum@yahoo.fr

Abstract—In this work, we have conducted a comprehensive study to investigate the impact of bromine substitution on the structural and ferroelectric properties of CsGeI_3 , specifically examining the compositions $\text{CsGeI}_{(3-t)}\text{Br}_t$ ($t = 1,2$). Our first-principles calculations reveal that the bandgap energies of these mixed-halide perovskites vary from 1.34 to 1.72 eV, making them highly suitable for visible light absorption and photovoltaic applications. We also observe a significant variation in polarization values, with CsGeI_2Br exhibiting a higher polarization than CsGeIBr_2 . Moreover, the shift current analysis indicates that these materials, due to their lack of inversion symmetry, can generate spontaneous photocurrents through the Berry connection, positioning them as promising alternatives to traditional p-n junction solar cells. Our findings highlight the potential of $\text{CsGeI}_{(3-t)}\text{Br}_t$ compounds for future solar energy harvesting technologies, combining favorable electronic, optical, and ferroelectric properties with efficient bulk photovoltaic effects.

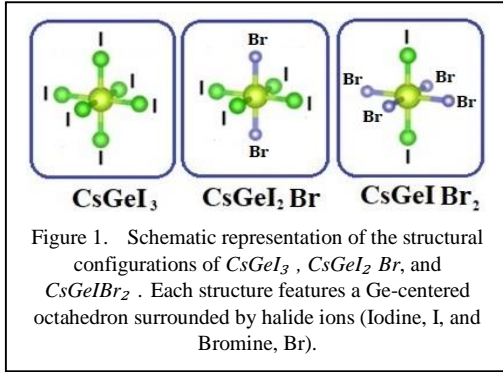
Keywords - shift current, photocurrent, BPVE, ferroelectrics

I. INTRODUCTION

Ferroelectric materials, which exhibit reversible spontaneous polarization in non-centrosymmetric crystals [1-3], generate a bulk photovoltaic effect (BPVE) through second-

order optical responses [4,5], known as shift current [6-8]. This phenomenon produces a rectified current in response to linearly polarized light, with potential applications in optoelectronics [9-11] and terahertz emission [12-14]. Unlike traditional p-n junction solar cells that rely on built-in potentials for charge separation, BPVE arises from the real-space shift of charge centers in noncentrosymmetric materials, resulting in a less dissipative photocurrent not limited by the Shockley-Queisser efficiency [15-17]. Although promising for photovoltaic applications due to their ability to absorb a large portion of the solar spectrum [18,19], ferroelectric materials like BiFeO_3 , BaTiO_3 , and SbSI have shown limited shift current conductivity in the UV-Vis-NIR range [20-23]. Metal-halide perovskites, particularly mixed-halide types like $\text{CsGeI}_{(3-t)}\text{Br}_t$ ($t = 1,2$) offer unique opportunities to study the impact of crystal structure and chemical composition on shift current conductivity, thanks to their flexibility and ability to support ion migration while maintaining excellent electronic transport properties [24-27]. This study uses Density Functional Theory (DFT) calculations to investigate the effect of mixed halogen composition on shift current in





$\text{CsGeI}_{(3-t)}\text{Br}_t$ ($t=1,2$), focusing on the relationship between structure and BPVE, an area that has not been fully explored despite previous studies on the material's electronic and optical properties [28].

II. COMPUTATIONAL METHOD

We performed DFT calculations on the optimized structure using the Full-Potential Linearized Augmented Plane Wave (FP-LAPW) method as implemented in WIEN2k [29], with the Perdew-Burke Ernzerhof (PBE) formulation [30] of the generalized gradient approximation (GGA). Both internal coordinates and lattice parameters were fully relaxed. To address the typical GGA bandgap underestimation, we employed the Tran-Blaha modified Becke-Johnson (TB-mBJ) potential [31]. The shift current conductivity was calculated using the Wannier90 package [32], which utilizes a high-quality tight-binding model incorporating $Ge-s$, $Ge-p$, $I-p$, and $Br-p$ orbitals as basis sets. Polarization was determined using the Berry phase method with the BerryPI program [33-35].

III. RESULTS AND DISCUSSION

In this work, the crystal structures of $\text{CsGeI}_{(3-t)}\text{Br}_t$ ($t=1,2$) compounds were constructed by mixing two halides into the structure of CsGeI_3 in its ferroelectric phase before performing geometry optimization. The specific effect of halide mixing may be associated with the reduction of local symmetry along the z-direction. The initial geometries of the $\text{CsGeI}_{(3-t)}\text{Br}_t$ compounds were relaxed using the PBE-GGA approach. We found that all compounds adopt a non-centrosymmetric hexagonal structure with the P3m1 space group, exhibiting subtle distortions in local bonding.

TABLE I. THE FORMATION ENERGY OF $\text{CsGeI}_{(3-t)}\text{Br}_t$ ($t=1,2$).

Compounds	ΔH (Ry)	Bandgap (eV)	$P_s(\mu\text{C}/\text{cm}^2)$
CsGeI_2Br	0.0300	1.34	18.31
$\text{CsGeI}_2\text{Br}_2$	0.3039	1.72	8.88
CsGeI_3 [36]	-	1.53	15.82

To investigate the stability of these materials, we calculated the formation energies using the formula below.

$$\Delta H = E(\text{CsGeI}_{3-t}\text{Br}_t) - \{xE(\text{CsGeI}_3) + (1-x)E(\text{CsGeBr}_3)\} \quad (1)$$

Here $E(\text{CsGeI}_{(1-t)}\text{Br}_t)_3$, $E(\text{CsGeI}_3)$ and $E(\text{CsGeBr}_3)$ are the total energies of the mixed halide and the pure halides, respectively. All the compounds showed positive formation energies; For the lower energy configuration of CsGeI_2Br is close to 0.0 Ry. Hence this mixed halide must be formed and are stable with respect to the added anion (see Table I).

To evaluate the potential of ferroelectric $\text{CsGeI}_{(3-t)}\text{Br}_t$ ($t=1,2$) as photovoltaic applications, we performed electronic structure calculations using the TB-mBJ approach. The band structures and density of states (DOS) for CsGeI_2Br and CsGeIBr_2 , are shown in Fig. 2 (a) and (b), show that both materials are direct bandgap semiconductors, with bandgap energies ranging from 1.34 to 1.72 eV, making them suitable for visible light absorption. Notably, the bandgap of CsGeIBr_2 is larger than that of pristine CsGeI_3 (1.53 eV), a trend consistent with previous findings for CsPbI_2Br [37]. The electronic states near the band edges are mainly composed of p orbitals from Br , I , and Ge atoms, with minor contributions from Ge_s orbitals, which guided our selection of Wannier basis sets for shift current calculations. These features underscore the materials' potential as effective ferroelectric photovoltaic absorbers.

Studying the optical absorption in optoelectronic devices is essential, which

explains the behavior of materials under incident light, it is determined by the formula based on the frequency-dependent dielectric function $\varepsilon(\omega)$.

$$\alpha(\omega) = \sqrt{2}\omega \left[\sqrt{(\varepsilon_1^2(\omega) + \varepsilon_2^2(\omega)) - \varepsilon_1(\omega)} \right]^{\frac{1}{2}}. \quad (2)$$

Fig. 2 presents the absorption coefficient, $\alpha(\omega)$, of $CsGeI_2Br$ (labeled in purple) and $CsGeIBr_2$ (labeled in cyan) as a function of energy, ranging from the infrared (IR) region to the ultraviolet (UV) region. $\alpha(\omega)$ for $CsGeI_2Br$ and $CsGeIBr_2$ shows that both materials exhibit low absorption in the infrared region (0-1.5 eV), with a significant increase in absorption as the energy enters the visible range, indicating their potential for photovoltaic applications. In the UV region, the absorption coefficient rises sharply with different peaks indicating distinct electronic transitions at higher energies, highlighting strong UV absorption capabilities, which is useful for UV photodetectors. The

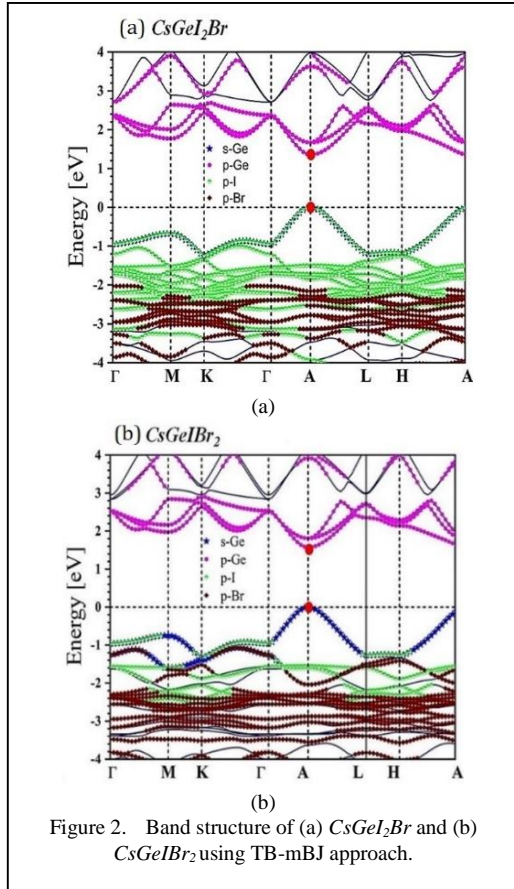


Figure 2. Band structure of (a) $CsGeI_2Br$ and (b) $CsGeIBr_2$ using TB-mBJ approach.

anisotropy in absorption, shown by the different behavior for E_{xx} and E_{zz} polarizations, suggests direction-dependent optical properties that could be harnessed in device design. Overall, the materials demonstrate effective absorption across the visible and UV spectra, with $CsGeI_2Br$ showing slightly higher absorption in the visible range compared to $CsGeIBr_2$.

The results indicate that the candidate materials possess electronic and optical properties ideal for solar energy harvesting. Additionally, the material adopts a polar space group (P3m1), which lacks inversion symmetry, leading to distinct spontaneous polarization. In ferroelectric materials, opposite charges are displaced in opposite directions, creating a dipole moment, and the spontaneous electric polarization is directly related to the extent of atomic distortions from a centrosymmetric structure. This polarization was calculated using the Berry phase method developed by King-Smith and Vanderbilt [34], which defines spontaneous polarization as the sum of ionic and electronic components:

$$Ps = P_{ion} + P_{el}. \quad (3)$$

This polarization can be expressed as:

$$Ps = \frac{e}{\Omega} \sum_S^{atoms} Z_s^{ion} r_s - \frac{2ei}{(2\pi)^3} \sum_n^{occ-bands} \int_{BZ} dk \langle U_{nk} | \nabla_k | U_{nk} \rangle. \quad (4)$$

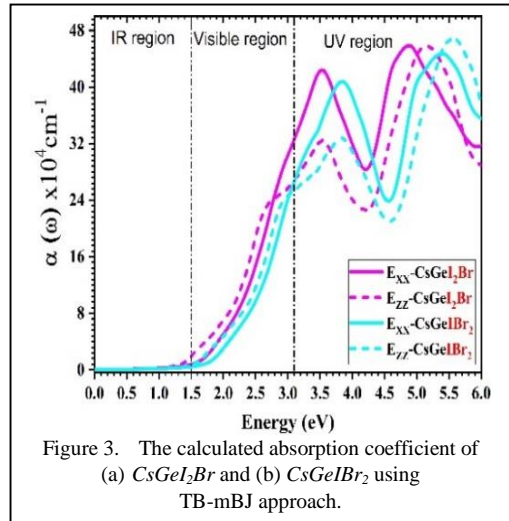


Figure 3. The calculated absorption coefficient of (a) $CsGeI_2Br$ and (b) $CsGeIBr_2$ using TB-mBJ approach.

Where Ω is the volume, e is the elementary charge, Z_s is the ionic charge represented by the number of valence electrons in atom s , and r_s is its position vector. The significant influence of halide substitution on the ferroelectric properties of $CsGeI_2Br$ ($18.31 \mu\text{C}/\text{cm}^2$) and $CsGeIBr_2$ ($8.88 \mu\text{C}/\text{cm}^2$) is clear when compared to pure $CsGeI_3$ ($15.82 \mu\text{C}/\text{cm}^2$) [36]. Bromine's smaller atomic radius compared to iodine leads to greater lattice distortion, enhancing the displacement of the Ge atom within the octahedral structure and resulting in increased polarization in $CsGeI_2Br$. However, further substitution in $CsGeIBr_2$ leads to reduced polarization, likely due to additional distortions counteracting each other, thereby decreasing the overall displacement of Ge and the resulting polarization. The introduction of bromine also modifies the crystal's symmetry and charge distribution, where the polarization is affected by the interplay between increased distortion and potential phase transitions. Therefore, while moderate halide substitution can boost ferroelectric properties by increasing lattice distortion and breaking symmetry, excessive substitution may lead to structural configurations that reduce overall polarization. In materials with broken inversion symmetry, the shift current response [5] a second-order nonlinear effect becomes significant. The BPVE is described by the nonlinear conductivity tensor σ^{abc} , which relates the current density J^i to the electromagnetic field E_j :

$$J^i = \sigma^{abc}(0, \omega, -\omega) E_j E_k. \quad (5)$$

The conductivity tensor $\sigma^{abc}(0, \omega, -\omega)$ is given by [20]:

$$\begin{aligned} \sigma^{abc}(0, \omega, -\omega) = \\ = \frac{ie^3 \pi}{\hbar V} \sum_{\vec{k}} \sum_{m,n} f_{nm} (r_{nm}^i r_{nm}^j + r_{nm}^j r_{nm}^i) \delta(\hbar\omega - E_{nm}), \end{aligned} \quad (6)$$

where n and m are band indices, $f_{nm} = f_n - f_m$ represents the Fermi-Dirac distribution difference, $r_{nm}^i = A_{nm}^i (1 - \delta_{n,m})$ is the inter-band Berry connection, $r_{nm}^{i,j} = \partial_{k_j} r_{nm}^i - i(A_m^j - A_n^j) r_{nm}^i$ depends on intermediate virtual states, and $E_{nm} = E_n - E_m$ is the energy difference between two bands. The photovoltaic effect is directly

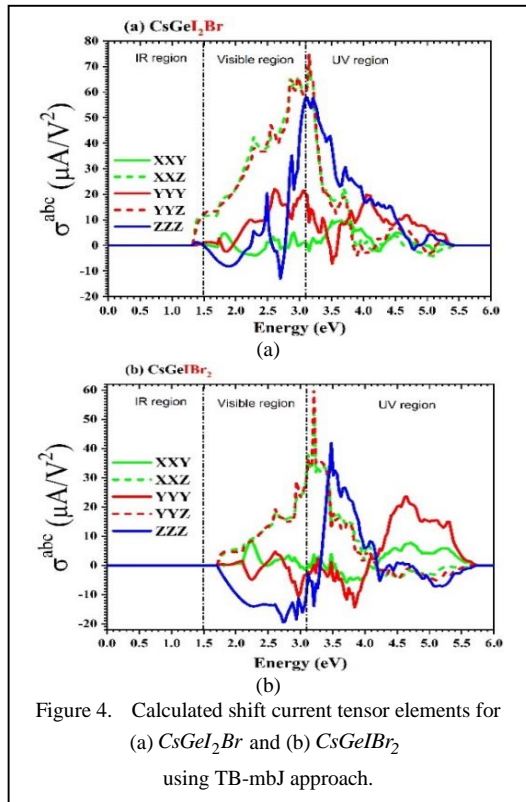


Figure 4. Calculated shift current tensor elements for (a) $CsGeI_2Br$ and (b) $CsGeIBr_2$ using TB-mbJ approach.

proportional to light intensity and is influenced by the third rank tensor of σ^{abc} . Our studied materials belong to the point group $P3m1$, which permits five nonzero tensorial components of $\sigma^{abc}(0, \omega, -\omega)$, namely σ^{xyx} , σ^{xzx} , σ^{yyy} , σ^{yyz} , and σ^{zzz} . Here, the upper-case letter represents the direction of shift current susceptibility, while the lowercase letters represent light polarization. Fig. 3 (a) and (b) illustrate the nonzero components of the shift-current spectrum for $CsGeI_2Br$ and $CsGeIBr_2$ as a function of photon energy. The calculated shift current response for $CsGeI_2Br$ and $CsGeIBr_2$ reveals distinct differences in their nonlinear optical properties, particularly in the visible spectrum. $CsGeI_2Br$ exhibits a pronounced shift current response with significant peaks around 3.0 eV, especially in the σ^{yyz} component, reaching nearly $80 \mu\text{A}/\text{V}^2$ (see Fig. 4a). The σ^{zzz} component also shows significant activity in the visible region, with a peak around 3.2 eV, indicating strong anisotropic behavior ideal for visible light absorption in photovoltaic applications. In contrast, $CsGeIBr_2$ (Fig. 4b) shows a reduced overall shift current response, with lower peak

values and a broader distribution across the visible and UV regions. This reduction in response for $CsGeIBr_2$ aligns with its lower spontaneous polarization, suggesting that while it remains responsive to visible light, the additional bromine substitution leads to complex distortions that diminish the overall efficiency of charge separation.

In conclusion, we provide a comprehensive analysis of the electronic, optical, ferroelectric, and bulk photovoltaic properties of the mixed-halide perovskites $CsGeI_2Br$ and $CsGeIBr_2$. Both materials exhibit a direct bandgap, with $CsGeI_2Br$ showing better alignment with the visible spectrum and superior light absorption. $CsGeI_2Br$ also has a higher spontaneous polarization ($18.31 \mu\text{C}/\text{cm}^2$) compared to $CsGeIBr_2$ ($8.88 \mu\text{C}/\text{cm}^2$), attributed to increased lattice distortion from bromine substitution. The shift current analysis further highlights $CsGeI_2Br$ stronger photovoltaic potential, especially in the visible range, due to a more concentrated shift current response. The real-space charge center shift between the valence and conduction electrons in I , $Br-p$, and $Ge-4p$ orbitals play a crucial role in this enhanced performance. As results, $CsGeI_2Br$ emerges as a promising candidate for photovoltaic applications, combining favorable electronic and optical properties with strong ferroelectric polarization and an efficient shift current response.

REFERENCES

- [1] Röhm, H., Leonhard, T., Schulz, A. D., Wagner, S., Hoffmann, M. J., & Colsmann, A. (2019). Ferroelectric properties of perovskite thin films and their implications for solar energy conversion. *Advanced Materials*, 31(26), 1806661.
- [2] Nechache, R., et al. (2015). Bandgap tuning of multiferroic oxide solar cells. *Nature photonics*, 9(1), 61-67.
- [3] Paillard, C., et al. (2016). Photovoltaics with ferroelectrics: current status and beyond. *Advanced Materials*, 28(26), 5153-5168.
- [4] Kraut, W., & von Baltz, R. (1979). Anomalous bulk photovoltaic effect in ferroelectrics: a quadratic response theory. *Physical Review B*, 19(3), 1548.
- [5] von Baltz, R., & Kraut, W. (1981). Theory of the bulk photovoltaic effect in pure crystals. *Physical Review B*, 23(10), 5590.
- [6] Nastos, F., & Sipe, J. E. (2006). Optical rectification and shift currents in GaAs and GaP response: Below and above the band gap. *Physical Review B—Condensed Matter and Materials Physics*, 74(3), 035201.
- [7] Nastos, F., & Sipe, J. E. (2010). Optical rectification and current injection in unbiased semiconductors. *Physical Review B—Condensed Matter and Materials Physics*, 82(23), 235204.
- [8] Morimoto, T., & Nagaosa, N. (2016). Topological nature of nonlinear optical effects in solids. *Science advances*, 2(5), e1501524.
- [9] Tan, L. Z., Zheng, F., Young, S. M., Wang, F., Liu, S., & Rappe, A. M. (2016). Shift current bulk photovoltaic effect in polar materials—hybrid and oxide perovskites and beyond. *Npj Computational Materials*, 2(1), 1-12.
- [10] Rangel, T., Fregoso, B. M., Mendoza, B. S., Morimoto, T., Moore, J. E., & Neaton, J. B. (2017). Large bulk photovoltaic effect and spontaneous polarization of single-layer monochalcogenides. *Physical review letters*, 119(6), 067402.
- [11] Matsyshyn, O., Dey, U., Sodemann, I., & Sun, Y. (2021). The Berry phase rectification tensor and the solar rectification vector. *Journal of Physics D: Applied Physics*, 54(40), 404001.
- [12] Harrel, S. M., Milot, R. L., Schleicher, J. M., & Schmittenmaer, C. A. (2010). Influence of free-carrier absorption on terahertz generation from ZnTe (110). *Journal of Applied Physics*, 107(3).
- [13] Somma, C., Reimann, K., Flytzanis, C., Elsaesser, T., & Woerner, M. (2014). High-field terahertz bulk photovoltaic effect in lithium niobate. *Physical review letters*, 112(14), 146602.
- [14] Ghalgaoui, A., Reimann, K., Woerner, M., Elsaesser, T., Flytzanis, C., & Biermann, K. (2018). Resonant second-order nonlinear terahertz response of gallium arsenide. *Physical Review Letters*, 121(26), 266602.
- [15] Choi, T., Lee, S., Choi, Y. J., Kiryukhin, V., & Cheong, S. W. (2009). Switchable ferroelectric diode and photovoltaic effect in BiFeO₃. *Science*, 324(5923), 63-66.
- [16] Yang, S. Y., et al. (2010). JW, LW Martin, and R. Ramesh. Above-bandgap voltages from ferroelectric photovoltaic devices. *Nature Nanotechnology*, 5(2), 143-147.
- [17] Ogawa, N., Sotome, M., Kaneko, Y., Ogino, M., & Tokura, Y. (2017). Shift current in the ferroelectric semiconductor SbSI. *Physical Review B*, 96(24), 241203.
- [18] Sturman, B., & Fridkin, V. (2021). *Photovoltaic and photo-refractive effects in noncentrosymmetric materials*. Routledge.
- [19] Brehm, J. A., Young, S. M., Zheng, F., & Rappe, A. M. (2014). First-principles calculation of the bulk photovoltaic effect in the polar compounds LiAsS₂, LiAsSe₂, and NaAsSe₂. *The Journal of chemical physics*, 141(20).
- [20] Young, S. M., & Rappe, A. M. (2012). First principles calculation of the shift current photovoltaic effect in ferroelectrics. *Physical review letters*, 109(11), 116601.
- [21] Pal, S., Muthukrishnan, S., Sadhukhan, B., NV, S., Murali, D., & Murugavel, P. (2021). Bulk photovoltaic effect in BaTiO₃-based ferroelectric oxides: An experimental and theoretical study. *Journal of Applied Physics*, 129(8).

- [22] Yang, S. Y., et al. (2009). Photovoltaic effects in BiFeO₃. *Applied Physics Letters*, 95(6).
- [23] Sotome, M., et al. (2019). Spectral dynamics of shift current in ferroelectric semiconductor SbSI. *Proceedings of the National Academy of Sciences*, 116(6), 1929-1933.
- [24] Rehman, W., et al. (2017). Photovoltaic mixed-cation lead mixed-halide perovskites: links between crystallinity, photo-stability and electronic properties. *Energy & Environmental Science*, 10(1), 361-369.
- [25] Jacobsson, T. J., et al. (2016). Exploration of the compositional space for mixed lead halogen perovskites for high efficiency solar cells. *Energy & Environmental Science*, 9(5), 1706-1724.
- [26] Parrott, E. S., Green, T., Milot, R. L., Johnston, M. B., Snaith, H. J., & Herz, L. M. (2018). Interplay of structural and optoelectronic properties in formamidinium mixed tin-lead triiodide perovskites. *Advanced Functional Materials*, 28(33), 1802803.
- [27] Zhao, B., et al. (2017). High open-circuit voltages in tin-rich low-bandgap perovskite-based planar heterojunction photovoltaics. *Advanced materials*, 29(2), 1604744.
- [28] Elfatouaki, F., Farkad, O., Ibnouelghazi, E. A., Abouelaoualim, D., & Outzourhit, A. (2022). Electronic and optical properties of CsGeX₂M (X, M= Br, Cl, I) perovskites for solar cell applications: First-principles study using PBE and TB-mBJ potentials. *Materials Science in Semiconductor Processing*, 143, 106488.
- [29] Blaha, P., Schwarz, K., Madsen, G. K., Kvasnicka, D., & Luitz, J. (2002). *Wien2k, an augmented plane wave plus local orbitals program for calculating crystal properties*. Vienna University of Technology, Austria.
- [30] Perdew, J. P., Burke, K., & Ernzerhof, M. (1996). Generalized gradient approximation made simple. *Physical review letters*, 77(18), 3865.
- [31] Tran, F., & Blaha, P. (2009). Accurate Band Gaps of Semiconductors and Insulators with a Semilocal Exchange-Correlation Potential. *Physical review letters*, 102(22), 226401.
- [32] Mostofi, A. A., Yates, J. R., Lee, Y. S., Souza, I., Vanderbilt, D., & Marzari, N. (2008). wannier90: A tool for obtaining maximally-localised Wannier functions. *Computer physics communications*, 178(9), 685-699.
- [33] Ahmed, S. J., Kivinen, J., Zaporzan, B., Curiel, L., Pichardo, S., & Rubel, O. (2013). BerryPI: A software for studying polarization of crystalline solids with WIEN2k density functional all-electron package. *Computer Physics Communications*, 184(3), 647-651.
- [34] King-Smith, R. D., & Vanderbilt, D. (1993). Theory of polarization of crystalline solids. *Physical Review B*, 47(3), 1651.
- [35] Resta, R., & Vanderbilt, D. (2007). *Theory of polarization: a modern approach*. In *Physics of ferroelectrics: a modern perspective* (pp. 31-68). Berlin, Heidelberg: Springer Berlin Heidelberg.
- [36] Chelil, N., Sahnoun, M., Benhalima, Z., Larbi, R., & Eldin, S. M. (2023). Insights into the relationship between ferroelectric and photovoltaic properties in CsGeI₃ for solar energy conversion. *RSC advances*, 13(3), 1955-1963.
- [37] Gao, R., et al. (2021). Tunable electronic properties and large optical anisotropy in the CsPbX_nY_{3-n} (X, Y= Cl, Br, I) perovskite. *Solar Energy*, 217, 165-172.

Numerical Simulation and Optimization of Stable $\text{CH}_3\text{NH}_3\text{PbI}_3$ -based 2D/3D Mixed Dimensional Perovskite Solar Cell

Walagedara Gamage Ayomi Pabasara¹, Galhenage Asha Sewvandi²

^{1,2}Department of Materials Science and Engineering, University of Moratuwa, Katubedda, Sri Lanka

¹ayomiwalagedara@gmail.com, ²galhenage@uom.lk

Abstract—Over the recent decades, solar power has gained significant attention globally as a sustainable and cost-effective source of energy outpacing other renewable energy alternatives. Perovskite Solar Cells (PSCs) have been identified as a powerful photovoltaic technology due to their exceptional characteristics including improved efficiency and affordability. The perovskite material demonstrates superior properties such as higher absorption coefficients, adjustable band gaps and extended charge carrier lifetime. However, conventional 3D perovskite solar cells face instability issues upon exposure to elevated temperatures and moisture delaying commercialization. 2D perovskite materials demonstrate a higher stability level than their 3D counterparts. Therefore, 2D/3D mixed-dimensional PSCs have been developed to overcome these challenges and achieve balanced performance and long-term stability simultaneously. In this study, a 2D/3D mixed dimensional PSC was numerically simulated by incorporating 2D-MAPbI₃ capping layer on the top of 3D-MAPbI₃ using SCAPS-1D solar cell simulation software. The proposed device architecture is FTO/TiO₂/3D-MAPbI₃/2D-MAPbI₃/Cu₂O/Au. The device performance was optimized by varying the thickness and the defect density of 3D-MAPbI₃ layer. The optimized device demonstrates maximum power conversion efficiency (PCE) of 24.52% at 1 μm thickness and defect density range of 10¹⁰-10¹² cm⁻³. This analysis reveals that the 2D/3D mixed-dimensional PSC delivers enhanced efficiency while ensuring the prolonged operational stability of the solar cell.

Keywords - perovskite solar cell, capping layer, stability enhancement, power-conversion efficiency, defects

I. INTRODUCTION

Global energy demand is rising day by day due to rapid industrialization and population growth. It is anticipated that global energy demand will triple by 2050, even the timely conservation measures are implemented. The availability of fossil fuel sources is limited making it challenging to fulfill the rising energy demand [1]. Moreover, the emission of greenhouse gases and air pollution caused by burning fossil fuels has become a pressing environmental issue emphasizing the need for energy alternatives. In recent decades, solar power has evolved as a clean and sustainable energy source providing solutions for both increasing energy demand and environmental pollution. Currently, Si-based solar cells dominate the solar cell market with enhanced power conversion efficiency [2]. However, their high manufacturing cost and associated environmental concerns limit their widespread adoption.

Perovskite Solar Cell is a promising solar cell technology due to its remarkable power conversion efficiency levels and simple and affordable manufacturing practices [3]. Organic-inorganic halide perovskites are rapidly gaining prominence in the solar cell industry due to their unique photovoltaic characteristics such as adjustable optical bandgap, greater absorption



coefficient, improved carrier transportation and weak exciton binding energy [4]. Since the inception of PSCs, they have achieved 20% efficiency improvements in the past few decades due to technological advancements in the photovoltaic field. As per the efficiency chart published by the National Renewable Energy Laboratory 2023, the maximum certified PCE achieved by single-junction perovskite-based solar cells is 26.1% [5].

ABX₃ is the standard chemical formula of perovskites. Here, A is denoted as monovalent cations such as methylammonium [MA⁺: CH₃NH₃⁺], formamidinium [FA⁺], Cesium (Cs⁺), or their blend. B is divalent cations usually metals, such as Pb²⁺, Sn²⁺, Ge²⁺, or a blend of these. Monovalent anions are indicated by X, typically halides, including I⁻, Br⁻, Cl⁻, or a mixture of them [6]. 3D-MAPbI₃ based PSCs are considered the most prominent PSCs in the market due to their higher PCE and low production cost. However, they are highly prone to degradation under external environmental factors such as heat, moisture and UV radiation resulting in deterioration of performance in long-term operation [7]. This is the main barrier behind the commercialization of MAPbI₃ based solar cells.

2D perovskite materials show excellent moisture, heat and UV stability over their 3D counterparts. Ruddlesden–Popper (RP), Dion–Jacobson (DJ), and Alternation cation in the interlayer space perovskites (ACI) are the most prevailing 2D perovskite types [8]. The incorporation of 2D materials as a capping layer on the 3D perovskite has been proven as a successful way to boost the stability of the 3D perovskite materials. The resultant 2D/3D hybrid solar cell shows balanced efficiency and long-term stability compared to the PSCs [9-11]. For instance, [10] developed phenethylammonium based 2D with 3D perovskites. The stability of the system is enhanced, and it achieved a PCE of 19.98% with Voc of 1.17 V. Further, [11] incorporated thin 2D n-butylamine with 3D perovskite film to form a 2D/3D mixed dimensional solar cell which remained at 93% of the initial PCE after 55 days in the air with humidity of about 50% at room temperature.

The 2D form of MAPbI₃ perovskite material is more environmentally stable than its 3D counterpart making them an excellent candidate for incorporation as a capping layer [12].

The layered structure facilitates reducing issues such as moisture sensitivity and thermal instability in 2D-MAPbI₃. Furthermore, 2D structures can enhance charge transport properties resulting in greater carrier mobility and fewer recombination losses. Consequently, it offers better higher power conversion efficiencies in the PSCs. Nipuna L et al numerically simulated a solar cell inserting 3D-MAPbI₃ between two 2D-MAPbI₃ layers with the cell architecture of Glass/ITO/PEDOT: PSS/2D-MAPbI₃/3D-MAPbI₃/2D-MAPbI₃/PC BM/Ag. Here, it has been investigated the effect of deep defect density of 3D-MAPbI₃ layer on the performance of the PSC. The results show that the highest performance of the device is given when the deep defect density ranges from 10¹⁰-10¹² cm⁻³ [13].

In this study, a 2D/3D hybrid solar cell was numerically simulated by applying 2D-MAPbI₃ capping layer on the top of the 3D-MAPbI₃ layer to reduce the degradation of the 3D-MAPbI₃ upon exposure to heat and moisture. The simulated p-i-n device architecture was FTO/TiO₂/3D-MAPbI₃/2D-MAPbI₃/Cu₂O/Au. The effect of the thickness and defect density of the absorber layers were investigated to optimize the performance of the solar cell.

II. METHODOLOGY

The 2D/3D mixed dimensional PSC with the device architecture of FTO/TiO₂/3D-MAPbI₃/2D-MAPbI₃/Cu₂O/Au was simulated in this study. The front contact electrode was made of Fluorine-doped tin oxide (FTO) while Cu₂O was utilized as the hole transport layer (HTL) which is a p-type hole-accepting material where the majority of carriers are holes. As the perovskite active absorber materials 3D-MAPbI₃ was utilized and as a protective layer 2D-MAPbI₃ was applied. In the proposed structure, TiO₂ layer acts as the electron transport layer (ETL) and Gold (Au) acts as the back contact cathode material as depicted in Fig 1.

The Solar Cell Capacitance Simulator (SCAPS-1D) software was employed to simulate the proposed device. It is commonly used in the simulation of optoelectronic devices particularly for solar cells, due to its capability of solving the Continuity equation and Poisson equation, allowing accurately forecast the output of photovoltaic devices [14]. The presented cell structure was drawn in the software and simulation was performed using the drift-

diffusion model at 300 K temperature upon one sun illumination (AM1.5G, 100 mW/cm²).

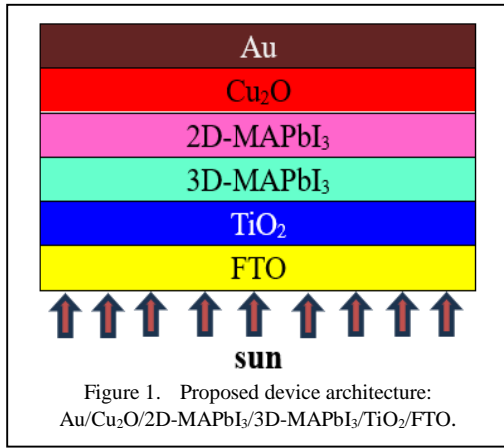


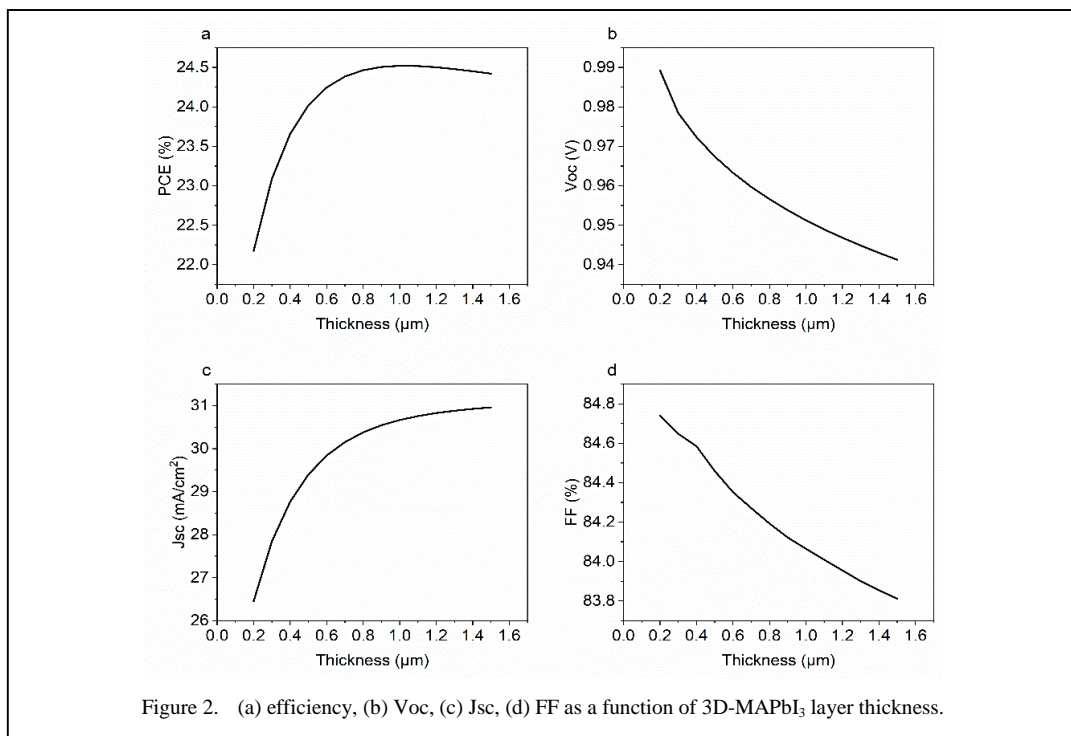
TABLE I. OPTICAL AND ELECTRONIC PARAMETERS USED IN SIMULATION FOR CHARGE TRANSPORT LAYERS AND FRONT ELECTRODE.

S/ No	Description of the parameter	FTO [15]	TiO ₂ [14,16]	Cu ₂ O [14,16]
1	Thickness (μm)	0.5	0.1	0.4
2	Band gap (eV)	3.5	3.26	2.22
3	Electron affinity (eV)	4	4.2	3.40
4	Dielectric permeability relative	9	38	7.11
5	VB effective density of state (states/cm ³ /eV)	2.2x 10 ¹⁸	2.2 x 10 ¹⁷	2.02x 10 ¹⁷
	CB effective density of state (states/cm ³ /eV)	1.8x 10 ¹⁹	1.8x 10 ¹⁸	3.0x 10 ²⁰
6	Hole thermal velocity (cms ⁻²)	1x10 ⁷	1x10 ⁷	1x10 ⁷
	Electron thermal velocity (cms ⁻²)	1x10 ⁷	1x10 ⁷	1x10 ⁷
7	Hole mobility (cm ² /Vs)	20	2x10 ⁴	30
	Electron mobility (cm ² /Vs)	10	1x10 ⁴	30
8	Shallow uniform donor density (cm ⁻³)	10 ¹⁵	6x10 ¹⁹	0
	Shallow uniform donor density (cm ⁻³)	0	0	1x10 ¹⁸
9	ElectronCapture cross section (cm ²)	1x 10 ⁻¹⁵	1x10 ⁻¹⁵	1x10 ⁻¹⁵
10	Hole Capture cross section (cm ²)	1x 10 ⁻¹⁵	1x10 ⁻¹⁵	1x10 ⁻¹⁵
11	Defect density	1x10 ¹²	1x10 ¹²	1x10 ¹²

The thickness of the 3D-MAPbI₃ varied between 0.2 μm-1.5 μm as reported in the literature. The 2D-MAPbI₃ should be a thin layer so that its thickness is kept at 0.03 μm as reported in previous studies [13]. In this theoretical study, the defect density of 3D layers varied from 10¹⁰-10¹⁷ cm⁻³ to explore the impact of defect densities on the overall performance of the device keeping the thickness of the layers at the optimum values. The parameters used in SCAPS-1D simulations for the different absorber materials, transport layers and electrodes were adopted from previously published reports as depicted in Tables I and II.

TABLE II. OPTICAL AND ELECTRONIC PARAMETERS USED IN THE SIMULATION FOR ABSORBER LAYERS.

S/No	Description of the parameter	3D-MAPbI ₃ [14,17]	2D-MAPbI ₃ [13]
1	Thickness (μm)	varied	0.03
2	Band gap (eV)	1.55	1.63
3	Electron affinity (eV)	6.90	3.9
4	Dielectric permeability relative	6.50	6.5
5	VB effective density of state (states/cm ³ /eV)	2.75x 10 ¹⁸	1.94x10 ²⁰
	CB effective density of state (states/cm ³ /eV)	3.9 x 10 ¹⁸	1.94x10 ²⁰
6	Hole thermal velocity (cms ⁻²)	1x10 ⁷	1x10 ⁷
	Electron thermal velocity (cms ⁻²)	1x10 ⁷	1x10 ⁷
7	Hole mobility (cm ² /Vs)	11.8	414
	Electron mobility (cm ² /Vs)	11.8	1184
8	Shallow uniform donor density (cm ⁻³)	2.2x10 ¹⁸	1x10 ¹⁶
	Shallow uniform donor density (cm ⁻³)	9x10 ²⁰	1x10 ¹⁶
9	ElectronCapture cross section (cm ²)	1x10 ⁻¹⁵	1x10 ⁻¹⁵
10	Hole Capture cross section (cm ²)	1x10 ⁻¹⁵	1x10 ⁻¹⁵
11	Defect density	varied	2.5x10 ¹²



III. RESULTS AND DISCUSSION

A. Effect of 3D-MAPbI₃ Absorber Layer Thickness on the Performance of the PSC

As illustrated in Fig. 2a, the PCE of the device increases with the thickness of the 3D-MAPbI₃ layer until a threshold thickness of 1 μm and then starts to decline further increasing the thickness. The recorded maximum PCE is 24.52%. The main reason behind this behavior can be related to the thickness-dependent absorption characteristics of the active absorber layer. In the relatively lower thicknesses, the absorption in the longer wavelength is limited leading to the creation of limited electron-hole pairs. Increasing the perovskite layer thickness promotes the absorption of longer wavelengths resulting in improved electron-hole pair generation [14]. However, when further enhancing the thickness beyond a critical value, even a greater percentage of the solar spectrum can be absorbed, the generated charge carriers are required to travel long distances to reach the electrodes which increases the likelihood of carrier recombination [18]. Subsequently, the PCE of the device declines after the thickness surpasses a critical threshold. As per Fig. 2b and Fig. 2d the V_{oc} and FF are decreasing when the absorber layer thickness rises. This is mainly

caused by the increased carrier recombination and series resistance due to thickness enhancement. The thicker absorber layer introduces more series resistance leading to voltage drop under the current flow and reducing the effectiveness of charge collection, thereby reducing the V_{oc} . The decrement in the V_{oc} drops the maximum output power and thereby reduces the FF [19]. At the optimum thickness value, the device shows V_{oc} of 0.95 V, J_{sc} of 30.66 mA/cm² and FF of 84.07%.

B. Effect of 3D-MAPbI₃ Absorber Layer Defect Density on the Performance of the PSC

The defect density of the perovskite absorber layer greatly affects the photovoltaic characteristics of the PSCs. If the defect density is high, it declines the efficiency and the overall performance of the device as it increases the recombination losses. The behavior of photovoltaic parameters with defect density of the 3D-MAPbI₃ layer is shown in Fig. 3. As per Fig. 3a, when defect density increases up to 10^{12} the PCE remains unchanged at 24.52%, however, when further increases the defect density, PCE starts to decline. Similar behavior can be observed in V_{oc} , J_{sc} and FF as well. To determine the impact of the defect density of the perovskite layer, the Shockley – Read – Hall (SRH) model can be used. This model portrays

the way defects within the bandgap of a semiconductor can behave as recombination centers for charge carrier pairs influencing carrier dynamics and device performance as mentioned in Eqs. (1) and (2) [18].

$$R_{SRH} = \frac{np - n_i^2}{\tau_p(n + n_i) + \tau_n(p + p_i)}, \quad (1)$$

$$\tau_{n,p} = \frac{1}{\sigma v_{th,n,p} N_t}. \quad (2)$$

Here R_{SRH} is denoted by the rate of the Shockley–Read–Hall recombination, n and p are the concentration of electron and hole respectively. τ_p , τ_n are the lifetime of electron and hole. $v_{th,n,p}$ are the thermal velocities of electrons and holes, respectively. With relatively low defect density levels, the recombination rate (R_{SRH}) is small. Therefore, the majority of the photo-generated carriers can be effectively collected by the electrodes before recombination [14]. Hence, up to a certain defect density value,

the device performance remains unaffected. However, at moderate and higher defect density levels the trap states become significant, and the performance starts to decline. As per equation 2, defect density (N_t) is inversely proportional to the lifetime of the electron and hole. When increasing the defect density, the non-radiative recombination enhances and thereby reduces the overall performance of the device [13].

The I-V characteristics of the proposed device after optimizing the thickness and the defect density of 3D-MAPbI₃ absorber layer is depicted in Fig. 4. In the same graph, IV curves MAPbI₃ based solar cells without the capping layer for the same device architecture is also included. The two curves are identical. In this study, a thin capping layer was incorporated so that it does not have a substantial impact on bulk properties of solar cells such as charge transport and light absorption. Therefore, incorporating 2D capping layer has a limited effect on overall performance.

The effect of the other parameters such as interface defect densities, recombination rates, series, shunt resistance and light intensities can

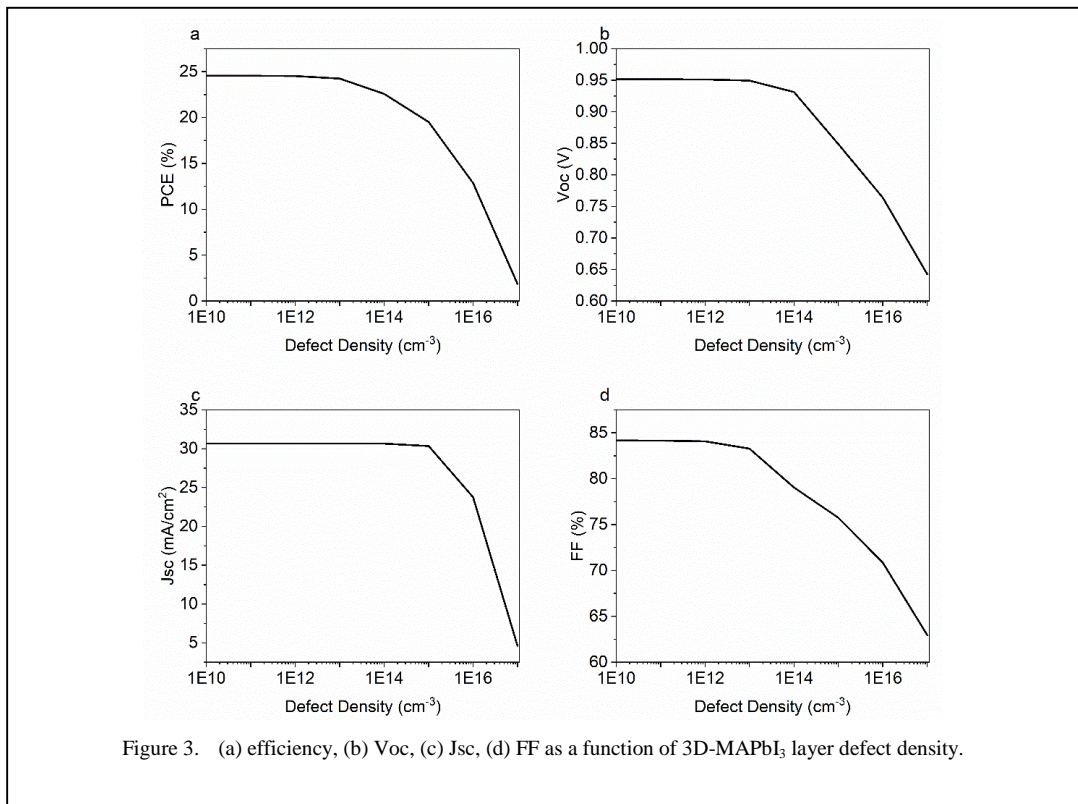


Figure 3. (a) efficiency, (b) Voc, (c) Jsc, (d) FF as a function of 3D-MAPbI₃ layer defect density.

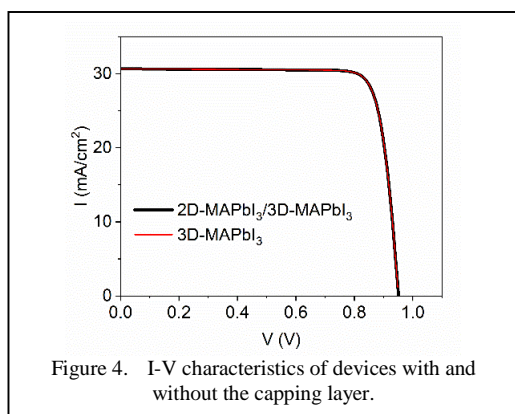


Figure 4. I-V characteristics of devices with and without the capping layer.

be comprehensively analyzed to further optimization for the device. In addition to that, by changing the number of layers in 2D-MAPbI₃, the overall efficiency of the hybrid device can be enhanced as increasing the number of layers results in lower bandgap and enhanced carrier mobilities [12]. Further, the literature suggests that performance and stability enhancement of these 2D/3D mixed dimensional PSCs can be achieved by changing the composition by substituting different organic spacer cations [20,21].

The previous research studies have shown that 2D perovskite exhibits enhanced thermal and moisture stability compared to their 3D counterparts. Furthermore, several studies have demonstrated that incorporating 2D capping layers on 3D perovskite materials can enhance the stability of the 3D perovskite without compromising the performance. Therefore, the proposed 2D-MAPbI₃ capping layer is expected to enhance the stability of 3D MAPbI₃-based hybrid cell by providing additional resistance to environmental degradation. However, a comprehensive investigation of stability enhancements through experimental validation would be beneficial. Based on the findings of this numerical study, future experiment studies can be built to confirm the stability of enhancement afforded by 2D-MAPbI₃.

IV. CONCLUSION

In this research, the 2D/3D mixed dimensional solar with device architecture of Au/Cu₂O/2D-MAPbI₃/3D-MAPbI₃/TiO₂/FTO was numerically simulated using SCAPS-1D software. The 2D-MAPbI₃ layer is capped on top of the 3D-MAPbI₃ layer to boost the long-term operational stability of 3D perovskite. The performance of the PSC was optimized by

varying the thickness and the defect density of the 3D-MAPbI₃ layer. At the optimum thickness of 1 μm and defect density range of 10¹⁰-10¹² cm⁻³, the proposed device achieved a PCE of 24.52%. This study offers valuable insight into the designing and optimization of 2D/3D mixed dimensional PSCs with balanced efficiency and long-term stability. Ultimately, it enables laboratory-scale fabrication of PSCs with minimal effort and cost-effective manner.

ACKNOWLEDGMENT

The authors sincerely recognize Prof. Marc Burgelman and his team at the University of Gent, Belgium, for creating, maintaining and freely distributing the SCAPS-1D software, which was essential in performing the solar cell simulations in this research.

REFERENCES

- [1] Abedini-Ahangarkola, H., Soleimani-Amiri, S., & Gholami Rudi, S. (2022). Modeling and numerical simulation of high-efficiency perovskite solar cell with three active layers. *Solar Energy*, 236(February), 724–732
- [2] Rathore, N., Panwar, N. L., Yettou, F., & Gama, A. (2021). A comprehensive review of different types of solar photovoltaic cells and their applications. *International Journal of Ambient Energy*, 42(10), 1200–1217.
- [3] Mahmud, M. A., et al. (2022). Origin of efficiency and stability enhancement in high-performing mixed dimensional 2D-3D perovskite solar cells: A review. *Advanced Functional Materials*, 32(3), 1–26.
- [4] Wang, R., Mujahid, M., Duan, Y., Wang, Z. K., Xue, J., & Yang, Y. (2019). A review of perovskite solar cell stability. *Advanced Functional Materials*, 29(47), 1–25.
- [5] National Renewable Energy Laboratory. (2024). No title. <https://www.nrel.gov/pv/cell-efficiency.html>.
- [6] Yu, Y., Xia, J., & Liang, Y. (2022). Basic understanding of perovskite solar cells and passivation mechanism. *AIP Advances*, 12(5).
- [7] Meng, L., You, J., & Yang, Y. (2018). Addressing the stability issue of perovskite solar cells for commercial applications. *Nature Communications*, 9(1), 1–4.
- [8] Ahmad, S., & Guo, X. (2018). Rapid development in two-dimensional layered perovskite materials and their application in solar cells. *Chinese Chemical Letters*, 29(5), 657–663.
- [9] Kim, E. B., Akhtar, M. S., Shin, H. S., Ameen, S., & Nazeeruddin, M. K. (2021). A review on two-dimensional (2D) and 2D-3D multidimensional perovskite solar cells: Perovskites structures, stability, and photovoltaic performances. *Journal of Photochemistry and Photobiology C: Photochemistry Reviews*, 48(January).
- [10] Yang, J.-H., Yuan, Q., & Yakobson, B. I. (2016). Chemical trends of electronic properties of two-dimensional halide perovskites and their potential applications for electronics and optoelectronics.

- Journal of Physical Chemistry C*, 120(43), 24682–24687.
- [11] Zhang, W., et al. (2023). Enhanced stability of carbon-based perovskite solar cells by using n-butylamine to assemble 2D capping layer. *Organic Electronics*, 115, 106757.
- [12] Kumavat, S. R., Sachdeva, G., Sonvane, Y., & Gupta, S. K. (2022). Structural and compositional properties of 2D CH₃NH₃PbI₃ hybrid halide perovskite: A DFT study. *RSC Advances*, 12(40), 25924–2593.
- [13] Adihetty, N. L., Ratnasinghe, D. R., Attygalle, M. L., Narayan, S., & Jha, P. K. (2021, July). The Effect of Deep Defects on the Efficiency Variation of CH₃NH₃PbI₃ Perovskite Solar Cells. In *2021 Moratuwa Engineering Research Conference (MERCOn)* (pp. 659-663). IEEE.
- [14] Son, C., Son, H., & Jeong, B.-S. (2024). Enhanced conversion efficiency in MAPbI₃ perovskite solar cells through parameters optimization via SCAPS-1D simulation. *Applied Sciences*, 14(6), 239.
- [15] Ou, M., et al. (2024). Dion-Jacobson perovskite solar cells: Further optimize the performance by SCAPS-1D simulation techniques. *Materials Today Communications*, 39(2103), 108955.
- [16] Raoui, Y., et al. (2019). Performance analysis of MAPbI₃-based perovskite solar cells employing diverse charge selective contacts: Simulation study. *Solar Energy*, 193, 948–955.
- [17] Chakrabarty, J., Islam, M. A., & Reza, S. (2021). Performance analysis of highly efficient 2D/3D bilayer inverted perovskite solar cells. *Solar Energy*, 230(October), 195–207.
- [18] Chaurasia, S., et al. (2024). Highly efficient and stable Dion–Jacobson(DJ) 2D-3D perovskite solar cells with 26% conversion efficiency: A SCAPS-1D study. *Journal of Physics and Chemistry of Solids*, 191(January), 11203.
- [19] Chen, M., et al. (2020). Enhanced efficiency and stability of perovskite solar cells by 2D perovskite vapor-assisted interface optimization. *Journal of Energy Chemistry*, 45, 103–109.
- [20] Choi, H.-S., & Kim, H.-S. (2020). 3D/2D bilayered perovskite solar cells with enhanced stability and performance. *Materials (Basel)*, 13(17).
- [21] Grancini, G., et al. (2017). One-year stable perovskite solar cells by 2D/3D interface engineering. *Nature Communications*, 8, 15684.

Influence of Different Recommendations for Walls Pressure Coefficients in a Pavilion under Natural Ventilation

Paulo Cesar Mioralli¹, Ricardo Nunes Pereira Junior², Elson Avallone³

^{1,2,3}Federal Institute of São Paulo - IFSP, Catanduva-SP, Brazil

¹mioralli@ifsp.edu.br, ²junior.nunes@aluno.ifsp.edu.br, ³elson.avallone@ifsp.edu.br

Abstract—Natural ventilation by the combined action of winds and the chimney effect in pavilions constitutes an important mechanism for air renewal. In this context, this study computationally compares air flow rates in a pavilion using different recommendations from the literature for the values of external pressure coefficients on the walls, with the flows driven by the action of winds and the chimney effect. Computational simulations, based on a theoretical mathematical model of flow, were conducted considering changes in the area of the pavilion's air openings and changes in the height between the air inlet and outlet openings. The normative methods NBR 6123 (1988), British Standards (1991), Liddament (1986), Lamberts (2014) and Swami and Chandra (1987) were used to obtain the pressure coefficients on the walls. These parameters may be different among these sources and, consequently, imply in disparate flow rate values obtained by the same model. The results showed, using the tested normative methods, that changes in the area of the pavilion's air inlet and outlet openings have a more significant impact on natural ventilation than changes in the height between them. It was also observed that, with the change in these parameters, the Swami and Chandra (1987) method overestimates the flow rate values when compared to the others, while the British Standards (1991) method underestimates them.

Keywords - thermal comfort, natural convection, building, computational analysis

I. INTRODUCTION

Natural ventilation is a fundamental component in promoting thermal comfort and indoor air quality in buildings, which can occur jointly through the mechanisms of wind action and the chimney effect. The action of wind is a process in which the difference in pressure between the faces of a building, due to the incidence of wind, causes air to move through strategic openings. The chimney effect is a phenomenon that occurs due to the difference of density between hot air and cold air, promoting the upward movement of hot air and the entry of fresh air at the base of the building.

To obtain the air flow rate in natural ventilation in buildings, theoretical models that consider external pressure coefficients on the walls can be used. These coefficients, which depend on the direction of the wind and geometric data of the building, are recommended by different sources in the literature [1-5]. Significant differences in the calculation of air flow rate can be found when obtained by the same theoretical model, depending on the source chosen.

Theoretical models for analyzing air flow rate by natural convection in buildings have been developed by researchers over the years [6-19]. However, users of these models usually adopt one of the recommendations for pressure coefficients to calculate air flow rate in their analyses, knowing in advance that different results could be obtained if another



recommendation were used. The recommendation used by the user is often the one adopted or prescribed by regulatory standards in their country or location.

The estimation of values for pressure coefficients in building walls is usually performed empirically through experiments, which explains the difference in results among existing recommendations. Thus, the comparative analysis of the use of different pressure coefficients available in the literature is crucial to understand the level of disparity in the air flow rate results obtained by the models. In this work, a theoretical model of natural ventilation by the joint action of winds and the chimney effect available in the literature is used [16]. The air flow rate is obtained in a pavilion using different recommendations for the values of the external pressure coefficients on the windward and leeward walls of the building. The flow rate results are compared between the different cases considering the change in two parameters that influence the natural convection process: the area of the air inlet and outlet openings and the height between them.

II. NATURAL VENTILATION IN A PAVILION

In natural ventilation in a pavilion, air moves through openings, some functioning as inlets and others as outlets [20]. This air movement can occur through the following mechanisms: by the action of winds; by the difference in density of internal and external air (a mechanism known as the chimney effect) or; by the mechanisms of wind action and chimney effect simultaneously.

Considering natural ventilation exclusively by the action of winds, the walls of the pavilion exposed to the wind will be subject to positive pressures (overpressures), while the walls not exposed to the wind and the upper horizontal surface of the building will be subject to negative pressures (underpressures) [20]. Thus, ventilation conditions in the pavilion can occur through openings in the walls subject to positive pressures (air inlet) and in the walls subject to negative pressures (air outlet). The pressure exerted on the pavilion wall depends on the wind speed and its angle of incidence. Fig. 1 illustrates a pavilion exposed to the action of winds in an open field, with air inlet and outlet openings. The indications *A, B, C* and *D* are the walls of the pavilion and θ is the angle of incidence of the wind. The parameters *L, W* and *H* are, respectively, the length, width and height of the

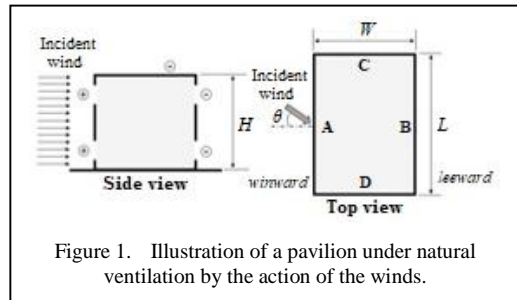
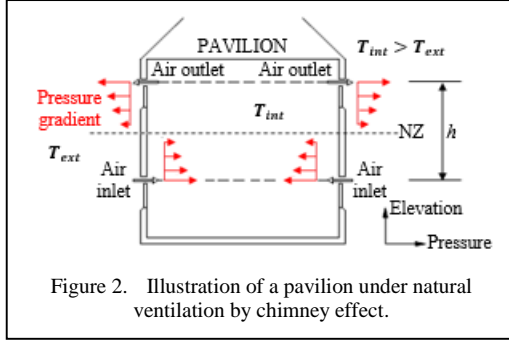


Figure 1. Illustration of a pavilion under natural ventilation by the action of the winds.

pavilion. The region of the pavilion in which the wind is incident is called windward and the region opposite to that where the wind blows is called leeward.

In natural ventilation exclusively by the chimney effect, the origin of the difference in density of the internal and external air is the difference in temperature between these two environments. The difference in density causes pressure gradients in the internal and external regions of the building. Ventilation inside the building occurs by the displacement of the air mass from the zone of higher pressure (lower temperature) to the zone of lower pressure (higher temperature) [21]. Fig. 2 illustrates the pressure difference in these regions, assuming a room with vertical openings in its lower and upper parts for air entry and exit, considering the internal temperature, T_{int} , higher than the external temperature, T_{ext} . The parameter h represents the difference in elevation between the centers of the openings. If the internal temperature is higher than the external temperature, the external air (colder) enters the room through the openings positioned closer to the ground, while the internal air (hotter) leaves the room through the openings located closer to the roof. If the internal temperature is lower than the external temperature, a reverse flow will occur. Fig. 2 shows the existence of a line at a certain height, called the neutral zone (NZ), in which the difference between internal and external pressure is zero. The presence of an opening at this height does not produce either air inlet or outlet. The elevation of the neutral zone is a function of the distribution and characteristics of the openings.

Whether by the chimney effect, by the action of the winds or by the simultaneity of these mechanisms, the air flow rate through natural ventilation inside a pavilion can be obtained through theoretical mathematical models developed by researchers [22], which require

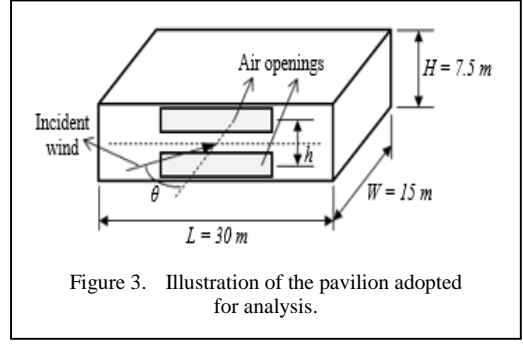


knowledge of the difference between the external pressure coefficients on the windward and leeward walls of the building. These coefficients are generally obtained empirically and define what portion of the kinetic energy of the wind is transformed into pressure energy on the vertical surfaces of the pavilion [23]. Recommendations for their values are found in the literature.

III. PROCEDURE AND METHODOLOGY

The natural convection analysis was conducted considering a small industrial pavilion with a parallelepiped shape, as illustrated in Fig. 3. The air inlet and outlet openings are positioned on opposite walls (on the walls that indicate the length L of the pavilion), with two openings per wall. The openings are considered to have equal areas and are positioned at the same height. The building will be considered to be isolated in an open field.

For natural ventilation by wind action and chimney effect simultaneously, considering steady-state flow and identical air inlet and outlet openings, [16] proposes two independent models for obtaining air flow rate, that is, an exclusive model for obtaining flow rate by wind action and another exclusive for calculating flow rate by chimney effect. Equation (1) corresponds to the model of [16] for calculating air flow rate in natural ventilation by wind action, Q_w (m^3/s), in a building. Equation (2) refers to the model for obtaining air flow rate by chimney effect, Q_c (m^3/s). Equation (3) corresponds to the total air flow rate, Q_T (m^3/s), which computes the action of winds and the chimney effect simultaneously. In Eq. (1), A is the area of the air inlet or outlet opening (m^2), considered equal, V is the average wind speed (m/s) on the windward side and the parameters c_{pe} and c_{ps} are the external pressure coefficients (dimensionless) on the windward side (at the air inlet) and on the leeward side (at



the air outlet), respectively. For the parameter K , [20] recommend $K = 0.6$. In Eq. (2), A is the area of the air inlet or outlet opening (m^2), taken as the smallest in the case of different areas, h is the vertical distance between the centers of the air inlet and outlet openings (m) and $\Delta T(K)$ is the difference between the temperatures of the air leaving and entering the pavilion. The coefficient K_0 is given by $K_0 = 0.139$ for equal air inlet and outlet areas.

$$Q_w = \frac{KAV}{\sqrt{2}} \sqrt{(c_{pe} - c_{ps})}, \quad (1)$$

$$Q_c = K_0 A \sqrt{h \Delta T}, \quad (2)$$

$$Q_T = \sqrt{Q_w^2 + Q_c^2}. \quad (3)$$

The external pressure coefficients, c_{pe} and c_{ps} , are established primarily based on the geometric dimensions of the pavilion and the incidence angle of the wind. These coefficients are also subject to changes resulting from the presence of bulkheads. Their values were obtained from five recommendations in the literature [1-5]: Brazilian standard NBR 6123 (1988); English standard British Standards Institution (1991); Liddament (1986); Lamberts, Dutra and Pereira (2014) and; Swami and Chandra (1987). Table I shows how to obtain the pressure coefficients for each recommendation and their respective values obtained for the pavilion analyzed in this work.

A computational code in *Python* programming language was written to compute Eqs. (1), (2) and (3) necessary for analyzing natural ventilation by wind action and by chimney effect simultaneously, considering the different recommendations in the literature

TABLE I. EXTERNAL PRESSURE COEFFICIENTS.

Recommendation	Method of obtaining	Values
NBR 6123 (1988)	From table	$c_{pe} = 0.7;$ $c_{ps} = -0.5$
British Standards (1991)	From table	$c_{pe} = 0.7;$ $c_{ps} = -0.25$
Liddament (1986)	From table	$c_{pe} = 0.5;$ $c_{ps} = -0.7$
Lamberts, Dutra and Pereira (2014)	From equation	$(c_{pe} - c_{ps}) = 1.2$
Swami and Chandra (1987)*	From equation	$c_{pe} = 1.2;$ $c_{ps} = -0.7$

*With the equation of Swami and Chandra (1987) it is possible to obtain only c_{pe} . For this case, the value of c_{ps} was considered to be the same as that of Liddament (1986).

TABLE II. SIMULATED CASES IN THE COMPUTER PROGRAM.

CASES	$\Delta T(^{\circ}C)$	$V(m^3/s)$	$\theta(^{\circ})$
- Changing the area of openings: $10 \leq A \leq 150m^2$ - Fixed height between openings: $h = 3m$	4	1.994	0
- Changing the height between openings: $0.5 \leq h \leq 5m$ - Fixed area of openings: $A = 70m^2$			

adopted for the pressure coefficients. For each recommendation, the total air flow rate was calculated considering two different cases, shown in Table II, in which the prescription of the values of the area of the air inlet and outlet openings, and also of the elevation difference measurements between them, was based on the geometric dimensions of the pavilion. Each of the cases in Table II was simulated for each of the recommendations presented in Table I, implying different values of the pressure coefficients among the simulations.

IV. RESULTS AND DISCUSSION

Using the computer program, with the data set obtained and duly tabulated for the two cases in Table II simulated for the five literature recommendations for pressure coefficients, a comparative analysis of the results was

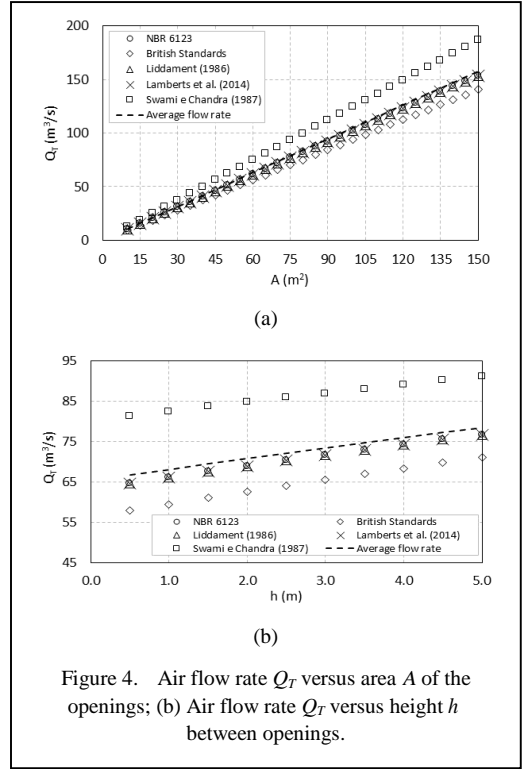


Figure 4. Air flow rate Q_T versus area A of the openings; (b) Air flow rate Q_T versus height h between openings.

performed. Figs. 4(a) and 4(b) show, respectively, the total air flow rate as a function of the area A of the openings and the height h between them, for the five pressure coefficient recommendations. In both graphs, all methods exhibit a linear trend, where the air flow rate increases with A and h . However, there are variations in the slope of the lines, indicating different rates of increase in the air flow rate. The dashed line represents the average flow rate value obtained among the five methods for each fixed value of A and h . It is noted that, in both figures, the [2] recommendation is the one that presents the highest air flow rate and the only one with flow rate values higher than the average values. It is also the recommendation whose flow rate values are most distant from the values obtained by the other recommendations. The recommendations of [1,4,5] present equal flow rate results as A and h vary, which is explained by the fact that these methods have the same difference value $(c_{pe} - c_{ps}) = 1.2$. The recommendation of [3] is the most conservative, presenting the lowest flow rate values. These differences highlight how the choice of method can influence the results in the calculation of natural ventilation.

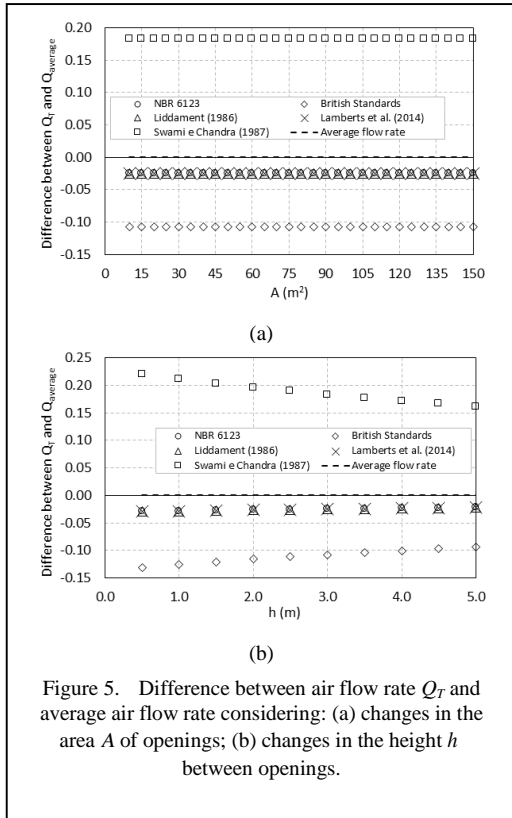


Figure 5. Difference between air flow rate Q_T and average air flow rate considering: (a) changes in the area A of openings; (b) changes in the height h between openings.

Figs. 5(a) and 5(b) show, respectively, the relative difference between the flow rate values obtained by each literature recommendation and the average flow rate value for each fixed value of A and h , taking the average flow rate as reference for the calculation. Both graphs show that the recommendations that differ most from the average values are [2,3], with the highest differences close to 20% and 12% respectively. Another characteristic is that the differences between the average flow rate and the total flow rate obtained for all methods do not change with the variation of the area A in Fig. 5(a). This is because the area A is present in Eqs. (1) and (2), for Q_w and Q_c , which make up the calculation of the total flow Q_T , acting as a multiplying parameter that keeps constant the difference between Q_T and the average flow rate. This is different in Fig. 5(b) where there are changes in the relative difference values as h varies, since this parameter only appears in the calculation of the chimney effect. In this case, the largest differences correspond to the smallest values of h .

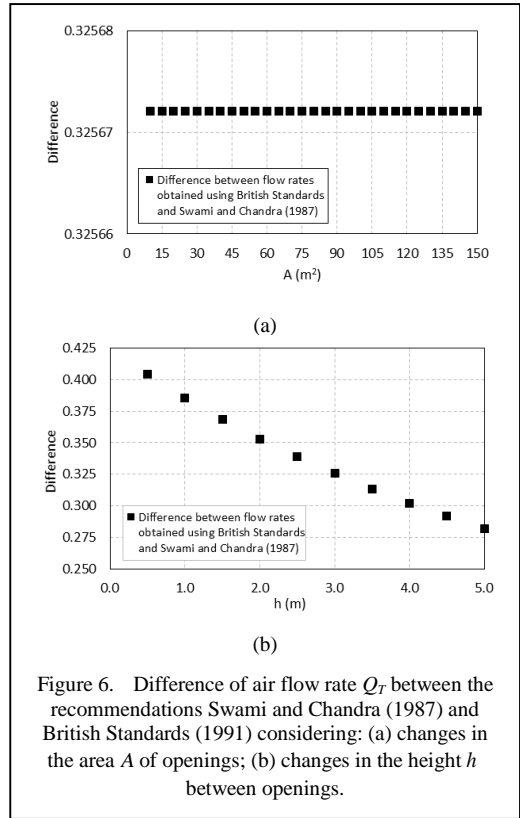


Figure 6. Difference of air flow rate Q_T between the recommendations Swami and Chandra (1987) and British Standards (1991) considering: (a) changes in the area A of openings; (b) changes in the height h between openings.

The recommendations of [2,3] are those that present the highest difference in results between them. Figs. 6(a) and 6(b) show, respectively, a comparison between the total flow rate values obtained by these methods as a function of the A and h . In Fig. 6(a), considering changes in the area A of the openings, the difference between the flow rate values is constant, around 32%, for any area value. In this case, the constant difference is explained by the act that the area A constitutes a multiplying parameter in the value of the flow rates Q_w and Q_c and, consequently, Q_T . In Fig. 6(b) it can be seen that the difference between the flow rate values reaches 40% for small values of h and around 27% for the highest values of h simulated, showing to be significant.

V. CONCLUSIONS

For all tested recommendations for pressure coefficients, changing the area of the pavilion's air inlet and outlet openings has a more significant impact on natural ventilation than changing the height between them. This is because increasing the area provides more space for air flow rate, favoring both wind ventilation and the chimney effect.

Observing the behavior of the parameters A and h as influencers of natural convection, it can be seen that to maximize the efficiency of this mechanism, the area of the openings should be prioritized. However, the height between the openings is not insignificant, influencing the process moderately.

The choice of the recommendation also plays an important role, with [2], providing more optimistic predictions and [3], presenting a more conservative approach. It was found that the [2] method overestimated the average flow rate values when compared to the others, while the [3] method underestimated them. Furthermore, significant differences were found between the flow rate values obtained by these two methods.

Finally, it is worth noting that the external pressure coefficients are influenced by the geometric dimensions of the pavilion, the angle of incidence of the wind and the presence of bulkheads in the wind path. Therefore, the results of this study cannot be generalized to other building or pavilion configurations with geometric dimensions and angles of incidence of the wind different from those observed in the pavilion analyzed. Additionally, climate changes involving different wind speeds and temperature variations do not change the values of the pressure coefficients, but they interfere in the calculation of the air flow rate predicted by theoretical models of natural ventilation that take into account the action of winds and the chimney effect simultaneously in buildings.




ACKNOWLEDGMENT

To the PIBIFSP/IFSP program for the support.

REFERENCES

- [1] Liddament, M. W. (1986). *Air infiltration calculation techniques: an applications guide*. The Air Infiltration and Ventilation Centre. Bracknell, England: Oscar Faber Partnership.
- [2] Swami, M. V., & Chandra, S. (1987). Procedures for calculating natural ventilation airflow rates in buildings. *ASHRAE Research Project 448-RP*, Final report FSEC-CR-163-86.
- [3] British Standards Institution (1991). *Code of practice for design of buildings: ventilation principles and designing for natural ventilation*. London: BS 5925.
- [4] Brazilian Association of Technical Standards (1998). *ABNT NBR 6123: Forces due to wind in buildings*. Rio de Janeiro: ABNT.
- [5] Lamberts, R., Dutra, L., & Pereira, F. O. R. (2014). *Energy efficiency in architecture* (3rd ed.). Rio de Janeiro: Eletrobras/Procel.
- [6] Emswiler, J. E. (1926). The neutral zone in ventilation. *Journal of the American Society of Heating and Ventilation Engineers*, 32(1), 1-16.
- [7] Randall, W. C., & Conover, E. W. (1931). Predetermining the airtightness of industrial buildings. *ASHVE Transactions*, 37, 605-618.
- [8] Centre Scientifique et Technique du Batiment (C.S.T.B.). (1958). *Hygrothermique et ventilation - R.E.E.F.* 58. Paris: D5.
- [9] Toledo, E. (1967). *Natural ventilation of buildings*. Lisbon: National Civil Engineering Laboratory.
- [10] Van Straaten, J. F. (1967). *Thermal performance of buildings*. Elsevier Pub. Co.
- [11] Jorgensen, R. (Ed.). (1970). *Fan engineering - an engineer's handbook* (7th ed.). Buffalo Forge Company.
- [12] Baturin, V. V. (1976). *Fundamentals of industrial ventilation*. New York: Pergamon Press.
- [13] Daly, B. B. (1978). *Woods practical guide to fan engineering* (3rd ed.). Woods of Colchester Limited.
- [14] Costa, E. C. da. (1982). *Ecological architecture: natural thermal conditioning*. Edgard Blucher.
- [15] Constance, J. D. (1986). *Simplified method for sizing gravity ventilation. Air conditioning, heating ventilation*, (n.p.).
- [16] Frota, A. B. (1989). *Ventilation of industrial buildings: parametric model for dimensioning natural ventilation systems by stack effect* (Doctoral Thesis). Faculty of Engineering and Architecture, University of São Paulo, São Paulo, Brazil.
- [17] Clezar, C. A., & Nogueira, C. R. (1999). *Industrial ventilation*. Florianópolis: UFSC.
- [18] American Society of Heating, Refrigerating and Air Conditioning Engineers. (2001). *Handbook fundamentals*. ASHRAE.
- [19] Silvani, M. (2005). *Subsídios para o projeto da ventilação natural em pavilhões industriais* (Master's Dissertation). Faculty of Engineering and Architecture, University of Passo Fundo, Passo Fundo, Brazil.
- [20] Frota, A. B., & Schiffer, S. R. (2001). *Thermal comfort manual* (5th ed.). Studio Nobel.
- [21] Toledo, A. M. (2006). *Avaliação do desempenho da ventilação natural pela ação do vento em apartamentos: uma aplicação em Maceió/AL* (Doctoral Thesis). Faculty of Civil Engineering, Federal University of Santa Catarina, Florianópolis, Brazil.
- [22] Awbi, H. B. (2003). *Ventilation of buildings* (2nd ed.). Spon Press.
- [23] Srebric, J. (2011). Ventilation performance prediction. In: Hensen, J. L. M.; Lamberts, R. (Eds.). *Building performance simulation for design and operation*. (pp. 143-179). Spon Press.

Modeling the Effects of Wall Orientations on Indoor Temperature During the Autumn Season : A Case Study of Ouled Sidi Brahim (Algeria)

Nabila Ihaddadene¹, Mohamed Chouidira², Razika Ihaddadene³

^{1,2,3}Department of Mechanical Engineering, M'Sila University, M'Sila, Algeria.

^{1,3}Water, Environment and Renewable Energies Laboratory, Med Boudiaf University, M'Sila, Algeria

¹nabila.ihaddadene@univ-msila.dz, ²mohamed.chouidira@univ-msila.dz,

³razika.ihaddadene@univ-msila.dz

Abstract—The construction sector is globally recognized for its substantial energy consumption and environmental impact. Proper orientation of buildings presents a cost-effective strategy to enhance thermal comfort for occupants while reducing energy expenditure associated with heating and cooling. This study, conducted in Ouled Sidi Brahim (Algeria), aims to assess and model the influence of wall orientation (East, West, North, and South) on the internal temperature of a small cubic brick room during the autumn season. Four temperature sensors were strategically installed at the center of each external wall face to continuously monitor their temperatures at one-minute intervals over various days throughout the study period. The indoor temperature was also recorded using the same methodology. During autumn, the temperature variation within the chamber closely aligns with that observed on the exterior surface of the north-facing wall. Furthermore, the indoor temperature of the chamber is significantly affected by the temperature of its north-facing wall (T_{North}), whereas the impact from other orientations ranges from moderate to weak. The proposed model, which employs multiple linear regression for each month of autumn, demonstrates proficiency in accurately predicting internal temperatures based on external surface temperatures of the walls.

Keywords – modelling, temperature, building, wall orientation

I. INTRODUCTION

The construction sector is known worldwide for its high-energy consumption and pollution [1,2]. Indeed, the International Energy Agency (IEA) reports that construction activities constitute 30% of global final energy consumption and 26% of global energy-related emissions [1]. Moreover, this consumed energy is utilized for various purposes, including the construction processes, air conditioning, heating, and illumination of both residential and commercial properties, in addition to powering the appliances and equipment found within these spaces.

The same situation can be found in Algeria, where the building sector consumed 18053 kTep, or 36% of the country's total energy consumption, in 2021, ahead of any other sector [3]. Furthermore, it is thought that Algerian buildings overuse of energy is mostly caused by the air conditioning and heating systems that are in place to give residents thermal comfort. As a consequence of this overuse of energy, the building sector releases a huge amount of CO₂ into the atmosphere. For instance, in 2017, greenhouse gas emissions amounted to 41487



tonnes of CO₂ equivalent [4]. The main sources of this pollution in Algeria are heating systems that burn natural gas and air conditioning units that run on conventional electricity.

Through its envelope (walls and roofs), the building continuously exchanges thermal energy with its surrounding environment. In warm periods, air conditioning units mitigate energy gains, while in cold periods; heating systems serve to offset thermal energy losses.

Enhancing the building materials' thermal properties [5], selecting an appropriate building orientation and design [6], and integrating renewable energies [7] are among the approaches being adopted in the world to overcome the problems related to buildings' energy efficiency.

Thermal comfort is greatly impacted by the building orientation [8]. A right orientation can maximize the amount of heat and light received from the sun, hence lowering the need for energy-intensive heating and cooling appliances. For instance, in the northern hemisphere, north-facing walls typically receive the smallest amounts of direct solar radiation, whereas east-facing walls benefit from the morning sun. It's important to pay attention to the dominant winds as well since they can be beneficial for natural ventilation and comfort in general. Climate, sun path, wind direction, and other elements all contribute to deciding upon the ideal building orientation.

Numerous studies have tried to explain the relationship between orientation and thermal comfort [8-10]. Reference [8] concluded that a north-south orientation is preferable to an east-west orientation for buildings constructed from compressed earth blocks in the Ouagadougou (Burkina Faso) climate conditions. Reference [9] investigated the effect of building orientation, wind speed, and direction on the overall thermal performance of building modules in Newcastle, Australia. They observed that the northern wall (windows side) of the Insulated Cavity Brick module consistently gave the most heat to the room through the window, allowing the sun to enter the building in winter and heat it while avoiding the major wind stream. Reference [10] investigated the impact of different orientations on enhancing internal air temperature and thermal comfort in mud-brick dwellings located in the hot and arid climate of Tarim City, Yemen. Based on the maximum percentage of hours spent in thermal

comfort, they concluded that the south orientation is the best. According to the study conducted by [11] in the Ghardaia region of south Algeria, the orientation of thermally isolated buildings has no considerable effect on interior temperature, particularly during the hot season. Furthermore, the south is the best orientation for residents of dry and semi-arid locations since it provides better yearly thermal comfort.

Correctly orienting the building is an inexpensive way to enhance occupant thermal comfort and save energy consumption for heating and cooling. Thus, a good building orientation allows beneficial winter radiation to enter while reducing harmful summer radiation as well as providing proper ventilation in the hot season.

The current study performed in Ouled Sidi Brahim (Algeria) intends to evaluate and model the effect of wall orientation on temperature inside a small cubic brick room throughout the autumn season without taking ventilation into account.

II. MATERIAL AND METHODS

A. Site and Study Period

The current experimental investigation was conducted in Ouled Sidi Brahim, a town in northern Algeria that has the geographic coordinates 35° 17' 49" latitude, 4° 10' 27" longitude, and 541 m elevation above sea level [12]. This location is characterized by a semi-arid climate marked by dryness and cold temperatures.

Autumn in the northern hemisphere is typically referred to as the interval from September 21 marked by the autumnal equinox, when day and night are of equal length, to December 21, the winter solstice, which is the shortest day of the year. There is a notable decline in temperature throughout autumn. The current trials were carried out over this season.

B. Experimental Chamber

In order to investigate the influence of orientation on indoor temperature, a small chamber with internal dimensions of 20×20×20 cm³ was constructed using hollow red brick, as illustrated in Fig. 1. The walls, each measuring 5 cm in thickness, are properly cemented, reflecting the construction practices commonly employed in residential buildings throughout Algeria. As seen in Fig. 1, it should be noted that

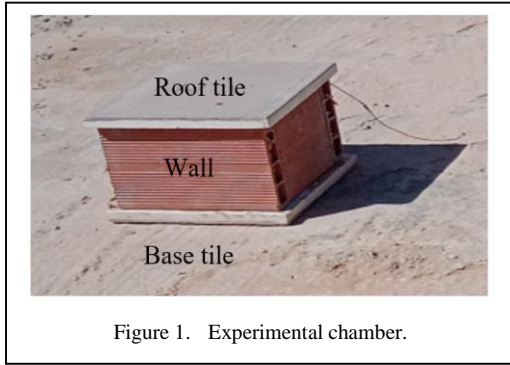


Figure 1. Experimental chamber.

the brick structure is covered by the same kind of floor tiles (slabs) that support it at ground level.

C. Digital Acquisition System

A digital tracking device, shown in Fig. 2, was designed to record the temperature for a duration of 24 hours at a time interval of one minute in the middle of the chamber and at the center of each of the four external wall faces. By the way, our earlier study [13] contains further information about the Digital Acquisition System's composition.

D. Experimental Procedure

As illustrated in Fig. 3, the constructed chamber was positioned away from any external obstacles, with its four walls oriented towards the four cardinal directions (East, West, North, and South). Four temperature sensors of the acquisition system were mounted at the center of each of the four external wall faces (Fig. 3) to constantly monitor their temperatures for a full day in one-minute increments on various days in September, October, November, and December. In the same manner, the indoor temperature was recorded also in the middle of the chamber. Moreover, the hours of sunrise and sunset were collected during the trial days.

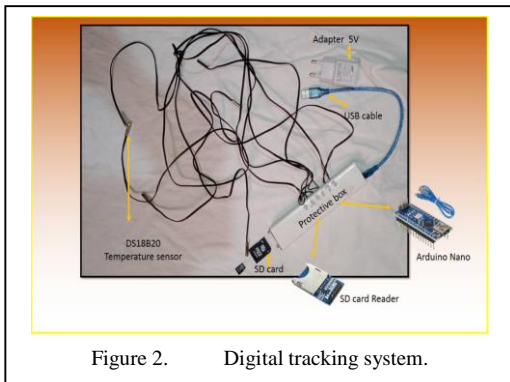


Figure 2. Digital tracking system.

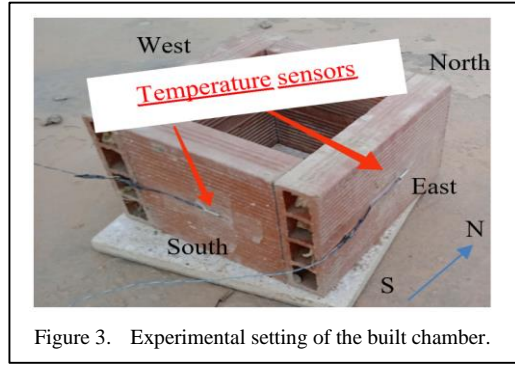


Figure 3. Experimental setting of the built chamber.

III. RESULT AND DISCUSSION

The constructed chamber measures $20 \times 20 \times 20 \text{ cm}^3$ (small-scale model), which corresponds to a scale of 1/15 of the actual size. The chosen model's dimensions remain suitable for thermal analysis, as evidenced by the findings of [14], who indicate that the model can be reduced in size to a maximum scale of 1/24.

The chamber is warmed by solar radiation that attains and heats the earth. Moreover, the sun's radiation heats the chamber's envelope first, and conduction subsequently brings this thermal energy inside the chamber. Furthermore, during the day, the incident radiation on the chamber's enclosure varies depending on the orientation and inclinations of its surfaces. In this study, we specifically focus on the vertical walls of the chamber.

Fig. 4 illustrates an example of the temperature evolution of the four outer wall faces at the end of September, which is solely a result of the radiation received by them. In fact, the walls are heated differently based on the amount of incident radiation (trapped heat). According to most research [8,15], the north-facing wall in the northern hemisphere gets the least amount of solar energy, which explains why it has the lowest measured temperature when compared to the other orientations as shown in Fig. 4. On the other hand, the south-facing wall gets the maximum solar radiation during the winter and autumn seasons when the sun is low in the sky [15]. This observation justifies the highest temperature recorded on the south wall's outer face at the end of September. As reported by [16] and illustrated in Fig. 4, solar radiation hits the eastern wall during the morning and the western wall in the afternoon.

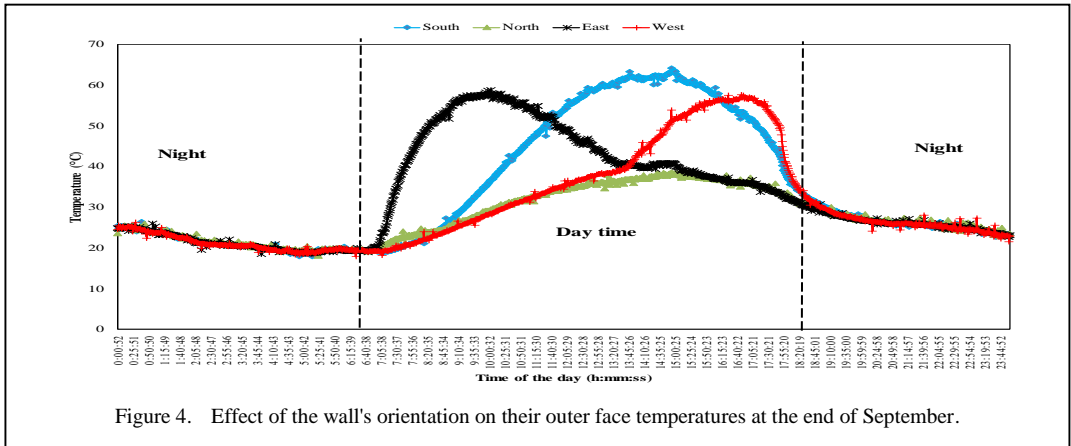


Figure 4. Effect of the wall's orientation on their outer face temperatures at the end of September.

Once again, the results found on the reduced model are reasonable and consistent with those reported in the literature pertaining to full-scale studies, thereby affirming the validity of our research.

A building's orientation is determined by the direction of its longest axis. For instance, if the longest sides are oriented towards the north and south, the building is classified as north-south oriented. However, in our case, the cubic chamber has no specific orientation, despite the fact that these walls are oriented towards the four cardinal points.

Fig. 5 illustrates a comparison of the temperatures recorded within the chamber and on the external faces of each of its four walls at the end of September. As can be observed, the curve representing the temperature evolution within the chamber most closely approximates the one found on the north-facing wall's outer surface. Indeed, the highest temperatures observed within the chamber and on the external surface of its north-facing wall were 42.9 °C and 38.6 °C, respectively, while the lowest recorded temperatures were 18.8 °C and 18 °C, respectively. Additionally, it is noteworthy that there was no time lag; these extreme values

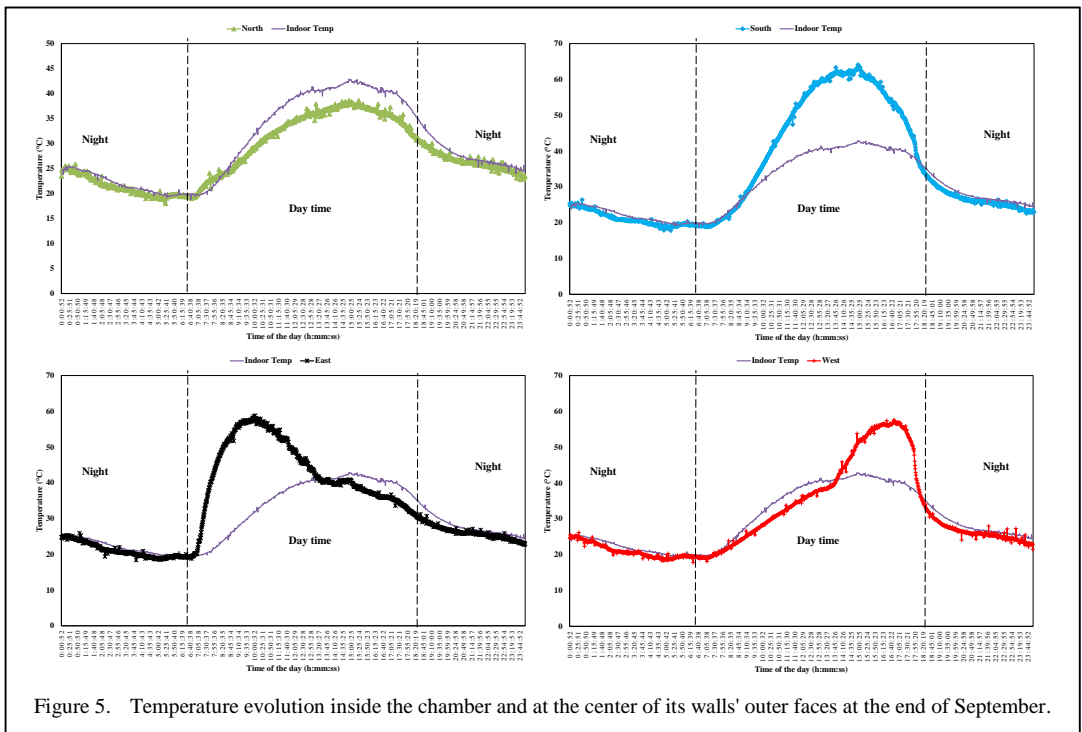


Figure 5. Temperature evolution inside the chamber and at the center of its walls' outer faces at the end of September.

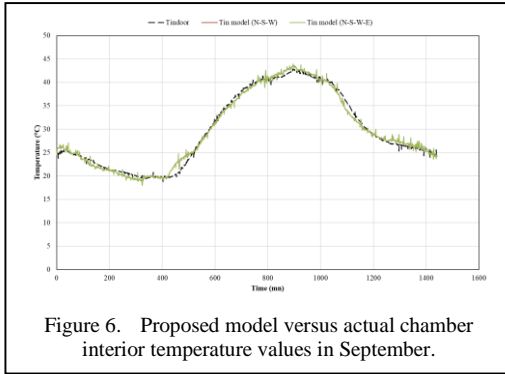


Figure 6. Proposed model versus actual chamber interior temperature values in September.

occurred almost concurrently. In relation to the other orientations, it is observed that the temperature of the outer surface of the wall facing east exhibits a distinct variation compared to the temperature recorded within the chamber during morning hours. Conversely, for the west orientation, a clear difference is noted in the afternoon. The temperature profiles for both the inside of the chamber and the outer surface of the wall facing south display similar trends; however, it is important to note that the outer surface generally maintains a higher temperature than that of the inside, particularly during daylight hours, where discrepancies can reach up to 21 °C. The relationship between the temperature inside the chamber T_{in} and the

temperature of its four walls' outer surfaces was ascertained using a statistical approach called multiple linear regression. The following model is then proposed:

$$T_{in} = -3.42 + 0.054T_{South} + 1.109T_{North} + 0.022T_{West} - 0.003T_{East} \quad (1)$$

As seen, the indoor temperature of the chamber is strongly influenced by the temperature of its north-facing wall (T_{North}), moderately by the temperature of its south (T_{South}) and west (T_{West}) walls, while the east wall has a little impact on the inside temperature in September. Furthermore, this statistical analysis confirms the results shown in Figs. 5 and 6. When combined, the walls in the four orientations account for 98.9% of the variance in the inside temperature of the chamber ($R^2 = 0.982$). This suggests an excellent fit of the model to the data, as shown in Fig. 6.

The temperatures within the chamber and on the outside surfaces of each of its four walls in October are compared in Fig. 7. Most observations regarding the temperature curves in various orientations relative to the temperature curve inside the chamber in September remain

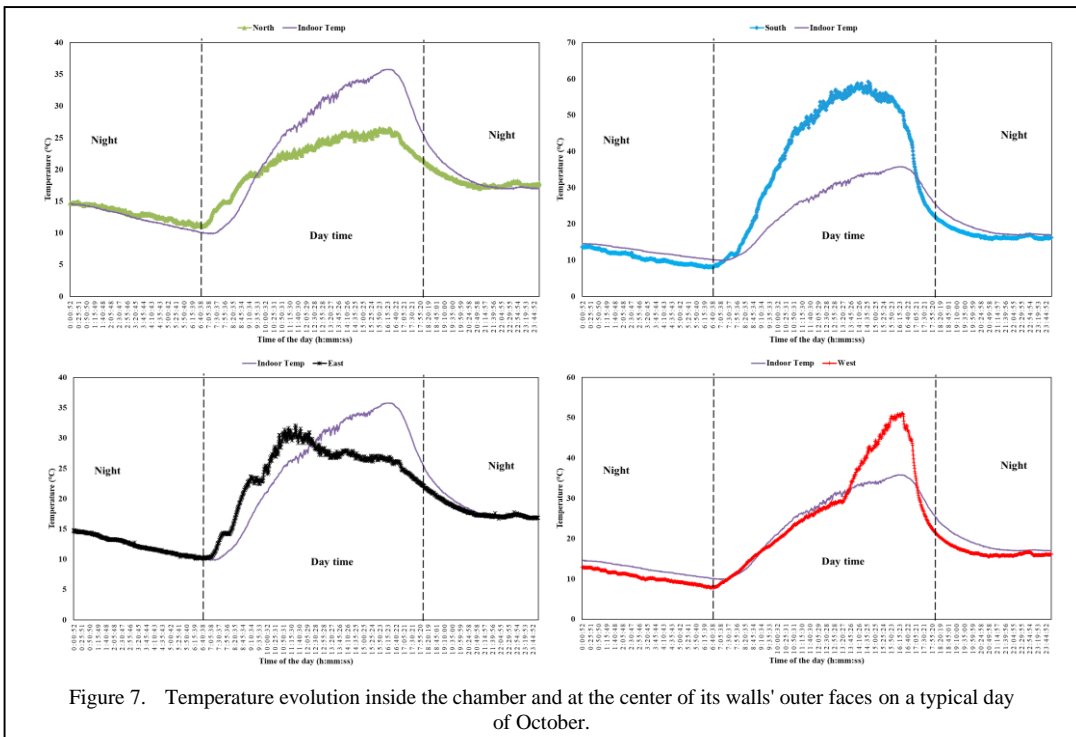


Figure 7. Temperature evolution inside the chamber and at the center of its walls' outer faces on a typical day of October.

relevant for October. The following model was used to determine the relationship between the temperature inside the chamber (T_{in}) and the temperature of the outer surfaces of its four walls on a typical day of October:

$$T_{in} = -6.00 + 0.06T_{South} + 1.35T_{North} + 0.20T_{West} - 0.21T_{East} \quad (2)$$

As observed, the indoor temperature of the chamber is strongly influenced by the temperature of its north-facing wall (T_{North}) and moderately by the temperatures of its west (T_{West}), and east (T_{east}) walls, even though the latter has a negative effect on the indoor chamber temperature in October. Moreover, its south wall, however, has less impact-full effect compared to the remaining orientations. The walls oriented in the four cardinal directions collectively explain 97.2% of the variance in the chamber internal temperature ($R^2 = 0.972$). This suggests a very strong model-data fit, as seen in Fig. 8. Considering the excellent correlation observed between the model and the measured data (Fig. 8), it can be concluded that the proposed model is capable of reliably predicting

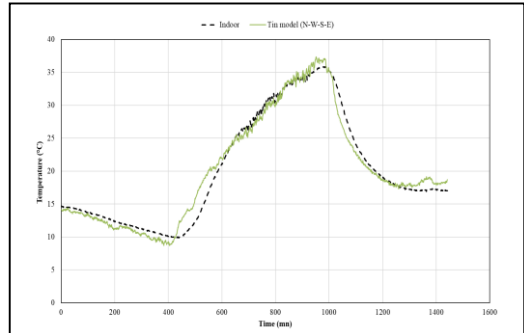


Figure 8. Proposed model versus actual chamber interior temperature values on a typical day of October.

the temperature within the chamber based on the external surface temperatures of its walls.

The majority of observations concerning the temperature profiles in different orientations, in relation to the temperature curve observed inside the chamber in September, continue to be applicable for November and December, as shown in Figs. 9 and 10, respectively. Moreover, when compared to the exterior surfaces of the walls facing east, west, and south, the temperature variation within the room is more stable in November. The relationship between

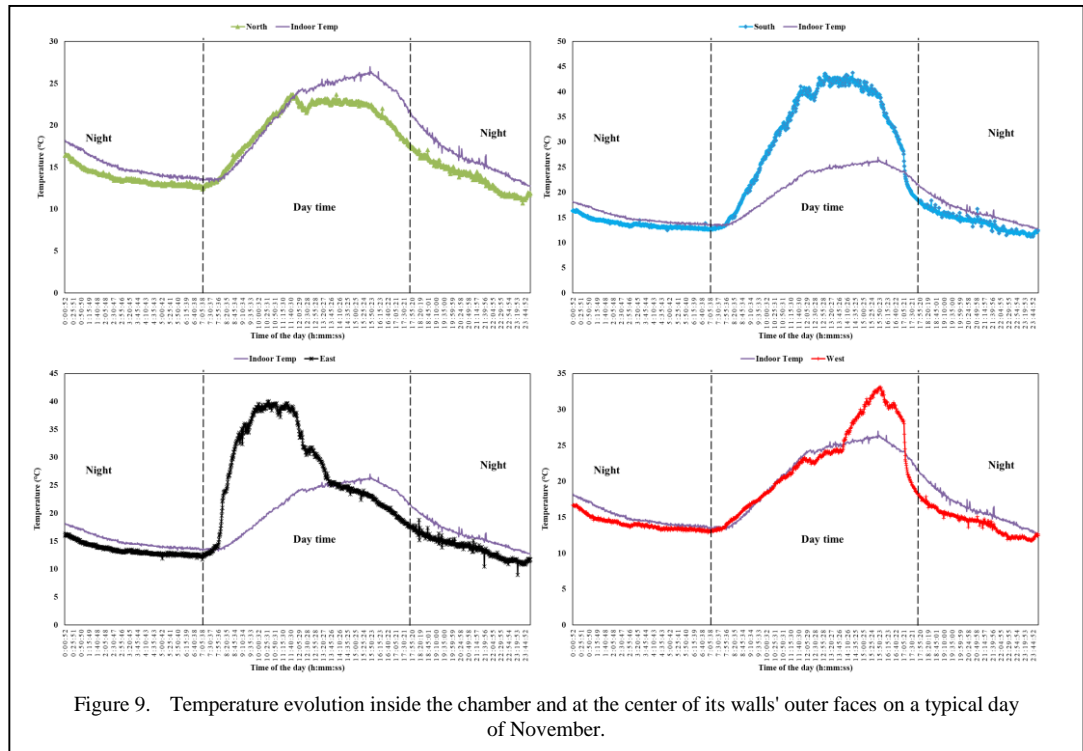


Figure 9. Temperature evolution inside the chamber and at the center of its walls' outer faces on a typical day of November.

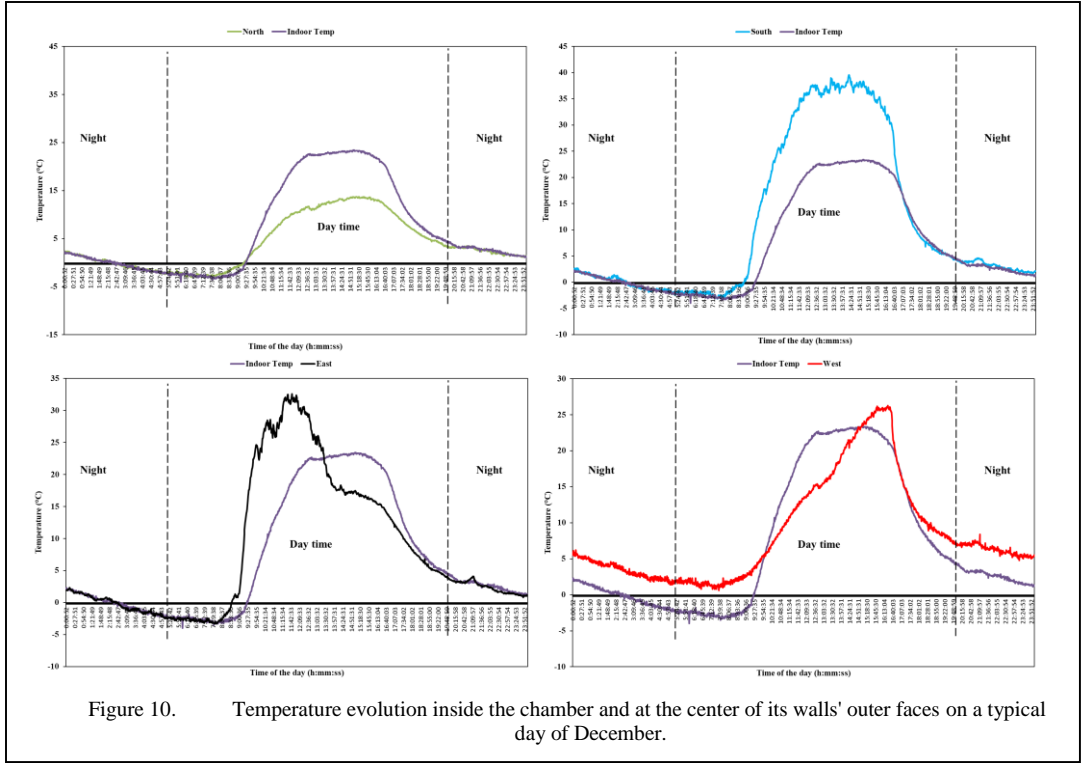


Figure 10. Temperature evolution inside the chamber and at the center of its walls' outer faces on a typical day of December.

the temperature inside the chamber T_{in} and the temperature of its four walls' outer faces was determined using the following model:

$$T_{in} = -3.08 - 0.10T_{South} + 1.5T_{North} + 0.13T_{West} - 0.19T_{East} \quad (3)$$

As observed, the indoor temperature of the chamber is strongly influenced by the temperature of its north-facing wall (T_{North}), moderately by the temperature of its west wall

(T_{West}), and weakly by the temperatures of its south (T_{South}), and east (T_{East}) walls.

The walls aligned with the four cardinal directions account for 97.8% of the variance in the internal temperature of the chamber ($R^2 = 0.978$). This indicates a highly robust fit between the model and the data, as illustrated in Fig. 11. It can be inferred that the proposed model is proficient in accurately forecasting the temperature within the chamber based on the external surface temperatures of its walls.

Again, when compared to the exterior surfaces of the walls facing east, west, and south, the temperature variation within the room is more stable in December. The correlation between the inside chamber temperature T_{in} and the external temperatures of its four walls was established using the subsequent model:

$$T_{in} = 0.28 + 0.33T_{South} + 1.22T_{North} - 0.13T_{West} - 0.12T_{East} \quad (4)$$

When combined, the walls in the four orientations account for 99.3% of the variance in the inside temperature of the chamber ($R^2 = 0.993$). This suggests an excellent fit of the model to the data, as shown in Fig. 12.

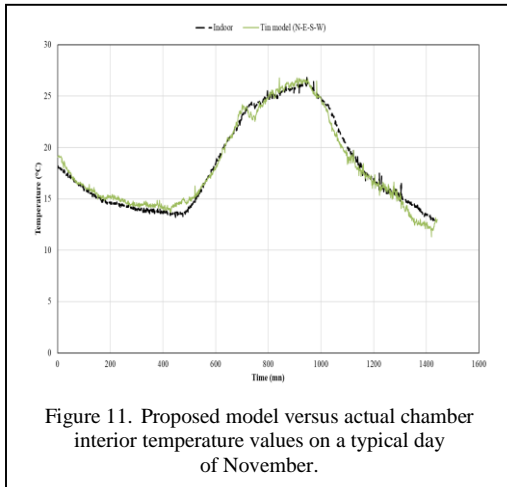
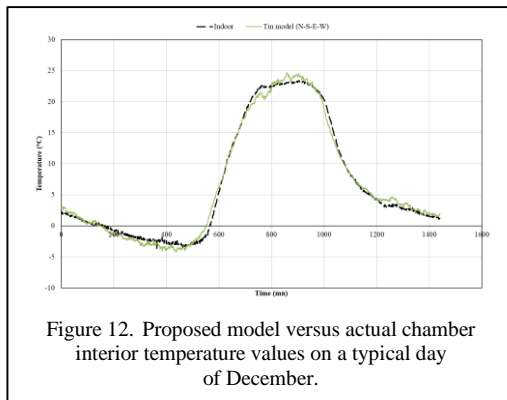


Figure 11. Proposed model versus actual chamber interior temperature values on a typical day of November.



IV. CONCLUSION

During autumn, the temperature variation within the chamber closely aligns with that observed on the exterior surface of the north-facing wall. Furthermore, the indoor temperature of the chamber is significantly affected by the temperature of its north-facing wall (T_{North}), whereas the impact from other orientations ranges from moderate to weak.

REFERENCES

- [1] IEA (2023). *Building*. Available at: <https://www.iea.org/energy-system/buildings>
- [2] Hadji, F., Ihaddadene, N., Ihaddadene, R., Betga, A., Charick, A., & Logerais, P. O. (2020). Thermal conductivity of two kinds of earthen building materials formerly used in Algeria. *Journal of Building Engineering*, 32, 101823.
- [3] Ministère de l'énergie et des mines, Bilan énergétique nationale (2021). Bilan énergétique nationale. Available at: https://www.energy.gov.dz/Media/galerie/bilan_energetique_2021_63df78f2b775e.pdf
- [4] Algerian Ministry of Environment and Renewable Energy (2023), *First updated biennial report of algeria*. Available at: <https://unfccc.int/sites/default/files/resource/BUR1%20Alg%C3%A9rie%20r%C3%A9vis%C3%A9%2022102023%20rev%207>.
- [5] Ahmed, S., El Attar, M. E., Zouli, N., Abutaleb, A., Maafa, I. M., Ahmed, M. M., ... & Ragab, A. (2023). Improving the thermal performance and energy efficiency of buildings by incorporating biomass waste into clay bricks. *Materials*, 16(7), 2893.
- [6] Sinha, A. (2020). Building orientation as the primary design consideration for climate responsive

architecture in urban areas. *Architecture and Urban Planning*, 16(1), 32-40.

- [7] Chen, L., Hu, Y., Wang, R., Li, X., Chen, Z., Hua, J., ... & Yap, P. S. (2024). Green building practices to integrate renewable energy in the construction sector: a review. *Environmental Chemistry Letters*, 22(2), 751-784.
- [8] Oumarou, F. A., Ouedraogo, A., Ky, S. M. T., Bhandari, R., Konfe, A., Konate, R., ... & Kam, S. (2021). Effect of the Orientation on the Comfort of a Building Made with Compressed Earth Block. *Smart Grid and Renewable Energy*, 12(7), 99-112.
- [9] Albatayneh, A., Alterman, D., Page, A., & Moghtaderi, B. (2018). The significance of the orientation on the overall buildings thermal performance-case study in Australia. *Energy procedia*, 152, 372-377.
- [10] Bakhlah, M. S., Hassan A. S. (2015). Effect of Orientation on Indoor Air Temperature in Hot and Dry Climate in Hadramout, Yemen. *American Transactions on Engineering & Applied Sciences*, 4(2).
- [11] Bekkouche, S. M. E. A., Benouaz, T., Cherier, M. K., Hamdani, M., Yaiche, M. R., & Khanniche, R. (2013). Influence of building orientation on internal temperature in Saharan climates, building located in Ghardaïa region (Algeria). *Thermal Science*, 17(2), 349-364.
- [12] Ouled Sidi Brahim, Available at: <https://fr.db-city.com/Alg%C3%A9rie--M'Sila--Ouled-Sidi-Brahim--Ouled-Sidi-Brahim>. [Accessed 31 August 2022]
- [13] Choudira, M., Ihaddadene, N., Zggane, H., & Ihaddadene, R. (2022, December). Effect of solar radiation on the temperature of house walls facing the four cardinal points in the summer in Ouled Sidi Brahim (Algeria). In *2022 13th International Renewable Energy Congress (IREC)* (pp. 1-6). IEEE.
- [14] Lirola, J. M., Castañeda, E., Lauret, B., & Khayet, M. (2017). A review on experimental research using scale models for buildings: Application and methodologies. *Energy and Buildings*, 142, 72-110.
- [15] Choudira, M., Ihaddadene, N., Ihaddadene, R., El Hacén, J. M., & Kherbiche, Y. (2024). An Experimental Study on the Effect of Surface Orientation and Inclination on Incident Solar Irradiation: Application to Buildings. *Journal of Renewable Energy and Environment*, 11(1), 157-167.
- [16] Rosado, P. J., & Levinson, R. (2019). Potential benefits of cool walls on residential and commercial buildings across California and the United States: Conserving energy, saving money, and reducing emission of greenhouse gases and air pollutants. *Energy and Buildings*, 199, 588-607.

Implementation of an Automatic Feedback Control Unit for a Double-pass Thermoelectric-assisted Solar Air Heater

Chinemerem Jerry Chukwu¹, Izuchukwu Kenneth Onyenwe², Chibundu Ogbonnia³

¹University of Nigeria, Nsukka, Nigeria.

²University of Nigeria, Nsukka, Nigeria. ³Technical University Chemnitz, Chemnitz, Germany,

¹chinemeremchukwu@outlook.com, ²onyenweizuchukwu@gmail.com,

³chibunduogbonnia@gmail.com

Abstract—This project presents the modification and implementation of an arduino-based automatic feedback control unit for an existing double-pass thermoelectric solar air heater. Upgrades and modifications were done on the aluminium absorber plate, thermal fin and fan assembly of an already existing thermoelectric solar air heater. An arduino-based automatic feedback control unit was implemented on the system to switch the power source of the micro fans from a rechargeable battery to TEGs (Thermoelectric generators) as soon as the power output of the TEGs is enough to power the micro fans and to charge the battery with excess power from the TEGs. A performance test on the workability of the system was conducted. The preliminary tests showed that the arduino-based automatic feedback control unit was capable of switching the power source of the microfans from the batteries to the TEGs and also charging the batteries.

Keywords - thermo-electric generator, solar air heater, arduino

I. INTRODUCTION

Global warming is real and its effect can be seen in rises in sea level, melting of solar ice caps, etc. If we must leave the average world temperature at a lower or same pedestal as we met it, there is need to use alternative fuel sources to produce energy. Thermal electricity is a promising area that can help us produce cleaner energy.

Solar energy is an environment-friendly resource that has been utilized since ancient times. It stands out as the most promising in terms of meeting energy demands without adverse environmental effects. Thermoelectric (TE) power generator converts heat directly to electricity. TEs are unique, environmentally friendly solid-state energy generators that has no moving parts and are very reliable. It consists of n and p semiconductors connected electrically in series and thermally in parallel. A source of heat is supplied at one end of the TE, while the other end is maintained at a lower temperature.

II. JUSTIFICATION OF STUDY

In the past, there were numerous studies on the simultaneous generation of PV (photovoltaic) and TE electric power but only few attempts have been made to simultaneously generate heat and TE power. So, proposing to undertake this project is a way to research deeper into simultaneous generation of heat and TE power from solar thermal systems.

III. LITERATURE REVIEW

The concept of solar air heating is not a new discovery. Over the years, many solar air heaters have been designed, constructed and tested. Some references claim that there were



numerous inventions in America since the 1700s on how one could harness the sun's energy for heating a home.

In 1894, a Frenchman, Jean Charles Athanase Peltier, discovered that when a current is passed through dissimilar metals or semiconductors (n-type and p-type) that are connected to each other at two junctions, the current drives a transfer of heat from one junction to the other, one junction cools off while the other heats up. This is known as Peltier effect. The Peltier heat \dot{Q} , generated at the junction per unit time equals:

$$\dot{Q} = (\pi_A - \pi_B)I, \quad (1)$$

where π_A and π_B are the Peltier coefficients of conductors A and B and I is the electric current from A to B.

Reference [1] considered heat sink optimization by varying the number of channels in closed-finned ducts under forced convection. For a fixed pressure drop, [2] introduced a criterion to determine the optimal heat sink dimensions of water-cooled heat sinks.

An alternative procedure based on the extended flat plate surface model for simulating natural convection cooling was later described by [3].

Reference [4] studied an approximate analytical-numerical procedure used to model natural convection cooling of heat sinks using computational fluid dynamics.

Reference [5] presented an analytical study for a forced convection cooled, shrouded plate fin array, and presented their results for their average heat transfer rate in tabular form. Reference [6] presented a study of flow bypass effects on plate fin heat sinks, and recommended the use of the developing flow correlation of [7], which was modified from its original log-mean temperature formulation. Reference [8] developed the existing solar air heater with a symbiotic thermoelectric module power source, which was tested under the climatic conditions of Nsukka, Nigeria. The result of the experiment showed an average thermal efficiency of 48% at an average solar radiation of 423.35 W/m^2 . The system generated approximately 4.3V from the TEGs.

IV. STUDY AIM AND OBJECTIVES

The main aim of this study is to implement an automatic feedback control unit for a double-pass thermoelectric solar air heater and the set objectives are:

- For the control unit to switch the power source of the fans from a backup rechargeable battery to TEGs as soon as the power output of the TEGs are sufficient to power the fans.
- For the control unit to charge the battery using excess power generated by the TEGs.
- To carry out performance test to illustrate the work-ability of the system.

V. SCOPE OF WORK

This project will be limited to the following:

- Modifying/upgrading the absorber plate, thermal fin and fan assembly of an existing double-pass solar TE collector.
- Developing an Arduino-based feedback control unit for the collector system.
- Writing Arduino codes to govern the power switching and battery charging functions of the feedback control unit.
- Carrying out performance test on the system.

VI. MATERIALS AND METHODS

The already existing double-pass thermoelectric solar air heater is composed of a wooden box made from gmelina wood, 82cm×55cm aluminium absorber plate, thermoelectric modules, three (3) 5cm×5cm micro fans, an air gap and rectangular heat sinks.

A. Modification/Upgrade Procedure

1) A black coated aluminium absorber plate of 96cm×55cm was used to replace the existing one. This was done in order to increase the area of insolation. Aluminium was used because of its high absorptivity, durability, corrosive resistance and low cost. The edge of the glazing was sealed with silicon sealant to avoid escape of hot air from

the system and the primary function of the glazing is to transmit radiation to the absorber plate and minimize the heat losses, convection and radiation from the absorber plate.

2) The micro fans were changed from three (3) 5cm×5cm to four (4) 7cm×7cm micro fans. This was done to increase the amount of air sucked from the system. An adhesive was used to hold the micro fans at the inlet channel of the collector. Seven (7) uniform rectangular thermal fins were installed in the system. A hole was made on the absorber plate using a 3mm drill bit on the drilling machine. The thermal fins were attached to the absorber plate using a screw and 7 TEGs were placed between the absorber plate and the thermal fins. The thermal fins were placed on the cold surface of the TEGs at the inlet channel so as to be cooled by the incoming air Fig. 4

shows an Arduino-based automatic feedback control unit that switches the powersource of the microfans from a rechargeable battery to TEGs as soon as the power output of the TEGs is enough to power the microfans was incorporated into the solar air heater and 116 lines of Arduino codes were written to govern the switchover and charging functions.

3) Next is the program flow chart (Fig. 1).

B. Electronic Circuit of the Control Unit

Prior to the actual construction of the Arduino-based automatic feedback control unit, the conceptual design and simulation of the system were done using Proteus. The major work was soldering the electronic components on the vero board. The electronic circuit of the Arduino-based automatic feedback control unit is shown in Fig. 2. The unit consists of rechargeable batteries (B2)

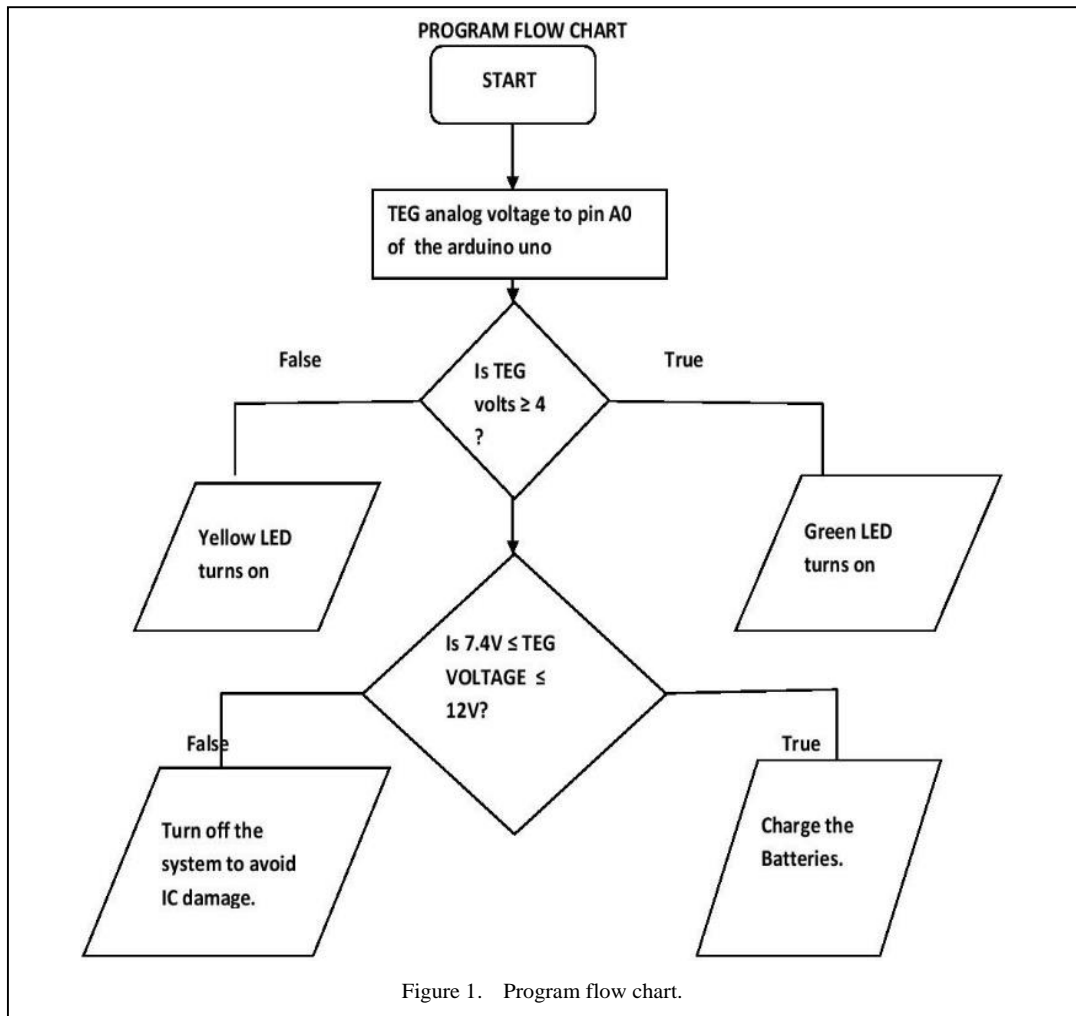
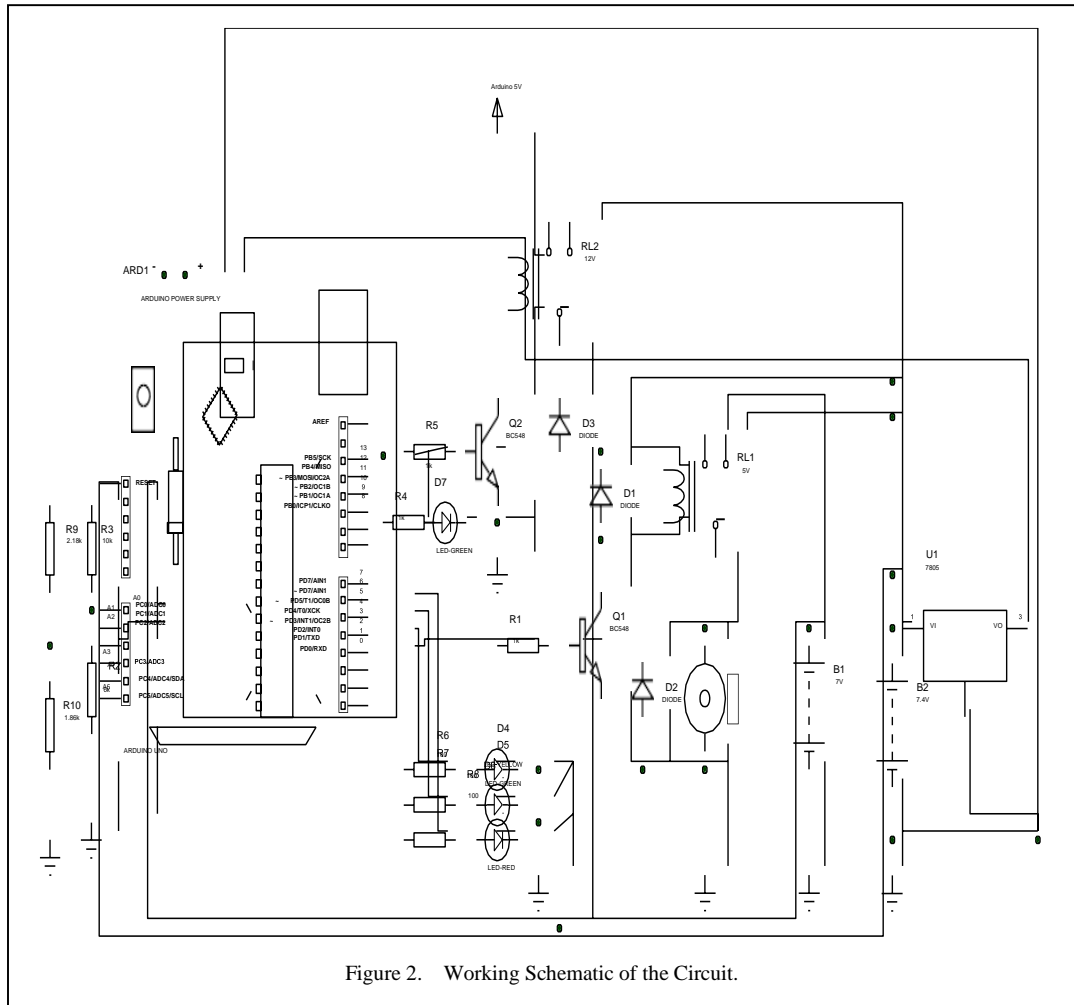


Figure 1. Program flow chart.

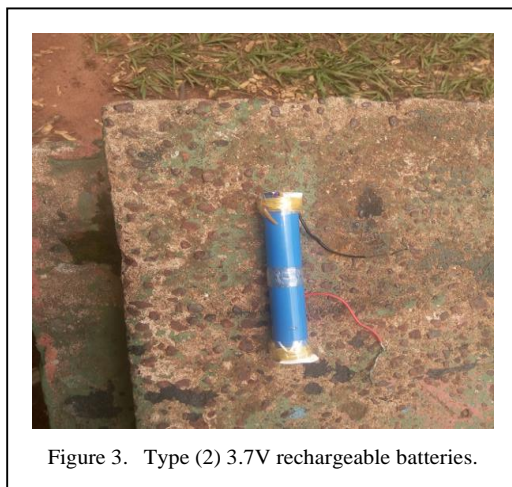


and TEGs (B1) that power the micro-fans depending on the set priority.

C. LEDs

These are semiconductor devices that emits visible light when an electric current passes through it. Three LEDs (yellow, green & red in colour) of 2V, 20mA and 5mm size were used in the control unit. The yellow one indicates that the micro fans are being powered by the battery, the green one indicates that the switch-over function has been actualized, the red one indicates high voltage while the green one on the charging circuit shows that the batteries are being charged by the charging circuit.

D. The Rechargeable Batteries



E. Diodes

These are two terminal devices that allows current flow in one direction. In this circuit, 3 IN4007 diodes with voltage drop of 0.7V were used for protecting the components that are vulnerable to reverse current.

F. Cables and Jumper Wires

J21 pin plg and premium male/male jumper wires of 20 × 6 inches (152.4mm) were used as connecting wires in the system (Figs. 4-6).

VII. THERMAL EFFICIENCY OF THE COLLECTORS

The performance of a collector is usually evaluated in terms of efficiency, which is defined as the ratio of the useful energy delivered by the collector during a given time period to the incident solar radiation on the collector during the same period. Based on previous analysis, the mass of air entering our solar air heater in kg/s is given by:

$$\dot{m}_f = \dot{Q}_f Av . \quad (2)$$

Thermal power delivered by the solar air collector:

$$\dot{Q}_f = \dot{m}_f C_{pa} \Delta T . \quad (3)$$

The efficiency (η) of solar collector:

$$\eta = \frac{\dot{Q}_f}{I_{av} \times Ac} , \quad (4)$$

where \dot{Q}_f is the thermal power delivered by the solar collector absorber plate, C_{pa} is the specific heat capa, \dot{m}_f is the mass flow rate of air, Ac is the area of the city of air and ΔT is the temperature difference between the air at inlet and outlet. I_{av} is the average solar irradiance in W/m² and ρ_f is density of the fluid in kg/m³. v is the fluid velocity, and A is the cross-sectional area of the flow.

VIII. RESULTS AND DISCUSSIONS

The result obtained in this project work is limited to the measurement of the TEGs output voltage only. The proposed performance test to check the thermal efficiency and thermal power output of the solar air heater for improvement was not carried out. This is due to the unfavorable weather conditions (heavy rainfall) as at the time the collector was ready for the test. Because of this, only a workability test on the different sections of the collector assembly was carried out. This was done at the Electrical Engineering Department of University of



Figure 4. Physical appearance of the control unit.

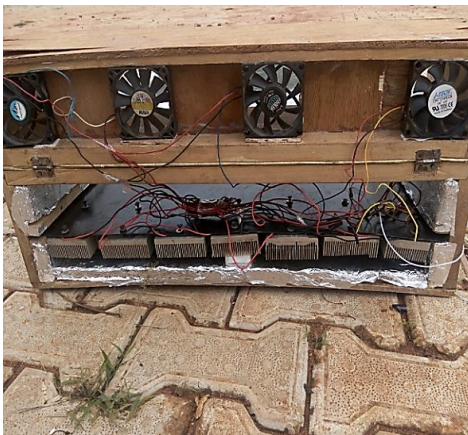


Figure 5. Fin/fan assembly.



Figure 6. Coupled finished system.

Nigeria, Nsukka on the 9th of August, 2017, which is different from the proposed test location (National Centre for Energy Research and Development, University of Nigeria, Nsukka.)

The maximum measured TEG voltage recorded was 0.42V. Other parameters like absorber plate temperature, air outlet temperatures, ambient temperature, solar irradiance and TEG cold side temperature needed to compute the collector's thermal efficiency and thermal power were not measured as the test was not carried out at the proposed test location where access to such measuring instruments would have been granted.

However, another demonstration test to check the functionality of the Arduino- based control unit to switch power and charge the rechargeable batteries was done using a 9V dc battery as the TEGs power source. When the 9V dc battery was connected to the TEG terminal, the yellow LED turned off and a green LED switch on automatically. This showed that the microfans power source have been switched from the initially lithium-ion rechargeable battery powering it to the 9V d.c battery representing the TEGs generated voltage. This confirmed that the control unit is perfectly working.

For scalability, a robust Arduino system with capacity above 12v, my experimental benchmark, can be built. This will allow the system to power higher voltage batteries and provide more current for battery storage. A possible challenge with the scalability of our system will involve the maintenance of the battery unit in the long run due to battery efficiency reduction with usage over time.

On a cost basis, the modified system will cost more compared to the original system due to the addition of the Arduino-based control unit. For commercial purpose, our modification brings in automation [automatic fan power switching from back up battery to TEG] into the system and will heat up air faster for a prolonged period since the Arduino switching will help prolong backup battery life.

IX. RECOMMENDATIONS AND CONCLUSIONS

In this project work, an Arduino-based feedback control unit, an external battery

power source and a charging unit was incorporated into an existing thermo-electric solar air heater. Few other modifications were made and the workability of the entire system was tested under the climatic condition of Nsukka, Nigeria by August, 2017.

This section discusses the major shortcomings and limitations encountered in this project work and suggested recommendations to overcome it. The limitations include the following:

- This project was time-bound and considering the time of work, performance evaluation tests happened only during rainy season. Conducting tests during dry season will provide concrete empirical data and will be an area for further research. For this reason, it would be suggested that a comprehensive test be done on the solar thermoelectric collector system during the dry season.
- The thermal efficiency of the unmodified system is 48% with TEG output voltage of 4.3v. The outdoor test on our improved system only captured the workability of the power switching system. No tests were conducted to assess the durability and reliability of the system over extended periods.

Beyond addressing weather conditions, other plans to further enhance the system's capabilities involves incorporating advanced sensors for current and temperature data capture. Also, with Arduino systems i/o pins limited to 40ma before they are damaged [The limits of arduino uno board - Using Arduino / General Electronics - Arduino Forum], subsequent enquiry can employ the use of more advanced PLC(programmable logic controller) systems, in place of Arduino, for better current filtering at higher working temperatures.

REFERENCES

- [1] Knight, R. W., Goodling, J. S., & Hall, D. J. (1991). Optimal design of forced convection. *ASME Journal of Electronic Packaging*, 113, 313–321.
- [2] Sasaki, S., & Kishimoto, T. (1986). Optimal structure for microgroove cooling fin for high-power LSI devices. *Electronics Letters*, 22, 1332–1334.

- [3] Culham, J. R., Yovanovich, M. M., & Lee, S. (1995). Thermal modeling of isothermal cuboids and rectangular heat sinks cooled by natural convection. *IEEE Transactions on Components, Packaging and Manufacturing Technology*, 18, 559–566.
- [4] Narasimhan, S., & Majdalani, J. (2012). Characterization of compact heat sink models in natural convection. *IEEE Transactions on Components and Packaging Technologies*, 25(1), 572–579.
- [5] Sparrow, E. M., Baliga, B. R., & Patankar, S. V. (1978). Forced convection heat transfer from a shrouded fin array with and without tip clearance. *Journal of Heat Transfer*, 100(4), 572–579.
- [6] Wirtz, R. A., Chen, W., & Zhou, R. (1994). Effect of flow bypass on the performance of longitudinal fin heat sinks. *Journal of Heat Transfer*, 116(3), 206–211.
- [7] Shaw, R. K., & London, A. L. (1978). *Laminar flow forced convection in ducts*. Academic Press.
- [8] Orizu, & Onyekwe. (2016). Development of an active solar air heater with a symbiotic TEM power source. Unpublished undergraduate project, University of Nigeria, Nsukka.

Exploring Organic Photovoltaic Systems: A Sustainable Solution for Energy-efficient Building Facades in Northeastern Brazil

Dafne Negrão Cordeiro e Silva¹, Taynara G. S. Lago²

^{1,2}Graduate Program in Renewable Energy (PPGER), Center for Alternative and Renewable Energies (CEAR), Federal University of Paraíba (UFPB), Brazil

¹dafne.silva@estudante.cear.ufpb.br, ²taynara@cear.ufpb.br

Abstract—In response to the pressing need to reduce greenhouse gas emissions brought on by the rapid industrial and demographic growth in Northeastern Brazil, this article explores the potential of organic photovoltaic (OPV) systems as a new source of sustainable energy for building facades. A bibliometric review of databases like Scopus and Web of Science is part of the process, which examines the viability and suitability of these systems in a particular geographic setting. OPV stand out because to their molecular flexibility, which makes them perfect for semi-transparent solar cell (STC) applications where transparency to visible light and energy conversion efficiency are prioritized. By substituting traditional materials in various structural components, the integration of these systems into building facades not only encourages urban energy sustainability but also greatly improves building energy efficiency by lowering the requirements for lighting and cooling. This study emphasizes how crucial it is to keep investigating and creating novel photovoltaic technologies as a means of effectively and sustainably addressing local and global energy issues.

Keywords - greenhouse, sustainable, efficiency, building, energy

I. INTRODUCTION

The quality of life in local communities and the sustainability of the environment are greatly impacted by the diverse climatic conditions found on Earth. This emphasizes the urgent need

for sustainable energy solutions that are tailored to the unique features of each region, such as the Northeast region of Brazil. The abundance of solar radiation in this semi-arid region with its socioeconomic issues contrasts with the lack of water [1]. Recurrent droughts worsen long-term trends in declining precipitation while raising local temperatures [2]. Energy conversion has increased significantly in a few countries due to the rise in photovoltaic (PV) energy conversion and the sharp decline in the cost of solar kWh relative to thermal and hydroelectric generation in a number of those regions, including Brazil. For regions plentiful in solar energy, such as the Northeast of Brazil [1], solar photovoltaic technology offers itself as a very appealing choice to support a new growth paradigm based on the most abundant resource: the sun.

The ongoing advancement of renewable energy technology is fueled by expanding energy demand and global environmental concerns, which opens new avenues for the investigation of sustainable energy sources. Even now, solar energy stands out as the most plentiful, endless, and pure renewable energy source [3]. Considering the rise in industrialization and population expansion, finding alternatives to conventional energy sources, such as fossil fuels, is crucial for reducing greenhouse gas emissions.

Owing to their adaptability and translucent nature, Organic Photovoltaic (OPV) modules represent a novel choice for uses not addressed by traditional photovoltaic systems, including



commercial or industrial settings, windows, integrated architectural elements, rooftop installations, and solar plants. This energy requirement can be considerably met by photovoltaic systems, particularly if they are used extensively. Nevertheless, despite their potential, photovoltaic plants that are already in operation only provide “1%” of the world's electrical energy needs [2]. The dearth of data and academic studies emphasizes how critical it is to increase the widespread and effective application of photovoltaic and renewable energy technology.

Even though China's coal capacity and energy output have grown significantly, coal consumption did not keep up with this expansion in 2022. The production of wind, solar, and photovoltaic energy has significantly increased, mitigating this tendency, with coal accounting for around three-fifths of the energy mix utilized to generate power. Growth in the world's demand for energy has been substantially slower than the average over the previous ten years [4].

Conversely, there was a minor decline in direct emissions resulting from construction activities in 2022 as compared to the previous year, deviating from an average yearly growth trend of over “1%” between 2015 and 2021. This decline can be attributed to the increasing use of clean energy technology, like electric cars, heat pumps, and renewable energy, all of which have greatly reduced the amount of CO₂ emissions that would have otherwise occurred [4].

Building-integrated photovoltaics (BIPV) is being developed in response to the pressing demand for energy sustainability, which aims to lessen the negative effects of large fossil fuel consumption [5]. The integration of solar technologies, including windows and roofs on urban building surfaces, offers prospects to greatly increase energy sustainability. Decarbonization of energy systems necessitates a significant growth of photovoltaic areas.

This article's goal is to examine and assess organic photovoltaic systems' (OPV) potential as a fresh, environmentally friendly energy source for use on building facades in northeastern Brazil. To lessen reliance on fossil fuels and cut greenhouse gas emissions, it is critical to identify workable alternatives to traditional energy sources in light of the global difficulties brought about by fast industrial and population growth. The creation of novel and reasonably priced technology for the conversion of renewable

energy is essential and calls for large contributions from a variety of sectors. The flexibility and transparency of OPV modules make them a standout option for applications like windows, integrated construction elements, and building facades that aren't often covered by traditional solar systems. BIPV Requirements and Benefits.

Many alternatives exist for the integration of solar systems on a building's support, such as building integrated photovoltaics (BIPV), which has emerged as a very promising method for producing power since the late 1990s [5]. The idea behind multifunctional building components is to replace traditional materials for sun protection elements, windows, roofs, and facades with photovoltaic technology that integrates into the building structure to produce useful energy. An effective way to balance natural light penetration into a structure and lessen the need for lighting and cooling is using glazed windows with an average transmittance in the visible area of between “10%” and “60%” [6]. These extra advantages are made possible by semi-transparent solar cells, which convert sunlight into power in addition to letting light through.

In addition to providing advantages for natural light transmission and lowering energy consumption for lighting and cooling, semi-transparent solar cells also increase the amount of power they can produce [7]. For instance, compared to plain windows, semi-transparent solar cells installed on one side of an office building with lighting control might save electricity by up to “12%” [8].

The annual reports that the National Renewable Energy Laboratory (NREL) publishes on developments in the efficiency of solar photovoltaic technology and related materials are well-known. The most efficient solar module on the market can reach an efficiency of “47%”, per the most recent NREL report [7]. However, monocrystalline modules-which, according to the 2020 report, can achieve up to “27.6%” efficiency under laboratory conditions-make up most conventional solar cells that are sold for use in common applications [9].

II. METHODOLOGY

The Scopus and Web of Science platforms were chosen for this study because of their extensive coverage of academic fields pertinent to the investigation of the viability and implementation of organic photovoltaic (OPS) systems on building facades in Northeastern Brazil. Comprehensive bibliometric research is made possible by the scope and quality of these databases, which are acknowledged for their ability to index scientific publications, conferences, and other academic information sources. When combined, they will provide a thorough picture of pertinent articles, making it easier to spot technological advancements and knowledge gaps pertaining to the topic at hand.

The criteria were utilized in the process of bibliometric and bibliometric network analysis to enhance the research. The utilization of the Scopus and Web of Science platforms facilitated a more comprehensive and extensive exploration of pertinent literature about organic photovoltaic (OPV) systems installed on building facades. The interdisciplinary method gave a wider picture of the various viewpoints engaged, while the temporal analysis showed changes in research patterns over time. Additionally, the geographical research showed differences in the viability and challenges associated with OPV implementation in various geographic locations.

A thorough and organized methodology is needed for a bibliometric study on the viability and application of organic photovoltaic (OPS) systems on building facades in Northeast Brazil.

Research on the production of transparent OPV panels with an emphasis on optical and electrical characteristics, energy efficiency, and useful applications was one of the selection criteria. The documents were obtained, and then the metadata was processed and examined. Next, networks of co-occurrence of terms (words) and co-citation of authors, sources, and references were developed and presented as part of the study's progress. These criteria and search terms were essential for directing the bibliographical investigation and locating pertinent papers to comprehend and assess transparent microalgae OPS panels' ability to produce electricity.

This methodology aims to provide a solid and organized basis for bibliometric research on the feasibility and application of organic photovoltaic systems on building facades in Northeastern Brazil. Below, in Fig. 1, we have

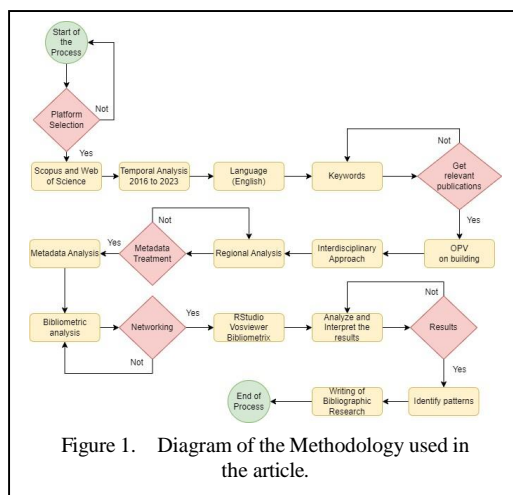


Figure 1. Diagram of the Methodology used in the article.

the diagram of the methodology, where its steps and processes are highlighted until reaching the final state of the article.

III. SYSTEM AND APPLICATION FOR ORGANIC PHOTOVOLTAIC SYSTEMS (OPS)

Even though Paraíba has historically experienced water shortages, the region presents a significant opportunity for the use of photovoltaic technology due to its constant and ample solar exposure [10]. This strategy benefits the local economy by generating revenue and jobs, but it also has a significant social impact. Solar systems help to uplift living circumstances and foster social inclusion by giving rural, low-income, and low-consumption families access to more reasonably priced electricity.

In the educational setting, the construction of photovoltaic systems provides a valuable chance to expose solar technology concepts to academic institutions, thereby preparing future generations to address future energy concerns. The most prevalent application in semi-arid regions is water pumping using engines powered by solar panels; nevertheless, there is significant potential to expand the usage of this technology to other more powerful applications [10]. This not only broadens the opportunities for solar energy use, but it also has a significant impact on the region's long-term development, contributing to resilience and economic growth.

Brazil competes on an equal footing with other countries in the field of researching thin organic films capable of converting solar energy into electricity [11]. This illustrates the Brazilian scientific community's ability and skill to

contribute to the advancement of this technology on a worldwide scale.

To overcome these restrictions, substantial research is being conducted in Brazil and around the world to develop new materials and manufacturing procedures for more efficient and cost-effective solar cells. As a result, a new generation of solar cells has evolved, with lower manufacturing costs than the silicon wafers now used in modules. These cells, known as third-generation solar cells (the first being silicon and the second being inorganic films), are classified into two types: organic cells (OPS, or organic photovoltaic) and sensitized cells (DSSC, or dye-sensitized) [12].

DSSCs rely on a chemical oxidation-reduction mechanism to convert light into electricity, whereas OPV cells use semiconductor materials. DSSCs, also known as hybrid cells, use a liquid electrolyte that frequently contains iodine salt and blend inorganic and organic materials between two glass layers. In order to produce energy, the dyes in these cells absorb solar radiation and separate positive and negative charges. Organic and hybrid cells aren't currently generally available for purchase, though.

A. Law 14.300 - MMGD Legal Framework

The Normative Resolution N° 482, published in 2012, establishes that the isolated Brazilian market consumers can produce electricity from renewable sources or qualified cogeneration and supply the surplus to the distribution network. Besides introducing the distributed micro-generation and mini-generation concepts, this resolution implements the Electric Energy Compensation System (EECS). With EECS implementation, when the consumers with micro or mini-generation systems produce more energy than they consume, the surplus is injected into the distribution network. Therefore, the consumer uses this injected energy to reduce his consumption, with credits calculated at full price. However, over the years, this text was modified with Normative Resolutions No. 687/2015 and No. 786/2017 [13].

When the EECS is used, the utility company replaces the conventional energy meter, which measures energy in only one direction, through a bidirectional meter or two conventional meters.

According to Normative Resolution No. 482 and its revisions, consumers who find themselves in one of the following situations can participate

in the compensation system: consumption units with distributed micro or mini-production, members of companies with multiple consumption units, consumers participating in common production or remote self-consumption. The remote self-consumption allows energy credits generated by a decentralized production consumption unit to be offset in another unit, if both have the same ownership and are in the same concession area. On the other hand, joint production refers to a consortium or cooperative that uses excess energy from a production unit [14].

With the approval of the Legal Framework for Distributed Micro-generation and Mini-generation, titled Law 14,300, all existing units or those that register access within 12 months of its publication are guaranteed to preserve the benefits obtained until 2045. Additionally, the law defined the rules that will be applied during and after the regulatory transition [13].

Starting in 2029, all tariff components that are not related to the cost of energy will be charged, thus ignoring the benefits of distributed generation (DG) for the network. ANEEL should evaluate these benefits according to the guidelines of the National Energy Policy Council [15].

IV. RESULTS AND DISCUSSION

Significant developments in solar cell classes have focused mostly on semitransparent applications. These technologies can be classified into inorganic, such as CdTe, Cu₂ZnSnS₄, or CuInSe₂ materials, organic, such as massive heterojunctions of poly(3-hexylthiophene): phenyl-C61-butyric acid methyl ester (BHJ), and perovskites, such as lead iodide and meth, which use thin or mesoporous films as dyes or quantum dots to sensitize the solar cell architecture [16].

Brazil has a competitive edge in the manufacture of photovoltaic silicon due to its ideal features for photovoltaic technology, including high solar incidence and an abundance of high-quality quartz. Brazilian researchers advanced their study of thermal solar systems, such as solar collectors, stoves, and distillation systems, and created novel solar cells between the 1970s and 1983 [17].

The solar market in the country was also boosted by the production of silicon photovoltaic modules and the implementation of field projects

TABLE I. LIST OF ARTICLES CHOSEN FOR THE BIBLIOGRAPHIC ANALYSIS.

1. Ding, Z., et. al. (2016). Spray coated silver nanowires as transparent electrodes in OPVs for Building Integrated Photovoltaics applications. <i>Solar Energy Materials and Solar Cells</i> , 157, 305-311.	13. Ali, A. Y., Holmes, N. P., Ameri, M., Feron, K., Thameel, M. N., Barr, M. G., ... & Zhou, X. (2022). Low-Temperature CVD-Grown Graphene Thin Films as Transparent Electrode for Organic Photovoltaics. <i>Coatings</i> , 12(5), 681.
2. Park, Y., et. al. (2016). Efficient flexible organic photovoltaics using silver nanowires and polymer based transparent electrodes. <i>Organic Electronics</i> , 36, 68-72.	14. Bellchambers, P., et. al. (2021). High-performance transparent copper grid electrodes fabricated by microcontact lithography for organic photovoltaics. <i>ACS Applied Energy Materials</i> , 4(4), 4150-4155.
3. Park, Y., Nehm, F., Müller-Meskamp, L., Vandewal, K., & Leo, K. (2016). Optical display film as flexible and light trapping substrate for organic photovoltaics. <i>Optics Express</i> , 24(10), A974-A980.	15. Burwell, G., et. al. (2022). Scaling considerations for organic photovoltaics for indoor applications. <i>Solar RRL</i> , 6(7), 2200315.
4. Bazaka, K., Ahmad, J., Oelgemöller, M., Uddin, A., & Jacob, M. V. (2017). Photostability of plasma polymerized γ -terpinene thin films for encapsulation of OPV. <i>Scientific reports</i> , 7(1), 45599.	16. Moreno, A., Riverola, A., Chemisana, D., Vaillon, R., & Solans, A. (2022). Design and characterization of an OPV-ETFE multi-layer semi-transparent glazing. <i>Energy Reports</i> , 8, 8312-8320.
5. Chiba, T., Kumagai, D., Udagawa, K., Watanabe, Y., & Kido, J. (2018). Dual mode OPV-OLED device with photovoltaic and light-emitting functionalities. <i>Scientific reports</i> , 8(1), 11472.	17. Dolaro, A., Leva, S., Manzolini, G., Simonetti, R., & Trattenero, I. (2022). Outdoor performance of organic photovoltaics: Comparative analysis. <i>Energies</i> , 15(5), 1620.
6. Li, Y., et. al. (2019). Enhanced light utilization in semitransparent organic photovoltaics using an optical outcoupling architecture. <i>Advanced Materials</i> , 31(40), 1903173.	18. Waller, R., Kacira, M., Magadley, E., Teitel, M., & Yehia, I. (2022). Evaluating the performance of flexible, semi-transparent large-area organic photovoltaic arrays deployed on a greenhouse. <i>AgriEngineering</i> , 4(4), 969-992.
7. Pereira, H. J., & Hatton, R. A. (2019). High figure-of-merit transparent copper–zinc oxide window electrodes for organic photovoltaics. <i>Frontiers in Materials</i> , 6, 228.	19. Schopp, N., et. al. (2022). Unraveling device physics of dilute- donor narrow- bandgap organic solar cells with highly transparent active layers. <i>Advanced Materials</i> , 34(31), 2203796.
8. Li, Y., et. al. (2020). Color-neutral, semitransparent organic photovoltaics for power window applications. <i>Proceedings of the National Academy of Sciences</i> , 117(35), 21147-21154.	20. Nair, N. M., et. al. (2023). Self- Powered e- Skin Based on Integrated Flexible Organic Photovoltaics and Transparent Touch Sensors. <i>Advanced Intelligent Systems</i> , 5(10), 2300103.
9. Pascual-San-José, E., et. al. (2020). Towards photovoltaic windows: scalable fabrication of semitransparent modules based on non-fullerene acceptors via laser-patterning. <i>Journal of Materials Chemistry A</i> , 8(19), 9882-9895.	21. Huang, J., et. al. (2023). Intrinsically stretchable, semi-transparent organic photovoltaics with high efficiency and mechanical robustness via a full-solution process. <i>Energy & Environmental Science</i> , 16(3), 1251-1263.
10. Chang, J. K., et. al. (2020). Solution-processed, semitransparent organic photovoltaics integrated with solution-doped graphene electrodes. <i>Scientific Reports</i> , 10(1), 20010.	22. Liu, X., et. al. (2023). High- Performance Colorful Organic Photovoltaics with Microcavity Resonance Color Filter. <i>Advanced Energy Materials</i> , 13(34), 2301361.
11. Lee, B., Lahann, L., Li, Y., & Forrest, S. R. (2020). Cost estimates of production scale semitransparent organic photovoltaic modules for building integrated photovoltaics. <i>Sustainable Energy & Fuels</i> , 4(11), 5765-5772.	23. Waller, R., et. al. (2021). Semi-transparent organic photovoltaics applied as greenhouse shade for spring and summer tomato production in arid climate. <i>Agronomy</i> , 11(6), 1152.
12. Huang, X., Fan, D., & Forrest, S. R. (2021). Scalable semitransparent prototype organic photovoltaic module with minimal resistance loss. <i>Organic Electronics</i> , 97, 106276.	24. Güler, E. N., Distler, A., Basu, R., Brabec, C. J., & Egelhaaf, H. J. (2022). Fully solution-processed, light-weight, and ultraflexible organic solar cells. <i>Flexible and Printed Electronics</i> , 7(2), 025003.

implementation of this technology in Brazil still faces obstacles, such as the lack of incentives for its mass adoption.

This limited adoption of photovoltaic technology in Brazil may be linked to the historical cost of conventional energy sources. According to the “Empresa de Pesquisa Energética” (EPE), the price of photovoltaic solar energy per kW, including charges and taxes, ranges from R\$130 to R\$150 per kW/year, considering an economic lifespan of 25 years and an average payment period of 12 months. On the other hand, floating photovoltaic technology has a cost of R\$160 per kW/year over the same period, which forments a more gradual adoption [18].

A study that looked at solar plants that were partially incorporated into greenhouses served as an example of how photovoltaic systems can be integrated. The results showed that electrical output rose with increasing greenhouse coverage, from less than 65 kWh/m² annually for partially shaded greenhouses to almost 190 kWh/m² annually for fully covered greenhouses [19]. Moreover, photovoltaic solar energy generation contributed to a decrease in CO₂ emissions. Reference [20] examined the use of semitransparent organic photovoltaic cells to lessen the effects of shade on indoor areas. However, although these cells produced electricity, they also raised the need for artificial illumination. Nonetheless, up to 40% of the demand might be satisfied by the electricity generated.

The absence of sufficient incentives, such as lower taxes on solar equipment and government subsidies, is one of the challenges facing Brazil's OPV technology advancement. Additionally, it is essential to mandate greater energy efficiency in housing projects and new construction, permit the sale of excess energy, and exempt non-profit institutions from paying taxes [17]. The construction industry, which is dominated by family-run businesses with little investment in skilled labor and technology, continues to rely on conventional solutions like masonry and concrete, putting short-term profits ahead of energy efficiency. It is important to view photovoltaic technology as a flexible architectural material that considers various scales and physical properties [17].

The opaque nature of Si- based crystalline solar cells has generated interest in developing novel photovoltaic technologies for use in

building integrated systems (BIPV). Efficient STC designs incorporate technologies such as perovskites [21].

Table I shows the papers selected for the literature review: 10 from the WoS platform and 16 from the Scopus platform. These papers are acknowledged as references by scholars working on this topic and are limited to scientific articles published in English over the last seven years that have reached the final stage of publication.

V. CONCLUSION

Based on the analysis of the viability and suitability of organic photovoltaic systems (OPV) for building facades in the northeast region of Brazil, it's necessary to consider the specific environment of this geographical area and its unique climatic characteristics. Although the challenges related to the efficiency and stability of OPVs might be relevant, it is important to recognize the great potential of these systems, especially in areas with high solar incidence, such as the northeast of Brazil.

Energy diversification is crucial to ensure energy security and reduce dependence on non-renewable energies. In this sense, OPVs are a promising alternative, especially when integrated into building facades, where they can efficiently exploit the available sunlight.

Even though it is essential to overcome technical hurdles, it's encouraging to see continuous progress in the research and development of these systems. Collaboration between academic, governmental, and industrial institutions is fundamental to stimulate innovation and accelerate the large-scale adoption of OPVs.

Therefore, it is concluded that, despite the inherent challenges, organic photovoltaic systems (OPV) represent a promising solution for sustainable energy generation in building facades in the Northeast region of Brazil. With adequate support and continuous research and development, these systems have the potential to play an important role in the region's transition to a more sustainable and diversified future.

REFERENCES

- [1] ANEEL. (2024). *Metadata dictionary of the dataset. National Electric Energy Agency*. Available at: <https://dadosabertos.aneel.gov.br/dataset/5e0fafd2-21b9-4d5b-b622-40438d40aba2/resource/27b24236-3974-462d-ae35-64ab16661ef7/download/dm-empreendimentos-geracao-distribuida-colica-informacoes-tecnicas.pdf>

- [2] ABSOLAR—Brazilian Solar Photovoltaic Energy Association. (2023). *Statistics and exclusive analyses of the solar photovoltaic market*. Available at: <https://www.absolar.org.br>
- [3] ABSOLAR—Brazilian Solar Photovoltaic Energy Association. (2021). *Solar Photovoltaic Energy in Brazil, ABSOLAR infographic*. Available at: <https://www.absolar.org.br>
- [4] Albert, M. J. (2021). The climate crisis, renewable energy, and the changing landscape of global energy politics. *Alternatives*, 46(3), 89-98.
- [5] Bayoumi, M. (2017). Impacts of window opening grade on improving the energy efficiency of a façade in hot climates. *Building and Environment*, 119, 31-43.
- [6] Bigas, A., & Lamberti, P. (2024). How law can ensure solar energy for all Brazilians. *Revista Jurídica Direito, Sociedade e Justiça*, 11(17).
- [7] Ferreira, A., Kunh, S. S., Fagnani, K. C., De Souza, A. T., Tonezer, C., Rodrigues Dos Santos, G. H., & Coimbra-Araújo, C. (2018). Economic overview of the use and production of photovoltaic solar energy in Brazil. *Renewable and Sustainable Energy Reviews*, 81(1), 181-191.
- [8] Dolara, A., et al. (2022). Outdoor performance of organic photovoltaics: Comparative analysis. *Energies*, 15(5), 1620.
- [9] International Energy Agency (IEA). (2023). *CO₂ emissions in 2022*. Available at: <https://www.iea.org/reports/co2-emissions-in-2022>
- [10] Diodato, V. P. (1994). *Dictionary of bibliometrics*. Haworth Press.
- [11] Romaní, J., Pérez-Rodríguez, A., & Salom, J. (2023). Performance of prototype tandem UV filter and organic transparent photovoltaic windows. *Journal of Building Engineering*, 68, 106111.
- [12] Scharber, M. C., & Sariciftci, N. S. (2013). Efficiency of bulk-heterojunction organic solar cells. *Progress in Polymer Science*, 38(12), 1929-1940.
- [13] Albert, M. J. (2021). The climate crisis, renewable energy, and the changing landscape of global energy politics. *Alternatives*, 46(3), 89-98.
- [14] Trindade, W. J., Diniz, J., Dias, J. A. A., & Rodrigues, E. P. (2012). Study of solar energy and analysis of its potential in Brazil, Northeast, and the state of Paraíba. In *VII North-Northeast Research and Innovation Congress*.
- [15] Souza, B. A., et al. (2020). Technical and economic feasibility study for the application of organic photovoltaics (OPV) in a residential building.
- [16] Ruther, R. (2004). *Photovoltaic solar buildings: The potential of photovoltaic solar energy integrated into urban buildings and interconnected with the public electricity grid in Brazil* (1st ed.). LABSOLAR.
- [17] Dias, S. H., & Schmid, A. L. (2024). *Photovoltaic buildings: Energy in architectural genesis*. Insight.
- [18] Ministry of Mines and Energy. (2024). *PDE 2034: Generation and Transmission Cost Book*. Available at: https://www.gov.br/mme/pt-br/assuntos/secretarias/sn-tep/publicacoes/plano-decadal-de-expansao-de-energia/pde-2034/caderno-de-custos-geracao-e-transmissao_pde2034-1.pdf
- [19] La Notte, L., et al. (2020). Hybrid and organic photovoltaics for greenhouse applications. *Applied Energy*, 278, 115582.
- [20] Bambara, J., & Athienitis, A. K. (2019). Energy and economic analysis for the design of greenhouses with semi-transparent photovoltaic cladding. *Renewable Energy*, 131, 1274-1287.
- [21] Davenport, T. H., De Long, D. W., & Beers, M. C. (1998). Successful knowledge management projects. *MIT Sloan Management Review*, 39(2), 43-57.

Numerical Study on the Performance Comparison of Classical and Elliptical Savonius Turbines with Various Parameters at Different Wind Variations

Sri Kurniati¹, Sudirman Syam², Nursalim³, Wellem F. Galla⁴

^{1,2,3,4}Electrical Engineering Department, Faculty of Science and Technology, University of Nusa Cendana, 85228 Kupang-Nusa Tenggara Timur, Indonesia

¹sri_kurniati@staf.undana.ac.id, ²sudirman_s@staf.undana.ac.id, ³nursalim@staf.undana.ac.id, ⁴wellem_galla@staf.undana.ac.id

Abstract—The Savonius turbine is a wind turbine that is simple and easy to make. However, this turbine has low performance at low wind speeds. The Savonius turbine can be modified to an elliptical shape to improve its performance. This research uses numerical simulations to compare the performance of classic and elliptical Savonius turbines with different wind variations. Numerical simulations were conducted using ANSYS Fluent version 15 software to solve the unstable Reynolds – Navier – Stokes (URAN) equation. The simulation results show that the velocity contour shows less wake generated by the conventional blade than the elliptical blade. The results of calculating power coefficient (CP) values with various variations in wind speed show that elliptical blades have a greater CP than conventional blades. The elliptical Savonius turbine has a higher power coefficient, greater torque, higher efficiency, and lower rotation ratio. Therefore, elliptical Savonius turbines are more suitable for various applications. The elliptical type turbine can be applied at wind speeds between 5-12 m/s, but for wind speeds of 10-12 m/s, it is better to use a classic blade because it has a higher CP than the elliptical blade.

Keywords - blade, wind power, power coefficient, wind speed

I. INTRODUCTION

Renewable energy is the main focus in overcoming global energy sustainability challenges. Wind turbines are one of the prominent innovations in the search for energy resources that are environmentally friendly and reliable. Savonius turbines, with their unique design, have become a highlight in developing renewable energy technologies. The Savonius turbine, first introduced by Sigurd Johannes Savonius in 1922 [1], differentiates itself from conventional wind turbines by its more straightforward design and ability to produce energy at low wind speeds [2,3]. This turbine consists of two or more U-shaped blades mounted on a vertical shaft. Savonius turbine blades catch the wind and direct it towards the turbine shaft. The Savonius wind turbine is a popular type of wind turbine because of its simple design and easy construction [4-6]. However, this classic Savonius turbine has several weaknesses: performance is not very good at low wind speeds, it produces fluctuating torque and low efficiency. Therefore, to increase its efficiency, research continues to be carried out to compare the performance of the Savonius turbine with more innovative designs.

Various studies have been conducted to overcome these weaknesses and develop a better shape for the Savonius turbine blade. One of the



Savonius turbine blade shapes developed is the elliptical blade shape. The Savonius wind turbine is a vertical axis wind turbine (VAWT), which consists of curved blades arranged in an elliptical shape. The Savonius elliptical turbine has a design similar to the classic Savonius turbine, but the rotor is elliptical. In contrast to traditional horizontal axis wind turbines requiring a constant and direct wind flow, Savonius turbines can operate effectively in turbulent or low wind speeds. This design is expected to overcome several limitations of the classic Savonius turbine, such as low power coefficient and unstable torque. Therefore, it is necessary to carry out in-depth studies to understand the performance comparison between the classic Savonius turbine and the elliptical variant, especially in different wind speed variations. To explore the performance of the Savonius turbine, several methods were used, as has been done by previous researchers, including computational fluid dynamics (CFD) [7-12], experimental [13-16], and a combination of experimental and numerical [17-19].

Several studies have been carried out to improve the performance of elliptical turbines, and they can be found widely in the literature. [20] carried out a parametric investigation on the power coefficient of a two-bladed Savonius rotor and found that the power coefficient can be significantly improved by selecting important geometric parameters such as height, diameter, overlap ratio, end plate dimensions, etc. Then, [12] investigated the geometry optimization of a dynamic torsion elliptical-shaped Savonius Turbine blade. The cut angle, cut corner location and overlap ratio were optimized using Solidwork's two-dimensional simulation via response surface methodology. The results of an optimization study using a central composite design show that the cutting angle, the location of the cutting angle, the interaction of the location of the cutting angle with the cutting angle, and the overlap ratio are significant factors. Other researchers have also done the same by researching general structures or optimizations on wind turbines. Many variations affect the performance of Savonius wind turbines, such as blade shape, number of blades, gap ratio, overlap ratio, and end plates [20-26].

Moreover, wind speed is essential to improve Savonius turbine performance [27]. In contrast, [28] conducted a 2D Computational Fluid Dynamic (CFD) analysis on a three-blade hybrid Savonius rotor combined with a three-blade

Darrieus turbine to increase productivity. They analyzed the flow field around a three-bladed Savonius wind turbine using a $k-\epsilon$ turbulence model. They found that an overlap of 19.87% was the optimal overlap, with the highest pressure and speed differences across the rotor. High performance of the triple-split Savonius rotor can be expected under such overlapping conditions. In addition, [29] performed 2D CFD simulations to analyze the detailed flow field and performance of the Savonius rotor using the commercial code Star-CCM+. They solved the unstable Reynolds Averaged Navier-Stokes equations using the SIMPLE (Semi-Implicit Method for Pressure-Linked Equations) algorithm for coupling speed, pressure and a realizable $k-\epsilon$ model for turbulence modelling.

Furthermore, numerical research has become a practical approach to understanding and modelling fluid flow characteristics in wind turbines. Using numerical simulations, we can gain deep insight into the flow patterns, pressure distribution, and other performance parameters in classical Savonius and elliptical turbines. In this context, this numerical study investigates the performance comparison between a classical Savonius turbine and an elliptical turbine, considering variations in wind speed. Previous research shows that elliptical Savonius turbines perform better than classical Savonius turbines at low wind speeds. However, only a few numerical studies have been carried out to compare the performance of these two types of turbines at various wind speeds. Therefore, this research aims to conduct a comparative numerical study between classical and elliptical Savonius turbines using variations in wind speed as a parameter. With a further understanding of the performance comparison of these two types of turbines, we can identify the advantages and disadvantages of each design. The results of this research are expected to provide new insights into the development of renewable energy technology and assist in selecting optimal designs for specific applications. In addition, it can contribute to developing the Savonius wind turbine to support more efficient use of renewable energy. More specifically, it is hoped to obtain optimal geometry by looking for considerable momentum and power coefficients at lower speeds, which cause low Reynolds numbers in the 4-9 m/s range according to weather conditions in Kupang, East Nusa Tenggara, Indonesia.

II. METHODOLOGY

A. Methods

This paper uses ANSYS Fluent version 15 software simulation to solve the unstable Reynolds-Naiver–Stokes equation (URAN). A coupling algorithm was used to solve the pressure-based clutch pressure speed using ANSYS Fluent. The spatial discretization concerning wind for the second-order algorithm is used for all pressure, momentum, and turbulence equations. In contrast, the least squares cell-based algorithm uses gradients to achieve high accuracy. Sliding mesh is used to model turbine rotation versus time. The moment value or moment pitching (P_m) obtained is used to calculate the moment coefficient (C_m) as follows:

$$C_m = \frac{\text{Moment Pitching}}{\text{Moment Dynamic}} = \frac{M}{\frac{1}{4} \rho A_s d V_\infty^2}, \quad (1)$$

where:

- C_m = moment coefficient
- ρ = air density (Kg/m³)
- M = moment of force on the blade (Nm)
- A_s = swept cross-sectional area (m²)
- dV^2 = air fluid speed (m/s power coefficient).

The (C_p) is calculated using the equation:

$$C_p = \frac{\text{Rotor power}}{\text{Wind power}} = \frac{Pr}{\frac{1}{2} \rho A_s d V_\infty^3}, \quad (2)$$

where: $C_p = C_m \times \lambda$, (λ = tip speed ratio).

In this simulation, two main zones are planned: the stationary domain and the rotating domain. The stationary domain includes the inlet velocity and outlet pressure. For the inlet velocity, a free wind velocity that reaches V_∞ 9 m/s in the x direction is used, the outlet is pressured, and the walls are symmetrical. The rotating domain includes turbine blades that rotate counterclockwise according to a time step. The time steps for all 2D simulations were set to 274-time steps per rotation. The rotational speed domain depends on the turbine, which is based on the speed angle and can be calculated by the

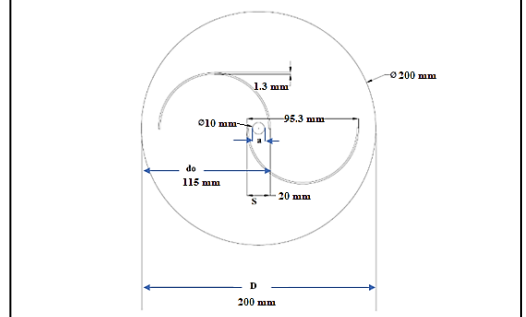


Figure 1. Classic Savonius turbine.

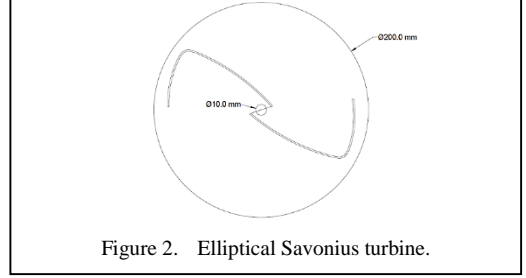


Figure 2. Elliptical Savonius turbine.

tip speed ratio (λ), defined as the linear speed of the blade tip to the undisturbed flow speed. To calculate λ , the following equation is used:

$$\lambda = \frac{\omega R}{v_\infty}, \quad (3)$$

where:

- λ is the Tip Speed Ratio (TSR) (without units)
- ω is the rotor angular speed (rad/s)
- R is the radius of the turbine rotor (m)
- V is wind speed (m/s).

B. Geometry

The classic turbine geometry to be tested is shown in Fig. 1.

Information:

- do = turbine diameter
- a = diameter of the shaft located at the centre of the rotor
- S = rotor overlap, and
- D = rotor diameter.

Fig. 1 shows a classic type turbine from Savonius, which consists of two semicircular blades, usually called conventional blades. In this case, the simulation domain has two main zones: the inner domain is the outer domain. The inner domain is a rotating circular domain close to the

turbine to simulate the rotor mechanism and its angular changes over time. As a comparison, to find out whether there is a difference in power coefficient, the conventional type turbine will be engineered by changing the blade to an elliptical type. To find out the difference between the conventional type and the elliptical model, numerical studies or CFD are numerical calculations to solve partial differential equations (PDE) into algebraic equations that can be calculated using computer assistance. Fig. 2 shows the geometry of an elliptical-type turbine.

III. RESULTS AND DISCUSSION

A. Simulation

The pressure and velocity contours of the conventional Savonius blade and the elliptical blade design are shown in Figs. 3 and 4, respectively. The velocity contours show that the conventional blade generates less wake than the elliptical blade. The pressure contour plot shows the pressure difference between upstream and downstream around the rotor. The red area on the blade indicates a higher-pressure rise, while the blue area indicates a lower pressure. The pressure increase on the original blade is relatively more significant than the modified blade because it has a more circular blade shape. In contrast, the

elliptical blade only has a circular shape at the tip of the blade. This shape optimization makes the difference between these two blades.

On the convex side of both blades, static pressure can be seen under the concave side of the blade. However, in reality, there is negative pressure on the convex side of the blade due to the high flow velocity at the convex tip of the blade. Therefore, there is a pressure difference between the convex and concave sides of the blade, which provides the torque required to rotate the blade.

B. Angular Speed Calculation

1) Angular speed value of TSR variations

Savonius turbine performance is influenced by various factors, including TSR (λ). TSR (λ) is the ratio between the tip speed of the turbine blade and the wind speed. The optimal TSR value for Savonius turbines ranges between 0.5 and 1.5. At a lower TSR, the turbine cannot produce enough power, while at a higher TSR, the turbine will stall, and Figefficiency will decrease. The effect of TSR variations based on Eq. (3) will directly impact the turbine's angular speed. Using a rotor radius of 0.1 m at an air

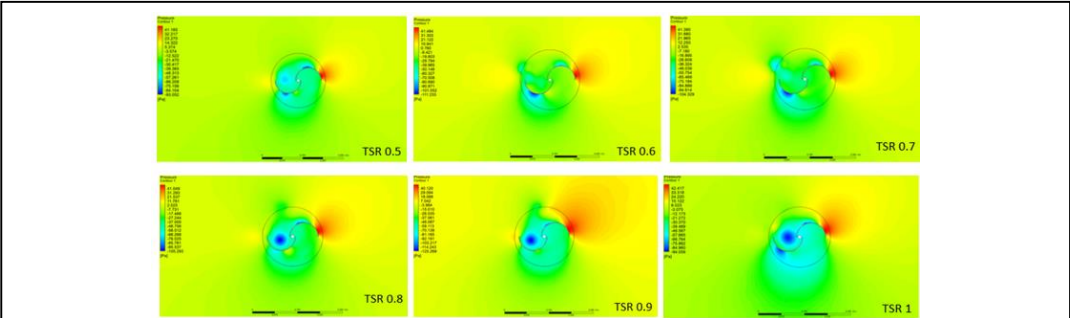


Figure 3. Classic Savonius turbine simulation (TSR 0.5 - 1).

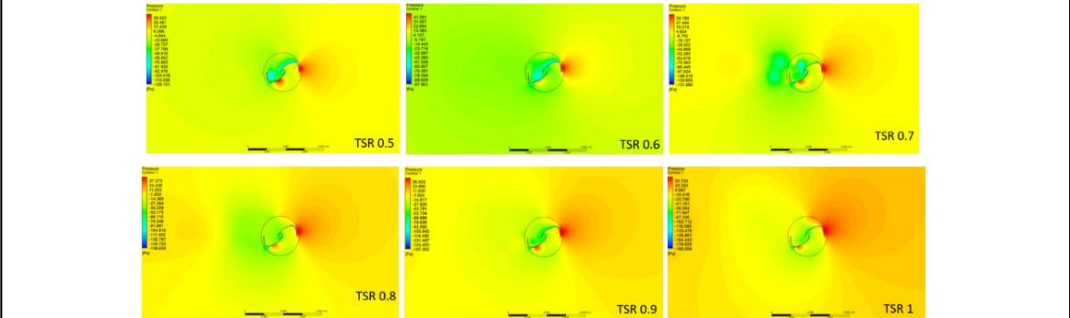


Figure 4. Elliptical Savonius turbine simulation (TSR 0.5 - 1).

TABLE I. ANGULAR SPEED VALUES ACCORDING TO TSR .

ω	0.5	0.6	0.7	0.8	0.9	1	1.5
Rad/s	45	54	63	72	81	90	135

TABLE II. ANGULAR SPEED VALUES ACCORDING TO VARIATIONS IN WIND SPEED .

V	m/s	6	7	8	9	10	11	12
ω	rad/s	48	56	64	72	80	88	96

speed of 9 m/s shows that the higher the TSR, the higher the turbine angular speed (Table I).

Based on Table I, the effect of TSR on angular speed is that at low TSR, the angular speed of the Savonius turbine increases linearly with TSR. At optimal TSR, the angular velocity reaches its maximum value, and at high TSR, the angular speed decreases due to the stall effect on the turbine blade. Furthermore, other factors influencing angular speed are turbine blade design (shape, curvature, angle), diameter, number of turbine blades, and load applied to the turbine.

2) Angular speed value from variations in wind speed

The angular speed value of a Savonius turbine is directly proportional to the wind speed. The constant of proportionality between wind speed and angular speed depends on the turbine's design, size and material. Apart from wind speed, several other factors can influence the turbine's angular speed, such as wind incidence angle, resistance torque, and inertia. To get optimal performance, the angular speed value needs to be optimised. That can be done by adjusting the turbine design: The shape and dimensions of the blades and the materials used can influence the angular speed value and set the TSR. The optimal TSR value for a Savonius turbine is generally between 0.8 to 1.2.

Furthermore, the angular speed value from variations in wind speed significantly influences the Savonius turbine's performance. Savonius turbine designers and users can maximize the energy produced by understanding and optimizing this relationship. A high angular speed value can produce greater torque and faster rotation. *Torque* is the rotating force produced by the turbine. The higher the torque, the greater the power produced. In addition, fast rotation allows the turbine to produce more electrical energy. However, it should be noted that an angular

speed value that is too high can cause turbine instability and excessive noise, which can cause the turbine to vibrate and sway violently, damaging turbine components. This paper uses the optimal angular speed, namely 0.8, with wind speed variations of 6 – 12 m/s, as shown in Table II.

3) Moment of force on the blade (Moment pitching)

The moment of force on the blade, known as the moment pitching (Pm), is the force generated by fluid flow around the blade, which causes the blade to rotate about the pitch axis (the axis perpendicular to the blade chord). This force moment is essential in blade aerodynamic performance, including pitch control, stability, and performance. The moment of force is used to control blade pitch, which determines the blade's angle of attack and the resulting lift force. The moment of force helps maintain blade stability and prevents it from vibrating or rotating uncontrollably. Therefore, the force moment can be optimized to increase blade efficiency and power output.

Several factors influence the moment of force, including angle of attack, flow speed, blade shape, air density and fluid viscosity. The blade's angle of attack relative to the airflow is the main factor influencing the moment of force. A larger angle of attack results in a more significant moment of force. A higher airflow velocity will produce a more significant force moment, where the blade shape, such as aerodynamic profile and thickness, influences the force moment. Additionally, higher air density results in greater force moments and fluid viscosity can influence fluid flow around the blade. The moment of force on the blade can produce various effects, such as rotation, stability and blade performance. An optimistic moment of force causes the blade to rotate upwards, while a negative moment causes the blade to rotate downwards. Meanwhile, a stable moment of force helps keep the blade in position, while an unstable moment can cause the blade to vibrate or sway. In other words, the optimal moment of force helps the blade produce maximum power. Fig. 5 compares the moment of force on the blade between a classic and elliptical turbine. It can be seen that the elliptical turbine has a higher moment of force compared to the classical turbine, with an angular speed variation of 0.5 -1.

C. Moment Dynamic (DM)

Moment dynamic is used to calculate the torque produced by the Savonius turbine. This torque can generate electricity, pump water, or drive machinery. In other words, the dynamic moment is the force that causes the Savonius turbine rotor to rotate. The difference in air pressure between the front and rear sides of the rotor generates this force. The curved shape of the rotor causes this pressure difference. That means that dynamic moments affect the performance of the Savonius turbine. High torque is needed to accelerate the rotor and overcome friction forces. The high moment of inertia makes it more difficult for the rotor to accelerate and stop. Therefore, the Savonius turbine design can be optimized to increase the dynamic moment. That can be done by increasing the rotor area, increasing the power coefficient, reducing the rotor mass, and reducing the friction force. The dynamic moment with a speed variation of 5-9 m/s shown in Fig. 6.

D. Moment Coefficient (CM)

The moment coefficient (CM) is an essential parameter in understanding the performance of Savonius wind turbines. CM indicates the turbine's ability to produce torque, ultimately determining the power produced. CM is defined as the ratio between the moment generated by the wind turbine (moment pitching) and the moment dynamic, as formulated in Eq. 1. CM is influenced by several factors, including TSR, wind speed, shape, blade design, and number of

blades. Higher TSR generally results in higher CM and increases with wind speed. Additionally, more blades generally result in a higher CM but can increase cost and complexity.

Furthermore, CM is an essential parameter in predicting the performance of Savonius wind turbines: CM can be used to predict the torque and power produced by the turbine under certain wind conditions. CM can also be used to optimize the Savonius wind turbine design by modifying the factors that influence it. CM's effects on Wind Turbine Performance include producing higher power and efficiency. Thus, to maximize CM in various operating conditions, the Savonius wind turbine design must be optimal. By using Eq. (1), the C_m value obtained in a classic turbine with a wind speed of 9 m/s and an angular speed of 0.5 is as follows:

$$C_m = \frac{0.00804}{4.96 \text{ Kg}m / s^2} = 0.001621 \quad (4)$$

Next, Fig. 7 show the C_m value based on TSR variations and moment coefficient variations on speed variations. The images compare the C_m value concerning variations in TSR and speed, showing that the elliptical turbine is higher than the classical turbine.

E. Input Power (Wind power)

The relationship between wind power and wind speed variations can be explained through Betz's Law, which states that the maximum power that can be extracted from the wind by a wind turbine is 59.3% of the available wind kinetic power. Wind power is proportional to the cube of wind speed. That means that if the wind speed is doubled, the wind power will increase eightfold.

Table III shows the results of calculating wind power variations with wind speed variations from 5–12 m/s. As a sample calculation at a speed of 9 m/s.

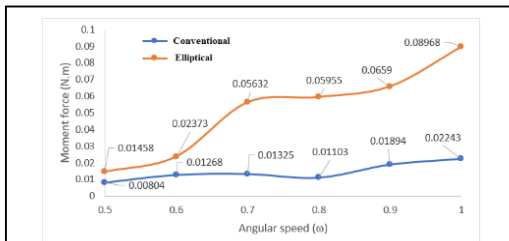


Figure 5. Moment of force on the blade.

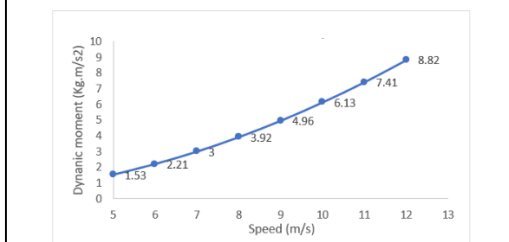


Figure 6. Moment dynamics at varying speeds.

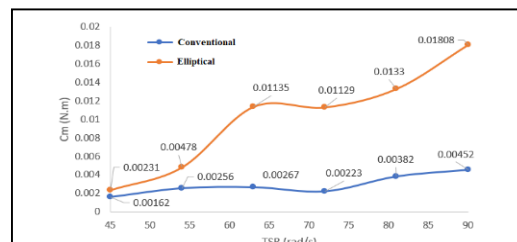


Figure 7. C_m vs TSR variations.

TABLE III. WIND POWER AT VARYING WIND SPEED.

No.	Speed (m/s)	Windpower (Kg.m ² /s ³)
1.	5	15.31
2.	6	26.46
3.	7	42.02
4.	8	62.72
5.	9	89.30
6.	10	122.50
7.	11	163.05
8.	12	211.68

Based on Table III, it can be seen that wind power is proportional to the square of the wind speed. If the wind speed doubles, the wind power will be squared or increased fourfold. That can happen because an increase in wind power causes an increase in wind kinetic energy. An increase in kinetic energy causes an increase in wind speed.

F. Power Coefficient (CP)

Power coefficient (C_p) is an essential parameter in the performance of wind turbines, including Savonius turbines. C_p shows how efficiently the turbine converts wind energy into mechanical energy. The higher the C_p , the greater the turbine's power for a certain wind speed. That is important to maximize the energy obtained from the turbine. It indicates high torque is required to drive a generator or other load. Likewise, C_p is closely related to turbine efficiency. The higher the C_p , the more efficient the turbine converts wind energy into mechanical energy. Fig. 8 compares the magnitude of C_p between classical and elliptical turbines with varying TSR. Based on this, the elliptical turbine shows more excellent C_p performance than the classical design. Just as in the calculation, the moment value of the elliptical blade shows a significant pitching moment compared to conventional blades by the simulation results at TSR 0.5-1.

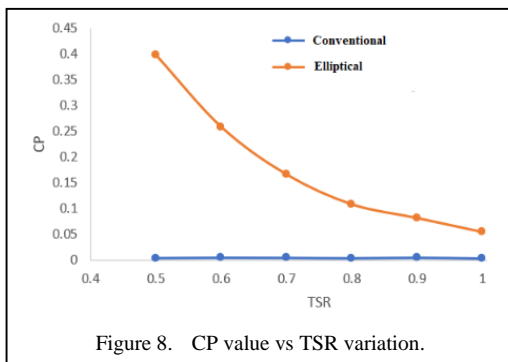


Figure 8. C_p value vs TSR variation.

IV. DISCUSSION

A comprehensive overview of the rapid use of CFD in the past two decades has seen significant improvements in numerical flow simulations in Savonius turbine performance testing. Based on the simulation results, the elliptical Savonius turbine performs better than the classic Savonius turbine in all wind variations. The same thing has been reported numerically by [9], namely, that elliptical blades have higher coefficients than conventional blades. Several factors influence this, including the elliptical design having a slimmer elliptical shape, which produces less aerodynamic resistance so that the turbine can rotate more efficiently [8]. In addition, the elliptical Savonius turbine has a larger area than the classic Savonius turbine with the same aspect ratio. That allows the turbine to capture more wind energy. In addition, because the Savonius elliptical turbine has a larger area, the surface area increases, which results in a higher aspect ratio. As a result, a higher aspect ratio results in a larger turbine surface area, making it possible to capture more wind energy. A higher aspect ratio produces greater torque, thereby increasing the power produced by the turbine. That has been proven experimentally by [29] that determining a blade with an optimal configuration involving aspect ratio, turbine height, and overlap ratio is necessary to obtain high power and torque in an elliptical turbine.

V. CONCLUSIONS

Overall, using analysis of various parameters shows that the Savonius elliptical wind turbine performs better than the classic Savonius turbine. All parameters such as TSR, angular speed, pitching moment, dynamic moment, wind power, coefficient moment and power coefficient were tested numerically with varying wind speeds of 6 – 12 m/s. A comparison of the simulation and calculation results of the two turbines shows significant differences where the elliptical blades dominate with higher values at low speeds. For the record, the classic Savonius turbine with a wind speed of 10 – 12 m/s has a higher C_p than the elliptical blade, which shows that this type of turbine is suitable for application at higher wind speeds than the elliptical blade.

ACKNOWLEDGEMENT

The author would like to thank the Dean of the Faculty of Science and Engineering, Nusa Cendana University-Kupang, for carrying out

this research activity in the form of DANA DIPA PNBP. This research activity was carried out under Contract Agreement No. No. SP-DIPA 023.17.2.677528/2023, 30 November 2022, Fiscal Year 2023, with Activity Code 4471.DBA.004.051.B MAK 52511 Fiscal Year 2023.

REFERENCES

- [1] Tabassum, S., et al. (2015). Design and analysis of different types of rotors for pico-turbine. *Smart Grid and Renewable Energy*, 6(6), 141–147.
- [2] Abraham, J. P., et al. (2012). Summary of Savonius wind turbine development and future applications for small-scale power generation. *Journal of Renewable and Sustainable Energy*, 4(4).
- [3] Worasinchai, S., & Suwannakij, K. (2018). Performance characteristics of the Savonius turbine. *IOP Conference Series: Materials Science and Engineering*, 297(1).
- [4] Zemamou, M., Aggour, M., & Toumi, A. (2017). Review of Savonius wind turbine design and performance. *Energy Procedia*, 141, 383–388.
- [5] Maldonado, R. D., et al. (2014). Design, simulation, and construction of a Savonius wind rotor for subsidized houses in Mexico. *Energy Procedia*, 57, 691–697.
- [6] Mahmoud, N. H. (2012). An experimental study on improvement of Savonius rotor performance. *Alexandria Engineering Journal*, 51(1), 19–25.
- [7] Pranta, M. H., Rabbi, M. S., & Roshid, M. M. (2021). A computational study on the aerodynamic performance of modified Savonius wind turbine. *Results in Engineering*, 10.
- [8] Alom, N., et al. (2016). Aerodynamic design optimization of elliptical-bladed Savonius-style wind turbine by numerical simulations. *Proceedings of the International Conference on Offshore Mechanics and Arctic Engineering (OMAE, Vol. 6)*.
- [9] Kacprzak, K., Liskiewicz, G., & Sobczak, K. (2013). Numerical investigation of conventional and modified Savonius wind turbines. *Renewable Energy*, 60, 578–585.
- [10] Saeed, H. A. H., Nagib Elmekawy, A. M., & Kassab, S. Z. (2019). Numerical study of improving Savonius turbine power coefficient by various blade shapes. *Alexandria Engineering Journal*, 58(2), 429–441.
- [11] Kaya, A. F., Acir, A., & Kaya, E. (2023). Numerical investigation of wind-lens combinations for improving aerodynamic performance of an elliptical-bladed Savonius wind turbine. *Journal of the Brazilian Society of Mechanical Sciences and Engineering*, 45(6), 3–4.
- [12] Fetalver, C. F., & Mortel, C. M. (2022). Numerical simulation of two-dimensional elliptical shape Savonius wind turbine blade using response surface methodology. *AIP Conference Proceedings*, 2534.
- [13] Kamoji, M. A., Kedare, S. B., & Prabhu, S. V. (2009). Experimental investigations on single stage modified Savonius rotor. *Applied Energy*, 86(7–8), 1064–1073.
- [14] Wenehenubun, F., Saputra, A., & Sutanto, H. (2015). An experimental study on the performance of Savonius wind turbines related with the number of blades. *Energy Procedia*, 68, 297–304.
- [15] Al Absi, S. M., et al. (2021). An experimental test of the performance enhancement of a Savonius turbine by modifying the inner surface of a blade. *Materials Today: Proceedings*, 42, 2233–2240.
- [16] Al-shammari, S. A., et al. (2020, October). Optimization and experimental investigation of Savonius wind turbine performance at low wind speed conditions. *International Journal of Mechanic and Mechatronics Engineering*, 20(5), 128.
- [17] Akkus, M. B., Haksever, Z., & Teksin, S. (2022). Experimental and numerical analysis of Savonius wind turbine with end plate on various types. *Energy and Environmental Storage*, 2(2), 54–63.
- [18] Kalluvila, J. B. S., & Sreejith, B. (2018). Numerical and experimental study on a modified Savonius rotor with guide blades. *International Journal of Green Energy*, 15(12), 744–757.
- [19] Al-Gburi, K. A. H., et al. (2022). Experimental and simulation investigation of performance of scaled model for a rotor of a Savonius wind turbine. *Energies*, 15(23).
- [20] Altan, B. D., Atilgan, M., & Özdamar, A. (2008). An experimental study on improvement of a Savonius rotor performance with curtaining. *Experimental Thermal and Fluid Science*, 32(8), 1673–1678.
- [21] Zhao, Z. (2009). Research on the improvement of the performance of Savonius rotor based on numerical study. *2009 International Conference on Sustainable Power Generation and Supply*, 1–6.
- [22] Altan, B. D., & Atilgan, M. (2012). A study on increasing the performance of Savonius wind rotors. *Journal of Mechanical Science and Technology*, 26(5), 1493–1499.
- [23] Bhutta, M. M. A., et al. (2012). Vertical axis wind turbine: A review of various configurations and design techniques. *Renewable and Sustainable Energy Reviews*, 16(4), 1926–1939.
- [24] Morshed, K. N., et al. (2013). Wind tunnel testing and numerical simulation on aerodynamic performance of a three-bladed Savonius wind turbine. *International Journal of Energy and Environmental Engineering*, 4(1), 1–14.
- [25] Rassoulinejad-Mousavi, S. M., Jamil, M., & Layeghi, M. (2013). Experimental study of a combined three-bucket H-rotor with Savonius wind turbine. *World Applied Sciences Journal*, 28(2), 205–211.
- [26] Ying, P., Chen, Y. K., Xu, Y. G., & Tian, Y. (2015). Computational and experimental investigations of an omni-flow wind turbine. *Applied Energy*, 146, 74–83.
- [27] Teksin, S., Azginoglu, N., & Akansu, S. O. (2022). Structure estimation of vertical axis wind turbine using artificial neural network. *Alexandria Engineering Journal*, 61(1), 305–314.
- [28] Gupta, R., & Biswas, A. (2011). CFD analysis of flow physics and aerodynamic performance of a combined three-bucket Savonius and three-bladed Darrieus turbine. *International Journal of Green Energy*, 8(2), 209–233.
- [29] Zhou, T., & Rempfer, D. (2013). Numerical study of detailed flow field and performance of Savonius wind turbines. *Renewable Energy*, 51, 373–381.

Numerical Study of Nanofluid Forced Convection in a Channel with Flexible Vortex Generators

Khaoula Dedouh¹, Brahim Fersadou², Henda Kahalerras³

^{1,2,3}University of Sciences and Technology Houari Boumediene (USTHB), Algeria.

¹kdedouh@usthb.dz, ²bfersadou@usthb.dz, ³hkahalerras@usthb.dz

Abstract—A numerical study was conducted to analyze the effect of the fluid-structure interaction of a flexible vortex generator (FVG) integrated into a channel filled with a nanofluid in an unsteady laminar regime. The channel walls feature alternating hot and cold sources separated by an adiabatic zone. A hydrothermal performance study was undertaken by adapting several configurations while modifying the position and number of FVGs. The results were presented as temporal evolutions of isotherms, iso-velocities, and iso-pressures. Time-averaged results presented the evolution of the average Nusselt number, pressure drop, and Performance Evaluation Coefficient (PEC) for the different FVG configurations. The finite element method (FEM) was used to solve the system of equations along with the associated boundary conditions. The Arbitrary Lagrangian-Eulerian (ALE) method was employed to track the dynamic movement of the structures within the nanofluid. The results show that the oscillatory motion of the FVG effectively reduces the thermal boundary layer, thereby enhancing heat transfer. The highest average Nusselt number at the upper heated boundaries was achieved with an asymmetric FVG configuration, where the lower FVG was positioned at the front. The maximum PEC of 1.54 was obtained with a symmetric FVG configuration.

Keywords - flexible vortex generator, fluid structure interaction, thermal mixing, electronic cooling systems

I. INTRODUCTION

Heat transfer is a crucial area that has been widely investigated and has extensive applications in industry and engineering. If the heat generated during the operation is not effectively managed, it can compromise the reliability and effectiveness of the devices. In recent years, the militarization of electronic devices has increased energy consumption due to the elevation of electronic device's temperature. Researchers have geared toward effective cooling solutions to address the thermal management challenges that ensure effective heating extraction with minimized energy consumptions. In the literature, the mixing of cold fluid flow with a heated surface has been investigated; a passive rigid or flexible obstacle has been integrated into flow channels to generate the vortex-shedding effect. This approach has demonstrated its effectiveness in reducing thermal boundary layers and enhancing the overall heat transfer of these systems. The study [1] investigated the flow behavior and heat transfer features of two flexible wings mounted at the bottom of a channel's wall. The authors reported that the flexible wings deflect in three modes: deflection, vibration, and flapping mode. Additionally, they found that the vortices induced by the fluid-structure interaction promoted heat transfer, where at $E = 0.4$ MPa and $Re = 1625$, a PEC of 1.145 was achieved. In the study by [2], an inclined flexible vortex



was mounted at the bottom channel's wall. The authors investigated the dynamics and thermal performances of the systems and found that augmentation in the inclination angle promotes heat transfer. The study also found that the maximum heat flux is obtained when the transition mode occurs as the bending rigidity increases. Reference [3] numerically analyzed the heat transfer in a channel equipped with a pair of flexible vortex generators mounted in an asymmetric configuration on the upper and lower channel walls. The parametric study revealed that thermal performance improved by 122% compared to the baseline flow at a bending rigidity of 0.06, an initial inclination angle of 75° , and a gap distance of 2.4 times the length of the vortex generators. In the study conducted by [4], a square obstacle is placed at the centerline of a microchannel, followed by a flexible vortex fixed at its lower wall. The analysis confirmed that the overall average Nu, the mixing index, and thermohydraulic performance factor were increased by 31.4%, 14.5%, and 32%, respectively, compared to a channel with a rigid vortex generator. [5] studied the fluid-structure interaction effect on heat transfer enhancement of flexible structures attached vertically at a heated surface. The authors observed that the baffle oscillates in a stable or periodic vibration mode. When the baffle flaps are in periodic mode, heat transfer improves by up to 12%. They also noted that the maximum heat transfer improvement, ranging from 9% to 12%, occurs at the highest Rayleigh number ($Ra = 3.5 \times 10^9$) and a bending rigidity of $EB = 3.5 \times 10^5$. In this paper, we investigate the thermal behavior of nanofluid flow undergoing a self-sustained oscillation process, along with the associated flow and structural dynamics. Five configurations differ in the number and position of flexible vortex generators (FVGs) and are compared. The optimal configuration is identified within the specified range of parameters.

II. MATHEMATICAL MODELING

The present study examines unsteady forced convection in a channel. Heat sources with a constant temperature of $T_h = 363.15$ [K] are placed on the first section of the upper wall and the second section of the lower wall of the channel. The center section is insulated, while the remaining surfaces are maintained at a cold temperature of $T_c = 298.15$ [K] as illustrated in Fig. 1. The working fluid is MWCNT-water

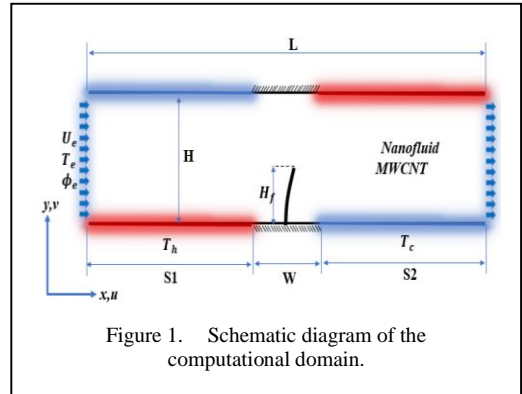


Figure 1. Schematic diagram of the computational domain.

nanofluid, which enters the channel with a pulsed velocity of $f = 10$ [Hz], an initial velocity of $u_0 = 0.04$ [m/s], and a constant cold temperature of $T_i = 298.15$ [K]. A flexible vortex generator (FVG) with a length of $H_f = 0.45$ [cm] and a Young's modulus of $E = 5 \times 10^6$ [Pa] is attached to the channel walls in different arrangements, corresponding to five configurations:

- Configuration C1: The FVG is mounted at the midpoint of the lower wall.
- Configuration C2: The FVG is placed at the midpoint of the upper wall.
- Configuration C3: Two FVGs are symmetrically positioned on the upper and lower walls.
- Configuration C4: Two FVGs are asymmetrically arranged, with the bottom FVG and the top FVG positioned at the front and the rear, respectively.
- Configuration C5: Two FVGs are asymmetrically distributed. The upper FVG is positioned at the front, while the lower FVG is placed at the rear.

The governing equations used to solve the described physical problem, along with their boundary conditions, are formulated as follows:

For nanofluid domain:

Continuity equation:

$$\frac{\partial u}{\partial x} + \frac{\partial v}{\partial y} = 0 \quad (1)$$

Momentum equation:

$$\rho_{nf} \frac{\partial u}{\partial t} + \rho_{nf} \left((u - u_m) \frac{\partial u}{\partial x} + (v - v_m) \frac{\partial v}{\partial y} \right) = -\frac{\partial p}{\partial x} + \mu_{nf} \left(\frac{\partial^2 u}{\partial x^2} + \frac{\partial^2 u}{\partial y^2} \right), \quad (2)$$

$$\rho_{nf} \frac{\partial v}{\partial t} + \rho_{nf} \left((u - u_m) \frac{\partial u}{\partial x} + (v - v_m) \frac{\partial v}{\partial y} \right) = -\frac{\partial p}{\partial y} + \mu_{nf} \left(\frac{\partial^2 v}{\partial x^2} + \frac{\partial^2 v}{\partial y^2} \right). \quad (3)$$

Energy Equation:

$$(\rho C_p)_{nf} \left((u - u_m) \frac{\partial T}{\partial x} + (v - v_m) \frac{\partial T}{\partial y} \right) = K_{nf} \left(\frac{\partial^2 T}{\partial x^2} + \frac{\partial^2 T}{\partial y^2} \right), \quad (4)$$

where u_m and v_m represent the mesh displacement velocity components. In the coupling iteration, and are determined by the displacement of the structure interface and mesh deformation of the fluid domain [6].

For the solid domain, geometric nonlinearity is considered to analyze the large deformations occurring in the solid. Additionally, the Neo-Hookean model is applied to characterize the stress-strain nonlinear behavior of the hyper-elastic material under large deformations [7].

Displacement equation:

$$\rho_s \frac{\partial^2 u}{\partial t^2} = \nabla \cdot \mathbf{F} \mathbf{S}, \quad (5)$$

$$\mathbf{F} = \mathbf{I} + \nabla \mathbf{u}, \quad (6)$$

$$\mathbf{S} = 2 \frac{\partial \mathbf{W}}{\partial \mathbf{C}}. \quad (7)$$

\mathbf{W} is the strain energy density function and \mathbf{C} is the right Cauchy-Green deformation tensor, defined as:

$$\mathbf{C} = \mathbf{F}^T \mathbf{F}. \quad (8)$$

The strain energy density is defined as:

$$\mathbf{W} = \frac{1}{2} \mu (\mathbf{I}_1^c - 3) - \mu \ln J + \frac{1}{2} \lambda (\ln J)^2. \quad (9)$$

Energy Equation of the solid domain:

$$(\rho C_p)_s \left(\frac{\partial T}{\partial t} \right) - \nabla \cdot (\mathbf{K} \nabla T) = 0. \quad (10)$$

Boundary conditions:

At the inlet:

$$u_i = u_o \times (1 + \text{Amp} \times \sin(2\pi ft)), \quad v = 0, \quad T_i = 298.15K. \quad (11)$$

At the outlet:

$$\frac{\partial u}{\partial x} = v = p_{out} = 0, \quad \frac{\partial T}{\partial x} = 0. \quad (12)$$

At the fin surface:

We assumed a continuity of dynamic motion and kinematic forces:

$$\frac{\partial d_s}{\partial t} = u; [-P + \mu_{nf} \nabla u] n - \sigma n = 0. \quad (13)$$

Energy balance equation:

$$K_{nf} \left. \frac{\partial T}{\partial n} \right|_{nf} = K_s \left. \frac{\partial T}{\partial n} \right|_s. \quad (14)$$

Energy balance equation:

$$u = v = 0, T_h = 363.15K. \quad (15)$$

At the cold source:

$$u = v = 0, T_c = 398.15K. \quad (16)$$

Insulated surfaces:

$$u = v = 0, \frac{\partial T}{\partial y} = 0. \quad (17)$$

Heat transfer is represented by the local Nusselt number defined as:

$$Nu_i = \frac{hH}{K_{nf}}, \quad (18)$$

where $i=1, i=2$ refer to the bottom heated source and upper heated source, respectively.

While the average Nusselt number is determined by the following expression:

$$Nu_{av} = \frac{1}{S} \int_0^S Nu dx. \quad (19)$$

The average Nusselt number of the two hot surfaces is defined by:

$$Nu_{av} = (Nu_{av1} + Nu_{av2}) / 2. \quad (20)$$

The time-averaged global Nusselt number is expressed as:

$$Nu_{g1,2} = \frac{1}{t} \int_0^{t_{max}} Nu_{av1,2} dt, \quad (21)$$

$$Nu_g = \frac{1}{t} \int_0^{t_{max}} Nu_{av} dt. \quad (22)$$

The pressure loss between the cavity inlet and outlet is given by:

$$\Delta P = p_{av}(x=0) - p_{av}(x=L). \quad (23)$$

The average pressure drops over time is given by:

$$\Delta P = \frac{1}{t} \int_0^{t_{max}} \Delta P dt. \quad (24)$$

A Performance Evaluation Coefficient is used to compare heat transfer improvements to pressure drop losses. It is defined as:

$$PEC = \frac{Nu_g / (Nu_g)_{ref}}{\left(\frac{\Delta P}{\Delta P_{ref}} \right)^{1/3}}. \quad (25)$$

The reference case corresponds to a non-pulsed flow case ($Amp = 0$) with a rigid turbulator ($u_m = 0$) in each configuration.

III. NUMERICAL PROCEDURES

The unsteady, no-linear studied system is numerically solved using the finite element method. The interaction between the solid and fluid domains is computed using the Arbitrary Lagrangian-Eulerian (ALE) approach, which is widely used to compute the coupling of the fluid field with the structure dynamics. The computational domain is discretized into the unstructured triangular mesh and refined near the solid-fluid surface interface. A grid with 37,118 cells has been adopted to ensure the accuracy and time convergence of the solutions.

IV. RESULTS AND DISCUSSION

Fig. 2 shows the instantaneous velocity field for the five configurations at four different time instants. It is evident that the flow layers are separated and disturbed. Additionally, the velocity in all configurations increases as the flexible vortex generator (FVG) deflects. The FVG deforms due to the periodic dynamic forces exerted by the nanofluid flow. As the FVG bends, its frontal area decreases, causing the restoring force to dominate over the dynamic force, which diminishes due to the reduction in pulsed flow inlet velocity. Subsequently, the elastic flags attempt to return to their original state.

The motion of the nanofluid over the oscillating FVG generates circulating vortices downstream of the FVG, which move toward the channel outlet. When the position of the FVG is reversed on the upper wall, as shown in configuration C2, the same self-induced vibration process occurs. The upward and backward motion of the free end of the FVG causes rotating eddies to form and Move along the upper heated surface. The high-velocity core flow is redirected toward the lower wall instead of the upper wall, as seen in configuration C1.

In configuration C3, the nanofluid flow is obstructed by pair symmetric FVGs, forcing it through the confined section with increased velocity. Vortices are generated downstream of both FVGs, distributing the flow. A small volume of nanofluid continues to flow close to the centerline of the channel. At $t = 3$ [s], the vortices near the upper wall dissipate, while those near the lower wall develop and deflect the accelerated core flow toward the upper heated surface.

Configuration C4 involves two FVGs with an asymmetrical distribution. Despite the presence of a pair of FVGs, vortex shedding is only observed from the upper FVG. The accelerated core flow is deflected by the upper FVG toward the lower wall, suppressing the vortices generated downstream of the lower FVG.

Two asymmetric FVGs are also involved in configuration C5, where the upper FVG is located at the front, while the lower FVG is placed further back. Similar to the flow behavior of configuration C4, the oscillating motion of the rear FVG produces rotating eddies. In contrast, the nonfluid flow deviated by the lower FVG dissipates those generated by the upper FVG.

From the temperature field illustrated in Fig. 3, we observe the effect of fluid-structure interaction on the reduction of the thermal boundary region, mainly where the upper heat boundary layer experienced more disruption than the lower one. The number and location of FVGs significantly impact the layer near the heat source, as illustrated in Fig. 4 and supported by Nu number results in Fig. 6.

In configuration C1, despite the circulation of vortices near the cold surface, the accelerated nanofluid flow changes direction toward the upper heated surface. This is expected to enhance convective heat transfer near the upper hot region compared to the area upstream of the FVG, where the velocity is lower and more uniform.

In configuration C2, the hot zone is located behind the upper FVG; its thermal boundary is disturbed by the oscillating eddies advancing along it. In configuration C3, we notice that the nanofluid flow is highly disrupted by the dynamics of the two symmetric FVGs; as a result, the rotating vortices interact with hot thermal boundaries with high velocity. In addition, they break the nanofluid flow into segments; those segments penetrate the thermal boundary layer and enhance the convective heat flux.

In configuration C4, the flow moves across the two asymmetric FVGs at an elevated velocity and is deflected toward the lower wall, allowing vortices to develop and circulate near the upper heated surface. The circulation of stretched eddies mixes the hot near-wall nanofluid with the colder mainstream, reducing the temperature of the upper heat source.

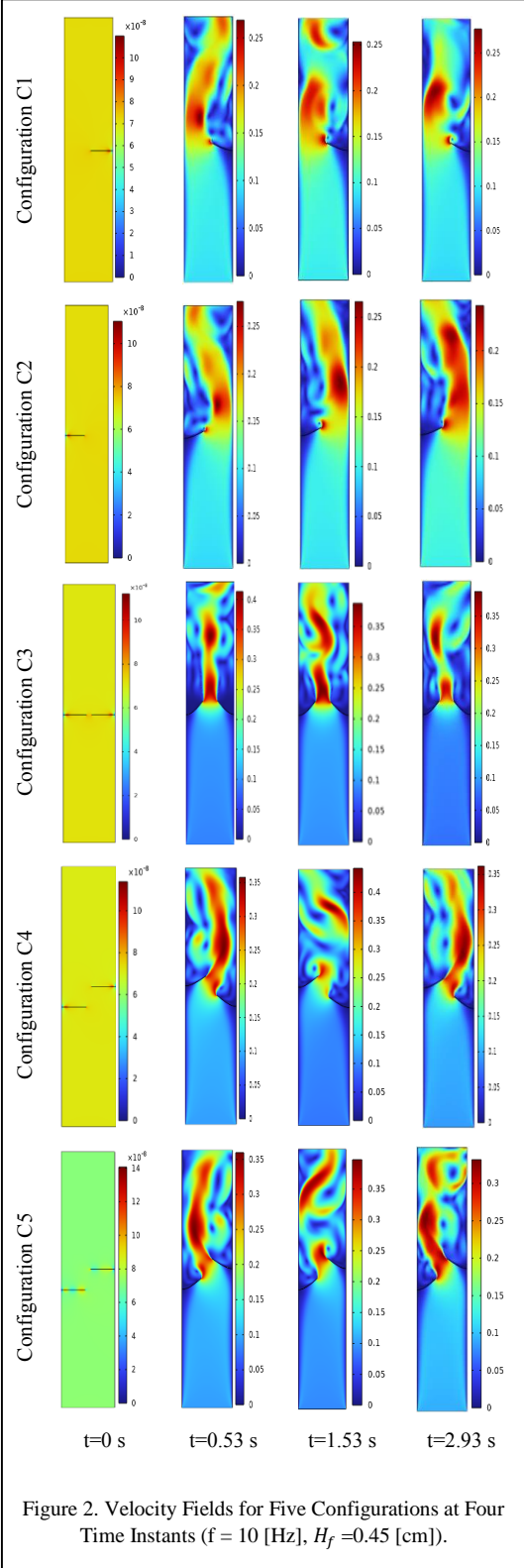
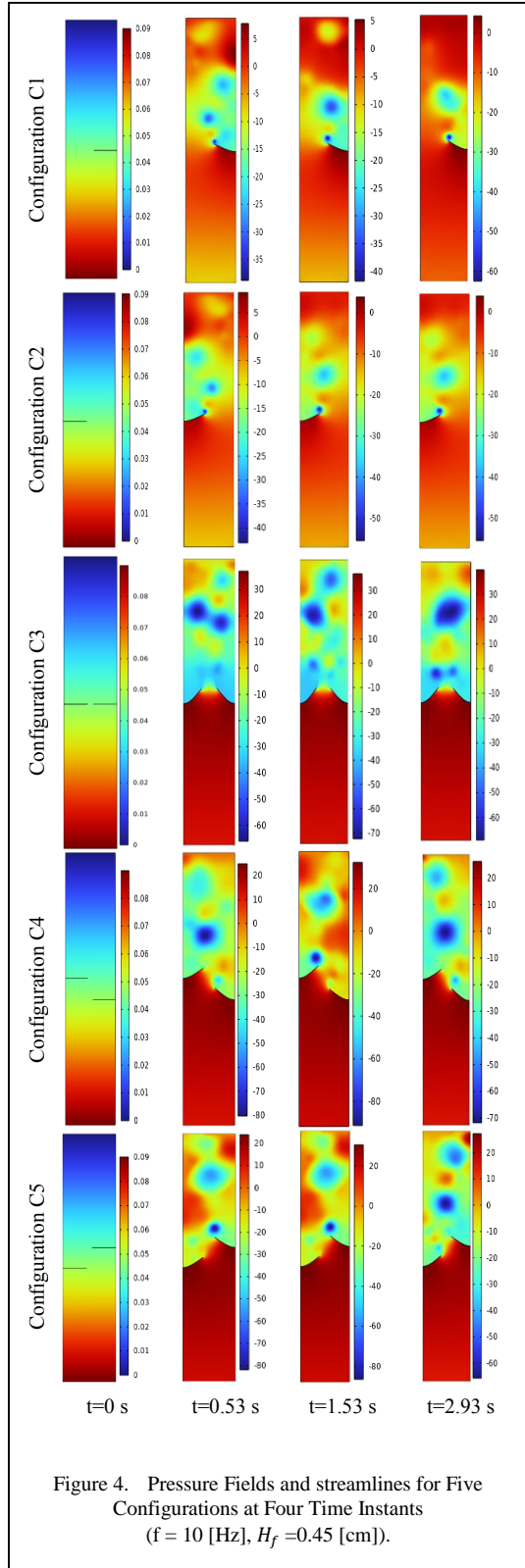
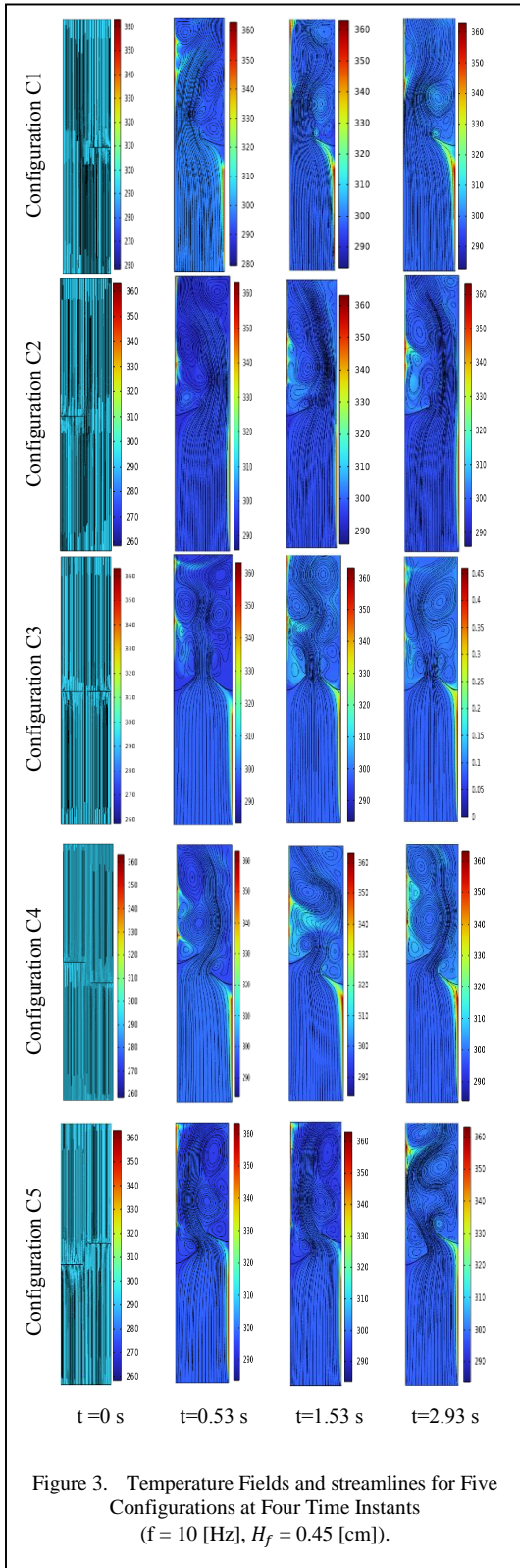


Figure 2. Velocity Fields for Five Configurations at Four Time Instants ($f = 10$ [Hz], $H_f = 0.45$ [cm]).



In configuration C5, the lower bending FVG directs the accelerated nanofluid flow toward the heated surface. Additionally, the vortex core developed downstream of the lower FVG pushes the cold core flow to continuously contact and interact with the upper heat source, thereby increasing heat removal.

Fig. 4. Shows pressure contours for the five configurations at four different instants. It is observed that the flapping motion of the FVG (Flexible Vortex Generator) changes the pressure distribution in the second part of the channel. A low-pressure region forms behind the FVG, demonstrating that the oscillation of the FVG reduces pressure losses. Configurations with two FVGs exhibit more pronounced weak regions as the velocity increases, compared to configurations with a single FVG, where the flow is more restricted.

Fig. 5, show Superimposed Positions of the Flexible Vortex Generator for Five Configurations. The oscillatory motion is governed by the hydrodynamic force of the nanofluid flow and the restoring force of the elastic FVG (Flexible Vortex Generator). Configurations with two FVGs experience larger amplitude oscillations compared to those with a single FVG. The maximum FVG displacement of $d = 27$ [mm] is observed in configuration C3. In this configuration, the flow passage is restricted.

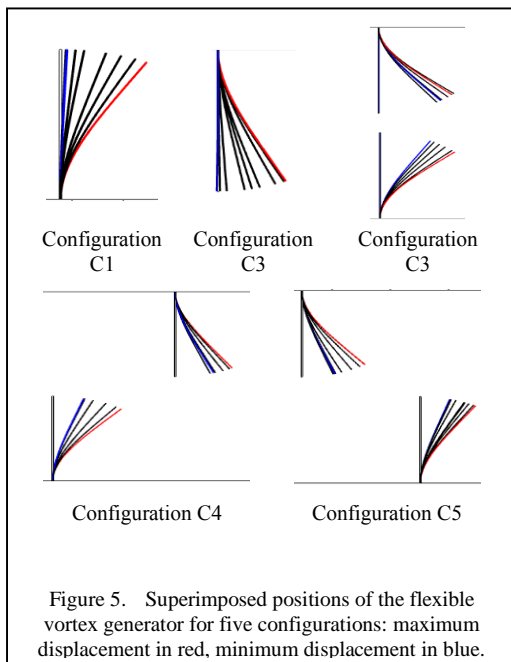


Figure 5. Superimposed positions of the flexible vortex generator for five configurations: maximum displacement in red, minimum displacement in blue.

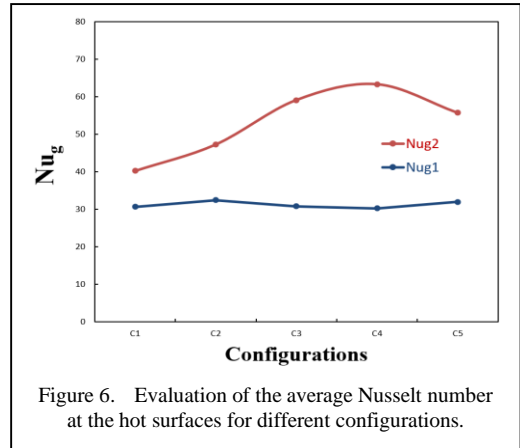


Figure 6. Evaluation of the average Nusselt number at the hot surfaces for different configurations.

Intensifying the velocity and resulting in a larger oscillation amplitude of the FVG.

Configurations C1 and C2 exhibit the same deformation of $d = 16$ [mm]. The maximum bending amplitude is observed for the lower FVG at $d = 22$ [mm] in configuration C4 and the upper FVG at $d = 21$ [mm] in configuration C5.

In Fig. 6, it is observed that Nu_{g2} is higher than Nu_{g1} , which demonstrates the ability of oscillation to enhance heat transfer. The lowest value of Nu_{g2} is obtained with configuration C1. When a FVG is located on the upper wall (C2, C3, C4, C5), the shedding vortex interacts with the heated surface located behind the FVG, resulting in a higher Nu_{g2} . The maximum Nu_{g2} number is achieved in configuration C4. In this configuration, the presence of two asymmetric FVGs, with the upper FVG placed in

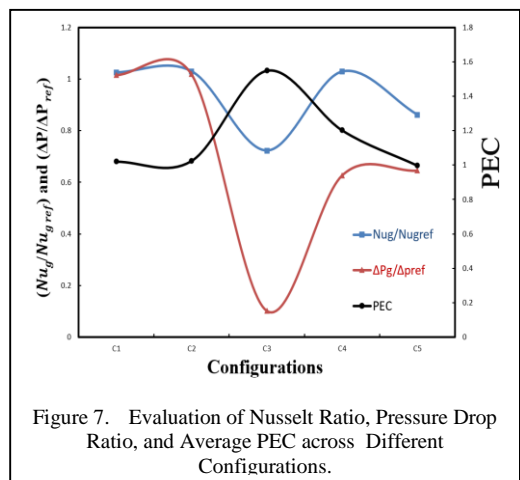


Figure 7. Evaluation of Nusselt Ratio, Pressure Drop Ratio, and Average PEC across Different Configurations.

the rear position, accelerates the velocity of the nanofluid and the circulating vortex, leading to improved heat transfer.

The Evaluation of Nusselt Ratio and Pressure Drop Ratio follow the same pattern as noticed in Fig. 7, indicating that heat transfer enhancement is associated with mechanical energy losses [8]. The pressure drops in the configuration with two FVGs are lower than in the configuration with a single FVG, which is less than 1, demonstrating that FVGs create less resistance to flow than rigid vortex generators (RVGs). The Nu number values for configurations C1, C2, and C4 are more significant than 1, which indicates that FVGs have significantly enhanced heat transfer compared to rigid configurations. Configuration C3 shows the highest PEC value ($PEC = 1.54$), so the reduction in pressure drop is greater than the reduction in the Nusselt number.

V. CONCLUSION

In this study, we investigated the effect of self-induced vibration on flow patterns and thermal characteristics using five different flexible vortex generators (FV)G distributions. The Arbitrary Lagrangian-Eulerian (ALE) method was employed to compute the interaction between the FVGs and the surrounding nanofluid flow. Flow dynamics and temperature distributions were visualized by plotting velocity, pressure, and temperature contours at four different well-selected times. The average Nusselt number, pressure drops, and Performance evaluation coefficient were examined for the different configurations. The results found that the generated vortices reduce the thermal boundary layers when it is located behind the FVG.

The results found that the generated vortices reduced the thermal boundary layers when the heat source is located behind the FVG and, as a result, enhanced convective heat exchange. Additionally, configuration with two FVGs

improves thermal mixing more effectively than the channel with one FVG due to the increased mainstream velocity and the intensified circulating vortices. Furthermore, asymmetric and symmetric configurations exhibit large-scale deformation compared to a single FVG case. The pressure drops in a channel with two FVGs is lower than that with rigid RVGs, and the flow resistance with FVGs is reduced. Finally, the symmetric configurations depict the maximum PEC , with a value of 1.54.

REFERENCES

- [1] Wang J., Wang X., & Liu X. (2022). Numerical investigation on flow behavior and heat transfer feature of flexible wings located at the bottom of a two-dimensional channel. *Applied Thermal Engineering*, 206, 118112.
- [2] Park, S. G. (2020). Heat transfer enhancement by a wall-mounted flexible vortex generator with an inclination angle. *International Journal of Heat and Mass Transfer*, 148, 119053.
- [3] Kang, M. S., Park, S. G., & Dinh, C. T. (2023). Heat transfer enhancement by asymmetric flexible vortex generators and thermal performance prediction using machine learning algorithms. *International Journal of Heat and Mass Transfer*, 200, 123518.
- [4] Hosseini, S., Aghebatandish, S., Dadvand, A., & Khoo, B. C. (2021). An immersed boundary-lattice Boltzmann method with multi-relaxation time for solving flow-induced vibrations of an elastic vortex generator and its effect on heat transfer and mixing. *Chemical Engineering Journal*, 405, 126652.
- [5] Kang, M. S., Park, S. G., & Dinh, C. T. (2023). Heat transfer enhancement by a pair of asymmetric flexible vortex generators and thermal performance prediction using machine learning algorithms. *International Journal of Heat and Mass Transfer*, 200, 123518.
- [6] Shi, J., Hu, J., Schafer, S. R., & Chen, C.-L. (2014). Numerical study of heat transfer enhancement of channel via vortex-induced vibration. *Applied Thermal Engineering*, 70, 838-845.
- [7] Ogden, R. W. (1997). *Non-linear elastic deformations*. Courier Corporation.
- [8] Amini, Y., & Habibi, S. E. (2022). Effects of multiple flexible vortex generators on the hydrothermal characteristics of a rectangular channel. *International Journal of Thermal Sciences*, 175, 107454.

Conversion of Castor Oil Plant through a Biorefinery Scheme for Sustainable Aviation Fuel and Succinic Acid Production

Carlos Eduardo Guzmán-Martínez¹, Claudia Gutiérrez-Antonio²

^{1,2}Universidad Autónoma de Querétaro, Facultad de Ingeniería, Querétaro, Mexico

¹dcicqcarlos@gmail.com, ²claugtez@gmail.com

Abstract—The search for renewable and sustainable sources for producing fuels and value-added products has driven the development of biorefinery schemes that take advantage of waste. One of the raw materials of most interest is the castor oil plant (*Ricinus communis*), which stands out for its ability to grow in adverse conditions and its high oil content. This oil, rich in triglycerides, is a potential source for the production of biofuels, while its coproducts, such as lignocellulosic fractions, can synthesize chemical products with high added value. In this context, the present work presents the conversion of a castor oil plant through a biorefinery scheme to obtain sustainable aviation fuel (SAF) and succinic acid, two crucial products in the transition towards a low-carbon economy. This research concludes that the proposed biorefinery is technically feasible. However, an economic evaluation and a supply chain study are essential.

Keywords - biorefinery, succinic acid, biofuels Aspen Plus, *Ricinus communis*

I. INTRODUCTION

Humanity has enormous challenges, such as waste management, climate change, and sustainable energy sources. To tackle these, biofuels are presented as a sustainable option to decrease the planet's negative impact and support an eco-friendly solution to energy demand. Biofuels are defined as those coming from renewable biomass.

SAF (Sustainable Aviation Fuel) is a promising solution for decreasing CO₂ emissions in the aeronautic sector. This industry emits

ISBN: 978-86-82602-05-7

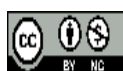
2-3% of the global carbon emissions [1]. SAF can be produced from different kinds of waste. It contributes to improving waste management by using valorizing processes and adding to sky decarbonization; besides, it develops more sustainable supply chains [2].

The castor oil plant (*Ricinus communis*) is popular for its resistance to drought conditions and marginal soils, which makes it an attractive option for semiarid regions, tropical areas, or lands with agricultural limitations [3]. The most attractive attribute of the castor oil plant is its high lipidic content, which is mainly characterized by ricinoleic acid. By using this fatty acid, the production of SAF is possible [3].

A biorefinery scheme is a unit operation set that transforms biomass into added-value products, energy, and biofuels to achieve a sustainable operation [4].

In the case of the castor oil plant, in addition to producing SAF from castor oil, it is possible to generate other valuable compounds from its biomass using biorefinery schemes. One of these products is succinic acid, which can be produced through biomass fermentation. This compound is relevant in the chemical industry since it is an important precursor for manufacturing bioplastics, resins, solvents, food additives, and other high-value-added products [5]. Succinic acid is part of the growing demand for “green” and sustainable chemicals; therefore, the research aim is to evaluate the feasibility of a conceptual biorefinery scheme for sustainable aviation fuel and succinic acid production.

175



II. METHODOLOGY

To develop this research, six steps were implemented:

1. Define the case study. In this first stage, the case of study is defined for establishing a calculus base; it corresponds to a biorefinery feed stream as raw material. Then, the castor oil plant must be described chemically. Therefore, a literature search was conducted to find its composition regarding lignin, cellulose, and hemicellulose.
2. Develop a conceptual design for a biorefinery. Knowing all the products that can be obtained from the raw material is imperative for designing a biorefinery. Once the products are viewed, the design must select those with an industrial interest due to their value added.

When the products have been specified, unit operations must be proposed to transform the incomes from the raw materials to the value-added molecules aimed.

3. Collect thermodynamic and chemical kinetic data. Experimental data are essential for validating process modeling; therefore, thermodynamic and chemical kinetic data reported in the literature must be compiled according to the unit operations defined in the conceptual design of the biorefinery.
4. Simulate the scheme in Aspen Plus. The conceptual design is modeled and simulated in the Aspen Plus® V14 software at a steady state. Manipulated variables are selected according to each unit operation, and the model is resolved using rigorous methods.
5. Evaluate the technical feasibility. This stage measures the biorefinery's capacity to transform castor oil plants into biofuels and value-added molecules. The technical indicators employed to describe the whole process are component recovery (rec), conversion (cv), yield (Y_d), and product mass ratio (pmr), Eqs. (1)-(4) [6]:

$$rec = oms / fms , \quad (1)$$

$$cv = (r_{in} - r_{out}) / r_{in} , \quad (2)$$

$$Y_d = pmf / tpm , \quad (3)$$

$$pmr = mp / rmm , \quad (4)$$

where: rec = component recuperation, oms = output mass flow (kg/h), fms = feed mass flow (kg/h), cv = conversion, r_{in} = reactant input to process (mol/h), r_{out} = reactant output to process (mol/h), Y_d = Yield, pmf = moles of desired product formed (mol), tpm = theoretical product moles (mol), pmr = product mass ratio, mp = product mass flow (kg/h), rmm = raw material mass flow (kg/h).

It is essential to highlight that this research does not include an economic evaluation.

III. RESULTS

According to the information provided by the Consultation Agri-Food Information System in Mexico (SIACON) [7], the production in the Mexican state of Sonora is 274.8 tons/year, which represents 92.43% of the Mexican output; therefore, this flow is contemplated as a study case. Besides, it is essential to mention that this research does not include the supply chain. Consequently, it assumes that a biorefinery in Sonora state, a place with significant castor oil plant production, is not affected by the implications of raw material transportation. To finalize the study case definition, it must be pointed out that 8760 hours per year are considered.

The castor oil plant comprises three components: seeds, leaves, and stems. The seeds represent 46.8 wt%, leaves 14.4 wt% and stems 38.8 wt%. Seeds can be subdivided into shells, representing 30 wt%, and the balance is known as kernel [8].

The lipidic content in the castor oil plant is located in the kernel, representing 45 wt%. The balance is mainly constituted by hydrocarbons and proteins [8].

The conceptual design of the biorefinery is described in Fig 1. The main products selected are succinic acid, sustainable aviation fuel (SAF), and biodiesel.

For simulation, Aspen Plus V.14 is used. The Thermodynamic models implemented are SOLIDS, NRTL, PENG ROBINSON, and BK10. The Carlson algorithm is employed to determine them [9].

The 31.368 kg/h of castor oil plant is fed to the Solid separation section. As the first step, stems and leaves are separated from the raw material to get the seeds. Then, the shell is removed from the rest of the seed to obtain the kernel. It is essential to highlight that these two-unit operations constitute a separation section.

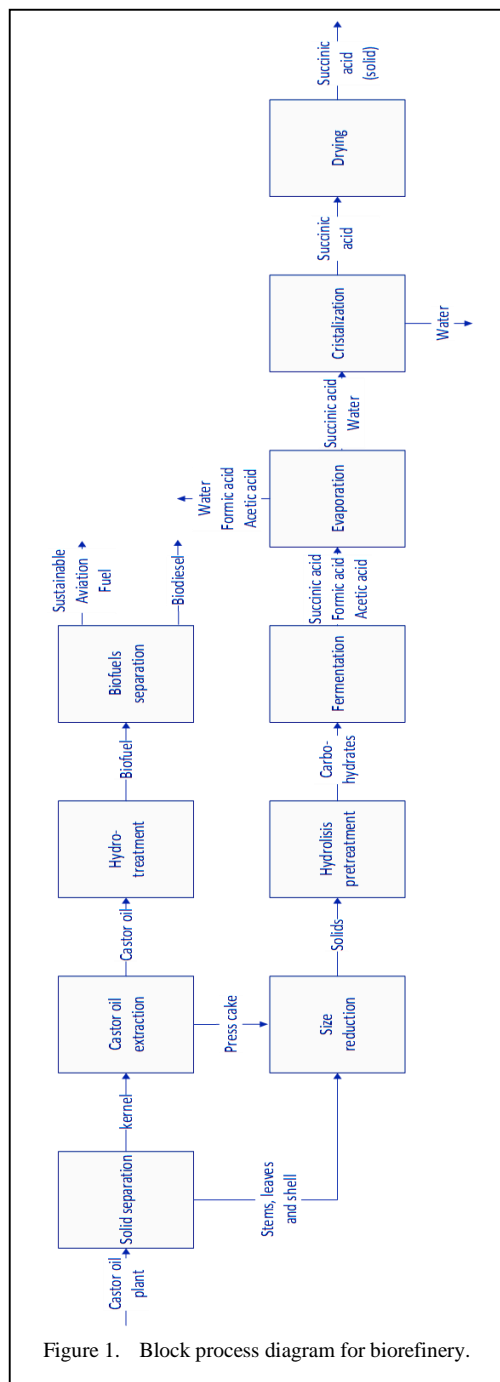


Figure 1. Block process diagram for biorefinery.

On the other hand, these two are modeled using the Sep block in Aspen Plus. The thermodynamic model used for them is SOLIDS. The lignocellulosic residues from the Solid separation section are sent to the size reduction section to be pre-treated for succinic acid production. Table I shows the chemical composition of castor oil plants [8,10-13].

As mentioned before, the lipidic fraction is located in the kernel and is employed to produce biofuels, according to the experimental data provided by Belaid et al.

According to [14], it must be preheated to 100 °C, as pretreatment, for oil extraction. A Heater block and SOLIDS as a thermodynamic model were used to model it. The oil extraction is carried out in an expeller by mechanical pressing. Patel et al. (2016) show the importance of preheating; without it, just 45 wt% can be extracted [15].

The expeller has two outputs: press cake and castor oil with impurities, which correspond to 10 wt% of total solids. The expeller is modeled using SOLIDS as a thermodynamic model and two blocks: a Crusher and a Sep; the second one is employed to separate the press cake.

The oil from the expeller is refined using a Filter block, which removes suspended solids to get clean oil. The 1 wt% of oil leaves the filter with the solids removed, and the press cake is sent to the reduction size section.

The next section of the process is the oil hydrotreatment. According to [16], this process is carried out at 395 °C and 50 bar; therefore, the castor oil is heated and pressurized using Pump and Heater blocks. At the same time, a hydrogen stream is fed to this section; its flow is 0.12 kg/h at standard conditions. It is pressurized and heated at the same point as castor oil to prepare the hydrogen using a Compr Block and Heater Block, respectively. All these unit operations use PENG ROBINSON as a thermodynamic model.

The castor oil and hydrogen streams are fed to the plug reactor. This one operates to 395 °C and 50 bar. Its geometry is defined by 0.6 and 0.15 meters of length and diameter, respectively. Besides, the reactor is loaded with 5 kg of catalyst (NiMo/ γ -Al₂O₃) [16]. The catalyst has a particle density of 0.72 g/cm³ [16]. The reactor is modeled by using an RPlug block. As the last unit operation, it also employs PENG ROBINSON as a thermodynamic model. The

reactions inside the reactor are described in Table II. These correspond to the hydrogenation of triglycerides and the isomerization of some hydrocarbons [17]. The kinetic parameters are shown in Table III [16]. It assumes that all reactions follow a first-order Power Law kinetic.

When the biofuels are released from the reactor, they are cooled at 20 °C and depressurized at 1 atm; this is performed by employing Flash2 Block and NRTL as thermodynamic models. CO, CO₂, H₂, and water vapor are separated from liquid biofuels from the top of the flash unit. With this process, the biofuels separation section Starts.

As mentioned, the gas outcome from the flash unit contains H₂, which is recuperated by membrane technology [18]. With it, it is possible to recirculate 99.5 wt% of the unreacted hydrogen. The other gases are released into the environment. Hydrogen purification is modeled using a Sep Block and NRTL as thermodynamic models.

The liquid biofuels are separated by using rigorous methods based on MESH equations. A Rad Frac block is employed, and BK10 is the thermodynamic model implemented in this unit's operation. The distillation column has 24 stages, fed at the #7 stage. It has a column pressure drop of 10 psi. It works with a total condenser and kettle reboiler. The distillate rate is 1.5359 kg/h, and its mass reflux ratio is 0.42. From the column top is obtained SAF, defined as the mixture of hydrocarbons until carbon #16. From the column bottom is biodiesel, specified as the mixture of hydrocarbons from carbon #17 onwards [17]. Table III shows the product flows attained by the whole biorefinery.

Lignocellulosic solids from solid separation and castor oil extraction are sent to the size reduction section. This last one is implemented to reduce the particle size of solid wastes to 1mm of particle diameter. This unit operation aims to increase the contact area to improve the reactive pretreatment later employed. The block and thermodynamic models used are Crusher and Solids, respectively. The type of Crusher is Gyratory.

Once the size of the lignocellulosic material has been reduced, it is sent to the hydrolysis pretreatment section. It consists of a batch reactor where cellulose and hemicellulose are reduced to simple carbohydrates, such as glucose and xylose; formulas 26 to 27 describe the reaction.

TABLE I. CHEMICAL COMPOSITION OF CASTOR OIL PLANT.

Plant section	Component	Mass percentage
Stems, leaves, and shells [8]	Cellulose	47 wt%
	Hemicellulose	28 wt%
	Lignin	25 wt%
Castor oil [9-10]	Triricinolein	89 wt%
	Trilinolein	5 wt%
	Triolein	4 wt%
	Trilinolenin	2 wt%
Press cake [11]	Cellulose	4 wt%
	Hemicellulose	5 wt%
	Lignin	36 wt%
	Proteins	24 wt%
Proteins [12]	Arginine	23.09 wt%
	Glutamic acid	31.45 wt%
	Tryptophan	19.45 wt%
	Aspartic acid	15.27 wt%
	Leucine	10.73 wt%

To carry out these reactions, it is important to use acid-diluted conditions. Therefore, diluted acid is added to the reactor, a flow of 40 kg/h 5 wt.% H₂SO₄. This reactor is modeled using an RBatch block and uses PENG ROBINSON as a thermodynamic method. It works at a constant temperature of 170 °C and 12 atm [19]. The total cycle time is 15 minutes. Table III shows the kinetic parameters used [19].

As lignin is not degraded under pretreatment conditions [19], it must be removed using a Filter Block. It uses SOLIDS as a thermodynamic model. This unit operation separates the 99 wt.% of liquids from the reactor outlet mixture. It works at atmospheric pressure. It is essential to mention that the lignin and proteins retained in this section are considered solid waste from biorefinery.

The glucose and xylose-rich hydrolysate are sent to the fermentation section. *Actinobacillus succinogenes* is the bacteria responsible for succinic acid production by transforming glucose and xylose into succinic acid, formic acid, and acetic acid, reactions 28 to 29 [20]. These reactions are carried out in a fermenter modeled by RBatch block, which employs NRTL as a

thermodynamic model. The reactor operates at a constant temperature, 37 °C, and 1 atm. The total cycle time of operation is 24 hours. It assumes that the reactions involved obey the first-order power-law kinetics. Thus, the kinetic parameters used are shown in Table III [20]. It is essential to highlight that the succinic acid process requires a

CO₂ supply as a co-substrate for obtaining large-scale production [20]. Thus, a CO₂ stream, with a mass flow of 7 kg/h at standard conditions, is fed to the fermenter. Once fermentation has finished, the resultant stream is filtered to remove the remaining solids in suspension. It is

TABLE II. REACTION FORMULAS.

REACTION	#
$C_{57}H_{104}O_6 + 9.375H_2 \rightarrow C_5H_{12} + C_6H_{14} + C_7H_{16} + 4.375C_8H_{18} + CO_2 + H_2O + 3CO$	(5)
$C_{57}H_{104}O_6 + 6.64286H_2 \rightarrow C_9H_{20} + 0.5C_{10}H_{22} + C_{11}H_{24} + 0.5C_{12}H_{26} + C_{13}H_{28} + 0.642857C_{14}H_{30} + CO_2 + H_2O + 3CO$	(6)
$C_{57}H_{104}O_6 + 5.2353H_2 \rightarrow C_{15}H_{32} + C_{16}H_{34} + 0.2353C_{17}H_{36} + C_{18}H_{38} + CO_2 + H_2O + 3CO$	(7)
$C_{57}H_{104}O_6 + 4.63158H_2 \rightarrow 0.631579C_{19}H_{40} + C_{20}H_{42} + C_{21}H_{44} + CO_2 + H_2O + 3CO$	(8)
$C_{57}H_{98}O_6 + 12.375H_2 \rightarrow C_5H_{12} + C_6H_{14} + C_7H_{16} + 4.375C_8H_{18} + CO_2 + H_2O + 3CO$	(9)
$C_{57}H_{98}O_6 + 9.64286H_2 \rightarrow C_9H_{20} + 0.5C_{10}H_{22} + C_{11}H_{24} + 0.5C_{12}H_{26} + C_{13}H_{28} + 0.642857C_{14}H_{30} + CO_2 + H_2O + 3CO$	(10)
$C_{57}H_{98}O_6 + 8.2353H_2 \rightarrow C_{15}H_{32} + C_{16}H_{34} + 0.2353C_{17}H_{36} + C_{18}H_{38} + CO_2 + H_2O + 3CO$	(11)
$C_{57}H_{98}O_6 + 7.63158H_2 \rightarrow 0.631579C_{19}H_{40} + C_{20}H_{42} + C_{21}H_{44} + CO_2 + H_2O + 3CO$	(12)
$C_{57}H_{104}O_9 + 6H_2 \rightarrow C_5H_{12} + C_6H_{14} + C_7H_{16} + 4C_8H_{18} + CO_2 + H_2O + 6CO$	(13)
$C_{57}H_{104}O_9 + 3.42857H_2 \rightarrow C_9H_{20} + 0.5C_{10}H_{22} + C_{11}H_{24} + 0.5C_{12}H_{26} + C_{13}H_{28} + 0.42857C_{14}H_{30} + CO_2 + H_2O + 6CO$	(14)
$C_{57}H_{104}O_9 + 2.0588H_2 \rightarrow C_{15}H_{32} + C_{16}H_{34} + 0.0588C_{17}H_{36} + C_{18}H_{38} + CO_2 + H_2O + 6CO$	(15)
$C_{57}H_{104}O_9 + 1.47368H_2 \rightarrow 0.47368C_{19}H_{40} + C_{20}H_{42} + C_{21}H_{44} + CO_2 + H_2O + 6CO$	(16)
$C_{57}H_{92}O_6 + 15.375H_2 \rightarrow C_5H_{12} + C_6H_{14} + C_7H_{16} + 4.375C_8H_{18} + CO_2 + H_2O + 3CO$	(17)
$C_{57}H_{92}O_6 + 12.6429H_2 \rightarrow C_9H_{20} + 0.5C_{10}H_{22} + C_{11}H_{24} + 0.5C_{12}H_{26} + C_{13}H_{28} + 0.642857C_{14}H_{30} + CO_2 + H_2O + 3CO$	(18)
$C_{57}H_{92}O_6 + 11.2353H_2 \rightarrow C_{15}H_{32} + C_{16}H_{34} + 0.2353C_{17}H_{36} + C_{18}H_{38} + CO_2 + H_2O + 3CO$	(19)
$C_{57}H_{92}O_6 + 10.6316H_2 \rightarrow 0.63158C_{19}H_{40} + C_{20}H_{42} + C_{21}H_{44} + CO_2 + H_2O + 3CO$	(20)
$C_8H_{18} \rightarrow C_8H_{18}$	(21)
$C_9H_{20} \rightarrow C_9H_{20}$	(22)
$C_{10}H_{22} \rightarrow C_{10}H_{22}$	(23)
$C_{12}H_{26} \rightarrow C_{12}H_{26}$	(24)
$C_{16}H_{34} \rightarrow C_{16}H_{34}$	(25)
$Hemicellulose + H_2O \rightarrow C_5H_{10}O_5$	(26)
$Cellulose + H_2O \rightarrow C_6H_{12}O_6$	(27)
$C_5H_{10}O_5 + CO_2 \rightarrow C_4H_6O_4 + CH_2O_2 + 3C_2H_4O_2$	(28)
$C_6H_{12}O_6 + CO_2 \rightarrow C_4H_6O_4 + CH_2O_2 + C_2H_4O_2$	(29)

TABLE III. VALUES OF KINETIC PARAMETERS.

Equation	k (s ⁻¹)	AE (kJ/mol)
(5)	1.29x10 ¹¹	216.69
(6)	2.38 x10 ⁵	123.43
(7)	1.03 x10 ⁴	103.82
(8)	1.03 x10 ⁴	103.82
(9)	1.29x10 ¹¹	216.69
(10)	2.38 x10 ⁵	123.43
(11)	1.03 x10 ⁴	103.82
(12)	1.03 x10 ⁴	103.82
(13)	1.29x10 ¹¹	216.69
(14)	2.38 x10 ⁵	123.43
(15)	1.03 x10 ⁴	103.82
(16)	1.03 x10 ⁴	103.82
(17)	1.29x10 ¹¹	216.69
(18)	2.38 x10 ⁵	123.43
(19)	1.03 x10 ⁴	103.82
(20)	1.03 x10 ⁴	103.82
(21)	2.38 x10 ⁵	123.43
(22)	2.38 x10 ⁵	123.43
(23)	2.38 x10 ⁵	123.43
(24)	2.38 x10 ⁵	123.43
(25)	2.38 x10 ⁵	123.43
(26)	3.34 x10 ¹⁸	176.7
(27)	1.54 x10 ¹⁸	179.5
(28)	1.38 x10 ⁹	81.56
(29)	1.38 x10 ⁹	81.56

performed using a filter block. The 99 wt.% of liquid defines the filtering.

The filtering goes to the evaporation section, where the temperature is increased to 125°C at atmospheric pressure to eliminate water vapor, acetic acid, and formic acid. Flash Block and NRTL model this stage as a thermodynamic model. A mixture of water, sulfuric acid, and succinic acid is obtained.

The diluted succinic acid from the evaporator is mixed with 21.23 kg/h of ethanol at 8.3 mol% [21], which will later be solidified in the crystallizer block. This is because succinic acid is being commercialized as a solid product.

The crystallization is carried out at 4 °C and 1 atm. The saturation calculation method is the solubility function, which follows (30).

$$L_n(K_{sp}) = A + B/T + C \cdot L_n(T) + DT, \quad (30)$$

where K_{sp} = solubility, T = temperature, A , B , C , and D are constants. For this research, the values of $A = 68.89$, $B = -6960.9$, $C = -8.74$, and $D = 0$ are used. The thermodynamic model used is SOLIDS.

Once succinic acid has been crystallized, the solid particles are separated from the matrix using a Filter block. It separates 99 mass % of liquid.

Finally, the last section dries the solid succinic acid. The Dryer block operates at 110°C and 1 atm.

Table IV shows the product flows and the values obtained for technical indicators.

With a relation 1:3 of biofuels and succinic acid, respectively, it could seem that SAF and biodiesel production is low; however, it is essential to highlight that the primary source of them is the lipidic fraction of castor oil plant, which represents only the 14.74 wt% of the whole plant. In this sense, 52.82 wt% of the raw

TABLE IV. CONCENTRATE OF RESULTS.

Product mass flow	
Succinic acid (kg/h)	9.76
Sustainable aviation fuel (kg/h)	1.536
Biodiesel (kg/h)	1.625
Technical indicators	
$rec_{succinic\ acid}$	98.69%
$rec_{hydrogen}$	99.49%
$Cv_{hemicellulose}$	100%
$Cv_{cellulose}$	100%
$Cv_{glucose}$	95.91%
Cv_{Xilose}	99.83%
$Cv_{Trioletin}$	99.15%
$Cv_{Trilinolein}$	99.16%
$Cv_{Trilinoenin}$	99.17%
$Cv_{Triricinolein}$	100%
$Yd_{succinic\ acid}$	37.19%
Yd_{SAF}	63.2%
$pmr_{succinic\ acid}$	31.11%
pmr_{SAF}	4.9%
$pmr_{biodiesel}$	5.18%

material is cellulose and hemicellulose, which are sent to be transformed into succinic acid, explaining the mass production of the value-added molecule.

The biorefinery achieves attractive values in its performance; technical indicators, such as product recovery and material conversion, reach rates greater than 95%. However, it might seem contradictory if succinic acid and SAF yields are considered. In this sense, the value of $Y_{dsuccinic\ acid}$ is justified because the result of the fermentation, Eqs. (28) to (29), is not only succinic acid, as it was desired in a utopic case but also acetic acid and formic acid are included; it is essential to mention that this condition is not possible to change due to it is part of microorganism metabolism. On the other hand, Y_{dSAF} is not an undesirable result because the secondary product, which is the cause of this parameter not being more significant than the one obtained, is another essential biofuel, biodiesel. Thus, the technical indicator that better describes the process of biofuel production is the conversion of lipids. Besides, it is necessary to remember that Eqs. (5) to (20) in involved reactions, CO, CO₂, and H₂O are generated, reducing biofuel production.

The product mass ratios of biofuels are consistent with the lipidic content in castor oil plants. The same case happens for $pmr_{succinic\ acid}$ according to plant composition in cellulose and hemicellulose and the secondary products production. However, it is essential to highlight that pmr_{SAF} value could be improved if lignin were not wasted; it represents 26.17 wt% of the raw material fed to the biorefinery. Lignin cannot be employed to increase SAF production using some thermochemical process or to obtain phenolic/value-added products by implementing chemical or biological treatments. On the other side, proteins are not used either; they represent 6.23 wt% of the total mass, which, added to lignin, corresponds to 32.4 wt%, and that can directly impact biofuels production; besides, it can directly decrease the waste released by biorefinery.

The acetic and formic acids are not recovered. However, it might be considered for reaching mass flows of 7.87 and 3.85 kg/h, respectively. It represents 2.49- and 1.22-times biofuel production.

The energy involved, for the most representative unit operations, is Pump for oil 0.39kW, Hydrogen compressor 0.34kW, Plug

reactor 25.77kW, Distillation column 0.91kW, Biomass hydrolysis reactor 2.64kW, evaporator 6 403.4kW, Dryer 0.55kW. In this sense, the evaporation to remove succinic acid from the fermenter matrix consumes 99.49% of the total process energy because evaporating water requires a lot of energy due to its heat capacity. Besides, efforts to decrease this consumption must be focused on developing another way to purify succinic acid.

In previous work [22], where a biorefinery for wine effluent (BWE) valorization was developed, it got two products: SAF and Levulinic acid. Comparing BWE and the biorefinery of castor oil plant (BCOP), BCOP shows better performance because it reaches 63.2% in SAF yield, and BWE just 2.94%. Besides, the add-value-product yield is 37.20% for BCOP and 2.68% for BWE. These results exhibit that BCOP is more efficient than BWE. It is important do not forget that both biorefineries have different structures and co-products. About sustainable terms, BWE presents an energy consumption of 64 829.44kW and BCOP 6 431.36kW, which means 9.92% of the energy that BWE employs.

The simulations show that the proposed biorefinery emits 3.5287 kg/h of CO₂. This value comes from the balance between the CO₂ input, a needed stream in succinic acid production, CO₂ outputs, an undesired product of reactions in the hydrotreatment and fermentation section, and CO₂ for utility use. Although the correct way to make a comparison between this process and the traditional fuel production methods should be through Cycle life Analysis, it is possible to affirm that the proposed scheme has a lower environmental impact since the castor oil plant employs the CO₂ in the atmosphere to biodiesel production, unlike fossil diesel comes carbon trapped in underground.

Finally, since Sonora state has the highest production of castor oil plants in Mexico, it is the unique region where this biorefinery can operate. This is based on the fact that the supply chains focused on biofuels, which involve significant distance, tend to be not economically and environmentally feasible [23].

IV. CONCLUSIONS

This research confirms that converting castor oil plants through a biorefinery scheme for sustainable aviation fuel and succinic acid production is technically feasible. On the other

hand, the proposed scheme does not take advantage of the whole biomass because an essential quantity of lignin is still wasted; therefore, the biorefinery can potentially improve biofuel production, mainly SAF, by providing another thermochemical process.

Finally, it is essential to consider both an economic evaluation and a supply chain to guarantee project feasibility.

ACKNOWLEDGMENT

The authors appreciate the financial support provided by CONAHCyT through the Carlos Eduardo Guzmán Martínez postdoctoral scholarship (Call: 2022 (1). Project: 2397403).

REFERENCES

- [1] Raman, R., Gunasekar, S., Dávid, L. D., & Nedungadi, P. (2024). Aligning sustainable aviation fuel research with sustainable development goals: Trends and thematic analysis. *Energy Reports*, *12*, 2642-2652.
- [2] Matos-Rios, D. M., Martínez-Guido, S. I., Ortega, J. M. P., Gómez-Castro, F. I., García-Trejo, J. F., & Gutiérrez-Antonio, C. (2022). Optimal supply chain design for renewable aviation fuel production in Mexico considering the full use of nonedible biomass. *ACS Sustainable Chemistry & Engineering*, *10*(30), 9770-9786.
- [3] Dimian, A. C., Iancu, P., Plesu, V., Bonet-Ruiz, A. E., & Bonet-Ruiz, J. (2019). Castor oil biorefinery: Conceptual process design, simulation, and economic analysis. *Chemical Engineering Research and Design*, *141*, 198-219.
- [4] Naik, S. N., Saxena, D. K., Dole, B. R., & Khare, S. K. (2018). Potential and perspective of castor biorefinery. In *Waste biorefinery* (623-656).
- [5] Nghiem, N. P., Kleff, S., & Schwegmann, S. (2017). Succinic acid: technology development and commercialization. *Fermentation*, *3*(2), 26.
- [6] Felder, R. M., Rousseau, R. W., & Bullard, L. G. (2020). *Elementary principles of chemical processes*. John Wiley & Sons.
- [7] Secretaría de Agricultura y Desarrollo Urbano. (2024). *Sistema de Información Agroalimentaria de Consulta*. Available at: <https://www.gob.mx/siap/documentos/si-acon-ng-161430>.
- [8] Kaur, R., Gera, P., Jha, M.K., & Bhaskar, T. (2018). Pyrolysis kinetics and thermodynamic parameters of castor (*Ricinus communis*) residue using thermogravimetric analysis. *Bioresour Technol.* *250*, 422-428.
- [9] Carlson, E. C. (1996). Don't Gamble with Physical Properties for Simulations. *Chemical Engineering Progress*, 35-46
- [10] Hincapie, G. (2011). Transesterificación de aceite de higuera crudo utilizando catalizadores heterogéneos - estudio preliminar. *Dyna Rev. Fac. Nac. Minas* *78*, 176-181.
- [11] Huang, F., Zhu, G., Chen, Y.S., Meng, F., Peng, M., Chen, X., He, Z., Zhang, Z., & Chen, Y.J. (2016). Seed characteristics and fatty acid composition of castor (*Ricinus communis* L.) varieties in Northeast China. *Phyton Int. J.* *84*, 26-33.
- [12] Hilioti, Z., Michailof, C.M., Valasiadis, D., Iliopoulou, E. F., Koidou, V., & Lappas, A. A. (2017). Characterization of castor plant-derived biochars and their effects as soil amendments on seedlings. *Biomass Bioenergy*, *105*, 96-106.
- [13] Chambi, H. N. M., Lacerda, R. S., Makishi, G. L. A., Bittante, A. M. Q. B., Gomide, C. A., & Sobral, P. J. A. (2014). Protein extracted from castor bean (*Ricinus communis* L.) cake in high pH results in films with improved physical properties. *Ind. Crops Prod.*, *61*, 217-224.
- [14] Belaid, M., Muzenda, E., Mitilene, G. & Mollagee, M., (2011). Feasibility study for a castor oil extraction plant in South Africa. *World Acad. Sci. Eng. Technol.*, *740-744*.
- [15] Patel, V. R., Dumancas, G. G., Viswanath, L. C. K., Maples, R., & Subong, B. J. J. (2016). Castor oil: properties, uses, and optimization of processing parameters in commercial production. *Lipid Insights*. *9*, 1-12.
- [16] Mederos-Nieto, F. S., Santoyo-López, A. O., Hernández-Altamirano, R., Mena-Cervantes, V. Y., Trejo-Zárraga, F., Centeno-Nolasco, G., & Ramírez-Jiménez, E. (2021). Renewable fuels production from the hydrotreating over NiMo/γ-Al₂O₃ catalyst of castor oil methyl esters obtained by reactive extraction. *Fuel*, *285*, 119168.
- [17] Romero-Izquierdo, A. G., Gómez-Castro, F. I., Hernández, S., & Gutiérrez-Antonio, C. (2022). Computer aided-design of castor bean fruit-based biorefinery scheme to produce sustainable aviation fuel. *Chemical Engineering Research and Design*, *188*, 746-763.
- [18] Du, Z., Liu, C., Zhai, J., Guo, X., Xiong, Y., Su, W., & He, G. (2021). A review of hydrogen purification technologies for fuel cell vehicles. *Catalysts*, *11*(3), 393.
- [19] Quintero, J. A., & Cardona, C. A. (2011). Process simulation of fuel ethanol production from lignocellulosic using Aspen Plus. *Industrial & engineering chemistry research*, *50*(10), 6205-6212.
- [20] Castro-Montoya, A. J., Méndez-Romero, T., Vargas-Tah, A. A., Aguilar-Rivera, N., & Lazato-Mixteco, P. E. (2023). Sugarcane molasses-based biorefinery: Organic acids and ethanol production. *Renewable Energy, Biomass & Sustainability*, *5*(1), 1-9.
- [21] Jiang, X., Hu, Y., Meng, Z., Yang, W., & Shen, F. (2013). Solubility of succinic acid in different aqueous solvent mixtures: Experimental measurement and thermodynamic modeling. *Fluid Phase Equilibria*, *341*, 7-11.
- [22] Guzmán-Martínez, C. E., Romero-Izquierdo, A. G., Martínez-Guido, S. I., Hernández, S., & Gutiérrez-Antonio, C. (2024). Wine effluents valorization through a biorefinery scheme. In *Computer Aided Chemical Engineering 53*, 2329-2334.
- [23] Martínez-Guido, et al. (2021). The integration of pelletized agricultural residues into electricity grid: Perspectives from the human, environmental and economic aspects. *Journal of Cleaner Production*, *321*, 128932.

Energy Management based on a Systems Approach to the Analysis of Energy Indicators, Strategies and Policies

Jelena Malenović-Nikolić¹ 

¹Faculty of Occupational Safety, Niš, Serbia

¹malenovicfznr@gmail.com

Abstract—The processes of transforming the primary energy of coal into thermal energy are a significant cause of environmental degradation and the reduction of energy potential at the national level. Failures in energy management lead to the degradation of air, water, and soil quality, as well as to threatened energy stability. Managing the energy sector is a complex task that can be addressed through a systematic approach to individual problems and through consideration of the overall situation. The adoption of an overly ambitious energy sector development strategy indicates the need to postpone proposed solutions, which are often part of procedures governed by legal norms. Energy indicators can largely reflect the level of implementation of energy policies. The analysis is based on the results of a timely and adequately implemented environmental system monitoring. Creating a more complex set of energy indicators can help improve the management of energy development. The use of alternative energy sources represents a significant shift in the perception of utilizing traditional energy sources. Technical conditions related to the provision of the electricity distribution network, transportation routes, and the importation of modern equipment should be aligned with the needs of energy development based on the application of solar, wind, hydromechanical, geothermal, and nuclear energy.

Keywords - energy, management, policy, indicators, strategy

I. LEGISLATION AS THE BASIS FOR THE USE OF ENERGY INDICATORS

The enforcement of laws in the energy sector is a complex task, especially in the face of limited financial resources. The most common justifications for non-compliance with legal norms are based on the high cost of implementing preventive environmental protection measures and mitigating their consequences. A properly planned energy management process requires that financial and technical issues be considered as early as the planning stage. Energy management in accordance with legal procedures means that energy transformations should only take place once the minimum requirements for the safety and health of workers and residents of nearby settlements are ensured. The ISO 50000 series of standards has adequately regulated energy management at the international level. Adherence to the principles of environmental and energy management based on the ISO 14000 and ISO 50000 standards is crucial for the successful implementation of the management process, especially in the planning and organizational stages. For the management process to improve, the standards must be applied across the entire company, not just to processes that are not the dominant sources of pollutants or that pertain solely to alternative energy sources. The use of energy indicators requires compliance with national and international legislation, implying legal coverage by national and international provisions and reporting obligations.



The National List of Environmental Indicators, within the topic of economic and social potentials and activities of environmental significance, includes the application of four energy indicators. Each of these indicators is legally covered by national regulations. According to the Rulebook on the National List of Environmental Indicators [1], attention should be paid to the guidelines of laws, strategies, and regulations (I). Energy management should be based on current legislation, both that adopted after the approval of the national list of indicators (II), and that pertaining to renewable energy sources (III), as presented in Table I. International legislation is presented in Table II.

TABLE I. NATIONAL LEGISLATION AND REGULATIONS.

	National legislation
I	<ul style="list-style-type: none"> • Law on Energy, Energy Sector Development Strategy of the Republic of Serbia [2] • Regulation on Amendments and Supplements to the Regulation on Establishing the Program for the Implementation of the Energy Sector Development Strategy of the Republic of Serbia [3] • Law on the Ratification of the Energy Community Treaty - Law on the Confirmation of the Statute of the International Renewable Energy Agency [4] • Energy Sector Development Strategy of the Republic of Serbia until 2015 [5] • National Environmental Protection Program [6]
II	<ul style="list-style-type: none"> • Law on Amendments and Supplements to the Law on Energy [7] • Law on Energy [8]
III	<ul style="list-style-type: none"> • Regulation on Conditions and Procedures for Acquiring the Status of a Privileged Producer of Electricity [9] • Regulation on Incentive Measures for Privileged Producers of Electricity [10] • Regulation on the Power Purchase Agreement [11] • Regulation on the Fee for Incentives for Privileged Producers of Electricity [12] • Regulation on the Amount of the Fee for Incentives for Privileged Producers of Electricity [13] • Regulation on the Method of Calculation and Distribution of Collected Funds from the Fee for Incentives for Privileged Producers of Electricity [14] • Regulation on Amendments to the Regulation on Determining the Program for the Implementation of the Energy Sector Development Strategy of the Republic of Serbia until 2015 for the 2007-2012 Period [15]

TABLE II. INTERNATIONAL LEGISLATION AND INTERNATIONAL INDICATORS [1].

	International legislation
I	<ul style="list-style-type: none"> • Directive 2001/77/EC on the promotion of electricity production from renewable energy sources • Directive 2003/30/EC on the promotion of the use of biofuels and other renewable fuels for transport
II	<ul style="list-style-type: none"> • Indicator CSI 027 / ENER 016 – Final energy consumption by sector • Indicator CSI 028 / ENER 017 – Total primary energy intensity • Indicator CSI 029 / ENER 026 – Primary energy consumption by fuel • Indicator CSI 030 / ENER 029 – Renewable primary energy consumption • Indicator CSI 031 / ENER 030 – Renewable electricity consumption

Energy management, according to the guidelines of the Rulebook on the National List of Indicators [1], shows that adherence to directives adopted at the international level (I) and the guidelines of internationally adopted indicators by the International European Environmental Agency (II) is necessary, as presented in Table II.

The National List of Environmental Indicators contains five groups of indicators/thematic areas including state, pressure, response, driving forces, and societal reaction.

The driving force indicators include Total primary energy consumption by energy sources and Final energy consumption by sectors, while the societal reaction indicators include Total energy intensity and Primary energy consumption from renewable sources. Table III presents the energy indicators from the National List of Environmental Indicators of the Republic of Serbia.

TABLE III. ENERGY INDICATORS FROM NATIONAL LIST OF ENVIRONMENTAL INDICATORS [1].

No.	Thematic area	Energy indicators
10.62	Driving forces	Total primary energy consumption by energy sources
10.63	Driving forces	Final energy consumption by sectors
10.64	Societal reaction	Total energy intensity
10.65	Societal reaction	Primary energy consumption from renewable sources

The use of energy indicators is significant for creating an energy management system, as the Rulebook on the National List prescribes reporting obligations, data availability, and deadlines for submitting information.

II. ENERGY SECTOR DEVELOPMENT STRATEGY OF THE REPUBLIC OF SERBIA AND MANAGEMENT

The Energy Sector Development Strategy of the Republic of Serbia until 2015 [5] and the Energy Sector Development Strategy of the Republic of Serbia until 2025, with projections up to 2030 [16] provide guidelines for managing the energy sector and economic development.

The current strategy [16] proposes the path of market restructuring and technological modernization of Serbia’s energy sector to better prepare for a period of increased demand for goods and services, in accordance with the requirements outlined in Table IV.

To reduce greenhouse gas emissions to the level outlined in the “Energy Roadmap 2050,” alongside the currently commercially available technologies, it would be necessary, in addition to the intensified application of energy efficiency measures and the introduction of renewable energy sources, to introduce nuclear facilities into the Serbian energy sector. Given Serbia’s available lignite reserves, the development of clean coal technologies, which include CO₂ storage, could be of crucial importance for the country [17].

TABLE IV. ENERGY MANAGEMENT SYSTEM REQUIREMENTS DEFINED BY STRATEGIC PLANS [17].

No.	Requirements defined by the Strategy
I	Ensure significant quantities of energy and energy resources, while aiming to reduce energy intensity, i.e., to lower consumption per unit of monetary product.
II	Introduce clean energy, i.e., energy management should increasingly rely on renewable energy sources and less on non-renewable resources.
III	Energy production and consumption should leave as few negative impacts as possible on the environment – water, air, and soil – and indirectly on the entire food chain, biodiversity, and human health.
IV	The retail price of energy must include environmental protection costs and other external costs – fees, taxes, penalties, or other economic and financial instruments.

The strategy stipulates the consideration of existing energy technologies while increasing the costs of energy transformations to secure funds for the implementation of new or less efficient technologies in the future.

Consideration of the energy situation at the European level is a serious task, which is why long-term plans began in 2011, when the European Commission planned the development for the following 40 years and created the document “Energy Roadmap 2050.” The goal of this document is to emphasize the need for a drastic reduction in greenhouse gas concentrations – by 80-95% compared to 1990 levels.

These plans should be implemented in line with the recommended guidelines, without compromising the satisfaction of energy needs and the competitiveness of the European market. The strategy also includes the education of experts in the use of renewable energy sources and for conducting project tasks to promote the development of renewable energy sources.

According to the National Energy and Climate Plan [17], the energy sector is projected to employ 2,000 to 2,500 workers for wind turbine and solar panel installation, as well as 1,000 to 1,400 workers in the biomass sector for similar tasks. For the maintenance of energy systems, the plan is to employ 600 to 1,200 workers in wind turbine maintenance, 300 to 700 workers in solar panel maintenance, and fewer than 100 workers for biomass processing plant maintenance by 2030 (Table V).

The Energy Sector Development Strategy [16] also includes the implementation of energy production from clean coal in highly efficient thermal power plants equipped with technologies for CO₂ capture and storage, following the stages outlined in Table VI.

TABLE V. EMPLOYMENT FACTORS BASED ON TECHNOLOGIES [17].

Technology	Installation (persons-years/MW)	Maintenance (tasks/MW)
Solar power plants	10-15	0.2-0.4
Wind turbines on land	10-15	0.2-0.4
Biomass processing facilities	15-20	0.2-0.4

TABLE VI. IMPLEMENTATION OF ENERGY PRODUCTION FROM CLEAN COAL [17].

No.	Production stages
I	Revitalization of existing and construction of new thermal power plants with increased efficiency and reduced emissions of CO ₂ , SO ₂ , NO _x , and particulate matter
II	Design and construction of thermal power plants with a high degree of utilization of 50%
III	Use of technologies that capture and store CO ₂

Energy development should meet the needs of electricity consumers, take into account the technical and financial capabilities of producers, ensure operational efficiency, and maintain the competitiveness of public companies in the energy market.

The planned tasks within the Energy Development Strategy pose a significant challenge, especially because these changes need to be implemented by 2030 while preserving environmental quality.

III. ENERGY POLICY AS THE FOUNDATION OF THE MANAGEMENT SYSTEM

Energy policy serves as the foundation for the development and improvement of Serbia's management system. It is essential to define the directions of energy transformations on a realistic basis, as overly ambitious plans often fail to materialize. The creation of energy policy and the adoption of defined proposals largely depend on the guidelines of the European Union's (EU) energy policy. Special attention is given to countries that are not yet EU members, as they are expected to harmonize their energy and environmental policies before joining the EU.

Energy policy should be created in accordance with the principles of sustainable development, security, and market competitiveness, with the primary goal of preserving environmental quality, preserving fossil fuel energy reserves, and utilizing available renewable energy sources.

The objectives of the national energy policy should align with the goals of the EU energy policy [18]. However, when formulating a policy, there is also the opportunity for each country to define the basic requirements so as to form its energy structure and utilize its energy resources according to the actual needs.

TABLE VII. ENERGY OBJECTIVES OF THE EU ENERGY POLICY [18].

No.	Energy objectives of the EU energy policy
I	Increase the share of final energy consumption from renewable sources to 42.5%
II	Increase the share of final energy consumption from renewable sources to 45% for member states
III	Reduce primary (approximate) and final energy consumption by 11.7% compared to the 2020 forecasts
IV	Ensure the interconnection of the EU's energy systems by at least 15%

The objectives of the EU energy policy include [18]: creating conditions for international cooperation and securing energy needs, ensuring the functioning of a common energy market with the free flow of energy between EU member states, improving energy efficiency, reducing dependence on energy imports, transitioning to low-carbon technologies, and developing research in the field of low-carbon and clean technologies (Table VII).

Serbia's energy policy should rely on the guidelines and goals defined by the EU, as it one of the candidate countries for EU accession.

IV. SYSTEMS APPROACH TO CREATING THE ENERGY MANAGEMENT MODEL

Energy management is a serious task, especially for countries that lack the financial capacity to implement renewable energy technologies and cleaner technologies.

Cross-border pollution of key environmental media is another reason to adjust established procedures and implement environmental legislation.

The creation of an energy management model should be based on available energy resources while ensuring that domestic needs are met. It is also unrealistic to irrationally consume energy resources, especially fossil fuels, in order to participate in the stability of the European energy market, while increasing regional and national air, water, and soil pollution. Fig. 1 presents the energy management model.

It is necessary to timely consider skilled personnel required for the installation and maintenance of installed energy capacities.



Figure 1. Energy management model.

Energy management based on a systems approach should rely on the analysis of national and supranational energy indicators (Primary energy Consumption, Final energy consumption, Final energy intensity in Industry, Final energy consumption per square meter in residential sector, climate corrected, Final energy consumption in transport, Final energy intensity in services sector), as they provide an opportunity to compare Serbia's energy policy with that of EU countries. The lack of financial resources is an obstacle to developing the energy sector towards the use of alternative energy sources, but it is not the only one. It is necessary

to ensure qualified personnel for the installation and maintenance of complex electrical systems, as well as to educate the population to better understand the importance of investing in modern technologies and sustainable energy development. The energy development strategy defines goals that often remain unmet due to a lack of financial resources, making it essential to set long-term goals realistically, according to the principles of sustainable development and within the limits of available energy capacities. Data on environmental quality are published in the Annual State of the Environment Report and they indicate that certain facilities exceed the pollutant limit values. According to current legislation, such facilities should cease operations until pollutant emissions are reduced within the limit values, but this could threaten energy stability.

V. CONCLUSION

The energy management model should be created through a multi-criteria decision analysis process in order to consider all aspects of the impact. The financial situation and technical conditions are also significant aspects, so decisions will generally depend on a wide range of factors (Systems Approach to the Analysis of Energy Indicators, Strategies and Policies).

ACKNOWLEDGMENT

This paper is supported by the Ministry of Science, Technological Development and Innovation of the Republic of Serbia pursuant to agreement № 451-03-66/2024-03/ 200148 with the University of Niš, Faculty of Occupational Safety.

REFERENCES

- [1] Pravilnik o Nacionalnoj listi indikatora zaštite životne sredine [Rulebook on the National List of Environmental Indicators], Official Gazette of the RS, No. 37/2011
- [2] Zakon o energetici, Strategija razvoja energetike Republike Srbije [Law on Energy, Energy Sector Development Strategy of the Republic of Serbia], Official Gazette of the RS, No. 84/04
- [3] Uredba o izmenama i dopunama Uredbe o utvrđivanju Programa ostvarivanja Strategije razvoja energetike Republike Srbije [Regulation on Amendments and Supplements to the Regulation on Establishing the Program for the Implementation of the Energy Sector Development Strategy of the Republic of Serbia], Official Gazette of the RS, No. 84/04
- [4] Zakon o ratifikaciji Ugovora o osnivanju Energetske zajednice – Zakon o potvrđivanju statuta Međunarodne Agencije za obnovljivu energiju [Law on the

- Ratification of the Energy Community Treaty - Law on the Confirmation of the Statute of the International Renewable Energy Agency], Official Gazette of the RS, No. 62/06
- [5] Strategija razvoja energetike Republike Srbije do 2015. godine [Energy Sector Development Strategy of the Republic of Serbia until 2015], Official Gazette of the RS, No. 44/200
- [6] Nacionalni program zaštite životne sredine [National Environmental Protection Program], Official Gazette of the RS, No. 12/10
- [7] Zakon o izmenama i dopunama Zakona o energetici [Law on Amendments and Supplements to the Law on Energy], Official Gazette of the RS, No. 62/2023
- [8] Zakon o energetici [Law on Energy], Official Gazette of the RS, No. 145/2014, 95/2018 – other law, 40/2021, 35/2023 – other law, and 62/2023
- [9] Uredba o uslovima i postupku sticanja statusa povlašćenog proizvođača električne energije [Regulation on Conditions and Procedures for Acquiring the Status of a Privileged Producer of Electricity], Official Gazette of the RS, No. 62/06
- [10] Uredba o merama podsticaja za povlašćene proizvođače električne energije [Regulation on Incentive Measures for Privileged Producers of Electricity], Official Gazette of the RS, No. 8/2013
- [11] Uredba o ugovoru o otkupu električne energije [Regulation on the Power Purchase Agreement], Official Gazette of the RS, No. 56/2016 i 61/2017
- [12] Uredba o naknadi za podsticaj povlašćenih proizvođača električne energije [Regulation on the Fee for Incentives for Privileged Producers of Electricity], Official Gazette of the RS, No. 8/2019
- [13] Uredba o visini naknade za podsticaj povlašćenih proizvođača električne energije [Regulation on the Amount of the Fee for Incentives for Privileged Producers of Electricity], Official Gazette of the RS, No. 3/2023
- [14] Uredba o načinu obračuna i načinu raspodele prikupljenih sredstava po osnovu naknade za podsticaj povlašćenih proizvođača električne energije [Regulation on the Method of Calculation and Distribution of Collected Funds from the Fee for Incentives for Privileged Producers of Electricity], Official Gazette of the RS, No. 8/2013
- [15] Uredba o izmenama i dopunama Uredbe o utvrđivanju Programa ostvarivanja Strategije razvoja energetike Republike Srbije do 2015. godine za period od 2007. do 2012. godine [Regulation on Amendments to the Regulation on Determining the Program for the Implementation of the Energy Sector Development Strategy of the Republic of Serbia until 2015 for the 2007-2012 Period], Official Gazette of the RS, No. 55/05, 71/05 – correction, 101/07, and 65/08
- [16] Strategija razvoja energetike Republike Srbije do 2025. godine [Energy Sector Development Strategy of the Republic of Serbia until 2025], Official Gazette of the RS, No. 101/2015
- [17] Integrisani nacionalni energetski i klimatski plan Republike Srbije za period do 2030. godine sa projekcijama do 2050. godine [Integrated National Energy and Climate Plan of the Republic of Serbia until 2030 with projections up to 2050], https://www.mre.gov.rs/extfile/sr/1138/INEKP_pre%C4%8Di%C5%A1%C4%87en_tekst_1.8.24.pdf
- [18] EU Energy Policy, <https://www.mre.gov.rs/tekst/1115/-integrisani-nacio-nalni-energetski-i-klimatski-plan-republike-srbije-za-period-do-2030-sa-vizijom-do-2050-godine.php>

Effect of Solar Radiation Intensity on the Drying of Tomatoes

Razika Ihaddadene¹, Nabila Ihaddadene², Réda Khama³, Hachemi Benouadah⁴

^{1,2}Departement of Mechanical Engineering, Faculty of Technology, University of M'sila, M'sila, Algeria,

^{1,2}Water, Environment and Renewable Energies Laboratory, Faculty of Technology, University of M'sila, M'sila, Algeria,

³Departement of Process Engineering, University of Batna2, Batna, Algeria,

⁴Departement of Finance and Accounting, University of M'sila, M'sila, Algeria

¹razika.ihaddadene@univ-msila.dz, ²nabila.ihaddadene@univ-msila.dz, ³r.khama@univ-batna2.dz, ⁴hachemi.benouadah@univ-msila.dz

Abstract—In this study, the effect of radiation intensity was investigated using a new device (halogen lamp) which simulate the solar radiation. The experiments were carried out in the laboratory, varying the radiation intensity between 2655 W/m² and 619.5 W/m² through 1062 W/m² and 1327.5 W/m². The results show that the shape of the MR curves is similar to that obtained with other drying methods, and the drying time of this new technique is reduced. Similarly, increasing the radiation intensity reduces the drying time. A mathematical model that describes the variation of MR as a function of time and solar radiation has been proposed. These results are in agreement with the experimental results.

Keywords - draying, solar radiation, tomatoes

I. INTRODUCTION

Lycopersicon esculentum, often known as tomato, is the fruit of a Herbacée plant native to Perou. After potatoes, it is currently the second most consumed agricultural product worldwide [1]. In tomatoes, considerable content of vitamin C and an extensive variety of phytochemicals reported health advantages. The primary elements with the strongest antioxidant action are lycopene and vitamin C [2]. Nevertheless, because of its high moisture content, tomato fruit has a limited shelf life and deteriorates quickly after harvest [3]. To solve

this problem, the drying technique is the most used to preserve tomatoes.

Drying is an important approach in the processing of agricultural products [4]. Many food products are dried to reduce their final weight and volume, increase their shelf life, reduce packaging costs, and lead to an important decrease in transportation and storage costs. Interest in the production of dried tomatoes is increasing due to the possibility of using them in salads, pizza, soups, willows, and other dishes [5]. It is possible to dry tomatoes as halves, slices, quarters, and powders [6].

Numerous solar drying techniques can be used to carry out the drying process [7]. There are several methods of drying tomatoes that affect the final product quality, including tomato variety, size, shape, and thickness of the tomato, air temperature, air humidity, air velocity, drying speed, and efficiency of the drying process [8]. Convection hot air drying is the most suitable technique at the commercial level. This technique has shown its superiority over other applicable methods in terms of quality preservation (color and carotenoid content) and low operating cost [9]. The temperature, speed and drying time are the only factors that can affect the final product quality [10]. The moisture content of dried tomatoes varies between 4% and 20% [11-14] according to the form of tomato



samples dried b (tomato slices, peels, pomace) [13-15]. Nevertheless, depending on the tomato sample form, the drying temperature and duration must be carefully selected in order to preserve the tomato final quality.

In this study, we investigated the possibility of drying using radiation as a drying mode as opposed to high-temperature convection, which is the most popular method. Solar radiation was simulated by a halogen lamp, and the experiments were carried out in the laboratory. The effect of radiation intensity on drying kinetics was studied. This study is structured into three sections. The first section, Materials and Methods, summarizes the sample preparation, experimental procedure, and drying kinetics. The results and their discussion are gathered in the second section, and this work is concluded with a conclusion.

II. MATERIALS AND METHODS

A. Sample Preparation

Fresh tomatoes (variety Roma) were purchased from a market in the city of M'sila (Algeria) and brought to the laboratory at ambient temperature. A selection of tomatoes was washed with water without any kind of treatment. Using a coupe-tomato, the tomatoes were cut into 6 mm pieces.

B. Experimental Procedure

In this study, the tomatoes were dried using the experimental ET200 (flat plan solar collector) described in detail in our previous work [16]. This device simulated the solar radiation by a halogen lamp. Although the main radiation from these lamps is in the visible spectrum (light), they also emit infrared rays (heat) and a small amount of UV. To limit this UV emission, halogen lamps are equipped with UV filters or a protective coating on the lamp glass, which blocks or considerably reduces UV rays. The lamp used in this study, is equipped with a protective coating.

To this end an experimental setup was built, it consists of four levels, each one receiving a different intensity (from top to bottom): (1) 2655 W/m², (2) 1327,5 W/m², (3) 1062 W/m² and 619,5 W/m² as illustrated in Fig. 1.

The tomatoes are placed in the four levels (1, 2, 3, 4), and the monitoring of their drying process is carried out by measuring the variation in their mass over time. The experiments were taking in the laboratory conditions. The tomato mass was measured by an electric digital scale

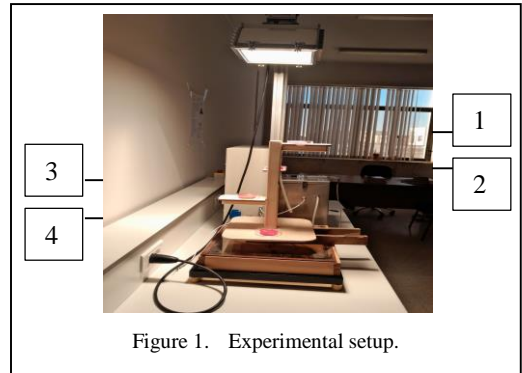


Figure 1. Experimental setup.

(JOANLAB model, range 0–600 g ±0.001 g, China). Measurements were made every half hour for the first level and every hour for levels 2, 3, and 4.

C. Drying Kinetics

Measuring the variation in dried tomato mass is a crucial parameter for comprehending the drying process. The (1) was used to determine the tomatoes' moisture content (M_t) at time t [17-19]:

$$M_t = \frac{w_i - w_d}{w_d} \times 100, \quad (1)$$

where w_i and w_d refer for the tomato's starting weight and the tomato's dry weight respectively. The moisture ratio (MR) of the draying tomato is expressed as [17-19]:

$$MR = \frac{M_t - M_e}{M_0 - M_e} \approx \frac{M_t}{M_0}, \quad (2)$$

where M_t , M_e and M_0 are the tomatoes' moisture content, the tomatoes' equilibrium water content and the tomatoes' initial water content.

The drying ratio DR is calculated using (3) as noted in [17,19], which is the ratio of the difference between two successive values of M_t times the difference Δt .

$$DR = \frac{M_{t+\Delta t} - M_t}{\Delta t}. \quad (3)$$

During this study the evolution of the MR was carried out according to a Gaussian model and its validation was carried out using two indices; the

coefficient of determination (R^2) and root mean square error $RMSE$. A good model is characterized by a high R^2 and a low value of $RMSE$. The R^2 and $RMSE$ are given by as:

$$R^2 = \sqrt{1 - \frac{\sum_{j=1}^N (MR_{jmod} - MR_{jexp})^2}{\sum_{j=1}^N (MR_m - MR_{jexp})^2}}, \quad (4)$$

$$RMSE = \sqrt{\frac{\sum_{j=1}^N (MR_{jmod} - MR_{jexp})^2}{N}}, \quad (5)$$

where:

MR_{jmod} : the moisture ratio predicted by the model of the j observation,

MR_{jexp} : the moisture ratio measured experimentally of the j observation,

MR_m : the mean value of the moisture ratio measured experimentally.

N : the number of observations.

III. RESULTS AND DISCUSSION

The evolution of the tomato moisture ratio (MR) over time for the different intensities (2655 W/m², 1327.5 W/m², 1062 W/m², and 619.5 W/m²) is illustrated in Fig. 2. All the MR curves follow the same pattern (it decreases during time). The same pattern was noted in the literature [20-22]. The drying time is affected by the radiation intensity. When the radiation intensity increases, the drying time decreases. The short time (200 min) was noted with the height intensity value (2655 W/m²) and the

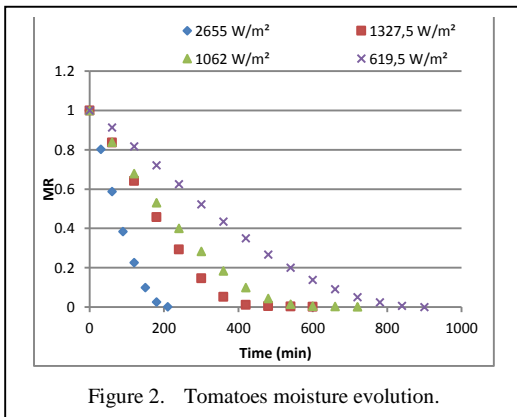


Figure 2. Tomatoes moisture evolution.

biggest time (840 min) was registered with the lowest intensity value (619.5 W/m²).

The degradation of MR over time (t) does not follow a linear law. The Gaussian function was chosen to see its evolution for the different intensities as illustrated in Figs. 3-6. The equations; (6)-(9) are used for the radiation intensities; 2655 W/m², 1327.5 W/m², 1062 W/m² and 619 W/m. respectively.

$$MR = 1.074 \exp \left[- \left(\frac{t + 33.36}{120.4} \right)^2 \right], \quad (6)$$

$$MR = 1.038 \exp \left[- \left(\frac{t + 53.63}{254} \right)^2 \right], \quad (7)$$

$$MR = 1.137 \exp \left[- \left(\frac{t + 134.7}{360.8} \right)^2 \right], \quad (8)$$

$$MR = 1.046 \exp \left[- \left(\frac{t + 124.3}{509.4} \right)^2 \right]. \quad (9)$$

As illustrated in Figs. 3-6, the Gaussian model fit well the MR evolution for all the tested radiations (2655 W/m², 1327.5 W/m², 1062 W/m² and 619.5 W/m²). Which is also confirmed by the statistical indices (R^2 and $RMSE$) grouped in Table I, the high values of R^2 (0.999) and the low values of $RMSE$ (0.012-0.013).

For the development of a general model that describes the MR evolution as a function of time

using the Gaussian model $a.exp \left(- \left(\frac{t-b}{c} \right)^2 \right)$,

the monitoring of the variation of the coefficients (a , b and c) of the Gaussian model as a function

TABLE I. STATISTICAL INDICES OF GAUSSIAN MODEL.

Radiation intensity	Statistical indices	
	R^2	$RMSE$
2655 W/m ²	0.999	0.0118
1327.5W/m ²	0.999	0.012
1062.5 W/m ²	0.999	0.012
619.5 W/m ²	0.999	0.013

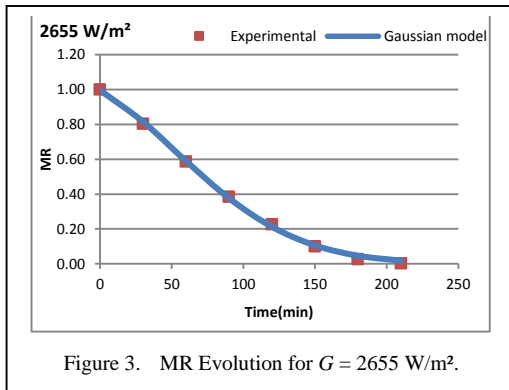


Figure 3. MR Evolution for $G = 2655 \text{ W/m}^2$.

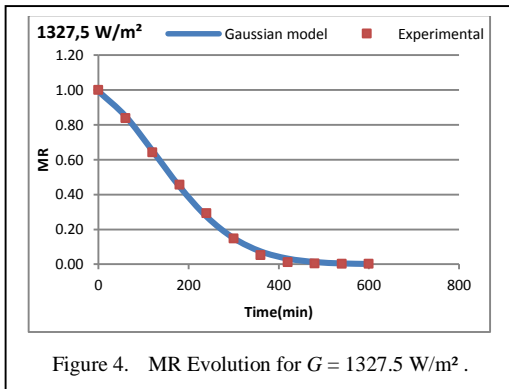


Figure 4. MR Evolution for $G = 1327.5 \text{ W/m}^2$.

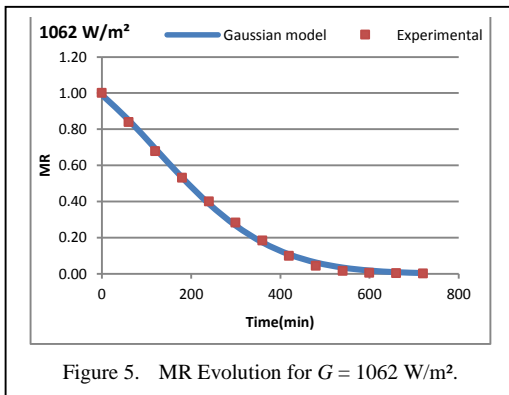


Figure 5. MR Evolution for $G = 1062 \text{ W/m}^2$.

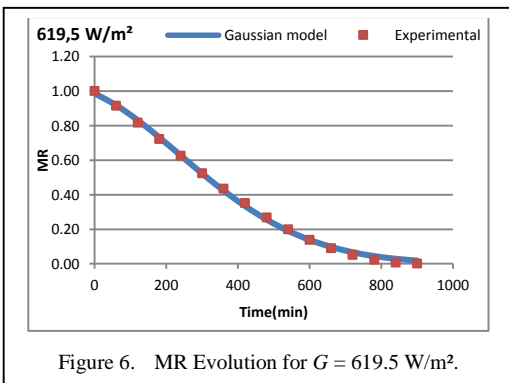


Figure 6. MR Evolution for $G = 619.5 \text{ W/m}^2$.

of the radiation intensity was carried out. The Eqs. (10), (11) and (12) represent the evolution of the coefficients a , b and c as a function of radiation intensity using the Fourier model.

$$a = 0.9635 - 0.1815\cos(0.003176G) + 0.01343\sin(0.003176G), \quad (10)$$

$$b = -9.491 + 102.5\cos(0.002722G) - 103.7\sin(0.002722G), \quad (11)$$

$$c = 307.4 + 241.6\cos(0.001588G) + 81.96\sin(0.001588G). \quad (12)$$

The Fourier model allows to calculate the values of the constants (a , b and c) of the Gaussian model used for the evolution of MR as a function of time with good precision, as shown in Figs. 7-9. As illustrated the comparison of the previously calculated values and the values calculated using the Fourier model reveals good agreement.

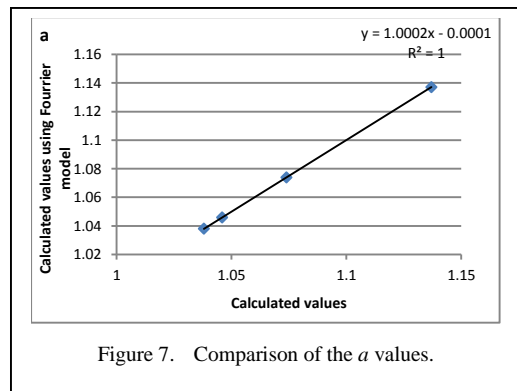


Figure 7. Comparison of the a values.

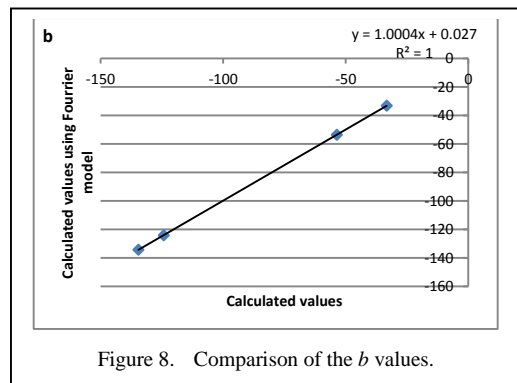
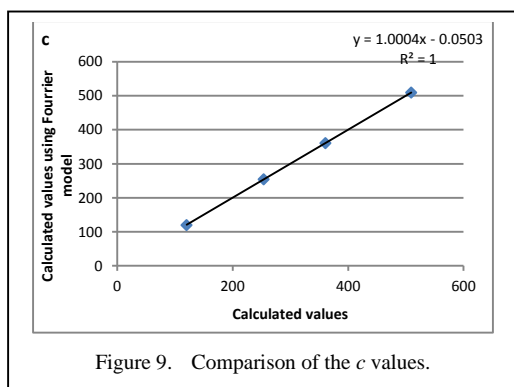


Figure 8. Comparison of the b values.



As a result, a generalized model can be presented in Eq. (13), which expresses the evolution of MR in time for any solar radiation value. The value of a , b and c are done in Eqs. (11), (12) and (13).

$$MR = a \exp \left[- \left(\frac{t+b}{c} \right)^2 \right]. \quad (13)$$

The validation of this model was done using the statistical parameters as illustrated in Table II. The generalized model's validation is supported by the R^2 values (0.999), which reveal large as well as small values (0.012-0.013) for the $RMSE$.

TABLE II. STATISTICAL INDICES OF THE GENERALIZED MODEL.

Radiation intensity	Statistical indices	
	R^2	$RMSE$
2655 W/m ²	0.999	0.0118
1327.5W/m ²	0.999	0.012
1062.5 W/m ²	0.999	0.012
619.5 W/m ²	0.999	0.013

IV. CONCLUSION

After during this study, a new drying technique was adapted for drying tomatoes in the laboratory. It is based on the use of a halogen lamp that simulates solar radiation.

The results have shown the possibility of drying by lamps in addition to the reduced drying time compared to other methods. Similarly, the intensity of the radiation affects the drying time; the drying time decreases with the increase in the intensity of the radiation.

A generalized model of the MR evolution as a function of time for the different intensities was developed using a Gaussian model. The results show a good agreement between the experimental and the simulated (model) results.

ACKNOWLEDGMENT




We thank ATRST (Agence Thématique de Recherche en Sciences et Technologie) in Algeria, which funded this work as part of a national research project entitled "Production, implementation and marketing of solar dryers and their products" PNR- 16/2023.

REFERENCES

- [1] Planetoscope. (2024). *World tomato production*. Available at: <https://www.planetoscope.com/fruits-legumes/1266-production-mondiale-de-tomates.html>
- [2] Stratakos, A. C., Delgado-Pando, G., Linton, M., Patterson, M. F., & Koidis, A. (2016). Industrial scale microwave processing of tomato juice using a novel continuous microwave system. *Food Chemistry*, 190, 622-628.
- [3] Kaur, R., Kaur, K., & Ahluwalia, P. (2020). Effect of drying temperatures and storage on chemical and bioactive attributes of dried tomato and sweet pepper. *Lwt*, 117, 108604.
- [4] Bennamoun, L., Khama, R., & Léonard, A. (2015). Convective drying of a single cherry tomato: Modeling and experimental study. *Food and bioprocesses processing*, 94, 114-123.
- [5] Movaghamejad, K., & Nikzad, M. (2007). Modeling of tomato drying using artificial neural network. *Computers and electronics in agriculture*, 59(1-2), 78-85.
- [6] Bakry, R. S., Khater, E. S. G., Bahnasawy, A. H., & Ali, S. A. (2021). Effect of drying methods on the quality of dried tomatoes. *Misr Journal of Agricultural Engineering*, 38(2), 155-180.
- [7] Khater, E. S. (2020). Effect of distillation methods on essential oil yield and composition of basil dried by different drying systems. *Annals of Agricultural Science, Moshtohor*, 58(2), 247-260.
- [8] Farooq, S., A. et al. (2020). Physicochemical and nutraceutical properties of tomato powder as affected by pretreatments, drying methods, and storage period. *International Journal of Food Properties*, 23(1), 797-808.
- [9] Lazzarini, C., et al. (2022). Sustainable drying and green deep eutectic extraction of carotenoids from tomato pomace. *Foods*, 11(3), 405.
- [10] Hussein, J. B., Oke, M. O., Ajetunmbi, R. I., & Agboola, F. F. (2022). Modelling the drying properties of tomato in a hot-air dryer using hybrid ANN-GA technique. *Journal of Applied Sciences*, 22(5), 262-272.
- [11] Albanese, D., Adiletta, G., D' Acunto, M., Cinquanta, L., & Di Matteo, M. (2014). Tomato peel drying and carotenoids stability of the extracts. *International Journal of Food Science & Technology*, 49(11), 2458-2463.

- [12] Hatami, T., Meireles, M. A. A., & Ciftci, O. N. (2019). Supercritical carbon dioxide extraction of lycopene from tomato processing by-products: Mathematical modeling and optimization. *Journal of food engineering*, 241, 18-25.
- [13] Khama, R., Aissani-Benissad, F., Alkama, R., Fraikin, L., & Léonard, A. (2022). Modeling of drying thin layer of tomato slices using solar and convective driers. *Agricultural Engineering International: CIGR Journal*, 24(1).
- [14] Tahmasebi, M., & Emam-Djomeh, Z. (2021). Lycopene degradation and color characteristics of fresh and processed tomatoes under the different drying methods: A comparative study. *Chemical Papers*, 75(7), 3617-3623.
- [15] Fărcaș, A. C., Socaci, S. A., Michiu, D., Biriș, S., & Tofană, M. (2019). Tomato waste as a source of biologically active compounds. *Bulletin UASVM Food Science and Technology*, 73(2), 55-60.
- [16] Razika, I., Nabila, I., Madani, B., & Zohra, H. F. (2014). The effects of volumetric flow rate and inclination angle on the performance of a solar thermal collector. *Energy Conversion and Management*, 78, 931-937.
- [17] Tawfik, M. A., Oweda, K. M., Abd El-Wahab, M. K., & Abd Allah, W. E. (2023). A New mode of a natural convection solar greenhouse dryer for domestic usage: performance assessment for grape drying. *Agriculture*, 13(5), 1046.
- [18] Rahmani, Y., & Khama, R. (2024). Improving open sun and indirect solar drying kinetics with physicochemical quality of regal seedless grapes by novel pretreatment solution. *Journal of Stored Products Research*, 106, 102292.
- [19] Badaoui, O., Hanini, S., Djebli, A., Haddad, B., & Benhamou, A. (2019). Experimental and modelling study of tomato pomace waste drying in a new solar greenhouse: Evaluation of new drying models. *Renewable energy*, 133, 144-155.
- [20] Jmai, S., Ben Slimane, N., Guiza, S., Messaoudi, S. E., & Mohamed, B. (2023). Experimental and modeling of tomato slices sorption isotherms and thin layer drying kinetics for a solar drying plant design. *Iran. J. Chem. Chem. Eng. Research Article Vol*, 42(8).
- [21] Doymaz, I. (2007). Air-drying characteristics of tomatoes. *Journal of Food engineering*, 78(4), 1291-1297.
- [22] Sogi, D. S., Shivhare, U. S., Garg, S. K., & Bawa, A. S. (2003). Water sorption isotherm and drying characteristics of tomato seeds. *Biosystems Engineering*, 84(3), 297-301.

Experimental Study of Fouling Effect on Feed Water Heaters: A CFD Modeling Approach in Steam Power Plants

Mkpamdi N. Eke¹, Emmanuel E. Duke², Imole A. Agunbiade³

^{1,2,3}Department of Mechanical Engineering, University Of Nigeria, Nsukka, Nigeria

¹mkpamdi.eke@unn.edu.ng, ²emmanuel.duke.243689@unn.edu.ng, ³imole.agunbiade.251910@unn.edu.ng

Abstract—This study examines the impact of fouling in feed water heaters within a 1320 MW steam power plant. Two models were created using Autodesk to represent the feed water heater model under clean and fouled conditions respectively. Acrylic was added to the fouled model, as an experimental foulant to understand the possible effect on the feed water heater. A computational fluid dynamics (CFD) analysis was performed on both heater models for the low-pressure heater 2 designed using Autodesk Fusion. The results show an increase in the outlet temperature for the fouled model by 8 °C from 118 °C to 126 °C indicating an impact of the fouling effect on the thermal efficiency of the feed water heater.

Keywords - fouling, temperature, feed water heater, low pressure heater, efficiency

I. INTRODUCTION

Feed water heaters are thermal power plant equipment designed to function as heat exchangers which transfer heat from a source to a sink. In fossil-fired plants, feed water heaters extract steam from the turbine to preheat feed water before entering the boiler. Preheating the water, increases the thermal efficiency of the plant by increasing the heat energy content [1]. As with heat exchangers, Across the feed water heater tubing, heat is transferred along and within the surfaces, as a result, there arises thermal resistance caused by fouling. Fouling is the build-up of scale, rust, dirt, precipitates on the heat transfer surfaces which creates an insulating layer which leads to resistance to heat transfer or

flow [2]. Fouling is caused by low fluid quality, chemistry, oxidation, polymerization and coking [3]. The effects of fouling are detrimental to the equipment, plant costs and efficiency. Due to fouling, there is increased maintenance costs equaling 2.5 to 3 times the initial heat exchanger purchasing price [4], other implications of fouling include higher pumping losses, spike in fuel usage, and reduced heat exchanger performance time. Troubleshooting techniques have been employed to understand and mitigate fouling effects in heat exchangers [5], amidst these techniques, modelling and simulating feed water heater behavior can offer important learnings that can be implemented in mitigating the effects of fouling.

Several studies have been made on fouling in heat exchangers, and simulation in low pressure heaters, a selection of them is discussed.

Reference [6] analyzed a low pressure closed feed water heater using a one-dimensional approach in a computational fluid dynamics (CFD) tool, The study prescribed an inlet tube temperature for improved efficiency of the steam power plant after considering the effect of inlet tube temperature on the outlet tube temperature, pressure of steam drum and steam drum level in transient condition. Reference [7] studied fouling layer thickness in exhaust gas recirculation systems by modeling with a dynamic mesh model in ANSYS Fluent, this approach provided insights into fouling deposition dynamics and fouling growth across the model geometry.



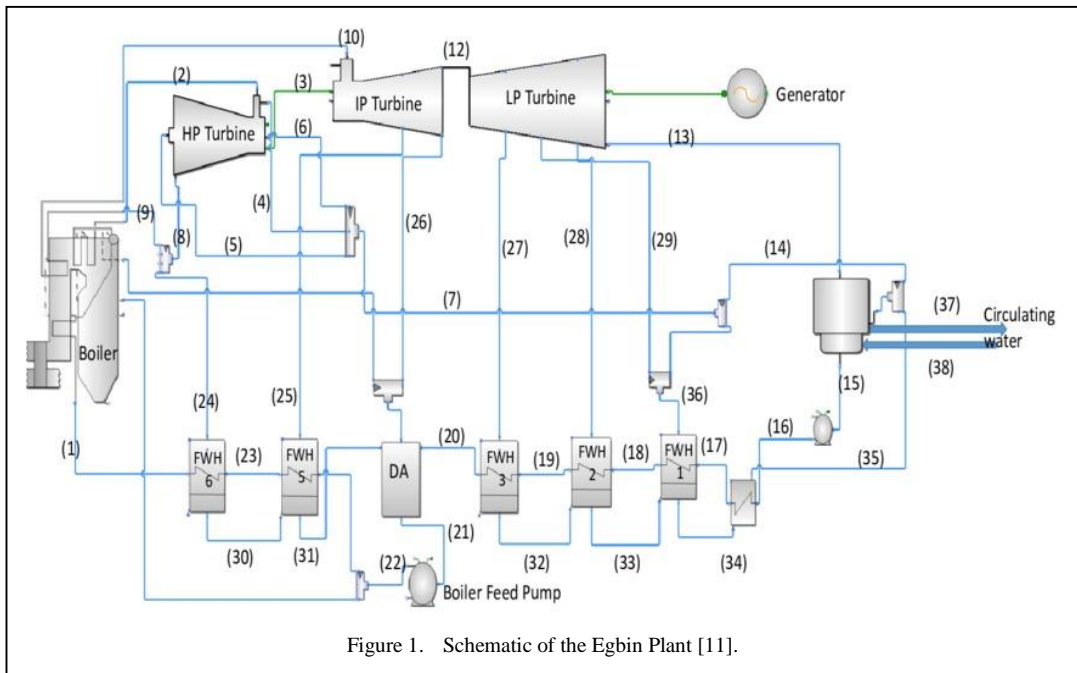


Figure 1. Schematic of the Egbin Plant [11].

Reference [8] used the DIAGAR software to investigate the performance of a shell and tube recuperative feed-water heater degraded by fouling. The fouling induced degradation resulted in an increase of the heater load, causing turbine set deficiency. Reference [3] developed a mathematical model to predict the fouling behavior in simulated cleaned and fouled operations in a single-shell heat exchanger at the hot end of a refinery preheat train. The study established that fouling on the shell side impairs heat transfer, increasing pressure difference, and resisting flow. Reference [9] showed that operating temperatures due to non-uniform fouling in shell-and-tube heat exchangers can exceed design limits, leading to equipment damage. Reference [10] implemented an approach that demonstrated the changing thermal and hydraulic reactions within a cooling tower and a heat exchanger. Reference [4] studied the behavior of brazed plate and shell-tube heat exchangers under daily ion and deposit formation fouling conditions in refrigerant condensers, through this approach, the presence of thermal resistance was confirmed, although it underestimated resistance in severe particulate fouling cases. Reference [12] incorporated a model, using mass, differential energy balance, and mechanical energy balance to determine fouling rates at each point along the exchanger surface.

Finally, [13] considered a sediment layer on heat exchanger surfaces, discovering that this build-up causes an increase in wall temperature on the affected area which leads to pressure rise and reduced thermal efficiency of the heat exchanger.

II. METHODOLOGY

A. Steam Power Plant

The steam power plant analyzed in this study is the Egbin 1320 MW thermal plant equipped with feed water heaters, turbines, and boilers that are standard for fossil-fueled plants. The equipment used for this study is the low-pressure feed water heater 2. The schematic representation of the components and their configuration within the plant is shown in Fig. 1.

B. Feed Water Heater

The feed water heater was modeled using Autodesk fusion and analyzed using computational fluid dynamics (CFD) to simulate both cleaned and fouled conditions. Based on equipment data obtained from the Egbin Thermal Plant, a three-dimensional computer aided design (CAD) model was created in Autodesk CAD environment. Fig. 2 shows a section of the CAD model

C. Fouling Estimation

Feedwater heater tubes are made of mostly stainless steel and other alloys. These materials

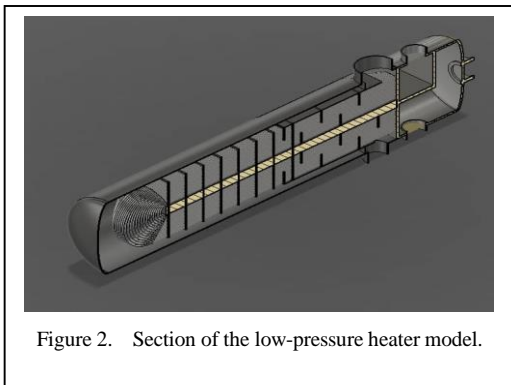


Figure 2. Section of the low-pressure heater model.

experience corrosion leading to exfoliation on the tube surfaces and on the steam side. Reference [1] observed that polymer composite tubes showed lower fouling compared to stainless steel tubes. In order to quantify the exfoliation or fouling due to corrosion, pellets of acrylic was experimented with. It was introduced to the feed water heater model in the Autodesk Fusion Simulation environment. The choice of acrylic was based on its nature as a polymer, solubility and aging behavior and assumption that scales, build-up in the feed water heater could become soluble over time reducing the likelihood of increased volume of outlet feedwater due to the presence of particles caused by fouling.

D. Computational Fluid Dynamics (CFD)

The objective of the computational fluid dynamics CFD analysis was to evaluate the impact of fouling on the thermal performance of the feed water heaters. The scope of the analysis includes both clean and fouled conditions for low-pressure heater 2. The computational fluid dynamics (CFD) analysis was performed in this study using Autodesk fusion, with geometric modeling and meshing performed in Autodesk Fusion 360. Given the focus on thermal efficiency and fouling in feed water heaters, the turbulence model selected was the $k-\epsilon$ model, suited for simulating heat transfer in industrial applications. In the simulation of the feed water heater model, certain assumptions were considered and applied such as (1) the fluid's specific heat is believed to be constant throughout the tube's length, (2) the fluid is compressible, (3) the value of the condensing and drains cooling sections of the feed water heater remain the same throughout the flow channel, (4) individual feed water heater tube behavior is uniform and heat loss through the outer shell side is negligible, (5) there is no

leakage through the baffle plates, (6) heat transfer by diffusion does not occur during the process. The CFD analysis was implemented first for the clean model with no presence of fouling. Subsequently, the fouled model was simulated, incorporating the effects of scale buildup on heat transfer efficiency using acrylic pellets along small increments of the tube length.

III. EXPERIMENTAL APPROACH

Plant feed water heater data for low pressure heater 2 was obtained for a period of two months after the heater has undergone cleaning. The plant design parameters are shown in Table I. The models for the study were created in the open-source computer aided design tool - Autodesk Fusion. A section of the model is seen in Figs. 2 and 3 shows the temperature distribution within the heater for the fouled model.

TABLE I. PLANT DATA.

Simulation Data	Low pressure feed water heater
Tube design pressure	3,700 kpa
Tube design temperature	1140 C
Design water velocity through tubes	2.01 m/s
Shell design pressure	150 kpa
Shell design temperature	1280 C
Internal dimensions of the tubes	15.9 mm
The tubes' wall thickness	115 mm
The number of tubes	530
Tube design pressure	3.700 kpa
Tubes length	304.5 mm

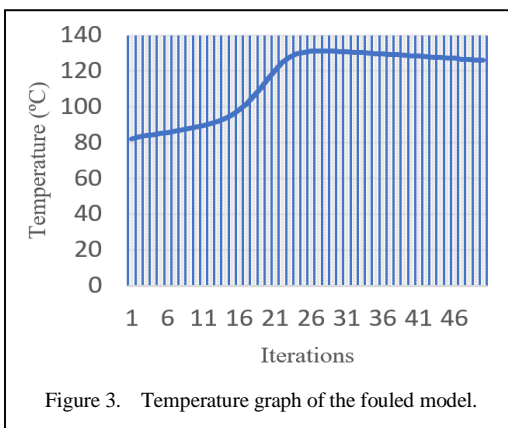


Figure 3. Temperature graph of the fouled model.

The geometry of the Feed water heater models including the number of tube passes, tube lengths, and tube diameters were created in the Autodesk work environment with specifications to determine the fluid paths for the hot and cold fluids, and the inlet and outlet locations. The heat exchanger model was implemented in the Autodesk fusion simulation environment by simulating the heat exchanger model with real time plant data. Following this approach, the relationship between the fouling process and intensive properties of the heat exchanger can be established. Reference [4] explained this approach in their work, where the formation of fouling deposit is calculated from measured data including pressure drop and inlet temperatures using Hexxcell Studio, an advanced thermo-hydraulic fouling prediction and analyzing tool.

IV. RESULTS AND DISCUSSION

From the simulation data, representations for clean and fouled model conditions are obtained. As fouling deposits accumulate on the heat transfer surfaces, insulating layers grow that hinder heat transfer between the fluids. This results in uneven temperature distributions across the surfaces as the fouling layer acts as a barrier to efficient heat exchange. The outlet temperature for the fouled model is significantly higher than the tube design temperature according to Table I supporting [9] analysis that non-uniform fouling could lead to temperatures

outside shell-and-tube heat exchangers design limits.

Fig. 4 shows a graph representing the graphical properties of the simulation obtained from the simulation data over fifty (50) iterations. The graph displays the variation of different properties that are important to understand the study, they include the flow velocity in the x-direction, pressure, turbulent kinetic energy, total energy dissipation over 50 iterations during the simulation. It is observed that the feed water heater goes through an input of feed water evident by the changes in the early iterations, as the simulation progresses as with actual plant running velocity, pressure and energy dissipation fluctuate before stabilizing. The stabilization suggests that the heater is approaching an equilibrium state, towards a steady state. The initial turbulence begins to settle, as indicated by the decline in turbulent kinetic energy (TKE) and total energy dissipation (TED).

Fig. 5 shows a graph representing the temperature variation for the clean model. In the graph, the temperature starts around 80 °C and increases gradually as the iterations progress. Around iteration 20, there is a rise in temperature owing to input from bled steam from the turbine, stabilizing around 120 °C after iteration 30, leaving at 125.87 °C, this behavior shows an ideal operation of the low-pressure feed water

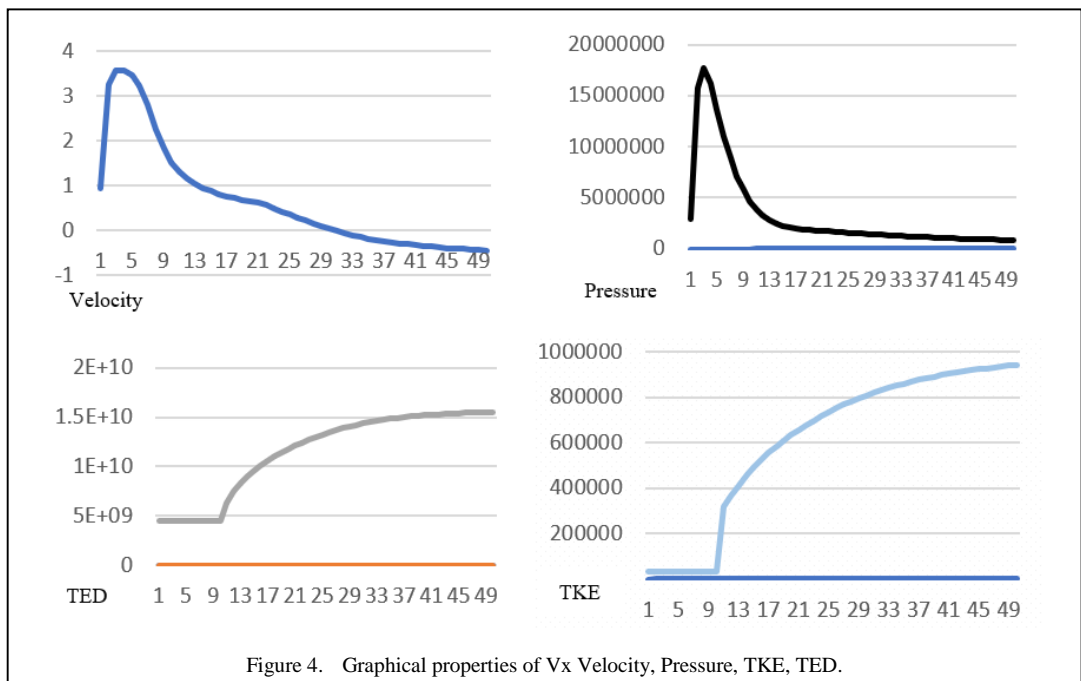
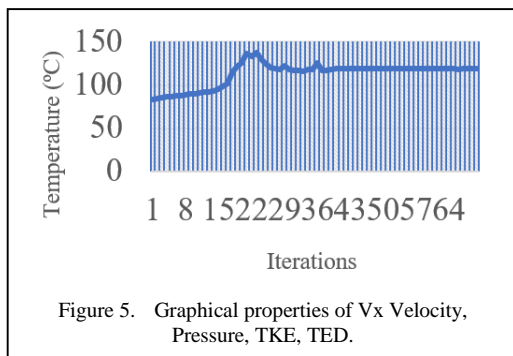


Figure 4. Graphical properties of Vx Velocity, Pressure, TKE, TED.



heaters without fouling. Fig. 3. shows the temperature distribution for the fouled model, initially the temperature follows a similar pattern as in Fig. 5, starting around 80 °C and increasing steadily until around iteration 20. However, after this point, the temperature shows some fluctuations, with a few peaks and troughs, before ending at 118 °C. The fluctuations observed after iteration 20 indicate some transient behavior or instability in the system, this fluctuation shows changes in heat transfer dynamics, caused by scale build up developed on the model, in the form of the acrylic pellets. Eventually, the heater reaches a stable temperature, similar to Fig. 4, but after experiencing these transient fluctuations.

The amount of fuel needed to produce steam is decreased when feedwater is pre-heated in the feed water heater before it enters the boiler, thus lowering running costs [14]. Higher feed water outlet temperature into the boiler is desired for improved efficiency and increased power output, however, the time it takes to pre-heat the feed water enroute to the boiler may be lengthened due to the presence of fouling leading to increased costs of running the pumps, and increased fuel consumed to heat the feed water to desired temperatures. Also, feed water inlet temperature and conditions are possible causative factors to fouling build up, thermal resistance and increased running costs. It is established that the presence of fouling can also contribute to increased temperature caused by presence of impurities or foulants in the feed water with differing properties.

V. CONCLUSION

The accumulation of fouling deposits on the internal surfaces of pipes and tubes within feed water heaters reduces heat transfer efficiency. This reduction is caused by the insulating properties of the fouling layer, which obstructs the effective transfer of thermal energy between

the feed water and the heating medium or source. This reduction leads to the increase in the feed water outlet temperature, time of heating and increasing fuel usage in pre-heating. This rise in temperature is a direct result of the impaired heat transfer, leading to a greater retention of thermal energy within the feed water. Consequently, the feed water exits the heater at a higher temperature than expected. In the low-pressure feed water heater 2, from Fig. 5 the outlet temperature of the fluid under clean conditions is at 118 °C, whereas it rises to 126 °C when fouling is present as seen in Fig. 3. Recent study by [1], showed that novel polymer composite tubes had fewer fouling tendencies proving a possibility of a migration to better material mix for tube manufacture. Investigating on possible feed water heater tube materials as an improvement or replacement for stainless steel being used in feed water heater tubes manufacturing could provide possible alternatives to ensure reduced fouling effect on feed water heater tubes.

ACKNOWLEDGMENT

The authors thank the Egbin power plc for supporting this study with relevant data.

REFERENCES

- [1] Schilling, S., Glade, H., & Orth, T. D. (2021). Investigation of Crystallization Fouling on Novel Polymer Composite Heat Exchanger Tubes. *Heat Transfer Engineering*, 43, 1326-1336.
- [2] Iloje, C. (2018). *Introductory course in heat and mass transfer (First)*. Nsukka: University of Nigeria Press.
- [3] Emilio, D., Francesco, C., & Sandro, M. (2019). Modeling and Prediction of Shell-Side Fouling in Shell-and-Tube Heat Exchangers. *Heat Transfer Engineering*, 40(11), 845-861.
- [4] Luai, A., Aftab, A., & Abdullah, A. (2012). Experimental Study of Fouling Resistance in Twisted Tube Heat Exchanger. *Heat Transfer Engineering*, 33(12), 1024-1032.
- [5] Nicolaas Hallatt (2019). The Development of a Test Rig to Determine Fouling Factors of Feed water Heaters (Unpublished master's dissertation). University of Cape Town, Cape Town, South Africa.
- [6] Byregowda K. Ca., S. N Amith kumarb, K. Preethic, H. A. Shivappad, & T. N. Raju (2014). Modelling and Simulation of Feed Water Heater for Steam Power Plant Systems. *International Journal of Ignited Minds*, 2, 1.
- [7] Concepción, P., Eduardo, S., Marcos, C., & Jesús, V.. (2020). Development of a Computational Fluid Dynamics Model for Predicting Fouling Process Using Dynamic Mesh Model. *Heat Transfer Engineering*, 41(2), 199-207.
- [8] Dariusz, B., Jerzy, G., Tomasz H., Marian, T., & Andrzej, G., (2009). Analysis of fouling thermal

- resistance of feed water heaters in steam power plants. *Polish Maritime Research, Special issue 2009/S1*, 3-8.
- [9] Les Jackowski, Peter R., & Rich S., (2017). Impact of Non-uniform Fouling on Operating Temperatures in Heat Exchanger Networks. *Heat Transfer Engineering*, 38(7-8), 753-76.
- [10] Lorenzo, C., & Xiaoxiao, W. (2015). Effect of Fouling on the Thermal Performance of Condensers and on the Water Consumption in Cooling Tower Systems. *Heat Transfer Engineering*, 36(7-8), 663-675.
- [11] Eke, M. N., Onyejekwe, D. C., Iloeje, O. C., Ezekwe, C. I., & Akpan, P. U. (2018). Energy and exergy evaluation of a 220MW thermal power plant. *Nigerian Journal of Technology*, 37(1), 115-123.
- [12] Souza, Aline R. C., Costa, André L. H. (2019). Chemical Engineering Research & Design. *Transactions of the Institution of Chemical Engineers Part A*, 141, 15-31.
- [13] Barszcz, T., & Czop, P. (2010). A Feed Water Heater Model Intended for Model-Based Diagnostics. *Applied Thermal Engineering*, 31, 8-9.
- [14] Okwabi, R., Mensah, G., Fiagbe, Y. A., & Davis, F. (2023). Towards the estimation of quantity of fuel consumed in steam generation through predictive modelling of feedwater temperature. *Scientific African*.

Exergetic Performance Analysis of a CPV/T-TEG System

Khaled Mouaici¹, Henda Kahalerras², Kamil Arslan³, Brahim Fersadou⁴, Selahattin Çelik⁵

^{1,2,4}Houari Boumediene University (USTHB), LTPMP, Algiers, Algeria,

^{3,5}Ankara Yıldırım Beyazıt University, Mechanical Engineering Department, Ankara, Türkiye,

^{3,5}Hydrogen Technologies and Energy Research Center (H2 TEAM),

Ankara Yıldırım Beyazıt University, Ankara, Türkiye

¹kmouaici@usthb.dz, ²hkahalerras@usthb.dz, ³kamilarslan@karabuk.edu.tr,

⁴bfersadou@usthb.dz, ⁵selahattincelik@aybu.edu.tr

Abstract—This article focuses on a numerical analysis of the exergetic performance of a photovoltaic-thermal hybrid collector equipped with a composite parabolic concentrator and a thermoelectric generator, comparing four different types of heat transfer fluids (HTF). The proposed system is exposed to solar radiation reflecting the climatic conditions of the southern region of Algeria, more precisely in the Ain Salah. The heat transfer fluid (HTF) is introduced into the tube at a constant mass flow rate of 0.01 kg/s and a concentration ratio (CR) of 7, maintaining a uniform temperature at the inlet. The equations describing the temporal variations of temperatures in each component of the CPV/T-TEG system are derived from the thermal balances and resolved using the fourth order Runge-Kutta method. The results show that exergetic production reaches its maximum during intense solar radiation. The CPV/T-TEG system has a significantly greater electrical exergy than thermal exergy, with a ratio of ten. In addition, the overall exergetic efficiency is negatively affected by the temperature of the photovoltaic (PV) component and is maximized when using hybrid water/Cu-Al₂O₃-MWCNT as a heat transfer medium. In addition, the Water/Cu-Al₂O₃-MWCNT ternary nanofluid performs better than other heat transfer fluids, achieving an average exergetic efficiency of 10.124%, which is significantly higher than the water yield of 5.935%.

Keywords - photovoltaic, HTF, exergy

I. INTRODUCTION

The integration of concentrated photovoltaic/thermal systems (CPV/T) with thermoelectric generators (TEG) represents a major advance in renewable energy technology, improving efficiency through efficient conversion and use of energy. The exergetic analysis of these hybrid systems is crucial, as it focuses on energy quality, allowing the identification of irreversibilities and the optimization of performance. Recent research suggests that coupling CPV/T systems with TEGs can significantly improve energy production by efficiently capturing and converting solar radiation and waste heat [1]. Studies have highlighted the importance of optimal concentration design and materials, which can improve thermal efficiency and minimize energy losses [2]. In addition, the incorporation of advanced thermoelectric materials has demonstrated its potential to improve the exergetic efficiency of the system [3]. Dynamic modelling of CPV/T-TEG systems under fluctuating environmental conditions was studied, which provided important information on their thermodynamic behaviour and optimisation potential [2]. In addition, the life cycle assessments by the exercise have highlighted the environmental benefits of these hybrid systems compared to traditional energy solutions [4]. Exergetic analyses are vital for advancing the design and efficiency of CPV/T-



TEG systems, supporting their role as sustainable energy solutions in the transition to a low-carbon future.

II. CONCEPTUAL DESIGN AND METODOLOGY

The CPV/T-TEG system utilized in this study is illustrated in Fig. 1. It operates under the climatic conditions of Ain Salah, a city in southern Algeria.

The CPV/T-TEG system can be modeled by applying the energy balance equation to each of its components as follows:

- Energy balance for the glazing

$$\rho_g \delta_g C_{pg} \frac{dT_g}{dt} = \alpha_g G \rho_{con} CR \gamma_t - (h_{conv,g-a} + h_{rad,g-s})(T_g - T_a) - (h_{conv,g-pv} + h_{rad,g-pv})(T_g - T_{pv}) \quad (1)$$

- Energy balance for the PV panel

$$\rho_{pv} \delta_{pv} C_{ppv} \frac{dT_{pv}}{dt} = (\tau \alpha)_{pv} G \rho_{con} \cdot CR \gamma_t \tau_g - E - (h_{conv,g-pv} + h_{rad,g-pv})(T_{pv} - T_g) - h_{cond,pv-cr}(T_{pv} - T_h) \quad (2)$$

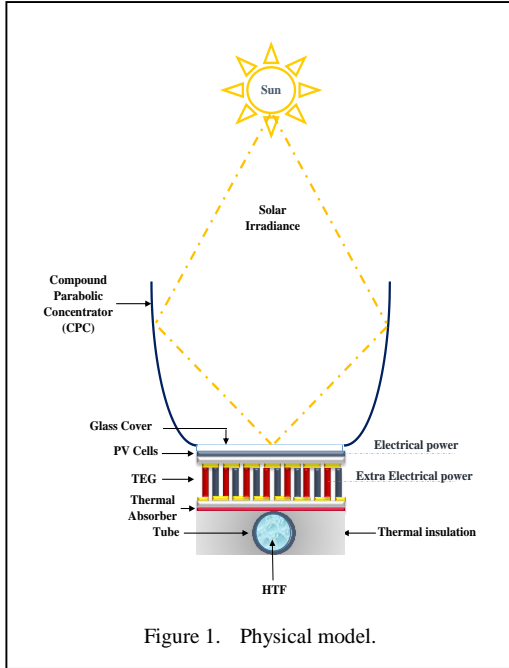


Figure 1. Physical model.

E is the electrical yield produced by the PV layer and provided by:

$$E = (\tau \alpha)_{pv} G \rho_{con} CR \gamma_t \cdot \tau_g P \eta_r (1 - \beta_r (T_{pv} - T_r)) \quad (3)$$

- Energy balance for the hot ceramic layer of TEG

$$\rho_{cr} \delta_{cr} C_{p,cr} \frac{dT_h}{dt} = h_{cond,pv-cr} (T_{pv} - T_h) - n_{TEG} \cdot [SI_{TEG} T_h + k_{TEG} (T_h - T_c) - 0.5 R_{int} I_{TEG}^2] \quad (4)$$

- Energy balance for the cold ceramic layer of TEG

$$\rho_{cr} \delta_{cr} C_{p,cr} \frac{dT_c}{dt} = -n_{TEG} [SI_{TEG} T_c + k_{TEG} (T_h - T_c) + 0.5 R_{int} I_{TEG}^2] - h_{cond,cr-abs} (T_c - T_{abs}) - \frac{A_{cr-t}}{A} h_{cond,cr-t} (T_c - T_t) \quad (5)$$

- Energy balance for the thermal absorber plate

$$\rho_{abs} \delta_{abs} C_{p,abs} \frac{dT_{abs}}{dt} = h_{cond,cr-abs} (T_c - T_{abs}) - \frac{A_{abs-t}}{A} h_{cond,abs-t} (T_c - T_t) - \frac{A_{abs-i}}{A} h_{cond,abs-i} (T_{abs} - T_i) \quad (6)$$

- Energy balance for the tube

$$M_t C_{p,t} \frac{dT_t}{dt} = A_{abs-t} h_{cond,abs-t} (T_{abs} - T_t) - A_{cr-t} h_{cond,cr-t} (T_c - T_t) - A_{HTF-t} h_{HTF-t} (T_t - T_{HTFm}) - A_{t-i} h_{cond,t-i} (T_t - T_i) \quad (7)$$

- Energy balance for the thermal insulation

$$M_i C_{p,i} \frac{dT_i}{dt} = A_{abs-i} h_{cond,abs-i} (T_{abs} - T_i) + A_{t-i} h_{cond,t-i} (T_t - T_i) - A h_{a-i} (T_i - T_a) \quad (8)$$

- Energy balance for the HTF

$$M_{HTF} C_{p,HTF} \frac{dT_{HTF}}{dt} = A_{HTF-i} h_{HTF} \cdot (T_i - T_{HTFm}) + (T_i - T_i) - Ah_{a-i} (T_i - T_a) \quad . (9)$$

$$\text{with } T_{HTFm} = \frac{T_{HTFi} + T_{HTFo}}{2} .$$

The fourth-order Runge-Kutta method was employed to solve the mathematical model that describes the operation of the CPV/T-TEG system. In this regard, the nanofluids used in the study were prepared using the "two-step" method, with a maximum volume fraction of 2% and a particle size of 10 nm. These characteristics of the nanofluids are essential for accurately predicting the thermophysical properties of the heat transfer fluid, which are determined using the following correlations [5]:

- Viscosity:

$$\mu_{mf} = \frac{\mu}{(1-\phi_{Cu})^{2.5} (1-\phi_{Al_2O_3})^{2.5} (1-\phi_{MWCNT})^{2.5}} \quad . (10)$$

- Density:

$$\rho_{mf} = (1-\phi_{MWCNT}) \cdot \left\{ (1-\phi_{Al_2O_3}) \left[(1-\phi_{Cu}) \rho_f + (\phi\rho)_{Cu} \right] + (\phi\rho)_{Al_2O_3} \right\} + (\phi\rho)_{MWCNT} \quad . (11)$$

- Thermal Conductivity:

$$k_{mf} = k_{mf} \cdot \frac{k_{MWCNT} + 2k_{mf} - 2\phi_{MWCNT} (k_{mf} - k_{MWCNT})}{k_{MWCNT} + 2k_{mf} + \phi_{MWCNT} (k_{mf} - k_{MWCNT})} \quad . (13)$$

$$k_{mf} = k_{nf} \frac{k_{Al_2O_3} + 2k_{nf} - 2\phi_{Al_2O_3} (k_{nf} - k_{Al_2O_3})}{k_{Al_2O_3} + 2k_{nf} + \phi_{Al_2O_3} (k_{nf} - k_{Al_2O_3})} \quad . (14)$$

$$k_{mf} = k_f \frac{k_{Cu} + 2k_f - 2\phi_{Cu} (k_{nf} - k_{Cu})}{k_{Cu} + 2k_f + \phi_{Cu} (k_{nf} - k_{Cu})} \quad . (15)$$

- Heat Capacity:

$$(\rho Cp)_{mf} = (1-\phi_{MWCNT}) \cdot \left\{ (1-\phi_{Al_2O_3}) \left[(1-\phi_{Cu}) (\rho Cp)_f + (\phi\rho Cp)_{Cu} \right] + (\phi\rho Cp)_{Al_2O_3} \right\} + (\phi\rho Cp)_{MWCNT} \quad . (12)$$

III. RESULTS AND DISCUSSION

Fig 2. shows the daily temperature change of the heat transfer fluid (HTF) at the tube outlet and the photovoltaic module temperature for a flow rate of 0,01 kg/s and a solar concentration ratio of 7. The figure also shows how the type of heat transfer fluid affects both temperatures. The two temperature curves present the same pace as solar irradiation, regardless of the type of heat transfer fluid. This trend is characterized by an initial rise in temperature throughout the day to a maximum at noon, followed by a gradual decline in the evening. The impact of heat transfer fluid (HTF) on these two key factors in CPV/T-TEG systems is inverse; a more efficient HTF improves the heat recovery of photovoltaic cells. This leads to a reduction in the temperature of the cells while increasing the temperature of the fluid at the outlet of the tube. Notably, the ternary nanofluid demonstrated the most significant positive effect on both parameters compared to other cooling fluids.

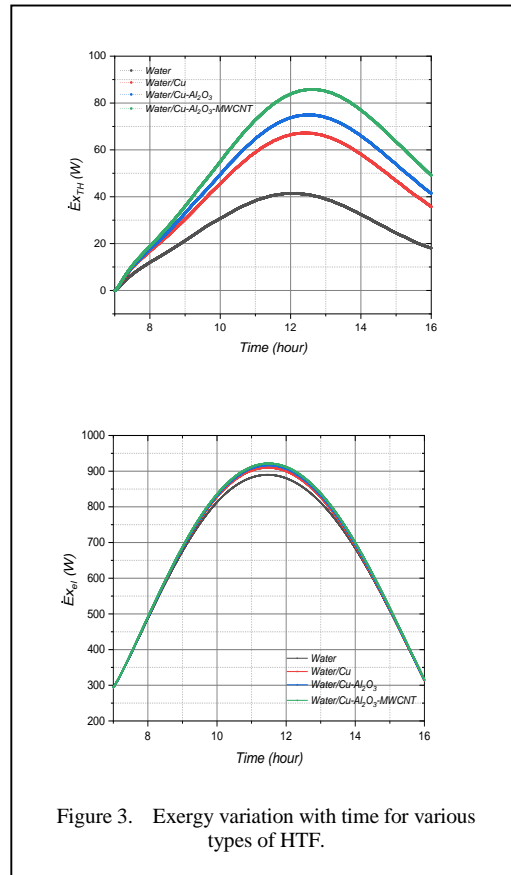
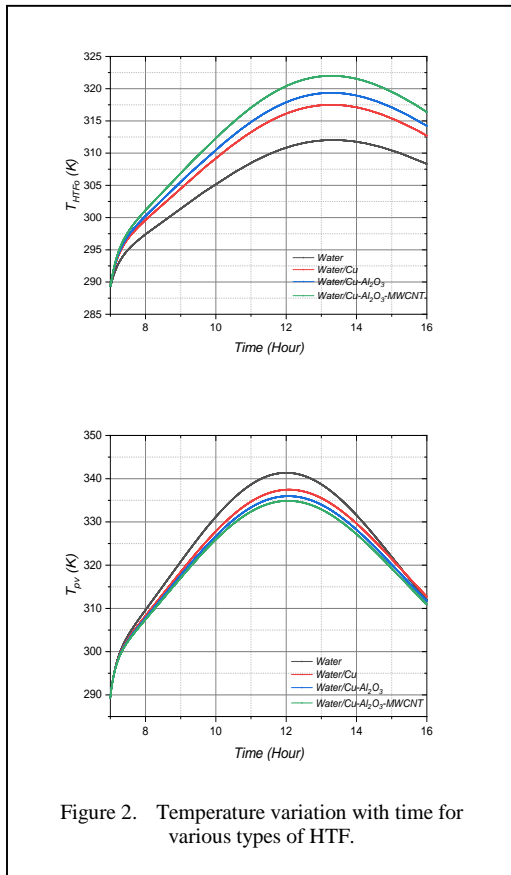
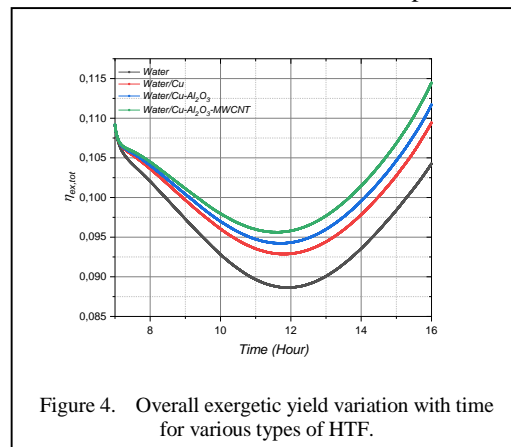


Fig. 3. displays the daily variation in thermal and electrical exergy for different types of heat transfer fluids. The outlet temperature of the heat transfer fluid and the temperature of the photovoltaic module shown in Fig. 2 are two factors that influence the exergy of the CPV/T-TEG system. As indicated in Fig. 3, both thermal and electrical exergy exhibit a similar evolution throughout the day, marked by a peak that follows an initial increase and subsequent decrease. The use of nanofluids enhances the quality of energy produced by the system. Following the figure, it is evident that the type of heat transfer fluid positively affects both types of exergy, with a more pronounced impact on thermal exergy. It's important to note that electrical exergy is ten times more significant than thermal exergy due to their inherent nature; electric exergy is of higher quality, whereas thermal exergy remains inherently limited.

The evolution of the overall exergetic yield is shown in Fig. 4. This parameter exhibits an inverse relationship with the curves in Fig. 3;

the exergetic yield of the system decreases until it reaches a minimum, after which it begins to rise. This trend is directly linked to temperature: as the temperature of the photovoltaic cells increases, exergy efficiency decreases, and vice versa. This behavior is primarily driven by electrical conversion capacity, which is adversely affected during peak solar irradiation. The use of nanofluids enhances this parameter,



as a high-quality heat transfer fluid mitigates the negative impact of temperature on overall exergetic performance and boosts its value. The ternary nanofluid significantly enhances the overall exergetic efficiency of the CPV/T-TEG system, achieving a daily average of 10.124%. This represents a 5.935% improvement over the efficiency of water.

IV. CONCLUSION





This study conducts a numerical analysis of the exergetic performance of a CPV/T-TEG system using different types of heat transfer fluids. The analysis is carried out in the specific weather conditions of Ain Salah, located in the southern region of Algeria. Exergetic production of the system demonstrates a significant dependence on weather conditions, as well as heat transfer outlet temperatures and PV temperature. Exergetic output of the system reflects fluctuations in T_{HTFO} and T_{PV} temperatures, reaching its peak during periods of intense solar irradiation. In addition, the CPV/T-TEG system generates electrical exergy almost ten times greater than its thermal exergy. The overall exergy efficiency of the CPV/T-TEG system is mainly influenced by exergetic electrical production, and it is negatively affected by the temperature of the photovoltaic component. The water ternary nanofluid/Cu-Al₂O₃-MWCNT made a significant contribution to the CPV/T-TEG system, positively impacting all parameters studied and

mitigating the negative effect of TPV on the overall efficiency of exergy. The TRHF has demonstrated superior performance compared to other heat transfer fluids, achieving an average exergetic efficiency of 10.124%, which is significantly higher than the water yield of 5.935%.

REFERENCES

- [1] Salari, A., Parcheforosh, A., Hakkaki-Fard, A., & Amadeh, A. (2020). A numerical study on a photovoltaic thermal system integrated with a thermoelectric generator module. *Renewable energy*, *153*, 1261-1271.
- [2] Zhou, H., Cai, J., Zhang, T., & Shi, Z. (2023, January). Sensitivity Analysis of the Concentrated Photovoltaic/Thermal Solar Air Collector with PCM. In *International Conference on Energy and Environmental Science* (pp. 201-218). Cham: Springer Nature Switzerland.
- [3] Tyagi, K., Gahtori, B., Kumar, S., & Dhakate, S. R. (2023). Advances in solar thermoelectric and photovoltaic-thermoelectric hybrid systems for power generation. *Solar Energy*, *254*, 195-212.
- [4] Zheng, N., Zhang, H., Duan, L., Wang, X., & Liu, L. (2022). Energy, exergy, exergoeconomic and exergoenvironmental analysis and optimization of a novel partially covered parabolic trough photovoltaic thermal collector based on life cycle method. *Renewable Energy*, *200*, 1573-1588.
- [5] Mouaici, K., Fersadou, B., Arslan, K., Kahalerras, H., & Traiche, M. (2025). Technological Limit of Solar Concentration Technique Applied to Hybrid Photovoltaic-Thermal Solar Collector Equipped With Thermoelectric Generator Incorporating Ternary Nanofluid. *Journal of Solar Energy Engineering*, *147*(2).

Obtaining Optical Radiation Splitters for Hybrid Photovoltaic and Thermal Systems

Philippe Pereira Moreira¹, Lucas Medeiros de França², Lucas Vinicius Borges Pereira³, José Felix da Silva Neto⁴, Pollyana Caetano Ribeiro Fernandes⁵

^{1,2,3,4,5}Federal University of Paraíba, João Pessoa - PB, Brazil

¹philippe.moreira@estudante.cear.ufpb.br, ²lucas.franca@estudante.cear.ufpb.br, ³lucas.pereira@cear.ufpb.br, ⁴josefelix@cear.ufpb.br, ⁵pollyana@cear.ufpb.br

Abstract—The need for energy has increased with the development of human activities and fossil fuels have been widely used. However, these fuels pollute the environment and are a finite resource. Therefore, investment in alternative and renewable energy sources is sought. It is possible to use solar radiation through photovoltaic cells, converting it directly into electrical energy, or through solar collectors, converting it into thermal energy. However, only solar radiation below 1100 nm in wavelength generates electrical current in the cells, while the other portion only heats the system and efficiency decreases. Thus, a hybrid generation system, Photovoltaic-Thermal Systems (PVT), with optical splitters, which reflect part of the incident radiation to the PV cells, transmitting radiation above 1100 nm to a solar collector, is used. Thus, the objective of this work is to investigate optical splitters based on Cr₂O₃, MoO₃ and Nb₂O₅ and compare the results obtained with the optical filters found in the literature (SiN and TiO₂). It was observed that the filters based on Cr₂O₃ and MoO₃ did not demonstrate good reflectivity from 300 to 1100 nm wavelength, mainly due to the contribution of absorptivity. The filter composed of Nb₂O₅, on the other hand, proved to be quite promising. After optimizing the dividers, varying the layer configurations and thicknesses, it was found that the Nb₂O₅ films had competitive results compared to the filters already found in the literature, varying the reflectivity from 80 to 90% and the transmissivity equal to approximately 90%, depending on the layer configuration.

Keywords - PVT systems, optical splitting, Nb₂O₅

ISBN: 978-86-82602-05-7

I. INTRODUCTION

Just like air and water, energy is a necessary ingredient for human life. In primitive societies, energy was used almost exclusively to heat the environment and cook food, through burning wood [1]. With the development of human activities, the need for energy increased and in the Industrial Revolution it was already necessary to use coal, oil and gas as energy sources to meet demand [1].

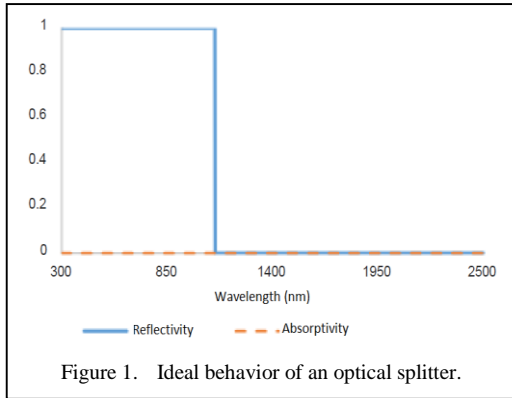
These sources, called fossil fuels, were and still are widely used. However, they are highly polluting, contributing to global warming and although there are still many reserves of these resources, they are finite, decreasing with use [2]. Due to these environmental issues and the growing demand for energy, efforts have been made to invest in renewable energy [3].

Among renewable energies, solar energy has gained considerable prominence in Brazil in recent years. The Brazilian northeast is one of the regions with the greatest potential for solar energy in the world, which makes investment in this sector quite advantageous [4].

It is possible to use solar energy through thermal conversion, where radiation is used to heat a fluid that in turn can be used for space heating or to generate mechanical or electrical power [4]. For this, a special heat exchanger is used, called a solar collector [3]. There is also photovoltaic conversion, where solar radiation is converted directly into electricity, where

207





equipment called a photovoltaic module or panel is used [2].

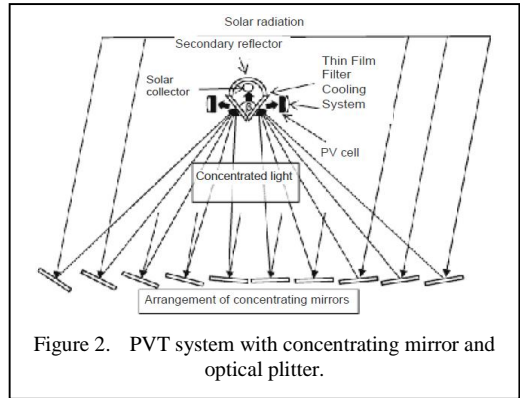
A difficulty faced in photovoltaic conversion is that the efficiency of the modules decreases approximately 0.5% for every 1 °C increase in temperature [5]. Therefore, some authors have proposed a hybrid system called PVT (Photovoltaic-Thermal Systems), which consists of taking advantage of the heat generated in the panels for use in thermal conversion [6,7].

As most photovoltaic (PV) cells are made of silicon, radiation with a wavelength equal to or greater than 1100 nm does not have enough energy to be converted into electricity and increases the module's temperature [8]. Thus, one way to implement a PVT system is through an optical splitter.

The optical splitter is a device that reflects a large part of the incident radiation (high reflectivity) of short wavelength to the PV cells, while the radiation of longer wavelength is transmitted (high transmissivity) to the solar collector. Therefore, it is not desirable for the divider to be a good radiation absorber (low absorptivity). The ideal behavior of an optical splitter can be seen in Fig. 1.

In addition to the optical divider, mirrors are used that concentrate, a cooling system in the photovoltaic panels, in which the heat removed is used in the thermal cycle. Therefore, it is possible to considerably improve the efficiency of the system and make maximum use of the incident radiation. The model described can be seen in Fig. 2.

Reference [9] analyzed optical filters based on SiNx-SiO₂ and demonstrated that the PV cell had an increase of 9.2 % in efficiency when using the equipment, while [10], when studying a filter composed of TiO₂-SiO₂, obtained an increase in

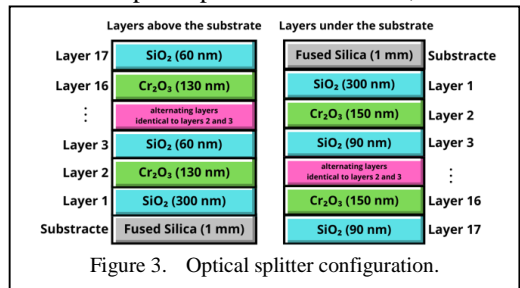


overall system efficiency of 4.94 % in relation to the system with unfiltered radiation. Thus, this work aims to study, through computational simulations, optical dividers made from some candidate materials and compare them with dividers found in the literature.

II. METHODOLOGICAL PROCEDURES

For comparison purposes, initially the chromium-based optical divider was made in the same configurations as that proposed by [9], consisting of 34 layers, 17 above the substrate and 17 below, as shown in Fig. 3.

The choice of chromium was made because researchers at the Federal University of Paraíba (UFPB) have studied selective surfaces based on Cr-SiO₂, obtaining good results [3,11,12]. As a comparison, other materials were sought for the theoretical construction of the filters. The materials investigated were: MgO, Nb₂O₅, MoO₃, Al₂O₃ and the selection of the best candidates was based on two properties optics: a) the extinction coefficient, which determines the degree of reduction of radiation as it penetrates the material and b) the refractive index, which indicates the degree of deviation of light when passing from an external medium to the material. After selection, the filters were constructed using the same settings as in the Fig. 3, just replacing Cr₂O₃ with the new compounds. Subsequently, with the help of Open Filters software, the filters



were optimized through modifications in the number and thickness of their layers. Both the optimization and the selection of materials were carried out based on a mathematical model that estimates that the reflectivity and transmissivity of a solid coated with a film is given by [13].

$$\rho_\lambda = \left| r_1 + r_2 e^{-2i\delta_1} / 1 + r_1 r_2 e^{-2i\delta_1} \right|^2, \quad (1)$$

$$\tau_\lambda = \left| t_1 t_2 e^{-i\delta_1} / 1 + r_1 r_2 e^{-2i\delta_1} \right|^2, \quad (2)$$

where ρ_λ and τ_λ is the spectral reflectivity and transmissivity (associated with a certain wavelength) respectively. The terms r_1, r_2, t_1 , and t_2 can be calculated using the expressions:

$$r_1 = \frac{n_0 - n_1 - i(k_0 - k_1)}{n_0 + n_1 - i(k_1 - k_0)}, \quad (3)$$

$$r_2 = \frac{n_1 - n_2 - i(k_1 - k_2)}{n_1 + n_2 - i(k_2 - k_1)}, \quad (4)$$

$$t_1 = \frac{2n_0 - i(k_0 - k_1)}{n_0 + n_1 - i(k_1 - k_0)}, \quad (5)$$

$$t_2 = \frac{2n_1 - i(k_1 - k_2)}{n_1 + n_2 - i(k_2 - k_1)}, \quad (6)$$

$$\delta_1 = \frac{2\pi}{\lambda} (n_1 - ik_1) d_1, \quad (7)$$

where n is the index of refraction, k is the extinction coefficient, λ is the wavelength of the incident radiation and d is the thickness of the layer. The indices 0, 1 and 2 are associated

with the properties of the medium through which the radiation passes (generally air), the films and the substrate, respectively [13]. It is still possible to calculate the spectral absorptivity (α_λ) using the Eq. (8) [14].

$$\alpha_\lambda = 1 - \rho_\lambda - \tau_\lambda. \quad (8)$$

For multi-layer coatings, Eqs. (1) and (2) can be applied considering the contribution of allayers through their refractive indices, extinction coefficient and their respective thicknesses. In this way, it is possible to calculate the configuration that corresponds to a reflectivity curve closest to the ideal, as seen in Fig. 1.

Then, the total reflectivity and transmissivity (independent of wavelength) of the filters obtained were calculated to compare with those found in the literature. To do this, the following mathematical expression can be used Eqs. (9) and (10) [14].

$$\rho = \frac{\int_0^\infty \rho_\lambda G_\lambda(\lambda) d\lambda}{\int_0^\infty G_\lambda(\lambda) d\lambda}, \quad (9)$$

$$\tau = \frac{\int_0^\infty \tau_\lambda G_\lambda(\lambda) d\lambda}{\int_0^\infty G_\lambda(\lambda) d\lambda}. \quad (10)$$

The evaluation of reflectivity and transmissivity was performed using global solar radiation data obtained from solarimetric databases. For reflectivity, the spectral range considered was 300-1100 nm, while for transmissivity, the range was 1100-250 nm, both with a spectral resolution of 1 nm. The light incidence angle was set to 0°, corresponding to perpendicular incidence on the surface.

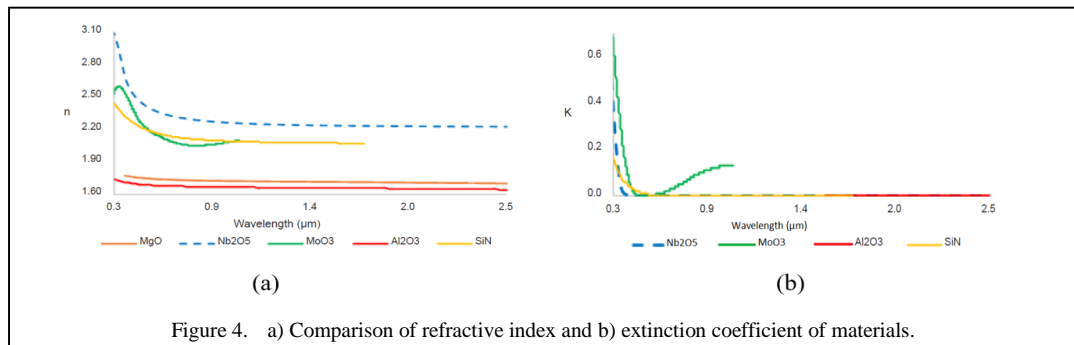


Figure 4. a) Comparison of refractive index and b) extinction coefficient of materials.

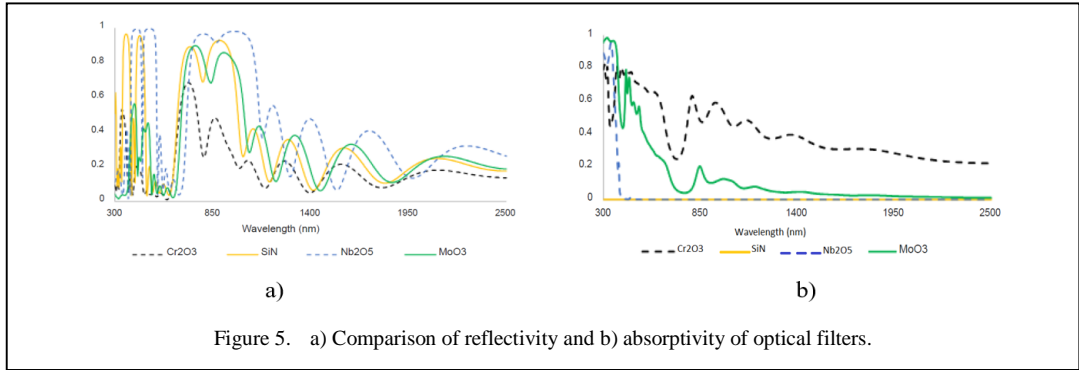


Figure 5. a) Comparison of reflectivity and b) absorptivity of optical filters.

The calculations were carried out using Eqs. (9) and (10), employing the trapezoidal rule for numerical integration. Due to the high density of data points and the low spectral resolution, the difference compared to more advanced methods, such as the 3/8 Simpson's rule, was less than the fourth decimal place. This ensures high precision and reliability in the results obtained.

III. RESULTS AND DISCUSSIONS

A. Selection of Materials

The bibliography [15-20] was searched for the index of refraction (n) and extinction coefficient (k) of the candidate materials and preference was given to those with values closest to those found for SiN, since the relationship between these properties of SiN and SiO₂ showed good results [9]. Fig. 4 show the comparison of these properties.

It is observed that Nb₂O₅ presents both properties with values close to SiN, showing promise for filter construction. Although, extinction coefficient (k) of MoO₃ presented a value that differs from SiN, the difference was due to a lower value that 1.5 at its peak and lack of data does not allow analysis for longer wavelengths, where the curve would reach

stability. Furthermore, its refractive index (n) was very similar to that found for SiN.

B. Theoretical Construction of Filters

Thus, Nb₂O₅ and MoO₃ were selected for theoretical construction of the films in the same configuration used for Cr₂O₃, shown in Fig. 3. Fig. 5 show the results.

It is noted that Cr₂O₃ has a considerable drop in reflectivity in the first wavelengths, this is due to the strong contribution of absorptivity. Several authors [3,11,12] have been studying chromium oxide applied to selective surfaces and found that this compound has good intrinsic absorptivity, making its application for optical splitters difficult.

On the other hand, Nb₂O₅ had excellent behavior, closely resembling that found for SiN. While MoO₃ had a slightly lower performance 300 to 700 nm wavelength, also due to its absorptivity.

C. Filter Optimization

The filters were then optimized based on varying the thickness of each layer, as shown in Fig. 6.

Although it has a lower wavelength of 300 to 400 nm, due to the contribution of absorptivity,

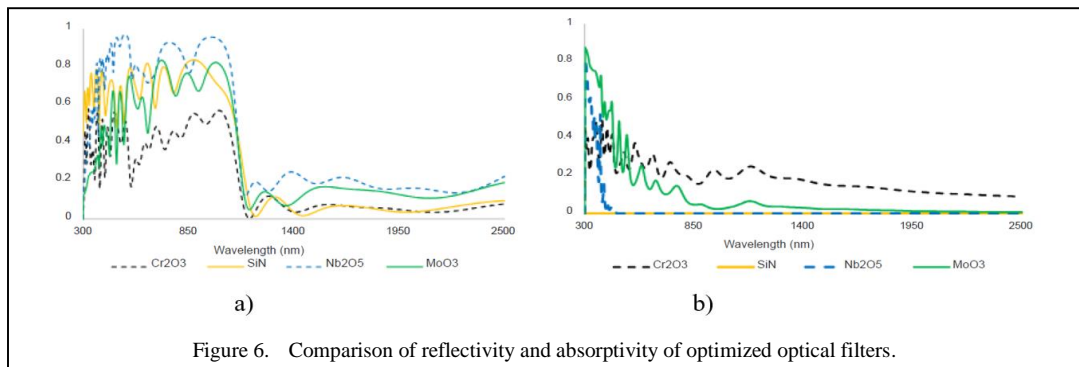


Figure 6. Comparison of reflectivity and absorptivity of optimized optical filters.

it still proved to be more promising than the too much. Cr_2O_3 and MoO_3 did not achieve very positive results, even after optimization of the thickness of its layers. This becomes evident when observing the absorptivity of these filters, which is of great relevance in the first lengths of wave for MoO_3 and throughout the spectrum studied for Cr_2O_3 .

Due to the high absorbance, MoO_3 and Cr_2O_3 , although not suitable for optical splitter applications compared to the other filters, may present good results as selective absorber surfaces in thermal system applications, improving radiation capture and converting it directly into heat, as demonstrated in other studies [3,21].

TABLE I. FILTER THICKNESS OBTAINED AFTER THE FIRST OPTIMIZATION.

Material	Thickness (nm)	Target Cost
Cr_2O_3	4077.17	263.95
SiN	6023.99	398.95
Nb_2O_5	3439.92	205.95
MoO_3	4224.94	335.95
TiO_2	No informed	343.95

TABLE II. TOTAL REFLECTIVITY AND TRANSMISSIVITY OF OPTICAL FILTERS.

Configurations	Reflectivity	Transmissivity
18-23	89.2 %	92.1 %
17-17	88.9 %	89.2 %
13-13	81.8 %	89.1 %
$\text{SiN}_x/\text{SiO}_2$	95 %	90 %
$\text{SiO}_2/\text{TiO}_2$	96.8 %	85 %

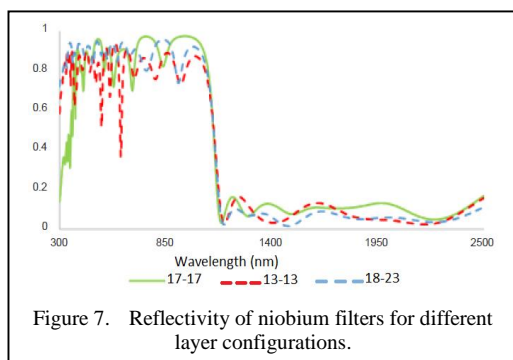


Figure 7. Reflectivity of niobium filters for different layer configurations.

Furthermore, the thickness obtained for the filters after this first optimization was different for each compound. Nb_2O_5 was the one with the smallest thickness among all, even presenting the best optical behavior. Although SiN also showed good results, the thickness required to achieve these values was almost double that used for niobium oxide. The thickness of the filters can be seen in the Table I.

Additionally, by comparing the values of the sputtering targets, it is possible to get a preliminary idea of the relative cost of the filters. All the compared targets had a purity of over 99% and dimensions of 2.00" diameter and 0.125" thickness, from the same supplier [22].

Thus, Nb_2O_5 achieves excellent results, with a lower market cost and requiring less material per target due to its considerably thinner thickness.

Therefore, it is important to explore layer configurations for Nb_2O_5 , in order to achieve the best results among the filters studied. To achieve this, we sought to optimize the filters under three different configurations: 18-23, 17-17 and 13-13, with the first term referring to the layers above the substrate and the second referring to those below. Configuration 18-13 was chosen considering the maximum possible reflectivity in the range of 400 to 1100 nm wavelength, through the addition of extra layers, while 17-17 was selected as a reference, since the results of [9] were obtained with this number of layers. The choice of configuration 13-13 was made considering economic issues and ease of construction, since it depends on a smaller number of layers and the equipment needed to build the films is expensive. The results of the optimized filters can be seen in the Fig. 7.

Using Eqs. (9) and (10), the total reflectivity and transmissivity were calculated within the spectral range of interest, as shown in the Table II, where the reflectivity of this work was calculated from 380 to 1100 nm, the reflectivity of $\text{SiN}_x/\text{SiO}_2$ from 713 to 1063 nm and that of $\text{SiO}_2/\text{TiO}_2$ from 400 to 100 nm and the transmissivity was calculated from 1100 to 2500 nm. The niobium filter composed of 17-17 and 18-23 layers demonstrated results, although slightly lower, still close to $\text{TiO}_2/\text{SiO}_2$ and $\text{SiN}_x/\text{SiO}_2$ obtained by [9,10], respectively. Although the 13-13 configuration filter performed below the others, it still had promising results, achieving a transmissivity close to the other compounds and reflectivity of 81.8%.

IV. CONCLUSION

It is concluded that the Nb₂O₅-based filter demonstrates highly promising results, being competitive with other extensively studied filters. In addition to its excellent optical performance, it stands out due to its lower market cost and reduced material requirements per target, thanks to its thinner thickness, reinforcing its technical and economic feasibility.

Conversely, optical dividers composed of Cr₂O₃ and MoO₃ exhibited below-expectation results in terms of reflectivity and transmittance, making them less competitive compared to widely adopted models in the literature. However, due to their high absorptivity properties, particularly in shorter wavelengths, these materials could be valuable as selective absorbing surfaces in solar thermal systems, where they can efficiently capture radiation and convert it directly into heat.

For future studies, it is suggested to conduct a detailed cost-benefit analysis of optical filters based on Nb₂O₅, SiN, and TiO₂, considering not only material costs and fabrication technologies but also the ease of implementation in diverse applications. This approach may provide a robust foundation for the selection and development of optimized optical filters for specific uses.

ACKNOWLEDGMENT

We extend our gratitude to the Microfabrication Laboratory (LMF) at CNPEM, the Thin Films Laboratory (LabFilm) at UFPB, the Center for Alternative and Renewable Energy Engineering (CEAR/UFPB), and the funding agencies CNPq, CAPES, and PROPESQ for their essential contributions in enabling this work.

REFERENCES

- [1] Goldemberg, J. & Lucon, O. (2007). Energia e meio ambiente no Brasil. *Estudos Avançados*, 21(59), 7-20.
- [2] Villalva, M. G. & Gazoli, J. R. *Energia solar fotovoltaica: conceitos e aplicações* (1th Ed.). Editora Érica, São Paulo.
- [3] Moreira, P. P., Forte, A. B. T., Leandro, L. B. C., Gomes, K. C. & Silva Neto, J. F. (2020). Aperfeiçoamento De Coletores Solares Térmicos Via Superfícies Seletivas. In *Proceedings of I CONIMAS and III CONDIS, Campina Grande, Brazil*.
- [4] Pacheco, F. (2006). CONJUNTURA & PLANEJAMENTO. Superintendência de Estudos Econômicos e Sociais da Bahia.

- [5] Abd-Elhady, M. S., Serag, Z. & Kandil, H. A. (2018). An innovative solution to the overheating problem of PV panels. *Energy Conversion and Management*, 157, 452–459.
- [6] Joshi, S. S. & Dhoble, A. S. (2018). Photovoltaic-Thermal systems (PVT): Technology review and future trends. *Renewable and Sustainable Energy*, 92, 848-882.
- [7] Abdelrazik, A. S., Al-Sulaiman, F. A., Saidur, R. & Ben-Mansour, R. (2018). *Renewable and Sustainable Energy*, 95, 110-129.
- [8] FOX, M. (2010). *Optical properties of solids* (2th Ed.). Oxford University Press, New York.
- [9] Crisostomo, F. et al. (2014). Experimental testing of SiN x /SiO₂ thin film filters for a concentrating solar hybrid PV/T collector. *Renewable Energy*, 72, 79–87.
- [10] Liang, H., et al. (2019). Experimental investigation on spectral splitting of photovoltaic/thermal hybrid system with two-axis sun tracking based on SiO₂/TiO₂ interference thin film. *Energy Conversion and Management*, 188, 230–240.
- [11] Silva, Z. E. (1985). *Obtenção de Superfície Seletiva em Ni sobre Al para Conversão Térmica de Energia Solar*. [Master dissertation, Federal University of Paraíba].
- [12] Silva Neto, J. F. (2017). *Desenvolvimento de superfícies seletivas para coletores solares com deposição multicamadas de Cr e SiO₂*. [Doctoral theses, Federal University of Paraíba].
- [13] Heavens, O. S. (1991). *Optical properties of thin solid films*. Dover Publications, New York.
- [14] Bergman, T. L. (2017). *Incropera – Fundamentos de Transferência de Calor e de Massa* (8th Ed.), Grupo GEN, Rio de Janeiro.
- [15] Gao, L., Lemarchand, F. & Lequime, M. (2012). Exploitation of multiple incidences spectrometric measurements for thin film reverse engineering. *Optics Express*, 20(14), 15734–15751.
- [16] Stephens, R. E. & Malitson, I. H. (1952). Index of refraction of magnesium oxide. *Journal of Research of the National Bureau of Standards*, 49(4), 249-252.
- [17] Vos, M. F. J., et al. (2016). Atomic layer deposition of molybdenum oxide from (NtBu)₂(NMe₂)₂Mo and O₂ plasma. *Journal of Vacuum Science & Technology A*, 34(1), 01A103.
- [18] Boidin, R., Halenković, T., Nazabal, V., Beneš, L. & Nĕmec, P. (2016). Pulsed laser deposited alumina thin films. *Ceramics International*, 42(1, Part B), 1177-1182.
- [19] Kischkat, J., et al. (2012). Mid-infrared optical properties of thin films of aluminum oxide, titanium dioxide, silicon dioxide, aluminum nitride, and silicon nitride. *Applied Optics*, 51(28), 6789–6798.
- [20] Vogt, M. R. (2015). Development of physical models for the simulation of optical properties of solar cell modules. [Doctoral theses, Gottfried Wilhelm Leibniz Universität Hannover].
- [21] Wang, W., Huan, X., & Wang, C. (2020). Thermal annealing characteristics of solar selective absorber coatings based on nano-multilayered MoOx films. *Ceramics International*.
- [22] MSE Supplies (2024). Available at: <https://www.msesupplies.com/>

Performance Optimization of Solar Air Heater with Impinging Jet Technique

Siddhita Yadav¹, K. M. Pandey²

¹IIT Roorkee, Roorkee, India

²NIT Silchar, Silchar, India

¹syadav@ah.iitr.ac.in

Abstract—In response to rising pollution concerns, this study underscores the urgent need for a shift to clean energy sources, with a specific emphasis on solar energy, recognized as one of the most effective alternatives. This research paper explores the optimization of a solar air heater with jet impingement (SAHJI) by leveraging existing correlations for jet parameters. Utilizing established correlations for Nusselt number (Nu) and friction factor (ff), the study numerically evaluates the SAHJI system's performance in terms of effective efficiency with experimental validation. Effective efficiency is quantified by comparing the solar energy delivered with the equivalent thermal energy consumed to propel air within the system. The investigation identifies optimal values for geometric parameters (D_j/D_h , H_j/D_h , P/D_h , and $\alpha/90$) based on maximum effective efficiency, considering various temperature differences ($\Delta T/I$) and solar radiation intensities (I) within a Reynolds number range of 3500 to 17500. The research concludes that, according to the effective efficiency criterion, the optimum parameters are D_j/D_h of 0.065, H_j/D_h of 0.216, P/D_h of 1.30, and $\alpha/90$ of 0.094, resulting in optimal heat transfer with minimal pumping losses. Study features plots for the selection of optimal geometric parameters across diverse operating conditions, offering valuable insights for designers to improve efficiency of the system.

Keywords - jet impingement, solar air heater, effective efficiency, heat transfer

I. INTRODUCTION

However, as the world faces higher environmental issues and a greater need to stop climate change, the global community is looking to renewable energy sources as a solution. Of these, solar energy is one of the leading clean

energy sources because of it being plentiful and environmentally friendly. It is abundant, and an emerging, economic, and environmental optimum energy source in your area solar energy. Solar energy is facilitated by thermal and photovoltaic (PV) cells by converting the solar energy into electrical energy and thermal energy by appropriate use of fluids. Solar Air Heater (SAH) is one of the devices that help to utilize solar thermal energy in various applications like heating and cooling of buildings as well as agricultural crop drying [1].

Even though it has several benefits such as no leakages, freezing, and corrosion, SAH has a disadvantage of low heat transfer between the absorber and air. This issue has led researchers to investigate alterations like adding artificial roughness on the absorber, reducing heat losses, and improving turbulence in the duct [2]. In particular, the jet impingement method in SAH, studied experimentally, is attractive due to high heat transfer rates, low pumping power, minimum pressure losses and less cost.

II. LITERATURE AND OBJECTIVES

In the context of optimal utilization of solar energy, this study investigates solar air heaters (SAH), with an emphasis on solar air heater with jet impingement (SAHJI).

Reference [3] firstly proposed jet impingement using a jet plate in SAH, and was expanded upon by [4] preferred inline jets to staggered jet patterns. As [5] studied the energy balance equation and [6] elaborated on the thermo-hydraulic performance of the impinging

213



jet of SAH much later optimized by [7] using the PSI method.

Additionally, [8] focused on the implementation of an unglazed SAH along with jet impingement, while the further work of realized the effects of spanwise pitch and slots, both contributing to the promiscuous world of solar air heating devices [9]. A new configuration of SAHJI [10,11] was explored by Yadav and Saini, in which a conical jet idea was adopted on the jet plate, leading to the improved thermo-hydraulic performance up to 3.5 times over the conventional solar air heaters. They also investigated the influence of parameters of the jet, including height and angle of the cone, on the altered system. But these studies led to no correlations.

The literature reveals a plethora of works on solar air heaters, wherein they are significant in renewable energy applications. However, the optimization of solar air heaters in jet impingement scenarios and identification of optimal geometrical parameters into already existing correlation framework constitutes a research gap. This work is aimed at bridging this gap and providing practical insights to designers to maximize the efficiencies of SAHJIs.

This research stands out in its endeavor of studying solar air heating together with jet impingement, and interestingly looks at the maladies thereof in an investigation toward the maximization of system efficiency. Objectives of the study are to find optimal geometric parameters under various operating conditions, extending some useful knowledge into the greater sphere of solar energy utilization.

This paper looks at mathematical simulations performed using ANSYS FLUENT and MATLAB for performance analysis of SAHJIs. The thermo-hydraulic performance of SAHJIs has been predicted in terms of effective efficiency. Optimal values found within the standard conditions concerning changes in operating parameters are reported. Thus, an approach to optimization of effective efficiency is developed to obtain optimal values of the investigated design parameters for all operating conditions.

III. MATERIALS AND METHODS

Present study is performed on a duct with a cross-sectional area of 0.3 m (width) \times 0.025 m (depth) and 1 m in length with entry length of 575

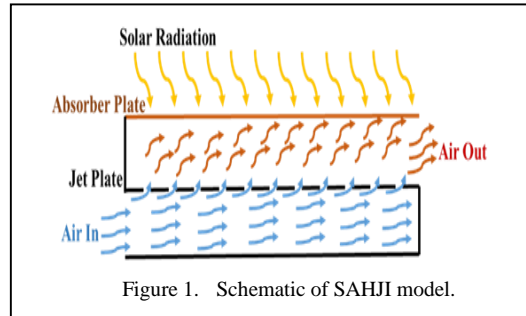


Figure 1. Schematic of SAHJI model.

mm and exit length of 400 mm for remainder as per ASHRAE guidelines [12]. This duct is equipped with an absorber plate and jet plate made of Aluminum. The sidewalls and backplate are insulated, and it is shown in Fig. 1. The 3D-model of SAHJI is generated via ANSYS Workbench. Model used for the present Study is discretized with Fine, unstructured, and non-uniform grid for the meshing. The top wall of the test section is considered as an absorber plate that has a uniform heat flux of 1000 W/m². The simulation was performed at different Reynolds numbers, and they fall in the range of 3500-16500 [11]. The duct's working fluid is assumed to be atmospheric air, and the absorber plate and jet plate are both constructed from Aluminum. In order to solve the continuity, momentum, and energy equations, *RNG k-ε* turbulence model is the preferred way to simulate the flow inside the duct [12,13]. The results are calculated with CFD POST.

Present study considers effective efficiency as a criterion for optimization as it considers effect of both heat transfer as well as frictional losses. In order to achieve the design parameters that will yield the maximum effective efficiency, it is necessary to vary the design and operating parameters separately within the range of the considered parameters while holding the other parameter constant. The ranges of variable parameters to be studied are listed in Table I.

TABLE I. CONSIDERED RANGES OF VARIABLE PARAMETERS.

Parameters	Range
Jet diameter ratio (D_j/D_h)	0.065 to 0.195
Jet height ratio (H_j/D_h)	0 to 0.433
Jet Pitch Ratio (P/D_h)	0.433 to 1.733
Jet angle ratio ($\alpha/90$)	0 to 0.269
Reynolds number (Re)	3500 to 17500

Traditional solar air heaters are low-efficient, mainly due to the laminar sub-layer which is overcome by impinging jet Solar Air Heater (SAHJI). Greater thermal efficiency in SAHJI also brings about a growth in friction losses, so therefore effective efficiency (η_ε) is recommended to be used for performance evaluation by Cortes and Piacentini (1990). Thus, the assessment of the SAHJI in terms of its performance and optimization should be designated by the η_ε . Therefore, η_ε becomes performance analysis and optimization criteria under the present study.

$$\eta_\varepsilon = \frac{(Qu - Pm/c)}{IA_p}, \quad (1)$$

where, $c=0.18$ is the conversion factor.

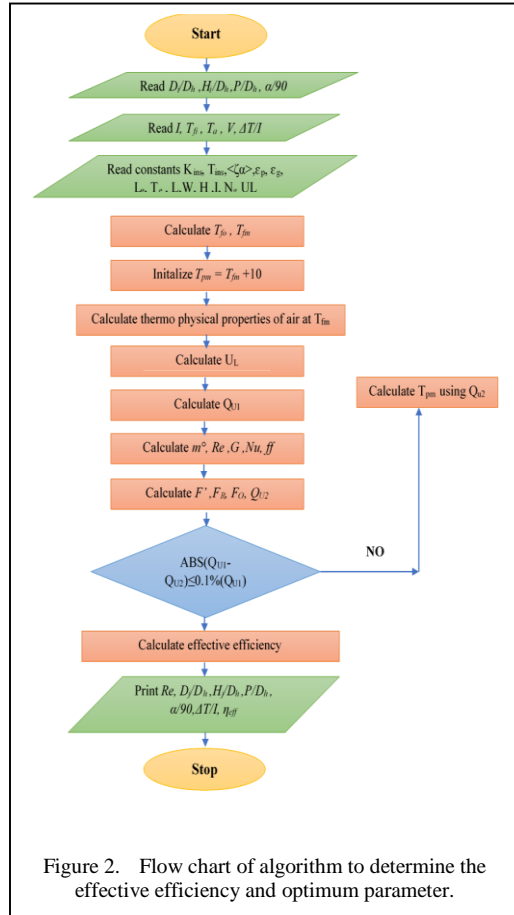


Figure 2. Flow chart of algorithm to determine the effective efficiency and optimum parameter.

The SAHJI system's performance optimization, employing design and operating parameters (Re), thus range of these parameters are shown in the Table I. The optimization method algorithm is described in Fig. 2 as a flow chart is accomplished by MATLAB. The optimum system parameters are assessed with respective effective efficiency. The Nu number and the friction factor are calculated via the correlation formula specified below in Eqs. (2) and (3), which are developed through CFD simulations using regression analysis.

$$Nu = 0.0001118Re^{0.85} \left(\frac{D_j}{D_h} \right)^{-4.36}$$

$$\left[\exp \left\{ -0.845 \left(\ln \left(\frac{D_j}{D_h} \right)^2 \right) \right\} \right]$$

$$\left(\frac{H_j}{D_h} \right)^{-1.03} \left[\exp \left\{ -0.28 \left(\ln \left(\frac{H_j}{D_h} \right)^2 \right) \right\} \right], \quad (2)$$

$$\left(\frac{P}{D_h} \right)^{0.012} \left[\exp \left\{ -0.62 \left(\ln \left(\frac{P}{D_h} \right)^2 \right) \right\} \right]$$

$$\left(\frac{\alpha}{90} \right)^{-1.06} \left[\exp \left\{ -0.21 \left(\ln \left(\frac{\alpha}{90} \right)^2 \right) \right\} \right]$$

$$ff = 0.83Re^{-0.108} \left(\frac{D_j}{D_h} \right)^{-0.32} \left(\frac{H_j}{D_h} \right)^{0.09}$$

$$\left(\frac{P}{D_h} \right)^{0.34} \left[\exp \left\{ -0.14 \left(\ln \left(\frac{P}{D_h} \right)^2 \right) \right\} \right]. \quad (3)$$

$$\left(\frac{\alpha}{90} \right)^{0.35} \left[\exp \left\{ 0.053 \left(\ln \left(\frac{\alpha}{90} \right)^2 \right) \right\} \right]$$

IV. VALIDATION

Experiments are conducted on SAHJI (D_j/D_h of 0.065, H_j/D_h of 0.0, P/D_h of 0.433, and $\alpha/90=0$) under varying flow conditions (Re) to validate the simulation results. SAHJI experimental outcomes were compared with Nu and ff values calculated using Eqs. (2) and (3). A 3D model for SAHJI is developed with similar geometric parameters replicating the experimental setup at IIT Roorkee as shown in Fig. 3.

The experimental data obtained for pressure and temperature during testing are reduced in terms of non-dimensional parameters: Nusselt number (Nu), friction factor (ff), and Reynolds number (Re) utilizing Eqs. (4), (5) and (6), respectively.

$$Nu = \frac{hD_h}{k}, \quad (4)$$

$$ff = \frac{2(\Delta P_d)D_h}{4\rho LV^2}, \quad (5)$$

$$Re = \frac{\rho v D_h}{\mu}. \quad (6)$$

In the current study, uncertainty analysis is performed using the methodology prescribed by [14]. The maximum uncertainties determined from the experiment are $\pm 3.82\%$ for Nu , $\pm 4.26\%$ for ff , and $\pm 2.73\%$ for Re .

CFD outcomes were illustrated in Fig. 4 and compared with experimental data for the RNG k- ϵ turbulence model. The maximum average absolute deviations are obtained from the plots of Nu and ff , which are found to be 7.62% and 8.44% respectively; such estimates indicates very good agreement and provide confidence in the reliability of the CFD approach.

V. RESULTS AND DISCUSSIONS

The Thermal performance of SAHJI is accentuated by the ratio of the temperature difference to irradiance ($\Delta T/I$). To reach maximum efficiency, it is critical to find the optimal values for key design parameters. The optimized parameter values of D_j/D_h , H_j/D_h , P/D_h , and $\alpha/90$ are illustrated in Fig. 5 as a function of $\Delta T/I$ (0.0020–0.038 K m²/W) and insolation (400–1000 W/m²) values.

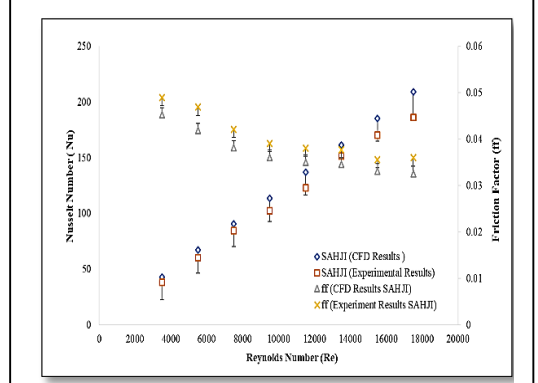


Figure 3. Experimental Validation of SAHJI.

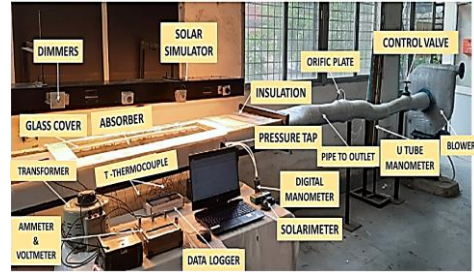


Figure 4. Image of Experimental Setup of SAHJI.

The D_j/D_h (Fig. 5a) shows decreasing values with increasing insolation, thus lower values are advised to increase efficiency under higher irradiance. In contrast, H_j/D_h (Fig. 5b) exhibits a reversed trend where values are recommended based on decreasing insolation, and optimized H_j/D_h increases with insolation decreasing.

Fig. 5c reveals that higher P/D_h values are favored under increased insolation, while the optimized P/D_h decreases as insolation levels decrease. Finally, Fig. 5d indicates that lower values of jet angle ratio ($\alpha/90$) are preferable for higher insolation, with the optimized $\alpha/90$ increasing as insolation decreases.

For researchers and manufacturers looking to create effective SAHJI systems suited to a variety of operating environments, these findings offer insightful information. A more informed and efficient approach to the development of SAHJI technology is made possible by correlation development between design parameters and environmental factors.

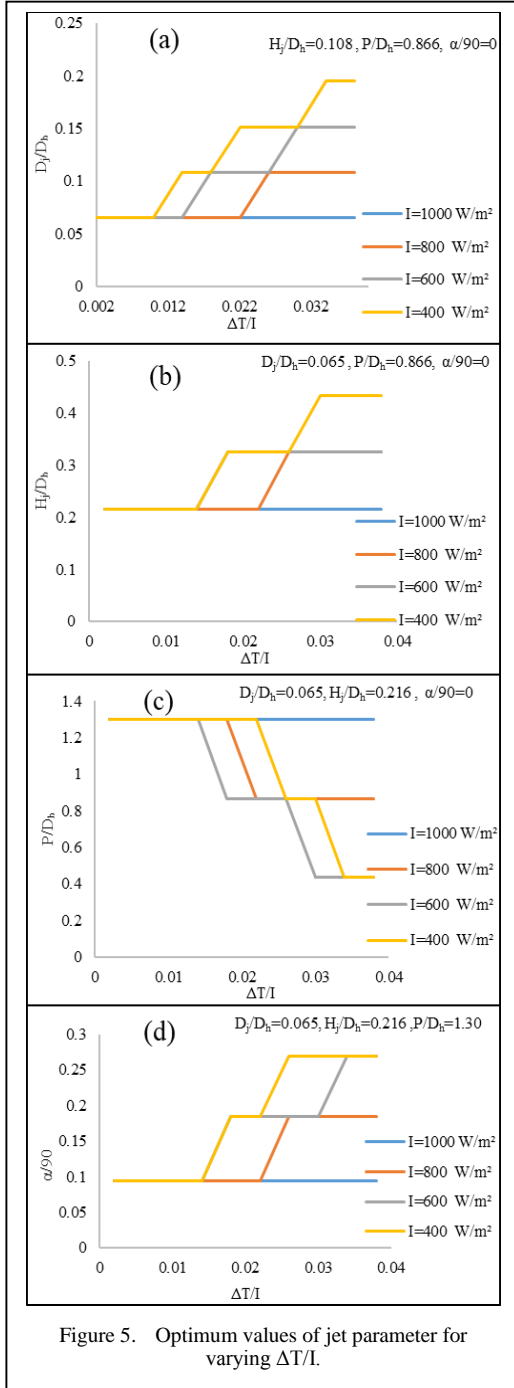


Figure 5. Optimum values of jet parameter for varying $\Delta T/I$.

VI. CONCLUSIONS

The energy provided by solar heating and the corresponding thermal energy required to move air through the system are taken into account while evaluating effective efficiency in this study. The ideal geometric parameters for

optimum heat transfer and minimal pump losses for Re that range between 3500 and 17,500 are found to be D_j/D_h of 0.065, H_j/D_h of 0.216, P/D_h of 1.30, and $\alpha/90=0.094$. Plots are also included to assist designers in choosing the best geometric parameters based on $\Delta T/I$ in a variety of scenarios. This study advances knowledge of SAHJI system efficiency and provides useful recommendations for advancing solar air heating technology.

Future Scope: The analysis can be expanded to take into consideration actual environmental variables like wind speed, humidity, and dust collection, allowing for the creation of SAHJI designs that are resilient and dependable in a variety of operating scenarios. Future research can also perform a thorough techno-economic analysis and lifespan cost assessment to assess how economical the suggested design modifications are as a result.

A. Abbreviations and Acronyms

Symbol	Parameter	Unit
P	Distance between two jet	[m]
D_j	Jet diameter	[m]
D_h	Hydraulic Diameter	[m]
α	Conical jet angle	(°)
ρ	Density of air	[kg/m ³]
Nu	Nusselt number	--
ff	Friction factor	--
Re	Reynolds Number	--
ΔT	Temperature difference	[K]
I	Solar Intensity	[W/m ²]
Q_u	Useful Energy gain	[W]
P_m	Mechanical Power	[W]
A_p	Absorber plate area	[m ²]

ACKNOWLEDGMENT

The authors express their sincere gratitude to the late Prof. R. P. Saini for his invaluable guidance and support throughout the completion of this research. Additionally, they extend their appreciation to the CFD lab at HRED IIT Roorkee for generously providing computational resources, and to MNRE for their financial support.

REFERENCES

- [1] Yu, N., Wang, R. Z., & Wang, L. W. (2013). Sorption thermal storage for solar energy. *Progress in Energy and Combustion Science*, 39(5), 489-514.
- [2] Prakash, C., & Saini, R. P. (2019). Heat transfer and friction in rectangular solar air heater duct having spherical and inclined rib protrusions as roughness on absorber plate. *Experimental Heat Transfer*, 32(5), 469-487.
- [3] Kercher, D. M., & Tabakoff, W. (1970). Heat transfer by a square array of round air jets impinging perpendicular to a flat surface including the effect of spent air. *J. Eng. Power*, 92(1), 73-82.
- [4] Metzger, D. E., Florschuetz, L. W., Takeuchi, D. I., Behee, R. D., & Berry, R. A. (1979). Heat Transfer Characteristics for Inline and Staggered Arrays of Circular Jets with Crossflow of Spent Air. *Journal of Heat Transfer*, 101(3), 526-531.
- [5] Choudhury, C., & Garg, H. P. (1991). Evaluation of a jet plate solar air heater. *Solar Energy*, 46(4), 199-209.
- [6] Chauhan, R., & Thakur, N. S. (2014). Investigation of the thermohydraulic performance of impinging jet solar air heater. *Energy*, 68, 255-261.
- [7] Chauhan, R., Singh, T., Thakur, N. S., & Patnaik, A. (2016). Optimization of parameters in solar thermal collector provided with impinging air jets based upon preference selection index method. *Renewable energy*, 99, 118-126.
- [8] Belusko, M., Saman, W., & Bruno, F. (2008). Performance of jet impingement in unglazed air collectors. *Solar Energy*, 82(5), 389-398.
- [9] Zukowski, M. (2013). Heat transfer performance of a confined single slot jet of air impinging on a flat surface. *International Journal of Heat and Mass Transfer*, 57(2), 484-490.
- [10] Yadav, S., Saini, R. P., & Pandey, K. M. (2023). Effect of jet angle and jet pitch on the Thermo-Hydraulic performance of solar air heater having absorber plate with jet impingement. *Thermal Science and Engineering Progress*, 45, 102146.
- [11] Yadav, S., & Saini, R. P. (2020). Numerical investigation on the performance of a solar air heater using jet impingement with absorber plate. *Solar Energy*, 208, 236-248.
- [12] ANSYS Fluent 14.0 User's Guide. 2011.
- [13] Gupta, A. D., & Varshney, L. J. T. S. (2017). Performance prediction for solar air heater having rectangular sectioned tapered rib roughness using CFD. *Thermal Science and Engineering Progress*, 4, 122-132.
- [14] Kline, S. J. (1985). The Purposes of Uncertainty Analysis. *Journal of Fluids Engineering*, 107(2), 153-160.

Performance Analysis of Maximum Power Point Tracking based on Perturb & Observe Algorithm and Fuzzy Logic Control

Yacine Bouali¹, Khoukha Imarazene², El Madjid Berkouk³

^{1,2}Power equipment Characterization and Diagnosis Laboratory (of USTHB), Algiers, Algeria

³Control Process Laboratory (of ENP), Algiers, Algeria

¹ybouali@usthb.dz, ²khoukhaimarazene@gmail.com, ³el_madjid.berkouk@g.enp.edu.dz

Abstract—Exploiting the full potential of a photovoltaic (PV) system requires the investigation of Maximum Power Point Tracking (MPPT). In this paper, two MPPT techniques are compared and evaluated, the Perturb and Observe (P&O) algorithm and the Fuzzy Logic Controller (FLC). This study includes theoretical analysis and experimental validation conducted using MATLAB/Simulink. Three modes of operation are tested. In the first mode, the system operates under varying irradiance with constant temperature and load. In the second mode, the temperature varies while the irradiance and load remain constant. In the third mode, only the load varies. Results demonstrate that the FLC MPPT algorithm significantly surpasses the P&O algorithm in terms of efficiency and precision. Additionally, the implementation cost of the P&O algorithm is lower than that of the FLC. This comparative analysis highlights the potential advantages of integrating advanced control strategies like fuzzy logic into PV systems for enhanced energy harvesting and system robustness.

Keywords - photovoltaic systems, Maximum Power Point Tracking, fuzzy logic controller, P&O algorithm

I. INTRODUCTION

Recently, there is great interest in renewable energy due to global warming, climate change, and pollution's economic and health effects. Renewable energy sources such as wind, solar, hydropower, geothermal, and biomass must

replace fossil fuels to reduce greenhouse gas emissions and benefit from clean energy [1,2].

Renewable energy sources are important for covering energy needs on a large scale, in addition to the possibility of achieving almost zero carbon dioxide emissions and greenhouse gases.

Solar energy is among the most important renewable sources due to its easy accessibility and ease of dealing with solar energy systems. This has led to a significant focus on the maximum exploitation of solar energy. However, the photovoltaic system has many challenges, such as extracting the maximum power and tracking the point of this power; this challenge leads to the development and refinement of Maximum Power Point Tracking (MPPT) algorithms.

Several works have investigated reviews of different MPPT algorithms [3,4]. Numerous categories of MPPT techniques have been proposed in the literature and classified [4,5]. MPPT techniques can be categorized into three groups based on operational principles. (1) Direct Methods: These techniques continuously monitor voltage and/or current to directly track the Maximum Power Point (MPP) without depending on empirical data, such as the Perturb and Observe (P&O) [6] and Incremental Conductance (INC) [7] methods. (2) Indirect Methods: based on monitoring voltage and current, these methods calculate the MPP using



empirical data. These techniques are typically less dynamic but more straightforward to implement. (3) Hybrid Methods: These methods combine the strengths of both direct and indirect approaches by utilizing real-time measurements and empirical data to track the MPP.

The most used of MPPT techniques is the Perturbe and Observe algorithm [8]; other techniques are also commonly used, such as Incremental Conductance [9], and Fractional Open Circuit Voltage (FOCV) [10]. Recently, new techniques have been proposed and compared with the known methods [11,12].

The aim of this paper is to investigate and compares two widely used MPPT algorithms: P&O and fuzzy logic control (FLC). Three modes are tested for evaluating both MPPT methods, where the environmental condition and the load value vary for each mode. This study evaluates their performance, efficiency, reliability, and suitability for different applications.

The remainder of this paper is as follows: Section II presents the principle working of MPPT and describes the P&O and FLC methods. In section III, the results of P&O and FLC MPPT are presented by evaluating three modes, where solar irradiance, temperature, and load vary for each mode. Finally, section IV presents the main conclusions of this work.

II. METHODOLOGY

A. Load Matching using MPPT

The power converter used to interface the PV panel and the load is known as MPPT, and it includes an algorithm (software part) used to control the DC-DC converter (hardware part), where the duty cycle is adjusted to meet the load matching between the PV module and the connected load in order to obtain the maximum power from the PV panel under present climatic conditions. According to an ideal DC-DC Buck converter, the input-output power can be described as:

$$P_{pv} = P_{load} , \quad (1)$$

$$\frac{V_{load}}{V_{pv}} = \frac{I_{pv}}{I_{load}} = d , \quad (2)$$

with the impedance Z_{pv} seen by the PV panel expressed in Eq. (3), this impedance can be

described as a function of the duty cycle and the output load impedance Eqs. (4) in (5).

$$Z_{pv} = \frac{V_{pv}}{I_{pv}} , \quad (3)$$

$$Z_{load} = \frac{V_{load}}{I_{load}} , \quad (4)$$

$$Z_{pv} = \frac{1}{d^2} Z_{load} . \quad (5)$$

By changing the duty cycle d , the value of the impedance seen by the PV module can be changed and matched to the optimal impedance Eq. (6), as shown in Fig. 1.

$$Z_{opt} = \frac{V_{mp}}{I_{mp}} . \quad (6)$$

Various MPPT algorithms have been investigated in the literature, including the P&O algorithm, incremental conductance (INC), Fractional Open-Circuit Voltage, Fractional Short-Circuit Current, and Fuzzy Logic Control. The output of the MPPT algorithm is the duty cycle used by the pulse width modulation (PWM) block generator to generate the PWM signal, based on the calculated duty cycle, as shown in Fig. 2.

B. Perturb and Observe MPPT

The principle of this technique is based on a trial-and-error method of varying the voltage of the PV panel and observing its effects on the output PV power, while comparing the current state with the previous state. This process is repeated periodically until the maximum power

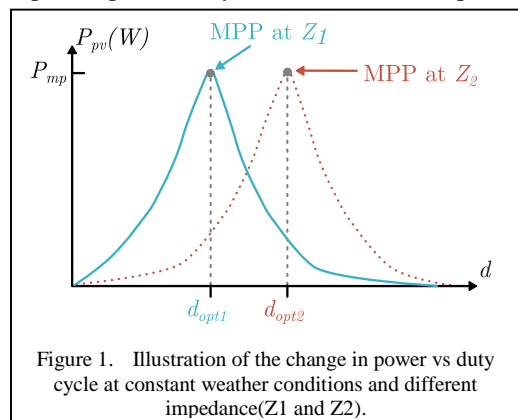


Figure 1. Illustration of the change in power vs duty cycle at constant weather conditions and different impedance(Z_1 and Z_2).

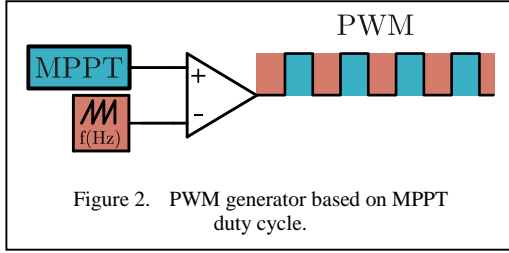


Figure 2. PWM generator based on MPPT duty cycle.

point is reached. However, the output of this control oscillates around the maximum power point; to minimize this oscillation, the perturbation step size is reduced.

The flowchart of the P&O algorithm is presented in Fig. 3. The algorithm starts by measuring the PV current and voltage to calculate the actual power $P(k)$ and compares it with the previous power $P(k-1)$. If there is no change in the power, the duty cycle stays the same. However, if $P(k)$ is greater than $P(k-1)$ and the actual voltage $V(k)$ is greater than the previous $V(k-1)$ the duty cycle is decreased. If $V(k)$ is less than $V(k-1)$, the duty cycle is increased. On the other hand, if $P(k)$ is less than $P(k-1)$, the duty cycle is increased if $V(k)$ is greater than $V(k-1)$, and it is decreased otherwise. To minimize the oscillation around the maximum power point, the perturbation step size Δd is usually reduced.

C. Fuzzy Logic Controller MPPT-based

The fuzzy logic was developed by Zadeh in 1965. The FLC is used to convert the human information to the rule-based model that can control a plant with linguistic explanations [13].

The typical FLC includes three main components: fuzzification, inference engine, and defuzzification, as shown in Fig. 4. The inputs to a MPPT fuzzy logic controller are usually an error E and a change in error ΔE as expressed in Eqs. (7) and (8), and the output is the change in duty cycle Δd . These inputs and output are scaled using the scaling factors S_E , $S_{\Delta E}$ and $S_{\Delta d}$ as shown in Fig. 4.

$$E(k) = \frac{\Delta P}{\Delta V} = \frac{P(k) - P(k-1)}{V(k) - V(k-1)}, \quad (7)$$

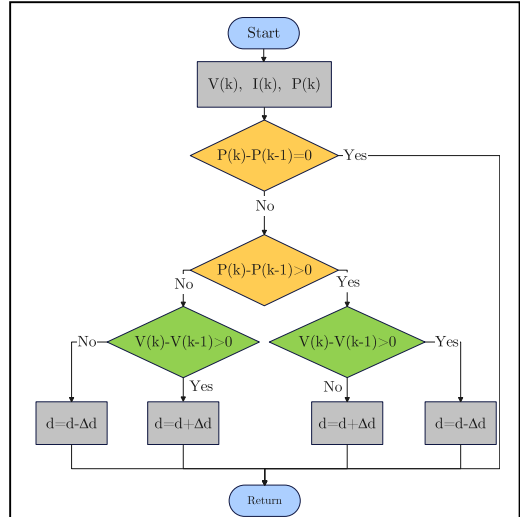


Figure 3. Flowchart of the perturb and observe MPPT algorithm.

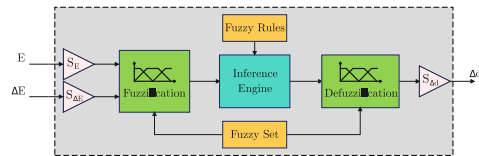


Figure 4. Structure of the FLC-MPPT technique.

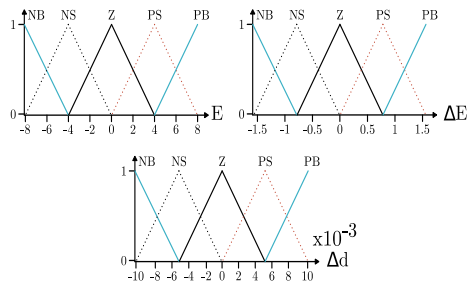


Figure 5. Membership functions of the FLC-MPPT algorithm.

$$\Delta E(k) = E(k) - E(k-1). \quad (8)$$

During fuzzification, numerical input variables are converted into linguistic variables based on a membership function. Five fuzzy linguistic variables are used: NB (negative big), NS (negative small), ZE (zero), PS (positive small), and PB (positive big).

In Fig. 5 the Membership functions for the inputs and output variables used in this paper are illustrated.

TABLE I. FUZZY LOGIC CONTROLLER RULES.

Δd		ΔE				
		<i>NB</i>	<i>NS</i>	<i>Z</i>	<i>PS</i>	<i>PB</i>
<i>E</i>	<i>NB</i>	<i>Z</i>	<i>Z</i>	<i>PB</i>	<i>PB</i>	<i>PB</i>
	<i>NS</i>	<i>Z</i>	<i>Z</i>	<i>PS</i>	<i>PS</i>	<i>PS</i>
	<i>Z</i>	<i>PS</i>	<i>Z</i>	<i>Z</i>	<i>Z</i>	<i>NS</i>
	<i>PS</i>	<i>NS</i>	<i>NS</i>		<i>Z</i>	<i>Z</i>
	<i>PB</i>	<i>NB</i>	<i>NB</i>	<i>NB</i>	<i>Z</i>	<i>Z</i>

The inference engine applies the fuzzy rules to the fuzzy inputs produced by fuzzification phase to generate the fuzzy outputs, 25 fuzzy IF-THEN rules are used as shown in Table I.

In the Defuzzification step the linguistic output variables was converted to real domain. The center of gravity defuzzification methods in Eq. (9).

$$\Delta d = \frac{\sum_{i=1}^n \Delta d_i \times \mu_i}{\sum_{i=1}^n \mu_i}, \quad (9)$$

where, Δd_i is the i^{th} crisp value of the output variable, μ_i is its corresponding membership degree, and n is the number of crisp values considered.

III. RESULTS AND DISCUSSION

The parameters of the PV panel used in the simulation are presented in Table II. The PV array is composed of two parallel rows, where each row contains five panels in series. The (I-V) and (P-V) characteristics of this array are shown in Fig. 6, for constant temperature and variable illumination, and vice versa.

TABLE II. PARAMETERS OF A SINGLE PV MODULE.

Parameter	Value	Unit
Rated power P_{mp}	290	W
Open circuit voltage V_{oc}	39.99	V
Short circuit current I_{sc}	9.67	A
Cells per module N_{cell}	60	-
Series resistor R_s	0.39545	Ω
Shunt resistor R_{sh}	390.5225	Ω
Temperature coefficient of V_{oc}	-0.3137	%/ $^{\circ}C$
Temperature coefficient of I_{sc}	0.052099	%/ $^{\circ}C$
Diode ideality factor n	1.0043	-

TABLE III. PARAMETERS OF THE BUCK DC-DC CONVERTER.

Parameter	Value	Unit
Inductance L	850	μH
Capacitor C	780	μF
Switching frequency f	5000	Hz

The short-circuit current of the PV array is affected by the variation of irradiation when the temperature is constant. On the other hand, if the irradiation is constant and the temperature is variable, the open-circuit voltage of the PV array decreases as the temperature increases. The values used to design the Buck converter are shown in Table III.

To evaluate the MPPT performance, three test modes were carried out using the system

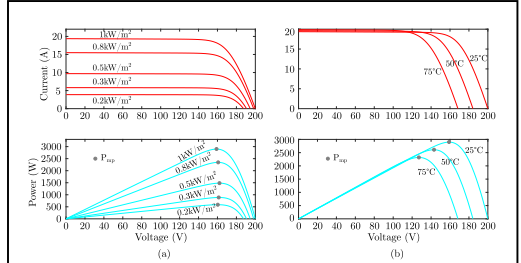


Figure 6. The (I-V) and (P-V) characteristic of PV array for (a) T=25 $^{\circ}C$ and variable G (b) G=1000 W/m² and variable T algorithm.

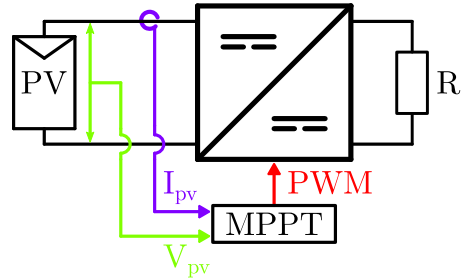


Figure 7. Synoptic schema of the PV system used to evaluate the MPPT performance.

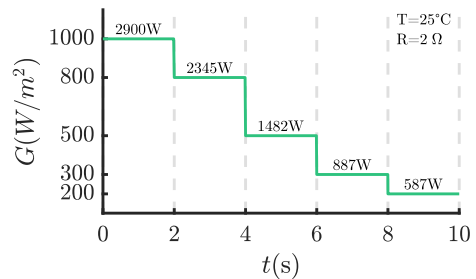


Figure 8. Parameters used in Mode 01.

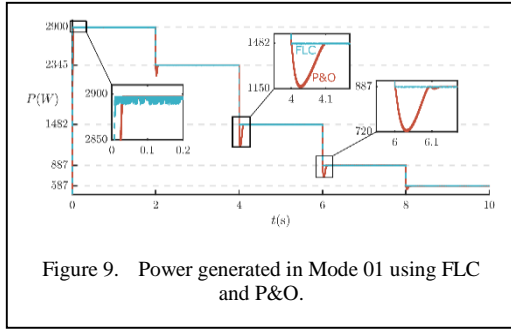


Figure 9. Power generated in Mode 01 using FLC and P&O.

presented in the schematic diagram shown in Fig. 7.

This system consists of a PV array that feeds a resistive load R through a DC-DC buck converter controlled by the PWM signal generated from the MPPT algorithm.

Mode 01: In this mode, the temperature and the load were fixed at constant values, while the illumination was varied as shown in Fig. 8. This mode was divided into five phases, each lasting two seconds. The expected power values for each phase were presented above the illumination plot.

The results of the generated power obtained from simulating the PV system controlled by the P&O algorithm and FLC for this mode are shown in Fig. 9.

The performance analysis of the MPPT algorithms responses in this mode is presented in Table IV.

Mode 02: In this mode, the illumination and load were fixed at constant values, while the temperature was varied as shown in Fig. 10. This mode was divided into three phases, and the maximum power for each phase was shown above the temperature plot.

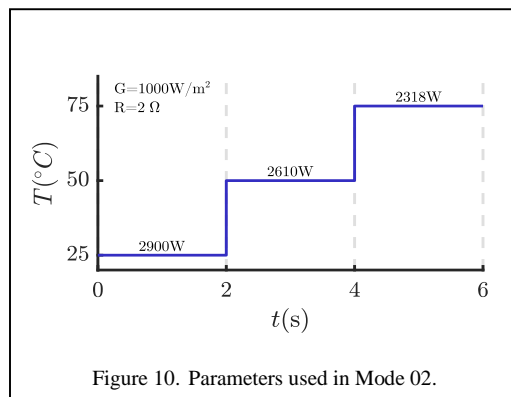


Figure 10. Parameters used in Mode 02.

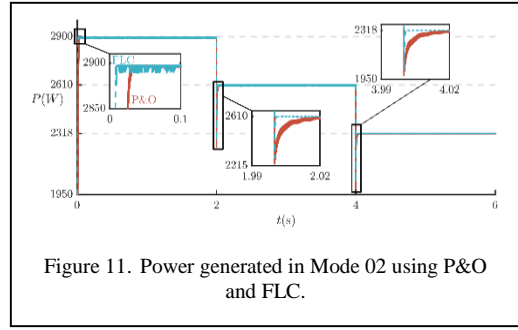


Figure 11. Power generated in Mode 02 using P&O and FLC.

TABLE IV. PERFORMANCES RESPONSES OF THE MPPT IN MODE 01.

G(W/m ²)	MPPT	Rise time (s)	Settling time (s)
1000	P&O	0.0166	0.0255
	FLC	0.0063	0.0078
800	P&O	0.0396	0.0665
	FLC	0.0079	0.0099
500	P&O	0.1414	0.1659
	FLC	0.0128	0.0159
300	P&O	0.2317	0.2525
	FLC	0.0213	0.0265
200	P&O	0.2902	0.3492
	FLC	0.0317	0.0394

The results of the generated power obtained from simulating the PV system controlled by the P&O algorithm and FLC for this mode are shown in Fig. 11.

The performance analysis of the MPPT algorithms responses in this mode is presented in Table V.

Mode 03: In this mode, the illumination and temperature were fixed at constant values, while the load was varied as shown in Fig. 12. This mode was divided into three phases, and the maximum power was 2900 W for all phases.

The results of the generated power obtained by the simulation of the PV system controlled by the P&O algorithm and FLC for this mode are shown in Fig. 13.

In the three presented modes, one parameter was always varied while the others were fixed during the simulation.

The converted power was found to be extremely close to the reference power, with an inaccuracy of less than 5%, when evaluating the efficiency of the MPPT in the test modes.

TABLE V. PERFORMANCES RESPONSES OF THE MPPT IN MODE 02.

T(°C)	MPPT	Rise time (s)	Settling time (s)
25	P&O	0.0166	0.0255
	FLC	0.0063	0.0078
50	P&O	0.0396	0.0665
	FLC	0.0055	0.0069
75	P&O	0.1414	0.1659
	FLC	0.0048	0.0060

Compared to the non-MPPT system, the MPPT algorithm resulted in a significant increase in power output under various circumstances.

The MPPT algorithms tested in different modes demonstrated stable performance under varying weather conditions and loads. Although the FLC-MPPT algorithm performed well under different conditions, there was a noticeable decrease in efficiency during a load change for the P&O algorithm.

The P&O and FLC MPPT algorithms responded quickly to changes in solar irradiance and temperature, providing optimal power output within seconds of a change in conditions. However, the P&O algorithm responded very slowly during a load change.

To perform a stability and reliability analysis, the rise and settling time should be compared under the same conditions.

Rise time: is defined as the time taken for the output power of the MPPT algorithm to reach 90% of the new optimal power value after a step change in solar irradiance or temperature.

Settling time: is the time taken for the output power of the MPPT algorithm to stabilize within 2% of the new optimal power value after a step change in solar irradiance or temperature.

From Table IV and V, the FLC algorithm demonstrates excellent stability, with minimal fluctuations in power output even under rapidly

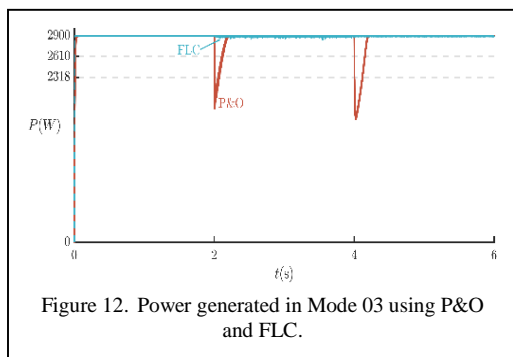


Figure 12. Power generated in Mode 03 using P&O and FLC.

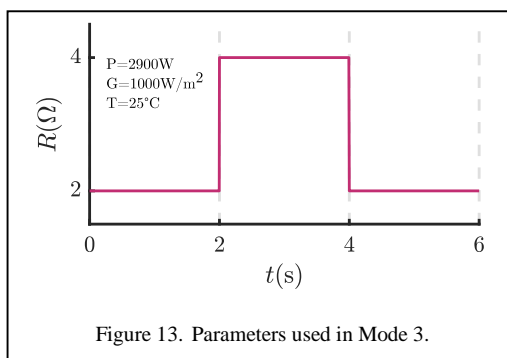


Figure 13. Parameters used in Mode 3.

changing conditions. Compared to the P&O algorithm, the FLC algorithm had faster response times and higher accuracy. The presented MPPT algorithms were robust and able to recover quickly from errors or failures, with no major disruptions to the power output observed during testing.

While the cost of implementing the FLC is higher and more complicated than the P&O method, the long-term benefits in terms of efficiency and reliability make the FLC a better solution for many applications, even with its higher cost of implementation in real hardware.

IV. CONCLUSION


This study focuses on two widely used Maximum Power Point Tracking (MPPT) algorithms, the Perturb and Observe (P&O) and Fuzzy Logic Control (FLC) algorithms; the paper investigates the drawbacks and benefits of FLC and P&O in photovoltaic systems. Three modes of parameters for the climate change and load value are applied. In conclusion, both MPPT methods can reach the MPP. However, the FLC demonstrated superior stability, faster response times, and higher accuracy, particularly in rapidly fluctuating conditions. On the other hand, P&O is easy to implement and less complicated.

REFERENCES

- [1] Qazi, A., Hussain, F., Rahim, N. A., Hardaker, G., Alghazzawi, D., Shaban, K., & Haruna, K. (2019). Towards sustainable energy: A systematic review of renewable energy sources, technologies, and public opinions. *IEEE Access*, 7, 63837-63851. <https://doi.org/10.1109/ACCESS.2019.2906402>
- [2] Jurasz, J., Canales, F. A., Kies, A., Guezgouz, M., & Beluco, A. (2020). A review on the complementarity of renewable energy sources: Concept, metrics, application and future research directions. *Solar Energy*, 195, 703-724. <https://doi.org/10.1016/j.solener.2019.11.087>
- [3] Mohapatra, A., Nayak, B., Das, P., & Mohanty, K. B. (2017). A review on MPPT techniques of PV system under partial shading condition. *Renewable and*

- Sustainable Energy Reviews*, 80, 854-867. <https://doi.org/10.1016/j.rser.2017.05.083>
- [4] Kathe, M. L., Makokha, A. B., Siagi, Z. O., & Adaramola, M. S. (2023). A comprehensive review of maximum power point tracking (MPPT) techniques used in solar PV systems. *Energies*, 16(5), 2206. <https://doi.org/10.3390/en16052206>
- [5] Sarvi, M., & Azadian, A. (2021). A comprehensive review and classified comparison of MPPT algorithms in PV systems. *Energy Systems*, 13(2), 281–320. <https://doi.org/10.1007/s12667-021-00427-x>
- [6] Elgendy, M. A., Zahawi, B., & Atkinson, D. J. (2012). Assessment of perturb and observe MPPT algorithm implementation techniques for PV pumping applications. *IEEE Transactions on Sustainable Energy*, 3(1), 21-33. <https://doi.org/10.1109/TSTE.2011.2168245>
- [7] Hsieh, G.-C., Hsieh, H.-I., Tsai, C.-Y., & Wang, C.-H. (2013). Photovoltaic power-increment-aided incremental-conductance MPPT with two-phased tracking. *IEEE Transactions on Power Electronics*, 28(6), 2895-2911. <https://doi.org/10.1109/TPEL.2012.2227279>
- [8] Fan, Z., Li, S., Cheng, H., & Liu, L. (2021). Perturb and observe MPPT algorithm of photovoltaic system: A review. In *2021 33rd Chinese Control and Decision Conference (CCDC)* (pp. 1413-1418). <https://doi.org/10.1109/CCDC52312.2021.9602272>
- [9] Ilyas, A., Ayyub, M., Khan, M. R., Jain, A., & Husain, M. A. (2017). Realisation of incremental conductance MPPT algorithm for a solar photovoltaic system. *International Journal of Ambient Energy*, 39(8), 873–884. <https://doi.org/10.1080/01430750.2017.1354322>
- [10] Baimel, D., Tapuchi, S., Levron, Y., & Belikov, J. (2019). Improved fractional open circuit voltage MPPT methods for PV systems. *Electronics*, 8(3), 321. <https://doi.org/10.3390/electronics8030321>
- [11] Naidu, I. E. S., Srikanth, S., Siva Sarapakara Rao, A., & Venkatanarayana, A. (2023). A novel mine blast optimization algorithm (MBOA) based MPPT controlling for grid-PV systems. *AIMS Electronics and Electrical Engineering*, 7(2), 135–155. <https://doi.org/10.3934/electreng.2023008>
- [12] Dkhichi, F. (2023). Improved MPPT algorithm: Artificial neural network trained by an enhanced Gauss-Newton method. *AIMS Electronics and Electrical Engineering*, 7(4), 380–405. <https://doi.org/10.3934/electreng.2023020>
- [13] Zadeh, L. A. (1965). Fuzzy sets. *Information and Control*, 8(3), 338-353. [https://doi.org/10.1016/S0019-9958\(65\)90241-X](https://doi.org/10.1016/S0019-9958(65)90241-X)

Substitution of Calcium at A-site in LaCaMnNiO₆ for Optimized Electrochemical Energy Storage Application

Dinesh¹, Mukul Gupta², Parasmani Rajput³, Ashok Kumar⁴ 

^{1,4}Department of Applied Sciences, National Institute of Technical Teachers Training and Research, Chandigarh 160019, India

¹J.C. Bose University of Science and Technology, YMCA, Faridabad, Haryana 121006, India

²UGC-DAE Consortium for Scientific Research, Khandwa Road, Indore 452017, India

³Beamline Development and Application Section, Bhabha Atomic Research Centre, Trombay, Mumbai 400085, India

⁴ashokku@nitttrchd.ac.in

Abstract—Double perovskite LaCaMnNiO₆ has been synthesized via sol-gel route to understand its potential for energy storage applications. Structural, morphological and electrochemical energy storage properties were investigated by X-ray diffraction, high-resolution transmission electron microscopy and cyclic voltammetry, respectively. The material exhibited cubic phase, $Fm\bar{3}m$ symmetry with uneven morphology. Energy storage behavior evaluated via CV curves revealed specific capacitance of 617 F/g at scan rate of 2 mV/s.

Keywords - energy storage, double perovskite, electrochemical

I. INTRODUCTION

The perovskite oxide are compounds with chemical composition ABO₃, where larger cation A occupies the center, smaller cations B corners and the oxygen anions, face centers of the unit cell with the B cation surrounded by the octahedron of O [1]. Double perovskites can host two elements of different sizes and valences at both A and B sites and have the chemical composition of AA'BB'O₆ [2]. The perovskites which offer both electronic and ionic conductivity are in great demand for the applications as electrode in fuel cells, random

access memories, solar cells, piezoelectric devices, supercapacitors and wireless communications [3]. Lanthanum has the largest ionic radius among the lanthanides and exhibits +3 oxidation state which provides stability and increased conductivity due to shielding of valence electrons provided by vacant 4f orbitals [4]. When A site is doped with bivalent smaller alkali earth metals (Ca²⁺), it creates charge imbalance throughout the crystal which leads to unstable oxidation states of B-site elements [5]. The smaller size of the Ca²⁺ may help in reducing the surface segregation which helps in better stability of the cathodes [6]. Hence, better electrochemical performance can be expected by hosting calcium at A site in double perovskites for energy storage applications [7]. B-site elements influence the properties like surface area, conductivity, morphology and energy storage behavior. Singh et al. reported the synthesis of Sm₂MnNiO₆ and La₂MnNiO₆ by hydrothermal and sol gel method respectively. The specific capacitance of Sm₂MnNiO₆ and La₂MnNiO₆ was calculated by galvanostatic charge discharge and cyclic voltammetry curves. The specific capacitance for Sm₂MnNiO₆ was found 525.2 F/g at the current density of 1 A/g [8] and 478 F/g at 2 mV/s for La₂MnNiO₆ [9]. Dhahiya et al. developed the A-site doped



perovskite BaLaMnFeO_6 , studied the electrochemical behavior, and reported the specific capacitance of 345 F/g at 5 mV/s [10]. Anup et al. synthesized LaCaCrMnO_6 and analyzed the electrochemical behavior of the material, and reported the specific capacitance of 281 F/g at 1 A/g current density [11]. Reference [12] reported the specific capacitance of $\text{La}_{0.5}\text{Sr}_{0.5}\text{Cu}_{0.1}\text{Mn}_{0.9}\text{O}_{3-\delta}$ as 464 F/g at 2 A/g. The above literature suggests that doping of divalent cations at A-site positively impacts the electrochemical performance of the compounds. In this study, Calcium (Ca^{2+}) is substituted at A-site to synthesize LaCaMnNiO_6 and the effect on electrochemical performance is studied.

II. EXPERIMENTAL

The precursors lanthanum nitrate hexahydrate ($\text{La}(\text{NO}_3)_3 \cdot 6\text{H}_2\text{O}$), calcium nitrate tetrahydrate ($\text{Ca}(\text{NO}_3)_2 \cdot 4\text{H}_2\text{O}$), manganese (II) nitrate hexahydrate ($\text{Mn}(\text{NO}_3)_2 \cdot 6\text{H}_2\text{O}$) and nickel nitrate hexahydrate ($\text{Ni}(\text{NO}_3)_2 \cdot 6\text{H}_2\text{O}$) were taken in stoichiometric ratio 1:1:1:1, and were added in 100 mL DI water and stirred at 140 °C for 1 hour. Citric acid and ethylene glycol were added to the above solution as chelating agents and stirred continuously until a gel is obtained. Afterwards, the obtained sample was heated at 160 °C for 24 hours. Then the sample was calcined at 1100 °C for 2 hours to obtain the desired material. The working electrodes used for electrochemical studies were made in lab. Polyvinylidene fluoride (PVDF), carbon black, and synthesized material were taken in ratio of 1:1:8 and dissolved in N-methyl 2-pyrrolidone (NMP) and stirred for 24 hours to make a homogeneous slurry. The slurry was casted on the nickel mesh on the approximate area of 1 cm². The electrodes were dried in the oven at 70 °C overnight and used for electrochemical studies.

III. CHARACTERIZATION

A. Structural and Morphological Analysis

The X-ray diffraction (XRD) pattern of LaCaMnNiO_6 with Rietveld refinement is shown in Fig. 1. X-ray diffraction (XRD) pattern was obtained using Bruker D8 Advance diffractometer equipped with Cu target and LYNXEYE XE-T detector. The peaks observed at (2θ) degrees 23.24°, 32.95°, 40.61°, 47.29°, 58.86°, 69.05°, 78.82° correspond to Bragg planes (100), (101), (111), (200), (211), (202), (301), respectively (JCPDS # 96-110-0105) [13].

The as-prepared compound has cubic structure with $Fm\bar{3}m$ symmetry. Minor peaks of NiO at (2θ) degrees 37.34°, 43.25° and 62.78 correspond to (111), (200) and (202) planes, respectively (JCPDS # 04-0835), as shown by “*” in Fig. 1 [14]. The high-resolution transmission electron microscopy images were obtained on JOEL JEM-2100 Plus to analyse the morphology of the compound as shown in Fig. 2. The particles are observed to have an uneven morphology.

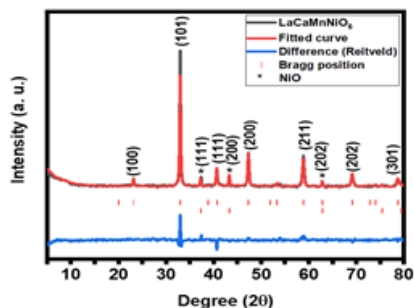


Figure 1. X-ray diffraction (XRD) pattern of LaCaMnNiO_6 with Rietveld refinement.

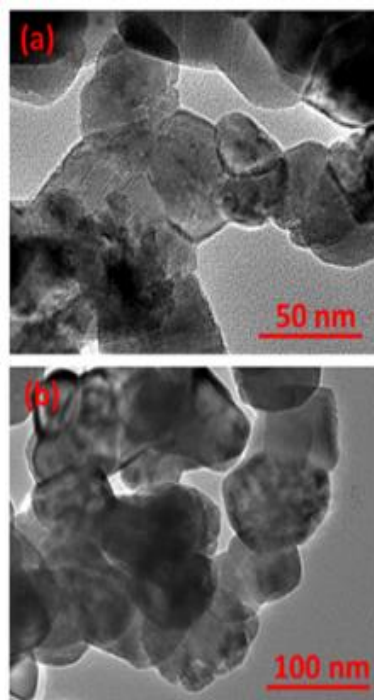
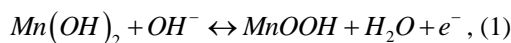


Figure 2. High-resolution transmission electron microscopy (HRTEM) images of as prepared LaCaMnNiO_6 .

B. Electrochemical Analysis

The electrochemical studies were done to analyze the electrochemical behavior of the material. The studies were done on a SP-150 Biologic potentiostat in 6M KOH solution using a three-electrode system. The cyclic-voltammetry (CV) curves were obtained at increasing scan rates from 2-100 mV/s (Fig. 3(a)). The CV curves are consistent at all scan rates which show the stability and reversibility. The oxidation and reduction peaks in the CV curves are due to the variable oxidation states of the B-site elements (Mn/Ni) [15]. The possible reactions take place at the surface of the electrodes in the KOH electrolyte are:



The specific capacitance is calculated from the CV curves using the expression:

$$C_{sp} = \int_{E_1}^{E_2} i(E)dE / 2mv(E_2 - E_1) , \quad (4)$$

where $\int_{E_1}^{E_2} i(E)dE$, m (1 mg), v and $(E_2 - E_1)$ represents the area under the CV curve, active mass loading, scan rate and applied potential respectively [16].

The specific capacitance is calculated to be 617, 551, 510, 473, 447 and 415 F/g at the scan rates 2, 10, 25, 50, 75 and 100 mV/s, respectively. The value of specific capacitance with respect to scan rate is shown in Fig. 3(b). It is evident that the specific capacitance decreases with increase in scan rates. At lower scan rates, the diffusion process is slow and the electrolyte OH^- ions get more time to interact with the inner active sites of the material at the interface resulting in high specific capacitance. At higher scan rates, the diffusion process is fast which does not allow to form a diffusion layer at the electrode-electrolyte interface results in lower specific capacitance values [11]. The such high performance of the LaCaMnNiO_6 as compared to $\text{La}_2\text{MnNiO}_6$ (specific capacitance~ 478 F/g at 2mV/s) can be attributed to the substitution of divalent Ca^{2+} at A-site which increase the conductivity and provide more active sites for the

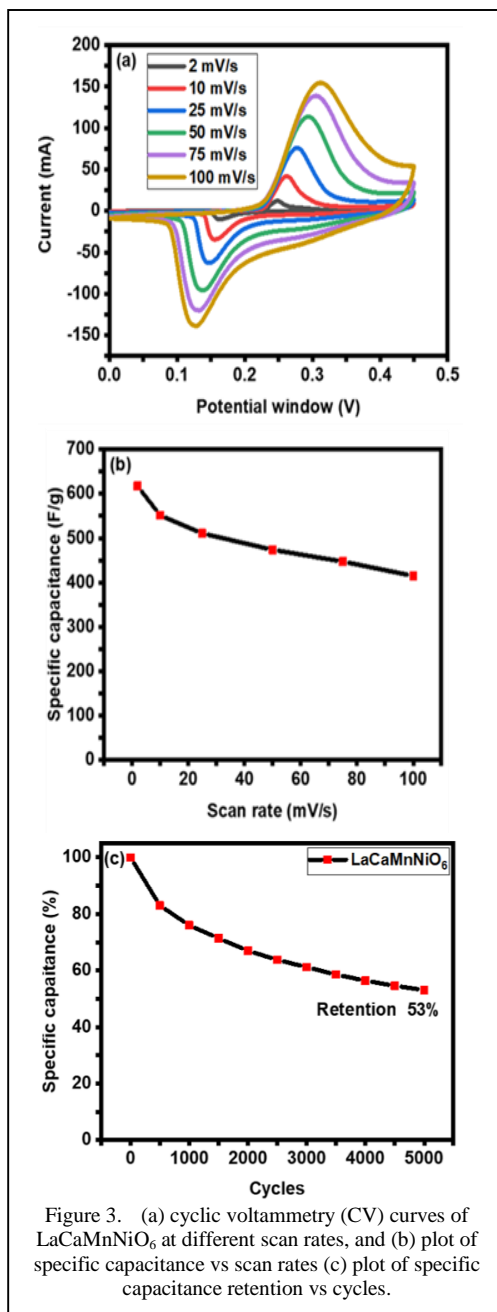


Figure 3. (a) cyclic voltammetry (CV) curves of LaCaMnNiO_6 at different scan rates, and (b) plot of specific capacitance vs scan rates (c) plot of specific capacitance retention vs cycles.

redox reactions [6]. Specific capacitance of various double perovskite materials has been given in Table I.

Cyclic stability of the electrode material was also analyzed over 5000 cycles. It is observed that the material has 53% specific capacitance retention over 5000 cycles. The plot of specific capacitance retention vs cycles is shown in Fig. 3(c). The material LaCaMnNiO_6 has potential

TABLE I. SPECIFIC CAPACITANCE OF VARIOUS DOUBLE PEROVSKITE MATERIALS.

S.No	Materials	Specific capacitance	Ref.
1	Sm ₂ MnNiO ₆	525.2 F/g at 1 A/g	[8]
2	La ₂ MnNiO ₆	478 F/g at 2mV/ s	[9]
3	BaLaMnFeO ₆	345 F/g at 5 mV/s	[10]
4	LaCaCrMnO ₆	281 F/g at 1 A/g	[11]
5	La _{0.5} Sr _{0.5} Cu _{0.1} Mn _{0.9} O _{3-δ}	464 F/g at 2 A/g	[12]
6	LaCaMnNiO ₆	617 F/g at 2 mV/s	This work

application as cathode in the supercapacitor and other energy storage devices.

Further work can be done towards optimizing the potential window and cyclic stability of the material for industrial applications. The electrochemical performance of the material may be further optimized by making composite with rGO, MXene or other carbon-based compounds.

IV. CONCLUSIONS

A-site doped LaCaMnNiO₆ has been synthesized by sol-gel method. The X-ray diffraction pattern shows that the material has cubic structure with *Fm $\bar{3}$ m* symmetry. The electrochemical studies show the maximum specific capacitance of 617 F/g at 2 mV/s which can be attributed to the substitution of divalent Ca²⁺ at A-site. Also, the material electrode attains a cyclic stability of 53% over 5000 cycles. The material has potential application in energy storage devices as cathode.

ACKNOWLEDGMENTS

Financial support from UGC-DAE-CSR is acknowledged by author (AK) (CRS/2021-22/01/459).




REFERENCES

- [1] Goel, P., et al. (2021). Perovskite materials as superior and powerful platforms for energy conversion and storage applications. *Nano Energy*, 80, 105552. <https://doi.org/10.1016/j.nanoen.2020.105552>
- [2] Saha-Dasgupta, T. (2020). Double perovskites with 3d and 4d/5d transition metals: compounds with promises. *Materials Research Express*, 7, 014003. <https://doi.org/10.1088/2053-1591/ab6293>
- [3] Kostopoulou, A., Vernardou, D., Savva, K., & Stratakis, E. (2019). All-inorganic lead halide perovskite nanohexagons for high-performance air-stable lithium batteries. *Nanoscale*, 11, 882. <https://doi.org/10.1039/C8NR10009H>
- [4] Singh, J., Goutam, U. K., & Kumar, A. (2019). Hydrothermal synthesis and electrochemical

performance of nanostructured cobalt free La₂ CuMnO₆. *Solid State Sciences*, 95, 105927.

- [5] Li, X., et al. (2021). A-site perovskite oxides: an emerging functional material for electrocatalysis and photocatalysis. *Journal of Materials Chemistry A*, 9, 6650. <https://doi.org/10.1039/d0ta09756j>
- [6] Choi, S., Park, S., Shin, J., & Kim, G. (2015). The effect of calcium doping on the improvement of performance and durability in a layered perovskite cathode for intermediate-temperature solid oxide fuel cells. *Journal of Materials Chemistry A*, 3, 6088. <https://doi.org/10.1039/c4ta05684a>
- [7] Liu, Y., et al. (2021). Recent advances in the heteroatom doping of perovskite oxides for efficient electrocatalytic reactions. *Royal Society of Chemistry*, 13, 19840. <https://doi.org/10.1039/d1nr05797a>
- [8] Singh, J., & Kumar, A. (2020). Solvothermal synthesis dependent structural, morphological and electrochemical behaviour of mesoporous nanorods of Sm₂ NiMnO₆. *Ceramics International*, 46, 11041. <https://doi.org/10.1016/j.ceramint.2020.01.122>
- [9] Singh, J., Kumar, A., & Kumar, A. (2021). Facile wet chemical synthesis and electrochemical performance of double perovskite- La₂ NiMnO₆ for energy storage application. *Materials Today: Proceedings*, 587. <https://doi.org/10.1016/j.matpr.2021.05.231>
- [10] Dahiya, R., Chauhan, N., & Kumar, A. (2024). Synergistic effect of reduced graphene oxide and BaLaMnFeO₆ in BaLaMnFeO₆/rGO composite on electrochemical behavior. *Physica Status Solidi (A) Applications and Materials Science*, 221, 2300638. <https://doi.org/10.1002/pssa.202300638>
- [11] Singh, A., et al. (2024). Synergistic effect of redox electrolyte and reduced graphene oxide on the electrochemical performance of LaCaCrMnO₆. *Journal of Energy Storage*, 87, 111489. <https://doi.org/10.1016/j.est.2024.111489>
- [12] Cao, Y., Lin, B., Sun, Y., Yang, H., & Zhang, X. (2015). Synthesis, structure and electrochemical properties of lanthanum manganese nanofibers doped with Sr and Cu. *Journal of Alloys and Compounds*, 638, 204.
- [13] Androulakis, J., et al. (2003). LaSrMnCoO₆: A new cubic double perovskite oxide. *Journal of Solid State Chemistry*, 173, 350. [https://doi.org/10.1016/s0022-4596\(03\)00109-9](https://doi.org/10.1016/s0022-4596(03)00109-9)
- [14] Wei, Z., Qiao, H., Yang, H., Zhu, L., & Yan, X. (2008). Preparation and characterization of NiO nanoparticles by anodic arc plasma method. *Journal of Nanomaterials*, 2009. <https://doi.org/10.1155/2009/795928>
- [15] Singh, N., Tanwar, S., Sharma, A. L., & Yadav, B. C. (2022). Advanced cyclic stability and highly efficient different shaped carbonaceous nanostructured electrodes for solid-state energy storage devices. *International Journal of Hydrogen Energy*, 47, 28254. <https://doi.org/10.1016/j.ijhydene.2022.06.162>
- [16] Mansoorie, F. N., Singh, J., & Kumar, A. (2020). Wet chemical synthesis and electrochemical performance of novel double perovskite Y₂ CuMnO₆ nanocrystallites. *Materials Science in Semiconductor Processing*, 107, 104826. <https://doi.org/10.1016/j.mssp.2019.10482>

Simplified Nusselt Correlations for Easier Estimation of Heat Exchange in Natural Convection in Vertical Cavities

Paulo Cesar Mioralli¹, Marcos Vinicios dos Santos², Elson Avallone³

^{1,2,3}Federal Institute of São Paulo - IFSP, Catanduva-SP, Brazil

¹mioralli@ifsp.edu.br, ²m.vinicios@aluno.ifsp.edu.br, ³elson.avallone@ifsp.edu.br

Abstract—In natural convection heat transfer processes in vertical cavities, the use of correlations to determine the Nusselt number is an easy-to-apply method for estimating the convective heat transfer coefficient. Such correlations are mostly dependent on the Rayleigh number and, many of them, also on the aspect ratio, a parameter that relates the height to the spacing between the vertical walls of the cavity. Some of these correlations have as a negative point their mathematical format, which can be extensive and somewhat complex. Furthermore, the literature is scarce on correlations that can be applied to laminar flow regimes and high aspect ratio values. The correlations proposed by a specific authors of literature fit the aforementioned conditions. Thus, the present study proposes correlations with a simple mathematical format, based on the application of the multivariate linear regression technique on a set of data from the correlations of literature, aiming to allow quick estimates of heat exchange inside the cavity. Five simple-application Nusselt correlations were obtained from two extensive correlations of literature by the same authors. The results obtained by the new correlations showed an agreement of over 90% with the data set from the correlations of literature, considering a maximum difference of 10% between them.

Keywords - heat transfer, computational analysis, natural convection, cavities

I. INTRODUCTION

Heat transfer by natural convection in cavities is a fundamental problem due to a wide

range of applications in fields related to thermal processes involved in various engineering systems, such as thermal insulation in buildings, fire hazards, solar energy collectors and electronic refrigeration equipment. An extensive literature review on natural convection in cavities was carried out by [1], demonstrating its importance and applicability in engineering systems.

A search of the literature reveals that, over the years, studies about cavities have been developed by researchers mainly due to their significant role in evaluating the thermal performance of fenestration products. Fenestration systems such as windows, doors and skylights are typical examples of cavities, constituting important components of buildings, residential or commercial, with the purpose of providing external views, fresh air during seasonal periods and natural light for interior spaces. However, fenestration systems also represent one of the largest sources of unwanted heat gain in the summer and significant heat loss in the winter for the internal environment of the building [2].

One way to quantify heat transfer by natural convection in vertical cavities is to use correlations to estimate the Nusselt number and evaluate the heat transfer coefficient. Such correlations are developed by researchers based on experimental or numerical results and are interesting because they constitute a spontaneous method for estimating heat transfer. The authors [3] present an interesting study on the evolution



of correlations in cavities over the course of forty years up to the date of publication of their manuscript.

Nusselt correlations for vertical cavities can be found in the literature and are generally written as a function of the Rayleigh number, which is used to express heat transfer in natural convection. Other Nusselt correlations are also expressed as a function of the aspect ratio of the cavity, in addition to the Rayleigh number.

The usability of these correlations has always been important. Some of them were used for years in computer programs developed in North America, THERM [4] and WINDOW [5], to evaluate the convective heat transfer coefficient in fenestration devices. These programs used a correlation based on the works of [6] and [7]. Later, [8], based on the results of [9], implemented improvements in this correlation, which was adopted by the American standard ASHRAE SPC-142P [10].

With the increase in computational power, many recent studies on heat transfer inside vertical cavities have been carried out by means of computational simulation that includes the use of numerical algorithms implemented with systems of differential equations that correlate the thermal and dynamic aspects of the flow and allow the application of initial conditions and boundary conditions to the problem under analysis. Examples of this application are the works [11] and [12]. However, the viability of this methodology sometimes requires significant simulation time and becomes unfeasible when a quick estimate of heat exchange inside the cavity is desired. The use of correlations provides reasonable approximations for such analysis and is also a very accessible and less complex approach.

Despite the practicality of using Nusselt correlations for thermal analysis in cavities, many correlations available in the literature, especially those considered more reliable by researchers in general, are extensive, intricate or somewhat complex in their presentation. These are negative aspects of their applicability. In contrast to these characteristics, this study develops correlations with a simple mathematical format to investigate heat transfer by natural convection in vertical cavities filled with air, based on the application of multivariate linear regression on a set of results obtained by the complex correlations of [2].

II. PROCEDURE AND METHODOLOGY

Classical literature [13-15] presents a cavity as a closed space in which two parallel walls are at different temperatures that induce a recirculation movement of the fluid confined inside. As a consequence of this process, there is heat transfer by convection from one wall to the other. Cavities are also presented in three configurations: vertical, horizontal and inclined, with the vertical cavity being the focus of analysis in this study.

Fig. 1 illustrates a typical vertical cavity filled with air. The cavity has side walls at different temperatures, T_1 and T_2 , with $T_1 > T_2$. The temperature difference between the walls causes air to recirculate inside the cavity and heat exchange by natural convection occurs in the direction of the wall with the highest temperature T_1 to the wall with the lowest temperature T_2 . The parameters H and L represent, respectively, the height of the cavity and the spacing between the walls. The aspect ratio (H/L) is an important parameter in the analysis of heat exchange by natural convection inside the cavity.

Correlations for Nusselt number, Nu_L , that are applicable to natural convection in cavities considering laminar flow regime (low Rayleigh values), together with high aspect ratio values, are rarely found in the literature. Meeting these requirements, there are two correlations, Eqs. (1) and (2), proposed by [2], developed from computational numerical results. Equation (1) is applicable for $5 \leq (H/L) < 30$ and (2) for $30 \leq (H/L) \leq 110$. Both correlations are valid for Prandtl number $Pr = 0.71$ and Rayleigh number $R_{aL} \leq 20.000$.

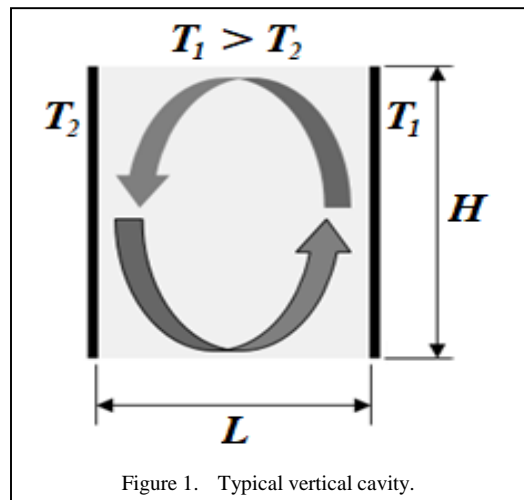


Figure 1. Typical vertical cavity.

$$Nu_L = \left\{ 1 + \frac{\left\{ 0.788335 \left[1.42227 - \frac{1.41845}{(H/L)} \right] \frac{Ra_L}{(H/L)} \right\}^{0.881073}}{\left\{ 139.677 + \left[1.42227 - \frac{1.41845}{(H/L)} \right] \frac{Ra_L}{(H/L)} \right\}^{0.724505}} \right\}^2 \quad (1)$$

$$Nu_L = \left\{ 1 + 0.00044265 \left[\frac{Ra_L}{(H/L)} \right]^{1.36869} \right\}^{0.326071} \quad (2)$$

For the development of Nusselt correlations in a simplified mathematical format, the prescription by [16] was used, which claims that, in general, the Nusselt number in the analysis of natural convection inside vertical cavities obeys the following relation, in which C , n and m correspond to constants that are functions of Ra_L and (H/L) .

$$Nu_L = CRa_L^n (H/L)^m \quad (3)$$

The correlations proposed in this work follow the format of Eq. (3), considering different Ra_L and (H/L) ranges and are valid for air-filled cavities with $P_r = 0.71$.

To linearize Eq. (3), the Napierian logarithm can be applied to both sides of the equation and the properties of logarithms can be used, so that:

$$\begin{aligned} \ln(Nu_L) &= \ln \left[CRa_L^n (H/L)^m \right] \Rightarrow \ln(Nu_L) = \\ &= \ln(C) + n \cdot \ln(Ra_L) + m \cdot \ln(H/L) \end{aligned} \quad (4)$$

Defining $\ln(Nu_L) = Y$, $\ln(C) = A$, $\ln(Ra_L) = X$ and $\ln(H/L) = Z$, (4) is rewritten in linearized form as:

$$Y = A + nX + mZ \quad (5)$$

With the data set obtained in accordance with linearized Eq. (5), multivariate linear regression can be applied. In this process, the constants A , n and m are obtained for each correlation proposed in this work. It should be noted that in the linearized form, the constant A will be obtained instead of the constant C which appears in (3), but since $\ln(C) = A$, then $C = e^A$.

The results obtained by each Nusselt correlation proposed in this work were compared with those from the correlations of [2] by calculating the relative error (ER) and the mean square error (MSE), parameters that evaluate the difference between the predicted value and the real value, as follows. High MSE values mean that the model did not perform well in relation to the predictions.

$$ER = \frac{Nu_{L \text{ pred}} - Nu_{L \text{ Zhao et al.}}}{Nu_{L \text{ Zhao et al.}}} \quad (6)$$

$$MSE = \frac{1}{n} \sum_{i=1}^n (Nu_{L \text{ pred}} - Nu_{L \text{ Zhao et al.}})^2 \quad (7)$$

where $Nu_{L \text{ pred}}$ is the value predicted by the correlations developed in this work and $Nu_{L \text{ Zhao et al.}}$ is the value provided by the correlations of [2]. The parameter n in Eq. (7) represents the quantity of Nusselt values calculated.

To generate the simplified Nusselt correlations, an acceptance criterion was established based on the following aspect: considering the entire data set obtained, at least 90% of the results from the developed correlations must be in agreement with the results calculated by the correlations of [2] within a relative error (RE) of 10%. This evaluation method was applied and analyzed for several Ra_L and (H/L) ranges. The ranges that did not reach the acceptability threshold were subdivided into smaller intervals, aiming at finer adjustments in search of results that met the acceptance criterion.

III. RESULTS AND DISCUSSION

Using the computer program, with the data set obtained by the correlations of [2] duly

TABLE I. CORRELATIONS DEVELOPED FOR NUSSELT WITH APPLICABILITY RANGES OF (H/L) , Ra_L AND ACCEPTANCE CRITERIA.

Correlation	Range of (H/L)	Range of Ra_L	Acceptance criteria (%): Percentage of agreement of all data within 10% difference
$Nu_L = 0.8532 R_{al}^{0.0581} (H/L)^{-0.0628}$	$5 \leq (H/L) \leq 30$	$10^2 \leq Ra_L \leq 5 \cdot 10^3$	96.43
$Nu_L = 0.2294 R_{al}^{0.2821} (H/L)^{-0.2614}$	$5 \leq (H/L) \leq 30$	$5 \cdot 10^3 < Ra_L \leq 2 \cdot 10^4$	100.00
$Nu_L = 1.0586 R_{al}^{0.0692} (H/L)^{-0.1285}$	$30 < (H/L) \leq 60$	$10^2 \leq Ra_L \leq 2 \cdot 10^4$	93.32
$Nu_L = 1.1090 R_{al}^{0.0428} (H/L)^{-0.0869}$	$60 < (H/L) \leq 80$	$10^2 \leq Ra_L \leq 2 \cdot 10^4$	100.00
$Nu_L = 1.1134 R_{al}^{0.0307} (H/L)^{-0.0657}$	$80 < (H/L) \leq 110$	$10^2 \leq Ra_L \leq 2 \cdot 10^4$	100.00

tabulated, an empirical procedure was performed in search of simplified Nusselt equations, so that multivariate linear regression was applied several times on this data set, considering several subdivisions for the ranges of values of Ra_L and (H/L) . After numerous tests, with the development of several correlations, five simplified Nusselt correlations were established, which are shown in Table I and are within the previously defined acceptance criteria. For all the correlations developed, if the result obtained is $Nu_L < 1$, then $Nu_L = 1$ should be considered.

Considering all the data obtained, referring to the five correlations presented in Table I, Fig. 2 shows the percentage relative error (RE) for all the calculated Nusselt values, which total 1,914 data. Fig. 3 shows a histogram with percentage ranges of the relative errors between the results obtained by the correlations of [2] and those calculated by the correlations proposed in

Table I. It can be seen in Figs. 2 and 3 that the vast majority of the data present a percentage difference of less than 10%. The data that present a percentage difference greater than 10% correspond to some related to the first and third correlation showed in Table I. The positive values on the abscissa axis of Figs. 2 and 3 correspond to the cases in which the values obtained by the correlations proposed in Table I overestimate the values obtained by the correlations of [2], while the negative values indicate the opposite.

Table II presents the mean square error (MSE) obtained for each Nusselt correlation in Table I. It can be seen that the highest MSE values were found for the first and third Nusselt correlations, which had lower values of the acceptance criterion. However, the MSE values for all correlations are low, indicating good performance of the models.

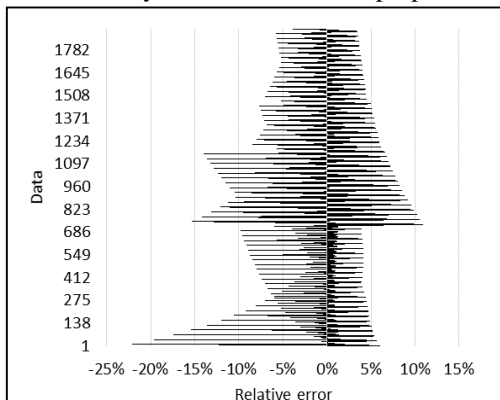


Figure 2. Percentage relative error as a function of the data set.

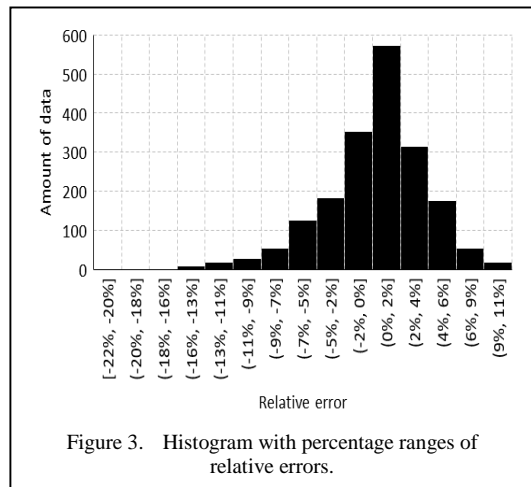


Figure 3. Histogram with percentage ranges of relative errors.

TABLE II. MSE FOR NUSSLETT CORRELATIONS OF TABLE I.

Correlation	MSE
$Nu_L = 0.8532 Ra_L^{0.0581} (H/L)^{-0.0628}$	0.0034
$Nu_L = 0.2294 Ra_L^{0.2821} (H/L)^{-0.2614}$	0.0003
$Nu_L = 1.0586 Ra_L^{0.0692} (H/L)^{-0.1285}$	0.0050
$Nu_L = 1.1090 Ra_L^{0.0428} (H/L)^{-0.0869}$	0.0018
$Nu_L = 1.1134 Ra_L^{0.0307} (H/L)^{-0.0657}$	0.0009

Fig. 4 represents a scatter plot that includes all the analyzed data, illustrating a comparison between the Nusselt values predicted by the correlations in Table I ($Nu_{L, pred}$) and those observed by the correlations of [2]. The dashed line corresponds to the ideal line that represents a perfect correspondence between the predicted and observed values, serving as a reference to evaluate the accuracy of the predictions from the models. The proximity of the points on the graph to the ideal line indicates a good agreement between the predicted and observed values, especially for higher Nusselt values, where the data tend to cluster closer to the ideal line. It is observed, in general, that the data are close to the ideal line, indicating an acceptable prediction of the Nusselt number by the correlations in Table I for the conditions analyzed. However, it is noted that for Nusselt values between $1.05 \leq Nu_{L, pred} \leq 1.35$, the data present greater deviation from the ideal line, suggesting that the models may be less reliable for Nusselt predictions in these cases. Fig. 4 also shows some Nusselt values $Nu_{L, pred} < 1$. These are the

cases in which $Nu_{L, pred} = 1$ should be considered, since this is the lowest value that can be obtained by the correlations of [2].

Fig. 5 shows the $Nu_{L, pred}$ values predicted by the correlations in Table I and those observed by the correlations of [2] as a function of Ra_L for four values of (H/L) , covering the use of all correlations in Table I. Fig. 5 shows some cases of greater discrepancy between the values, for $(H/L) = 10$ with $Ra_L = 5.000$ and also for $(H/L) = 40$ with $Ra_L \geq 17.000$. These cases correspond to values obtained by the first and third Nusselt correlations shown in Table I, exactly those whose acceptance criterion values were lower. This clearly indicates that these two correlations predict the Nusselt results with less reliability when compared with the others Nusselt correlations shown in Table I. Despite these specific cases, in general, the Nusselt correlations developed in this work provide values with good agreement with the values obtained by the correlations of [2]. Therefore, the developed correlations can be used with good reliability to obtain quick estimates of the Nusselt number values in natural convection in vertical cavities.

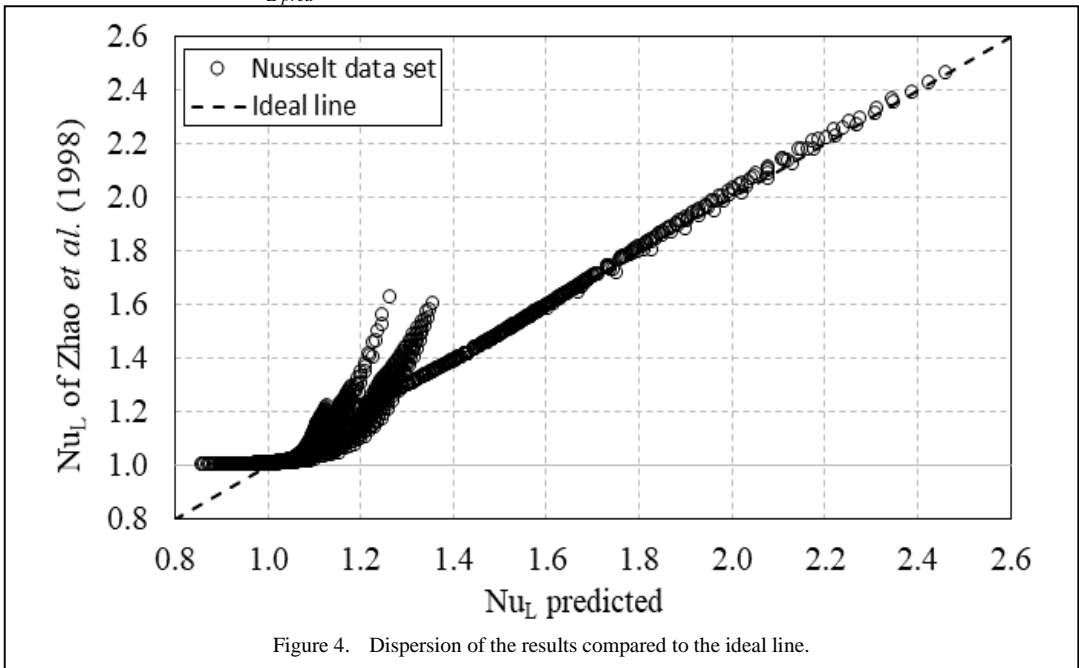


Figure 4. Dispersion of the results compared to the ideal line.

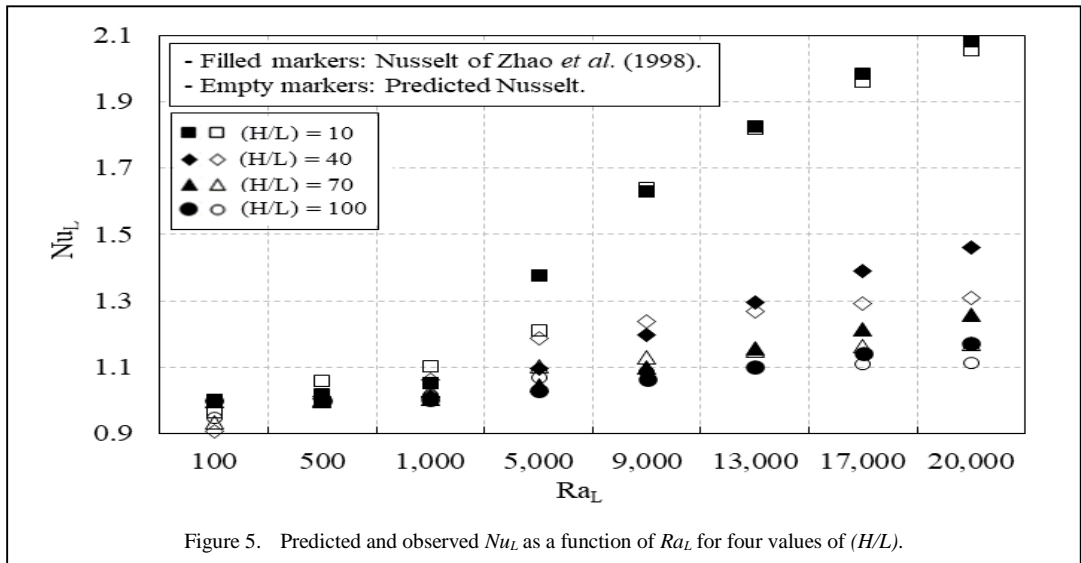


Figure 5. Predicted and observed Nu_L as a function of Ra_L for four values of (H/L) .

IV. CONCLUSIONS

This work proposed simple correlations for estimating the Nusselt number in the analysis of natural convection in vertical cavities. The application of the multivariate linear regression technique allowed the development of correlations that aggregate satisfactory results and easy handling, providing a valuable tool for researchers and professionals in the area.

The research also revealed the mathematical complexity of correlations in the literature. The simplicity of the mathematical model developed, compared to more complex correlations and methods proposed by other authors, confirms the viability of these correlations for real practical applications where quick estimates for the convective heat transfer coefficient are essential.

Further refinements in the Rayleigh number (Ra_L) and aspect ratio (H/L) ranges on the data set obtained from the correlations of [2] could imply the development of Nusselt correlations with better acceptance criteria than the correlations proposed in this work. However, a greater number of simplified correlations would possibly be generated, which would minimize the simplicity of application of the proposal.

The proposed model could be extended to analyses under turbulent flow regimes, however it would be necessary to incorporate other correlations from the literature that are valid for this condition. In this case, a greater number of simplified correlations would be obtained considering satisfactory acceptance criteria. Due

to the simplicity of the format of the proposed correlations, it is not feasible to obtain a smaller number of correlations that would be more comprehensive. For this, it would be necessary to obtain correlations with a more complex mathematical format, which is beyond the scope of this study.

A more comprehensive validation of the proposed correlations could also be performed by obtaining experimental data and by means of computational numerical simulations. Both analyses could incorporate different aspect ratios and flow regimes, as well as analyses of the temperature gradient inside the cavity. Such analysis would provide greater robustness to the correlations and greater reliability to the results, but would not guarantee obtaining a smaller number of correlations in a simplified format to cover the entire spectrum of aspect ratio (H/L) and Rayleigh number (Ra_L).

ACKNOWLEDGMENT

To the PIBIC/CNPq/IFSP program for the support.

REFERENCES

- [1] Ostrach, S. (1998). Natural Convection in Enclosures. *Journal of Heat Transfer*, 110, 1175-1190.
- [2] Zhao, Y., Curcija, D., Power, J. P., & Goss, W. P. (1998). Improved heat transfer correlations for quantifying laminar natural convection across fenestration glazing cavities. In *Proceedings of Thermal Performance of the Exterior Envelopes of Buildings VII*, ASHRAE Conference, Clearwater, FL.
- [3] Zhao, Y., Curcija, D., & Goss, W. P. (1999). Convective heat transfer correlations for fenestration

- glazing cavities: A review. *ASHRAE Transactions*, 105, Pt. 2.
- [4] LBNL. THERM 1.0. (1996). *A PC program for analyzing the two-dimensional heat transfer through building products*. Program description. Windows and Daylighting Group, Lawrence Berkeley National Laboratory, Berkeley, Calif.
- [5] LBNL. WINDOW 4.1. (1993). *A PC program for analyzing window thermal performance - Program description and tutorial*. Windows and Daylighting Group, Lawrence Berkeley National Laboratory, Berkeley, Calif.
- [6] Elsherbiny, S. M. (1980). *Heat transfer by natural convection across vertical and inclined air layers* (Ph.D. Thesis). Department of Mechanical Engineering, University of Waterloo, Canada.
- [7] Elsherbiny, S. M., Raithby, G. D., & Hollands, G. T. (1982). Heat transfer by natural convection across vertical and inclined air layers. *Journal of Heat Transfer*, 104, 96-102.
- [8] Wright, J. L. (1996). A correlation to quantify convective heat transfer between vertical window glazings. *ASHRAE Transactions*, 102, 940-946.
- [9] Shewen, E. C. A. (1986). *Peltier effect technique for natural convection heat flux measurement applied to the rectangular open cavity* (Ph.D. Thesis). Department of Mechanical Engineering, University of Waterloo, Canada.
- [10] ASHRAE draft standard SPC 142P. (1996). *Standard method for determining and expressing the heat transfer and total optical properties of fenestration products*. Atlanta: American Society of Heating, Refrigerating and Air-Conditioning Engineers, Inc.
- [11] Altaç, Z., & Ugurlubilek, N. (2016). Assessment of turbulence models in natural convection from two- and three-dimensional rectangular enclosures. *International Journal of Thermal Sciences*, 107, 237-246.
- [12] Rincón-Casado, A., Sanchez de la Flor, F. J., Chacón Vera, E., & Sanchez Ramos, J. (2017). New natural convection heat transfer correlations in enclosures for building performance simulation. *Engineering Applications of Computational Fluid Mechanics*, 11(1), 340-356.
- [13] Bergman, T. L.; Lavine, A. S. (2020). *Fundamentals of heat and mass transfer* (8th ed.). New York: Wiley.
- [14] Çengel, Y. A., & Ghajar, A. J. (2020). *Heat and mass transfer: fundamentals and applications* (6th. ed.). New York: McGraw-Hill.
- [15] Kreith, F., & Manglik, R. M. (2017). *Principles of heat transfer* (8th. ed.). New York: Cengage Learning.
- [16] Bejan, A. (1979). Note on Gill's solution for free convection in a vertical enclosure. *Journal of Fluid Mechanics*, 90(3), 561-568.

Prioritization of Measures for Achieving Energy and Climate Goals in Serbia

Gabrijela Popović¹, Aleksandra Fedajev², Petar Mitić³

¹University Business Academy in Novi Sad, Faculty of Applied Management, Economics and Finance, Belgrade, Serbia

²University of Belgrade, Technical Faculty in Bor, Serbia

³Institute of Economic Sciences, Belgrade, Serbia

¹gabrijela.popovic@mef.edu.rs, ²afedajev@tfbor.bg.ac.rs, ³petar.mitic@ien.bg.ac.rs

Abstract—The article proposes a hybrid Multiple-Criteria Decision-Making (MCDM) approach for assessing and prioritizing measures for achieving energy and climate goals in Serbia. The analysis was performed using the Simple weighted sum product (WISP), Measurement of Alternatives and Ranking according to COmpromise Solution (MARCOS), and Axial-Distance-Based Aggregate Measurement (ADAM) methods. The results emphasized *Research, innovation, and competitiveness* as measure that should be prioritized in current conditions.

Keywords - WISP, MARCOS, ADAM, energy, climate

I. INTRODUCTION

The growing global focus on sustainable energy transition and the need to mitigate climate change challenges have prompted countries to adopt more effective measures for achieving their energy and climate goals. In 2015, the multilateral climate change process was started with the primary goal of mitigating dangerous climate change by keeping global warming below 2°C and making an effort to reach 1.5°C. The Paris Climate Conference (COP21) resulted in the Paris Agreement, the first universal legally obligated agreement to cope with climate change. The Republic of Serbia ratified the Paris Agreement in 2016, and at the Berlin Process Western Balkans Summit 2022, signed a joint Declaration on Energy Security and Green Transition in the Western Balkans.

However, over the past two decades, Serbia has faced numerous challenges in achieving its energy and climate goals. The energy sector is one of the most important economic branches in Serbia [1], but there are numerous inefficiencies and inherited problems from socialistic regime. Serbia's energy sector faces challenges due to its reliance on fossil fuels and an ongoing energy deficit [2]. The country heavily depends on low-calorie lignite for electricity production, which provides energy independence and stable costs but is highly inefficient [3-4]. On the other hand, the current utilization of renewable energy sources in Serbia's energy mix remains insufficient to achieve the target of raising the share of renewable energy sources (RES) in gross final energy consumption [5]. In addition to an unfavorable energy mix, Serbia faces the significant issue of high energy intensity, driven by energy-intensive industries, a large share of household energy consumption, and unrealistic energy pricing [6]. Furthermore, the rate of temperature increase in Serbia is exceeding the global average, leading to projections of significantly higher average annual temperatures in the future [7].

The intensive use of lignite and high energy intensity in Serbia significantly contribute to growing GHG emissions, worsening the environmental impact of the electricity sector [3]. Consequently, this sector is a major polluter of air, water, and soil, threatening both the environment and public health [1], making



Serbia the largest CO₂ emitter in the Western Balkans from 2010 to 2020 [8]. The negative trends in Serbia's energy sector largely stem from an inefficient institutional environment and a lack of capacity to implement necessary reforms. Despite significant efforts to reform the energy sector since the 1980s, liberalization has progressed slowly and only in select segments [9].

Besides negative trends in energy sector, the underdeveloped circular economy significantly hampers the achievement of climate goals. The concept's utilization remains limited to a few successful examples, primarily due to a lack of awareness, insufficient funding, and consumer culture. Waste management is problematic, characterized by outdated policies and unresolved issues, while the market for secondary raw materials is poorly developed [10]. Most Serbian businesses lack awareness of environmental preservation, resulting in minimal use of waste as a production input. The country lags in waste management and recycling, largely due to inadequate infrastructure for waste collection, sorting, and treatment [11].

To effectively address all challenges, Serbia must advance its science and technology through substantial investment in research and development (R&D). Staying aligned with future trends is essential for maintaining competitiveness. However, Serbia invests less in R&D compared to EU peers adhering to the Lisbon Convention, largely due to low private investment [11].

Considering the complex nature of the necessary reforms, the Republic of Serbia developed the Integrated National Energy and Climate Plan (INECP) covering 2021 to 2030 [12] to achieve the perceived targets regarding decreasing GHG emissions and increasing energy efficiency and share of RES. Aligning with international sustainability standards and fulfilling national commitments requires a strategic approach to decision-making that takes into account diverse and often conflicting priorities. In this context, multiple-criteria decision-making (MCDM) methods can provide a comprehensive framework for evaluating and prioritizing the multiple aspects involved in formulation and implementation of energy and climate policy. In the recent literature in this research area, MCDM methods have been already used in analysis of energy transition [5],

optimizing energy mix [13], energy security assessment [14], and similar topics. This paper introduces a hybrid MCDM approach to support the prioritization of measures prescribed by INECP. The novelty of this research lies in the use of multiple MCDM methods (WISP, MARCOS, and ADAM), synthesized by usage of the Borda rule, to ensure a more objective prioritization of the proposed measures. Such approach supports policymakers in making more informed, evidence-based decisions, which are particularly crucial for energy and climate policymaking.

II. METHODOLOGY AND DATA

A. The Entropy Method

The Entropy method was introduced by Shannon [15], and Shannon and Weaver [16]. This method enables the calculation of the criteria's objective weighting coefficients, excluding the decision-makers influence. The Entropy method is based on the hypothesis that higher weight indication data is rather helpful than the opposite one [17]. Because of its relatively comprehensive computation procedure, the Entropy method has been used to facilitate various decision-making problems [18-22].

Defining the criteria weighting coefficients using the Entropy method is based on (1) as follows:

$$w_j = \frac{1 - e_j}{\sum_{j=1}^n (1 - e_j)}, \quad (1)$$

where $j = 1, \dots, n$.

The e_j value that represents the output entropy of the j_{th} factor is determined as follows:

$$e_j = -\frac{1}{\ln(m)} \sum_{i=1}^n r_{ij} \ln(r_{ij}), \quad (2)$$

where $j = 1, \dots, n$ and $\sum_{j=1}^n w_j = 1$.

B. The WISP Method

The WISP method [23] was proposed to create an approach that would be understandable and convenient for application even for users unfamiliar with MCDM methods. This method integrates four relationships between a set of benefit and cost criteria, defining the alternatives' total utility measure. Until now, the WISP

method has been used to facilitate different kinds of business and real-world problems [24-28].

The computation procedure for the WISP method involves the following steps:

Step 1. Define the initial decision-making matrix.

Step 2. Create the normalized decision-making matrix:

$$r_{ij} = \frac{x_{ij}}{\max_i x_{ij}}, \quad (3)$$

where r_{ij} represents a dimensionless number that designates a normalized rating of the i -th alternative regarding the j -th criterion.

Step 3. Compute the values of four utility measures as it is presented:

$$u_i^{wsd} = \sum_{j \in \Omega_{max}} r_{ij} w_j - \sum_{j \in \Omega_{min}} r_{ij} w_j, \quad (4)$$

$$u_i^{wpd} = \prod_{j \in \Omega_{max}} r_{ij} w_j - \prod_{j \in \Omega_{min}} r_{ij} w_j, \quad (5)$$

$$u_i^{wsr} = \frac{\sum_{j \in \Omega_{max}} r_{ij} w_j}{\sum_{j \in \Omega_{min}} r_{ij} w_j}, \quad (6)$$

$$u_i^{wpr} = \frac{\prod_{j \in \Omega_{max}} r_{ij} w_j}{\prod_{j \in \Omega_{min}} r_{ij} w_j}, \quad (7)$$

where u_i^{wsd} and u_i^{wpd} designate differences between the weighted sum and weighted product of normalized ratings of alternative i , respectively, additionally, u_i^{wsr} and u_i^{wpr} represent ratios between weighted sum and weighted product of normalized ratings of alternative i , respectively.

Step 4. Recalculate the four utility measure values in the following way:

$$\bar{u}_i^{wsd} = \frac{1 + u_i^{wsd}}{(1 + u_{max_i}^{wsd})}, \quad (8)$$

$$\bar{u}_i^{wpd} = \frac{1 + u_i^{wpd}}{(1 + u_{max_i}^{wpd})}, \quad (9)$$

$$\bar{u}_i^{wsr} = \frac{1 + u_i^{wsr}}{(1 + u_{max_i}^{wsr})}, \quad (10)$$

$$\bar{u}_i^{wpr} = \frac{1 + u_i^{wpr}}{(1 + u_{max_i}^{wpr})}, \quad (11)$$

where: \bar{u}_i^{wsd} , \bar{u}_i^{wpd} , \bar{u}_i^{wsr} and \bar{u}_i^{wpr} outline recalculated values of u_i^{sd} , u_i^{pd} , u_i^{sr} and u_i^{pr} .

Step 5. Determine the overall utility u_i of each alternative as follows:

$$u_i = \frac{1}{4} (\bar{u}_i^{wsd} + \bar{u}_i^{wpd} + \bar{u}_i^{wsr} + \bar{u}_i^{wpr}), \quad (12)$$

Step 6. Rank the alternatives in descending order, choosing the one with the highest u_i value as optimal.

C. The MARCOS Method

The essence of the MARCOS method [29] relies on finding the relations between ideal and anti-ideal alternatives and determining the compromise rankings according to ideal and anti-ideal solutions. Decisions are made regarding the utility functions representing the distance between an alternative and the ideal and anti-ideal solution. The alternative closest to the ideal solution and the most distant from the anti-ideal solution represents the optimal choice. The applicability of the MARCOS method has been proven in many research studies [30-33].

The MARCOS method calculation procedure is based on the following series of steps.

Step 1. As in the WISP method, define the initial decision matrix.

Step 2. Create the extended decision matrix that involves the ideal and anti-ideal solutions. The ideal solution is the alternative with the best performance regarding the particular criterion, while the alternative with the worst performance is designated as the anti-ideal solution. Ideal and anti-ideal solutions are defined in the following way:

$$AAI = \min_j x_{ij} \text{ if } j \in B \text{ and } \max_j x_{ij}, \quad (13)$$

$$\text{if } j \in C$$

$$AI = \max_j x_{ij} \text{ if } j \in B \text{ and } \min_j x_{ij}, \quad (14)$$

$$\text{if } j \in C$$

Step 3. Normalize the extended initial decision matrix in the following manner:

$$r_{ij} = \frac{x_{ai}}{x_{ij}} \text{ if } j \in C, \quad (15)$$

$$r_{ij} = \frac{x_{ij}}{x_{ai}} \text{ if } j \in B, \quad (16)$$

where x_{ij} and x_{ai} represent elements of the decision matrix.

Step 4. Define the weighted decision matrix as follows:

$$v_{ij} = r_{ij} \cdot w_j, \quad (17)$$

Step 5. Compute the utility degree of the alternatives K_i in the following way:

$$K_i^- = \frac{S_i}{S_{ai}}, \quad (18)$$

$$K_i^+ = \frac{S_{ai}}{S_i}, \quad (19)$$

where $S_i (i=1,2,\dots,m)$ is the sum of the elements of a difficult matrix:

$$S_i = \sum_{j=1}^n v_{ij}, \quad (20)$$

Step 6. Using (21) create the utility function of the alternatives $f(K_i)$:

$$f(K_i) = \frac{K_i^+ + K_i^-}{1 + \frac{1-f(K_i^+)}{f(K_i^+)} + \frac{1-f(K_i^-)}{f(K_i^-)}}, \quad (21)$$

where $f(K_i^-)$ is the utility function versus the anti-ideal solution and $f(K_i^+)$ is the utility function versus the ideal solution. Mentioned functions are defined in the presented way:

$$f(K_i^-) = K_i^+ / (K_i^+ + K_i^-), \quad (22)$$

$$f(K_i^+) = K_i^- / (K_i^+ + K_i^-). \quad (23)$$

Step 7. Rank the alternatives in descending order, with the best option designated by the highest value of the utility function.

D. The ADAM Method

The ADAM method [34] represents a pioneer as the first geometric MCDM method. The ranking process of the alternatives is performed by determining the volumes (aggregated measurement) of complex polyhedral defined by points in a three-dimensional coordinate system. Although relatively new, this method has been

recognized by scientists and used in various cases [35-38].

The following steps could illustrate the computation procedure of the ADAM method.

Step 1. As in previous cases, create the decision matrix.

Step 2. From the sorted decision matrix S :

$$S = [s_{ij}]_{m \times n}, \quad (24)$$

where s_{ij} denotes the sorted evaluations e_{ij} in descending order according to the criteria weightings.

Step 3. Normalize sorted decision matrix S :

$$n_{ij} = \left\{ \begin{array}{l} \frac{s_{ij}}{\max_i s_{ij}} \text{ for } j \in B \\ \frac{\min_i s_{ij}}{s_{ij}} \text{ for } j \in C \end{array} \right\}, \quad (25)$$

where n_{ij} is the normalized evaluations, B is the benefit set, and C is the cost set of the criteria.

Step 4. Determine the x, y and z coordinates of the R_{ij} reference and P_{ij} weighted reference points that define the complex polyhedron as follows:

$$x_{ij} = n_{ij} \times \sin \alpha_j, \quad \forall j = 1, \dots, n; \quad \forall i = 1, \dots, m, \quad (26)$$

$$y_{ij} = n_{ij} \times \cos \alpha_j, \quad \forall j = 1, \dots, n; \quad \forall i = 1, \dots, m, \quad (27)$$

$$z_{ij} = \begin{cases} 0, \text{ for } R_{ij} \\ w_j, \text{ for } P_{ij} \end{cases}, \quad \forall j = 1, \dots, m; \quad \forall i = 1, \dots, n, \quad (28)$$

where α_j is the angle that defines the orientation of the vector that outlines the alternatives' value, designated as follows:

$$\alpha_j = (j-1) \frac{90^\circ}{m-1}, \quad \forall j = 1, \dots, n, \quad (29)$$

Step 5. Compute the complex polyhedral V_i^C volumes as the sum of the volumes of the composing pyramids as shown:

$$V_i^C = \sum_{k=1}^{n-1} V_k, \quad \forall i = 1, \dots, n, \quad (30)$$

where V_k represents the volume of the pyramid defined as follows:

$$V_k = \frac{1}{3} B_k \times h_k, \forall k = 1, \dots, n-1, \quad (31)$$

where B_k designates the surface of the base of the pyramid determined by the reference and weighted reference points of two successive criteria computed in the following way:

$$B_k = c_k \times a_k + \frac{a_k \times (b_k - c_k)}{2}, \quad (32)$$

where α_k denotes the Euclidean distance between the reference points of two successive criteria, determined in the following way:

$$a_k = \sqrt{(x_{j+1} - x_j)^2 + (y_{j+1} - y_j)^2}, \quad (33)$$

b_k and c_k represent the magnitudes of the vectors corresponding to the weights of two successive criteria:

$$b_k = z_j, \quad (34)$$

$$c_k = z_{j+1}, \quad (35)$$

h is the height of the pyramid from the defined base to the top of discovered in the coordinate origin (O), which is calculated in the following way:

$$h_k = \frac{2\sqrt{s_k(s_k - a_k)(s_k - d_k)(s_k - e_k)}}{a_k}, \quad (36)$$

where s_k is the semicircumference of the triangle defined by the x and y coordinates of two successive criteria and the coordinate origin, computed using the following Eqs.:

$$d_k = \sqrt{x_j^2 + y_j^2}, \quad (37)$$

$$e_k = \sqrt{x_{j+1}^2 + y_{j+1}^2}, \quad (38)$$

Step 6. Rank the alternatives in descending order where the best-ranked alternative has the highest volume of complex polyhedral $V_i^c (i=1, \dots, m)$.

E. Data

The INECP [12] addresses five main dimensions that will enable reaching the national energy and climate goals. These dimensions include: 1. **Decarbonization** - increasing the RES share and GHG emissions reduction; 2. **Energy efficiency** - increasing energy efficiency across all sectors; 3. **Energy security** - diversification of the energy sources and establishing the cooperation between EU and Energy Community (EnC) countries to secure the energy supply; 4. **Internal energy market** - direction to establishing an integrated and functional market; 5. **Research innovation and competitiveness** - supporting cutting-edge low-carbon and clean energy technologies. Each of the presented dimensions, which could be considered as measure, is elaborated on a certain number of targets.

The presented measures contribute to energy and climate goals. To perform prioritization of these measures they are assessed by usage of following criteria: 1. implementation costs (billion €); 2. own funds over total implementation cost (%); 3. CAPEX WEM (billion €) - scenario with the existing measures; 4. CAPEX WAM (billion €) - scenario with the additional measures. Table I contains the initial data regarding the given question.

TABLE I. INITIAL DATA.

Alternatives	Criteria			
	Implementation costs	Own funds over total implementation cost	CAPEX WEM	CAPEX WAM
	billion €	%	billion €	billion €
	min	min	min	min
Decarbonization	5.19	77	1.16	4.03
Energy efficiency	20.94	61.2	12.31	8.62
Energy security	3.13	57.6	1.99	1.14
Internal energy market	1.19	85.0	1.19	0.00
Research innovation and competitiveness	0.11	45.7	0.11	0.00

III. RESULTS AND DISCUSSION

A. Results

The weighting coefficients were calculated using the Entropy method based on the data presented in Table I. The obtained results are presented in Table II.

The weighting coefficients revealed that the most influential criterion is **CAPEX WAM** (0.3462), while the least significant criterion is **Own funds over total implementation cost** (0.0107). The weighting coefficients necessary for the next procedure were obtained, so we continued with the procedure and applied the WISP, MARCOS, and ADAM method to define the ranking order of the considered measures.

Table III shows that **Research, innovation, and competitiveness** are the priority measure for all three methods. At the same time, **Energy efficiency** is the measure with the lowest priority for implementation. This result is confirmed by the performed sensitivity analysis, which involved varying the weighting coefficients, but the analysis results are not presented here due to the length of the article. The final results obtained using the Borda rule verified the first-ranked measure. The reason could be that energy efficiency is somewhat outdated as a measure of preserving climate change and improving the state of the energy sector. Modern conditions require innovative and modern approaches, which the first-ranked measure certainly offers. So, the emphasis has to be toward innovative strategies, as reflected in the best-ranked measure, which aligns with the need for modern, cutting-edge solutions to support decarbonization energy security, and competitiveness in the energy sector.

TABLE II. CRITERIA WEIGHTS.

Criteria	Weights
Implementation costs	0.3089
Own funds over total implementation cost	0.0107
CAPEX WEM	0.3342
CAPEX WAM	0.3462

TABLE III. FINAL RANKING ORDER.

Measures	WISP		MARCOS		ADAM		Final rank
	Score	Rank	Score	Rank	Score	Rank	
Decarbonization	0.4437	4	0.0427	3	0.0004	4	4
Energy efficiency	0.2558	5	0.0125	5	0.0001	5	5
Energy security	0.4832	3	0.0365	4	0.0008	3	3
Internal energy market	0.5334	2	0.2915	2	0.0070	2	2
Research, innovation, and competitiveness	1.0000	1	0.5000	1	0.1369	1	1

B. Discussion and Policy Recommendations

The results highlight several important points for policy recommendations. The restructuring of lignite mining and the diversification of mining regions should be prioritized in the energy transition. This is in line with [1], who emphasize that competition and setting electricity prices at an economically viable level are prerequisites for the energy transition in a liberalized market. In addition, circular economy principles should be introduced to reduce GHG emissions through sustainable production practices, the promotion of secondary raw materials usage and the development of an efficient waste management system [8]. To achieve this, a multi-layered and cross-sectoral integration of national policies is needed to promote favorable conditions for investment and consensus on the sustainable use of resources in line with circular economy objectives [10].

Low-Carbon (LC) technologies need to be integrated into the electricity market instead of relying solely on support mechanisms. However, current electricity prices are not sufficient to incentivize the necessary investments. To achieve the decarbonization targets by 2030, the authorities need to create a favorable environment with long-term incentives and share the investment risks between the state, end-users, and investors [9]. A model that links subsidies to market prices could reduce investment risks and ensure that support decreases when electricity prices rise. Improving consumer awareness of the electricity market and infrastructure enhancements, such as expanding transmission grids and promoting regional cooperation, will also optimize the integration of RES and avoid grid congestion [9].

To attract EU and other international funding for Serbia's green transition, the country needs to identify sectors with exceptional growth potential. Vertical industrial policy measures should ensure coherent integration of science and

industry, especially in the use of pioneering technologies such as green hydrogen, solar energy, and carbon capture, to create a new technological basis for climate-neutral production [2].

By using energy more productively, Serbia can increase its economic competitiveness while reducing consumer costs and emissions. Key measures include energy-efficient lighting, heating and cooling systems, industrial process automation, and improved energy data management. These efforts should be accompanied by a shift to RES and a reduction in energy losses during distribution. In addition, strengthening administrative capacity, and promoting a new energy culture are essential steps to drive the energy transition [3].

Finally, it is necessary to develop a basic infrastructure and create incentives for the individual players to make waste management profitable and thus contribute to Serbia's circular economy and sustainability goals [11].

IV. CONCLUSION

For Serbia to meet international sustainability standards and fulfill its national commitments, a strategic decision-making approach is essential to manage conflicting priorities. MCDM methods provide a robust framework for evaluating different aspects of energy and climate policy formulation and implementation. This paper presents a hybrid MCDM approach that combines several methods (WISP, MARCOS, and ADAM) by usage of Borda rule, allowing for a more objective assessment of measures aimed at achieving Serbia's energy and climate goals as outlined in the INECP. The results show that **Research, innovation, and competitiveness** are the highest priority, while **Energy efficiency** is the lowest priority for implementation.

This study underlines the urgent need for Serbia to adopt comprehensive strategies for its energy transition. Key policy measures include the restructuring of the lignite mining sector to bring it in line with market liberalization and sustainable practices, integration of circular economy principles to reduce GHG emissions. To achieve decarbonization targets, LC technologies need to be integrated into the electricity market, supported by market-based pricing mechanisms and long-term investment incentives to mitigate risks. At the same time, key infrastructure and incentives need to be

developed to support a profitable waste management sector and drive the circular economy. Parallel with that, strengthening governance, restructuring national energy companies and promoting a new energy culture is necessary.

This study has limitations, including possible biases due to the use of secondary data and the focus on Serbia, which could limit the generalizability of the results. The prioritization framework used could also oversimplify complex energy policy decisions. Future research should address these issues by incorporating primary data for greater accuracy and examining the long-term impacts of proposed measures. These primary data should include the sub-measures in the evaluation procedure, which will refine the final results. Furthermore, comparing Serbia with developed countries, such as European Union members, will give a more nuanced perspective on the effectiveness of the energy policy applied in Serbia.

REFERENCES

- [1] Bijelic, I. B., & Rajakovic, N. (2021). National Energy and Climate Planning in Serbia: From Lagging Behind to an Ambitious EU Candidate?. *International Journal of Sustainable Energy Planning and Management*, 32, 47-60.
- [2] Đurićin, D., Vuksanović, H. I., & Kuć, V. (2023). How a structural crisis is flipping the economic script and calling for the green transition in Serbia. *Ekonomika preduzeća*, 71(1-2), 1-29.
- [3] Madžar, L. (2022). Modelling the trend of energy productivity in the Serbian economy. *Ekonomika preduzeća*, 70(3-4), 179-190.
- [4] Djordjević, L., Pekez, J., Novaković, B., Bakator, M., Djurdjev, M., Čočkaló, D., & Jovanović, S. (2023). Increasing Energy Efficiency of Buildings in Serbia – A Case of an Urban Neighborhood. *Sustainability*, 15(7), 6300.
- [5] Pavlović, B., Ivezić, D., & Živković, M. (2021). A multi-criteria approach for assessing the potential of renewable energy sources for electricity generation: Case Serbia. *Energy Reports*, 7, 8624-8632.
- [6] Jednak, S., Minović, J., & Kragulj, D. (2020). A Review of Economic and Environment Indicators and Energy Efficiency: Evidence from the EU and Serbia. *Economic Themes*, 58(4), 459-477.
- [7] Milutinović, S. (2023). Climate change adaptation planning at the local level in Serbia: Current status and lessons learned. *Facta Universitatis, Series: Working and Living Environmental Protection*, 20(2), 63-76.
- [8] Ignjatović, J., Filipović, S., & Radovanović, M. (2024). Challenges of the green transition for the recovery of the Western Balkans. *Energy, Sustainability and Society*, 14, 2.
- [9] Čorović, N., Urošević, B. G., & Katić, N. (2022). Decarbonization: Challenges for the electricity market

- development—Serbian market case. *Energy Reports*, 8, 2200-2209.
- [10] Petrović, J., Pavlović, J., & Radivojević, A. (2022). Possibilities for implementing principles of a circular economy in the reconstruction and adaptation of buildings in Serbia. *Spatium*, 48, 40-48.
- [11] Đurićin, D., & Lončar, D. (2020). Shaping the future of Serbia's economy: The new growth model and related economic policy platform. *Ekonomika preduzeća*, 68(1-2), 1-21.
- [12] Ministry of mining and energy. (2023). *Integrated National Energy and Climate Plan (INECP) covering 2021 to 2030*. Available at: <http://skr.rs/z0Em>
- [13] Tomic Tomic, A. (2021). Multicriteria selection of the optimal energy mix during the world energy crisis. *Industry*, 49(3/4), 63-78.
- [14] Madžarević, A. R., Ivezić, D. D., Tanasijević, M. L., & Živković, M. A. (2020). The Fuzzy–AHP synthesis model for energy security assessment of the Serbian natural gas sector. *Symmetry*, 12(6), 908.
- [15] Shannon C. E. (1948). A Mathematical Theory of Communication, *Bell System Technical Journal*, 27(3), 379-423.
- [16] Shannon C. E., & Weaver W. (1964). *The mathematical theory of communication*. Urbana, The University of Illinois Press.
- [17] Dwivedi, P. P., & Sharma, D. K. (2022). Application of Shannon entropy and CoCoSo methods in selection of the most appropriate engineering sustainability components. *Cleaner Materials*, 5, 100118.
- [18] Punetha, N., & Jain, G. (2024). Integrated Shannon entropy and COPRAS optimal model-based recommendation framework. *Evolutionary Intelligence*, 17(1), 385-397.
- [19] Dwivedi, P. P., & Sharma, D. K. (2023). Evaluation and ranking of battery electric vehicles by Shannon's entropy and TOPSIS methods. *Mathematics and Computers in Simulation*, 212, 457-474.
- [20] Dwivedi, P. P., & Sharma, D. K. (2022). Application of Shannon Entropy and COCOSO techniques to analyze performance of sustainable development goals: The case of the Indian Union Territories. *Results in Engineering*, 14, 100416.
- [21] Brodny, J., & Tutak, M. (2021). Assessing the level of digital maturity of enterprises in the Central and Eastern European countries using the MCDM and Shannon's entropy methods. *Plos one*, 16(7).
- [22] Yazdani, M., Torkayesh, A. E., Santibanez-Gonzalez, E. D., & Otaghsara, S. K. (2020). Evaluation of renewable energy resources using integrated Shannon Entropy – EDAS model. *Sustainable Operations and Computers*, 1, 35-42.
- [23] Stanujkic, D., Popovic, G., Karabasevic, D., Meidute-Kavaliauskiene, I., & Ulutaş, A. (2021). An integrated simple weighted sum product method – WISP. *IEEE Transactions on Engineering Management*, 70(5), 1933-1944.
- [24] Diniz, B. P., de Moura Pereira, D. A., dos Santos, M., Moreira, M. A. L., et al. (2024). New Approach to Choosing an Aircraft Carrier for Brazil from the AHP and WISP Multicriteria Decision Methods. *Procedia Computer Science*, 242, 544-551.
- [25] Stanujkic, D., Fedajev, A., & Santos, M. (2023). Investment projects evaluation in a fuzzy environment using the simplified WISP method. *Serbian Journal of Management*, 18(2), 225-235.
- [26] Stanujkic, M. (2023). Comparative analysis of MULTIMOORA, WASPAS and WISP methods: The case of candidate selection. *Journal of Process Management and New Technologies*, 11(3-4), 79-88.
- [27] Ulutaş, A., Stanujkic, D., Karabasevic, D., Popovic, G., & Novaković, S. (2022). Pallet truck selection with MEREC and WISP-S methods. *Strategic Management*, 27(4).
- [28] Zavadskas, E. K., Stanujkic, D., Karabasevic, D., & Turskis, Z. (2022). Analysis of the simple WISP method results using different normalization procedures. *Studies in Informatics and Control*, 31(1), 5-12.
- [29] Stević, Ž., Pamučar, D., Puška, A., & Chatterjee, P. (2020). Sustainable supplier selection in healthcare industries using a new MCDM method: Measurement of alternatives and ranking according to COMPROMISE solution (MARCOS). *Computers & Industrial Engineering*, 140, 106231.
- [30] Mitra, A. (2024). Cotton fibre selection based on quality value using measurement of alternatives and ranking according to compromise solution (MARCOS) method. *Research Journal of Textile and Apparel*, 28(2), 299-316.
- [31] Tešić, D., Božanić, D., Puška, A., Milić, A., & Marinković, D. (2023). Development of the MCDM fuzzy LMAW-grey MARCOS model for selection of a dump truck. *Reports in Mechanical Engineering*, 4(1), 1-17.
- [32] Nguyen, H. Q., Nguyen, V. T., Phan, D. P., Tran, Q. H., & Vu, N. P. (2022). Multi-criteria decision making in the PMEDM process by using MARCOS, TOPSIS, and MAIRCA methods. *Applied Sciences*, 12(8), 3720.
- [33] Majidi, A., Mirzapour Al-e-Hashem, S. M., & Hashemkhani Zolfani, S. (2021). Sustainability ranking of the Iranian major ports by using MCDM methods. *Mathematics*, 9(19), 2451.
- [34] Krstić, M., Agnusdei, G. P., Tadić, S., Kovač, M., & Miglietta, P. P. (2023). A Novel Axial-Distance-Based Aggregated Measurement (ADAM) Method for the Evaluation of Agri-Food Circular-Economy-Based Business Models. *Mathematics*, 11(6), 1334.
- [35] Kalem, A., Tadić, S., Krstić, M., Čabrić, N., & Branković, N. (2024). Performance Evaluation of Railway Infrastructure Managers: A Novel Hybrid Fuzzy MCDM Model. *Mathematics*, 12(10), 1590.
- [36] Popovic, G., Fedajev, A., Mitic, P., & Meidute-Kavaliauskiene, I. (2024). An ADAM-based approach to unveiling entrepreneurial ecosystems in selected European countries. *Management Decision*.
- [37] Andrejić, M., Pajić, V., & Kilibarda, M. (2023). Distribution channel selection using FUCOM-ADAM: A novel approach. *Sustainability*, 15(19), 14527.
- [38] Agnusdei, L., Krstić, M., Palmi, P., & Miglietta, P. P. (2023). Digitalization as driver to achieve circularity in the agroindustry: A SWOT-ANP-ADAM approach. *Science of The Total Environment*, 882, 163441.

The Impact of Varying the Frequency and Amplitude of Porous Wavy Strip Inserts on the Hydrothermal Performance of a Nanofluid-filled Tube

Benelhaoues Mohamed¹, Fersadou Brahim², Nessab Walid³, Djeddou Hessem⁴

^{1,2,3,4}Laboratory of Multiphase Flows and Porous Media, University of Sciences and Technology Houari Boumedienne, Algiers, Algeria

¹mbenelhaoues@usthb.dz, ²brahim.fersadou@usthb.edu.dz, ³walid.nessab@usthb.edu.dz,

⁴Djeddou.sam@gmail.com

Abstract—The primary objective in the design and development of solar sensors is efficient heat extraction. Recent trends and innovative approaches, using both passive and active techniques, offer potential for further optimizing solar energy conversion systems. Among these innovations are the use of unconventional heat transfer fluids, such as nanofluids, and the insertion of wavy strips within the tubes of solar panels. This study follows such an approach, focusing on enhancing thermal performance in the cooling of a tube equipped with a corrugated, porous strip, through which a Water/MWCNT nanofluid circulates. The aim is to maximize heat transfer efficiency while minimizing the pressure drop penalty. A 3D laminar flow regime is simulated using the finite element method to solve the mass, momentum, and energy conservation equations. The Water/MWCNT nanofluid is modeled using a single-phase approach, and flow through the porous medium is described by the Darcy-Brinkman-Forchheimer model. By maintaining the tube wall at a constant hot temperature and fixing the Reynolds number at $Re = 400$, the study examines the effects of increasing forced convection by varying the frequency ($40 \leq n \leq 70$) and amplitude ($0.1D \leq Amp \leq 0.166D$) of the wavy strip for different permeability levels of the porous strip by adjusting the Darcy number ($10^{-6} \leq Da \leq 10^{-6}$). The results are displayed as velocity contours, isotherms, average Nusselt number trends, and pressure drops. They demonstrate that the velocity and

temperature fields are significantly affected by the frequency, amplitude of the corrugated strip, and the porous medium. The optimal frequency and amplitude are identified as $n=60$ and $Amp=0.133D$, respectively.

Keywords – heat transfer, wavy strip, nanofluid, porous medium, tube

I. INTRODUCTION

A heat exchanger plays a crucial role in energy conservation and management systems, as it often determines the system's overall efficiency and size. As a result, enhancing heat transfer has garnered significant interest from researchers. Pipes, a common component of heat exchangers, are frequently used in energy-related applications such as solar energy collection, waste heat recovery, and thermoelectric power generation [1]. Many efforts have been made to improve heat transfer in circular pipes. In other experimental study by [2] Using twisted tapes, perforated twisted tapes, and perforated twisted tapes with the alternate axis, increases the maximum heat transfer by 33%, 44.3%, and 48.12%, respectively; and maximum f by 15.85%, 17.6%, and 19.1% respectively. Reference [3] experimentally and numerically investigated the effect of inserting discrete V-winglets, finding that the maximum Nu and average friction factor increased by 3.8 and 18.8



times, respectively. Reference [4] developed a novel insert using pin fin arrays in parabolic trough collectors, achieving up to 12% and 9% increases in the Nusselt number. Reference [5] introduced a center-tapered wavy-tape insert inspired by cuttlefish fins. Their study showed an increase in the Nusselt number (Nu) by a factor of 5.2 to 9 compared to a plain tube. Additionally, reducing the free space ratio in regularly spaced quadruple twist tape elements increased the heat transfer rate, friction loss, and overall performance factor.

In the present study, corrugated porous inserts of varying frequency and amplitude are introduced to generate vortex flow in a straight pipe. Three-dimensional models are used to simulate the flow and heat transfer characteristics in the pipe.

II. MATHEMETICAL MODELING

A. Physical Model

Fig. 1 illustrates the schematic of the tube and the porous wavy-tape insert.

As shown, the wavy-tape insert is placed at the center of a straight pipe with an inner diameter (D) and a length (L). The tape, modeled as porous media, follows a sinusoidal pattern with a width of ($0.8D$) and three cases of the amplitude and the frequency. The tape has a fixed thickness of ($0.01D$). Additionally, two plain sections are located at both the front and rear ends, each with a length of ($L_i=2D$).

III. GOVERNING EQUATIONS

We analyze a three-dimensional, steady, incompressible laminar forced convection flow in a pipe, neglecting body forces, thermal radiation, and viscous dissipation. The wavy strip insert is treated as a porous medium. The Water/MWCNT nanofluid flow is modeled using a single-phase approach, with the porous medium flow governed by the Darcy-Brinkman-Forchheimer model.

In order to present the equations in their dimensionless form, we use the following variables:

$$(X, Y, Z) = \frac{(x, y, z)}{D}, \quad (1)$$

$$(U, V, W) = \frac{(u, v, w)}{U_i}, \quad (2)$$

$$P = \frac{p}{\rho_{nf} U_i^2}, \quad (3)$$

$$\theta = \frac{T - T_i}{T_w - T_i}. \quad (4)$$

Equations (5)-(7) describe the conservation of continuity, momentum, and energy.

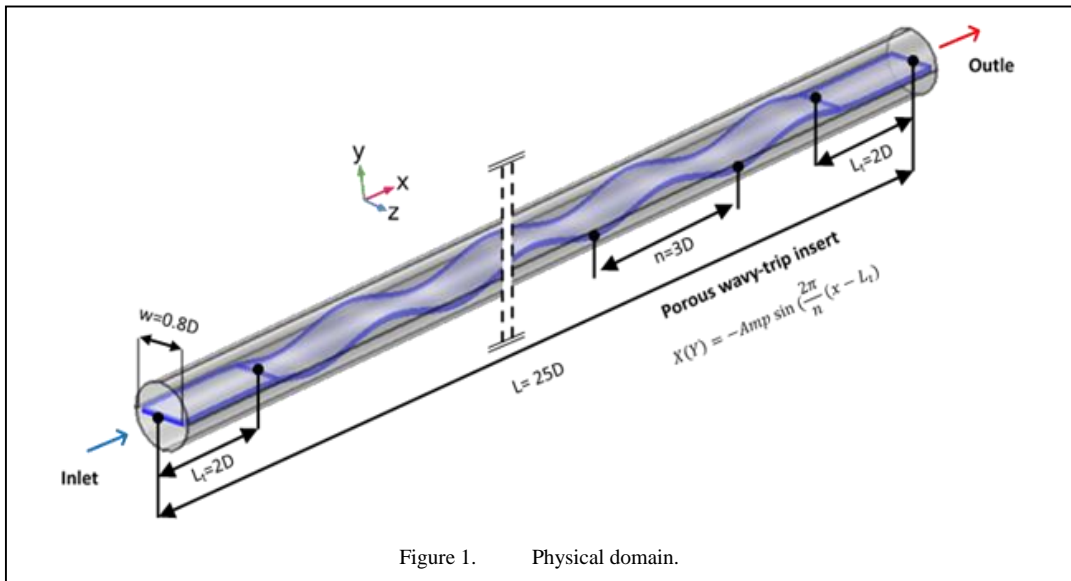


Figure 1. Physical domain.

Continuity:

$$\vec{\nabla} \cdot \left(\vec{\nabla} \right) = 0. \quad (5)$$

Momentum:

$$\frac{1}{\delta_1 \varepsilon^2} \vec{\nabla} \cdot \left(\vec{\nabla} \vec{\nabla} \right) = -\vec{\nabla} P + \frac{\rho_f \mu_{nf}}{\rho_{nf} \mu_f} \frac{R_\mu}{\text{Re}} \vec{\nabla}^2 \vec{\nabla} - \frac{\rho_f \mu_{nf}}{\rho_{nf} \mu_f} \frac{1}{\text{Re Da}} \vec{\nabla} \delta_2 - \frac{C}{\sqrt{\text{Da}}} \left| \vec{\nabla} \right| \vec{\nabla} \delta_2 \quad (6)$$

Energy:

$$\vec{\nabla} \cdot \left(\theta \vec{\nabla} \right) = \frac{(\rho C_p)_f}{(\rho C_p)_{nf}} \frac{R_K}{\text{Re Pr}} \vec{\nabla} \cdot \left(\vec{\nabla} \theta \right). \quad (7)$$

We take the constants $\delta_1 = \delta_2 = 1$; $\varepsilon = 0.97$ and $C = 0.1$ at the porous wavy-type insert.

We take the constants $\delta_1 = \frac{1}{\varepsilon^2}$ and $\delta_2 = 0$; $\mu_{eff} = \mu_{nf}$ and $k_{eff} = k_{nf}$ at the nanofluid region.

The dimensionless numbers apparent in the equations are:

$$\text{Re} = \frac{\mu_f \rho_f D}{\mu_f}, \quad (8)$$

$$\text{Pr} = \frac{\mu_f C_{pf}}{k_f}, \quad (9)$$

$$\text{Da} = \frac{K}{D^2}, \quad (10)$$

$$R_\mu = \frac{\mu_{eff}}{\mu_{nf}}, \quad (11)$$

$$R_K = \frac{\mu_{eff}}{\mu_{nf}}. \quad (12)$$

The governing equations are solved in conjunction with the following boundary conditions:

- Inlet: $V = W = \theta = 0; U = 1$
- Wall: $U = V = W = 0; \theta = 1$

- Outlet: $V = W = \frac{dU}{dX} = \frac{d\theta}{dX} = P = 0$

The Nusselt number is mainly used to evaluate the heat exchanges taking place between a wall and a fluid. It is defined as follows:

$$\text{Nu} = \frac{hD}{k_f} = \frac{k_{nf}}{k_f} \frac{\partial \theta}{\partial \eta}. \quad (13)$$

The temperature gradient on the tube wall is defined by:

$$\frac{\partial \theta}{\partial \eta} = \sqrt{\left(\frac{\partial \theta}{\partial X} \right)^2 + \left(\frac{\partial \theta}{\partial Y} \right)^2 + \left(\frac{\partial \theta}{\partial Z} \right)^2}, \quad (14)$$

$$\text{Nu}_m = \frac{1}{S} \int_0^S \text{Nu} ds. \quad (15)$$

S is the wall surface of tube.

The pressure drop is calculated by the following formula:

$$\Delta P = \frac{P_{m(X=0)} - P_{m(X=L)}}{L}. \quad (16)$$

P_m is the average pressure calculated at the inlet and outlet sections.

IV. NUMERICAL PROCEDURE

The governing equations, along with their boundary conditions, were solved using the Galerkin finite element method (FEM). Non-uniform triangular elements were employed to generate the mesh for both the nanofluid and porous media domains. To ensure numerical accuracy, the mesh was refined until the mean Nusselt number and pressure drop showed negligible differences between grids with 1,821,452 and 2,741,161 elements. Consequently, the mesh with 1,821,452 elements was selected for the numerical simulations to balance computational cost with acceptable accuracy.

V. RESULTS

In this study, as mentioned earlier, we conducted a hydrothermal analysis of the impact of a porous wavy strip insert. We maintained the wall at a constant hot temperature T_h , and set the Reynolds number to $Re = 400$. The frequency (n) was varied between 40 and 70, the amplitude

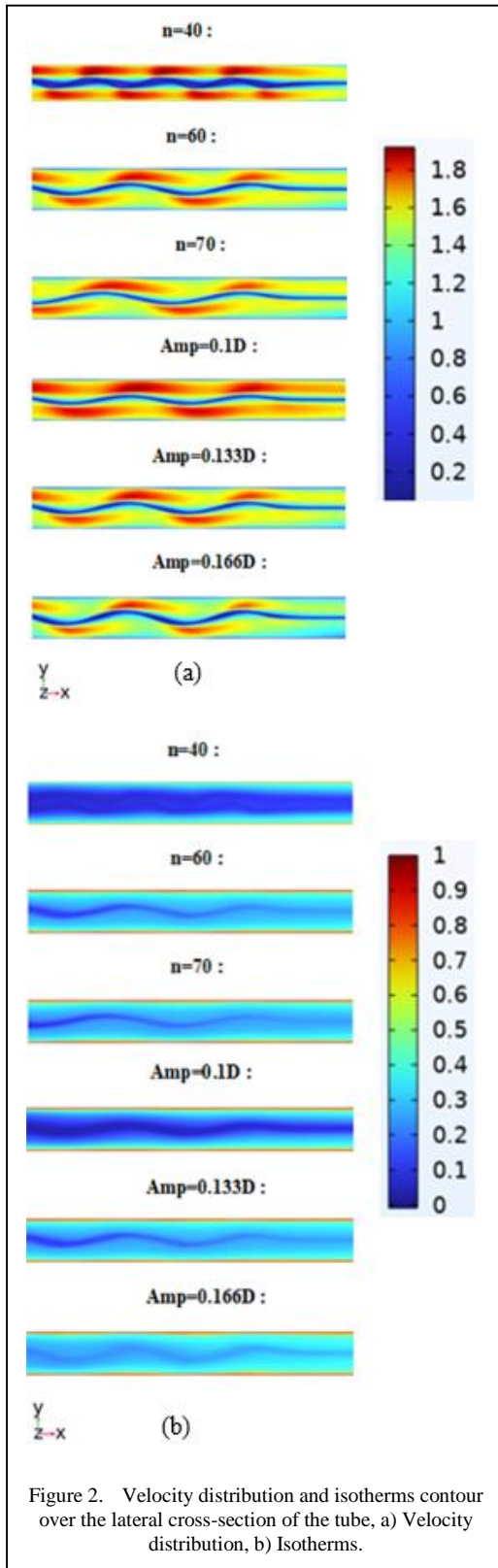


Figure 2. Velocity distribution and isotherms contour over the lateral cross-section of the tube, a) Velocity distribution, b) Isotherms.

between 0.1D and 0.166D, and the permeability of the wavy porous strip was adjusted by altering the Darcy number within the range ($10^{-6} \leq Da \leq 10^{-1}$). To study the frequency and amplitude effects, we fixed the Darcy number at 10^{-6} .

A. Frequency Effect

Adjusting the frequency of the wavy strip insert changes the number of waves. Specifically, lowering the frequency reduces the distance between adjacent waves, increasing their overall count, and the opposite occurs when the frequency is raised.

Fig. 2 shows the velocity distribution and isotherm contours along the lateral cross-section of the tube. The lateral cross-section coordinates (x) were selected between 350 and 400. The permeability of the wavy strip was held constant at $Da = 10^{-6}$ for all cases. When the amplitude was fixed and the frequency of the wavy strip varied, the velocity contours revealed a distinct distribution for all cases. At the frequency $n=40$, the nanofluid's movement is notably slower around the wavy strip compared to the other frequencies ($n = 60$ and $n = 70$). This is attributed to the increased number of ripples; for $n=40$, the greater number of waves impedes the nanofluid's flow, reducing its velocity and prolonging its passage through the tube. This results in an extended residence time and, consequently, greater heat absorption by the nanofluid. The isotherm contours and data from Table I support these findings, indicating that the outlet temperature for $n = 40$ ($\theta_{out} = 0.31514$) is higher than in the other two cases. This suggests that the cooling effect is greater in this scenario compared to the others. Table I also presents the pressure drop values. It can be observed that for $Da = 10^{-6}$, the pressure drop is highest for $n = 40$ and lowest for $n = 70$.

Therefore, we can conclude that $n = 60$ is the optimal frequency.

B. Amplitude Effect

To study the effect of the amplitude of the wavy strip, we carried out three cases: 0.1D, 0.133D, and 0.144D, by fixing the frequency at $n = 60$. As Fig. 2 also shows, the variation in amplitude influences the velocity distribution within the tube. For the case of 0.166D, we obtained a smaller volume and a smaller two-dimensional area between the corrugated strip and the tube wall. According to the velocity

TABLE I. THE VALUES OF THE OUTLET TEMPERATURE AND PRESSURE DROP FOR DIFFERENT FREQUENCIES.

Amplitude	Amp=0.133D		
Da	10^{-6}		
Frequency	40	60	70
θ_{out}	0.31514	0.28540	0.27757
ΔP	4.5681	4.0925	3.8354

TABLE II. THE VALUES OF THE OUTLET TEMPERATURE AND PRESSURE DROP FOR DIFFERENT AMPLITUDES.

Frequency	n=60		
Da	10^{-6}		
Amplitude	0.1D	0.133D	0.166D
θ_{out}	0.23727	0.28540	0.32239
ΔP	2.7956	4.0925	5.8694

contour, we observed a noticeable difference in the velocity distribution of the nanofluid. The maximum velocity for the two cases, 0.1D and 0.133D, covers more surface area than in the case of 0.166D. This means the nanofluid flows more quickly in the 0.1D and 0.133D cases compared to the 0.166D case. This is because the higher amplitude of the obstacles (waves) hinders the circulation of the nanofluid, increasing the residence time, bringing the hot nanofluid into the main flow, and intensifying the mixing of the nanofluid. This is clearly reflected in the isotherm contours and Table II, where the highest outlet temperature ($\theta_{out}=0.17448$), was recorded for Amp = 0.166D. This indicates a greater cooling effect in this case compared to the others.

Table II also displays the pressure drop values, showing that for $Da = 10^{-6}$, the highest pressure drop occurs at Amp = 0.166D, while the lowest is at Amp = 0.1D. Consequently, we can conclude that Amp = 0.133D represents the optimal amplitude.

C. Permeability Effect

Figs. 3-6 are used to investigate the thermo-hydraulic impact of using a porous corrugated strip with varying frequencies and amplitudes.

Figs. 3 and 5 illustrate the evolution of the Nusselt number average for different frequencies and Darcy numbers, and the evolution of the average Nusselt number for different amplitudes and Darcy numbers, respectively. We observe that, regardless of the amplitude or frequency of the wavy strip insert, as the Darcy number (which represents the permeability of the wavy strip inserts) increases,

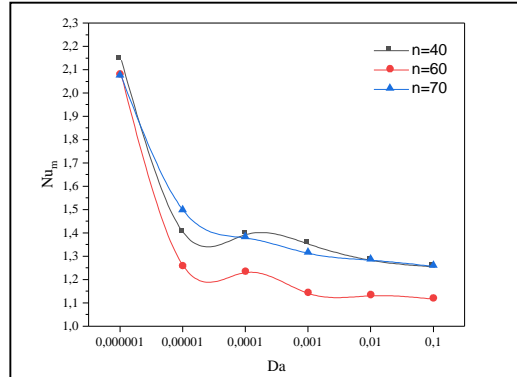


Figure 3. Evolution of Nusselt average for different Frequencies and Darcy numbers.

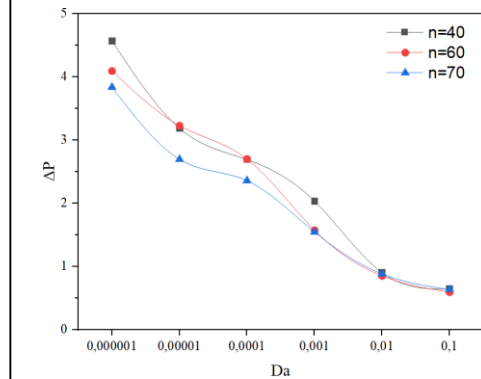


Figure 4. Evolution of Pressure drops for different Frequencies and Darcy numbers.

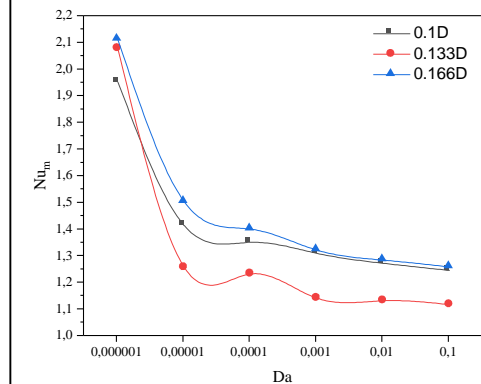
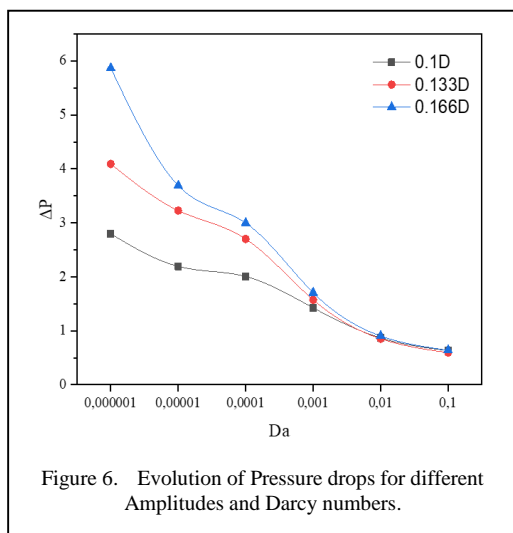


Figure 5. Evolution of Nusselt average for different Amplitudes and Darcy numbers.

the Nusselt number decreases. A similar trend is noted for the pressure drops: as the Darcy number increases, the pressure drops decreases, as shown in Figs. 4 and 6. These figures depict the evolution of pressure drops for different frequencies and Darcy numbers and the



evolution of pressure drops for different amplitudes and Darcy numbers, respectively.

Using a porous insert with higher permeability allows the nanofluid to flow more easily through the medium, which reduces the pressure drop.

As permeability increases, the fluid flows more easily through the porous medium. However, the flow becomes more dispersed rather than focused, potentially weakening convective heat transfer. At higher permeabilities, thermal dispersion effects (which typically enhance heat transfer) may diminish as the fluid flow becomes more uniform, further reducing the Nusselt number.

VI. CONCLUSION

The study explores the effects of frequency, amplitude, and permeability of the porous wavy-tape insert on nanofluid flow and heat transfer in a tube with its wall maintained at a hot temperature.

- **Frequency Effect:** Lowering the frequency ($n = 40$) increases the number of waves, slowing down the nanofluid's flow, enhancing heat absorption due to

prolonged residence time. However, it also leads to a higher pressure drop. The optimal frequency is found to be $n=60$, balancing heat transfer efficiency and pressure drop.

- **Amplitude Effect:** Increasing the amplitude reduces the nanofluid's velocity by creating more obstruction, which increases mixing and enhances heat absorption. However, it also increases pressure drop. The optimal amplitude is determined to be $\text{Amp}=0.133D$, balancing cooling performance and pressure drop.
- **Permeability Effect:** High permeability allows easier fluid flow but weakens convective heat transfer.

In summary, an optimal balance between frequency, amplitude, and permeability can enhance cooling performance while managing pressure drops.

REFERENCES

- [1] Zhu, X. W., Fu, Y. H., & Zhao, J. Q. (2016). A novel wavy-tape insert configuration for pipe heat transfer augmentation. *Energy Conversion and Management*, 127, 140-148.
- [2] Ponnadaa, S., Subrahmanyam, T., & Naidu, S. V. (2019). A comparative study on the thermal performance of water in a circular tube with twisted tapes, perforated twisted tapes, and perforated twisted tapes with alternate axis. *International Journal of Thermal Sciences*, 136, 530-535.
- [3] Promvong, P., Promthaisong, P., & Skullong, S. (2020). Experimental and numerical heat transfer study of turbulent tube flow through discrete V-winglets. *International Journal of Heat and Mass Transfer*, 151, 119351.
- [4] Xiangtao, G., Fuqiang, W., Haiyan, W., Jianyu, T., Qingzhi, L., & Huaizhi, H. (2017). Heat transfer enhancement analysis of tube receiver for parabolic trough solar collector with pin fin arrays inserting. *Solar Energy*, 144, 185-202.
- [5] Liang, Y., Liu, P., Zheng, N., Shan, F., Liu, Z., & Liu, W. (2019). Numerical investigation of heat transfer and flow characteristics of laminar flow in a tube with center tapered wavy-tape insert. *Applied Thermal Engineering*, 148, 557-567.

Estimating the Potentials for Indoor Comfort in Smart Green Buildings with BIPV

Nnabuiké Ngwu¹, Michael Ahanonu², Ken Chen³, Yongjun Sang⁴, Howard Njoku⁵, Gang Pei⁶

^{1,2,5}University of Nigeria, Nsukka, Nigeria

^{3,4,5,6}University of Science and Technology of China, Hefei, China

¹ngwu.chris.2@gmail.com, ²michael.ahanonu.c@gmail.com, ³chenken@mail.ustc.edu.cn,

⁴sangyongjun@ustc.edu.cn, ⁵howard.njoku@unn.edu.ng, ⁶peigang@ustc.edu.cn

Abstract—Increased emphasis on improving energy efficiency in buildings has arisen from the widespread focus on sustainable development. Promising solutions include smart and green buildings incorporating renewable energy systems, such as Building-Integrated Photovoltaics (BIPV). This study explores the potential of BIPV systems to maintain indoor thermal comfort across eight different climate regions. Simulation tools were used to determine the energy requirements for maintaining indoor comfort and evaluate the ability of BIPV systems to meet these demands while accounting for local climate, modes of HVAC operation (including the implementation of smart controls), and occupancy levels. The results show that all year round, more BIPV energy will be produced in the warm locations (Cairo, Mexico City, Mumbai, and Nsukka) than needed to maintain thermal comfort. However, in the cold locations (Beijing, Denver, Sofia, and Stuttgart), the energy generated by BIPV systems will be insufficient. Furthermore, implementing energy-saving and smart control strategies will significantly lessen HVAC loads in all locations, and energy deficits would be transformed into surpluses in all locations except Stuttgart, where only the implementation of smart HVAC controls will achieve the same effect. Additionally, the study revealed reductions in energy costs ranging between 10.2% and 995.9% (in instances where the costs were converted into revenues). These noteworthy cost reductions underscore the importance of incorporating energy-efficient solutions and smart technologies into building energy management systems.

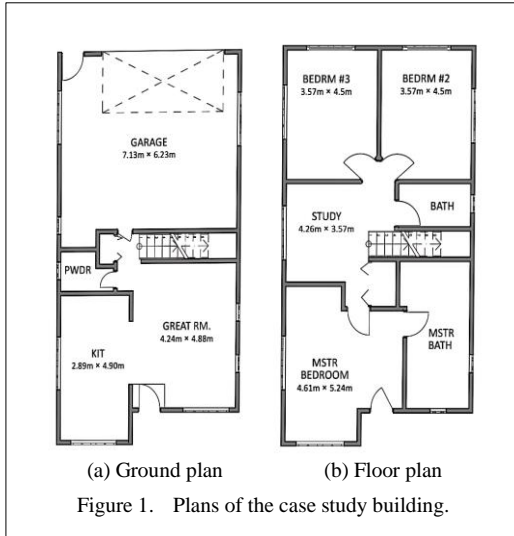
Keywords - indoor thermal comfort, smart buildings, BIPV, green buildings

I. INTRODUCTION

Buildings significantly contribute to climate change being responsible for one-third of global energy consumption and one-quarter of CO₂ emissions, and heating, ventilation and air conditioning (HVAC) systems, which are essential for maintaining indoor comfort, account for 38% of building energy use [1]. Indoor thermal comfort, defined by parameters such as temperature, humidity, and air quality, greatly influences the well-being and productivity of building occupants, and inadequate thermal conditions lead to discomfort, decreased productivity, and adverse health effects [2].

As the global population grows, projected to exceed 9 billion by 2050 [3], ensuring that building energy needs are met sustainably requires innovative approaches that balance human comfort with environmental stewardship. Green buildings enable the achievement of indoor thermal comfort while simultaneously reducing energy consumption [4]. They incorporate sustainable design principles and energy-efficient technologies that minimize environmental impact. Green building strategies, such as natural ventilation and thermal mass, can significantly improve indoor comfort levels [5], and the integration of renewable energy sources can further mitigate energy demands,

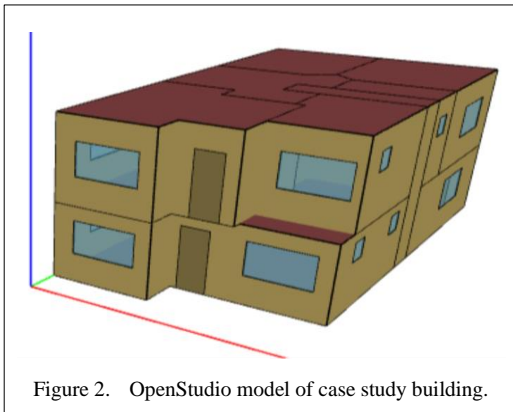




contributing to a more sustainable built environment [6].

Building-integrated photovoltaic (BIPV) systems, a green building design approach, provide an environmentally sustainable solution that reduces the dependence on grid power for maintaining indoor thermal comfort [7,8]. Recent advancements in BIPV technology have shown its potential to enhance energy efficiency while ensuring occupant comfort [9,10].

Considering the huge energy requirements of building HVAC systems, it is important to better understand the ability of BIPV systems to support HVAC loads in various climates. This study developed a residential building model to investigate the HVAC energy requirements for maintaining indoor comfort under the climate conditions at eight locations. The electricity generation potential of roof-mounted PV systems



on this building were then simulated for the selected locations. The model addressed the seasonal variations in the available solar resource as well as the cooling/heating demands of the studied building. Further analysis quantified the additional grid energy needs to offset any shortages, as well as the costs, and economic benefits of surplus energy produced when the BIPV systems are sized to fully satisfy the HVAC energy requirements. Thus, the economic implications of potential energy surpluses or deficits resulting from BIPV-HVAC interactions were quantified.

II. MATERIALS AND METHODS

A. Building Specifications

The building considered in this study is a one-storey residential building with eleven rooms (Fig. 1). The ground floor (Fig. 1(a)) comprises a garage, a guest bathroom, a kitchen, a guest toilet (PWDR) and a great room, while the first-floor features two bedrooms, a study room, a master bedroom, and two bathrooms (Fig. 1(b)). Fig. 2 shows the OpenStudio model of the building having the dimensions shown in Fig. 1 and a floor-to-ceiling height of 8m. The building's doors, windows, and other parts were specified using the FloorspaceJS tool as presented in Table I. The building roof has a flat dimension of 13.216m x 7.132m that was raised to form a double-pitched roof with two equal sloping surfaces. With a slope angle of 33°, the dimension of each sloping surface is 13.216m x 4.257m.

B. Cooling Loads

Thermal zones (TZ) were assigned to the spaces in the building to represent separate heat transfer regions as indicated in Table II and the contributions to a zone's internal cooling loads can be calculated for occupants using Eq. (1) and (2), for lighting using Eq. (3), and for electric equipment using Eqs. (4) and (5) [11].

$$Q_{Sensible} = N \times Q_S \times CLF, \quad (1)$$

$$Q_{Latent} = N \times Q_L, \quad (2)$$

$$Q_{Sensible} = 3.41 \times W \times F_{UT} \times F_{SA} \times CLF, \quad (3)$$

$$Q_{Sensible} = Q_{in} \times F_u \times F_r \times CLF, \quad (4)$$

$$Q_{Latent} = Q_{in} \times F_u, \quad (5)$$

where $Q_{Sensible}$ and Q_{Latent} represent the sensible and latent heat gains, the N represents the number of people in a space as specified in Table II, Q_S and Q_L indicate the sensible and latent heat gains per occupant with a combined value of 95 W/person split in a ratio of 70:30 as specified in ASHRAE [12] while CLF denotes the Cooling Load Factor by hour of occupancy. W stands for the power input (Watts) from the electrical lighting plan or lighting load data as given in Table II, and F_{UT} represents the lighting use factor while F_{SA} signifies the special ballast allowance factor. Q_{in} refers to the rated energy input from appliances, F_u is the equipment usage factor, and F_r is the radiation factor of the equipment. In consideration of the added heat generated by occupants, lighting and electrical equipment, the ANSI/ASHRAE/IES Standard 90.1-2016 Performance Rating was used to estimate the amount of latent heat (latent fraction), long-wave radiant heat (radiant fraction), and “lost” heat given off by the equipment in the spaces they occupy [6].

The lights were considered to have a radiant fraction of 0.38 and a visible fraction of 0.22.

TABLE I. DOOR AND WINDOW SPECIFICATIONS.

Construction	Dimension	Location
Regular door	2.03 m x 0.82 m	All the rooms
Overhead door	2.03 m x 4.72 m	Garage
Small window	0.61 m x 0.61 m	Bathroom, Staircase
Large window	1.07 m x 1.83 m	Other rooms

TABLE II. THERMAL ZONE AND SPACE LOAD SPECIFICATIONS.

Space	TZ	Max No. of People	Lighting Power (W)	Electrical Power (W)
Garage	1	4	20	-
Staircase	2	2	10	-
PWRD	3	1	10	-
Greatroom	4	4	15	1500
Kitchen	5	3	10	3000
Bedroom 2	6	3	10	300
M-Bedroom	7	3	10	300
Studyroom	8	4	10	150
M-Bathroom	9	1	10	-
Bathroom	10	1	10	-
Bedroom 3	11	3	10	300

For the electric equipment, the latent fraction was 0.25 while the radiant fraction was 0.3, and for the gas equipment, the latent fraction was 0.2, the radiant fraction was 0.4, and the lost fraction was 0.1.

C. Occupancy and Equipment Use Schedules

As the number of occupants and equipment usage influence the condition in the indoor spaces, schedules of the occupancy and equipment use was developed as shown in Table III, to model possible real-life conditions in the building under study. These also provided the hours of occupancy for determining values of CLF in Eqs. (1), (3) and (4). Importantly, the great room is usually unoccupied except during evenings, weekends and holidays, while the bedrooms are occupied in afternoons, nights, and weekends. In addition, on average, the garage is occupied for 3 hours per day, while the staircase is occupied for 10 hours per day.

A lighting schedule was created in which lights are on for 2 hours daily in the bathroom and for 5 hours in the bedroom, great room, kitchen, staircase, and study room. The garage lights are on for an average of 1.5 hours per day. A schedule was also created in which electrical equipment in the bedroom, great room, kitchen, and study room were specified to be used for an average of 3.6, 5, 4, and 3 hours per day, respectively.

TABLE III. OCCUPANCY SCHEDULES.

Day	Time			
	06:00 – 14:00	14:00 – 16:00	16:00 – 21:00	21:00 – 06:00
Greatroom				
Mon - Fri	0	0	3	0
Saturdays	0	0	5	0
Sundays	0	0	5	0
Holidays	0	2	5	0
M-Bedroom				
Mon - Fri	0	2	0	9
Saturdays	3	0	0	9
Sundays	2	0	0	9
Holidays	3	0	0	9
Kitchen				
Everyday	2	0	3	0
Studyroom				
Everyday	0	1	2	0
Bathroom				
Everyday	1	0	1	0

Meanwhile, the kitchen gas equipment was specified to be used for an average of 1.5 hours per day.

D. HVAC Operation Scenarios

Depending on weather conditions, HVAC systems will provide either heating or cooling to maintain indoor thermal comfort conditions. The desired indoor thermal conditions were fixed at an interior temperature of 25 °C and a humidity range of 30% to 60%. To investigate the energy consumed for maintaining indoor thermal comfort under different equipment use scenarios, three cases were considered, viz,

Case 1: Continuous HVAC operation in all building spaces. In this worst case scenario, HVAC equipment operate at maximum building cooling/heating load at all times.

Case 2: Continuous year-round HVAC operation only in living spaces. This represents an intermediate case that can be achieved by implementing energy efficiency measures at the building design stage to ensure that only the living spaces are provided with HVAC systems (although they may be operated without regards to the presence or absence of occupants), and that heating and cooling demands are not generated in spaces which are normally unoccupied.

Case 3: HVAC operation in living spaces according to occupancy schedule. Here, in addition to the energy efficiency measures described for Case 2, the system operates only when the spaces are occupied. This scenario can be achieved by deploying smart technologies to ensure that HVAC equipment in a living space only operates when needed, i.e., when occupants are identified or expected to be present in the space.

E. PV Power Generation Potential

The energy output of a solar PV system may be estimated using Eq. (6) [13]:

$$E = n_i r_p P_k H_i, \quad (6)$$

where E (kWh) is the generated electricity for the monthly or annual period with n_i number of days; r_p is a performance ratio (kWp/m²) that accounts for losses due to temperature and spectral effects and module inclination; P_k is the nominal installed peak power output (kWp) and H_i is insolation. The PVGIS online tool implements Eq. (6) and was used to estimate the

TABLE IV. BIPV PARAMETERS.

Parameter	Value
PV technology	Monocrystalline Silicon
PV type	Grid-connected
Number of cells	96
Module area	1.676 m ²
Number of modules	64
Installed Peak PV power	12.3354 KWp
System loss	14%
Mounting position	Roof-mounted
Slope	33°
Azimuth	0°/180°

BIPV energy production by specifying the module parameters.

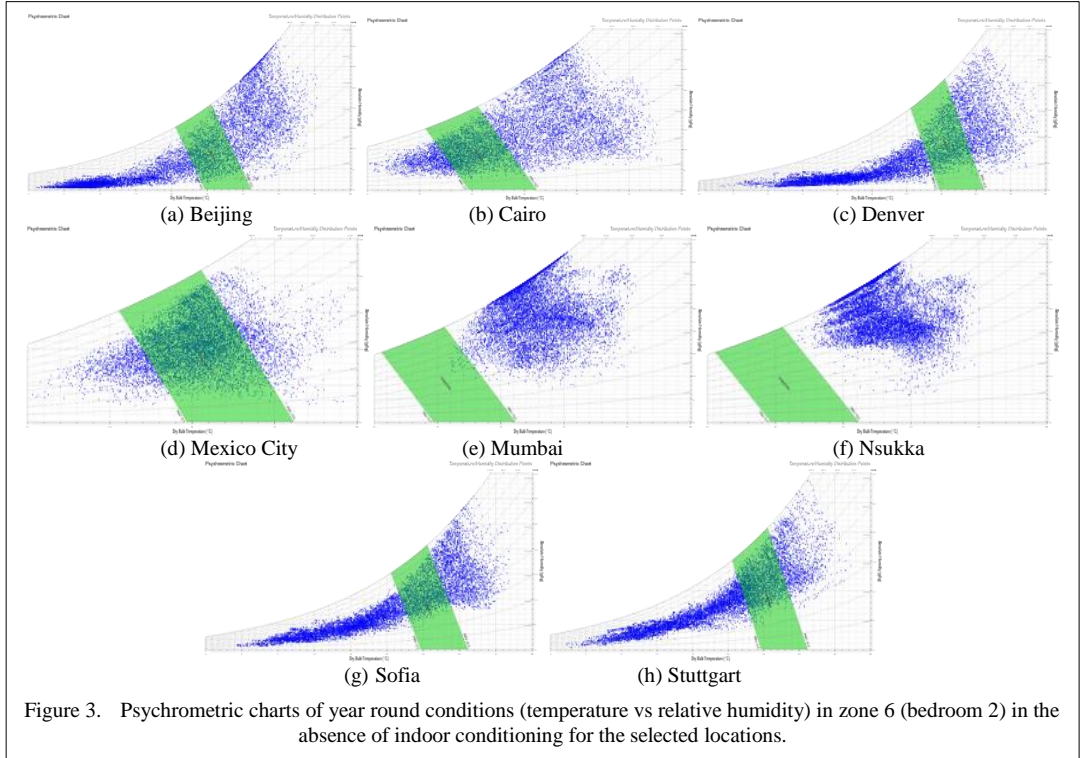
The model building is specified to align with the east-west direction and the roof-mounted BIPV system is designed for half of the PV modules to be mounted on the south-facing roof segment ($\gamma = 0$) and the other half on the north-facing roof segment ($\gamma = 180$). The properties of the selected PV module and its orientation are given in Table IV. The modules are based on monocrystalline silicon cells having conversion efficiencies of 23% and 64 of the selected modules will cover 95.328% of the building's roof area and provide an installed peak power of 12.3354kWp.

III. RESULTS AND DISCUSSION

The developed building and BIPV system models were implemented for eight selected locations with unique weather conditions as follows: Beijing, China (40.2 N, 116.4 E), Cairo, Egypt (30.1 N, 31.4 E), Denver, USA (39.8 N, 104.9 W), Mexico City, Mexico (19.4 N, 99.1 W), Mumbai, India (19.1 N, 72.9 E), Nsukka, Nigeria (6.9 N, 7.4 E), Sofia, Bulgaria (42.6 N, 24.0 E), and Stuttgart, Germany (48.7 N, 9.2 E). Typical Meteorological Year and Design Conditions files, to accurately represent the climates of the selected locations, were sourced from the PVGIS online database and OpenStudio Weather files website. Identical simulation parameters (Table II), occupancy schedules and HVAC operation modes were simulated for the eight locations.

A. Indoor Climate

The psychrometric charts in Fig. 3 show the year-round hourly (temperature and humidity) conditions in TZ 6 (bedroom) at the selected locations. With reference to the comfort zone (the shaded area in the charts), Mumbai, and



Nsukka require cooling for most periods of the year, while all the other locations experience cold conditions for significant portions of the year, necessitating heating. Also, the conditions Denver and Beijing suggest the need for humidification in addition to heating during the extreme cold season.

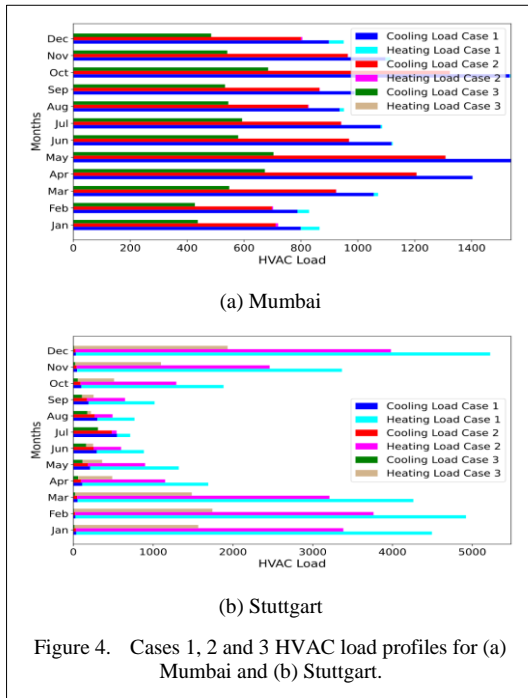
B. Heating/Cooling Load

Table V shows the annual cooling and heating loads for all eight locations and the three HVAC operation cases considered. We observe that the building will impose the highest cooling load on the HVAC systems in Mumbai (13237.3 kWh per annum), while the highest heating load will occur in Stuttgart (28592.1 kWh per annum).

This discrepancy is primarily due to Mumbai's hot and humid climate, which necessitates significant cooling throughout the year, whereas Stuttgart's colder climate requires substantial heating to maintain comfortable indoor temperatures during the colder months. The highest energy consumption will occur in Denver, where appreciable amounts of cooling in the warm season in addition to large amounts of heating in the cold season are required, whereas the least energy consumption will occur in Mexico City where the conditions fall within the comfort zone for more periods of the year as seen in Fig. 3.

TABLE V. ANNUAL HVAC LOADS.

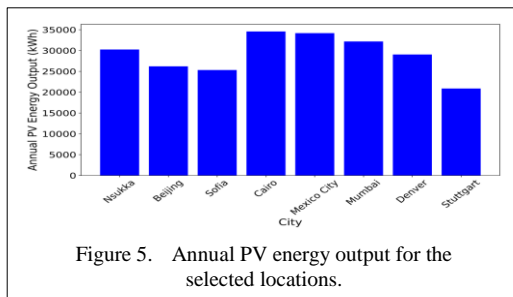
Location	Case 1 loads (kWh)			Case 2 loads (kWh)			Case 3 loads (kWh)		
	Heating	Cooling	Total	Heating	Cooling	Total	Heating	Cooling	Total
Nsukka	174.9	12947.0	13121.9	34.1	11185.8	11219.9	0.7	6881.8	6882.5
Beijing	24668.7	4367.7	29036.4	17792.4	3769.8	21562.2	8007.8	2325.5	10333.3
Sofia	26455.4	2482.4	28937.8	19061.3	2177.9	21239.2	8393.6	1369.7	9763.3
Cairo	5708.8	7500.1	13208.9	3288.59	6490.65	9779.24	892.38	3798.27	4690.65
Mexico City	8359.1	2764.7	11123.8	4655.48	2376.54	7032.02	1080.64	1523.26	2603.9
Mumbai	227.7	13237.3	13465	25.9	11534.2	11560.1	0.2	6749.5	6749.7
Denver	28463.6	2611.0	31074.6	20617.2	2248.7	22865.9	9606.9	1360.1	10967.0
Stuttgart	28592.1	1952.4	30544.5	20712.2	1703.3	22415.5	9154.5	1060.2	10214.7



C. Effect of the HVAC Operation Cases

The HVAC operation modes significantly affect HVAC loads, with the loads decreasing progressively from Case 1 to Case 3 (Table V). The loads are highest in case 1 due to the constant operation of the HVAC system in both occupied and unoccupied areas. By excluding non-living areas, the loads in Case 2 are reduced by 14.1%-36.8% compared to Case 1 loads. Case 3, however, results in the lowest load by minimizing unnecessary heating or cooling in the living spaces. This scenario reduces HVAC loads up to 47.5%-76.6% in comparison with Case 1 loads.

Fig. 4 shows the monthly variations in cooling and heating loads for locations needing the most cooling (Mumbai) and heating (Stuttgart). HVAC systems will experience the highest cooling load in May (Fig. 4(a)) and the

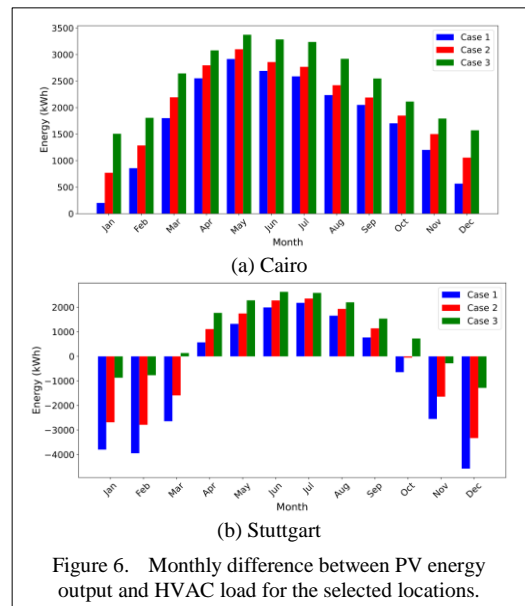


highest heating load in December (Fig. 4(b)) due to the seasonal temperature variations: May typically brings warmer weather, leading to increased cooling demands, while December, with its colder temperatures, results in higher heating requirements to ensure indoor comfort.

D. Comparison of BIPV Power Generation Potential and HVAC Loads

Predictions of the annual energy outputs of the BIPV system for the eight selected locations, are shown in Fig. 5. The highest energy output (34.577 kWh) is predicted for Cairo, while the least (20.877 kWh) is predicted for Stuttgart. Differences in the predicted outputs for different locations are mainly due to the location latitudes as the amount of incident solar radiation on the earth's surface varies widely with latitudes.

Fig. 6 shows the monthly differences between PV energy output and HVAC loads for the locations with the highest (Cairo) and least (Stuttgart) predicted PV outputs. Cairo (Fig. 6(a)) will consistently produce more PV energy than needed to maintain indoor comfort throughout the year. On the other hand, Stuttgart (Fig. 6 (b)) will experience energy deficits from October to March under Case 1 and Case 2, and from November to February under Case 3. Thus, the roof-mounted BIPV system will not be sufficient to meet the building's HVAC demand in Stuttgart's cold season, necessitating additional energy sources. Fig. 6 also reveals the expected increments in monthly surpluses and reductions in deficits as the HVAC operation



mode changes from Case 1 to Cases 2 and 3; this results from the reductions in HVAC loads in Cases 2 and 3.

Table VI presents the annual surpluses (+ve) and deficits (-ve) in PV energy output after fulfilling HVAC loads at the 8 locations for the three HVAC operation cases, along with the percentage reductions in deficits and increases in surpluses when transitioning from Case 1 to Case 3. Table VI suggests that apart from Stuttgart (Case 2), changing from Case 1 to Cases 2 and 3 will turn annual energy deficits (-ve) into surpluses for all other locations. These outcomes highlight significant energy savings that can be achieved when smart HVAC control solutions are implanted, especially for old buildings in colder regions where the alternative will be to rely on polluting fossil-based energy sources.

TABLE VI. ANNUAL SURPLUSES (+VE)/DEFICITS (-VE) IN BIPV ENERGY OUTPUT (KWH).

Location	Case 1	Case 2	Case 3
Nsukka	17129.6	19031.8 (11.1%)	23369.0 (36.4%)
Beijing	-2825.7	4648.5 (264.5%)	15877.4 (661.9%)
Sofia	-3619.6	4078.9 (212.7%)	15554.8 (529.7%)
Cairo	21368.1	24797.8 (16.1%)	29886.4 (39.9%)
Mexico City	23053.0	27144.7 (17.7%)	31572.8 (37%)
Mumbai	18718.6	20623.5 (10.2%)	25434.0 (35.9%)
Denver	-2019.0	6189.7 (406.6%)	18088.6 (995.9%)
Stuttgart	-9667.5	-1538.5 (84.1%)	10662.4 (210.3%)

E. Space Requirements for Additional BIPV to Meet Energy Deficits

The foregoing results show that the BIPV systems are unable to fully meet energy needs during certain months in Beijing, Sofia, Denver and Stuttgart (Table VI), whereas Nsukka, Cairo, Mexico City and Mumbai (Table VI) experienced all year-round energy surpluses. The extra PV peak power required to cover the deficits, and thus the additional space (m²) needed for installing additional PV generation capacity depends on the size of the energy deficit (larger deficits require more PV power). If the additional peak power requirements in the month with the highest peak demand were met, the requirements for all other months would also be met, and this month was identified to be December for all the locations. Table VII displays the peak power ratings of BIPV systems

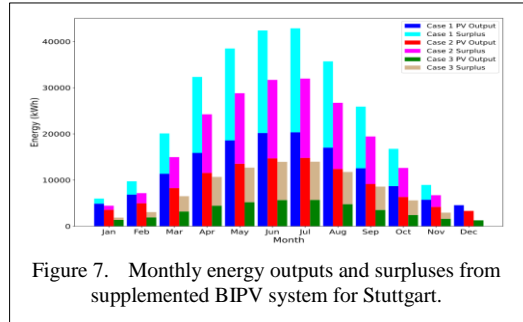


Figure 7. Monthly energy outputs and surpluses from supplemented BIPV system for Stuttgart.

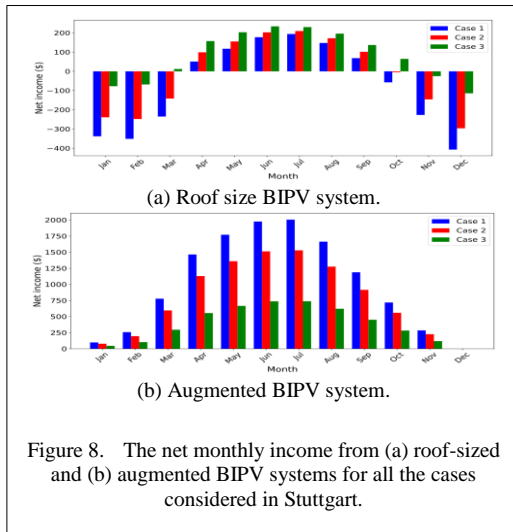
TABLE VII. PEAK POWER RATINGS(KWP) AND EXTRA AREA (M²) REQUIRED TO MEET ENERGY DEFICITS.

Location		Case 1	Case 2	Case 3
Beijing	Peak power	30.57	19.93	3.58
	Area	132.91	86.65	15.58
Sofia	Peak power	44.87	31.11	8.98
	Area	195.08	135.28	39.06
Denver	Peak power	36.71	24.84	6.53
	Area	159.61	108.01	28.41
Stuttgart	Peak power	86.73	108.01	24.32
	Area	377.10	274.57	105.73

that can meet HVAC loads at the four locations with deficits, along with the extra roof space required to accommodate these BIPV systems completely. For illustration, Fig. 7 provides a visual representation of the energy output from the additional PV modules necessary to offset the deficit for the three HVAC cases in Stuttgart, as well as the monthly energy surpluses produced. There is no surplus energy in December because the augmented PV peak power will produce the precise amount of energy needed to meet the December energy load and generate surpluses in other months.

F. Projected Incomes from Augmented BIPV Systems

By multiplying the energy deficits or surpluses by the location-specific cost of electricity per kWh, the net monthly incomes generated by BIPV systems were calculated. These are illustrated for Stuttgart in Fig. 8, from which it is observed that instead of energy expenditures between October to March when the roof-fit BIPV system will have to be supplemented with power purchased from the grid, surplus energy could be exported to the grid to earn up to USD 2,000 in July. This represents an incentive for implementing BIPV in older buildings, eliminating the high costs of maintaining indoor comfort conditions.



IV. CONCLUSION

The potential for maintaining indoor comfort in green buildings using BIPV-generated power has been investigated for eight locations under three HVAC operation scenarios. Indoor comfort was found to be sustained all year round by the BIPV systems in four locations (Nsukka, Cairo, Mexico City and Mumbai) with relatively warm climates, irrespective of the HVAC system operation mode. However, energy deficits were determined for four locations (Beijing, Sofia, Denver and Stuttgart) with colder climates. The least HVAC energy loads were projected to occur in Mexico City where indoor conditions are usually within the comfort zone for much of the year whereas the HVAC loads for Denver were the highest due to heating/cooling requirements for most of the year. The investigated BIPV system will generate the most energy in Cairo, benefiting from the high insolation levels experienced there, while the least BIPV energy output will occur in Stuttgart.

The study revealed that employing energy efficiency measures, such as eliminating HVAC operations from unoccupied spaces could lower energy usage by up to 36.78%, while introducing smart technologies for controlling HVAC operations could yield up to 76.59% reductions. Financial gains were similarly determined for the reduced-energy load cases, offering increased earnings from the surplus energy produced at the warm locations and converting energy costs to earnings in the cold locations.

ACKNOWLEDGMENT

This study was supported by the Chinese Academy of Sciences President's International Fellowship Initiative (PIFI) Grant No.: 2024VEA0011.

REFERENCES

- [1] González-Torres, M., et al. (2022). A review on buildings energy information: Trends, end-uses, fuels and drivers. *Energy Reports*, 8, 626–637.
- [2] Liu, G., Chen, H., Yuan, Y., & Song, C. (2024). Indoor thermal environment and human health: A systematic review. *Renewable and Sustainable Energy Reviews*, 191, 114164.
- [3] *World Population Prospects 2022: Summary of Results/Population Division*. (n.d.). Available at: <https://www.un.org/development/desa/pd/content/World-Population-Prospects-2022>
- [4] Boccalatte, A., Fossa, M., & Sacile, R. (2021). Modeling, Design and Construction of a Zero-Energy PV Greenhouse for Applications in Mediterranean Climates. *Thermal Science and Engineering Progress*, 25, 101046.
- [5] Hafez, F. S., et al. (2023). Energy efficiency in sustainable buildings: a systematic review with taxonomy, challenges, motivations, methodological aspects, recommendations, and pathways for future research. *Energy Strategy Reviews*, 45, 101013.
- [6] Hassan, Q., Algburi, S., Sameen, A. Z., Al-Musawi, T. J., Al-Jiboory, A. K., Salman, H. M., ... & Jaszczur, M. (2024). A comprehensive review of international renewable energy growth. *Energy and built environment*.
- [7] Aaditya, G., & Mani, M. (2013). Climate-responsive integrability of building-integrated photovoltaics. *International Journal of low-carbon technologies*, 8(4), 271-281.
- [8] González-Peña, D., García, I., Díez-Mediavilla, M., Dieste-Velasco, M., & Alonso-Tristán, C. (2021). Photovoltaic Prediction Software: Evaluation with Real Data from Northern Spain. *Applied Sciences*, 11, 5025.
- [9] Abdelrazik, A. S., et al. (2022). The recent advancements in the building integrated photovoltaic/thermal (BIPV/T) systems: An updated review. *Renewable and Sustainable Energy Reviews*, 170, 112988.
- [10] Pillai, D. S., Shabunko, V., & Krishna, A. (2022). A comprehensive review on building integrated photovoltaic systems: Emphasis to technological advancements, outdoor testing, and predictive maintenance. *Renewable and Sustainable Energy Reviews*, 156, 111946.
- [11] Bhatia, A. (n.d.). *Cooling Load Calculations and Principles Course No: M06-004 Credit: 6 PDH*. Available at: www.cedengineering.com
- [12] ASHRAE (2021) *ASHRAE Handbook-Fundamentals*. American Society of Heating, Refrigerating and Air-Conditioning Engineers, Inc.
- [13] Njoku, H. O. (2014). Solar PV Potential in Nigeria. *Journal of Energy Engineering*, 140, 4013020.

Systematic Literature Review for Recycling Cooperatives from the Perspective of Life Cycle Assessment: Interrelations and Gaps

Murilo dos Santos Oliveira¹, Julio Cesar Sales Bezerra², Andreza da Silva Santana Peruchi³,
Emerson Ribeiro Machado⁴, Raphael Abrahao⁵

^{1,2}Graduate Program in Renewable Energy, Federal University of Paraiba, Joao Pessoa, Brazil

³Department of Civil and Environmental Engineering, Federal University of Paraiba,
Joao Pessoa, Brazil

⁴Biolink soluções Estratégicas, Uberlândia, Brazil

⁵Department of Renewable Energy Engineering, Federal University of Paraiba, Joao Pessoa, Brazil

¹murilo.oliveira@estudante.cear.ufpb.br, ²julio.bezerra@estudante.cear.ufpb.br,

³deperuchi@gmail.com, ⁴emersonrm.bio@gmail.com, ⁵raphael@cear.ufpb.br

Abstract—The uncontrolled increase in solid waste worldwide is a complex issue that encompasses various environmental, social, and economic aspects. Conversely, recyclable materials cooperatives, through selective collection, represent a pragmatic and effective approach to managing this waste while promoting social inclusion and environmental protection. In this context, one possible strategic tool to aid in this endeavor is the use of Life Cycle Assessment (LCA): a methodology that evaluates the environmental impacts of a product, process, or service throughout all stages of its life cycle. Therefore, linking recycling cooperatives to this resource is essential to boost sustainable practices, optimize operations, and comply with environmental regulations, while transparently communicating their performance. Thus, the objective of this work was to conduct a comprehensive systematic review on the intersections between recycling cooperatives and LCA, aiming to understand the current landscape of knowledge, identify research gaps, and explore synergies between these two fields. The research methodology was based on a systematic literature review, combining bibliometrics and content analysis. Consequently, a portfolio containing 53 articles focusing on themes related to recycling cooperatives was created. The results showed that only 12% of these works relate to LCA, suggesting

a vast field for future research. Furthermore, the central focus of these resulting articles is divided among the following themes: GHG emissions and other pollution (29%), sorting of recycled materials (29%), costs involved in the recycling process (14%), occupational exposure (14%), and waste management (14%).

Keywords – sustainability, circular economy, selective collection, solid waste

I. INTRODUCTION

A greater amount of solid waste, exacerbated by urban development and accelerated consumption habits, increases environmental and climate impacts, since during the process of waste decomposition, methane gas, carbon dioxide and nitrous oxide, also known as CH₄, CO₂ and N₂O, are emitted. This accumulation of waste affects the ecosystem and public health, becoming a risk factor by protecting vectors and proliferating diseases [1,2].

In this way, recyclable materials cooperatives emerge as a type of central actor in the search for effective and sustainable responses. The role of such cooperatives is vital, since they are closely associated with the practice of selective collection, considered a fundamental practice for reducing waste and saving natural resources. In



this sense, they are an integral part of the recycling chain and act opportunistically by creating environmental and, in many cases, social value, involving members of local communities who, on the other hand, may face unemployment [3].

Even with great transformative potential, these cooperatives still have to contend with many accessible challenges. Inadequate infrastructure, lack of funding and difficulty accessing markets are just some of the problems these organizations face [4]. At the same time, the lack of adequate public policies and a constant struggle for institutional recognition, among other obstacles, continue to make sustainability and expansion difficult.

In this context, emerging as a strategy, Life Cycle Assessment (LCA) is a methodology that, throughout the stages of a product, process or service life cycle, examines the related environmental impacts. This analysis covers production, transportation, use and disposal, taking into account the natural resources used, pollutant emissions and waste generated. Therefore, from the above, LCA allows the assessment of all the significant environmental impacts of a system throughout its life, thus obtaining a more comprehensive perspective which, as mentioned by [5] could be used to help make more sustainable decisions.

For these reasons, it is crucial to connect studies involving recycling cooperatives to the LCA approach in order to obtain detailed information on the environmental impact of recycling operations and thus guide decision-making in waste management. By applying this methodology to the operations of a recycling cooperative, it is possible to describe and quantify the environmental impacts associated with the stages of collecting, sorting, processing and redistributing recycled materials. Described in this way, it will provide a comprehensive idea of how the cooperative is doing environmentally and where it needs to improve and optimize its operations. It can also make it less complicated for the cooperative to make its decisions, prioritizing efforts on reducing potential environmental impact.

Thus, with the aim of mapping the intersections of recycling cooperatives with LCA, a comprehensive review was carried out to assess the state of current knowledge, identify research gaps and, furthermore, investigate possible synergies in these areas.

II. METHODOLOGY

The study was structured in four stages. The first stage consisted of choosing the database and software. The search platform was the CAPES journal portal, using the Scopus database. Scopus contains high-impact academic articles and journals from various disciplines and fields, as well as being a widely used source of citation information worldwide [6].

The VOSviewer software [7], running on Java version 9, was used to process the data obtained. This is a tool commonly used in scientific research, especially in fields such as bibliometrics and information science. The software was chosen because it is an open-source program and includes the formats of the main academically consolidated databases. Using VOSviewer, it was possible to identify patterns of co-occurrence between the keywords of the publications analyzed. Microsoft Excel was also used to organize and manage the data, facilitating the manipulation and quantitative analysis of the information collected.

The second stage involved defining the terms to be searched for in the database (string) and then collecting the data from Scopus. Limited to articles published in English and defined as full or review articles published in journals, the following string was used: TITLE-ABS-KEY (“selective collection” OR “recycling” OR “selective waste collection”) AND (“recycling cent*” OR “recycling facility” OR “cooperative” OR “collector*”) AND (“LIFE CYCLE” OR “EMISSION*” OR “CARBON FOOTPRINT*” OR “LCA” OR “ENVIRONMENT* IMPACT*”). Thus, the search was carried out for these terms in the titles, abstracts and keywords of scientific articles in February 2024, with no time restriction on the initial period of the search.

In order to limit the number of documents obtained, they were read, as in step three. To do this, the Mendeley reference manager [8] was used, in which an initial screening of the research was carried out in order to dissociate divergent themes. At the same time, folders were created within the platform to group together articles dealing with similar themes.

The fourth stage comprises the processing and bibliometric analysis of the data resulting from stage three. After tabulating the data obtained (authors, affiliation, demographic region, etc.), analysis and mapping were carried

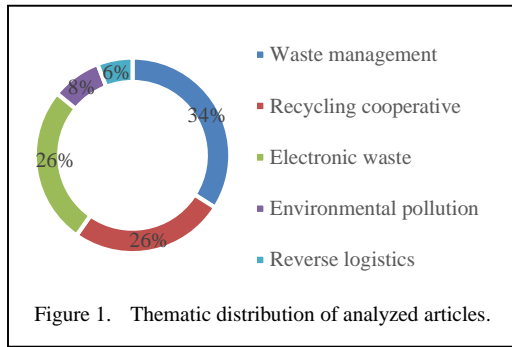


Figure 1. Thematic distribution of analyzed articles.

out, examining co-authors, co-citations, bibliographic links, and keyword co-occurrence networks.

III. RESULTS AND DISCUSSION

The search in the Scopus database, using the string defined in the methodology, resulted in the detection of 486 publications, of which 453 were articles (93.2%) and 33 reviews (6.8%). After reading the papers, in order to restrict them to the proposed topic, a total of 275 articles on different topics were discarded, leaving 211.

In order to select articles related to recycling cooperatives, the decision was made to include all papers that addressed the topic, regardless of their specific focus. This approach sought to broaden the range of studies analyzed, allowing for a more comprehensive and multifaceted view of the subject. In this way, different aspects can be observed, from operational and social aspects to economic and environmental challenges, ensuring a solid basis for discussing the role of cooperatives in the context of waste management. As a result, 54 articles focusing on recycling cooperatives were selected. The remaining articles addressed other relevant themes, namely: waste management (71), electronic waste (55), environmental pollution

(18), and reverse logistics (13), as illustrated in Fig. 1.

According to the presented data, it is observed that 34% of the articles are related to the broader theme of waste management. This significant portion indicates a trend in the scientific literature towards this field of study, reflecting the importance and relevance of proper waste management in global contexts of sustainability and environmental preservation.

The fractions related to recycling cooperatives and electronic waste account for 52% of the total, indicating a significant prioritization in these areas. This demonstrates a conscious commitment to activities involving the collection, sorting, processing, and recycling of materials, including electronic waste. This focus reflects the growing concern with the proper disposal of obsolete electronic equipment, which often contains toxic and polluting materials, requiring specific approaches for treatment and recycling.

Fig. 2 shows that the production of scientific articles involving the topics highlighted grew between 1989 and 2023. It is observed that publications focused on waste management remained intermittent throughout the analyzed period. On the other hand, the theme of electronic waste gained prominence in the last four years, peaking at 16 publications in 2023, revealing a growing research interest in the area. Investigations related to recycling cooperatives began in the late 1990s and progressed gradually, with a more significant expansion in 2022, when 10 publications on the topic were recorded.

Considering the purpose of this study, a bibliographic portfolio consisting of 54 articles focused on research on recycling cooperatives

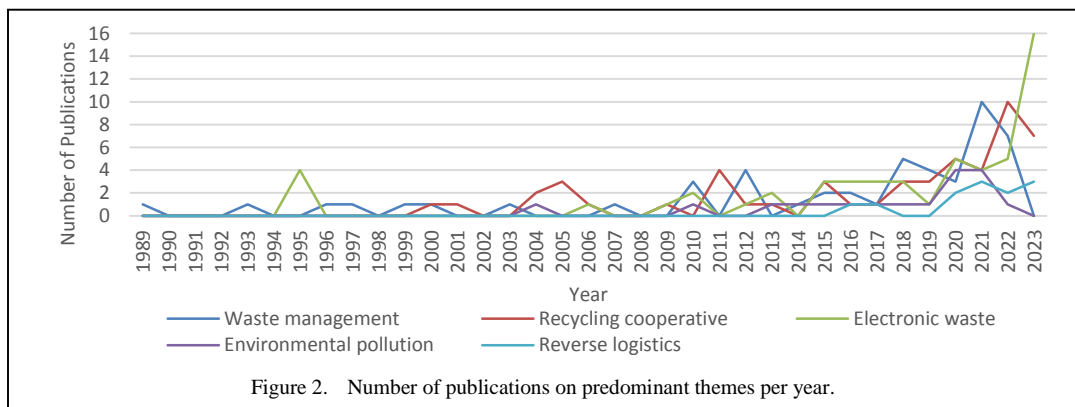


Figure 2. Number of publications on predominant themes per year.

was established. The journal “Waste Management” stood out in terms of the number of related research articles, holding 11 articles from 2004 to 2023. Among them, the most scientifically recognized article is authored by [9] from Switzerland, with 113 citations. Other prominent journals, each with three publications, include “Waste Management and Research,” “Journal of Cleaner Production,” “Journal of Hazardous Materials,” and “Science of the Total Environment.” The remaining articles are each linked to a single journal.

Regarding the geographical distribution of the studies, the 54 articles in the portfolio are derived from studies conducted in 25 countries (Fig. 3). The United Kingdom had the highest concentration of studies, totaling six publications. Among them, the most cited work is by researchers [10], with 27 citations. Following this, with four articles each, are Brazil, China, and the United States. The publication with the highest scientific recognition is by author [11] from Australia, with 439 citations.

The software VOSviewer, version 1.6.20, was used for the co-occurrence analysis of keywords based on the cluster concept, where keywords with similarities or common characteristics are represented by the same color group. Additionally, by the size of the node, it is possible to identify the most frequently occurring keywords, and the possibility of combining them with supplementary data helps identify gaps in the research.

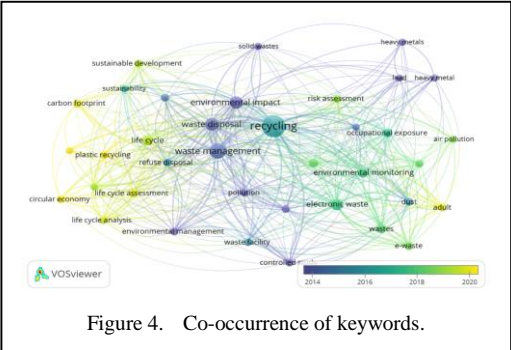


Figure 4. Co-occurrence of keywords.

According to the mapping performed, it is observed that the most prominent keyword is “recycling,” situated close to proportionally frequent words: “waste disposal,” “waste management,” and “environmental impact,” indicating the inextricable link between cooperatives and solid waste management and environmental issues (Fig. 4). According to [2], after evaluating the impact of recycling in reducing greenhouse gas (GHG) emissions through a waste picker cooperative, its significant contribution to gas reduction and energy savings was verified.

The frequent occurrence of the terms “risk assessment,” “occupational risks,” and “occupational exposure” demonstrates concern about the development of studies related to the health and well-being of waste pickers. According to researchers, collection activities are associated with a range of hazardous exposures (through contact with heavy metals, sharp and infected materials), which can result in respiratory diseases, eye infections, stomach

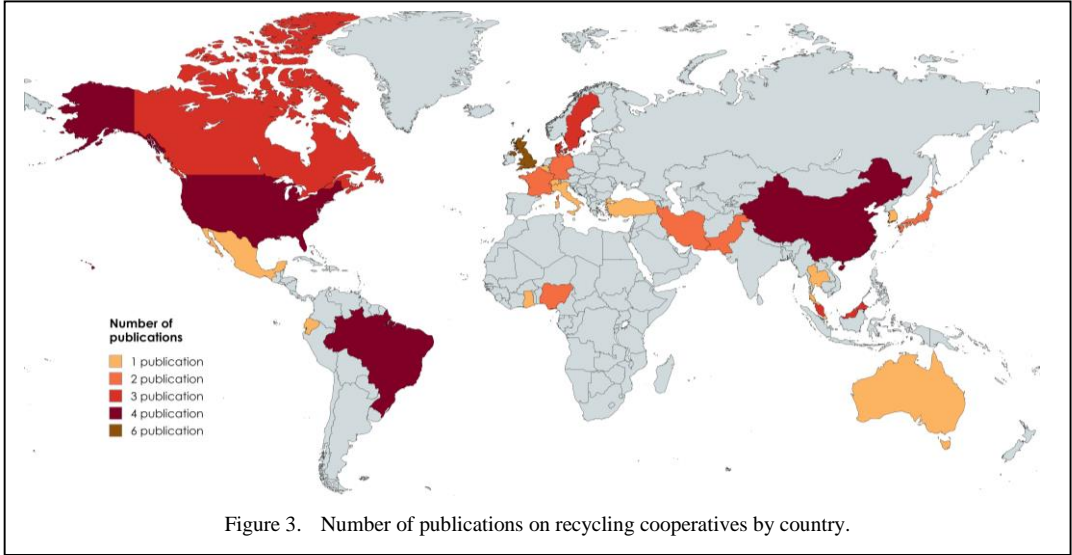


Figure 3. Number of publications on recycling cooperatives by country.

problems, typhoid fever, diarrhea, musculoskeletal disorders, carcinogenic effects, and other diseases, accidents, mutilations, and even deaths [12-15].

It is important to highlight that in 2010, Brazil enacted the National Solid Waste Policy, established by Law No. 12,305/10 [16], which aims to incorporate waste pickers as key players in the sustainable management of waste. This provides recognition, social and economic inclusion, values the work of these professionals, and significantly contributes to environmental preservation.

It is also observed, through the yellow cluster in Fig. 4, that some terms used in more recent publications have gained prominence in the last four years, such as: “life cycle analysis,” “cycle assessment,” and “circular economy.” While LCA proves to be a crucial tool in environmental management, allowing a comprehensive and systematic evaluation of the environmental impacts associated with a product, process, or activity, circular economy proposes a strategic context to promote sustainability through efficient resource management. Relating these terms to studies on recycling cooperatives may indicate that they are increasingly being incorporated into how companies operate, how governments make policies, and even how researchers direct their studies.

Terms such as “waste” and “electronic waste” have also gained prominence. In this context, [17] indicated that in France, approximately 1.5 billion batteries were sold in 2019, representing 273,000 tons of electronic material to be discarded. The study of the impact of electronic waste dismantling and recycling activities on contamination by brominated flame retardants (BFR) has been conducted in various regions of Asia and Africa, with China being the most extensively researched area in this context [18,19].

Within the analyzed portfolio, there is also a clear concern to highlight some issues related to the physical infrastructure of cooperatives. In Sweden, researchers [20] list a variety of problems, such as: visitor queues, material overload, and inadequate sorting. On the other hand, in Pakistan, there are no formal recycling facilities, and the process occurs informally, without any guidelines or safety measures [21,22]. The authors' approach to issues related to recycling cooperative facilities, as well as associated costs, working conditions of waste

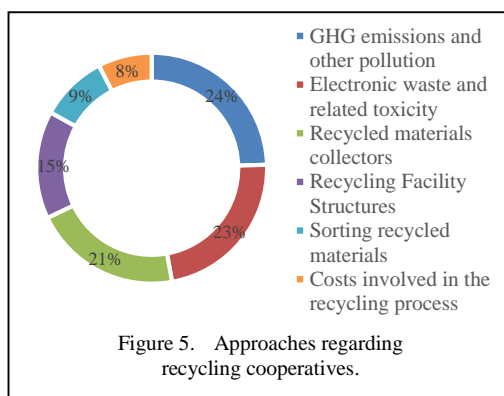


Figure 5. Approaches regarding recycling cooperatives.

pickers, and the impact of related activities, is detailed in Fig. 5.

By identifying GHG emissions as a priority area for research and intervention, it is evident that the authors are recognizing the need to address measures to minimize this environmental impact through recycling activities. Within this scope, some researchers address other forms of environmental pollution. For example [23], when comparing plastic recycling systems, highlight some impacts on climate change. On the other hand [24], discuss an action plan to reduce emissions of metallic aerosols from metal recycling facilities.

According to the research, twenty-three percent of the articles find an interconnection between recycling cooperatives and electronic waste management, which shows the importance of finding solutions to this increasing problem of e-waste, particularly in terms of the safe disposal of hazardous materials such as lead, copper, cobalt, barium, arsenic, cadmium, chromium, iron and nickel [25]. The least represented segments of the graph are connected with some particular internal matters of the cooperatives, such as the arrangement and configuration of their physical infrastructure, the actual sorting of materials content, and the costs incurred in their activities.

The studies which systematically looked for links between recycling cooperatives and the LCA methodology have been presented in Table I. These seven articles published representing only 12% of the publications published between 2015 and 2022. Such scarcity may be an implicit indicator that this approach has not been researched widely, and therefore not many people are aware of its usefulness and advantages. It is important to point out that cooperatives can leverage these tools to pinpoint

TABLE I. ARTICLES ABOUT RECYCLING COOPERATIVES RELATED TO LCA.

	References	Title	Periodic	Approach
1	[23]	Comparing the environmental performance of distributed versus centralized plastic recycling systems: Applying hybrid simulation modeling to life cycle assessment	Journal of Industrial Ecology	Environmental impacts
2	[29]	Occupational exposure to hazards and volatile organic compounds in small-scale plastic recycling plants in Thailand by integrating risk and life cycle assessment concepts	Journal of Cleaner Production	Occupational exposure of collectors
3	[30]	Application of a life cycle assessment for assessing municipal solid waste management systems in Bolivia in an international cooperative framework	Waste Management and Research	Waste management
4	[28]	The potential benefits of introducing informal recyclers and organic waste recovery to a current waste management system: The case study of Santiago de Chile	Resources	Environmental impacts
5	[26]	Combustible waste collected at Danish recycling centres: Characterisation, recycling potentials and contribution to environmental savings	Waste Management	Sorting recycled materials
6	[27]	Environmental life cycle cost assessment: Recycling of hard plastic waste collected at Danish recycling centres	Resources, Conservation and Recycling	Costs involved
7	[9]	Life cycle assessment of post-consumer plastics production from waste electrical and electronic equipment (WEEE) treatment residues in a Central European plastics recycling plant	Science of the Total Environment	Sorting recycled materials

the areas in which they need to improve on the detrimental effects they posed on the environment. This can lead to better collection routes, use of energy and water-efficient technologies, and reduction of wastes in the recycling operations.

Among the articles listed in Table I, the work with the highest scientific recognition is attributed to the Swiss authors [9], who have received 113 citations. The article uses the LCA approach to estimate the environmental effects associated with the recycling process of shredded electronic waste, which contains a significant amount of plastics from the treatment operations of electrical and electronic equipment waste. Also noteworthy are the Danish authors [26,27], who, through two articles published in 2019, conducted studies on waste sorting and associated costs using the LCA method.

It is observed that the use of LCA covers various aspects related to recycling cooperatives, with emphasis on the sorting of recyclable materials and environmental impacts (two articles each), as well as associated costs, occupational exposure of waste pickers, and

waste management (one article each). Regarding environmental impacts, [28] address the analysis of the environmental effects of different viable options for the collection, treatment, and recovery of urban solid waste using LCA. Meanwhile, [22], using this approach, highlight the environmental effects of plastic recycling systems, such as climate change and soil ecotoxicity.

Recycling cooperatives face several barriers in adopting LCA. Among the main difficulties are high costs, since the implementation of LCA requires significant financial resources for the acquisition of tools, software and specialized consultancies, and is more widely used in high-income countries [31]. This scenario is due to the need for high technical expertise, prior knowledge about the existence of this management tool and financial resources to acquire specialized software, which are fundamental for carrying out complete LCA studies. In addition, the models created in different countries depend on specific geographical data, which directly impacts the results of waste-related life cycle analysis [32].

The methodology is quite useful in tapping into areas that are now receiving little scientific attention such as environmental impacts and decision making. According to [26], this methodology offers a wider scope on evaluating environmental impacts of such systems such as waste management. This analysis strengthens decision-making as it improves understanding of environmental performance, and the results of employing varied waste management strategies.

Furthermore, LCA can also be beneficial when marketing the environmental achievements of recycling cooperatives to relevant stakeholders including customers, suppliers, and policymakers. Environmental transparency and management can increase the community trust and the trustworthiness of the cooperative.

VI. CONCLUSIONS

As a result of the bibliometric review on the available literature that concerns recycling cooperatives and the LCA methodology, it can be deduced that there are not many studies which link those terms. Only 12 % of the articles that are found in the search have connection to both of those problems. This is clearly an under-research gap and more importantly, understanding and awareness of this particular methodology and its importance to recycling cooperatives is quite low.

Nonetheless, even with those challenges, it is necessary to highlight the opportunities that a LCA approach can bring for the recycling cooperatives. It can be expected that the demand and researches on this subject will also increase in the coming times as the subject of this approach relates to enhancement of operational efficiency, lowered environmental effects, and improved clarity in communication.

Thus, establishing a connection between recycling cooperatives and life cycle assessment methodology is crucial to driving the adoption of more sustainable practices, improving operational efficiency, and ensuring compliance with environmental standards. Additionally, this approach encourages communication about the group's environmental performance, strengthening trust and commitment to environmental protection.

To promote the use of LCA, collaboration between recycling cooperatives, governments and academia is crucial. Governments can offer financial incentives, while academia can develop

tools adapted to cooperatives. Capacity building through training and university extension programs is also key. In addition, participatory approaches, with the involvement of cooperatives in planning and dialog forums, ensure that solutions are practical and effective. These joint efforts make the implementation of LCA more accessible and beneficial for cooperatives and for environmental sustainability.





In order to deepen the integration of LCA in recycling cooperatives, some propositions can be investigated, exploring different dimensions of this relationship. Among the main questions are: what are the environmental and economic benefits generated by the application of LCA in the operations of recycling cooperatives; how can the operational specificities of these organizations be translated into reliable inventories for LCA studies; and what financing models or partnerships would be most effective to enable the adoption of this methodology in cooperatives.

REFERENCES

- [1] Zolnikov, T. R., Silva, L. G. T., Marques, A., Cadena, M., & Rebelo, S. (2018). Ineffective waste site closures in Brazil: A systematic review on continuing health conditions and occupational hazards of waste collectors. *Waste Management*, 80, 26-39.
- [2] Mesquita, J. L. C., Cunha, J. F., & Monteiro, T. R. (2023). Greenhouse gas emission reduction based on social recycling: A case study with waste picker cooperatives in Brasília, Brazil. *Sustainability*, 15(12), 9185.
- [3] Dias, S. M., & Alves, F. C. G. (2008). Integration of the informal recycling sector in solid waste management in Brazil. Study prepared for GTZs sector project "Promotion of concepts for pro-poor and environmentally friendly closed-loop approaches in solid waste management."
- [4] Gutberlet, J. (2016). *Recovering resources-recycling citizenship: Urban poverty reduction in Latin America*. Routledge.
- [5] Laurent, A., et al. (2014). Review of LCA studies of solid waste management systems—Part II: Methodological guidance for a better practice. *Waste Management*, 34(3), 589-606.
- [6] Wang, Q., & Waltman, L. (2016). Large-scale analysis of the accuracy of the journal classification systems of Web of Science and Scopus. *Journal of Informetrics*, 10(2), 347-364.
- [7] Van Eck, N. J., & Waltman, L. (2020). *VOSviewer manual: Manual for VOSviewer version 1.6.15*. Leiden: Centre for Science and Technology Studies (CWTS) of Leiden University.
- [8] Mendeley Desktop. (2008). *Mendeley* Ltd. Available at: <https://www.mendeley.com>

- [9] Wäger, P. A., & Hischier, R. (2015). Life cycle assessment of post-consumer plastics production from waste electrical and electronic equipment (WEEE) treatment residues in a Central European plastics recycling plant. *Science of the Total Environment*, 529, 158-167.
- [10] Speirs, D., & Tucker, P. (2001). A profile of recyclers making special trips to recycle. *Journal of Environmental Management*, 62(2), 201-220.
- [11] Chi, X., Streicher-Porte, M., Wang, M. Y., & Reuter, M. A. (2011). Informal electronic waste recycling: A sector review with special focus on China. *Waste Management*, 31(4), 731-742.
- [12] Gutberlet, J., & Baeder, A. M. (2008). Informal recycling and occupational health in Santo André, Brazil. *International Journal of Environmental Health Research*, 18(1), 1-15.
- [13] Mol, M. P. G., Silva, M. C., & Gonçalves, M. E. (2017). Assessment of work-related accidents associated with waste handling in Belo Horizonte (Brazil). *Waste Management & Research*, 35(10), 1084-1092.
- [14] Chokhandre, P., Singh, S., & Kashyap, G. C. (2017). Prevalence, predictors and economic burden of morbidities among waste-pickers of Mumbai, India: a cross-sectional study. *Journal of Occupational Medicine and Toxicology*, 12(1), 1-8.
- [15] Jayakrishnan, T., Jeeja, M. C., & Bhaskar, R. (2013). Occupational health problems of municipal solid waste management workers in India. *International Journal of Environmental Health Engineering*, 2(1), 42.
- [16] Brasil. (2010). *Lei nº 12.305, de 2 de agosto de 2010. Institui a Política Nacional de Resíduos Sólidos. Diário Oficial da União*. Available at: https://www.planalto.gov.br/ccivil_03/_ato2007-2010/2010/lei/12305.htm
- [17] Hanser, O., Darracq, V., De Broucker, V., Abadie, E., & Marquet, P. (2022). Occupational exposure to metals among battery recyclers in France: biomonitoring and external dose measurements. *Waste Management*, 150, 122-130.
- [18] Ma, Y., Tang, X., Zhang, L., Cheng, H., & Li, X. (2021). Human exposure to halogenated and organophosphate flame retardants through informal e-waste handling activities - A critical review. *Environmental Pollution*, 268, 115727.
- [19] Ma, Y., Tang, X., Cheng, H., Zhang, L., & Li, X. (2022). Formal waste treatment facilities as a source of halogenated flame retardants and organophosphate esters to the environment: A critical review with particular focus on outdoor air and soil. *Science of the Total Environment*, 807, 150747.
- [20] Sundin, E., Jönsson, C., & Helander, A. (2011). Improving the layout of recycling centres by use of lean production principles. *Waste Management*, 31(6), 1121-1132.
- [21] Iqbal, M., et al. (2017). E-waste driven pollution in Pakistan: the first evidence of environmental and human exposure to flame retardants (FRs) in Karachi City. *Environmental Science & Technology*, 51(23), 13895-13905.
- [22] Umair, S., Anderberg, S., & Potting, J. (2016). Informal electronic waste recycling in Pakistan. *The Journal of Solid Waste Technology and Management*, 42(3), 222-235.
- [23] Kerdlap, P., Gheewala, S. H., & Bonnet, S. (2022). Comparing the environmental performance of distributed versus centralized plastic recycling systems: applying hybrid simulation modeling to life cycle assessment. *Journal of Industrial Ecology*, 26(1), 252-271.
- [24] Symanski, E., Juarez-Carrillo, P. M., & Hopkins, L. O. (2023). Data to action: community-based participatory research to address concerns about metal air pollution in overburdened neighborhoods near metal recycling facilities in Houston. *Environmental Health Perspectives*, 131(6), 067006.
- [25] Kumari, H., & Yadav, S. (2023). A comparative study on metal pollution from surface dust of informal and formal e-waste recycling sectors in national capital region of New Delhi and associated risk assessment. *Science of the Total Environment*, 904, 166791.
- [26] Faraca, G., Boldrin, A., & Astrup, T. (2019). Combustible waste collected at Danish recycling centres: Characterisation, recycling potentials and contribution to environmental savings. *Waste Management*, 89, 354-365.
- [27] Faraca, G., Martinez-Sanchez, V., & Astrup, T. F. (2019). Environmental life cycle cost assessment: Recycling of hard plastic waste collected at Danish recycling centres. *Resources, Conservation and Recycling*, 143, 299-309.
- [28] Rojas, A., Duarte, J., & Zambrano, L. (2018). The potential benefits of introducing informal recyclers and organic waste recovery to a current waste management system: The case study of Santiago de Chile. *Resources*, 7(1), 18.
- [29] Ansar, M. A., Jamsawang, P., Suwanprasisit, C., Kamphonsai, N., & Khummongkol, P. (2021). Occupational exposure to hazards and volatile organic compounds in small-scale plastic recycling plants in Thailand by integrating risk and life cycle assessment concepts. *Journal of Cleaner Production*, 329, 129582.
- [30] Ferronato, N., Torretta, V., Ragazzi, M., & Rada, E. C. (2020). Application of a life cycle assessment for assessing municipal solid waste management systems in Bolivia in an international cooperative framework. *Waste Management & Research*, 38(1), 98-116.
- [31] Khandelwal, H., Jain, S., & Choudhary, A. (2019). Application of life cycle assessment in municipal solid waste management: A worldwide critical review. *Journal of Cleaner Production*, 209, 630-654.
- [32] Gentil, E. C., Christensen, T. H., & Aoustin, E. (2010). Models for waste life cycle assessment: Review of technical assumptions. *Waste Management*, 30(12), 2636-2648.

Modeling and Simulation of the Light Water Nuclear Small Modular Reactor CAREM-25 with OpenMC Code

Karima Ziche¹, Amira Guessoum², Salah Eddine Bentridi³, Naima Amrani⁴

^{1,2,4}Ferhat ABBAS University, Setif, Algeria

³Khemis Miliana University, Ain Defla, Algeria

¹karimazh93@gmail.com, ²Maria.fievre@gmail.com, ³s.bentridi@univ-dbk.m.dz,

⁴naima.maiza@univ-setif.dz

Abstract—The idea of an integrated Small Modular Reactor (SMR) is not new, but has recently been revisited in today's energy context. SMRs are defined as nuclear reactors that produce 10 to 300 MWe of electrical output power. According to the publications of the International Atomic Energy Agency (IAEA), the use of this type of reactor has attracted the attention of many developed countries. According to the current situation, small and medium-sized reactors are in different stages of planning, approval and construction. Many technologies have been proposed, including the inherent concept of the widely used pressurized water reactor. The purpose of this study is to model and simulate a PWR-like SMR model using the OpenMC code. The Argentinian CAREM-25 reactor is studied within the framework of a neutronic analysis of a configuration with standard fuel made from metallic UO₂. Neutron flux, reaction rates and neutron spectrum of the reactor are obtained through OpenMC simulations.

Keywords - SMR, OpenMC, CAREM-25, neutronic, simulation

I. INTRODUCTION

The trend towards small integrated reactors has become more popular worldwide in recent years. Currently, numerous nations, including Canada, China, France, India, Italy, Japan, South Korea, the Russian Federation, South Africa, the United States and Argentina are conducting extensive researches on this kind of reactors [1].

The Argentinian project CAREM-25 reactor aimed to achieve the development, design and construction of an innovative, simple and small Nuclear Power Plant as well as energy production [2]. This project is coordinated by Argentina's National Atomic Energy Commission (CNEA) in collaboration with leading nuclear companies in Argentina to construct the first prototype designed to generate an electrical power of 25 MWe. The CAREM-25 is a small integrated PWR reactor type based on LWR technology [3,4] with a hexagonal geometry. It uses a modular approach, allowing flexible installation in remote areas, and its design incorporates intrinsic safety features and uses enriched uranium as fuel. The reactor operates under pressure with water as moderator and refrigerant.

This work focuses on modelling this reactor using the open-source code OpenMC, developed initially by researchers from CRPG at MIT since 2011, as part of a project to develop scalable parallel algorithms for future exascale supercomputers. It is relatively young Monte Carlo particle transport code [5,6]. The OpenMC simulations allowed us to obtain the relevant neutronic parameters of the core: Multiplication factor, Distribution of neutron flux, and the flux spectrum, neutron flux profiles.



II. METHODOLOGY

A. Physical and Geometrical Model

In this study, the CAREM-25 reactor is analyzed using OpenMC functions which by defining the geometry and materials involved in the design of the reactor core. Initially, we need to describe all materials used to build our reactor core [7]. Both Tables I and II give the needed characteristics to introduce the material definition of pincell, fuel assembly (FA), and finally the reactor core [8,9].

Two types of fuels are used, according to the U235 enrichment fraction, namely 1.8% and 3.1%. Besides that, Burnable Poison Rods (BPRs) made from a mixture of natural Uranium UO_2 and Burnable Poison Gadolinia Gd_2O_3 are also used in some of FAs (see Fig. 1). Each hexagonal FA contains 108 fuel rods, and according to the type of the used fuel and presence or not of BPRs, it is possible to differentiate four (4) main families of FA arranged as shown in Fig. 2.

Two families of FA configurations did not include BPRs. Only one central FA with enriched uranium fuel at 1.8% (light green) is used, and 18 FAs with enriched uranium fuel at 3.1% (light red) as shown in Fig. 2. While, two families with BPRs and the same U-enrichment of 3.1% are used in the core configuration. The first one is made with 6 BPRs (light red), and the second one is made with 12 BPRs (yellow).

As shown in Fig. 1, CAREM-25 core consists of 61 hexagonal FAs, each one contains 108 fuel pins (with 1.4 m active length). Each FA is introduced in the OpenMC code as follows:

- FA1800: 01 FA made with enriched uranium at 1.8% without BP rods. It contains 108 fuel rods, 18 thimble guides and 1 instrumentation guide.
- FA3100: 18 FAs made with enriched uranium at 3.1% without BP rods. Similarly, it contains 108 fuel rods, 18 thimble guides and 1 instrumentation guide.
- FA3106: 30 FAs, with enriched uranium at 3.1%. It contains 102 fuel rods, 06 BPRs, 18 thimble guides, 1 instrumentation guide.
- FA3112: 12 FAs, with enriched uranium at 3.1%. It contains 96 fuel rods, 12

BPRs, 18 thimble guides, and one instrumentation guide.

The reactor core of CAREM-25 is moderated and cooled with pressurized light water with a density of $0.706 [g/cc]$ considered at operating

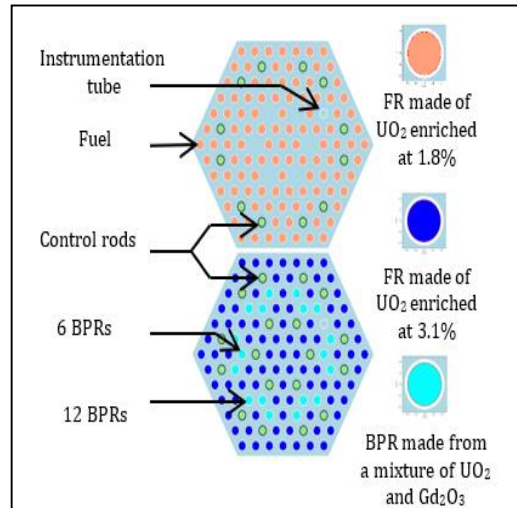


Figure 1. Configuration of CAREM-25 assemblies.

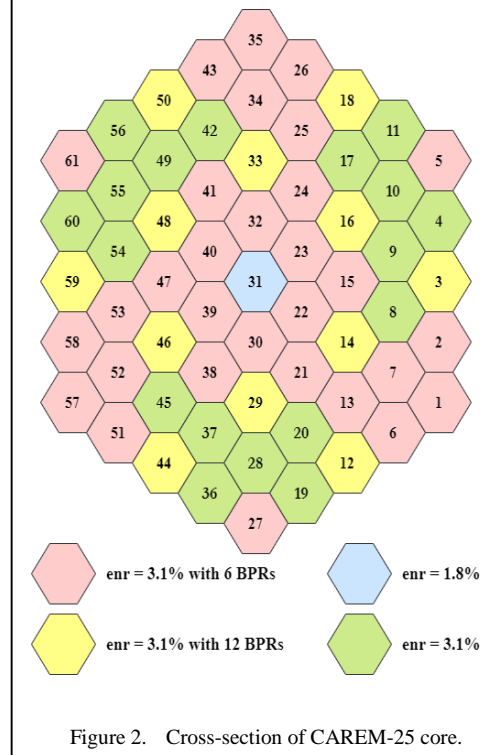


Figure 2. Cross-section of CAREM-25 core.

TABLE I. CHARACTERISTICS OF THE REACTOR CORE ELEMENTARY COMPONENTS.

Parameters	Fuel rods			Control rods		Instrumentation tube
	Fuel	Gap	Cladding	Absorbent	Cladding	
Outer radius (cm)	0.38	0.3875	0.4500	0.35	0.425	0.450
Density (g/cm ³)	10.412	0.166e-3	6.56	10.0775	8	--

TABLE II. CHARACTERISTICS OF CAREM-25 CORE REACTOR.

Parameters	Value
Electrical power (MWe)	25
Fuel Assembly geometry	hexagonal
Active length of fuel assemblies (cm)	140
Number of assemblies	61
Number of fuel rods per assembly	108
Number of guide tubes	18
Number of instrumentation tubes	1
<i>Fuel rod</i>	
Fuel composition 1 Fuel1 enrichment (%)	UO ₂ 1.8
Fuel composition 2 Fuel2 enrichment (%)	UO ₂ 3.1
Fuel composition 3	UO ₂ + Gd ₂ O ₃
Cladding material	Zry-4 (O, Cr, Fe, Zr, Sn, Hf)
Gap	He
<i>Control rod</i>	
Absorbent	Ag-In-Cd
Cladding material	AISI 316 L (C, Si, P, S, Cr, Mn, Fe, Ni, Mo)
Coolant/ moderator	Light water

temperature around 3000 °C and a pressure of 12[MPa].

After the definition of the reactor core materials, the geometry of the core is defined by including the detailed pincell (fuel pin, gap, cladding, and moderator), hexagonal fuel assembly configurations, and the whole core

with surrounding water of the Primary Vessel, according (see Table I and II) [7-9].

Once the model is correctly built, we can perform criticality calculation for the different fuel assemblies. Besides that, using suitable tallies it will be also possible to obtain different neutronic parameters such as the neutron flux

TABLE III. MCNP5 AND OPENMC COMPARATIVE OF CRITICALITY CALCULATIONS AT DIFFERENT LEVELS.

	<i>MCNP5/X</i>	<i>OpenMC (0.15)</i>
Pincells		
	$k_{\infty} \pm \sigma$	$k_{\infty} \pm \sigma$
UO2 (1.8%)	1.21508±0.00038	1.21389±0.00069
UO2 (3.1%)	1.37640±0.00039	1.37475±0.00062
Fuel assemblies		
FA18BP00	1.14151±0.00031	1.14274±0.00056
FA31BP00	1.32161±0.00041	1.31934±0.00061
FA31BP06	1.12334±0.00044	1.12253±0.00063
FA31BP12	0.95819±0.00048	0.95667±0.00062
Reactor Core		
	$k_{eff} \pm \sigma$	$k_{eff} \pm \sigma$
50%ACR 10%SCR	1.00027±0.00035	1.00035±0.00008

distribution over the whole core and some relevant reaction rates (fission and capture).

B. CAREM-25 Reactor Core

Fig. 3 depicts the CAREM-25 configuration based on the available control rods (CR) -made from neutron absorber materials such as silver, cadmium, and indium-- used to adjust the core reactivity. They are divided into two main groups: Adjustment Control Rods (ACRs) and Safety Control Rods (SCRs) used to urgent shutdown of the reactor. The control system is used to control reactivity during normal operation and to suddenly interrupt the core chain if necessary [10].

III. RESULTS

This work investigates the neutronic analysis of the CAREM-25 SMR by using OpenMC code. Therefore, multiplication factor is calculated using 700000 neutrons by cycle, with 300 active batches and 100 inactive batches. In addition, the reactor's criticality is determined with insertion of 10% of safety control rods and 50% of adjustment control rods. The first results of criticality calculation at different levels of the model: pincell, fuel assembly and whole core, allowed the validation of the OpenMC model with a good accuracy when compared to MCNP simulation as shown in Table III.

On the other hand, to complete this neutronic study, OpenMC functions to score neutrons data: Tallies are used to score neutrons spectrum, neutron flux distribution and profiles. Besides that, it is also possible to obtain the relevant reaction rates and deduce thermal power distribution. In the preliminary version of this

work discussed in the present paper, and as shown in Fig. 4, the neutron spectrum of the

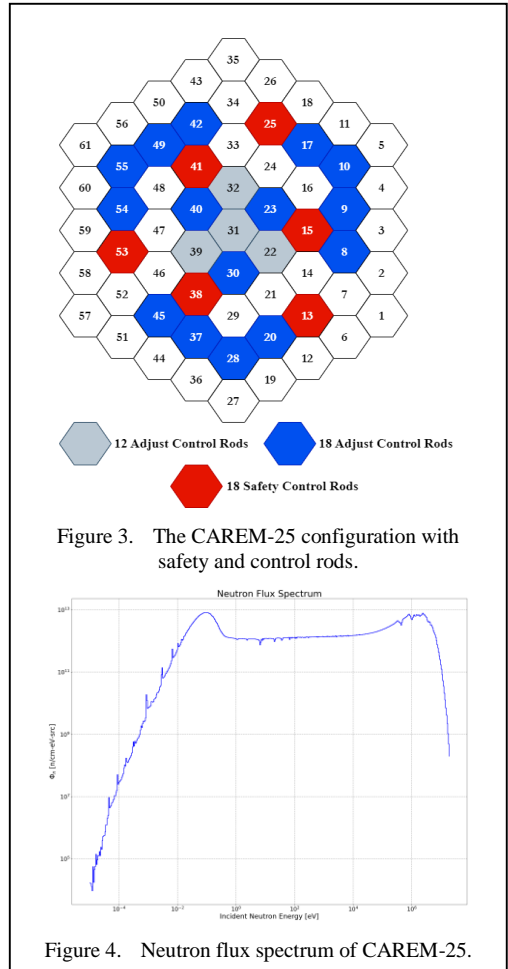


Figure 4. Neutron flux spectrum of CAREM-25.

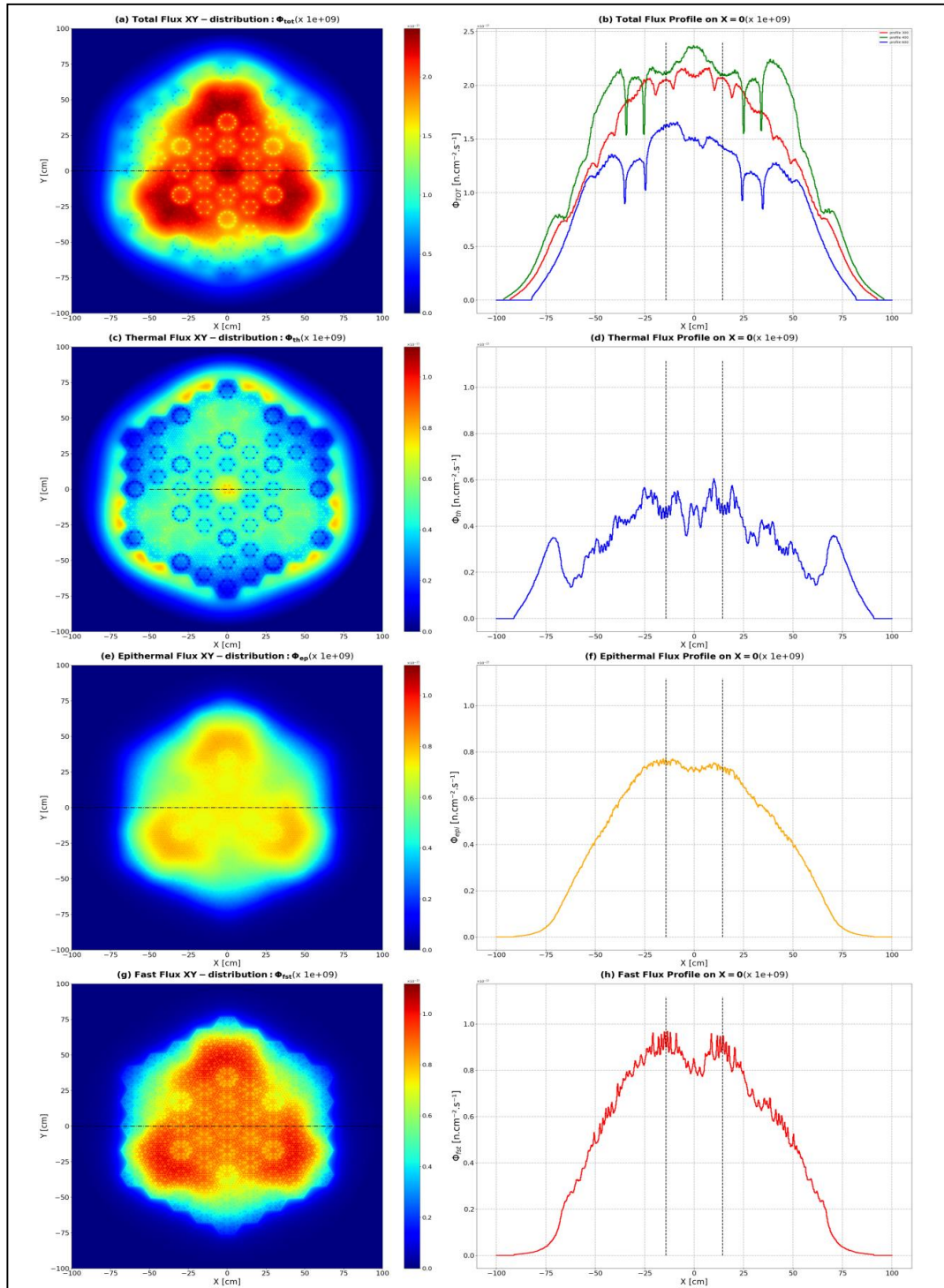


Figure 5. Neutron flux XY distribution and profiles: (a) Total neutron flux distribution, (b) Total neutron flux profile, (c) Thermal neutron flux distribution, (d) Thermal neutron flux profile, (e) Epithermal neutron flux distribution, (f) Epithermal neutron flux profile, (g) Fast neutron flux distribution, (h) Fast neutron flux profile.

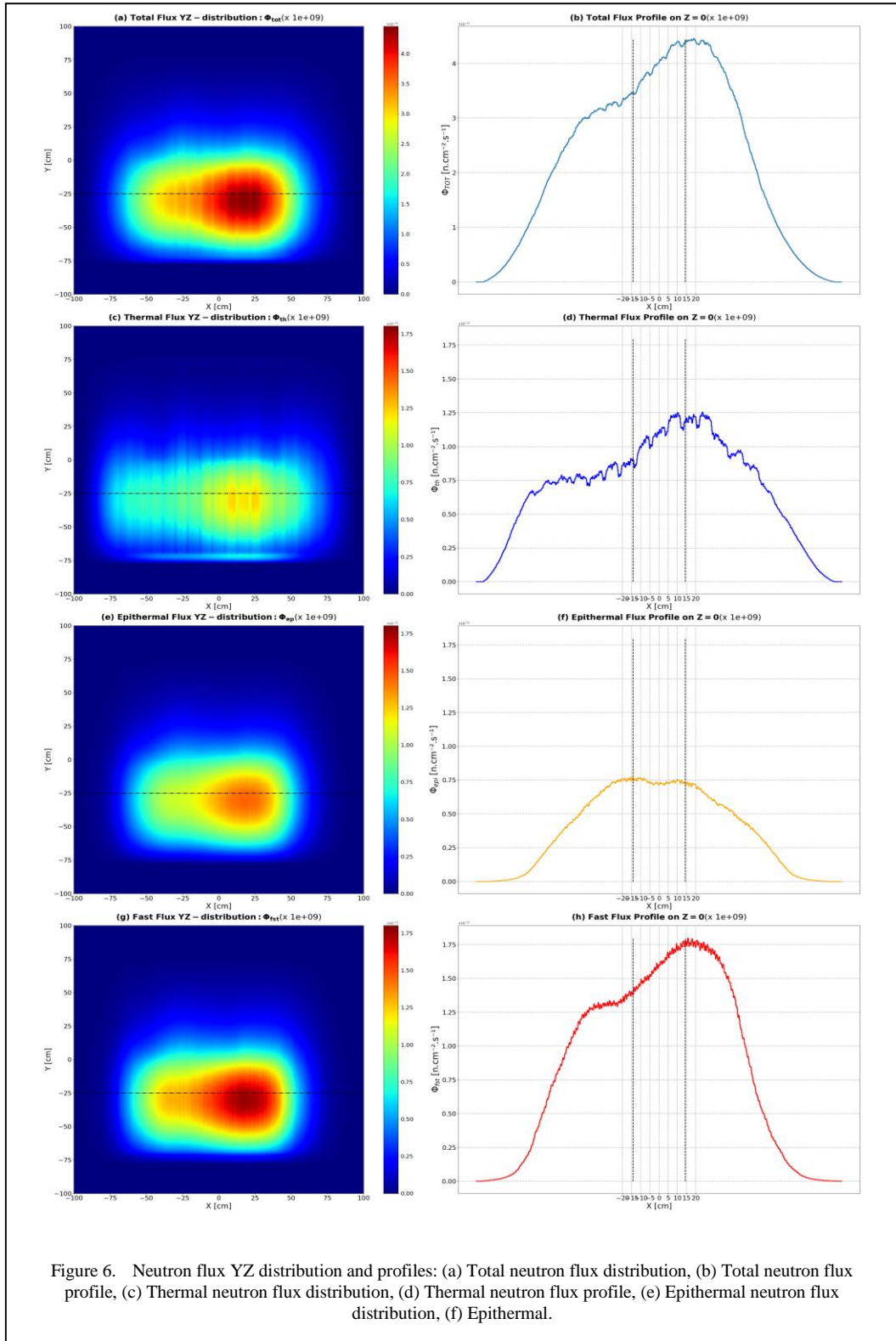


Figure 6. Neutron flux YZ distribution and profiles: (a) Total neutron flux distribution, (b) Total neutron flux profile, (c) Thermal neutron flux distribution, (d) Thermal neutron flux profile, (e) Epithermal neutron flux distribution, (f) Epithermal.

CAREM-25 represents a well thermalized reactor. In addition, relative neutron flux distribution within axial and radial cross-section of the core was obtained for total, thermal, epithermal and fast neutron (Figs. 5 and 6).

It could be seen that the total flux has triangular symmetry, according to the arrangement of fuel assemblies with BPRs, and it is also possible to distinguish poisoned FAs arrangement. The thermal flux distribution shows clearly the presence of BPRs, while epithermal is more diffused. The fast component is well shaped and depicts the FAs contributing actively in neutron generation.

IV. CONCLUSION


This study presented the neutron physics modeling and simulation of the CAREM-25 small modular reactor using the OpenMC code. The results confirmed the reliability of OpenMC for accurately capturing the key neutronic characteristics of the reactor core, including neutron flux distribution, effective multiplication factor, and fuel burnup evolution which is the next step of the study. These findings underline the potential of OpenMC as a robust tool for the analysis and optimization of small modular reactor designs.

The insights gained from this work contribute to a deeper understanding of the CAREM-25 reactor's performance and highlight the relevance of detailed Monte Carlo simulations in the development of innovative nuclear reactor technologies. Future work could focus on coupling neutronics with thermal-hydraulics analyses to provide a more comprehensive assessment of the reactor's behavior under operational and transient conditions.

REFERENCES

- [1] Nasiri, S., Ansarifar, G. R., & Esteki, M. H. (2022). Design of the CAREM nuclear reactor core with dual cooled annular fuel and optimizing the thermal-hydraulic, natural circulation, and neutronics parameters. *Annals of Nuclear Energy*, 169, 108939.
- [2] Marcel, C. P., Acuña, F. M., Zanocco, P. G., & Delmastro, D. F. (2013). Stability of self-pressurized, natural circulation, low thermo-dynamic quality, nuclear reactors: The stability performance of the CAREM-25 reactor. *Nuclear engineering and Design*, 265, 232-243.
- [3] International Atomic Energy Agency (2020). *Advances in Small Modular Reactor Technology Developments, A Supplement to: IAEA Advanced Reactors Information System (ARIS)*. IAEA, Austria.
- [4] Tashakor, S. et al. (2017). Neutronic simulation of CAREM-25 small modular reactor. *Progress in Nuclear Energy*, 99(185-195).
- [5] Romano, P. K., Horelik, N. E., Herman, B. R., Nelson, A. G., Forget, B., & Smith, K. (2015). OpenMC: A state-of-the-art Monte Carlo code for research and development. *Annals of Nuclear Energy*, 82, 90-97.
- [6] Raflis, H., Muhammad, I., Su'ud, Z., Waris, A., & Irwanto, D. (2021). Reflector materials selection for core design of modular gas-cooled fast reactor using OpenMC code. *International Journal of Energy Research*, 45(8), 12071-12085.
- [7] Official OpenMC code documentation website <https://docs.openmc.org/en/stable/usersguide/basics.html>.
- [8] Rivera, S.S., & Barón, J.H. *CAREM-25: a Low-Risk Nuclear Option*. Autoridad Regulatoria Nuclear e Instituto CEDIAC - Universidad Nacional de Cuyo Argentina.
- [9] Marcel, C. et al. (2017). CAREM-25: A Safe Innovative Small Nuclear Power Plant. Nuclear España.
- [10] Gajaroodi, S. Z., & Pazirandeh, A. (2020). Neutronic study of CAREM-25 advanced small modular reactor using Monte Carlo simulation. *Atw. Internationale Zeitschrift fuer Kernenergie*, 65(8-9), 435-439.

Red Deer Vocalizations based Optimization and Unique Football Player Skills inspired Algorithm for Active Power Loss Dwindling in Electrical Transmission System

Lenin Kanagasabai¹

¹Prasad V. Potluri Siddhartha Institute of Technology, Vijayawada, Andhra Pradesh, India

¹gklenin@gmail.com

Abstract—Red deer vocalizations based optimization (RDVO) algorithm and unique football player skills based (UFPS) optimization algorithm are applied for solving the actual power loss dwindling problem. Grunts, bleats, snorts, and barks, are utilized by the red deer to communicate in the cluster. General communication through vocalizations among the red deer's cluster is defined mathematically in the exploration segment of the algorithm. Adult male red deer roars and groans during the rut seasons to attract a female red deer. Adult male will keep the calling back and forth for half an hour or more, particularly during dawn and dusk. Red deer rut season originates in September and lasts until early November. Throughout this season, challenging males, propelled full of testosterone, will engross in a sequence of behaviours intended to showing off to female red deer and launching a supremacy over other red deer's. Unique football player skills based optimization algorithm is based on the playing skills of Diego Armando Maradona in the football sport. Maradona's revelation, passing, control, and dribbling talents are exceptional. His small physique provided a low centre of gravity and through that Maradona dominates in the sport than players. Red deer vocalizations based optimization (RDVO) algorithm and unique football player skills based (UFPS) optimization algorithm are validated in IEEE 30 test system.

Keywords - Red deer, vocalization, cluster, football player skills, Diego Armando Maradona

I. INTRODUCTION

Active power loss dwindling and voltage stability Amplification in electrical Transmission System is a universal problem. Copious methods are consecutively applied to solve the problem; Novel Stochastic Optimizer [1], Hybrid CAC-DE [2], Chaotic Turbulent Flow [3], and Adopting Scenario-Based approach [4] applied. These decades swarm and evolutionary based algorithms are applied to different problems [5-11].

In this paper Red deer vocalizations based optimization (RDVO) algorithm and unique football player skills based (UFPS) optimization algorithm are applied to solve the problem. RDVO algorithm is based on the different communications among the red deer (Fig. 1) [12] cluster. Grunts, bleats, snorts, and barks, are utilized by the red deer to communicate in the cluster. Fawns will bleat to call the mother red deer; adult red deer do grunt or snort to designate its presence to the cluster.

General communication through vocalizations among the red deer's cluster is defined mathematically in the exploration segment of the algorithm. Adult male red deer roars and groans during the rut seasons to attract a female red deer. Adult male will keep the calling back and forth for half an hour or more, particularly during dawn and dusk. Red deer rut





Figure 1. Red deer.



Figure 2. Diego Armando Maradona.

season originates in September and lasts until early November.

Throughout this season, challenging males, propelled full of testosterone, will engross in a sequence of behaviours intended to showing off to female red deer and launching a supremacy over other red deer's. Exploration section is modeled based on the general communication through vocalizations among the red deer's cluster. Grunts, bleats, snorts, and barks, are utilized by the red deer to communicate in the cluster. Fawns will bleat to call the mother red deer. This type of communication used among red deer's during exploration of food and parenting aspects in the cluster. When threat from predator happened, red deer roars and communicate fast to the clusters through various intensities of vocalizations.

Unique football player skills based (UFPS) optimization algorithm is based on the playing skills of Diego Armando Maradona in the football sport. Diego Armando Maradona (Fig. 2) [13] was an Argentine professional football player and generally observed as one of the outstanding players in the football sport.

Maradona's revelation, passing, control, and dribbling talents are exceptional. His small physique provided a low centre of gravity and through that Maradona dominates in the sport



Figure 3. Ball possession by Diego Armando Maradona.

than players. Maradona's presence and headship in the playing arena own a prodigious consequence on his team's overall performance, whereas Maradona would frequently be singled out by the opponent team.

Exploration section is mathematically designed, based on the Maradona's ball possession skills (Fig. 3) [14]. Maradona controls the ball while passing, receiving and shooting, decision making, dribbling and heading. His touching and running off the ball is magnificent while the ball moves into the opponent region. Maradona owns pronounced balance and harmonization while playing the sport. Maradona moves very fast in trivial spaces by means of interlacing the defenders. Exploitation segment is scientifically designed based on Maradona's turn skill by rotating the body 180 degrees. Maradona turn skill is most exceptional one and as the defender pulls the ball nearby, Maradona put the foot on top of the ball, by spinning the body 180 degrees the ball will be pulled back by Maradona. Through the body spin, the ball will be passed to another foot, continuing to rotate additional 180 degrees until Maradona face the original course of movement. Red deer vocalizations based optimization (RDVO) algorithm and unique football player skills based (UFPS) optimization algorithm are validated in IEEE 30 test system.

II. PROBLEM FORMULATION

Main Objective function of the problem is demarcated as:

$$\begin{aligned} \min \tilde{F}(\bar{g}, \bar{h}), \\ M(\bar{g}, \bar{h}) = 0, \\ N(\bar{g}, \bar{h}) = 0. \end{aligned} \quad (1)$$

Control (\bar{g}) and dependent (\bar{h}) vectors are defined as:

$$g = [VLG_1, \dots, VLG_{N_G}; QC_1, \dots, QC_{N_C}; T_1, \dots, T_{N_T}] \quad (2)$$

$$h = [PG_{slack}; VL_1, \dots, VL_{N_{Load}}; QG_1, \dots, QG_{N_G}; SL_1, \dots, SL_{N_T}] \quad (3)$$

$Q_C \rightarrow$ Reactive power compensator

$T \rightarrow$ Transformer tap

$V_G \rightarrow$ Generator voltage

$PG_{slack} \rightarrow$ Slack generator

$V_L \rightarrow$ Voltage in transmission lines

$Q_G \rightarrow$ Reactive power generator

Fitness functions are defined as follows:

$$F_1 = P_{min} = \min \left[\sum_m^{N_{TL}} G_m [V_i^2 + V_j^2 - 2 \times V_j \cos \phi_{ij}] \right],$$

$$F_2 = \min \left[\sum_{i=1}^{N_{LB}} |V_{Lk} - V_{Lk}^{desired}|^2 + \sum_{i=1}^{N_G} |Q_{GK} - Q_{GK}^{Lim}|^2 \right],$$

$F_3 =$ Minimize $L_{maximum}$,

$S_L \rightarrow$ Apparent power,

$$L_{max} = \max [L_j]; j = 1; N_{LB},$$

$$\begin{cases} L_j = 1 - \sum_{i=1}^{N_{PV}} F_{ji} \frac{V_i}{V_j} \\ F_{ji} = -[Y_1]^{-1} [Y_2] \end{cases} \quad (4)$$

$$L_{max} = \max \left[1 - [Y_1]^{-1} [Y_2] \times \frac{V_i}{V_j} \right],$$

Parity constraints:

$$0 = P_{Gi} - P_{Di} - V_i \sum_{j \in N_B} V_j \cdot [G_{ij} \cos[\phi_i - \phi_j] + B_{ij} \sin[\phi_i - \phi_j]] \quad (5)$$

$$0 = Q_{Gi} - Q_{Di} - V_i \sum_{j \in N_B} V_j \cdot [G_{ij} \sin[\phi_i - \phi_j] + B_{ij} \cos[\phi_i - \phi_j]] \quad (6)$$

N_B is the number of buses,

$P_G, Q_G \rightarrow$ real and reactive power

$G_{ij}, B_{ij} \rightarrow$ mutual conductance and susceptance

$P_D, Q_D \rightarrow$ real and reactive load

Disparity constraints:

$$\begin{aligned} P_{Gsl}^{min} &\leq P_{Gsl} \leq P_{Gsl}^{max}, \\ Q_{Gi}^{min} &\leq Q_{Gi} \leq Q_{Gi}^{max}, i \in N_G, \\ V_{Li}^{min} &\leq V_{Li} \leq V_{Li}^{max}, i \in N_L, \\ T_i^{min} &\leq T_i \leq T_i^{max}, i \in N_T, \end{aligned} \quad (7)$$

$$Q_C^{min} \leq Q_C \leq Q_C^{max}, i \in N_C,$$

$$|SL_i| \leq S_{L_i}^{max}, i \in N_{TL},$$

$$V_{Gi}^{min} \leq V_{Gi} \leq V_{Gi}^{max}, i \in N_G.$$

Multi objective fitness (MOF) =

$$\begin{aligned} &= F_1 + r_1 F_2 + u F_3 = \\ &= \left[\sum_{i=1}^{N_L} x_v [V_{Li} - V_{Li}^{min}]^2 \right] + \\ &+ \sum_{i=1}^{N_G} r_g [Q_{Gi} - Q_{Gi}^{min}]^2 + r_f F \end{aligned} \quad (8)$$

$$V_{Li}^{minimum} = \begin{cases} V_{Li}^{max}, V_{Li} > V_{Li}^{max} \\ V_{Li}^{min}, V_{Li} < V_{Li}^{min} \end{cases} \quad (9)$$

$$Q_{Gi}^{minimum} = \begin{cases} Q_{Gi}^{max}, Q_{Gi} > Q_{Gi}^{max} \\ Q_{Gi}^{min}, Q_{Gi} < Q_{Gi}^{min} \end{cases} \quad (10)$$

III. RED DEER VOCALIZATIONS BASED OPTIMIZATION ALGORITHM

Red deer vocalizations based optimization (RDVO) algorithm is based on the different communications among the red deer cluster. Grunts, bleats, snorts, and barks, are utilized by

the red deer to communicate in the cluster. Fawns will bleat to call the mother red deer; adult red deer do grunt or snort to designate its presence to the cluster. General communication through vocalizations among the red deer's cluster is defined mathematically in the exploration segment of the algorithm. Adult male red deer roars and groans during the rut seasons to attract a female red deer. Adult male will keep the calling back and forth for half an hour or more, particularly during dawn and dusk. Red deer rut season originates in September and lasts until early November. Throughout this season, challenging males, propelled full of testosterone, will engross in a sequence of behaviours intended to showing off to female red deer and launching a supremacy over other red deer's. This action has been scientifically designed in the exploitation segment of the algorithm.

Population is produced as follows

$$R = \begin{bmatrix} R_1 \\ \vdots \\ R_i \\ \vdots \\ R_N \end{bmatrix}_{N \times m} = \begin{bmatrix} r_{1,1} & \cdots & r_{1,m} \\ \vdots & \ddots & \vdots \\ r_{N,1} & \cdots & r_{N,m} \end{bmatrix}. \quad (11)$$

$R \rightarrow$ matrix of the population

$N \rightarrow$ members of the population

$m \rightarrow$ number of variables

$$r_{i,j} = \min_j + Z(\max_j - \min_j)$$

$\max_j, \min_j \rightarrow$ limits

$$Z \in [0,1]$$

Value of the objective function is computed as follows:

$$F = \begin{bmatrix} F_1 \\ \vdots \\ F_i \\ \vdots \\ F_N \end{bmatrix}_{N \times 1} = \begin{bmatrix} F(R_1) \\ \vdots \\ F(R_i) \\ \vdots \\ F(R_N) \end{bmatrix}_{N \times 1}. \quad (12)$$

Exploration section is modeled based on the general communication through vocalizations among the red deer's cluster. Grunts, bleats, snorts, and barks, are utilized by the red deer to communicate in the cluster. Fawns will bleat to call the mother red deer. This type of communication used among red deer's during exploration of food and parenting aspects in the cluster.

$$\begin{aligned} R_{i,j}^{L_1} &= R_{i,j} + Z \cdot (U_j - Z_1 \cdot R_{i,j}), \\ R_{i,j}^{L_1} &\rightarrow \text{General vocalizations}, \\ U_j &\rightarrow \text{Exploring actions of red deer}, \quad (13) \\ Z &\in [0,1], Z_1 \in \{1,2\}, \\ R_i &= \begin{cases} R_i^{L_1}, F_i^{L_1} \leq F_i \\ R_i, \text{ else} \end{cases} \end{aligned}$$

When threat from predator happened, red deer roars and communicate fast to the clusters through various intensities of vocalizations.

$$\begin{aligned} TH_i &= \{R_k, F_k > F_i\}, \\ k &= 1, 2, 3, \dots, N, \\ i &= 1, 2, \dots, N, \\ TH_i &\rightarrow \text{threat level}. \end{aligned} \quad (14)$$

$$\begin{aligned} R_{i,j}^{L_2} &= R_{i,j} + Z \cdot (R_{i,j} - Z_2 \cdot STH_{i,j}), \\ R_{i,j}^{L_2} &\rightarrow \text{location during threat}, \\ Z &\in [0,1], Z_2 \in \{1,2\}, \quad (15) \\ STH_{i,j} &\rightarrow \text{movement during threats}, \\ R_i &= \begin{cases} R_i^{L_2}, F_i^{L_2} \leq F_i \\ R_i, \text{ else} \end{cases} \end{aligned}$$

$$\begin{aligned} R_{i,j}^{L_3} &= R_{i,j} + R \cdot (1 - 2 \cdot R) \cdot \frac{\max_j - \min_j}{t}, \\ R_{i,j}^{L_3} &\rightarrow \text{altered vocalizations}, \\ Z &\in [0,1], \quad (16) \\ t &\rightarrow \text{iteration counter}, \\ R_i &= \begin{cases} R_i^{L_3}, F_i^{L_3} \leq F_i \\ R_i, \text{ else} \end{cases} \end{aligned}$$

- a. *Begin*
- b. *Create the population*
- c.
$$R = \begin{bmatrix} R_1 \\ \vdots \\ R_i \\ \vdots \\ R_N \end{bmatrix}_{N \times m} = \begin{bmatrix} r_{1,1} & \cdots & r_{1,m} \\ \vdots & \ddots & \vdots \\ r_{N,1} & \cdots & r_{N,m} \end{bmatrix}$$
- d. $r_{i,j} = \min_j + R(\max_j - \min_j)$
- e. *Compute the objective function*
- f.
$$F = \begin{bmatrix} F_1 \\ \vdots \\ F_i \\ \vdots \\ F_N \end{bmatrix}_{N \times 1} = \begin{bmatrix} F(R_1) \\ \vdots \\ F(R_i) \\ \vdots \\ F(R_N) \end{bmatrix}_{N \times 1}$$
- g. *For $t = 1:T$*
- h. *Classify the vocalizations*
- i. *For $i = 1:N$*
- j. *Apply the exploration phase*
- k. *Identify the general vocalization*
- l. $R_{i,j}^{L_1} = R_{i,j} + Z \cdot (P_j - Z_1 \cdot R_{i,j})$
- m.
$$R_i = \begin{cases} R_i^{L_1}, F_i^{L_1} \leq F_i \\ R_i, \text{ else} \end{cases}$$
- n. *Define the threat level*
- o. $TH_i = \{R_k, F_k > F_i\}$
- p. *Define the position during threat*
- q. $R_{i,j}^{L_2} = R_{i,j} + Z \cdot (R_{i,j} - Z_2 \cdot STH_{i,j})$
- r.
$$R_i = \begin{cases} R_i^{L_2}, F_i^{L_2} \leq F_i \\ R_i, \text{ else} \end{cases}$$
- s. *Apply exploitation phase*
- t. *Define the vocalization during rut season*
- u.
$$R_{i,j}^{L_3} = R_{i,j} + Z \cdot (1 - 2 \cdot Z) \cdot \frac{\max_j - \min_j}{t}$$
- v.
$$R_i = \begin{cases} R_i^{L_3}, F_i^{L_3} \leq F_i \\ R_i, \text{ else} \end{cases}$$
- w. $t = t + 1$
- x. *Output the preeminent solution*
- y. *End*

IV. UNIQUE FOOTBALL PLAYER SKILLS BASED OPTIMIZATION ALGORITHM

Unique football player skills based (UFPS) optimization algorithm is based on the playing skills of Diego Armando Maradona in the football sport. Maradona's revelation, passing, control, and dribbling talents are exceptional. Population generated in the bounded examination area as follows

$$O_{i,j} = lb_j + A(ub_j - lb_j) . \quad (17)$$

$ub_j, lb_j \rightarrow$ upper and lower bound ,

$$A \in [0,1] .$$

Exploration section is mathematically designed, based on the Maradona's ball possession skills. Maradona controls the ball while passing, receiving and shooting, decision making, dribbling and heading. His touching and running off the ball is magnificent while the ball moves into the opponent region. Maradona owns pronounced balance and harmonization while playing the sport. Maradona moves very fast in trivial spaces by means of interlacing the defenders. For this action excellent sum of balance and coordination has been maintained by Maradona. Maradona do appropriate body positioning; for short passes using the inside of the foot and for long passes instep is utilized by continuously keeping eyes on the target.

$$B_i = \{U_k\} ,$$

$$k = 1, 2, 3, \dots, N ,$$

$$i = 1, 2, \dots, N ,$$

$$G_k > G_i ,$$

$$U_i \rightarrow \text{ball movement} ,$$

$$U_{i,j}^1 = U_{i,j} + A \cdot (U_{i,j} - A_1 \cdot Q_{i,j}) , \quad (18)$$

$$U_{i,j}^1 \rightarrow \text{ball control by Maradona} ,$$

$$A \in [0,1] ,$$

$$A_1 \in \{1,2\} ,$$

$$Q_{i,j} \rightarrow \text{foot movement} ,$$

$$\begin{cases} U_i = U_i^1 \text{ if } G_i^1 \leq G_i \\ U_i = U_i \text{ otherwise} \end{cases} .$$

Maradona shooting skill towards scoring a goal is excellent and uses his feet or head for this action. A shot on target is precise and owns the capability of converting maximum attempts into

goal. During the penalty kick, Maradona plant the foot right behind the ball and lean to make the ball to move with high velocity towards the target. Maradona expert in free kick and owns outstanding concentration towards the target.

$$\begin{aligned}
 U_{i,j}^2 &= U_{i,j} + A \cdot (K_j - A_2 \cdot U_{i,j}), \\
 U_{i,j}^2 &\rightarrow \text{Maradona shooting skill}, \\
 K_j &\rightarrow \text{foot work}, \\
 A &\in [0,1], \\
 A_2 &\in \{1,2\}, \\
 \begin{cases} U_i = U_i^2 & \text{if } G_i^2 \leq G_i \\ U_i = U_i & \text{otherwise} \end{cases}
 \end{aligned} \quad . \quad (19)$$

Exploitation segment is scientifically designed based on Maradona's turn skill by rotating the body 180 degrees. Maradona turn skill is most exceptional one and as the defender pulls the ball nearby, Maradona put the foot on top of the ball, by spinning the body 180 degrees the ball will be pulled back by Maradona. Through the body spin, the ball will be passed to another foot, continuing to rotate additional 180 degrees until Maradona face the original course of movement. Maradona body spin is a dribbling talent through that control the ball possession.

$$\begin{aligned}
 U_{i,j}^3 &= U_{i,j} + A \cdot (1 - 2 \cdot A) \cdot P, \\
 U_{i,j}^3 &\rightarrow \text{turn skill of Maradona}, \\
 A &\in [0,1], \\
 P &= ub_j - lb_j / t, \\
 \begin{cases} U_i = U_i^3 & \text{if } G_i^3 \leq G_i \\ U_i = U_i & \text{otherwise} \end{cases}
 \end{aligned} \quad . \quad (20)$$

- a. Start
- b. Set the variables
- c. Engender the population
- d. Compute the fitness function
- e. Determine the exploration section
- f. $B_i = \{U_k\}$
- g. $U_{i,j}^1 = U_{i,j} + A \cdot (U_{i,j} - A_1 \cdot Q_{i,j})$
- h. $U_i = U_i^1, \text{if } G_i^1 \leq G_i$

- i. Otherwise
- j. $U_i = U_i$
- k. Define the ball shooting skill
- l. $U_{i,j}^2 = U_{i,j} + A \cdot (K_j - A_2 \cdot U_{i,j})$
- m. $U_i = U_i^2, \text{if } G_i^2 \geq G$
- n. Otherwise
- o. $U_i = U_i$
- p. Define the exploitation section
- q. $U_{i,j}^3 = U_{i,j} + A \cdot (1 - 2 \cdot A) \cdot P$
- r. $P = ub_j - lb_j / t$
- s. $U_i = U_i^3, \text{if } G_i^3 \geq G_i$
- t. Otherwise
- u. $U_i = U_i$
- v. End for
- w. $t = t + 1$
- x. Output the best solution
- y. End

V. RESULTS

Red deer vocalizations based optimization (RDVO) algorithm and unique football player skills based (UFPS) optimization algorithm are validated in IEEE 30 bus system [5].

Table I shows the active power loss (APO (MW)), voltage deviation (VDI (PU)) and voltage stability (VST (PU)). Fig. 4-6 gives the comparison of results.

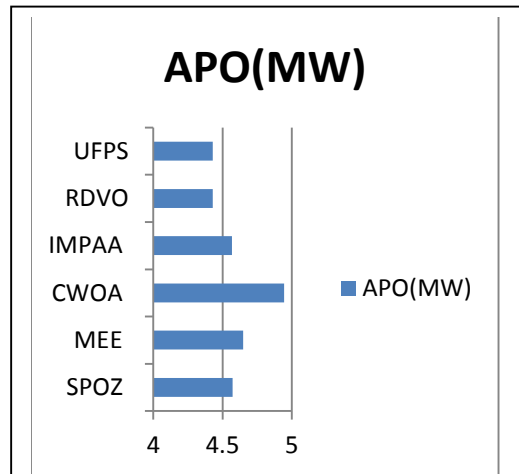


Figure 4. Comparison of active power loss (IEEE 30 bus).

TABLE I. VALUATION OF RESULT.

Method	APO(MW)	VDI(PU)	VST(PU)
SPOZ [1]	4.5730	1.8257	0.1262
MEE [2]	4.6482	0.0802	0.1394
CWOA [3]	4.9448	0.1212	0.1402
IMPAA [4]	4.5677	0.1250	0.1414
RDVO	4.4289	0.0786	0.1472
UFPS	4.4286	0.0782	0.1478

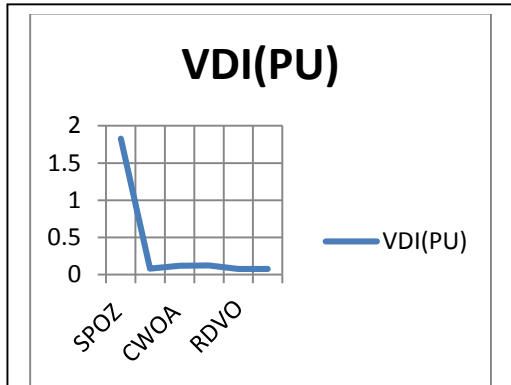


Figure 5. Comparison of voltage deviation (IEEE 30 bus).

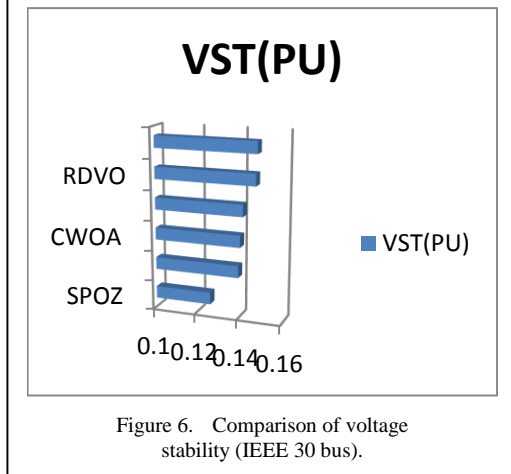


Figure 6. Comparison of voltage stability (IEEE 30 bus).

Table II shows the time taken by RDVO, UFPS algorithms.

TABLE II. TIME TAKEN BY RDVO, UFPS.

Technique	30 bus T(S)
RDVO	16.89
UFPS	16.76

VI. CONCLUSION

Red deer vocalizations based optimization (RDVO) algorithm and unique football player skills based (UFPS) optimization algorithm solved the problem competently. Grunts, bleats,

snorts, and barks, are utilized by the red deer to communicate in the cluster. Fawns will bleat to call the mother red deer; adult red deer do grunt or snort to designate its presence to the cluster. General communication through vocalizations among the red deer’s cluster is defined mathematically in the exploration segment of the algorithm. Adult male red deer roars and groans during the rut seasons to attract a female red deer. Adult male will keep the calling back and forth for half an hour or more, particularly during dawn and dusk. Red deer rut season originates in September and lasts until early November. Throughout this season, challenging males, propelled full of testosterone, will engross in a sequence of behaviours intended to showing off to female red deer and launching a supremacy over other red deer’s.












This action has been scientifically designed in the exploitation segment of the algorithm. Maradona controls the ball while passing, receiving and shooting, decision making, dribbling and heading. His touching and running off the ball is magnificent while the ball moves into the opponent region. Maradona owns pronounced balance and harmonization while playing the sport. Maradona moves very fast in trivial spaces by means of interlacing the defenders. Exploitation segment is scientifically designed based on Maradona’s turn skill by rotating the body 180 degrees. Maradona turn skill is most exceptional one and as the defender pulls the ball nearby, Maradona put the foot on top of the ball, by spinning the body 180 degrees the ball will be pulled back by Maradona. Through the body spin, the ball will be passed to another foot, continuing to rotate additional 180 degrees until Maradona face the original course of movement. Red deer vocalizations based optimization (RDVO) algorithm and unique football player skills based (UFPS) optimization algorithm are validated in IEEE 30 test system

REFERENCES

- [1] Ali, M. H., Soliman, A. M. A., Abdeen, M., Kandil, T., Abdelaziz, A. Y., & El-Shahat, A. (2023). A novel stochastic optimizer solving optimal reactive power dispatch problem considering renewable energy resources. *Energies*, 16(4), 1562.
- [2] PG, A. K., & Devaraj, D. (2022). Hybrid CAC-DE in optimal reactive power dispatch (ORPD) for renewable energy cost reduction. *Sustainable Computing: Informatics and Systems*, 35, 100688.
- [3] Abd-El Wahab, A. M., Kamel, S., Hassan, M. H., Mosaad, M. I., & AbdulFattah, T. A. (2022). Optimal reactive power dispatch using a chaotic turbulent flow

- of water-based optimization algorithm. *Mathematics*, 10(3), 346.
- [4] Khan, N. H., Jamal, R., Ebeed, M., Kamel, S., Zeinoddini-Meymand, H., & Zawbaa, H. M. (2022). Adopting Scenario-Based approach to solve optimal reactive power Dispatch problem with integration of wind and solar energy using improved Marine predator algorithm. *Ain Shams Engineering Journal*, 13(5), 101726.
- [5] Kanagasabai, L. (2023). Real power loss reduction by extreme learning machine based Panthera leo, chaotic based Jungle search and Quantum based Chipmunk search optimization algorithms. *International Journal of System Assurance Engineering and Management*, 14(Suppl 1), 55-78.
- [6] Rai, R., Das, A., Ray, S., & Dhal, K. G. (2022). Human-inspired optimization algorithms: Theoretical foundations, algorithms, open-research issues and application for multi-level thresholding. *Archives of Computational Methods in Engineering*, 29(7), 5313-5352.
- [7] Omelchenko, I. N., Lyakhovich, D. G., Aleksandrov, A. A., Vodchits, A. S., & Kunkov, N. V. (2020). Development of a design algorithm for the logistics system of product distribution of the mechanical engineering enterprise. *Вестник Московского государственного технического университета им. НЭ Баумана. Серия «Машиностроение»*, 3 (132), 62-69.
- [8] Khazali, A. H., & Kalantar, M. (2011). Optimal reactive power dispatch based on harmony search algorithm. *International Journal of Electrical Power & Energy Systems*, 33(3), 684-692.
- [9] Chen, G., Liu, L., Guo, Y., & Huang, S. (2016). Multi-objective enhanced PSO algorithm for optimizing power losses and voltage deviation in power systems. *COMPEL: The International Journal for Computation and Mathematics in Electrical and Electronic Engineering*, 35(1), 350-372.
- [10] Naderi, E., Narimani, H., Fathi, M., & Narimani, M. R. (2017). A novel fuzzy adaptive configuration of particle swarm optimization to solve large-scale optimal reactive power dispatch. *Applied soft computing*, 53, 441-456.
- [11] Lenin, K. (2023). Quasi opposition-based quantum pieris rapae and parametric curve search optimization for real power loss reduction and stability enhancement. *IEEE Transactions on Industry Applications*, 59(3), 3077-3085.
- [12] Rowe, Z. W., Robins, J. H., & Rands, S. A. (2023). Red deer Cervus elaphus blink more in larger groups. *Ecology and Evolution*, 13(3), e9908.
- [13] Palacios-Huerta, I. (2023). Maradona plays Minimax. *Sports Economics Review*, 1, 100001.
- [14] Halder, A. (2024). Diego Maradona: A Socio-Cultural Study. *Soccer & Society*, 25(8), 1200-1202.

Solar Distiller for Machining Cutting Fluid: An Alternative to Reduce Costs

Wesley Mateus Basso¹, Vinicius Souza Cardozo², Paulo César Mioralli³, Francine Martins Molinari⁴, Pablo Sampaio Gomes Natividade⁵, Paulo Henrique Palota⁶, Rodrigo Garcia da Silva⁷, Sílvio Aparecido Verdério Junior⁸, José Ferreira da Costa⁹, Jonas Rafael Antonio¹⁰, Elson Avallone¹¹

^{1,2,3,4,5,6,7,9,10,11}Federal Institute of Education, Science and Technology of Sao Paulo, Catanduva-SP, Brazil

⁸Federal Institute of Education, Science and Technology of Sao Paulo, Araraquara-SP, Brazil

¹wesley.basso@aluno.ifsp.edu.br, ²vinicius.cardozo@aluno.ifsp.edu.br, ³mioralli@ifsp.edu.br, ⁴francine.molinari@ifsp.edu.br, ⁵pablo.sgn@ifsp.edu.br, ⁶palota@ifsp.edu.br, ⁷rodrigo.garcia@ifsp.edu.br, ⁸silvioverderio@ifsp.edu.br, ⁹joseferreira@ifsp.edu.br, ¹⁰jonas.antonio@ifsp.edu.br, ¹¹elson.avallone@ifsp.edu.br

Abstract—Cutting fluids are soluble oils used in machining, extrusion and metal forming processes, where parts and tools are subjected to intense cutting, forming or grinding forces. The present work analyzes the thermal efficiency of a solar distiller for cutting fluid as an alternative to reduce costs for industrial wastewater treatment. The daily production for this equipment is 0.350 kg of distillate with an average efficiency of 3.05% and maximum efficiency of 26.33% at 3:00 pm. The chemical analysis showed a significant reduction in polluting compounds. The vibrational bands in the set of FTIR spectra obtained reveal that the functional groups present in the samples containing the cutting fluid, such as amides, vegetable esters and sulfonates were efficiently removed in the distillation process proposed in this study. In particular, the bands between 2800–3000 cm^{-1} , which indicate the presence of hydrocarbons, and the bands below 1500 cm^{-1} , related to amide and sulfonate functional groups, were significantly attenuated or eliminated. As it is very cheap and simple to build, the investment is justified, even with low efficiency, as it is possible to deliver to companies a distillate free of other contaminants, even if future treatment is necessary.

Keywords - solar distiller, cutting fluid, thermal efficiency

ISBN: 978-86-82602-05-7

I. INTRODUCTION

Cutting fluids are soluble oils used in machining, extrusion and metal forming processes, where parts and tools are subjected to intense cutting, forming or grinding forces. The function of these liquids is not only to reduce and control friction during machining, but also to control the heating of both the technologically worked parts and the tools used in these processes, thus increasing the useful life of the tools as well as reducing the stops necessary to redo the cutting geometry.

Cutting fluids are potentially carcinogenic because they are made up of organic and aromatic acid compounds [1].

The authors [2], in their 2005 work, report that the annual use of cutting fluids in England exceeds $2 \times 10^6 \text{ m}^3$ and waste can reach 10 times this amount. Annual world consumption is estimated at 1.25 billion liters.

In studies [2] and [3], cutting fluids are presented as carcinogenic substances that must be handled carefully and by qualified professionals.

In the work of [4], an alternative is presented for the treatment of cutting fluid waste using a

285



hybrid process with biological ozone [5] before disposal into the environment however, this process requires expenses with both electricity and chemical products.

According to [6] and [7], dry machining would be an alternative to reduce the use of cutting fluid, but countries such as Germany, which have a large industrial production, use only 12% of this resource [8].

Brazilian legislation is still incipient concerning the subject, but the only two laws, CONAMA 362/2005 and Decree 50.877/1961, refer to lubricant in general, classifying them as hazardous waste.

The authors [9] present a comparative table between several costs in machining and the disposal of cutting fluid is considered very high. In the works of [10] and [11], the authors present a value of 22% of costs related to the disposal of cutting fluid.

In the master's thesis of [12], important information is presented about the use and disposal of cutting fluids, and environmental pollution is a major concern.

In the work developed by [13] a system is presented using a UV-H₂O₂ process with a residue removal factor of around 60% and [14] achieves a removal factor of 95% using an ultrasonic-Fenton system.

The present work presents the construction and energy evaluation of a simple solar distiller, without the use of electricity or any other non-renewable and chemical energy, for the liquid separation of water from the cutting fluid, thus providing a significant reduction in the future costs of treatment of industrial effluents and improvement of the quality of the environment, in addition to preserving a significant portion of electrical energy, given the significant amount of use of this fluid in the metal-mechanic industry.

Reductions in disposal costs are also significant, especially considering small companies, which strongly justifies the present work.

II. MATERIAL AND METHODS

The solar distiller developed for this study was built from a wooden reservoir thermally insulated with Styrofoam and a transparent glass surface, with dimensions of 1.05 m x 0.49 m, i.e., a frontal area of 0.5145 m², as shown in Fig. 1. The fluid is poured into a tray housed inside the

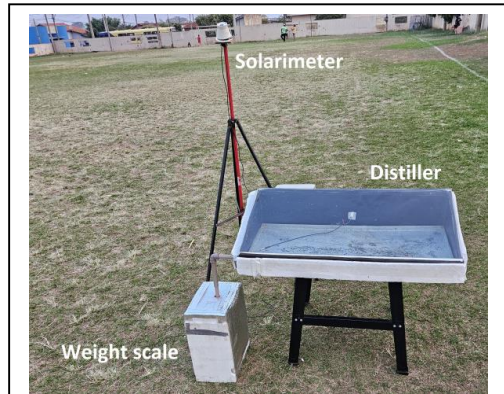


Figure 1. Solar distiller overview.



Figure 2. Solar distiller assembly.

reservoir and the process starts automatically when exposing the equipment to the sun with the glass side facing north.

The experiment was conducted in the city of Catanduva-SP, Brazil, at the coordinates - 21.146775156757585, -48.945651107197676.

Fig. 2 shows a schematic drawing of the distiller and its basic components, where 1 is the base, 2 the lower front cover, 3 sides, 4 rear covers, 5 channel for draining the distillate and 6 3 mm glass cover.

To measure the physical quantities involved in this project, an electronic data capture system of the Datalogger type was built using an ESP32 DevKit microcontroller [15].

The soluble oil used for the experiment is the Luc Sol 100 brand, consisting of mineral oil, additives, antifoam and bactericide, with a dilution of 1:20, i.e., one-part soluble oil to 20 parts waters.

Fig. 3 presents the electronic diagram of the system for measuring physical parameters, where 1 is the DHT22 humidity sensor [16] of relative humidity of the distiller's internal air, 2 is the indoor air temperature sensor (T_{int}) [17], 3

DHT22 [16] measuring the relative humidity of the ambient air, 4 is the room temperature sensor (T_{∞}) [17], 5 represents the fluid temperature sensor of fluid in the distiller tray (T_f) [17] and 6 is the temperature sensor installed on the outer surface of the glass (T_g) [17]. For solar radiation measurement, the number 7 represents the incident solar radiation sensor using a solarimeter, which has already been studied by the authors [18-22], with a calibration curve $G = 44.421 \times \Delta T_{rad}$, where ΔT_{rad} is the difference between hot and cold temperatures on the device's disk and environment, respectively. The set of numbers 8 and 9 represents respectively the module HX711 [23] and load cell referring to the distillate measuring scale. The button represented by the number 10 reset the scale before the beginning of each experiment.

The summarized First Law of Thermodynamics, presented in Eq. (1), was used

to determine the amount of transient heat absorbed by the system.

$$\dot{Q}_{abs} = \dot{m} \times cp_{flu} \times (T_{int} - T_{\infty}), \quad (1)$$

where, \dot{Q}_{abs} is the heat absorbed by the fluid [W], \dot{m} is the mass flow rate measured in [kg/s], using an electronic scale coupled to the measurement (Fig. 3), where the mass and all other physical properties are measured with a time variation of 60 seconds, T_{int} is the temperature inside the distiller [K] and T_{∞} is the room temperature [K]. The specific heat to constant pressure ($cp_{flu} = 4179 J / kg.K$) will be considered invariable to this study and so also all the cutting fluid will be considered like water, composed almost totality of the coolant.

The heat incident on the distiller surface is determined using the Eq. (2).

$$\dot{Q}_i = S_{dest} \times G, \quad (2)$$

where \dot{Q}_i is the heat incident on the distiller surface [W], S_{dest} is the front area of the distiller ($0.5145 m^2$) and G is the solar radiation incident measured by the solar radiation sensor [W/m²].

The system thermal efficiency is determined by the relation of the Eq. (3).

$$\eta = \frac{\dot{Q}_{abs}}{\dot{Q}_i}, \quad (3)$$

where η is the system thermal efficiency, which multiplied by 100 results in percentage values [%].

For the chemical analysis, the Thermo Fisher Scientific iS5 [24] infrared equipment is used with a high-intensity halogen infrared (near IR) radiation source and dTGS KBr detector, coupled to an iD3 ATR accessory, containing a Germanium window. Fig. 4 presents the equipment for the mentioned chemical analysis. The procedure included the collection of 16 sample scans and 16 background scans, with a collection duration of 25.6 seconds for each set. The spectrum resolution was $4,000 cm^{-1}$, covering the scan range of 600 a $4,000 cm^{-1}$. The method used Mertz phase correction and N-B Strong apodization, with an optical speed of

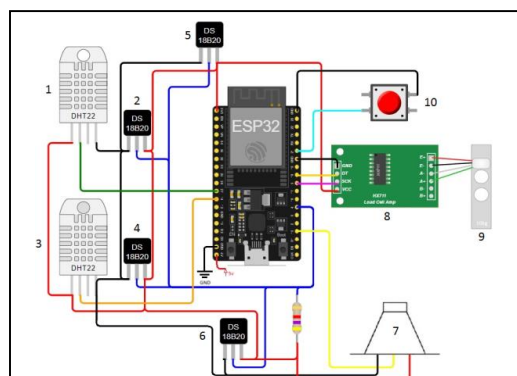


Figure 3. Electronic system (Datalogger).



Figure 4. Infrared Analyser Thermo Scientific.

0.4747 and data spacing of 0.482 cm^{-1} . The analyzer used a KBr beam splitter, ensuring accuracy in identifying the functional groups present. The analysis was conducted in absorbance mode and presented consistent results, with no collection errors or scan rejections.

The Fourier Transform Infrared Spectroscopy (FTIR) technique was selected and applied to evaluate and compare the chemical composition of the investigated samples, pre- and post-treatment, analyzing the sample recovered from the distillation process (called distillate), as well as the concentrated residues obtained and the pure cutting fluid (pure fluid). The residue containing concentrated fractions of the cutting fluid, constituting a heterogeneous water-oil system and with the presence of solid bodies, was separated into two aliquots: the less dense upper phase and the denser lower phase, entitled “Residue – Upper Phase” and “Residue – Lower Phase”, respectively.

III. RESULTS

A. Thermal Analysis

From the data collected by the Datalogger electronic system (Fig. 3), it is possible to work on the results, arriving at the transient values of energy absorbed by the cutting fluid, energy incident on the distiller surface and thermal efficiency of the system (Fig. 5).

Fig. 6 shows the transient graph of the thermal energies absorbed by the cutting fluid and incident on the distiller surface, respectively. The oscillations noticed in the absorbed thermal energy refer to small variations in the measurement of the distillate mass because the load cell presents instability with temperature, which induces oscillations in the graph.

The incident thermal energy depends only on the frontal area of distiller and the incident solar radiation. Therefore, variations in distilled mass do not influence the measurement of this parameter.

The energy losses of the system are presented in the graph in Fig. 7 highlighted in yellow, characterized by inefficient sealing, instability in the scale readings, heat loss through the system itself and the glass cover.

Fig. 8 is presented to evaluate the thermal efficiency of the system. It is noted that, between 6:47 am and 7:30 am, there are significant

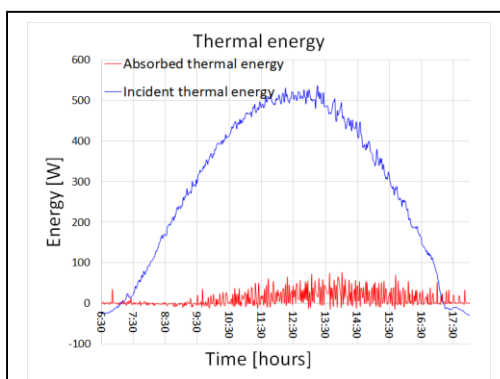


Figure 5. Thermal energy.

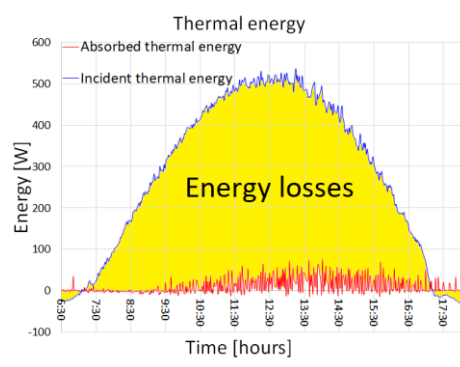


Figure 6. Energy losses of the solar distillation system.

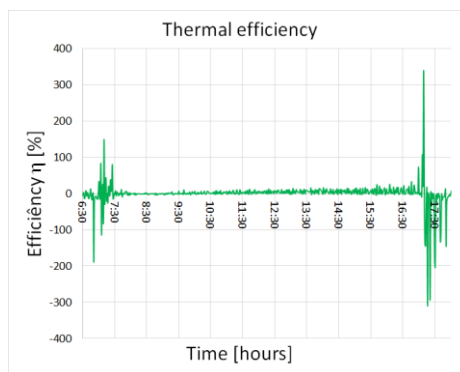


Figure 7. Transient thermal efficiency of the system.

variations in efficiency, as the incident solar radiation is still insufficient not only to raise the temperature of the solar radiation sensor, which uses the thermal principle, according to studies developed by authors [18-22], but also for a more effective distillation. There is also condensation at night due to the low ambient temperature and a small increase in internal temperature. In the period from 4:30 pm to 6:00 pm, the distiller still has distilled mass running down the glass, but

solar radiation is no longer sufficient to continue the distillation process, which causes an increase in efficiency, that is, there is thermal inertia for that period.

The period not only with the best efficiency but also where the equipment has the most consistent responses, is from 7:30 am to 4:30 pm. Fig. 9 presents the efficiency graph in this time interval and a polynomial trend line identifies that the highest value occurs at 3:00 pm with an approximate value of 26.33%. The average efficiency of 3.05% may seem small, but it is necessary to remember that this distiller is a

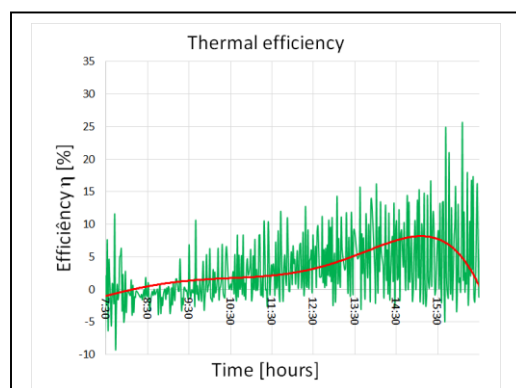


Figure 8. Transient thermal efficiency of the system with trend line.

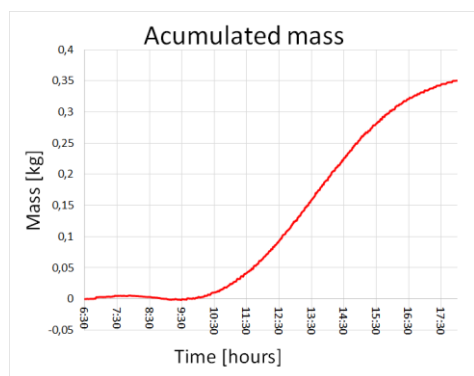


Figure 9. Accumulated Mass.

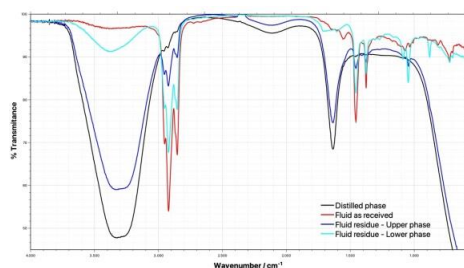


Figure 10. Infrared spectrum of the samples.

small piece of equipment and does not consume any electricity.

Fig. 10 presents the graph of the accumulated mass by the system in the period from 6:30 am to 6:00 pm, with the effective period of analysis for this study being from 7:30 am to 4:30 pm, where there are no abrupt variations in the measurement of mass.

The average thermal efficiency of the system is 3.05% and the distillate production in the period from 7:30 am to 4:30 pm is 0.316 kg.

B. Chemical Analysis

Fig. 10 presents the set of infrared spectra obtained for the different samples analyzed, comparing the vibrational behaviors throughout the wave number sweep, allowing the identification of functional groups based on the characteristic absorption frequencies, thus providing a molecular “fingerprint” of the samples. By comparing the spectra, the presence of compounds that were removed or secreted during the distillation process can be assessed, determining the qualitative efficiency of the system and the possibility of reprocessing or reusing the extracted water.

In the analysis of the spectra obtained, three main bands are observed in the region of $2800\text{--}3000\text{ cm}^{-1}$, typically attributed to the C–H stretching present in aliphatic bonds, for example, CH_2 and CH_3 , which indicate the presence of hydrocarbons in the cutting fluid analyzed. Such vibrations are characteristic of long aliphatic chains, often present in vegetable esters used as lubricating additives in biodegradable cutting fluids. The presence of these bands suggests that the cutting fluid contains a grease base (oily). In the spectrum of distilled water, these bands appear significantly reduced or absent, demonstrating that the distillation process managed to remove a large part of the organic compounds with aliphatic bonds.

In the region below 1500 cm^{-1} , a range known as the “fingerprint” of the spectrum, different bands can be visualized that provide detailed information about the chemical structure of the cutting fluid. In the case of this study, there are characteristic signals attributable to amides (with $\text{C}=\text{O}$ stretching bands around 1600 cm^{-1}) and sulfonate groups, whose $\text{S}=\text{O}$ vibration appears around $1200\text{--}1300\text{ cm}^{-1}$. These compounds are commonly used as additives to increase the solubility and surfactant properties

of the fluid. In the spectrum of the treated water, these bands are drastically reduced or absent, showing that the distillation process was effective in eliminating these compounds.

Comparing the spectra of the cutting fluid, as well as its post-distillation residues with the distilled water sample, there is a clear decrease in the intensity of the bands related to hydrocarbons, amides and sulfonates, confirming that distillation was able to remove most of the organic and inorganic contaminants present in the original sample. Distilled water displays a spectrum practically free of significant bands, suggesting a high degree of purity. The absence of important peaks indicates that the remaining residues are minimal and that the recovered water is suitable for reprocessing or reuse in industrial processes.

IV. CONCLUSIONS

The present work presents a solar distiller for cutting fluid as an alternative to reduce the costs of treating industrial effluents. An average efficiency of 3.05% and an accumulated mass of 0.316 kg of distillate were recorded in the period from 6:30 am to 6:00 pm, with a maximum efficiency of 26.33% at 3:00 pm. The analysis of the vibrational bands visualized in the set of FTIR spectra obtained reveals that the functional groups present in the samples containing the cutting fluid, such as amides, vegetable esters and sulfonates, were efficiently removed in the distillation process proposed in this study. In particular, the bands between $2800\text{--}3000\text{ cm}^{-1}$, which indicate the presence of hydrocarbons, and the bands below 1500 cm^{-1} , related to amide and sulfonate functional groups, were significantly attenuated or eliminated. This demonstrates that the recovery process was effective, allowing the reuse of water with a high degree of purity and making it suitable for reprocessing in industrial applications. Despite being a prototype with very small dimensions, the results presented are promising, as the distilled liquid can be reused in the industrial process or discarded in the environment and the remaining liquid can be transported to companies specialized in decontaminating cutting fluids in much smaller volumes, thus reducing subsequent costs. One solution to improve the 3.05% thermal efficiency is a more hermetic construction, forcing all distillate to flow into the collection reservoir, avoiding evaporation loss in the tank. As it is a very cheap and easy to build piece of equipment, the period of lower solar intensity will only have

lower production, without compromising the quality of the distilled fluid. Compared to authors cited in the bibliographic review, who use expensive systems that consume electrical energy, the equipment proposed in this work presents very interesting results, as it does not consume any type of energy other than solar energy. The efficiency of the system is significantly affected by the low solar intensity, as shown in Fig. 7, however, for effective distillation, free from instrumentation, the outlet of the distiller channel must be connected directly to the distillate collection tank, making the system more hermetic. Therefore, efficiency peaks can be considered negligible, considering the low cost of the equipment.

ACKNOWLEDGMENT

The authors would like to thank the Federal Institute of Education, Science and Technology of São Paulo for the constant encouragement and use of the facilities and laboratories available at the Catanduva-SP Campus.

REFERENCES

- [1] Motta, M. F. & Machado, A. R. (1995). Fluidos de corte: tipos, funções, seleção, métodos de aplicação e manutenção. *Revista Máquinas e Metais* 44–56.
- [2] Colbeth, H. L., Chen, K. T., Picciotto, S., Costello, S. & Eisen E. A. (2023). Exposure to Metalworking Fluids and Cancer Incidence in the United Auto Workers–General Motors Cohort. *American Journal of Epidemiology* 192, 171–81.
- [3] Friesen, M. C., Betenia N., Costello, S. & Eisen, E. A. (2012). Metalworking fluid exposure and cancer risk in a retrospective cohort of female autoworkers. *Cancer Causes Control*, 23 1075–82.
- [4] Jagadevan, S., Graham, N. J. & Thompson, I. P. (2013). Treatment of waste metalworking fluid by a hybrid ozone-biological process. *Journal of Hazardous Materials*, 244, 394–402.
- [5] Almeida, E., Assalin, M. R., Rosa, M. A. & Durán, N. (2004). Wastewater treatment by oxidation with ozone. *Quím. Nova*, 27, 818–24.
- [6] Klocke F. & Eisenblätter G. (1997). Dry Cutting. *CIRP Annals*, 46, 519–26.
- [7] Weinert, K., Inasaki, I., Sutherland, J. W. & Wakabayashi, T. (2004). Dry machining and minimum quantity lubrication. *CIRP Annals*, 53, 511–37.
- [8] Kalhöfer, E. & Kranzen, J. (2008). Usinagem a seco: passada a euforia, é hora de avaliar prós e contras. *Revista Máquinas e Metais*, 510, 48–55.
- [9] Benedicto, E., Carou, D. & Rubio, E. M. (2017). Technical, economic and environmental review of the lubrication/cooling systems used in machining processes. *Procedia Engineering*, 184, 99–116.
- [10] Armit, P. & Sing, C. S. (2014). *Role of minimum quantity lubrication in metal machining*. LAP Lambert Academic Publication.

- [11] Walker, T. (2013). *The MQL Handbook: a guide to machining with minimum quantity lubrication* (Vol. 1). Unist Inc.
- [12] Lima Junior, J. da S. (2021). *Análise técnico-econômica de fluidos de corte a base de óleo vegetal e sintético em operações de usinagem do aço SAE 1045*. Master Thesis (Brazil: universidade Federal de Pernambuco).
- [13] Assenhaimer, C., Seto, L. N., & Guardani, R. (2015). Avaliação Do Tratamento De Efluentes Contendo Resíduos De Fluidos De Corte Por Processo UV-H2O2. *Blucher Chemical Engineering Proceedings*, 1(2), 7730-7737.
- [14] Seo, D. C., Lee, H. J., Hwang, H. N., Park, M. R., Kwak, N. W., Cho, I. J., Cho, J. S., Seo, J. Y., Joo, W. H., Park, K. H. & Heo, J. S. (2007). Treatment of non-biodegradable cutting oil wastewater by ultrasonication-Fenton oxidation process. *Water Science and Technology*, 55, 251–9.
- [15] ESP 32. (2019). Espressif Systems ESP32.
- [16] Liu, T. (2020). DHT22 Data Sheet. *Guangzhou, China: Aosong Electronics Co., Ltd.* Maxim. (2012). DS18B20 Dallas Semiconductor.
- [17] Avallone, E., Mioralli, P. C., Scalon, V. L., Padilha, A. & Oliveira, S. del R. (2018). Thermal pyranometer using the open hardware Arduino platform. *International Journal of Thermodynamics* 21, 1–5.
- [18] Avallone, E., Mioralli, P. C., Scalon, V. L. and Padilha, A. (2016). Thermal pyranometer using the Arduino platform for data acquisition. In *Proceedings of 4th International Conference on Contemporary Problems of Thermal Engineering vol 1 (Katowice - Polen: Politechnika Slaska - ITC)* (pp. 303–11).
- [19] Avallone, E., Pansanato, C., Faro, Á. N., Silva, D. I. A. da, Silva, J. W. da, Gonçalves, G. B., Ito, M. C., Garcia, R. P. & Mioralli, P. C. (2021). Radiômetro solar de baixo custo usando a plataforma aberta Arduino. *Coleção desafios das engenharias: Engenharia mecânica*. Atena Editora (pp 79–91).
- [20] Avallone E. (2017). *Estudo de um coletor solar, tipo tubo evacuado modificado, utilizando um concentrador cilíndrico parabólico (CPC)*. PhD Thesis (Brazil: Universidade Estadual Paulista “Júlio de Mesquita Filho” - UNESP/FEB).
- [21] Pansanato C., Gonçalves G. B., Ito M. C., Scalon V. L., Avallone E. & Garcia R. P. (2018). Low cost thermal pyranometer using Dallas DS18B20 sensor and Arduino. In *Proceedings of ENCIT 2018 17th Brazilian Congress of Thermal Sciences and Engineering vol 1–8* (Águas de Lindóia - SP: ABCM).
- [22] Avia S. (2020). HX711.
- [23] Thermo S. (2014). Thermo Scientific Nicolet iS5 FT-IR Spectrometer.

Selection of Viable Areas for Geothermal Installations with Helical Probes using 3D Geophysical Modeling of the Subsoil

Víctor Pérez Fernández¹, Cristina Sáez Blázquez², Ignacio Martín Nieto³

¹Department of Cartographic and Terrain Engineering, University of Salamanca, Higher Polytechnic School of Avila, Hornos Caleros 50, 05003 Avila, Spain

¹vperez@usal.es, ²u107596@usal.es, ³nachomartin@usal.es

Abstract—In the context of current energetic transition, the shallow geothermal energy it presented as a sustainable and efficient alternative for energetic generation. This paper focuses on the identification optimal zones for the installation of shallow geothermal energy, with a comparison of two main approaches. Helicoidal system and Horizontal system. Through the detail analysis of the underground by applying Ground Penetrating Radar, the suitability of implementing helical design in the area under study has been confirmed. Finally, the research includes the calculation of this system through the use of own and specific geothermal software.

Keywords - helicoidal system, ground-penetrating radar, horizontal system

I. INTRODUCTION

Geothermal energy is a 100 % clean, non-emitting Green Houses Gases (GHG) and inexhaustible renewable energy that will be increasingly used in the upcoming years. Before performing a shallow geothermal project, it is necessary to know the composition and state of the subsoil, where the borehole or boreholes will be located to avoid possible fractures or leaks in the ground and to place the geothermal heat exchanger in the most suitable location.

In this context, several studies and geophysics techniques have been applied in geothermal surveys with the objective of defining the characteristics and properties of the underground. These practices include the use of

Electrical Tomography (ET) or Magneto Telluric (MT) to investigate the deeper structural levels in which the geothermal field is planned to be set.

Given the importance of knowing in detail the structure of the subsoil in geothermal applications, this research focuses on evaluating the different prospecting possibilities for shallow exploitation purposes,

A. Abbreviations and Acronyms

SGE: Shallow Geothermal Energy
GPR: Ground Penetrating Radar
ET: Electric Tomography
MT: Magnetotelluric
DCR: Direct Current Resistivity
SRT: Seismic Refraction Tomography
VES: Vertical Electrical Sounding
T^a: Temperatura
ERT: Electrical Resistivity Tomography
EM: Electro Magnetic
TRT: Thermal Response Test
 α : Attenuation
 μ : Magnetic permeability
 ω : signal frequency
 ϵ : cte dielectric
 σ : Conductivity
***T_m*:** Average annual ground temperature in ° C at a depth where temperature variations are not perceptible. As it difficult to know, the annual mean temperature of the ambient air above the ground surface is taken.
***A_s*:** Oscillation temperature in ° C



z : deep of the ground
 t : time in days
 t_0 : is the time lag in days
 α : thermal diffusivity of the ground
 $T_{w, in}, T_{w, out}$ = Water temperatures in and out of the ground heat exchanger
 ρ_w : water density
 c_w : specific heat capacity
PGHE: Pile Geothermal Heat Exchanger
 Q' : Water volumetric flow
HPS: Heat Pump System
EP: Energy Piles

UNITS

α = dB/cm
 μ = H/m
 ω = Hz
 ε = not have units
 σ = S/m or W/mK
 T_m = °C
 A_s = °C
 z = m
 t = days
 t_0 = days
 α = W/mK
 $T_{w, in}, T_{w, out}$ = °C
 ρ_w = kg/m³
 c_w = J/kg K
 Q' = m³/s

II. MATERIALS AND METHODS

A Shallow Geothermal Energy (SGE) system refers to the thermal energy reserves in the rock-soil body, groundwater, surface water and geothermal tail water at a depth of less than 200m, which is worthwhile to develop and utilize, and has a temperature lower than 25 °C. SGE has the characteristics of wide distribution, stable temperature, shallow buried depth and convenience for collection. The need for the development and utilization of SGE has been recognized by many countries [1] like China [2] Croatia [3], Germany [4], Turkey [5], Spain [6], and so on. Special interest is in the direct use of SGE and the numbers of shallow geothermal installations have continuously increased during the last decade [7].

This research focuses on a shallow geothermal energy system to be deployed in the province of Ávila (Centre of Spain), specifically at the Higher Polytechnic School of Avila (University of Salamanca), in which extensive research has been performed in the last years within the field of geothermal applications. As a

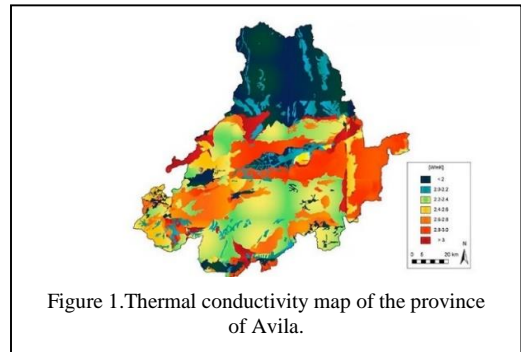


Figure 1. Thermal conductivity map of the province of Avila.

result of some these studies is the thermal conductivity map of the region presented in Fig. 1.

In the present case, this study aims to evaluate the possibilities of implementing a shallow geothermal system in the area shown in Fig. 2 below, where an existing borehole is located in which different studies of the thermal behavior of the ground have been carried out (such as a Thermal Response Test (TRT) [8]).

B. Geological Characteristics

From a geological point of view, the region of Ávila is divided into two distinct geological zones: an eminently sedimentary zone, which is located in the north-center of the province, and a second igneous area which extends from the south and east to the Central System [9]. The area under study (Figs. 2 and 3) is formed by colluviums that are deposits of loose materials with variable matrix, from nil to very abundant.

The extent and development depend on the morphology and slope angle, as well as on the structure and lithology of the source area structure and lithology of the source area. The northern part of the leaf exhibits a pronounced

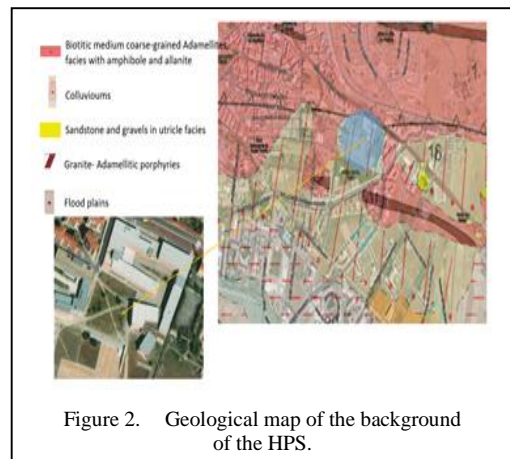


Figure 2. Geological map of the background of the HPS.

affinity with granites manifesting as a red pinkish hue.

This Colluviums are slope deposits which are found or at base or foot od slope. Two main groups of processes are usually involved in the development of a given slope deposit (a) Slope wash, hill wash or rain wash, that include soil erosion on agricultural land (b) mass wasting [10].

The history of colluvium and related terms follows changes in understanding of Earth processes and the needs to better describe varied environments in which Earth scientist work. While the definition of colluvium as changed a lot of time drastically from its origin [11].

C. Geophysical Methods

As previously discussed, the assessment of ground properties for geothermal purposes can be approached through various geophysical surveys. The main methods, including Magnetotelluric (MT), Direct Current Resistivity (DCR), Ground Penetrating Radar (GPR), Magnetostatic, Seismic Refraction, and Seismic Reflection, are compared below. These techniques are used to estimate ground characteristics and select the best location for the geothermal borehole. Table I provides an overview of these methods, while Table II outlines their properties and applications.

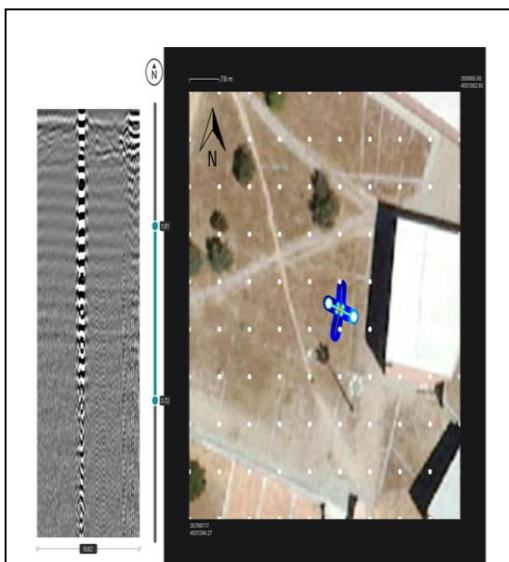


Figure 3. Location of the area under study at the Higher Polytechnic School of Ávila.

TABLE I. GENERAL CLASSIFICATION OF GEOPHYSICAL METHODS.

G. M	General Classification		
	Depth (km)	Application areas	Survey methods
Refract	0 – 150	Basin analysis Crustal studies Plate tectonics	Ground
Reflect	0-10	Basin Analysis	Ground
Gravi	Entire of the earth	Mining Hidrology Plate tectonics Paleo tectonics Core dynamics	Ground Airbone Spacebone
E	0 - 20 3000 - 6450	Basin Analysis Plate tectonics Paleo tectonics Core dynamics	Ground Airbone Spacebone
Induction	0 – 10	Geologic Mapping Ore minning Metal detection	Ground Airbone
GPR	0- 0,05	Geotechnology Hidrology Archaeology	Ground Airbone
MT	0-150	Hidrology Plate tectonics	Ground
DCR	0-0,01	Hidrology Ore Mining	Ground

TABLE II. CHARACTERISTICS AND PROPERTIES OF THE DIFFERENT GEOPHYSICS' METHODS.

G. M	Properties and Clasification		
	Measured property	Investigated physical property	Main practical obstacle
Refra	Seismic travel time	Seismic velocity	Seismic wave attenuation
Refl	Seismic travel time	Contrasts in acoustic wave impedance	Seismic wave attenuation
G	Acceleration vector and its gradient	Density contrast	small variations in densities of rocks
ME	Magnetic field vector	Magnetic permeability	Low magnetic strenght of rocks
DCR	Electric Potential Change	Resistivity	Low depth of penetration
MT	Amplitudes of electromagnetic fields	Resistivity,	Fast attenuation
EMI	Phase/amplitude of the magnetic field	Resistivity, Dielectric permittivity	Fast attenuation
GPR	Electromagnetic travel time	Contrast in electromagnetic wave impedance	Fast attenuation

Seismic Methods: Seismic methods involve the measurements of wave – fields produced by artificially or naturally generated seismic waves that propagate in the subsurface or near the soil surface. An earthquake is a common form of a seismic wave [12].

Gravity Methods: Gravity surveys play a crucial role in geothermal exploration, helping to detect lateral density variations that indicate deep magmatic bodies or heat sources. These methods can also reveal depth variations in crust-mantle interfaces and isotherms, which are critical for identifying geothermal potential.

Magnetic Methods: Magnetic surveys are particularly useful in mapping volcanic rocks near the surface, which are often relevant in geothermal contexts. These methods are designed to detect changes in magnetic properties, such as those occurring when rocks reach the Curie temperature, a critical point at which magnetic susceptibility is nearly lost [13].

Electrical and Electromagnetic Methods: Electrical and electromagnetic techniques are vital for characterizing geothermal reservoirs due to their sensitivity to subsurface resistivity changes caused by hydrothermal activity. Temperature influences the electrical properties of rocks, and these methods can measure the conductivity variations in groundwater. For example, between 350°C and 20°C, conductivity can increase sevenfold.

While all these methods can accurately determine the structure and status of geothermal systems, their high costs make them impractical for small-scale shallow geothermal systems, such as the one in this case study. Table III provides a cost comparison for these methods.

TABLE III. COST THE DIFFERENT GEOPHYSICAL METHODS.

Geophysical method	Price
	Cost of different methods (€)
Seismic refraction	9.200 - 46.000 (€/km)
Seismic reflexión	9.200 - 46.000 (€/km)
Gravimetry	4. 600 - 13.800 (€/km ²)
Magnetometry	920 - 4.600 (€/km ²)
Electrical Resistivity	1.840 - 9.200 (€/km ²)
Electromagnetic methods	2.760-18.400 (€/km ²)

D. Ground Thermal Response

Another possibility is to determine the underground thermal conductivity in shallow geothermal boreholes, reservoir or system by the use of TRT (Thermal Response Test). This technique is used to estimate subsurface and borehole thermal properties, which are required for the design and sizing of ground coupled heat pumps. The two properties estimated with this TRT are the thermal conductivity of the subsurface and the thermal resistance of the borehole.

TRTs involve a heat source that perturbs subsurface temperatures initially assumed to be at equilibrium, they are analogous to pumping test in hydrogeology, where groundwater is pumped to perturb hydraulic heads in an aquifer. This solution is used for the analysis of pumping tests is based on the infinite line -source equation for heat transfer

A TRT unit consist of a pump, purge valves, an electric heating element, temperature sensors, a flow meter, and a data logger.

For it doesn't have produced any fluctuation during this experiment or process be realized it will be recommended to measure the heat injection rate, from the temperature differential the water flow rate using the following equation [14]:

$$Q(t) = \dot{Q}(t) \times T_{w,in}(t) - (-T_{w,out}(t) \times \rho_w c_w) \quad (1)$$

Taking advantage of the existence of a tested borehole in the study area, this research provides data on the thermal properties of the surrounding soil from the implementation of a TRT [8].

E. Use of Ground Penetrating Radar for Geothermal Purposes

The Ground Penetrating Radar (GPR) generates through a transmitting antenna, electromagnetic pulses of very short duration which, on their way through the terrain, intercept objects and discontinuity surfaces where part of the energy is reflected and received by a receiver antenna.

The non- reflected part of energy continues its path by reflecting off new objects during its total damping.

The attenuation which determinates the penetration capacity of the electromagnetic waves and depends on the parameters $\mu, \epsilon, \sigma, \omega$ (magnetic permeability, dielectric constant, conductivity and signal frequency) is expressed by following math equation [15].

$$\alpha = \omega \sqrt{\frac{\mu\epsilon}{2} \left(\sqrt{1 + \left(\frac{\sigma}{\omega\epsilon} \right)^2} - 1 \right)} . \quad (2)$$

By continuously moving the radar antenna over the surface, traces are obtained with the reflections at each point. The continuous representation of these traces, assigning a color tone to each amplitude, gives rise to an image known as a radargram.

In this case, GPR was used to analyze the ground composition in the area under study (where there is an existing borehole) with the aim of evaluating the possible application of the method for establishing the optimal geothermal well field configuration.

The aim is to establish the possibility of implementing horizontal or helical systems due to the absence of rock formation at the selected depth.

F. Geothermal Well Field Design

As mentioned before, the possibilities of implementing surface geothermal systems (horizontal or helical) in a specific study area are being evaluated in this research. Some description about both configurations is included below.

1) Helical heat exchangers

Different geothermal heat exchangers can be used for low enthalpy geothermal energy installations. Despite the most popular are the vertical heat exchangers, the conditions of the project may imply the use of other alternative schemes.

The helical design involves cooling the pipes in a helical shape, which increases the surface in contact with the ground. This design enhances the heat exchange efficiency between the ground and the fluid circulating within the pipes. The helical system is particularly effective in areas with limited space, as it allows for a more compact installation compared to traditional vertical or horizontal systems

2) Horizontal geothermal design

The horizontal heat exchange has been extensively applied in GHP systems in several regions of the world. Thermal performance of the horizontal GHP system is comparatively lower than vertical ones given the seasonal soil temperature variation, thereby the horizontal GHP system needs larger land area and logger pipe [16].

However, this design is able to offer a cost-effective option as the drilling costs are avoided. Three different styles, linear, slinky – coil and spiral – coil arrangements are often implied in this horizontal design. The spiral and slinky configurations have higher heat transfer rates per trench unit length.

In term of the closed – loop system with sufficient ground area, the ground loop is arranged horizontally underneath the surface of ground within backfilled trenches. Three basic configurations including the trench, series and parallel loops are presented in the following figure.

The series and parallel layouts typically require smaller land regions and are able to be combined, improving the flexible horizontal fittings [17].

In addition, the technical differences between the geothermal designs here evaluated are included in the following Table IV [18-21].

TABLE IV. DIFFERENCES BETWEEN THE DIFFERENT GHES.

Characteristics	Design GHE	
	Helical GHE	Horizontal GHE
Installation	They used deep spiral - shaped pipes of boreholes to exchange heat with the ground in deeper and narrower trenches	They are installed at a depth 1,2 -1,5 m using High density polyethylene pipes
Space necessary	Requires less land area, more suitable for areas with limited space	Required a larger area of land for their installation
Climate conditions	Less affected by outdoor weather conditions due to their depth	their performance can be affected by outdoor climatic conditions due to their proximity to the surface
Cost, Prize	They tend to be more expensive to install due to the need for drilling	They are generally cheaper to install as they don't require deep drilling

III. RESULTS

A. GPR Application

The results of the GPR surveys are presented in the following Figs. 4 and 5.

To obtain the 3D model of the ground, the specific software GPR Insights was implemented.

The results of the Ground Penetrating Radar have allowed selecting the areas where it is possible to apply a drilling method compatible with the installation of helical probes at a viable depth (5-10 m). Given the greater performance of this type of design compared to traditional horizontal geothermal energy, in this case the helical ones will be chosen.

B. Real Application

Based on the data obtained from the TRT previously carried out in the survey and the geophysical readings obtained, a geothermal installation based on helical probes has been designed.

This has been possible given that the nature of the terrain surveyed with GPR makes the rotary drilling necessary for this type of installation possible.

The design program used was GES-CAL [22] which allows this type of probe to be included among the design options for the drilling field.

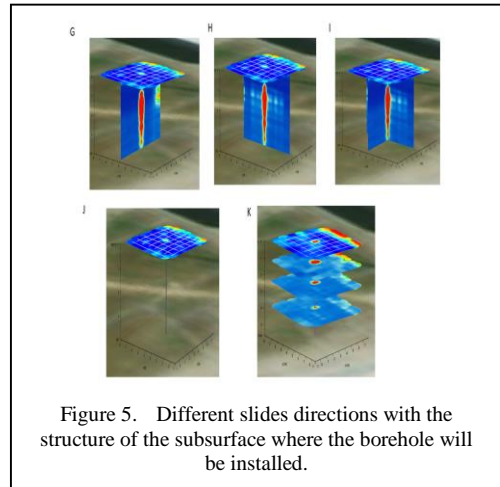


Figure 5. Different slides directions with the structure of the subsurface where the borehole will be installed.

In all the installations previously designed using this method, a significant economic improvement has been observed compared to the solution with conventional horizontal geothermal energy in areas where it is not possible to carry out more drilling.

The starting data considered were a thermal conductivity of the ground of 2.6 W/mK (from thermal resistance tests in the borehole), annual energy needs of 35,792 MWh (for a single-family home in the climatic zone of Ávila where the proposed location is located) and a land available for drilling of 100 square meters in surface area.

With all the above, results can be seen in the previous Figs. 6 and 7.

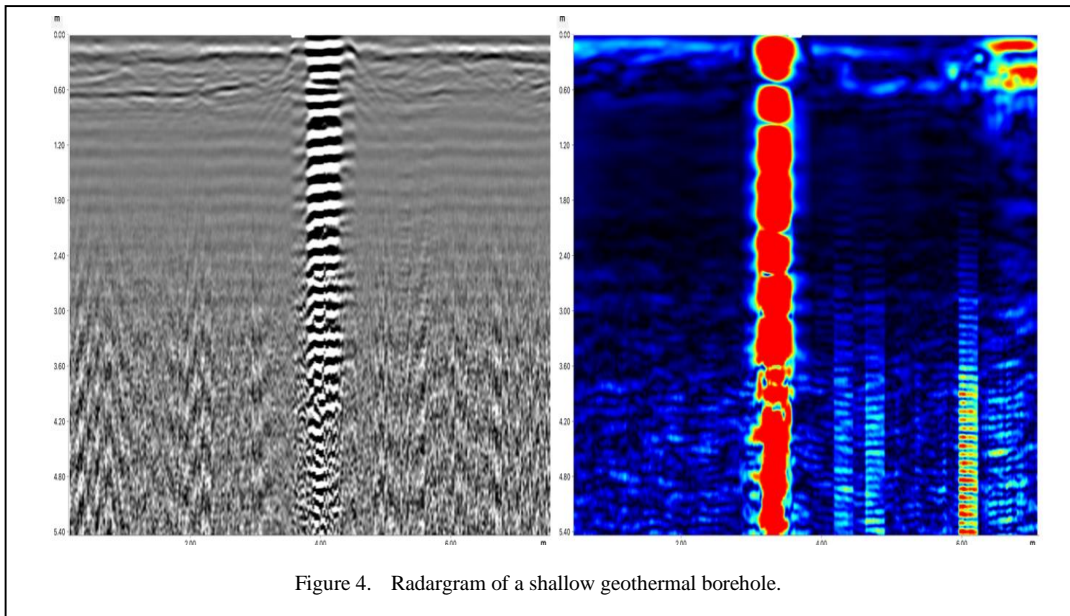


Figure 4. Radargram of a shallow geothermal borehole.

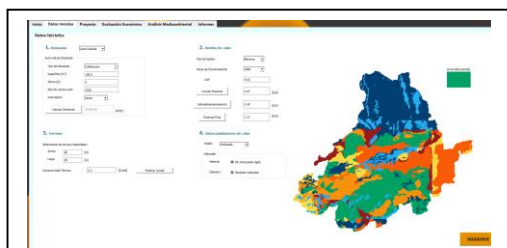


Figure 6. GES-CAL main window.

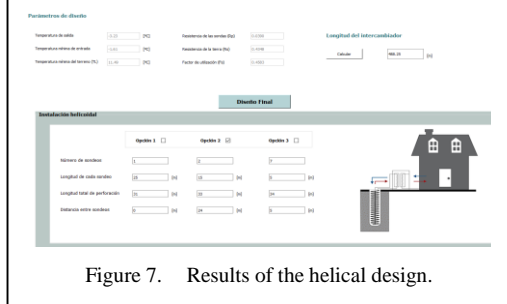


Figure 7. Results of the helical design.

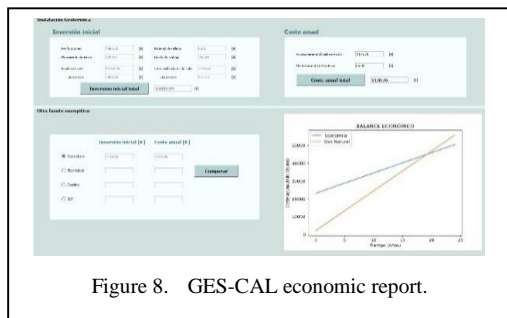


Figure 8. GES-CAL economic report.

As an additional result to the pure design of the installation, GES-CAL generates an economic report to estimate the amortization period of the installation compared to the most favorable alternative of those stored (in this case of the natural gas installation). This report can be seen in Fig. 8.

The selection of natural gas as a solution to be compared has been established after evaluating the available energy possibilities.

As can be seen, the inclusion of GPR in the tests prior to the direct implementation of a conventional horizontal geothermal system has allowed the selection of a more efficient method from an energy and economic point of view.

IV. CONCLUSIONS

This study demonstrates the potential of helical probe-based shallow geothermal energy systems (SGE) as an effective and sustainable energy source. It was feasible to precisely evaluate the ground's thermal characteristics and

choose the best locations for geothermal installation by using GPR and TRT. The findings show that the helical probe methods provide a notable energy efficiency benefits, particularly in locations with constrained installation space. The economic analysis also demonstrates that, while being initially more costly than natural gas systems the adoption of helical probes might result in a quicker return on investment because of their superior thermal performance.

The study highlights how crucial through the subsurface investigation is to geothermal projects. When assessing the feasibility of geothermal well fields and refining system designs, the incorporation of geophysical techniques like as GPR has proven crucial. By using less land and avoiding needless drilling, this method not only improves energy efficiency but also lessens its negative effects on the environment.

In order to reduce installation costs, future research should examine the wider applicability of this concept in various geological contexts as well as potential advancements in drilling technology.

SGE systems are an essential component of future energy landscapes due to the growing need for renewable energy and further study in this area will help to assure their successful deployment.

Future work will address the potential for scalability and exploitation of the systems evaluated in this research in other geological and energy contexts.

REFERENCES

- [1] Haehnlein, S., Bayer, P., & Blum, P. (2010). International legal status of the use of shallow geothermal energy. *Renewable and Sustainable Energy Reviews*, 14(9), 2611-2625.
- [2] Zhu, J., Hu, K., Lu, X., Huang, X., Liu, K., & Wu, X. (2015). A review of geothermal energy resources, development, and applications in China: Current status and prospects. *Energy*, 93, 466-483. Scopus.
- [3] Macenić, M., Kurevija, T., & Strpić, K. (2018). Systematic review of research and utilization of shallow geothermal energy in Croatia. *Rudarsko-Geološko-Naftni Zbornik*, 33(5), 37-46.
- [4] Somogyi, V., Sebestyén, V., & Nagy, G. (2017). Scientific achievements and regulation of shallow geothermal systems in six European countries – A review. *Renewable and Sustainable Energy Reviews*, 68, 934-952.
- [5] Yener, D., Ozgener, O., & Ozgener, L. (2017). Prediction of soil temperatures for shallow geothermal

- applications in Turkey. *Renewable and Sustainable Energy Reviews*, 70, 71-77.
- [6] Gil, A. G., & Moreno, M. M. (2019). Current Legal Framework on Shallow Geothermal Energy Use in Spain. *Journal of Sustainability Research*, 2(1).
- [7] Xu, Y.-S., Wang, X.-W., Shen, S.-L., & Zhou, A. (2020). Distribution characteristics and utilization of shallow geothermal energy in China. *Energy and Buildings*, 229, 110479.
- [8] Sáez Blázquez, C., Martín Nieto, I., Farfán Martín, A., González-Aguilera, D., & Carrasco García, P. (2019). Comparative analysis of different methodologies used to estimate the ground thermal conductivity in low enthalpy geothermal systems. *Energies*, 12(9), 1672.
- [9] Blázquez, C. S., Maté-González, M. Á., Nieto, I. M., Martín, A. F., & González-Aguilera, D. (2022). Assessment of the geothermal potential in the region of Ávila (Spain): An integrated and interactive thermal approach. *Geothermics*, 98, 102294.
- [10] Múcher, H., van Steijn, H., & Kwaad, F. (2018). Chapter 2—Colluvial and Mass Wasting Deposits. En G. Stoops, V. Marcelino, & F. Mees (Eds.), *Interpretation of Micromorphological Features of Soils and Regoliths (Second Edition)* (pp. 21-36). Elsevier.
- [11] Miller, B. A., & Juilleret, J. (2020). The colluvium and alluvium problem: Historical review and current state of definitions. *Earth-Science Reviews*, 209, 103316.
- [12] *Seismic Method—An overview | ScienceDirect Topics*. (s. f.). Recuperado 13 de noviembre de 2024, de <https://www.sciencedirect.com/topics/earth-and-planetary-sciences/seismic-method>
- [13] Georgsson, L. S. (s. f.). *Geophysical methods used in geothermal exploration*.
- [14] Raymond, J., Therrien, R., Gosselin, L., & Lefebvre, R. (2011). A Review of Thermal Response Test Analysis Using Pumping Test Concepts. *Groundwater*, 49(6), 932-945.
- [15] *Técnicas Geofísicas*. (s. f.).
- [16] Cui, Y., Zhu, J., Twaha, S., Chu, J., Bai, H., Huang, K., Chen, X., Zoras, S., & Soleimani, Z. (2019). Techno-economic assessment of the horizontal geothermal heat pump systems: A comprehensive review. *Energy Conversion and Management*, 191, 208-236.
- [17] Self, S. J., Reddy, B. V., & Rosen, M. A. (2013). Geothermal heat pump systems: Status review and comparison with other heating options. *Applied Energy*, 101, 341-348.
- [18] Geotermia: ¿Captación Horizontal o Vertical? T-Reunidas Asturias. (2017, febrero 7). *t-reunidas.es*. Available at: <https://www.t-reunidas.es/geotermia-captacion-horizontal-captacion-vertical/>
- [19] antoniolidia. (2023, enero 1). *Tipos de sistemas geotérmicos y su funcionamiento: Una guía completa*. Todo Ingenierías. Available at: <https://todoingenierias.com/tipos-de-sistemas-geotermicos-y-su-funcionamiento-una-guia-completa/>
- [20] Trillo, G. L., & Jimeno, C. L. (2009). Intercambiadores geotérmicos verticales. *Revista Digital del Cedex*, 156, Article 156.
- [21] León, J. de C. y. (s. f.). *Sistemas de intercambio geotérmico* (Castilla y León) [Text]. Junta de Castilla y León. Recuperado 2 de octubre de 2024, de <https://energia.jcyl.es/web/es/energias-renovables-ordenacion-energetica/sistemas-intercambio-geotermico.html>
- [22] Sáez Blázquez, C., Martín Nieto, I., Mora, R., Farfán Martín, A., & González-Aguilera, D. (2020). GES-CAL: A new computer program for the design of closed-loop geothermal energy systems. *Geothermics*, 87, 101852.

Numerical Study of Heat Transfer from a Nanofluid in a Waved Channel Equipped with a Rotating Cylinder in the Presence of a Magnetic Field

Nawal Guerroudj¹, Brahim Fersadou², Henda Kahalerras³

^{1,2,3}Faculty of Mechanical and Process Engineering, University of Sciences and Technology Houari Boumediene, Laboratory of Multiphase Transport and Porous Media, Algeria

¹nawal.guerroudj@usthb.edu.dz, ²brahim04@live.fr, ³kahalerrashenda@yahoo.fr

Abstract—The present study focuses on the intensification of heat transfer by coupling active and passive methods. To this end, a numerical study is carried out to explore the flow and heat transfer characteristics of a Cu-Al₂O₃-TiO₂/water tri-nanofluid in a corrugated-walled channel featuring a constriction at the inlet and equipped with three heat sources maintained at a constant temperature and organized alternately on the upper and lower walls. A rotating solid obstacle of circular shape is placed in center of channel, while a uniform magnetic field is applied throughout the channel. The governing equations and associated boundary conditions are solved numerically using Galerkin's weighted residual finite element method. The parametric study focuses on the impact of the opening rate at the channel entrance AR, the rotation speed of the solid obstacle and the magnetic field strength expressed by the Hartmann number Ha. The results reveal an intensification of the heat transfer rate with increasing Ha, Re₀ and decreasing AR.

Keywords - wavy channel, nanofluid, heat sources, magnetic field, rotatif solid obstacle

I. INTRODUCTION

In recent years, several techniques have been employed to enhance convective heat transfer in fluid-based cooling systems, including the adaptation of passive techniques by placing deflectors on the internal wall of heat sinks [1,2], or even the use of directed jets through open

cavities subjected to appropriate thermal boundaries to increase heat exchange [3-5]. Papers that are not formatted according to the instructions in the template will not be considered for review. The technique of enhancing heat transfer through wavy walls is a very important feature; indeed, numerous empirical studies and numerical analyses reported in the literature have focused on this technique [6-8]. The physical process of enhancing heat transfer arises from the fact that the wavy shape of the surface disrupts the boundary layer formed and allows for the continuous replacement of the fluid near the solid wall. Researchers have recently noted an innovative technique that involves using base fluids in which nanoparticles at very low concentrations are suspended to improve their thermal efficiency. These fluids are known as nanofluids. This new class of fluids can be used in a variety of technical applications, including boiling, condensation, cooling, and vehicle lubrication.

This work is situated within this context and involves a numerical simulation of the forced convection of a tri-nanofluid Cu-Al₂O₃-TiO₂/water in a wavy-walled channel featuring an inlet contraction and equipped with three heat sources maintained at a constant temperature, arranged alternately on the upper and lower walls. A rotating solid obstacle is positioned in several locations, while a uniform magnetic field



is applied throughout the channel. The governing equations and associated boundary conditions are solved numerically using the Galerkin weighted residual finite element method. The parametric study focuses on the impact of the inlet opening ratio AR , the rotation speed of the solid obstacle and the intensity of the magnetic field expressed by the Hartmann number Ha . The results reveal an enhancement in the heat transfer rate with increasing Ha , $Re\omega$ and a decrease in AR .

II. PHYSICAL DOMAIN

The study domain represented in Fig. 1 consists of a corrugated-walled channel of length ' L ' and height ' H ' featuring a constriction at the entrance with an opening ratio ' $AR = d/H$ ' and equipped with three heat sources maintained at a constant temperature, arranged alternately on the upper and lower walls. A circular rotating solid obstacle is placed in several positions, while a uniform magnetic field is applied to the upper wall of the channel.

The spatial functions defining the wall undulations are: $F_1(x) = 1 - Amp(1 - \cos(2\pi n))$ for the upper wall; $F_2(x) = Amp(1 - \cos(2\pi n))$ for the lower wall. A tri-nanofluid Water/Cu-Al₂O₃-TiO₂ enters the channel at a uniform velocity U_i and a uniform temperature T_i .

III. MATHEMATICAL FORMULATION

A. Governing Equations

In order to simplify the problem under study, several simplifying assumptions are considered: the flow is two-dimensional, laminar, with no internal heat generation and negligible viscous dissipation. The nanofluid is treated as

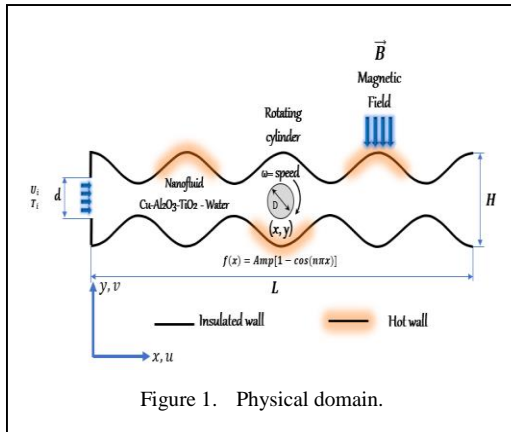


Figure 1. Physical domain.

Newtonian with constant thermophysical properties.

The dimensionless equations can be written as follows:

a) *Continuity:*

$$\frac{\partial U}{\partial Y} + \frac{\partial V}{\partial Y} = 0. \quad (1)$$

b) *Momentum:*

$$U \frac{\partial U}{\partial X} + V \frac{\partial V}{\partial Y} = -\frac{\partial P}{\partial X} + \frac{\mu_{nf}}{\mu_f} \cdot \frac{\rho_f}{\rho_{nf}} \cdot \frac{1}{Re} \cdot \left(\frac{\partial^2 U}{\partial X^2} + \frac{\partial^2 U}{\partial Y^2} \right) - \frac{Ha^2}{Re} \cdot \frac{\sigma_{nf}}{\rho_{nf}} \cdot \frac{\rho_f}{\rho_{nf}} \cdot U \quad (2)$$

$$U \frac{\partial V}{\partial X} + V \frac{\partial V}{\partial Y} = -\frac{\partial P}{\partial Y} + \frac{\mu_{nf}}{\mu_f} \cdot \frac{\rho_f}{\rho_{nf}} \cdot \frac{1}{Re} \cdot \left(\frac{\partial^2 V}{\partial X^2} + \frac{\partial^2 V}{\partial Y^2} \right) \quad (3)$$

c) *Energy:*

$$U \frac{\partial \theta}{\partial X} + V \frac{\partial \theta}{\partial Y} = \frac{1}{Re Pr} \cdot \frac{K_{nf}}{K_f} \cdot \frac{(\rho C_p)_f}{(\rho C_p)_{nf}} \cdot \left(\frac{\partial^2 \theta}{\partial X^2} + \frac{\partial^2 \theta}{\partial Y^2} \right) + \frac{Ec Ha^2}{Re} \cdot \frac{\sigma_{nf}}{\sigma_{nf}} \cdot \frac{(\rho C_p)_f}{(\rho C_p)_{nf}} \cdot U^2 \quad (4)$$

B. Boundary Conditions:

The associated boundary conditions are:

$$\text{Inlet: } U = 1; V = 0; \theta = 0, \quad (5)$$

$$\text{Exit: } \frac{\partial U}{\partial X} = 0; V = 0; \frac{\partial \theta}{\partial X} = 0, \quad (6)$$

$$\text{Upper wall: } \begin{cases} \frac{\partial \theta}{\partial Y} = T_c, & \text{under the blocks} \\ \frac{\partial \theta}{\partial Y} = 0, & \text{elsewhere} \end{cases} \quad (7)$$

$$U = V = 0 =$$

$$\text{Lower wall: } \begin{cases} \frac{\partial \theta}{\partial Y} = Tc, & \text{under the blocks} \\ \frac{\partial \theta}{\partial Y} = 0, & \text{elsewhere} \end{cases} \quad (8)$$

The expressions for the various dimensionless groupings are as follows:

$$Re = \frac{U_i H \rho_f}{\mu}; \quad Pr = \frac{\mu C p_f}{k_f}; \quad Ec = \frac{U_i^2}{C p_f \Delta T};$$

$$Ha = \frac{\sigma_f B_0^2 H^2}{\mu_f}.$$

C. Nusselt number

The local Nusselt number is given by:

$$Nu = -\frac{K_{thnf}}{K_f} \cdot \frac{\partial \theta}{\partial n},$$

$$\frac{\partial \theta}{\partial n} = \sqrt{\left(\frac{\partial \theta}{\partial X}\right)^2 + \left(\frac{\partial \theta}{\partial Y}\right)^2}. \quad (9)$$

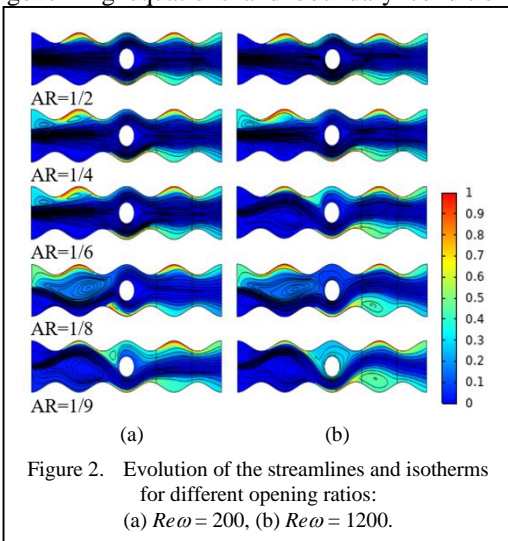
D. Pressure drop

The pressure drop is given by:

$$\Delta P = P_{m(x=0)} - P_{m(x=L)}. \quad (10)$$

IV. NUMERICAL PROCEDURE

The Galerkin weighted residual finite element method (FEM) was used to solve the governing equations and boundary conditions



mentioned above. Since FEM is employed to tackle the problem, the first step involves specifying the type of mesh. The geometric domain was transformed into a number of unstructured and non-uniform triangular elements, with finer meshes applied near the walls, resulting in a total of 60526 elements. The direct solver PARDISO was selected to solve the dynamic and thermal fields. To ensure converged solutions for different parametric studies, a convergence criterion of 10^{-6} was applied.

V. RESULTS AND DISCUSSION

Given the significant number of parameters involved in this study, some were varied while others were kept fixed. The focus was on the effects of rotational Reynolds number ($0 \leq Re\omega \leq 3000$) and the inlet aspect ratio of the channel ($1/9 \leq AR = d/H \leq 1/2$) and Hartmann number ($0 \leq Ha \leq 50$). The Reynolds number was fixed at $Re = 200$, the volumetric concentration of nanoparticles $\varphi_{Cu} = 2\%$, $\varphi_{Al_2O_3} = 2\%$, $\varphi_{TiO_2} = 1\%$ and the radius of the solid obstacle was fixed at $R = 0.2$.

Fig. 2 illustrates the evolution of the streamlines and isotherms for different opening ratios. The flow structures obtained adhere to the overall shape of the channel and the shape of the solid obstacle. It is observed that recirculation zones form just at the entrance of the channel, produced by the jet; thereafter, the nanofluid is again accelerated at the constrictions caused by the wave crests after the obstacle.

At high values of the opening ratio, the nanofluid flows symmetrically with respect to the central axis of the channel. At low values of Rp , an asymmetry is clearly visible in the flow, which is due to instabilities caused by the reduction of the jet. At the solid block, the flow is slowed down and diverts the nanofluid towards the channel walls, thus promoting heat exchange at the second source.

When comparing the situation as $Re\omega$ increases, it is noted that starting from $Re\omega = 1200$, the thermal and dynamic distribution is locally affected in the channel, particularly at the first wave of the channel, especially for very low opening ratios AR , because the rotation speed of the obstacle is significant.

The variation of the Nusselt global number as a function of $Re\omega$ for different opening ratios

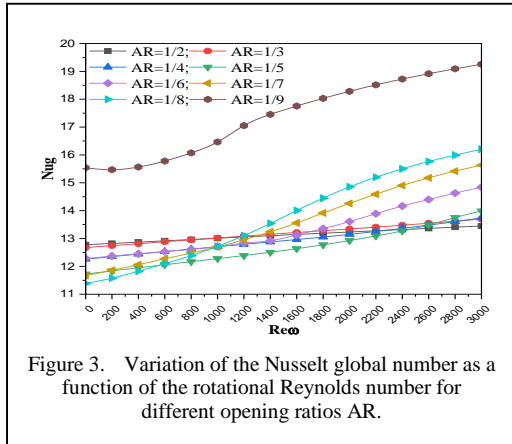


Figure 3. Variation of the Nusselt global number as a function of the rotational Reynolds number for different opening ratios AR.

AR is illustrated in Fig. 3. The heat transfer rate increases significantly, both with the decrease of the opening ratio AR and with the increase of Rew. The best heat transfer is achieved at AR = 1/9, due to the cooling of the primary source. Indeed, when the jet is reduced, it deflects toward this source and enhances its cooling (see Fig. 2).

Fig. 4 shows the evolution of pressure drop as a function of the opening ratio AR. It is clear that increasing the AR significantly raises the pressure drop. This is due to the constriction and subdivision of the nanofluid passage section at the first wave of the channel, which generates two wall jets redirected toward the centerline of the channel due to the existing harmony between the wavy structure and the shape of the solid obstacle. As a result, the flow will be revitalized at the second wave of the channel

To better understand the impact of the magnetohydrodynamic effect represented by the Hartmann number on the flow characteristics and heat transfer, we initially represented the

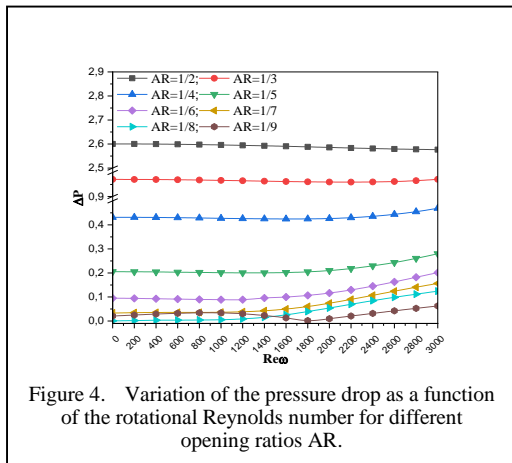


Figure 4. Variation of the pressure drop as a function of the rotational Reynolds number for different opening ratios AR.

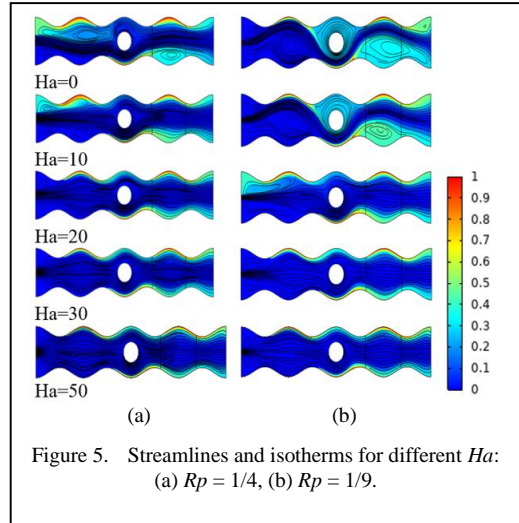


Figure 5. Streamlines and isotherms for different Ha: (a) $R_p = 1/4$, (b) $R_p = 1/9$.

streamlines and isotherms for various values of Ha in Fig. 5.

For $Ha = 0$, which corresponds to the absence of a magnetic field, the flow structure is disturbed and localized at the entrance of the channel due to the constriction. When the magnetic sources are activated, stagnation zones appear at the sources where the movement of the nanofluid is significantly slowed, and the velocity approaches zero. This is due to the effect of the Lorentz force, which acts in the opposite direction to the flow and is considered a resistive force. As a result, this leads to a disruption in the development of the thermal boundary layers, which will impact heat transfer.

At $Ha = 30$, the magnetic field accelerates the flow near the wavy walls by eliminating all the recirculation zones produced, thereby reducing the extent of the thermal boundary

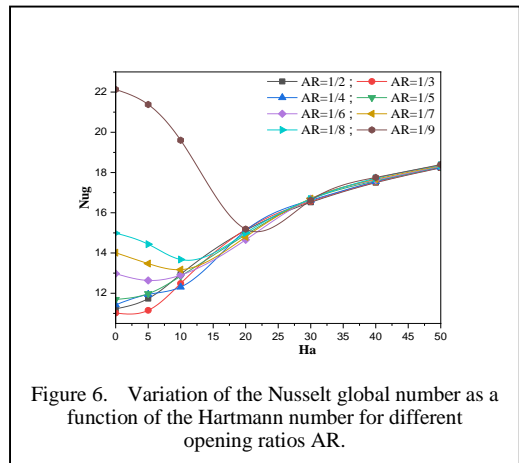


Figure 6. Variation of the Nusselt global number as a function of the Hartmann number for different opening ratios AR.

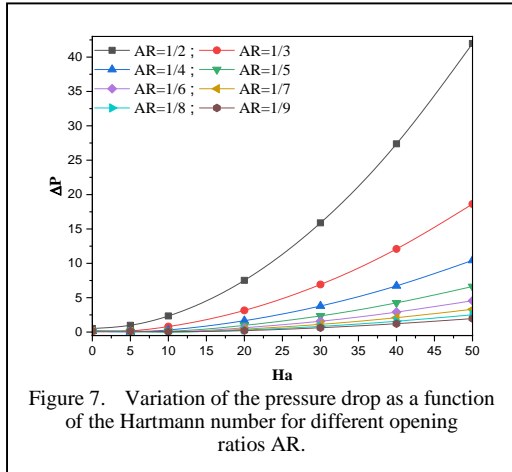


Figure 7. Variation of the pressure drop as a function of the Hartmann number for different opening ratios AR.

layers near this source. The application of the magnetic field creates an additional generalized resistance to the flow of the nanofluid. The Lorentz force is responsible for this behavior.

Fig. 6 illustrates the variation of the Nusselt global numbers with the Hartmann number for different values of AR. Increasing the intensity of the magnetic field is beneficial for heat transfer. Regarding the effect of the opening ratio, it appears that the jet flow only becomes significant at $AR = 1/9$, where the exchange between the nanofluid and the walls is favorable.

We can also distinguish two zones: the first corresponds to Hartmann numbers below 20, where heat exchange occurs in a non-monotonic manner. Thus, Nug initially increases with Ha . The critical intensity of the Lorentz force leading to the lowest heat transfer rate is closely related to the position of the obstacle relative to the entrance of the channel; the critical Ha is around 20.

The second zone concerns intensities such as $Ha = 20$, where it is evident from this figure that beyond a certain Hartmann number, increasing with the reduction of AR, heat transfer becomes insensitive to changes in the opening ratio. Indeed, this result is a direct consequence of the effect of magnetic sources on the dynamic and thermal fields discussed earlier, where increasing the intensity of the Lorentz force eliminates the flow structure created by the nanofluid jet.

As for the pressure drop, Fig. 7 illustrates the variations of the pressure drop as a function of Ha for different AR.

There is a continuous increase in pressure losses with the rise in Ha and AR. A slight pressure drop is also observed, which supports the results obtained above.

VI. CONCLUSION

Forced convection flow of a tri-nanofluid Cu- Al_2O_3 - TiO_2 /water in a wavy-walled channel featuring an inlet contraction and equipped with three heat sources maintained at a constant temperature has been numerically investigated. The key findings are as follows:

- The opening ratio AR has a significant effect on thermal performance.
- The heat transfer rate increases considerably, both with the decrease of the opening ratio AR and with the increase of $Re\omega$.
- A maximum heat transfer is achieved for an opening ratio of $AR = 1/9$ with a minimum pressure drop.
- Increasing the Hartmann number improves thermal transfer and affects the last source.

In conclusion, it can be said that to achieve a significant improvement in heat transfer, a careful choice must be made by combining the effects of the opening ratio, the rotational Reynolds number, and the intensity of the magnetic field.

In continuation of this work, we propose:

- The effect of the Reynolds number on the thermal performance : Increasing Re accelerates the jet velocity and creates larger velocity gradients, leading to a reduction in the development of thermal boundary layers and thus improving the heat transfer between the nanofluid and the channel walls.
- To highlight the effect of the nanofluid, it is preferable to choose a good combination of nanoparticles. Heat transfer increases with the volumetric concentration of nanoparticles due to the increase in the thermal conductivity of the mixture, resulting from the addition of metallic nanoparticles, which are much more heat-conductive than the base fluid.

REFERENCES

- [1] Mousavi, S. S., & Hooman, K. (2006). Heat and fluid flow in entrance region of a channel with staggered baffles. *Energy Conversion and Management*, 47(15-16), 2011-2019.
- [2] Wu, W., & Ching, C. Y. (2010). Laminar natural convection in an air-filled square cavity with partitions on the top wall. *Int J Heat Mass Transf*, 53, 1759-1772.
- [3] Deng, Q. H., Zhou, J., Mei, C., & Shen, Y. M. (2004). Fluid, heat and contaminant transport structures of laminar double-diffusive mixed convection in a two-dimensional ventilated enclosure. *International Journal of Heat and Mass Transfer*, 47(24), 5257-5269.
- [4] Bahlaoui, A., Raji, A., Hasnaoui, M., Naïmi, M., Makayssi, T., & Lamsaadi, M. (2009). Mixed convection cooling combined with surface radiation in a partitioned rectangular cavity. *Energy Conversion and Management*, 50(3), 626-635.
- [5] Naphon, P., Nakharintr, L., & Wiriyaart, S. (2018). Continuous nanofluids jet impingement heat transfer and flow in a micro-channel heat sink. *International Journal of Heat and Mass Transfer*, 126, 924-932.
- [6] Rashidi, S., Mahian, O., & Languri, E. M. (2018). Applications of nanofluids in condensing and evaporating systems: a review. *Journal of Thermal Analysis and Calorimetry*, 131, 2027-2039.
- [7] Rashidi, S., Karimi, N., Mahian, O., & Abolfazli Esfahani, J. (2019). A concise review on the role of nanoparticles upon the productivity of solar desalination systems. *Journal of Thermal Analysis and Calorimetry*, 135, 1145-1159.
- [8] Mahian, O., Kolsi, L., Amani, M., Estellé, P., Ahmadi, G., Kleinstreuer, C., ... & Pop, I. (2019). Recent advances in modeling and simulation of nanofluid flows-Part I: Fundamentals and theory. *Physics reports*, 790, 1-48.

Xylitol Production from Sugar and Alcohol Industry Waste

Lucas Vinicius Borges Pereira¹, Laís Campos Teixeira de Carvalho Gonçalves², Joelda Dantas³

¹Postgraduate Program in Renewable Energy - UFPB, João Pessoa/PB, Brazil

²Department of Sugar and Alcohol Technology - UFPB, João Pessoa/PB, Brazil

¹lucas.pereira@cear.ufpb.br, ²lais.goncalves@academico.ufpb.br,

³joelda.dantas@cear.ufpb.br

Abstract—Biotechnological alternatives are increasingly being discussed in order to promote the application of renewable materials in the industrial field, such as the use of lignocellulosic materials for the production of xylitol. Xylitol is a substitute sweetener for common sugar, and it also stands out for its low glycemic index, anticariogenic properties, and other benefits to human health. This additive can be manufactured from hemicellulose present in materials such as coconut shells, corn straw, corncobs, wheat straw, and sugarcane bagasse. Thus, this article sought to analyze the forms of production, the biomasses from sugarcane that can be used, microorganisms used in the process, and applications of this sugar in various areas. To this end, the study was carried out through a literature search in the Web of Science and Google Scholar databases. Therefore, the residual biomasses present in the sugar and alcohol sector were highlighted due to the creation of environmental guidelines aimed at eliminating burning in the field. The literature describes the pretreatments applied to biomass fractionation, such as physical, chemical, biological or physicochemical. Among the studies analyzed, yeasts of the *Candida* genus were the most used for the production of Xylitol, representing 66% among the other microorganisms reported. The set of findings highlights the importance of the topic in question, which in turn is aligned with SDGs 12, 9, 13, 3 and 7, proposed in the UN 2030 Agenda, thus highlighting the positive impact in terms of sustainability, innovation, health and the environment.

Keywords - agricultural waste, xylitol production, sweetener, residues, xylose

ISBN: 978-86-82602-05-7

I. INTRODUCTION

This template, modified in MS Word 2007 provides authors with most of the formatting specifications needed for preparing electronic versions of their papers. All standard paper components have been specified for three reasons: (1) ease of use when formatting individual papers, (2) automatic compliance to electronic requirements that facilitate the concurrent or later production of electronic products, and (3) conformity of style throughout a conference proceedings. Margins, column widths, line spacing, and type styles are built-in; examples of the type styles are provided throughout this document and are identified in italic type, within parentheses, following the example.

Currently, the bioprocessing industry is increasingly converting and applying lignocellulosic materials to obtain value-added products. The use of polymerized carbohydrates (cellulose and hemicellulose) from biomass represents an energy alternative for various sectors, with application and consonance in obtaining biofuels, pharmaceuticals, enzymes and food additives, such as xylitol [1,2].

Xylitol is a polyol (sugar-alcohol) with the molecular formula $C_5H_{12}O_5$ (1,2,3,4,5-pentahydroxypentane) and is found naturally in fruit and vegetables. It is a sweetener perfectly capable of replacing ordinary sugar, with only around 2.4 cal/g (40% less than sucrose), and it does not need insulin to be metabolized, so it is

307



Creative Commons Non Commercial CC BY-NC: This article is distributed under the terms of the Creative Commons Attribution-Non Commercial 4.0 License (<https://creativecommons.org/licenses/by-nc/4.0/>) which permits non-commercial use, reproduction and distribution of the work without further permission.

tolerated by diabetics [3,4]. It also has benefits such as anti-cariogenic properties, preventing respiratory infections and osteoporosis, helping with weight loss and stimulating collagen production [5].

The global xylitol market reached a value of more than US\$ 823.6 million in 2017. On the other hand, the company Mordor Intelligence argues that new growth estimates suggest that by 2029 the xylitol market will reach US\$ 1.37 billion, representing a percentage growth of 5.11% compared to the 2024-2029 period [6]. Xylitol is one of the main chemical products to be obtained from lignocellulosic biomass, highlighting the transformation of lignocellulosic waste into high value-added products [7].

Xylitol can be produced mainly by chemical and biotechnological synthesis [8]. Chemical synthesis is based on the reduction and catalytic hydrogenation of D-xylose under high temperatures and pressures, however, this process requires high purity conditions and has proven to be uneconomical and energy-intensive. On the other hand, the biotechnological route stands out as an alternative with a positive impact on the economy, as well as being low cost and easy to operate [9]. In this context, pentose fermenting microorganisms convert xylose into xylitol.

The biotechnological synthesis of xylitol can be presented as a sustainable process using residual biomass. Thus, the sugar-alcohol sector produces large quantities of lignocellulosic waste that can be reused to produce xylitol. The aim of this article was therefore to analyze the forms of production, the sugarcane biomass that can be used, the microorganisms used in the process and the applications of this sugar in various areas, such as medicine, pharmaceuticals and food.

II. BIOMASSES FROM THE SUGAR AND ALCOHOL INDUSTRY

The sugar-alcohol industry is responsible for producing high value-added products, the main ones being sugar and alcohol. Sugarcane is one of the main crops grown in the world [10]. In Brazil, production of 731.2 million tons of sugar cane was estimated for the 2023/24 harvest, of which 45.6 million tons were destined for sugar production, an increase of 26.8% compared to the 2022/23 harvest [11]. In addition to this high production, the industrial process is linked to the generation of waste that negatively affects the socio-environmental sphere when managed

inappropriately. In this context, by-products are generated such as sugarcane straw and bagasse, lignocellulosic biomass that can be used to produce various bioproducts with high added value [12].

It is important to highlight the production systems that still exist in the sugarcane industry, as the bagasse generated during the milling stage is currently used to produce energy within the mill itself and the surplus is used in applications such as fodder, briquette production, 2G ethanol production, fiber cement, concrete and bioplastics production [13,14]. Thus, for every ton of sugarcane processed, 250 kg of bagasse and 204 kg of straw and dry ends are generated [15]. Therefore, according to the biotechnological potential of these residues, they can be used in industrial processing to produce important products, including xylitol.

Sugarcane straw is a by-product from the mechanized harvesting stage and is generally kept on the ground to prevent erosion, with the surplus being removed to prevent the formation of straw mattresses. The burning of this biomass causes the release of soot and toxic products, mainly affecting children and the elderly who live in areas close to the sugarcane fields. Given this social and environmental aggravation, some states have regulated laws that prohibit the use of burning in connection with cutting sugarcane, such as Law 14.944/24, which deals with fire management in rural areas, and Law 1.778/07, which prohibits burning in sugarcane fields [16]. Thus, an increase in straw in the field is expected, which could represent a new route for bioconversion of its constituents.

Sugarcane bagasse and straw stand out as lignocellulosic biomass composed of (40-44%) cellulose, (30-32%) hemicellulose and (22-25%) lignin [17]. Cellulose consists of a homopolymer of glucose. Hemicellulose is classified as a heteropolymer made up of D-xylose, D-galactose, D-mannose and D-arabinose units [18]. Lignin is a hydrophobic macromolecule that surrounds both components. This macromolecule is the main barrier to enzymatic hydrolysis, as it provides greater resistance to attack by microorganisms [19,20]. Thus, the high availability of these lignocellulosic biomasses in the sugar-alcohol sector makes it possible to incorporate them into biotechnological processes for the production of xylitol.

Within this context, it can be said that this topic is aligned with several SDGs, for example,

the production of xylitol from sugar and alcohol industry waste contributes to SDG 9, by promoting technological innovations that modernize industrial processes, and SDG 12, by promoting the use of waste and more sustainable production practices. It is also related to SDG 7, because in this type of industry, the use of waste contributes to greater efficiency in the use of energy resources. It is also in line with SDG 13, by mitigating greenhouse gas (GHG) emissions through the recovery of by-products. Finally, the production of xylitol, a sweetener beneficial to health, reflects a link with SDG 3, highlighting its potential to improve quality of life, especially in relation to oral health and glycemic control.

Therefore, the use of sugarcane straw and bagasse for the production of xylitol is characterized as an opportunity for product diversification and value generation in the sugar and alcohol industry. It is worth noting that the adoption of this practice on a large scale will be possible through the construction of policies aimed at creating carbon credits and sustainability and circular economy certifications within the scope of xylitol production.

III. PRE-TREATMENT OF SUGAR AND ALCOHOL BIOMASS

In the production of xylitol, waste such as bagasse and sugar cane straw are fundamental raw materials in the process. This process consists of pre-treatment, enzymatic hydrolysis, concentration, detoxification, fermentation, purification and crystallization. Due to the recalcitrant nature of these lignocellulosic biomasses, enzymatic hydrolysis is slow and it is difficult to achieve high sugar yields, which is why pre-treatment is a crucial step in obtaining this additive [21].

Various pre-treatment mechanisms applied to sugar-alcohol biomass have been analyzed and can be classified as physical, chemical, biological, physicochemical and a combination of these on the same material. Pretreatment influences all the other stages in the manufacture of xylitol [22]. In this way, an efficient methodology should promote a reduction in the crystallinity of the residue, removal of lignin, high digestibility of hemicellulose in enzymatic hydrolysis, produce no or low amounts of fermentative inhibitors, good recovery of the sugars released in the hydrolysate and low energy demand [23,24].

Physical pre-treatment methods aim to increase the surface area of the biomass, so grinding and comminution processes are widely used, with high energy consumption. Physical pre-treatment together with chemical action can be applied in order to reduce costs and increase efficiency. This aspect can be seen in the literature, as there are several examples of this methodology, such as steam pretreatment with the addition of a catalyst, hydrothermolysis, wet oxidation and explosion with ammonia [25]. Physical processes cause a strong environmental impact due to the high amount of energy required, electrical or thermal. Furthermore, the fragmentation of biomass promotes the dispersion of small particles that can cause problems to human health and the environment.

Chemical pre-treatment involves the use of acid and alkaline substances to release monosaccharides for use in industrial processing. From this perspective, time and temperature factors are linked to this process in order to influence it positively or negatively, since at high temperatures acid pretreatment causes the degradation of hemicellulose into low-yield compounds [26].

Pretreatment with dilute acid is the method most commonly used on an industrial scale due to its low cost and greater efficiency. Furthermore, different types of compounds can be used in this system, such as hydrochloric, sulphuric and phosphoric acid [27]. Thus, given its non-crystalline nature, the hemicellulose present in the biomass is hydrolyzed into sugars such as xylose and arabinose, increasing the digestibility of the material. However, due to the severity of this type of pre-treatment, the biomass undergoes structural changes that promote the degradation of important sugars, resulting in toxic compounds such as furfural, hydroxymethylfurfural and organic acids that correspond to strong inhibitors of the fermentation process.

The main advantage of acid pretreatment is the solubilization of macromolecular components. Reference [28] demonstrated good results in their experiments on the use of cashew stalk bagasse to produce xylitol using the yeast *Candida guilliermondii CCT 3544*. The results obtained showed high levels of xylose in the hydrolyzed liquor obtained from acid pretreatment.

Alkaline pre-treatment uses compounds such as sodium hydroxide, potassium hydroxide or

ammonia to remove the lignin present in the residue. This mechanism can be carried out at low pressures and temperatures, promoting lignin degradation and low rates of sugar decomposition compared to acid treatment [29]. Thus, it promotes the swelling of biomass, increasing the contact surface to improve the enzyme's action on hemicellulose, breaking the bonds between lignin and carbohydrates [30]. Despite the advantages in lignin removal, this process requires subsequent steps to remove inhibitory compounds, also highlighting its low efficiency in removing the lignocellulosic complex in biomasses with high structural resistance.

Reference [31] obtained 1.86 g/L in reducing sugars after the alkaline pretreatment of sugarcane bagasse pretreated under conditions of 4% sodium hydroxide, autoclaved at 121 °C for 45 minutes. In addition, in the study carried out by Oliveira, Nunes and Sousa (2020) [32], the authors reported significant removal of lignin in the samples pretreated with 2% sodium hydroxide, and the hemicellulose fraction was preserved with a relevant degree of purity. Both the aforementioned studies show the delignifying potential of alkaline pre-treatment.

Biological pre-treatment involves the action of enzymes or microorganisms responsible for depolymerizing the biomass and degrading the lignin fraction. Compared to the other methods discussed here, the literature [33] highlights the low reaction speed of this process for industrial application. Biological pre-treatment is a cleaner

process when compared to physical and chemical means, as it has lower energy consumption and less severe process conditions [34].

Among the pretreatment alternatives mentioned above, hydrothermal pretreatment stands out for using high pressures and temperatures to promote the rupture of lignin-carbohydrate bonds. This process is recognized for its separation efficiency, lower production of degradation products and non-use of chemical reagents.

IV. XYLOSE FERMENTING MICROORGANISMS

Among the various ways of obtaining xylitol, fermentation processes have gained prominence for achieving yields of over 85% [35]. The literature shows studies on yeast species used to produce xylitol, such as *Candida*, *Pichia* and *Debaryomyces*. It is necessary to highlight the species most commonly used in this application, namely *Candida Tropicalis*, *Guilliermondii* and *Parapsilosis*; with regard to *Pichia*, *Stiptis* and *Anomala* stand out; while with regard to the yeast *Debaryomyces*, the *Hansenii* species stands out. Table I shows the microorganisms used in the production of xylitol, as well as some of the biomasses used in this area.

The two studies that used residual biomass from the sugar and alcohol industry stand out. In study 3, sugarcane bagasse hydrolysate was used as a substrate for the production of xylitol by *Candida tropicalis* JA2. The authors obtained 109.5 g/L of xylitol with a productivity of

TABLE I. XYLITOL PRODUCTION BY DIFFERENT MICROORGANISMS AND BIOMASSES.

Studies	Microorganism	Biomass	Xylitol	Reference
1	<i>CANDIDA TROPICALIS GS18</i>	RICE STRAW	34.21	[36]
2	<i>CANDIDA ALBICANS</i>	CASSAVA HUSK	0.27	[37]
3	<i>CANDIDA TROPICALIS JA2</i>	SUGARCANE BAGASSE	109.5	[38]
4	<i>PICHIA STIPTIS CBS 5773</i>	CORNHUSK	0.62	[39]
5	<i>TRAMETES MEMBRANACEA</i>	SUGARCANE BAGASSE	5.65	[40]
6	<i>CANDIDA TROPICALIS</i>	BANANALEAF	11.2	[41]

2.81 g-L-h in the optimized process. In contrast, study 5 evaluated the simultaneous production of ethanol and xylitol by *Trametes membranacea*, with the highest xylose production obtained by strain TM158/10 with 5.65 g/L, pH 4, 28 °C and 288h of fermentation. These aspects highlight the plurality of potentially effective microorganisms that can be applied to xylitol production.

V. BIOTECHNOLOGICAL PRODUCTION OF XYLITOL

Among the ways of producing xylitol, the biotechnological route is the most widely used, as it is not a polluting process, is low cost and does not require high temperatures and pressures like the chemical route [42]. The challenges of this production are linked to the complexity of the biomasses used in the process due to the pre-treatment techniques, scalability and industrial integration. These aspects are justified by the need for more selective pre-treatments for xylose and the difficulty in implementing promising technologies, on a laboratory scale, for pilot scale. The microorganism used in the process is the main factor, as all the conditions used in the process revolve around it [43]. Fig.1 illustrates the scheme for the production of xylitol by the biotechnological route.

The biotechnological production of xylitol consists of using microorganisms that reduce D-xylose using the enzyme xylose reductase, converting xylose into xylitol. D-xylose is used by the yeast for respiration and cell growth under

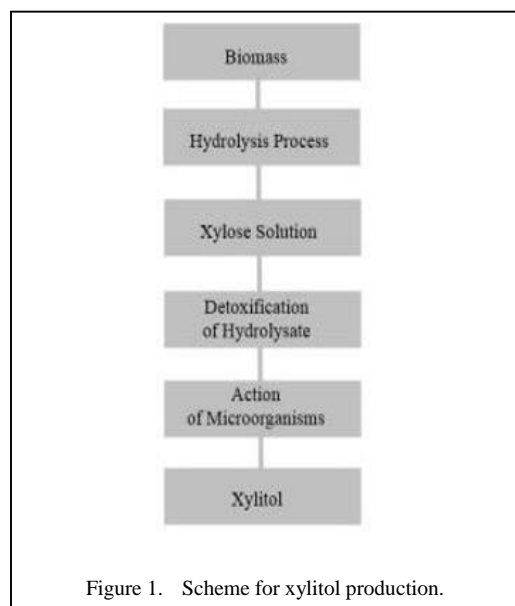


Figure 1. Scheme for xylitol production.

aerobic conditions, but in the absence of oxygen the yeast will produce xylitol [44]. It is worth noting that in the biotechnological production of xylitol, pre-treatment is the initial stage of the process, with the aim of releasing fermentable sugars from the hemicellulosic fraction of the biomass by removing the lignin complex [45].

The hydrolysis of lignocellulosic materials results in the production of compounds that prevent microorganisms from metabolizing xylose, such as the concentrations of furfural, hydroxymethylfurfural, acetic acid and some aromatic compounds found in pretreatment with concentrated acid. Thus, the detoxification stage is specified as being responsible for removing these low molecular weight compounds [46].

Reference [47] evaluated the efficiency of pretreating sugarcane bagasse with sulfuric acid - H₂SO₄ without the presence of detoxifying agents, obtaining 17 g/L of xylose and 12 g/L of glucose. However, [48] demonstrated superior results when working with the same process factors, biomass and chemical compound, and using activated carbon in the detoxification process. In the aforementioned study, the authors obtained 50 g/L of xylose, highlighting the application of this agent as an enhancer in the production of xylitol.

The literature reports various types of fermentation processes used to obtain xylitol, such as batch, fed-batch and continuous, with batch fermentation being the most widely used method for producing bioproducts such as xylitol due to the ease with which possible contamination can be controlled [49].

Through the process of pre-treatment and hydrolysis of sugarcane bagasse, it is possible to recover more than 80% of the pentoses contained in the hemicellulose fraction for biotechnological application [50]. The recovery of xylitol is linked to its purification, as a high purity product is sought. The crystallization process is reported as a promising principle in this area [51]. However, it should be noted that the purification process must be carried out before crystallization due to the impurities coming from the hydrolysis of the lignocellulosic complex. In addition, the use of activated carbon, ion exchange resins, pH adjustment, chromatographic methods, liquid-liquid extraction and precipitation are reported as good methodologies for purifying the fermented medium [52].

Therefore, the biotechnological production of xylitol is essential for the use of agricultural waste, integrating these materials into a production process, promoting the reduction of the carbon footprint by not using petroleum derivatives and less toxic industrial production due to the removal of catalysts.

VI. APPLICATIONS OF XYLITOL

Xylitol is characterized as a sugar rich in several applications, such as in the pharmaceutical, food and medical industries, presenting several benefits to human health. Due to its rapid drying and crystallization, it is commonly used to coat chewing gum, being considered the main application in the world. This sugar does not participate in the reactions that cause food browning, Maillard reactions, a factor that highlights its applicability in the food sector, since products with xylitol do not lose their nutritional value during storage [53]. The National Health Surveillance Agency - Anvisa establishes in RDC No. 18 - March 24, 2008 that xylitol must be used in sufficient quantity to obtain the desired effect, “quantum satis” [54]. Xylitol can bring benefits to human health, with anticariogenicity being one of its most relevant properties, since this food additive improves oral health and stimulates salivation, causing the remineralization of teeth. However, consumption of this sugar in quantities greater than 60g/day may have a laxative effect [55]. Xylitol does not pose health risks, as it has a low glycemic index and is commonly used by diabetics, without affecting the level of insulin present in the blood. It is absorbed by the liver and intestinal tract, and the liver cells are responsible for metabolizing it, transforming it into energy. The absorption of xylitol by the intestine is considerably slow, consequently, all metabolized D-glucose is stored as glycogen in the liver and released progressively [56]. Therefore, xylitol can be used in several industrial applications, including areas directly linked to consumer health. Thus, its regulated use in the diet enables a healthy life with better body functioning, in addition to limiting obesity. New research is promoting the production of this sugar through routes that provide greater productivity at a low cost, as well as its use in hospital networks in order to prevent the formation of biofilms in hospitalized patients, given its activity on bacteria.

VII. CONCLUSION

The biotechnological production process of xylitol has gained prominence, mainly due to the

extensive purification steps involved in the chemical route. In the context of biotechnology, waste produced in the sugar and alcohol sector, such as sugarcane straw and bagasse, can be applied in this area through the pre-treatment stage that increases the access of microorganisms to hemicelluloses. Xylitol is commonly used as a substitute for regular sugar due to its benefits to human health, and it also has relevant applications in the pharmaceutical, medicinal, biotechnological, and food sectors, among others. Therefore, the production of xylitol through lignocellulosic residual biomass represents a promising alternative to conventional models, as well as enabling environmental and human health improvements, in line with the Sustainable Development Goals (SDGs) and the principles established in Green Chemistry.

REFERENCES

- [1] Lima, T. M., & Quattrocchi, D. G. (2023). Catalytic hydrogenation reactions of compounds from lignocellulosic biomass as a strategy for obtaining value-added products. *Virtual Journal of Chemistry*, 15(5).
- [2] Tambor, J. H. H. M., & Rodrigues, M. C. (2018). Biofuels and their impacts on society. *Brazil For All - International Journal*, 6(1), 59-70.
- [3] Rédua, R. B., et al. (2019). Is there justification for the use of xylitol in caries prevention? A literature review. *Full Dentistry Science*, 128-134.
- [4] Kumar, K., Singh, E., & Shrivastava, S. (2022). Microbial xylitol production. *Applied Microbiology and Biotechnology*, 106(3), 971-979.
- [5] Oliveira, G. G. C., et al. (2018). Propriedades antibacterianas e anticariogênicas do xilitol: uma revisão da literatura. *Revista Brasileira de Odontologia*, 75, 1-7.
- [6] Mordor Intelligence. (2024). *Mercado de xilitol – Análise da indústria*. Available at: <https://www.mordorintelligence.com/pt/industry-reports/xylitol-market>
- [7] Santos, J. R., Rambo, M. K. D., & Scapin, E. (2024). Recent advances in xylitol production in biorefineries from lignocellulosic biomass: a review study. *Revista Brasileira de Ciências Ambientais*, 59, e1814-e1814.
- [8] Xu, Y., et al. (2019). Biosynthetic strategies to produce xylitol: an economical venture. *Applied Microbiology and Biotechnology*, 103(13), 5143-5160.
- [9] Queiroz, S. S., et al. (2023). Xylitol and ethanol co-production from sugarcane bagasse and straw hemicellulosic hydrolysate supplemented with molasses. *Biomass Conversion and Biorefinery*, 13(4), 3143-3152.
- [10] Pessoa, G. G. F. A., et al. (2021). Dinâmica temporal da produção de cana-de-açúcar em um município do Brejo Paraibano, Brasil (1995-2019). *Scientific Electronic Archives*, 14(11).

- [11] National Supply Company (CONAB). (2024). *Sugarcane production in the 2023/24 harvest reaches 713.2 million tons, the highest in historical series*. Brasília, DF. Available at: <https://conab.gov.br/ultimas-noticias/5489-producao-de-cana-de-acucar-na-safra-2023-24- chega-a-713-2-milhoes-de-toneladas-a-maior-da-serie-historica#:~:text=Apesar%20da%20prioriza%C3%A7%C3%A3o%20na%20produ%C3%A7%C3%A3o,29%2C69%20bilh%C3%B5es%20de%20litros>
- [12] Mountraki, A. D., et al. (2017). Selection of biorefinery routes: The case of xylitol and its integration with an organosolv process. *Waste and Biomass Valorization*, 8, 2283-2300.
- [13] Santos, J. V., et al. (2020). Effects of addition and replacement of sugarcane bagasse ash in cement matrices. *Brazilian Journal of Development*, 6(10), 77494-77509.
- [14] Feitosa, C. J. D., et al. (2022). Characterization and application of sugarcane bagasse ash in dry concrete mixes. *Principia Journal, Early View*, 1-15.
- [15] Gabriel, L. C. (2021). Thermoelectric generation in Brazil from sugarcane biomass. *Revista do Clube Naval*, 1(397), 14-19.
- [16] Domingues, R. C., et al. (2023). Sugarcane biomass burning and hospitalizations of children and elderly people due to respiratory diseases in Pernambuco, Brazil. *Cadernos de Saúde Pública*, 39, e00238422.
- [17] Carvalho, N., et al. (2021). Physical and chemical characterization of biomass used as solid fuel in a boiler. *Química Nova*, 44(1), 35-40.
- [18] Costa, L. F. M. (2018). Lignocellulosic degradation by enzymatic hydrolysis aiming at ethanol production. *IFSC Technical-Scientific Journal*, 2(7), 52-61.
- [19] Dresch, A. P., Bender, J. P., & Mibielli, G. M. (2020). Characterization, pretreatment and enzymatic hydrolysis of elephant grass biomass. In *Scientific and Technological Initiation Conference*, 1(10).
- [20] Mitri, S., et al. (2022). Valorization of brewers' spent grains: pretreatments and fermentation, a review. *Fermentation*, 8(2), 50.
- [21] Lorenzi, B. R., & Andrade, T. N. (2019). Second-generation ethanol in Brazil: policies and sociotechnical networks. *Brazilian Journal of Social Sciences*, 34(100), 1-32.
- [22] Muller, C., et al. (2019). Sugarcane and corn residues as raw material for 2G ethanol: current events and perspectives. *Impacts of Technologies in Chemical Engineering*, 3(1), 8-22.
- [23] Teixeira, G. M., et al. (2019). Analysis of the efficiency of steam explosion pretreatment of coconut mesocarp fiber. In *Student Seminar on Academic Production*, 17.
- [24] Yao, L., et al. (2018). Understanding the influences of different pretreatments on recalcitrance of *Populus* natural variants. *Bioresource Technology*, 265, 75-81.
- [25] Fuhr, J. F. (2019). Pretreatment and enzymatic hydrolysis of millet lignocellulosic biomass. In *SEPE-UFFS Teaching, Research and Extension Seminar*, 9.
- [26] Cheng, M.-H., et al. (2019). Economic analysis of cellulosic ethanol production from sugarcane bagasse using a sequential deacetylation, hot water, and disk refining pretreatment. *Processes*, 7(10), 642.
- [27] Godinho, E. Z., et al. (2019). Alkaline and alkaline-oxidative hydrothermal pretreatment on cellulose and lignin contents in BRS Capiaçú elephant grass biomass. *Journal of Bioenergy and Food Science*, 6(3), 51-65.
- [28] Medeiros, L. L. de, et al. (2017). Bioconversion of cashew peduncle bagasse hydrolysate for ethanol and xylitol production. *Brazilian Journal of Agricultural and Environmental Engineering*, 21(7), 488-492.
- [29] Dong, L., et al. (2018). Alkali/urea pretreatment of rice straw at low temperature for enhanced biological hydrogen production. *Bioresource Technology*, 267, 71-76.
- [30] Galbe, M., & Zacchi, G. (2017). Pretreatment of lignocellulosic materials for efficient bioethanol production. In *Advances in Biochemical Engineering/Biotechnology*, 108, (pp. 41-65). Springer Verlag.
- [31] Resende, J. F., et al. (2019). Study of pretreatments for the provision of reducing sugars from sugarcane bagasse. *Brazilian Journal of Development*, 5(10), 19219-19227.
- [32] Oliveira, R. M. M., Nunes, M. T. A. S., & Sousa, R. M. S. (2020). Chemical pretreatment and characterization of sugarcane bagasse: a perspective for ethanol production from agro-industrial waste. *Brazilian Journal of Development*, 6(11), 87865-87879.
- [33] Gueri, M. V. D., et al. (2021). Pretreatment of lignocellulosic waste aiming at increasing methane generation in anaerobic digestion processes: a review. *Geama Journal*, 7(3), 13-27.
- [34] Shrestha, S., Fonoll, X., Khanal, S. K., & Raskin, L. (2017). Biological strategies for enhanced hydrolysis of lignocellulosic biomass during anaerobic digestion: Current status and future perspectives. *Bioresource Technology*, 245, 1245-1257.
- [35] Arcaño, Y. D., et al. (2020). Xylitol: A review of the advances and challenges of its chemical production. *Catalysis Today*, 344, 2-14.
- [36] Kaur, S., et al. (2022). Efficient process for xylitol production from nitric acid pretreated rice straw derived pentosans by *Candida tropicalis* GS18. *Biomass and Bioenergy*, 166, 106618.
- [37] Pereira, T. N., Aguiar, A. A., & Gerre, E. B. (2020). Biotechnological production of xylitol from cassava peel (*Manihot esculenta*). *Journal of Biotechnology and Biodiversity*, 8(3), 187-191.
- [38] Morais Junior, W. G., et al. (2019). Xylitol production on sugarcane biomass hydrolysate by newly identified *Candida tropicalis* JA2 strain. *Yeast*, 36(5), 349-361.
- [39] Neeru, C., Chandrajit, B., & Vidyasagar, J. (2013). Biological production of xylitol from corn husk and switchgrass by *Pichia stipitis*. *Research Journal of Chemical Science*, 3, 58-64.
- [40] Rissi, S., et al. (2018). Production of ethanol and xylitol by *Trametes membranacea*. *Bioprocess and Biosystems Engineering*, 41, 1017-1028.
- [41] Shankar, K., et al. (2020). Co-production of xylitol and ethanol by the fermentation of the lignocellulosic hydrolysates of banana and water hyacinth leaves by individual yeast strains. *Industrial Crops and Products*, 155, 112809.

- [42] Jain, V., & Ghosh, S. (2023). Biotransformation of lignocellulosic biomass to xylitol: An overview. *Biomass Conversion and Biorefinery*, 13(11), 9643-9661.
- [43] Reis, G. A., et al. (2024). The importance of mycology in high school. *Revista Acervo Educacional*, 6, e14552.
- [44] Ur-Rehman, S., et al. (2015). Xylitol: A review on bioproduction, application, health benefits, and related safety issues. *Critical Reviews in Food Science and Nutrition*, 55(11), 1514-1528.
- [45] Luo, Y., et al. (2019). The production of furfural directly from hemicellulose in lignocellulosic biomass: A review. *Catalysis Today*, 319, 14-24.
- [46] Santos, C. T., Soares, J. R., & Esteves, T. S. M. (2022). Evaluation of 2G ethanol production by the in-vivo route with the yeast *S. stipitis* in sugarcane straw hydrolysate. *Journal of Scientific Initiation Works*.
- [47] Senatham, S., et al. (2016). Enhanced xylose fermentation and hydrolysate inhibitor tolerance of *Scheffersomyces shehatae* for efficient ethanol production from non-detoxified lignocellulosic hydrolysate. *SpringerPlus*, 5, 10140.
- [48] Dussán, K. J., et al. (2016). Evaluation of oxygen availability on ethanol production from sugarcane bagasse hydrolysate in a batch bioreactor using two strains of xylose-fermenting yeast. *Renewable Energy*, 87, 703-710.
- [49] Chogi, M. A. N., et al. (2020). Production of biofuel and organic acids to add value to cassava effluent. *Virtual Journal of Chemistry*, 12(1), 89-98.
- [50] Arruda, P. V., et al. (2017). Scale up of xylitol production from sugarcane bagasse hemicellulosic hydrolysate by *Candida guilliermondii* FTI 20037. *Journal of Industrial and Engineering Chemistry*, 47, 297-302.
- [51] Zhang, L., et al. (2021). Production of platform chemicals and bio-fuel from paper mill sludge via hydrothermal liquefaction. *Journal of Analytical and Applied Pyrolysis*, 155, 105032.
- [52] Martínez, E. A., et al. (2015). Strategies for xylitol purification and crystallization: A review. *Separation Science and Technology*, 50(14), 2087-2098.
- [53] Pivetta, L. R., Arruda, P. V., & Felipe, M. G. A. (2008). Comparison of detoxification methodologies of sugarcane bagasse hydrolysate for the production of xylitol by fermentation. In *Proceedings of the XII Latin American Meeting of Scientific Initiation*.
- [54] ANVISA – National Health Surveillance Agency. (2008). Resolution of the Board of Directors of the National Health Surveillance Agency No. 18, dated March 24, 2008, which establishes the Technical Regulation authorizing the use of sweeteners in foods, with their respective maximum limits. Official Gazette of the Union, Brasília, March 23, 2008.
- [55] Salli, K., et al. (2019). Xylitol's health benefits beyond dental health: A comprehensive review. *Nutrients*, 11(8), 1813.
- [56] Santos, K. E. R., & Ricci, G. C. L. (2016). Gut microbiota and obesity. *Uningá Review*, 26(1).

Selection of Electric Vehicle Charging Station using PROMETHEE II and Shannon Entropy: A Case Study from Niš, Serbia

Petar Vranić¹, Ivana Petkovski²

^{1,2}Mathematical Institute of the Serbian Academy of Sciences and Arts, Belgrade, Serbia

¹petarvvv@mi.sanu.ac.rs, ²ivana993@turing.mi.sanu.ac.rs

Abstract—The selection of an optimal Electric Vehicle Charging Station (EVCS) improves user experience, decrease costs and emissions, and contribute to sustainable urban mobility and energy efficiency. In solving this optimization problems, the application of decision support methods has an important role. This study focuses on the problem of selecting the best EVCS by analyzing real data from five stations in a specific area in Nis, Serbia. The most optimal station was chosen based on eight factors divided into two categories: benefit and cost. Their weights were determined using the Shannon Entropy objective approach. The PROMETHEE II approach was used to complete the ranking process.

Keywords - electric vehicle, charging station, Entropy, PROMETHEE II

I. INTRODUCTION

Along with rise of urban environmental problems related to carbon emission and climate change effects, the sustainable transport initiative has gained increased attention in recent years worldwide [1]. Sustainable transport discourse considers various concepts like expansion and diversification of transportation network, promotion of energy efficient vehicles and “green” transport options like walking and cycling [2-4].

The current transportation sector is one of the most significant contributors to global greenhouse gas (GHG) emissions with an approximate share of 23% in the world's total energy-related CO₂, and adds considerably to

climate change and global warming [5,6]. Sustainable transport solutions attempt to mitigate these consequences by diversifying fuel options and using renewable energy sources (RES), playing a significant role in improving public health. The increasing issues of air quality in urban areas, followed by numerous respiratory and cardiovascular diseases, largely come from vehicle emissions [7]. Transition to cleaner forms of transport, can reduce the prevalence of these health issues, improve quality of life and reduced healthcare costs for governments.

Transition process considers the development of smart infrastructure. In line with that, one of the most discussed issues is establishing an extensive network of EV charging stations (EVCS) [8,9]. With the expanding market of EV demand for accessible, reliable, and fast-charging options increases. The poor charging infrastructure is the major obstacle to the adoption of EV, since it may produce range anxiety [10,11]. To address this, investments in the widespread deployment of EVCS, ensure they are strategically located to meet the needs of urban, suburban, and rural areas alike.

Another significant segment of transition represents the integration of smart technologies into existing transportation infrastructure, which, among others includes connected vehicles, intelligent traffic management systems, and digital payment platforms. This, and other technologies will contribute to better efficiency and safety of transportation networks [12-14], enabling real-time monitoring and management



of traffic flows, contribute to the reduced energy consumption, and better driver's experience.

Selecting the optimal EVCS plays a key role in protecting the environment and helping drivers pick the best choices. When drivers can choose optimal EVCSs considering criteria like proximity, cost, or charging speed, they're more likely to make choices that cut down on their impact on the environment. Informed selection cuts back on extra driving, lowers emissions, and makes sure drivers can finish their trips without a hitch striking a balance between ease and being "sustainable". By giving drivers the information, they need to make smart choices, we can keep drivers satisfied and help the environment at the same time.

The goal of this paper is to offer a multi-criteria decision support approach for selection for the optimal charging station from the driver's perspective. Study employs a real-world data from the city of Niš, Serbia. The paper firstly presents a brief literature review, secondly explain methodology, thirdly applies methodology on the case study and finally discuss results.

II. LITERATURE REVIEW

As a site selection problem, as far as literature suggests selecting optimal EVCS inevitably consider multi-criteria decision-making (MCDM) methods because this problem involves evaluating multiple, often conflicting factors that cannot be easily aggregated into a single metric. There are numerous studies that considers single or hybrid approach with more than one MCDM method to solve the site selection problem. Some of them are presented below.

For instance, in evaluating performances of nine EVCS in Istanbul [15] applied three MCDM: Analytic Hierarchy Process (AHP), Decision Making Trial and Evaluation Laboratory (DEMATEL), and Technique for Order of Preference by Similarity to Ideal Solution (TOPSIS) to compare four main and twenty-one sub-criteria. Solving the charging problem for taxi service in [16], integrate fuzzy AHP to weight six main and twenty-five sub criteria, GIS for spatial analysis and TOPSIS for final ranking of electric taxi charging stations. To assess the effectiveness and applicability of EVCSs suggested for the Shanghai region [17] developed a Pythagorean fuzzy VlseKriterijumska Optimizacija I Kompromisno

Resenje (PF-VIKOR) model, while VIKOR and TOPSIS methodologies were applied to assess feasibility, as well as economic, social, and environmental issues. Evaluating the EVCSs in the [18] combined Analytic Network Process (ANP), Preference Ranking Organization Method for Enrichment Evaluation (PROMETHEE) and integrated cloud model considering geographical, environmental, social, service, engineering, and economic issues. Reference [19], introduced another integrated approach utilizing gray DEMATEL, to determine criterion weights, and UL - Multiple Objective Optimization on the basis of Ratio Analysis plus Full Multiplicative Form (UL-MULTIMOORA) to assess and rank the best EVCS location based on several linked parameters. Studying current and most suitable potential EVCS locations in Ankara. Reference [20] combined AHP method for weighting fifteen criteria, GIS for create a suitability map, while potential EVCS locations were identified, and alternative EVCSs were rated using the TOPSIS methodology. Reference [21] suggested a practical model for location decision of EV photovoltaic charging station combining a GIS for suitability analysis and entropy and Iterative Multi-criteria Decision Making (TODIM) method are extended to the mixed attribute value environment. For selecting island photovoltaic charging station [22] applied the hybrid fuzzy approach that include AHP, entropy weight method, λ - fuzzy measure method and VIKOR. To evaluate criteria for site selection for shared charging and swapping stations [23] utilized Simultaneous Evaluation of Criteria and Alternatives (SECA) method to determine the weight of each secondary criterion, and the TRUST method to rank the alternatives. While planning the establishment of battery swapping station in Kolkata, [24] applied fuzzy based TFN method with consideration of the preference within the criteria; weights of the criteria are obtained, and Complex Proportional Assessment (COPRAS) methodology is applied to rank the selected locations. In their research, [25] studied location decision framework of electric vehicle battery swapping station fuzzy DEMATEL method is applied to determine the weights of criteria then, the Fuzzy ordered Weighted Averaging (FOWA) operator is adopted to aggregate the evaluation values on alternatives of experts and the fuzzy MULTIMOORA is used to rank the alternatives. In analyzing location of the offshore wind station [26] utilized a hybrid fuzzy ANP fuzzy DEMATEL and fuzzy Elimination

and Choice Expressing Reality (ELECTRE) techniques. Reference [27] applied the Weighted Suitability Analysis (WSA) and Grey Relation Analysis (GRA) method to find the most suitable site of industrial wastewater discharge in coastal regions. Reference [28] proposed a model to evaluate the site selection problem of car sharing stations using Weighted Aggregated Sum Product Assessment (WASPAS) based TOPSIS method. In analyzing optimal site selection in Istanbul [29] employed FUCOM-GIS hybrid method.

III. METHODOLOGY

For selecting the optimal EVCS this study employs a real word data for the city of Niš Serbia, where all of the analyzed criteria are quantifiable. Therefore, a hybrid Shannon Entropy - PROMETHEE II method is applied to secure objective distribution of criteria weights, based on the variability of observed data and enable efficient balance between costs and benefits criteria.

The Shannon entropy method is often applied in MCDM and for objective determination of the weights of various criteria based on the data set. Shannon was the first scientist to develop the notion of entropy in information theory in the mid-twentieth century. The Shannon entropy technique assesses the disorder in existing data [30]. The authors Claude Shannon and Warren Weaver (1948) illustrate the following steps involved in applying this method below [31]. The initial step in the calculation of weight coefficients is the normalization of the decision matrix. Then, in the next step, the share of the value of the alternatives in the total value of the criteria is calculated. Based on the obtained values, entropy is calculated for each criterion, and then the calculated entropy value is subtracted from the maximum possible entropy value. This step indicates the calculation of the degree of variation among the entropy values, on the basis of which the weighting coefficients are calculated.

In this example, the PROMETHEE II method was used to solve the set multi-criteria problem. The PROMETHEE II method enables the prioritization of alternatives in relation to a larger number of criteria, taking into account the preferences of the decision maker [32]. The choice in the application of the PROMETHEE II method was based on the assumption that this method enables a complete ranking of

alternatives even in situations where conflicting criteria appear [33].

There are several basic steps in PROMETHEE II. These are (1) defining criteria and alternatives, (2) giving each criterion a weight value, (3) picking a preference function, (4) calculating preference indices, (5) calculating positive and negative preference flows, (6) calculating net preference flow, and (7) ranking the alternatives [34]. PROMETHEE II offers six preference functions that define the preference relationship between alternatives: the usual criterion (Type I), the U-shape criterion (Type II), the V-shape criterion (Type III), the level criterion (Type IV), the linear criterion (Type V), and the Gaussian criterion (Type VI) [34]. The choice of the preference function depends on the nature of the available data and the research problem [35]. The net preference flow is obtained by subtracting the positive preference flow from the negative preference flow [34]. In order for an alternative to be highly ranked, it is necessary to have the highest possible value of the positive flow of preference, because it shows how much this alternative outranks the other alternatives, and the lowest value of the negative flow of preference, because it indicates how much this alternative is outranked in relation to the others [34]. This step enables a complete ranking of the alternatives.

For selection of EVCS infrastructural, spatial and environmental criteria are considered.

A. Infrastructural Criteria

Charger type. The EV charger type is important criterion for EVCS selection. It is reciprocal to charging time and cost. There are different types of chargers like Level 1, Level 2 or DC fast chargers, with its pros and cons. However, network with variety of chargers types can satisfy different needs that consequently can encourage adoption of EVs.

Number of chargers. More chargers at EVCSs increase drivers' chances of finding an available port, especially during peak hours, and decrease congestion that in turn improves the drivers experience and charging predictability. This is especially important in high-density urban area where the larger volume of traffic and users are expected. Stations with more chargers makes a better use of the infrastructure and distribution of load, optimizing the energy use and overall environmental impact.

Charging Price. Charging affordability increases the likelihood of driver selecting particular station. The price affects the total cost of the ownership of EV, especially the ones who totally rely on public EVCSs. It also influences competitiveness between the stations; thus, driver may give lower priority to stations with higher charging prices that do not offer some additional benefits (e.g. membership tokens, faster charging, proximity to important POIs etc.).

Available chargers' information. The access to real time information about EVCS contribute to the driver's convenience in several ways: prevent unnecessary trips, minimize waiting time, optimize route planning, book a charging spot in advance, allow price comparison and avoid unexpected costs.

B. Spatial Criteria

Distance. The range anxiety may considerably affect driver's psychological comfort, thus the proximity and accessibility to the EVCSs is an important criterion. Closer station is more probable choices for EV drivers, since it adds to less deviation from the planned route, saves time and energy.

Population density. EVCSs located in high-density areas may experience higher load that can affect the efficiency of service (e.g. waiting time), since larger number of residence (potential EV owners) are in higher proximity to the station. Also, higher usage rates influence station

demand, and economic viability which can result in better maintenance and service in the long run.

Proximity to arterial road. Strategic placement of EVCS along arterial road enhances accessibility, increases utilization rates, and improves convenience for drivers, encouraging EV adoption. Furthermore, accessibility to EVCS in high-traffic areas supports more efficient energy distribution and can optimize operational costs for charging networks.

C. Environmental Criteria

Charging Efficiency. The conversion from Alternating Current (AC) to Direct Current (DC) during the charging process cause energy losses. DC fast chargers, perform lower efficiency than slower Level 2 chargers. Additionally, inefficient charging practices, particularly frequent use if fast chargers, accelerate battery degradation i.e. shorten their life. The production of new batteries considers high emissions from mining essential materials, and thus, contribute to environmental degradation.

Renewable energy source. EVCS powered by RES reduce carbon emission and contribute to environmental sustainability, energy efficiency and encourage sustainable behavior of drivers promoting cleaner transportation.

IV. CASE STUDY

For the selected criteria case study is conducted for the city of Niš, Serbia. Though online and on-site analysis fourteen EVCSs are identified. Ten of them are located within the

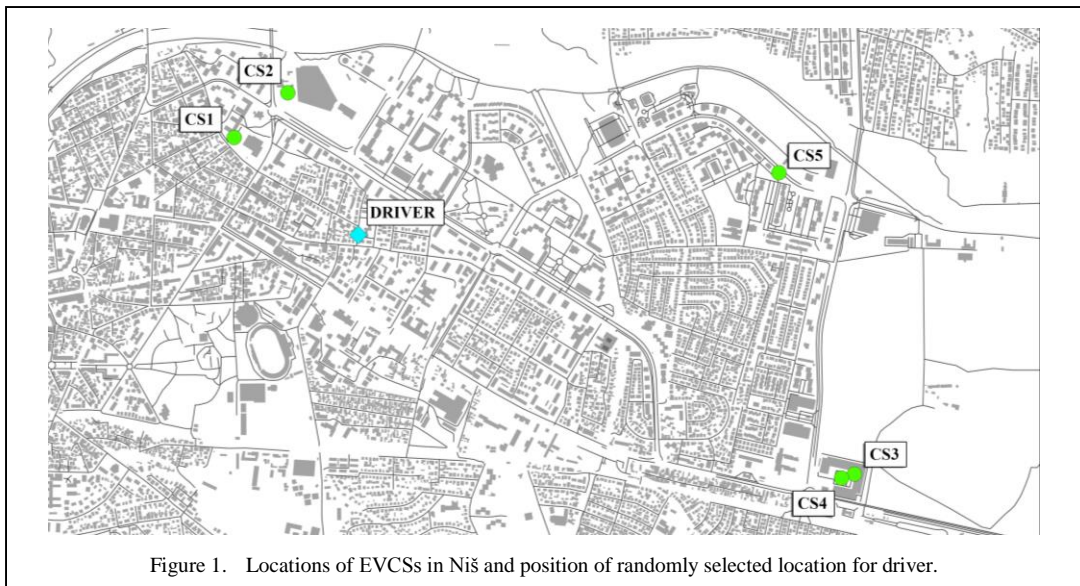


Figure 1. Locations of EVCSs in Niš and position of randomly selected location for driver.

TABLE I. CRITERIA INFO.

Criterion	Unit	Abbreviation
Charger type	kW/hour	C1
Number of chargers	number	C2
Price	RSD/minute	C3
Distance	km	C4
Population density	Low (0), Medium (1), High (2)	C5
Available charger information	No (0), Yes (1)	C6
Charging Efficiency	Low (0), Medium (1), High (2)	C7
Proximity to arterial road	Low (0), Medium (1), High (2)	C8

TABLE II. INITIAL DECISION MAKING MATRIX.

ID	EVCS	C1	C2	C3	C4	C5	C6	C7	C8
Criterion type	-	Benefit	Benefit	Cost	Cost	Cost	Benefit	Cost	Benefit
Preference function	-	Usual	Usual	Usual	Usual	Usual	Usual	Usual	Usual
CS_1	Goran Ostojevic	11	2	0	1.3	High	No	High	Medium
CS_2	Delta Planet	11	10	15	0.95	High	Yes	High	High
CS_3	StopShop	100	2	153	2.7	Medium	Yes	Low	High
CS_4	Liikennevirta Oy (CPO)	120	2	153	2.7	Medium	Yes	Low	High
CS_5	Kemoimpex	22	2	15	2.5	Medium	Yes	Medium	High

commercial facilities lots (like hotels or factories), while only four that are located in the wider city central zone. Only the former are considered for this example, since the remaining ones either includes additional costs (like any kind of service in hotel) or are strictly allocated for the employees (Fig. 1). For the selected EVCSs criteria info are shown in Table I.

In the first iteration conceptual model considered EVCS powered by RES. However, field study showed that in the given context none of the identified EVCS is powered by RES, thus, we decided to omit this criterion from the final model since all of the selected cases would receive equal weight.

The initial decision matrix was formed for the purposes of creating the hybrid Entropy-PROMETHEE II in order to select the most optimal charging station for an EV. The criteria are divided according to whether they are positive/benefit or negative/cost in relation to the decision-making objective. The usual type of preference function was chosen because even minor differences in the alternatives affect the choice [35]. In accordance with the defined units

of measure in the previous table, this decision matrix was transformed into a form where all criteria have numerical values (Table II).

V. RESEARCH RESULTS AND DISCUSSION

The Shannon entropy method was used to calculate the value of the weighting coefficients of the criteria. The calculation was carried out on the basis of eight criteria and five alternatives. The initial decision matrix is normalized to show uniform values of the comparison criteria. The weight coefficients' values are presented in the Table III. The results indicate that the decision-maker places significant importance on the calculated price of charging an EV. The importance of charging efficiency and charger type is approximately equal, with the former having a slight preference. The type of charger is then the next important criterion in choosing the most optimal station. Charging speed carries more weight because rapid chargers are more convenient than slower chargers and provide significant savings in charging time. The least important in the prioritization process is the proximity to arterial roads.

The application of the PROMETHEE II method necessitates the normalization of the decision matrix based on the benefit and cost type criteria. The next step, based on the values of the normalized matrix and the selection of the preference function, calculates the preference indices whose aggregate results can be seen in the Table IV.

The Table V shows the results of the calculation of the positive and negative flow of preference for each offered alternative. In order to approach the final ranking, the net value of the preference flow was calculated, which is obtained by subtracting the positive preference flow from the negative preference flow. The ranking prioritizes higher values of the net flow of preference, placing CS_2 Delta Planet at the top. The lowest-ranked station is CS_1 Goran Ostojic.

The results obtained using the hybrid Entropy-PROMETHEE II model show the feasibility of prioritizing the optimal EV charging station according to criteria of diverse characteristics. Considering the weight values determined objectively in this case study, the price of charging is a crucial factor in the decision-making process, highlighting the importance of cost criteria. Another criterion that prioritizes chargers with high charging efficiency approves the use of slower charger types because they cause less energy losses. In addition, the type and number of chargers play a significant role in selecting the most optimal EVCS, because a faster type of charger with a larger number of free charging stations allows for a shorter waiting time and more efficient use of resources. The wide availability of the option to monitor the state of free chargers has significantly reduced the influence of this criterion on the ranking.

TABLE III. OBJECTIVE CRITERIA WEIGHT CALCULATED BY SHANNON’S ENTROPY METHOD.

Abbreviation	Criterion	Weight coefficient
C1	Charger type	0.193
C2	Number of chargers	0.144
C3	Price	0.288
C4	Distance	0.035
C5	Population density	0.028
C6	Available charger information	0.105
C7	Charging Efficiency	0.194
C8	Proximity to arterial road	0.013

TABLE IV. AGGREGATED PREFERENCE FUNCTION RESULTS CALCULATED BY PROMETHEE II.

	CS_1	CS_2	CS_3	CS_4	CS_5
CS_1	1	0.028	0.317	0.317	0.052
CS_2	0.268	1	0.439	0.439	0.175
CS_3	0.498	0.380	1	0.000	0.235
CS_4	0.533	0.415	0.035	1	0.270
CS_5	0.262	0.145	0.264	0.264	1

TABLE V. PRIORITIZATION RESULTS BY PROMETHEE II.

ID	Charging station	Positive flow (Phi+)	Negative flow (Phi-)	Net flow (Phi)	Rank
CS_1	Goran Ostojic	0.178	0.390	-0.212	5
CS_2	Delta Planet	0.330	0.242	0.088	1
CS_3	StopShop	0.278	0.264	0.014	4
CS_4	Liikennevirta Oy (CPO)	0.313	0.255	0.059	2
CS_5	Kemoimpex	0.234	0.183	0.051	3

Decision-making places less emphasis on distance from users and population density, suggesting that even more distant stations or those in highly urbanized locations that are close to high priority roads could be suitable options if the other criteria are satisfied. Accordingly, using the PROMETHEE II method, the choice was reduced to the Delta Planet station, which offers a low EV charging price, with slow types of chargers, but with the largest number of installed charging points. Charging efficiency of this station is high leading to the energy-saving charging process. The station offers the possibility to check the availability of chargers, with services being covered by a smartphone application. Although the station is located in a densely populated area that is close to high-order roads, its distance from users is the shortest compared to other stations.

VI. CONCLUSION

In conclusion, the application of the hybrid Entropy-PROMETHEE II method for selecting optimal EVCS demonstrates to be a useful MCDM approach in EVCS optimization problems. This study analyses the importance of numerous parameters, with the cost of charging calculated as the crucial one. The analysis finds that, while charger type and energy efficiency are essential, cost efficiency and the number of available charging lots are more relevant in identifying the best option.

The presented model can be applied in other regions, but with context-specific adaptation that takes into consideration local infrastructure, energy policies and socio-economic conditions. For instance, in cities/regions with highly developed EVCS infrastructure factors like station density, network interoperability, or integration with smart grid networks may become more relevant. On the other side in region with poor EVCS network accent can be on accessibility, availability of public land and network capacity. The PROMETHEE II method can easily accommodate these additional criteria without compromising the decision-making logic, while Shannon Entropy can dynamically reflect the varying relevance of these factors based on regional data availability.

Further studies should consider more further analysis of the relevant criteria that are out of scope of the presented research, and consider several axis:

Analysis of the environmental impact (like source of electricity) i.e., how different EVCS locations and technologies (existing and emerging) impact the environment, supporting more informed decisions that align with sustainability goals.

A detailed geospatial analysis to understand how spatial factors like infrastructure, spatial distribution (density and proximity) of EVCS, or traffic pattern and population density influence EVCS placement and accessibility.

Exploration of the potential integration of EVCS with renewable energy sources, and its effect on station selection, i.e., how green energy solutions can enhance the sustainability and attractiveness of charging stations.

ACKNOWLEDGEMENT



This work was supported by the Serbian Ministry of Science, Technological Development and Innovation through the Mathematical Institute of the Serbian Academy of Sciences and Arts.

REFERENCES

- [1] Eswaranathan, K., Sivakumar, T., De Silva, M. M., & Kumarage, A. S. (2024). Modelling the factors influencing carbon efficiency of consumer choice to promote energy-efficient vehicles. *Transport Economics and Management*, 2, 130-142.
- [2] Ullah, Z., Qazi, H. S., Rehman, A. U., Hasanien, H. M., Wang, S., Elkadeem, M. R., & Badshah, F. (2024). Efficient energy management of domestic loads with electric vehicles by optimal scheduling of solar-powered battery energy storage system. *Electric Power Systems Research*, 234, 110570.
- [3] Naik, M. B., Kumar, P., & Majhi, S. (2019). Smart public transportation network expansion and its interaction with the grid. *International Journal of Electrical Power & Energy Systems*, 105, 365-380.
- [4] Monazzam, M. R., Karimi, E., Shahbazi, H., & Shahidzadeh, H. (2021). Effect of cycling development as a non-motorized transport on reducing air and noise pollution-case study: Central districts of Tehran. *Urban Climate*, 38, 100887.
- [5] Leicht, J. B., & Leicht, M. (2024). Climate change and transportation companies: A bibliometric and systematic literature review. *Transportation Research Part F: Traffic Psychology and Behaviour*, 101, 160-185.
- [6] Wang, T., Qu, Z., Yang, Z., Nichol, T., Clarke, G., & Ge, Y. E. (2020). Climate change research on transportation systems: Climate risks, adaptation and planning. *Transportation Research Part D: Transport and Environment*, 88, 102553.
- [7] Pradhan, R. P., Nair, M. S., Hall, J. H., & Bennett, S. E. (2024). Planetary health issues in the developing world: Dynamics between transportation systems, sustainable economic development, and CO₂

- emissions. *Journal of Cleaner Production*, 449, 140842.
- [8] Goli, P., Gampa, S. R., Kumar, N. M., Jasthi, K., Parimi, A. M., Das, D., ... & Guerrero, J. M. (2023). Strategic planning of distribution network integrated with EV charging stations using fuzzy pareto optimality for performance improvement and grid-side emission reduction benefits. *Sustainable Energy, Grids and Networks*, 36, 101199.
 - [9] Saldanha, J. J., Nied, A., Trentini, R., & Kutzner, R. (2024). AI-based optimal allocation of BESS, EV charging station and DG in distribution network for losses reduction and peak load shaving. *Electric Power Systems Research*, 234, 110554.
 - [10] Goncencaruc, A., De Cauwer, C., Sapountzoglou, N., Van Kriekinge, G., Huber, D., Messagie, M., & Coosemans, T. (2024). The barriers to widespread adoption of vehicle-to-grid: A comprehensive review. *Energy Reports*, 12, 27-41.
 - [11] Pamidimukkala, A., Kermanshachi, S., Rosenberger, J. M., & Hladik, G. (2024). Barriers and motivators to the adoption of electric vehicles: a global review. *Green Energy and Intelligent Transportation*, 100153.
 - [12] Ouallane, A. A., Bakali, A., Bahnas, A., Broumi, S., & Talea, M. (2022). Fusion of engineering insights and emerging trends: Intelligent urban traffic management system. *Information Fusion*, 88, 218-248.
 - [13] Yang, M., Jiang, K., Wijaya, B., Wen, T., Miao, J., Huang, J., ... & Yang, D. (2024). Review and Challenge: High Definition Map Technology for Intelligent Connected Vehicle. *Fundamental Research*.
 - [14] Mogaji, E., & Nguyen, N. P. (2024). Evaluating the emergence of contactless digital payment technology for transportation. *Technological Forecasting and Social Change*, 203, 123378.
 - [15] Karaşan, A., Kaya, İ., & Erdoğan, M. (2020). Location selection of electric vehicles charging stations by using a fuzzy MCDM method: a case study in Turkey. *Neural Computing and Applications*, 32, 4553-4574.
 - [16] Kaya, Ö., Alemdar, K. D., & Çodur, M. Y. (2020). A novel two stage approach for electric taxis charging station site selection. *Sustainable Cities and Society*, 62, 102396.
 - [17] Cui, F. B., et al. (2018). Optimal siting of electric vehicle charging stations using Pythagorean fuzzy VIKOR approach. *Mathematical Problems in Engineering*. 2018(1), 9262067.
 - [18] Wu, Y., Xie, C., Xu, C., & Li, F. (2017). A decision framework for electric vehicle charging station site selection for residential communities under an intuitionistic fuzzy environment: A case of Beijing. *Energies*, 10(9), 1270.
 - [19] Liu, H. C., Yang, M., Zhou, M., & Tian, G. (2018). An integrated multi-criteria decision making approach to location planning of electric vehicle charging stations. *IEEE Transactions on Intelligent Transportation Systems*, 20(1), 362-373.
 - [20] Erbaş, M., Kabak, M., Özceylan, E., & Çetinkaya, C. (2018). Optimal siting of electric vehicle charging stations: A GIS-based fuzzy Multi-Criteria Decision Analysis. *Energy*, 163, 1017-1031.
 - [21] Zhou, J., Wu, Y., Wu, C., He, F., Zhang, B., & Liu, F. (2020). A geographical information system based multi-criteria decision-making approach for location analysis and evaluation of urban photovoltaic charging station: A case study in Beijing. *Energy Conversion and Management*, 205, 112340.
 - [22] Dang, R., Li, X., Li, C., & Xu, C. (2021). A MCDM framework for site selection of island photovoltaic charging station based on new criteria identification and a hybrid fuzzy approach. *Sustainable Cities and Society*, 74, 103230.
 - [23] Lu, F., Yan, L., & Huang, B. (2022). Site selection for shared charging and swapping stations using the SECA and TRUST methods. *Energy Reports*, 8, 14606-14622.
 - [24] Koirala, K., & Tamang, M. (2022). Planning and establishment of battery swapping station-A support for faster electric vehicle adoption. *Journal of Energy Storage*, 51, 104351.
 - [25] Wang, R., Li, X., Xu, C., & Li, F. (2020). Study on location decision framework of electric vehicle battery swapping station: Using a hybrid MCDM method. *Sustainable Cities and Society*, 61, 102149.
 - [26] Fetanat, A., & Khorasaninejad, E. (2015). A novel hybrid MCDM approach for offshore wind farm site selection: A case study of Iran. *Ocean & Coastal Management*, 109, 17-28.
 - [27] Li, Y., Lin, C., Wang, Y., Gao, X., Xie, T., Hai, R., ... & Zhang, X. (2017). Multi-criteria evaluation method for site selection of industrial wastewater discharge in coastal regions. *Journal of Cleaner Production*, 161, 1143-1152.
 - [28] Deveci, M., Camtez, F., & Gökaşar, I. (2018). WASPAS and TOPSIS based interval type-2 fuzzy MCDM method for a selection of a car sharing station. *Sustainable Cities and Society*, 41, 777-791.
 - [29] Gökler, S. H. (2024). Optimal site selection for electric vehicle charging stations: analysis with hybrid FUCOM and geographic information systems. *Energy*, 132659.
 - [30] Wu, J., Sun, J., Liang, L., & Zha, Y. (2011). Determination of weights for ultimate cross efficiency using Shannon entropy. *Expert Systems with Applications*, 38(5), 5162-5165.
 - [31] Shannon, C. E. (1948). A mathematical theory of communication. *The Bell system technical journal*, 27(3), 379-423.
 - [32] Martínez-Maldonado, V., Barragán-Escandón, A., Serrano-Guerrero, X., & Zalamea-Leon, E. F. (2023). Optimal routing for mass transit systems using multicriteria methodologies. *Energy Strategy Reviews*, 47, 101077.
 - [33] Oubahman, L., & Duleba, S. (2021). Review of PROMETHEE method in transportation. *Production Engineering Archives*, 27(1), 69-74.
 - [34] Brans, J. P., & De Smet, Y. (2016). PROMETHEE methods. *Multiple criteria decision analysis: state of the art surveys*, 187-219.
 - [35] Zhaoxu, S., & Min, H. (2010, June). Multi-criteria decision making based on PROMETHEE method. In *2010 international conference on computing, control and industrial engineering* (Vol. 1, pp. 416-418). IEEE.

The Promise of Indium Gallium Nitride Solar Modules for Sustainable Energy

Sabira Nour¹, Abdelhak Merabti², Houcine Aissani³, Rachid Abdeldjebbar⁴, Abdelkader Benslimane⁵, Ahmed Djatout⁶

^{1,2,3,4,5,6}Higher Normal School of Bechar- Department of Physics, Bechar, Algeria,

^{1,2,3,4,5}Laboratory of Semiconductor Devices Physics - Tahri Mohamed University, Bechar, Algeria

¹nour.sabira@ensbechar.dz, ²merabti.abdelhak@ensbechar.dz, ³aissani.houcine@ensbechar.dz, ⁴abdeldjebbar.rachid@ensbechar.dz, ⁵benslimane.abdelkader@ensbechar.dz, ⁶djatout.ahmed@ensbechar.dz

Abstract—Indium Gallium Nitride (InGaN) solar modules offer a compelling alternative to traditional silicon-based solar cells, boasting enhanced efficiency, improved performance, and longer lifespans. This paper explores the advantages of InGaN solar technology, including its tunable bandgap for wider light absorption, higher absorption coefficient, and remarkable stability under extreme conditions. The theoretical potential for efficiencies exceeding 40%, particularly in multi-junction configurations, far surpasses the typical 20-26% efficiency of silicon cells. Despite current challenges in achieving high-quality growth and p-type doping, ongoing research addresses these obstacles through advanced growth techniques and innovative device architectures. Computational modeling and simulation play a crucial role in optimizing design parameters and predicting performance, accelerating the development of efficient InGaN solar cells. The paper highlights the potential of InGaN solar modules to revolutionize sustainable energy production, pushing the boundaries of solar technology and contributing to a cleaner, more sustainable future.

Keywords - InGaN, performance, renewable energy

I. INTRODUCTION

The sun, a limitless source of energy, has long held promise for powering our planet. While solar energy technology has made

significant strides, it faces limitations in terms of efficiency and cost. Traditional silicon-based solar cells, while ubiquitous, struggle to capture a large portion of the sun's spectrum and often require vast land areas for deployment. However, a new generation of solar materials is emerging, poised to revolutionize the field. Among these is Indium Gallium Nitride (InGaN), a material with unique optical and electronic properties that offer a pathway to dramatically enhanced solar energy conversion. This paper explores the potential of InGaN solar modules, arguing that they present a compelling alternative to conventional technologies, capable of achieving higher efficiencies and unlocking a brighter future for solar energy.

II. THE ADVANTAGES OF INGAN SOLAR MODULES

A. Enhanced Efficiency

Indium Gallium Nitride (InGaN) possesses unique optical properties that make it highly effective for light absorption and energy conversion in scientific applications. Its nanowire arrays, due to increased surface area and optimized structural parameters, exhibit enhanced light trapping, improving absorption efficiency by up to 5% compared to uniform arrays [1]. Additionally, InGaN core-shell structures are capable of broader solar spectrum absorption by adjusting the indium composition



to match the solar irradiance, resulting in enhanced energy conversion [2]. Furthermore, the ability of InGaN to form multiple quantum wells (MQWs) enhances light absorption through waveguiding effects and refractive index differences [3]. The material's tunable bandgap and high absorption coefficients make it suitable for tandem solar cells, which capture a broad range of the solar spectrum, potentially reaching efficiencies exceeding 40%, far surpassing traditional silicon-based solar cells [4,5]. Despite advances in silicon technology, silicon's fixed bandgap and lower resistance to high temperatures limit its maximum efficiency, unlike InGaN, which remains resilient even in high-radiation environments [6]. Multi-junction solar cells incorporating InGaN, such as InGaN/Si configurations, have been theoretically predicted to achieve efficiencies up to 46.45%, making InGaN a highly promising material for both terrestrial and space-based solar applications [7,8].

B. Improved Performance

Indium Gallium Nitride (InGaN) solar modules show great potential for high performance across various conditions, particularly in low-light environments and high temperatures. The tunable bandgap of InGaN allows it to capture a wide range of the solar spectrum efficiently, even in low-light conditions, where its high absorption capabilities remain effective [9]. Additionally, InGaN cells maintain their efficiency in high-temperature environments due to near-zero or positive temperature coefficients, unlike traditional silicon-based cells, which degrade at elevated temperatures [10]. These properties make InGaN ideal for use in hot climates or hybrid photovoltaic-thermal systems that operate above 150°C [11], with innovative approaches such as the introduction of quantum wells further boosting performance under solar concentration and heat [12].

Furthermore, InGaN offers key advantages over conventional materials due to its wide bandgap tunability (0.7 to 3.4eV), heat resistance, and durability. Its resilience against radiation and chemical corrosion makes it particularly suited for harsh environments like space or deserts, where silicon-based cells deteriorate more quickly. Advanced growth techniques like plasma-assisted molecular beam epitaxy (PAMBE) have been shown to enhance the crystalline quality of InGaN, reducing defect

densities and extending its operational lifespan [13,14]. Efforts to optimize solar cell technologies focus on improving junction designs, contact materials, and anti-reflective coatings (ARCs). Techniques such as laser thermal processing with specialized coatings enhance the efficiency of ultra-shallow junctions [15], while multilayer ARCs have reduced reflectance in triple-junction solar cells [16]. Metal contacts like titanium further improve conductivity and efficiency [17], and anti-reflective nanostructures have been integrated with multilayer coatings to enhance light transmission in multijunction devices [18].

Computational modeling, such as TCAD simulations, provides valuable insights into optimizing InGaN solar cells by fine-tuning parameters like layer thickness and doping levels, achieving up to 29% efficiency in GaN/InGaN/Si tandem cells [19]. Tools like SLALOM allow for multivariate optimization, significantly improving solar cell design [20]. These models help refine real-world designs by predicting performance under various conditions, offering a faster path to developing high-efficiency InGaN solar cells [20].

III. CURRENT RESEARCH AND DEVELOPMENTS

C. Refining Growth Techniques

Growing high-quality InGaN crystals for solar cell production faces several scientific challenges, primarily due to lattice mismatches between GaN and InGaN, which cause strain and defects like dislocations that negatively affect solar cell efficiency [21]. The high vapor pressure of indium further complicates uniform incorporation during growth, increasing the risk of defects [22]. Phase separation, particularly at higher indium concentrations, also degrades crystal quality, though step-graded interlayers and optimized growth conditions such as temperature and pressure help mitigate these issues [21,22].

Advancements in epitaxial growth techniques, such as Molecular Beam Epitaxy (MBE) and Metal-Organic Chemical Vapor Deposition (MOCVD), have greatly improved the production of high-quality semiconductor materials. MBE allows for precise control of thin films and is effective for fabricating complex heterostructures like quantum wells and transistors, with recent low-temperature process improvements reducing defect densities [23]. MOCVD, more suitable for large-scale

production, has made strides with hot-wall technology, achieving high growth rates and reduced defect densities, particularly in materials like β -Ga₂O₃, promising for high-power electronics [24]. Research continues to enhance InGaN solar cells by focusing on crystal quality and defect reduction. Optimizing growth parameters, such as reducing ammonia flow and adjusting pressure, has enhanced external quantum efficiency in multi-quantum well (MQW) structures [25].

Moreover, introducing AlGaIn electron-blocking layers has reduced recombination losses in GaN–InGaIn MQW solar cells, increasing efficiency, while nanostructure techniques like GaN nanowires on silicon substrates show promise in further reducing dislocations and enhancing light absorption [24,26]. These advancements in growth techniques and novel structures are driving significant improvements in InGaIn-based solar cell performance.

D. Optimizing Design

The scientific design of Indium Gallium Nitride (InGaIn) solar cells is critical to their efficiency, with factors such as indium content, layer thickness, and defect management playing key roles. For example, higher indium content enhances short-circuit current density and absorption but can lower open-circuit voltage and fill factor, ultimately affecting overall efficiency [27]. In heterojunction structures, high indium can lead to polarization effects that reduce efficiency, though single-homojunction cells with optimized designs can achieve efficiencies up to 17% [28]. Additionally, ultra-thin layers like AlN help reduce defects and improve current density, enhancing conversion efficiency [29]. Simulations indicate that InGaIn multijunction cells, when optimized for current matching, can reach very high efficiencies of up to 46% [30].

Advancements in solar cell architectures have improved efficiency through innovations in junction design, contact materials, and anti-reflective coatings (ARCs). Rear-junction silicon heterojunction (SHJ) cells, for example, achieved cost reductions and maintained performance by replacing indium tin oxide (ITO) with aluminum-doped zinc oxide (ZnO) for the front Transparent Conductive Oxide (TCO) layer [31]. In GaInP/GaAs cells, efficiency improved by 4.16% when traditional gold contacts were replaced with a titanium/gold

combination [32]. Nanostructured ARCs, mimicking natural anti-reflective surfaces, have outperformed traditional coatings, improving efficiency by 0.8% [33], while a four-layer ARC increased short-circuit current density by 34.4% in inverted metamorphic triple-junction solar cells [34]. Computational modeling plays a pivotal role in optimizing InGaIn solar cell structures.

Simulations allow researchers to fine-tune parameters like layer thickness, doping concentrations, and defect densities, enabling efficient designs before fabrication. Studies have shown that simulations can optimize InGaIn single-junction cells to reach efficiencies of 27.3% and improve GaN/InGaIn/cSi tandem cells to 29% efficiency using graded layers [35,36]. Multijunction cells have achieved over 40% efficiency under concentrated sunlight by optimizing junctions and material compositions for current matching [37]. Overall, computational models are essential for reducing costs and accelerating the development of high-efficiency solar cells.

IV. CHALLENGES AND FUTURE DIRECTIONS

E. Current Challenges

The adoption of InGaIn solar technology is hindered by several challenges, primarily related to material quality and production costs. A key issue is achieving consistent, high-quality growth of InGaIn due to lattice mismatches and phase separation during fabrication, which affects the efficiency and reliability of the solar cells. Additionally, optimizing light absorption across the solar spectrum remains a technical challenge. High production costs also limit the commercial viability of InGaIn technology compared to other solar technologies [38]. To make InGaIn solar cells more competitive, reducing manufacturing costs, improving scalability, and enhancing long-term stability are essential. Lattice mismatch defects drive up production costs, and current fabrication techniques struggle with large-scale production.

Research into better fabrication methods and materials is crucial for mass production without compromising efficiency. Long-term stability under environmental stress is another concern, requiring further studies to improve material resilience and durability. Innovations such as improved encapsulation and new coatings may help enhance the longevity and performance of InGaIn solar cells [39].

F. Future Directions

To address the challenges in InGaN solar technology, several solutions have been proposed, such as improving material growth techniques like advanced molecular beam epitaxy, which reduces defects and enhances efficiency while lowering costs. Employing innovative materials such as quantum wells can also improve light absorption and stability, tackling the issue of long-term performance. Automated fabrication methods are suggested to scale production efficiently, reducing costs and enhancing scalability. Advancements in encapsulation methods will further protect solar cells from environmental degradation, ensuring long-term stability [40].

Future research in InGaN materials focuses on exploring new alloys, improving indium content control to boost device efficiency, and utilizing InGaN's tunable bandgap for optoelectronic and photovoltaic applications. Cubic-phase InGaN alloys are being explored for overcoming structural limitations and enhancing light emission, while InN/InGaN quantum dots offer high absorption and carrier mobility, showing potential in quantum computing and photodetectors. Additionally, quantum dot-based devices are being researched for solar hydrogen generation, with promising results for stable, efficient renewable energy solutions [41,42].

Integrating InGaN with other materials, such as GaN, using buffer layers and advanced epitaxial growth techniques, helps reduce lattice mismatches, improving the quality and performance of devices. This integration has demonstrated potential for improving both optoelectronic and photovoltaic efficiencies. InGaN solar cells stand out for their tunable bandgap, allowing efficient light absorption across a wide solar spectrum, which can increase conversion efficiencies, particularly in tandem structures. Moreover, these cells are stable under extreme conditions like high temperatures, making them suitable for both terrestrial and space applications. Their resilience to radiation and temperature variations offers a robust solution for long-term energy generation in harsh environments, helping reduce reliance on fossil fuels and promote renewable energy adoption. With ongoing optimizations, such as quantum well structures and multi-junction cells, InGaN technology holds great promise for advancing global energy sustainability [43,44].

V. COMPARISON WITH OTHER EMERGING PHOTOVOLTAIC TECHNOLOGIES

InGaN solar cells are emerging as promising photovoltaic materials due to their tunable bandgap and high absorption coefficients, allowing utilization of a broad solar spectrum. Comparing these with other technologies like perovskite and thin-film photovoltaics reveals key strengths and limitations.

A. Bandgap Tunability and Spectrum Utilization

InGaN alloys provide a wide bandgap range from 0.7eV to 3.4eV, covering the full solar spectrum. This tunability enables high theoretical efficiencies, particularly for tandem or multi-junction designs [45]. Perovskite cells also exhibit high efficiency due to their high absorption coefficients and defect tolerance but face stability challenges compared to InGaN [46].

B. Temperature Stability

InGaN solar cells maintain performance at high temperatures, making them suitable for hybrid thermal-photovoltaic systems. They exhibit a near-zero or positive temperature coefficient, unlike silicon or perovskite cells, which degrade at elevated temperatures [47].

C. Efficiency and Stability

Perovskite solar cells achieve power conversion efficiencies (PCEs) exceeding 25% in laboratory settings but are hindered by degradation due to moisture and light exposure [46]. In contrast, InGaN cells exhibit PCEs up to 27.3% in simulations, with greater potential for reliability in extreme environments [35].

D. Material Challenges

InGaN faces difficulties in achieving uniform, high-quality films due to phase separation and doping limitations. Progress in growth technologies, such as using super-thin interlayers or quantum well structures, has enhanced performance [48]. Perovskites benefit from simpler fabrication processes but require advancements in stability for commercial viability [46].

E. Specialized Applications

InGaN solar cells are promising for space and high-temperature applications, thanks to radiation hardness and thermal stability. For example, nonpolar m-plane InGaN/GaN

multiple quantum well cells perform well at high temperatures and solar concentrations [49].

VI. CONCLUSION

Indium Gallium Nitride (InGaN) solar modules have a tunable bandgap, enhancing energy conversion efficiency. They have a high absorption coefficient, radiation tolerance, and carrier mobility, making them suitable for diverse environmental conditions. InGaN-based designs, like *p*-layer-free Schottky solar cells and multiple quantum wells, show potential for high efficiencies. Research is focused on novel growth methods to improve homojunction device performance. InGaN solar cells offer superior stability and durability, while perovskite cells lead in efficiency but lag in robustness.

ACKNOWLEDGMENT

This work is supported by the University Training Research Project PRFU-2022 (Grant Nos. B00L02EN080120220001). The authors also appreciate the support of the Semiconductor Devices Physics Laboratory.

REFERENCES

- [1] Cao, Z., Liu, L., Lu, F., Cheng, H., & Guo, X. (2023). Optical absorption enhancement in inhomogeneous InGaN nanowire arrays photocathode. *Nanotechnology*, *34*(49), 495701.
- [2] Bae, H., Hwang, S. M., Seo, I., & Kim, Y. (2016). Electrochemical lithium recycling system toward renewable and sustainable energy technologies. *Journal of the Electrochemical Society*, *163*(7), E199.
- [3] Gu, Y., Shen Liu, Y., Yang, G., Xie, F., Zhu, C., Yu, Y., ... & Chen, G. (2021). 3D fluorescence confocal microscopy of InGaN/GaN multiple quantum well nanorods from a light absorption perspective. *Nanoscale Advances*, *3*(9), 2649-2656.
- [4] Peng, Y., Sanati, S., Morsali, A., & García, H. (2023). Metal-organic frameworks as electrocatalysts. *Angewandte Chemie International Edition*, *62*(9), e202214707.
- [5] Passaro, A., Spitaleri, G., Gyawali, B., & de Marinis, F. (2019). Immunotherapy in non-small-cell lung cancer patients with performance status 2: clinical decision making with scant evidence. *Journal of Clinical Oncology*, *37*(22), 1863-1867.
- [6] Hossain, A. S., Teparić, R., & Mrša, V. (2019). Comparison of two models of surface display of xylose reductase in the *Saccharomyces cerevisiae* cell wall. *Enzyme and microbial technology*, *123*, 8-14.
- [7] Nacer, S., & Aissat, A. (2015). Simulation and optimization of current matching multi-junction InGaN solar cells. *Optical and Quantum Electronics*, *47*(12), 3863-3870.
- [8] Chang, J. Y., Yen, S. H., Chang, Y. A., Liou, B. T., & Kuo, Y. K. (2013). Numerical investigation of high-efficiency InGaN-based multijunction solar cell. *IEEE transactions on electron devices*, *60*(12), 4140-4145.
- [9] Fabien, C. A., & Doolittle, W. A. (2014). Guidelines and limitations for the design of high-efficiency InGaN single-junction solar cells. *Solar Energy Materials and Solar Cells*, *130*, 354-363.
- [10] Ren, X., Li, J., Gao, D., Wu, L., & Pei, G. (2021). Analysis of a novel photovoltaic/thermal system using InGaN/GaN MQWs cells in high temperature applications. *Renewable Energy*, *168*, 11-20.
- [11] Polykovskiy, D., Zhebrak, A., Sanchez-Lengeling, B., Golovanov, S., Tatanov, O., Belyaev, S., ... & Zhavoronkov, A. (2020). Molecular sets (MOSES): a benchmarking platform for molecular generation models. *Frontiers in pharmacology*, *11*, 565644.
- [12] Chen, Z., Zheng, X., Li, Z., Wang, P., Rong, X., Wang, T., ... & Wang, X. (2016). Positive temperature coefficient of photovoltaic efficiency in solar cells based on InGaN/GaN MQWs. *Applied Physics Letters*, *109*(6).
- [13] Luna, E. L., & Vidal, M. Á. (2024). Review of the Properties of GaN, InN, and Their Alloys Obtained in Cubic Phase on MgO Substrates by Plasma-Enhanced Molecular Beam Epitaxy. *Crystals*, *14*(9), 801.
- [14] Tsai, I. J., Burt, A., & Koufopanou, V. (2010). Conservation of recombination hotspots in yeast. *Proceedings of the National Academy of Sciences*, *107*(17), 7847-7852.
- [15] Hernandez, M., Venturini, J., Berard, D., Kerrien, G., Sarnet, T., Debarre, D., ... & Akhouayri, H. (2004). Laser thermal processing using an optical coating for ultra shallow junction formation. *Materials Science and Engineering: B*, *114*, 105-108.
- [16] Schubert, M. F., Mont, F. W., Chhajed, S., Poxson, D. J., Kim, J. K., & Schubert, E. F. (2008). Design of multilayer antireflection coatings made from co-sputtered and low-refractive-index materials by genetic algorithm. *Optics express*, *16*(8), 5290-5298.
- [17] Ataser, T., Akin Sonmez, N., Ozen, Y., Ozdemir, V., Zeybek, O., & Ozcelik, S. (2018). Developing of dual junction GaInP/GaAs solar cell devices: effects of different metal contacts. *Optical and Quantum Electronics*, *50*, 1-13.
- [18] Perl, E. E., McMahon, W. E., Bowers, J. E., & Friedman, D. J. (2014). Design of antireflective nanostructures and optical coatings for next-generation multijunction photovoltaic devices. *Optics express*, *22*(105), A1243-A1256.
- [19] Nawaz, M., & Ahmad, A. (2012). A TCAD-based modeling of GaN/InGaN/Si solar cells. *Semiconductor Science and Technology*, *27*(3), 035019.
- [20] Boudaoud, C., Hamdoune, A., & Allam, Z. (2020). Simulation and optimization of a tandem solar cell based on InGaN. *Mathematics and Computers in Simulation*, *167*, 194-201.
- [21] Jani, J., Nicolaides, K. H., Keller, R. L., Benachi, A., Peralta, C. F. A., Favre, R., ... & Antenatal-CDH-Registry Group. (2007). Observed to expected lung area to head circumference ratio in the prediction of survival in fetuses with isolated diaphragmatic hernia. *Ultrasound in obstetrics & gynecology*, *30*(1), 67-71.
- [22] Yamamoto, A., Takagishi, K., Osawa, T., Yanagawa, T., Nakajima, D., Shitara, H., & Kobayashi, T. (2010). Prevalence and risk factors of a rotator cuff tear in the

- general population. *Journal of shoulder and elbow surgery*, 19(1), 116-120.
- [23] Martin, M. A., Boaky, E. A., Boyd, E., Broadgate, W., Bustamante, M., Canadell, J. G., ... & Zhao, Z. J. (2022). Ten new insights in climate science 2022. *Global Sustainability*, 5, e20.
- [24] Gogova, D., Ghezellou, M., Tran, D. Q., Richter, S., Papamichail, A., Persson, A. R., ... & Darakchieva, V. (2022). Epitaxial growth of β -Ga₂O₃ by hot-wall MOCVD. *AIP Advances*, 12(5).
- [25] Jafar, N., Jiang, J., Lu, H., Qasim, M., & Zhang, H. (2023). Recent research on indium-gallium-nitride-based light-emitting diodes: Growth conditions and external quantum efficiency. *Crystals*, 13(12), 1623.
- [26] Johnson, J., Alahi, A., & Fei-Fei, L. (2016). Perceptual losses for real-time style transfer and super-resolution. In *Computer Vision—ECCV 2016: 14th European Conference, Amsterdam, The Netherlands, October 11–14, 2016, Proceedings, Part II 14* (pp. 694–711).
- [27] Feng, S. W., Lai, C. M., Chen, C. H., Sun, W. C., & Tu, L. W. (2010). Theoretical simulations of the effects of the indium content, thickness, and defect density of the i-layer on the performance of pin InGa_N single homojunction solar cells. *Journal of applied physics*, 108(9).
- [28] Fabien, C. A., & Doolittle, W. A. (2014). Guidelines and limitations for the design of high-efficiency InGa_N single-junction solar cells. *Solar Energy Materials and Solar Cells*, 130, 354–363.
- [29] Sang, L., Liao, M., Ikeda, N., Koide, Y., & Sumiya, M. (2011). Enhanced performance of InGa_N solar cell by using a super-thin AlN interlayer. *Applied Physics Letters*, 99(16).
- [30] Chang, J. Y., Yen, S. H., Chang, Y. A., Liou, B. T., & Kuo, Y. K. (2013). Numerical investigation of high-efficiency InGa_N-based multijunction solar cell. *IEEE transactions on electron devices*, 60(12), 4140–4145.
- [31] Cruz, A., Wang, E. C., Morales-Vilches, A. B., Meza, D., Neubert, S., Szyszka, B., ... & Stannowski, B. (2019). Effect of front TCO on the performance of rear-junction silicon heterojunction solar cells: Insights from simulations and experiments. *Solar Energy Materials and Solar Cells*, 195, 339–345.
- [32] Ataser, T., Akin Sonmez, N., Ozen, Y., Ozdemir, V., Zeybek, O., & Ozcelik, S. (2018). Developing of dual junction GaInP/GaAs solar cell devices: effects of different metal contacts. *Optical and Quantum Electronics*, 50, 1–13.
- [33] Perl, E. E., McMahon, W. E., Bowers, J. E., & Friedman, D. J. (2014). Design of antireflective nanostructures and optical coatings for next-generation multijunction photovoltaic devices. *Optics express*, 22(105), A1243–A1256.
- [34] Yan, X., Poxson, D. J., Cho, J., Welsler, R. E., Sood, A. K., Kim, J. K., & Schubert, E. F. (2013). Enhanced omnidirectional photovoltaic performance of solar cells using multiple-discrete-layer tailored-and low-refractive index anti-reflection coatings. *Advanced Functional Materials*, 23(5), 583–590.
- [35] Akter, N., Sharmin, S., & Afrose, R. (2018). Design of a Highly Efficient InGa_N Single Junction Solar Cell Designed from Numerical Analysis. *International Journal for Research in Applied Science & Engineering Technology*, 6, 2614–2618.
- [36] Nawaz, M., & Ahmad, A. (2012). A TCAD-based modeling of GaN/InGa_N/Si solar cells. *Semiconductor Science and Technology*, 27(3), 035019.
- [37] Caselli, D., & Ning, C. Z. (2012, June). Full-spectrum laterally-arranged multiple-bandgap InGa_N solar cells. In *2012 38th IEEE Photovoltaic Specialists Conference* (pp. 002518–002520). IEEE.
- [38] Bhuiyan, M., Siwar, C., Ismail, S., & Islam, R. (2012). The role of ecotourism for sustainable development in East Coast Economic Region (Ecer), Malaysia. *OIDA International Journal of Sustainable Development*, 3(9), 53–60.
- [39] Novas, N., Garcia, R. M., Camacho, J. M., & Alcaide, A. (2021). Advances in solar energy towards efficient and sustainable energy. *Sustainability*, 13(11), 6295.
- [40] Dada, M., & Popoola, P. (2023). Recent advances in solar photovoltaic materials and systems for energy storage applications: a review. *Beni-Suef University Journal of Basic and Applied Sciences*, 12(1), 1–15.
- [41] Luna, E. L., & Vidal, M. Á. (2024). Review of the Properties of GaN, InN, and Their Alloys Obtained in Cubic Phase on MgO Substrates by Plasma-Enhanced Molecular Beam Epitaxy. *Crystals*, 14(9), 801.
- [42] Xiao, L., & Zhao, F. (2024). Exploring the frontier of microbiome biomarker discovery with artificial intelligence. *National Science Review*, 11(11), nwae325.
- [43] Kolesnikov, A., Beyer, L., Zhai, X., Puigcerver, J., Yung, J., Gelly, S., & Houlsby, N. (2020). Big transfer (bit): General visual representation learning. In *Computer Vision—ECCV 2020: 16th European Conference, Glasgow, UK, August 23–28, 2020, Proceedings, Part V 16* (pp. 491–507).
- [44] Mars 2020: Perseverance Rover - NASA Science. Available at: <https://science.nasa.gov/mission/mars-2020-perseverance/>
- [45] Fabien, C. A., Moseley, M., Gunning, B., Doolittle, W. A., Fischer, A. M., Wei, Y. O., & Ponce, F. A. (2013). Simulations, practical limitations, and novel growth technology for InGa_N-based solar cells. *IEEE Journal of Photovoltaics*, 4(2), 601–606.
- [46] Park, N. G. (2015). Perovskite solar cells: an emerging photovoltaic technology. *Materials today*, 18(2), 65–72.
- [47] Ren, X., Li, J., Gao, D., Wu, L., & Pei, G. (2021). Analysis of a novel photovoltaic/thermal system using InGa_N/Ga_N MQWs cells in high temperature applications. *Renewable Energy*, 168, 11–20.
- [48] Sang, L., Liao, M., Ikeda, N., Koide, Y., & Sumiya, M. (2011). Enhanced performance of InGa_N solar cell by using a super-thin AlN interlayer. *Applied Physics Letters*, 99(16).
- [49] Zhao, Y., Huang, X., Fu, H., Chen, H., Lu, Z., Montes, J., & Baranowski, I. (2017, August). InGa_N-based solar cells for space applications. In *2017 IEEE 60th International Midwest Symposium on Circuits and Systems (MWSCAS)* (pp. 954–957). IEEE.

Photovoltaic Solar Energy to Mitigate Emissions Associated with Public Buildings: A Bibliometric Study

Ana Paula Freire de Araújo¹, Andrezza Pereira de Matos², Joelda Dantas³, Monica Carvalho⁴

^{1,2,3,4}Federal University of Paraíba, João Pessoa, Brazil

¹ana.freire@cear.ufpb.br, ²andrezza.matos@cear.ufpb.br, ³joelda@cear.ufpb.br,

⁴monica@cear.ufpb.br

Abstract—This article is a bibliometric review on the use of photovoltaic solar energy to reduce greenhouse gas (GHG) emissions using the life cycle assessment (LCA) methodology. Publications from the Scopus and Web of Science (WoS) databases were used, and the RStudio and VOSviewer software were extensively applied to perform the bibliometric analysis. The study identified that the use of the LCA methodology in studies utilizing photovoltaic solar energy to reduce GHG emissions grew significantly between 2013 and 2022. It also revealed that the countries with the highest number of publications in this research field were China, the United States, Spain, and Italy. The terms “environmental impact,” “life cycle,” and “greenhouse gases” were the main keywords used by the authors. Additionally, a gap was identified in publications on the topic in Africa, Brazil, and other Latin American countries. Therefore, the results of this work aim to contribute to addressing the research gap identified.

Keywords - life cycle assessment (LCA), carbon emissions, photovoltaic solar energy, photovoltaic systems, environmental impacts

I. INTRODUCTION

Anthropogenic greenhouse gas (GHG) emissions are a significant concern due to their contribution to the amplification of climate change [1]. The energy generation sector has been one of the major culprits in the increase of GHG emissions in recent years, responsible for 34% of global GHG emissions in 2019 [2].

As a result, numerous global challenges have emerged, which have been disseminated through the Sustainable Development Goals (SDGs) established by the United Nations (UN) in the 2030 Agenda. The transition to renewable energies plays a pivotal role in promoting sustainable development, as it is interconnected with various SDGs and contributes to the mitigation of negative environmental and social impacts.

In this way, the proper and rational use of energy represents a significant and imminent challenge for society in the coming years so that future generations can access these resources with sufficient quality and minimal environmental impact [3]. To achieve this goal, the widespread adoption of various renewable energy sources over the past decades has proven to be a great ally in reducing GHG emissions from the electricity sector, thus aiding in the energy transition [4].

Therefore, the efficient and rational use of energy plays a crucial role in promoting sustainable development, reducing environmental impact, and improving people's quality of life. It is linked to a series of Sustainable Development Goals (SDGs), which include, in this interconnected order, SDG 7 (Affordable and Clean Energy), SDG 13 (Climate Action), SDG 12 (Responsible Consumption and Production), SDG 9 (Industry, Innovation, and Infrastructure), SDG 11 (Sustainable Cities and Communities), SDG 8



(Decent Work and Economic Growth), and SDG 17 (Partnerships for the Goals).

Among the various renewable sources, photovoltaic solar energy proves to be an excellent strategy to promote sustainability in the energy generation sector and positively contribute to mitigating the impacts of climate change. According to [5], since 1993, Council Directive 93/76/EEC explicitly recognizes the significant role of buildings in total CO₂ emissions.

Thus, the use of solar energy is a favorable strategy to reduce GHG emissions associated with buildings. This is because it is a clean energy source that does not emit carbon during electricity generation, contributing to combating climate change and the use of photovoltaic panels in buildings aligns with SDG 13 and SDG 7.

Furthermore, the installation of photovoltaic panels on buildings aligns with ESG principles, referring to environmental, social, and governance criteria. These aspects are becoming increasingly relevant for investors, companies, and financial institutions seeking to comply with environmental regulations in their operations and investments.

In order to quantify carbon emissions related to photovoltaic panels and contribute to minimizing emissions associated with public buildings, Life Cycle Assessment (LCA) proves to be a well-established methodology. It can encompass the entire lifecycle of a product or service, including raw material extraction, production, distribution, use, and final disposal [6,7]. LCA is an internationally standardized methodology by the International Organization for Standardization (ISO) in ISO 14040 (2006) and ISO 14044 (2006) standards. LCA studies are based on concepts of energy consumption and mass and energy balances (the first law of thermodynamics), which allow for the quantification of environmental impacts through thermodynamic analyses, accounting for resource use [8].

A bibliometric and systemic analysis is an approach that enables a comprehensive quantitative evaluation of the most important scientific studies on a subject. This approach is a tool that allows researchers to identify trends, track the subject's evolution over the years, map existing knowledge on the subject, and identify knowledge gaps. The bibliometric review

method requires a protocol that specifies the systematic search in databases, inclusion and exclusion criteria, the research period, analysis, and the format of presenting results [9].

This work provides a review of LCA research applied to photovoltaic panels, focusing on the challenges and main conclusions regarding emissions related to electricity consumption in buildings. It examines the evolution and dynamics of LCA studies disseminated over the past decade (2013 to 2022). Finally, it identifies areas that require further research and development so that LCA can be useful in assisting decision-makers in defining more suitable renewable energy policies in Brazil and worldwide.

II. METHODOLOGY

In this work, a bibliometric review was conducted using the renowned Scopus and Web of Science (WOS) databases. Bibliometric review represents a systematic approach to assess the effectiveness and gaps in existing knowledge, identifying areas where there is a scarcity or absence of relevant research and, consequently, where new studies are needed [10]. The choice of Scopus and WOS is due to both being considered as some of the most important multidisciplinary databases in the academic context [11].

In constructing this research, the keywords used in the databases were: “solar”, “life cycle assessment”, “photovoltaic”, “carbon emissions”, “greenhouse gases”, “public buildings”, and “environmental impacts”. Searches were applied to find publications related to the topic through the title, abstract, or keywords. According to these conditions, the search string applied in both databases was: (“solar” OR “solar energy” OR “photovoltaic*” OR “PV”) AND (“Life cycle” OR “LCA” OR “Life cycle assessment” OR “carbon emission*” OR “carbon footprint*” OR “GHG” OR “greenhouse gas emission*”) AND (“universit*” OR “public building*” OR “college” OR “campus*”) AND (“environmental impact*” OR “environmental load*”).

The results obtained from the Scopus database were subjected to the following inclusion criteria: (i) articles or reviews; (ii) in the final stage of publication; (iii) published in the English language; and (iv) with a publication period between 2013 and 2022. For the results obtained in the Web of Science (WOS) database, similar inclusion criteria were applied: (i) articles

or reviews; (ii) published in the English language; and (iii) with a publication period between 2013 and 2022.

After applying the inclusion criteria, the results from both databases were imported into the Rstudio software to remove duplicate publications. Rstudio is an open-source, free software that was selected for this purpose. Data packages such as Bibliometrix and Biblioshiny were used, allowing for the mapping of scientific studies to reveal a dynamic structure of the data [12]. With the help of these data packages, it became possible to analyze the following data: number of publications per year, number of publications per country, making it easier to identify nations with more significant academic influence; ranking of the most relevant journals in the field according to Bradford's Law; identification of the most productive affiliations; recognition of authors with the highest publication volume using Lotka's Law; and mapping articles that received the highest number of citations over the years, aiding in identifying publications with greater academic diffusion. Investigating these data helps in understanding the diffusion of the subject over the years, allowing the identification of prominent topics and potential research gaps.

To further investigate the subject, the results obtained after applying the inclusion criteria were submitted to VOSviewer software version 1.6.8, using Java version 9. Among other tools, VOSviewer was chosen as it is free and open-source, accepts the formatting of the databases used and other major ones like PubMed and Google Scholar. In this study, the software was used to map academic trends, the connection between results, and evaluate academic production on the subject by cross-referencing metadata obtained from the two platforms, based on the concept of clustering.

Analyzing publications using VOSviewer and Rstudio software allowed for an in-depth quantitative assessment of academic output, trend detection, and identification of research gaps requiring further academic investigation.

III. RESULTS AND DISCUSSION

According to the Scopus database, a total of 90 publications were disseminated between 2013 and 2022, where the Life Cycle Assessment (LCA) methodology was applied to assess the emissions of greenhouse gases (GHG) in buildings related to the use of photovoltaic

panels. These publications comprised 53 articles (58.8%), 27 conference papers (30%), and 5 reviews (5.5%). Regarding books, book chapters, and conference reviews, only one publication of each format was detected, accounting for 1.1% of the total publications found. After applying inclusion criteria, 56 publications were included, consisting of 51 articles (91.07%) and 5 reviews (8.92%).

The search in the Web of Science (WOS) database resulted in 56 publications, including 44 articles (78.57%), 13 conference papers (23.21%), and 4 reviews (7.14%). After applying inclusion criteria, 33 publications were obtained, comprising 30 articles (90.9%) and 3 reviews (9.1%).

Among the 90 publications found in the Scopus database and the 56 publications obtained in the WOS database, the Rstudio software identified 20 duplicated articles. Tracking the volume of publications on a specific topic over the years allows for the identification of trends in the subject of study. As illustrated in Fig. 1, between 2013 and 2017, there was a reduction in the number of publications from 6 articles to 2 articles. However, between 2018 and 2020, publications reached a record high of 9 articles published in 2020. The period between 2020 and 2021 witnessed a significant drop in the number of publications, possibly due to the sharp reduction in global activities resulting from the COVID-19 pandemic. However, in 2022, the theme returned to a growth in publications, reaching a total of 6 articles published, indicating that the interest in the topic was only temporarily delayed.

Furthermore, among the analyzed publications, the application of the 'cradle to grave' and 'cradle to cradle' methods stood out, highlighting the growing interest of researchers in these approaches. Notably, the 'cradle to

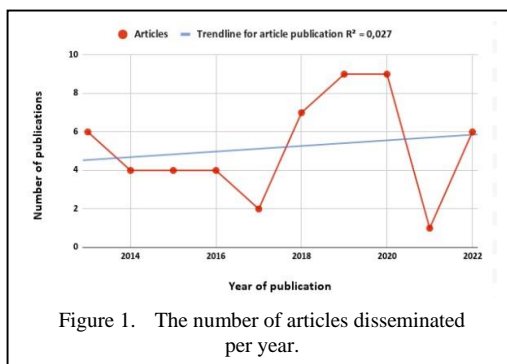


Figure 1. The number of articles disseminated per year.

cradle' method can be identified as a trend for future research. One of the possible catalysts for this renewed interest in the topic was the strengthening of the debate on the contributions of human activities to climate change, evident during the pandemic period [2]. This increased public awareness and sparked political and economic interest in research and technologies aimed at carbon emissions mitigation.

An analysis of the trend line of the number of publications over the years revealed that even though there was a growth trend in research related to the topic between 2017 and 2020, the trend line alone cannot definitively ensure the continuous growth of the topic in the subsequent years. It's important to note that this trend might have reached a higher percentage if we hadn't considered the pandemic-related drop between 2020 and 2021. Therefore, this suggests that other factors may influence this dynamic. However, the resurgence of publications in 2022 represents a renewal of interest and academic production related to the topic.

Publications on the use of photovoltaic solar energy to reduce carbon emissions in buildings have been significant, as illustrated in Fig. 2, particularly in countries such as the United States (27 publications), China (18 publications), Spain (12 publications), Italy (12 publications), and Portugal (9 publications). This analysis highlights that regions with a strong presence also demonstrate a significant investment in scientific research in the area, reflecting these countries' commitment to the United Nations' Sustainable Development Goals (SDG) 12, related to sustainable consumption and production.

Keyword co-occurrence analysis is a tool for research in the field of photovoltaic solar systems and carbon emissions due to its ability to identify emerging trends, interdisciplinary research areas, key concepts, interconnections between the two fields, literature gap identification, literature review support, and guidance for future academic investigations and relevant study planning.

Co-occurrence maps group closely related keywords into clusters identified by colors. The publications obtained from the Scopus database are divided into five clusters, as shown in Fig. 3.

Among the cluster members, the following keywords stand out: the red cluster "carbon footprint" with 14 occurrences, the purple cluster

"sustainable development" with 18 occurrences, the blue cluster "greenhouse gases" with 22 occurrences, the yellow cluster "solar power" with 24 occurrences, and the green cluster "environmental impact" with 59 occurrences, making it the most relevant keyword. The keyword "environmental impact" was widely used by authors to create connections between other topics.

The publications obtained from the WOS database showed a different keyword trend

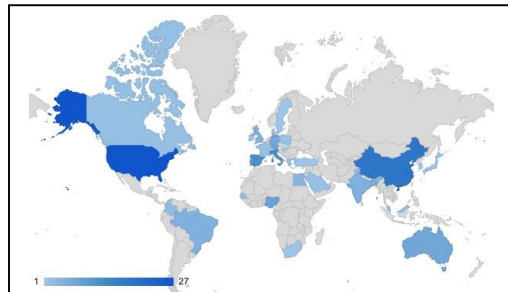


Figure 2. Map of number articles published by country.

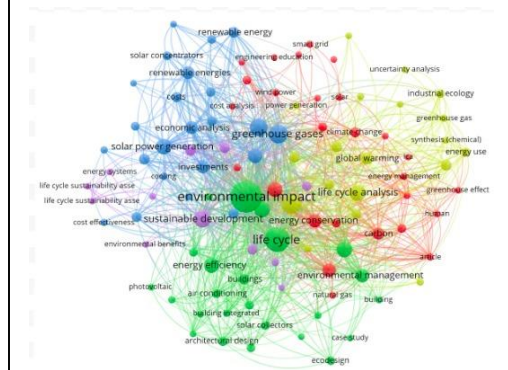


Figure 3. Keyword Co-Occurrence visualization map in the scopus database.

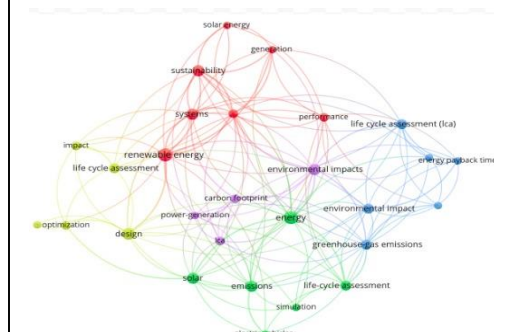


Figure 4. Keyword Co-Occurrence visualization map in the Web of Science (WOS) database.

compared to those identified in the Scopus database. As shown in Fig. 4, the map was organized into five clusters, and the main keywords for each group were as follows: the blue cluster with 5 occurrences each for “environmental impact”, “life cycle assessment (LCA)” and “greenhouse gas emissions”; the purple cluster “environmental impacts” with 6 occurrences; the yellow cluster “design” with 7 occurrences; the red cluster “renewable energy” with 8 occurrences; and the green cluster “energy” with 8 occurrences.

When crossing the databases and excluding duplicate publications, Zipf/s Law for keyword distribution is observed. This is a statistical principle that describes the distribution of keywords in a body of text or dataset, stating that a few keywords are very common, while the majority of keywords are rare [13]. As a result, the main keywords in the two databases and their respective frequencies of occurrence were identified.

These keywords are: “environmental impact” (25), “life cycle” (15), “living cycle analysis” (11), “greenhouse gases” (9) and “energy conservation” (8). Over the years, the words that have shown the greatest growth are “environmental impact,” increasing from 8 occurrences in 2013 to 21 occurrences in 2022, and “life cycle,” rising from 8 occurrences in 2013 to 15 in 2022. This indicates a persistent

interest in these issues. It demonstrates a growing trend in research to identify environmental impacts related to photovoltaic solar energy generation methods. It also shows that topics such as mitigating impacts, such as recycling solar panels, are still areas that require further study.

Bradford's Law of Scientific Dissemination, formulated by Bradford in 1934, provides a way to assess the importance of scientific journals in a specific field of study. According to this law, journals that publish the highest number of articles on a specific topic are identified as the “core” journals, presumably representing greater quality or relevance within that particular area [13]. To apply Bradford's method, the following data were identified: journals, frequency, cumulative frequency, and zone. Ranking the journals involves organizing them based on the significant number of publications related to the topic under consideration. Cumulative frequency, in turn, represents the cumulative sum of publication frequencies of all journals up to a specific point in the ranking. Based on the descending order of journals, they can be divided into three categories, each comprising one-third of the total publications. The first category includes a limited number of highly productive journals. The second category includes a larger number of journals but with lower productivity. Finally, the third category encompasses an even greater number of journals, although each of

TABLE I. RANKING OF THE MOST RELEVANT SOURCES ON SOLAR ENERGY FOR REDUCING CARBON EMISSIONS IN BUILDINGS ACCORDING TO THE BRADFORD LAW.

Journal	Ranking	Frequency	cumFreq	Zone
Journal of Industrial Ecology	1	6	6	Zone1
Applied Energy	2	5	11	Zone1
Energies	3	5	16	Zone1
Energy Reports	4	3	19	Zone1
Renewable And Sustainable Energy Reviews	5	3	22	Zone1
Alexandria Eng. Journal	6	2	24	Zone1

TABLE II. APPLICATION OF LOTKA’S LAW.

Documents written	Number of authors	Proportion of authors
1	220	0.936170213
2	13	0.055319149
4	1	0.004255319
5	1	0.004255319

TABLE III. MOST CITED PUBLICATIONS.

Paper	Total citation	Reference
Renewable energy technologies for sustainable development of energy efficient building	166	[19]
Life Cycle Assessment of a Building Integrated Concentrated Photovoltaic scheme	82	[18]
Life cycle energy and climate change implications of nanotechnologies: A Critical Review	72	[17]
Assessment of technical and economic feasibility for a hybrid PV-wind-diesel-battery energy system in a remote community of north central Nigeria	62	[16]
Design and assessment of solar PV plant for girls hostel (GARGI) of MNIT University, Jaipur city: A case study	49	[15]

them is characterized by even lower productivity [14].

Following Bradford's methodology, journals are classified as: zone 1 (core), zone 2 and zone 3 (peripheries)'. The six journals listed in Table I constitute "Zone 1", that is, the "core", and were considered highly productive and influential in the thematic field. "Zone 2" is made up of 18 journals that showed a lower level of productivity and "Zone 3", with 22 journals, which demonstrated even lower productivity compared to the journals in "Zone 2". The Journal of Industrial Ecology secured first place, being the most productive, with a frequency of 6 publications.

To recognize the most influential authors within a topic, it is essential to apply Lotka's Law. This law argues that the relationship between the number of authors and the quantity of articles they publish, in any field of science, follows a pattern described by the Inverse Square Law, represented by the formula $1/n^2$. In simple terms, during a specific period of time and when examining n articles, the number of scientists contributing four articles would be about $1/16$ of the number of scientists contributing a single article [14].

To apply this law, as presented in Table II, the number of authors who published a certain number of articles was recorded. By applying the Inverse Square Law, it was possible to calculate the publication frequency. Based on 220 authors, accounting for 93.61% of the total, the frequency data obtained, we observed published only one article on the subject in question. Following the same line of reasoning, 13 authors (5.53%) published two articles, 1 author (0.42%) published four articles, and 1 author (0.42%) published five articles. As a result of applying Lotka's Law, we were able to identify highly

productive authors in terms of the volume of articles published on the subject.

Among the most productive authors, two authors with significant prominence were identified: Lamnatou, C., from the University of Lleida, Spain, with four publications, and Chemesiana, D., also from the University of Lleida, Spain, with five publications. The presence of authors from the University of Lleida as the most productive ones reinforces the importance of this affiliation. Furthermore, the existence of publications on the same topic in collaboration between the authors strengthens the relevance and impact of their work in the research field.

In addition to highlighting the top authors, to determine the articles that found greater relevance and dissemination in the scientific community, the volume of citations is analyzed, as presented in Table III.

The article "Design and assessment of solar PV plant for girls hostel (GARGI) of MNIT University, Jaipur city: A case study" [15] was the fifth article with the highest volume of publications in the analyzed period, with a total of 49 citations. This study contributed to identifying gaps in energy policies and strategies, providing useful information for countries or states seeking to reduce their greenhouse gas emissions and make solar energy technology more attractive and financially viable.

The article "Assessment of technical and economic feasibility for a hybrid PV-wind-diesel-battery energy system in a remote community of north-central Nigeria" [16] received a total of 62 citations, ranking fourth. This study contributes by offering a techno-economic analysis that can be adopted in other developing areas or in locations where rural populations lack access to grid electricity,

providing an efficient model for the adoption of renewable energy sources and environmental impact mitigation. The third publication with the highest number of citations was “Life Cycle Energy and Climate Change Implications of Nanotechnologies” [17] with 72 citations. The authors pointed that significant variations were observed in the studies due the article “Assessment of technical and economic feasibility for a hybrid PV-wind-diesel-battery energy system in a remote community of north-central Nigeria” [16] received a total of 62 citations, ranking fourth. o inconsistent parameters and the lack of reliable data, attributed to the immature stage of many nanotechnologies. Despite the high energy demands in the production of nanostructured materials, these demands are often diluted over the product's life cycle, resulting in net efficiency benefits. This highlights the need for more LCA studies to confirm these findings due to uncertainties and frequent hypothetical scenarios in the analyzed studies [17].

The second publication with the highest number of citations was “Life Cycle Assessment of a Building Integrated Concentrated Photovoltaic scheme”, with 82 citations. This article presents a life cycle assessment (LCA) of a Building Integrated Concentrated Photovoltaic (BICPV) scheme at the University of Lleida, Spain, focusing on the assembly phase and its environmental impact. According to [18], the results indicate that Concentrated Photovoltaic (CPV) technology has significantly lower environmental impact compared to the PV system, representing only 10% of the total impact in the BICPV scheme. Furthermore, replacing BICPV with Building Integrated Photovoltaic (BIPV) increases the environmental impact by about 13.5 times, with the PV system being 2.35 times more impactful than the CPV system. This impact is mainly caused by cooling tubes and reflectors. The authors emphasize the importance of choosing between BICPV and BIPV technologies based on environmental considerations and highlight areas for improving efficiency and material selection.

The publication with the highest number of citations was “Renewable energy technologies for sustainable development of energy-efficient buildings”, with 162 citations and is a collaboration between authors from Spain and Italy, two of the countries that have the largest number of publications. The article states that there are several ways to reduce conventional

fossil fuel energy use to meet the energy needs of a building. As pointed out [19], this reduction can occur through energy conservation strategies, such as the use of passive solar design and low-embodied-energy building materials, by promoting renewable energy technologies to meet building energy needs, aiming for zero carbon emissions from buildings, increasing the share of renewable sources in the energy matrix and reinforcing the need for global policies to integrate renewable energy systems into buildings.

In this way, based on the set of findings obtained in this study, it is said that despite the searches using specific keywords directly related to the explored topic, reflecting interest in the field, on the other hand, it is also inferred that, to the present moment, the number of publications is still low when considering the degree of importance encompassed in the particular field of photovoltaic solar energy to reduce emissions associated with public buildings. Thus, this work constitutes a contribution to filling this research gap, which needs to be further addressed, especially in the case of Brazil, where none of the considered fields, such as the presence of authors, affiliations, and journals, were identified.

IV. CONCLUSION

This study conducted a bibliometric review on the use of photovoltaic solar energy as a means to mitigate greenhouse gas emissions through the application of the Life Cycle Assessment (LCA) methodology.

The bibliometric review utilized the Scopus and Web of Science databases, applying the VOSviewer software and the RStudio software with the Biblioshiny and Bibliometrix libraries.

A total of 146 publications from 2013 to 2022 were analyzed, with 90 sourced from Scopus and 56 from Web of Science. An analysis of the number of publications over time revealed a growing trend in research on this topic. The main methods employed in the studies were “cradle to grave” and “cradle to cradle,” demonstrating the increasing interest of researchers in applying these methods within LCAs.

The countries that contributed the most to the dissemination of the topic were China, the United States, Spain, and Italy, respectively, reinforcing the commitment of these nations-

signatories of the 2030 Agenda-to promoting scientific advancement and innovation to achieve the Sustainable Development Goals (SDGs) established by the United Nations (UN). Additionally, a research gap on this topic was identified in Africa, Brazil, and other Latin American countries.

Thus, this work not only highlights the growing interest in research on the use of photovoltaic solar energy to mitigate greenhouse gas emissions but also contributes to identifying and addressing the research gap observed.






ACKNOWLEDGMENT

The authors wish to acknowledge the support of the Laboratory of Environmental and Energy Assessment (LAvAE) at the Federal University of Paraíba, the Paraíba State Research Support Foundation (FAPESQ) for the M.Sc. scholarship and postdoctoral grant (№. 1990/2022, №. 17/2022) and project 3063/2021 (call N° 09/2021 Universal Demand). Thanks are extended to the Coordination for the Improvement of Higher Education Personnel (CAPES) for the M.Sc. scholarship, and to the National Council for Scientific and Technological Development (CNPq) for the Productivity Grant (№. 309452/2021-0) and project 424173/2021-2.

REFERENCES

- [1] Jones, M. W., et al. (2023). National contributions to climate change due to historical emissions of carbon dioxide, methane, and nitrous oxide since 1850. *Scientific Data*, 10(1), 155.
- [2] Pathak, M., Slade, R., Shukla, P. R., Skea, J., Pichs-Madruga, R., & Ürge-Vorsatz, D. (2022). Technical Summary. In: *Climate Change 2022: Mitigation of Climate Change. Contribution of Working Group III to the Sixth Assessment Report of the Intergovernmental Panel on Climate Change*. Cambridge University Press, Cambridge, UK and New York, NY, USA.
- [3] Pereira, M. T. R. M., Carvalho, M., & Mady, C. E. K. (2022). Addressing energy demand and climate change through the second law of thermodynamics and LCA towards a rational use of energy in Brazilian households. *Entropy*, 24(11), 1524.
- [4] Sathaye, J., O. Lucon, A. Rahman, J. Christensen, F. Denton, J. Fujino, G. Heath, S. Kadner, M. Mirza, H. Rudnick, A. Schlaepfer, & A. Shmakin, (2011). Renewable Energy in the Context of Sustainable Development. In *IPCC Special Report on Renewable Energy Sources and Climate Change Mitigation*. Cambridge University Press, Cambridge, United Kingdom and New York, NY, USA.
- [5] Carvalho, M., Serra, L. M., & Lozano, M. A. (2011). Optimal synthesis of trigeneration systems subject to environmental constraints. *Energy*, 36(6), 3779-3790.
- [6] Associação Brasileira de Normas Técnicas [Brazilian Association of Technical Standards]. (2014). Avaliação do ciclo de vida - Princípios e estrutura: NBR ISO 14040 [Life Cycle Assessment - Principles and structure: NBR ISO 14040], Rio de Janeiro.
- [7] Associação Brasileira de Normas Técnicas. [Brazilian Association of Technical Standards]. (2014). Avaliação do ciclo de vida - Requisitos e orientações: NBR ISO 14044 [Life Cycle Assessment - requisitos and orientations: NBR ISO 14040], Rio de Janeiro.
- [8] Nwodo, M. N., & Anumba, C. J. (2020). Exergetic life cycle assessment: A review. *Energies*, 13(11), 2684.
- [9] Waddington, H., et al. (2012). How to do a good systematic review of effects in international development: A tool kit. *Journal of Development Effectiveness*, 4(3), 359-387.
- [10] Petticrew, M., & Roberts, H. (2006). *Frontmatter. In Systematic Reviews in the Social Sciences*. Wiley.
- [11] Wang, Q., & Waltman, L. (2016). Large-scale analysis of the accuracy of the journal classification systems of Web of Science and Scopus. *Journal of Informetrics*, 10(2), 347-364.
- [12] Cobo, M. J., López-Herrera, A. G., Herrera-Viedma, E., & Herrera, F. (2011). An approach for detecting, quantifying, and visualizing the evolution of a research field: A practical application to the Fuzzy Sets Theory field. *Journal of Informetrics*, 5(1), 146-166.
- [13] Rodrigues, C., & Godoy Viera, A. F. (2016). Estudos bibliométricos sobre a produção científica da temática Tecnologias de Informação e Comunicação em bibliotecas [Bibliometric studies on the scientific production of the topic Information and Communication Technologies in libraries]. InCID: *Revista de Ciência da Informação e Documentação*[*Journal of Information Science and Documentation*], 7(1), 167.
- [14] Alberto, C. (2023). Bibliometrics: historical development and current issues. *Em Questão*; 24(2), 32-11.
- [15] Khatri, R. (2016). Design and assessment of solar PV plant for girls hostel (GARGI) of MNIT University, Jaipur city: A case study. *Energy Reports*, 2, 89-98.
- [16] Salisu, S., Mustafa, M. W., Olatomiwa, L., & Mohammed, O. O. (2019). Assessment of technical and economic feasibility for a hybrid PV-wind-diesel-battery energy system in a remote community of north central Nigeria. *Alexandria Engineering Journal*, 58(4), 1103-1118.
- [17] Kim, H. C., & Fthenakis, V. (2013). Life cycle energy and climate change implications of nanotechnologies: A critical review. *Journal of Industrial Ecology*, 17(4), 528-541.
- [18] Menoufi, K., Chemisana, D., & Rosell, J. I. (2013). Life cycle assessment of a building integrated concentrated photovoltaic scheme. *Applied Energy*, 111, 505-514.
- [19] Chel, A., & Kaushik, G. (2018). Renewable energy technologies for sustainable development of energy efficient building. *Alexandria Engineering Journal*, 57(2), 655-669.

The Importance of Implementing Artificial Neural Networks in Boiler Automation Systems

Stefan Popović¹ , Dejan Djukić² , Nebojsa Denić³ , Sonja Djukić Popović⁴ ,
Jelena Stojanović⁵ 

^{1,2,5}Faculty of Information Technologies – Alfa BK University, Belgrade, Serbia

³Faculty of Sciences and Mathematics - University of Pristina, Kosovska Mitrovica, Serbia

⁴Faculty of Mathematics - University of Belgrade, Serbia

¹stefan.popovic@alfa.edu.rs, ²dejan.djukic@alfa.edu.rs, ³nebojsa.denic@pr.ac.rs,

⁴sonjica27@yahoo.com, ⁵jelena.stojanovic@alfa.edu.rs

Abstract—The twenty-first century brings significant energy challenges such as the scarcity of fossil fuels, the reduction in the number of nuclear power plants, and insufficient capacities of power plants that operate on the principle of renewable energy sources. In addition to this, ecological problems that we have been facing for more than a century are emerging, with global warming, the greenhouse effect, and the extensive devastated areas resulting from the large amounts of ash being particularly noteworthy. Increasingly frequent military conflicts disrupt the uninterrupted flow of energy resources among countries, leading to a natural gas deficit. This problem especially affects the European continent, which must turn to renewable energy sources such as biomass. In order to reduce pollution, increase the utilization of existing fuels, and maintain the quality and comfort of life during the heating season, a solution must be found so that with existing reserves and the production of biomass we can achieve the same or better results. This paper presents an example of the application of artificial neural networks in small capacity boilers and the potential for energy savings. Savings not only yield economic results but also visibly reduce small particles PM 2.5 and PM 10, while also decreasing the emission of harmful carbon and sulfur gases.

Keywords - artificial neural networks, boiler automation systems, mathematical models, optimization of combustion parameters

I. INTRODUCTION

The rapid development of technology and modern lifestyle are introducing artificial intelligence and machine learning into all aspects of life. Pollution problems have plagued the planet for more than a century and are the result of excessive consumption of fossil fuels. The last few decades have brought innovations in heating smaller facilities, phasing out the use of oil and coal in boiler rooms, while introducing boilers with automatic heating systems powered by gas and biomass. This significantly reduces pollution, but not sufficiently. Hence, there is a need for greater application of artificial intelligence and machine learning in the control of combustion in boilers with automatic loading.

Neural networks, although introduced as a mathematical model in the mid-twentieth century, are only experiencing their full expansion today, at the end of the first quarter of the twenty-first century. The application of neural networks is very broad; there is almost no area where they have not played a key role in the functioning of automated control systems, object recognition, decision-making systems, and many other fields that surround us [1]. The application of neural networks in controlling combustion in automatic loading boilers is gaining significance. It is important to note that until just a year ago,



practical application was virtually negligible in small boiler systems. Research on this topic remains relatively modest and almost unnoticed, except in large boiler systems. Through considerations of potential applications, it has been concluded that neural networks can be applied to the automatic calibration of combustion control systems [2]. Due to all this, the issue of controlling the operation of boilers with automatic ignition is very relevant, and the implementation of neural networks and machine learning for managing calibration during operation allows for significant fuel savings, contributing to the reduction of harmful environmental impacts and leading to an inevitable improvement in the quality of life. The safe and stable operation of boilers has been a challenge since ancient times, and combustion is fundamental to their operation; therefore, it is essential to monitor the state of combustion to ensure economical operation of the boilers. [3,4]. The number of devices connected to various Internet servers around the world is rapidly increasing. Supporting this is Gartner's research, which indicated that in 2015 there were over twenty billion connected internet devices [5]. Today that number is around 27 billion, while according to IHS Markit research, it will rise to as many as 125 billion by 2030 [6]. Additionally, the issue of impaired air quality, resulting from the emissions of harmful substances from industrial and thermal power plants, local boiler houses, and traffic, prompts various research aimed at analyzing and assessing gas emissions and their impact on air quality and finding solutions for improvement and control [7]. Global warming and climate change, the impacts on the melting of ice caps, and the extinction of plant and animal species—all of these lead to the necessity of developing cheap hardware and software solutions for monitoring that would be an integral part of every energy system.

This necessitates the development of a model that will integrate artificial intelligence with the basic living needs of the population. The paper presents experimental confirmation of how artificial neural networks can, with satisfactory probability, predict combustion parameters, allowing for recalibration during combustion that will reduce energy consumption and increase the efficiency of fuel utilization.

II. LITERATURE REVIEW

Accurate modeling and simulation of components are very important for training,

strategic planning and maintenance, techno-economic decisions as well as continuous monitoring of construction work. With increasing concern for the environment and a more competitive market after electricity deregulation, the need for better and simpler simulation and monitoring tools is growing [8]. Department of Energy Sciences, Lund University has conducted several researches in this area and artificial neural networks have been shown to be good candidates for fault diagnosis, process identification and modeling of nonlinear systems in the energy field [8-11]. The boiler is undoubtedly an important element of the power plant. Physical modeling of the boiler is difficult and complicated [12-15]. Several authors have reported various applications, such as monitoring, diagnostics, optimization, fault diagnosis, etc., using data-driven modeling. In [16] an artificial neural network is used to optimize load allocation, and in [17] a neural network is used for fault diagnosis and is trained with operational data from a nuclear power plant. Other examples of the use of artificial neural networks include [18,19] where they are used for turbofan motor diagnosis and fault diagnosis in a power plant [20]. According to all these studies, artificial neural networks have proven to be a good candidate for modeling nonlinear energy systems. Although we find many examples of the use of artificial neural networks in energy systems, we do not find the application of parameter control in low and medium power systems in research. Accordingly, the idea of checking the model on the OZON 55 boiler system is arrived at.

III. MODEL SETUP

During the 2019/2020 heating season, a problem was observed with boilers with automatic ignition, which was reflected in unusual shutdown and impossibility of ignition. Then comes the idea that neural networks and machine learning can be applied to problem solving [2]. By monitoring the operation of the boiler, it was determined that whenever pellets from another manufacturer are introduced, there is a stoppage in operation. Then a reason is sought for the uncontrolled shutdown of the boiler and the impossibility of automatic ignition. It is recognized that the automation system that works according to already defined parameters for the quality of wood pellets cannot work with pellets of lower quality. When pre-calibration is carried out in order to burn pellets with a higher humidity or a lower heat value, the

problem of uncontrolled overheating occurs in case of encountering pellets of better quality. Here comes the idea of introducing a recalibration system during combustion [21]. Inevitably there was a need for a system that could take the input pellet quality and perform an independent recalibration during operation to eliminate the major problem of downtime.

In order to adequately approach the finding of causes and possible solutions, the issue of monitoring the operation of the boiler was imposed. The possibility of using one of the existing data recording systems was analyzed. After a comprehensive review of the complexity, it was decided to implement a special purpose system that will collect data from sensors that are embedded in the boiler system in a way that does not disturb the system and has no contact points with combustion. For the experimental data collection, which has been carried out since March 2022 and is still ongoing, an Arduino Uno was used to which K-type temperature probes, humidity meters and gas meters are connected. Temperature probes are placed at the probe points that control the operation of the boiler, but also directly under the firebox, in the smoke channel one meter above the smoke exit from the boiler, as well as for measuring the external and internal air temperature. Humidity sensors monitor the relative humidity of air and pellets. Gas sensors are placed in the chimney to measure the amount and type of gases that are a product of combustion. By May 2022, the system has undergone a series of hardware and software changes to adapt for more accurate and purposeful measurements. Experimental measurements for the research part are being carried out from October 2022 [21].

In parallel with the development of the hardware used in the measurements, the selection of a mathematical model that would describe the system was approached. Therein lies the difficulty that is reflected in predicting the functioning, order and size of the system. This is important so they can start collecting data.

Searching for possible mathematical models, we came to the conclusion that the model used is multivariate and non-linear. On the other hand, the nature of the collected data in the form of time series imposes a dynamic discrete time model for this system. For this reason, the required model is of the following form:

$$y(t) = f(Y(t, D_Y), X_1(t, D_1), X_2(t, D_2), \dots), \quad (1)$$

where $f: \mathbf{R}^{D_Y + D_{X_1} + D_{X_2} + \dots} \rightarrow \mathbf{R}$ is a continuous non-linear map representing the required model, and where:

$$Y(t, D_Y) = (y(t-1), y(t-2), \dots, y(t-D_Y)),$$

$$X_1(t, D_{X_1}) = (x_1(t-1), x_1(t-2), \dots, x_1(t-D_{X_1})),$$

$$X_2(t, D_{X_2}) = (x_2(t-1), x_2(t-2), \dots, x_2(t-D_{X_2})),$$

etc., are vectors of data samples acting as arguments of function f .

The problem solved initially is the determination of the dimensions of vectors Y, X_1, X_2, \dots , i.e. D_Y, D_1, D_2, \dots which are the orders of the models autoregressive and trans regressive dependencies of the system. The method used for this has been described in [10]. The essence of this method consists in computation of probability that the collected data are produced by a system whose model is a linear map.

$$p_D(\varepsilon, \delta) = P(d(y(t_1), y(t_2)) < \varepsilon | d(X(t_1, D), X(t_2, D)) < \delta) \quad (2)$$

This probability is, in fact, being estimated from the counts of favourable events using an indicator function:

$$\Psi_\varepsilon(\zeta) = \begin{cases} 1 & |\zeta| \leq \varepsilon \\ 0 & |\zeta| > \varepsilon \end{cases} \quad (3)$$

Thus, we compute the counts:

$$\psi_D(\varepsilon, \delta) = \sum_{1 \leq i < j \leq N_D} \Psi_\varepsilon(y(i) - y(j)) \prod_{k=1}^D \Psi_\delta(x(i-k) - x(j-k)) \quad (4)$$

and from these counts, the probability is estimated:

$$p_D(\varepsilon, \delta) = \frac{\psi_D(\varepsilon, \delta)}{\psi_D(\delta)} \quad (5)$$

In order to facilitate the estimation of the order, the estimated probabilities have been compounded into the cumulative complement of probability:

$$\rho_D = \int_0^{\infty} (1 - p_D(\varepsilon)) d\varepsilon, \quad (6)$$

and finally, the differential increment of predictability:

$$\Delta_D = \frac{(\rho_{D-1} - \rho_D)}{\rho_0}. \quad (7)$$

This value decreases as the supposed order of the model D increases, until it reaches zero value. After that, for the collected data, the prediction of outputs cannot be improved with an increase in value of D . Thus, we have reached the conclusion that this value of D is the correct order of the model [22].

Once model orders of the autoregressive component D_Y , and of the trans-regressive components D_1 , D_2 etc. have been estimated, the dynamical regression model has been constructed from a neural network effectuating the non-linear mapping f . In this case, the three-layer perceptron network structure has been used, $y = f(X)$, where all the delayed input and output samples have been combined into input vector $X = (Y, X_1, X_2)^T$. This function has been identified using the data collected by the measurements on the system.

The mapping performed by the neural network is being computed as:

$$y = f(X) = \sigma_3 \left(W_3 \left(\sigma_2 \left(W_2 \sigma_1 \left(W_1 X - W_{1,0} \right) - W_{2,0} \right) - W_{3,0} \right) \right). \quad (8)$$

In this model, non-linear sigmoidal functions σ_1 , σ_2 , σ_3 are, for all the layers, the hyperbolic tangent $\sigma_1(s) = \sigma_2(s) = \sigma_3(s) = th(s)$.

The synaptic and the activation coefficients of the neuronal network, represented by matrices $W_1, W_{1,0}, W_2, W_{2,0}, W_3, W_{3,0}$ have been optimised using the method of back-propagation of the error gradient.

IV. EXPERIMENT AND RESULTS

An artificial neural network was used for data processing. It should be remembered that the neural network determines one sequence element at a time. We bring a set of measured values to the input and after that we start the calculation. The next mesh is added only after the calculation for the previous mesh has already been performed. The network maintains a so-called hidden state and has the current hidden state at each step. For a given input, given that input and the current hidden state, it computes a new hidden state as a linear combination of the matrices with the vectors of the current hidden state and the current input. An activation function is applied to the obtained result and thus a new hidden state is obtained. After that comes a new set of measurements, based on the current state and representation of the set, with the help of the same matrices, linear transformations are performed, activation functions are applied, a new state is obtained and so on for all sets of measurements. At each step, some output can be generated from the hidden state [21].

The complete system designed with the methodology approach given in this paper is shown in the Fig. 1 including the entire approach for effective training of neural networks.

A carefully designed methodology integrates multiple components to ensure correct and efficient neural network training and evaluation in case of network intrusion detection. A strategic combination of parameters such as the number of epochs, batch size and callbacks ensure an effective performance-oriented training phase.

By using this model, and after comparing the results, deviations were observed between the computationally obtained hidden states and the

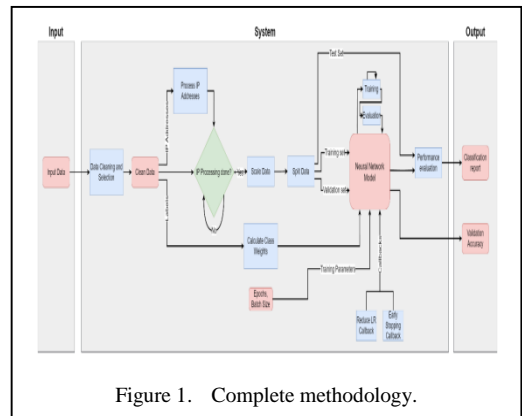


Figure 1. Complete methodology.

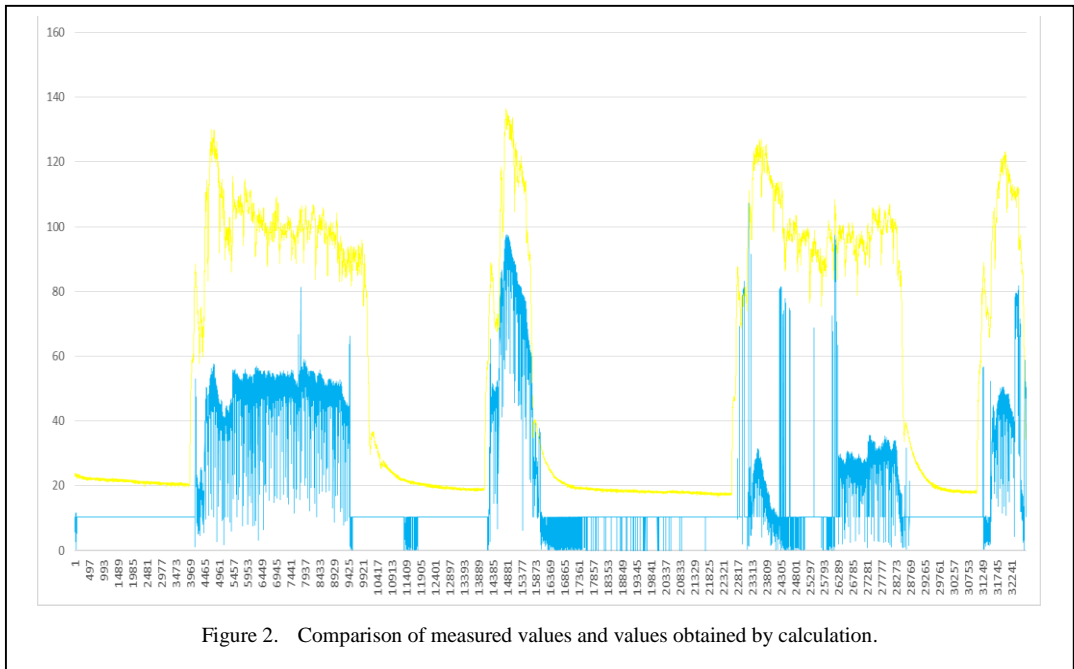


Figure 2. Comparison of measured values and values obtained by calculation.

actual measured values. By increasing the number of measurement points, the error decreased.

The Fig. 2 shows the relationship between the measured values (blue color) and the calculated values (yellow color), it can be seen that the calculated value mostly follows the measured value, but there is an error. In this research, the neural network obtained an approximate value to the measured value. The error decreased with increasing number of measurements. And in some cases, a neural network of this type gave results that did not agree with the measured results.

V. CONCLUSION

Although there are systems with better results [23], using knowledge from the field of neural networks for application in combustion control in boilers with automatic ignition would greatly improve the degree of fuel utilization, ensure more stable operation of boilers, which would lead to significant energy savings, and this would help to preserve the environment, reducing the emission of harmful gases, reducing the amount of ash and reducing the consumption of biomass and fossil fuels, which are decreasing every day on planet Earth.

Therefore, the development of a neural network model that will be applied to optimize the control parameters of boilers with automatic

firing can lead to a significant reduction in fuel consumption and an increase in the degree of fuel utilization. Forecasting the temperature of the combustion chamber, the energy power of the pellets, the amount of oxygen in the air mixture can significantly improve the operation of the heating system, thereby increasing the comfort of the population and contributing to environmental protection [21]. The importance of the development of algorithms and machine learning is inevitable today. All engineering solutions used must contain an artificial intelligence component in their software part, which is the conclusion of this paper. A big problem in the development of this model is the short period of operation of the boiler, which is contributed by uneven weather conditions. We see the need to develop a model that, in addition to the parameters necessary to maintain the fire and monitor the quality of the pellets, will also include parameters related to the climatic conditions of the microregion where the measurements are made.

VI. PROPOSAL FOR FURTHER WORK AND OTHER RESEARCH

To all researchers working on this topic, we offer, as a team, selfless cooperation and the desire to exchange information and further work on improving the model. In addition, after the completion of the first phase of the project, all

obtained results will be publicly published on the file server.

ACKNOWLEDGMENT

Since 2023, this research has been included in the project “Smart cities and modern technologies” registered under the number U03/2023.

REFERENCES

- [1] Popovic, S., Kopanja, L., Djukic Popovic, S., & Djukic, D. (2022). Neural networks and their application in object recognition. In *Proceedings of the 12th International Conference on Applied Internet and Information Technologies (AIIT 2022)*, Zrenjanin, Serbia.
- [2] Popovic, S., Djukic, D., Djukic Popovic, S., & Kopanja, L. (2022). Preliminary research on the application of neural networks to the combustion control of boilers with automatic firing. In *Proceedings of the 8th Virtual International Conference on Science, Technology and Management in Energy*, Belgrade, Serbia.
- [3] Fernández-Alemán, J. L., López-González, L., González-Sequeros, O., Jayne, C., López-Jiménez, J. J., Carrillo-de-Gea, J. M., & Toval, A. (2016). An empirical study of neural network-based audience response technology in a human anatomy course for pharmacy students. *Journal of Medical Systems*, 40(4), 1-12.
- [4] Soltani, A., Battikh, T., Jabri, I., & Lakhoua, N. (2018). A new expert system based on fuzzy logic and image processing algorithms for early glaucoma diagnosis. *Biomedical Signal Processing and Control*, 40, 366-377.
- [5] Tomanović, I. (2017). Implementation of Internet of Things in retail development. *InfoM*, 64, 18–25.
- [6] Forbes. *Digital Asset*. Available at: <https://www.forbes.com/digital-assets/research/?sh=754256e487b64cf1>, Accessed on 09/25/2024.
- [7] Borić, J., & Goletić, Š. (2014). Dispersion modelling of pollutants emitted from road traffic in the area Zenica using the software model AERMOD. *Proceedings on Metallic & Nonmetallic Materials*, 419-426.
- [8] Smrekar, J., Assadi, M., Fast, M., Kuštrin, I., & De, S. (2009). Development of artificial neural network model for a coal-fired boiler using real plant data. *Energy*, 34(2), 144-152.
- [9] Chu, J. Z., Shieh, S. S., Jang, S. S., Chien, C. I., Wan, H. P., & Ko, H. H. (2003). Constrained optimization of combustion in a simulated coal-fired boiler using artificial neural network model and information analysis. *Fuel*, 82(6), 693-703.
- [10] Rusinowski, H., & Stanek, W. (2007). Neural modelling of steam boilers. *Energy Conversion and Management*, 48(11), 2802-2809.
- [11] Mellit, A., & Kalogirou, S. A. (2008). Artificial intelligence techniques for photovoltaic applications: A review. *Progress in energy and combustion science*, 34(5), 574-632.
- [12] Kesgin, U., & Heperkan, H. (2005). Simulation of thermodynamic systems using soft computing techniques. *International journal of energy research*, 29(7), 581-611.
- [13] Boccaletti, C., Cerri, G., & Seyedan, B. (2001). A neural network simulator of a gas turbine with a waste heat recovery section. *J. Eng. Gas Turbines Power*, 123(2), 371-376.
- [14] Mathioudakis, K., Stamatis, A., Tsalavoutas, A., & Aretakis, N. (2001). Performance analysis of industrial gas turbines for engine condition monitoring. *Proceedings of the Institution of Mechanical Engineers, Part A: Journal of Power and Energy*, 215(2), 173-184.
- [15] Fantozzi, F., & Desideri, U. (1998). Simulation of power plant transients with artificial neural networks: Application to an existing combined cycle. *Proceedings of the Institution of Mechanical Engineers, Part A: Journal of Power and Energy*, 212(5), 299-313.
- [16] Cerri, G., Borghetti, S., & Salvini, C. (2006). Neural management for heat and power cogeneration plants. *Engineering Applications of Artificial Intelligence*, 19(7), 721-730.
- [17] Weerasinghe, M., Gomm, J. B., & Williams, D. (1998). Neural networks for fault diagnosis of a nuclear fuel processing plant at different operating points. *Control Engineering Practice*, 6(2), 281-289.
- [18] Joly, R. B., Ogaji, S. O. T., Singh, R., & Probert, S. D. (2004). Gas-turbine diagnostics using artificial neural networks for a high bypass ratio military turbofan engine. *Applied energy*, 78(4), 397-418.
- [19] Simani, S., & Fantuzzi, C. (2000). Fault diagnosis in power plant using neural networks. *Information Sciences*, 127(3-4), 125-136.
- [20] Fast, M., & Palme, T. (2010). Application of artificial neural networks to the condition monitoring and diagnosis of a combined heat and power plant. *Energy*, 35(2), 1114-1120.
- [21] Popovic, S., Djukic, D., Djukic Popovic, S., & Gligorićević, M. (2023). Neural networks in pellet combustion control: An overview of the group's research work in 2022/2023. In *Proceedings of the 9th Virtual International Conference on Science, Technology and Management in Energy*, Belgrade, Serbia.
- [22] D. Djukic. (1997). Modelisation des systemes non lineaires, *These No 1739, EPFL, Lausanne*.
- [23] Wen, H. T., Lu, J. H., & Phuc, M. X. (2021). Applying artificial intelligence to predict the composition of syngas using rice husks: A comparison of artificial neural networks and gradient boosting regression. *Energies*, 14(10), 2932.

Theoretical Studies on the Hydrogen Adsorption Properties of Transition Metal Decorated Covalent Organic Framework

Valarmani M. Vasanthakannan¹, Kittusamy Senthilkumar²

^{1,2}Department of Physics, Bharathiar University, Tamil Nadu, India

¹vasanthakannangasc@gmail.com, ²ksenthil@buc.edu.in

Abstract—In this work, we study metal (Sc and Y) atom decorated quinoxaline and benzene connected covalent organic framework (MCOF) for H₂ molecule storage application using the density functional theory calculations. Total of 18 metal (Sc and Y) atoms are bonded on covalent organic framework (COF) with the binding energy of 4.3 eV per Sc atom and 4.4 eV per Y atom. We observed that each metal atom of MCOFs successfully adsorbs six H₂ molecules with H₂ adsorption energy of approximately -0.35 eV/H₂ molecule. The adsorbed H₂ molecules interact with MCOFs through Kubas interaction. The computed H₂ molecule storage capacity is 8.4 and 6.5 % with desorption temperature of 436 and 447 K for Sc atom decorated COF and Y atom decorated COF, respectively. The computed H₂ molecule storage capacity of MCOFs reaches the required H₂ gravimetric weight percentage reported by U. S. Department of Energy (US-DE). Abinitio molecular dynamics simulation study confirms the structural stability of MCOFs at 450 K. These computed findings show that MCOFs are suitable adsorbent for reversible H₂ adsorption.

Keywords - covalent organic framework, hydrogen molecule storage, Abinitio molecular dynamics, desorption temperature.

I. INTRODUCTION

Researchers are working to find an accessible, sustainable and environmentally friendly energy source due to the harmful effects of traditional energy sources like fossil fuels on the environment. In recent days, hydrogen

energy is becoming more important because of its pollution free nature. Hydrogen is stored in three phases: as gas, liquid, and solid. In gas and liquid phase storage, the process is expensive and requires high energy to compress and cool the hydrogen [1,2]. So, researchers are trying to store the hydrogen on solid adsorbents called hydrogen storage material (HSM). In this method, hydrogen is stored either as H₂ molecule or as hydride. Hydrides are formed when hydrogen atoms are chemically bonded with adsorbent material, while H₂ molecule is adsorbed via weak van der Waals interactions or hydrogen bonds [2]. To connect this, the U. S. Department of energy (US-DE) has recommended the target for effective adsorbents is that they should exhibit a minimum of 6.5 % H₂ molecule uptake (in weight percentage, wt%) and have average adsorption energy between -0.2 and -0.6 eV [3].

Recently, numerous carbon based materials such as carbon nitride [4], fullerene [5], graphene [6] and covalent organic framework (COF) [3] have been explored for reversible hydrogen storage. Among these adsorbents, COFs are suitable because they are lightweight, affordable and have a large surface area for H₂ adsorption. However, previous studies show that the pure carbon based materials have lesser H₂ adsorption property [3,7]. Therefore, researchers are studying several COFs to enhance their hydrogen adsorption property by modifying their structure, and adding transition metals by either doping or decoration. By modifying the size, shape, and



functionality of the organic linkers, it is possible to control the pore size, surface area and distribution of binding sites, all of which play important roles in hydrogen storage application.

Reference [8] investigated Pd-decorated tetra (di-hydroxyboryl-phenyl) methane-based COFs (TDM-COFs) for hydrogen storage applications. They confirmed Pd decoration through energy dispersive X-ray (EDX) spectra and TEM analysis and measured the hydrogen storage capacity of the Pd-decorated TDM-COFs using the Sievert's apparatus. Their results showed H₂ storage capacity of 0.38 and 0.42 wt% for 3.5 and 9.5 wt% Pd decoration, respectively.

Recently, holey graphene with Sc and Y were studied by V. Mahamiya et al. and M. Singh et al. respectively for hydrogen adsorption application and they found that the H₂ molecule adsorption capacity of Sc decorated holey graphene and Y decorated holey graphene is 9.80 and 9.34 % with average H₂ adsorption energy of -0.36 and -0.34 eV [6,9]. B. Chakraborty et al. studied the H₂ molecule adsorption ability of Sc metal atom decorated triazine-graphitic carbon nitride (T-gCN) and reported that each Sc atom of Sc decorated T-gCN adsorbs 7 H₂ molecules, resulting in H₂ storage capacity of 8.55 % [10]. Further, the hydrogen storage properties of Y atom decorated T-gCN were studied by [4] and they found that each Y atom of Y decorated T-gCN adsorbs 9 H₂ molecules, showing H₂ storage capacity of 8.55 %. Furthermore, [5,9] studied the Sc decorated C₂₄ fullerene and Y decorated C₂₄ fullerene for H₂ storage and reported that each metal atom (Sc and Y) of metal decorated C₂₄ fullerene adsorbs 6 H₂ molecules with H₂ storage capacity of 13.02 % for Sc decorated C₂₄ fullerene and 8.84 % for Y decorated C₂₄ fullerene. These studies show that the Sc and Y decorated adsorbents show higher hydrogen storage capacity than the isolated carbon frameworks.

Recently, [11] recently synthesized a Co atom decorated COF (CoCOF) using the poly-condensation reaction method and confirmed the metal decoration through XPS and TEM analysis. They also reported that the CoCOF showed excellent catalytic performance for the oxygen evolution reaction (OER). Therefore, in the present work we have studied the Sc and Y atom decorated quinoxaline and benzene connected COFs as adsorbent for hydrogen storage. The hydrogen storage ability of metal atom decorated COFs is studied by adsorption

energy, interaction distance, Bader charge analysis, density of states, H₂ molecule storage capacity and desorption temperature. The calculated results from the present study show that the studied metal (Sc and Y) atom decorated COFs are suitable for hydrogen storage application.

II. COMPUTATIONAL DETAILS

Electronic structure calculations were carried out to study the H₂ adsorption property of pristine COF and transition metal decorated COFs by using the Vienna ab initio simulation package (VASP) with projector augmented wave (PAW) method [12]. Generalized gradient approximation is used with Perdew Burke Ernzerh exchange correlation functional [13]. Furthermore, Grimme's DFT-D3 correction is applied to account the van der Waals long range interaction [14]. The cutoff energy of plane waves and convergence criterion for the total energy were set to 400 and 10⁻⁵ eV, respectively throughout the electronic structure calculations. The 1 X 1 X 1 centered k-point sampling of Brillouin zone is used. The adsorption energy (E_{ads}) of H₂ molecule on the studied covalent organic frameworks (COFs, isolated COF and metal atom decorated COFs) was computed by the equation [15]:

$$E_{ads} = \frac{E_{nH_2+COF} - (nE_{H_2} + E_{COF})}{n}, \quad (1)$$

where, n represents the total amount of adsorbed H₂ molecules on the COF. E_{nH_2+COF} , E_{COF} and E_{H_2} are the energy of COF with nH_2 molecules, isolated COF and isolated H₂ molecule, respectively. The interaction between metal atom (Sc and Y) and COF was analyzed at four various positions (S1-S4). The binding energy (E_{BE}) of metal atom on COF was computed by given below equation:

$$E_{BE} = \frac{(mE_M + E_{COF}) - E_{MCOF}}{m}, \quad (2)$$

where, m represents number of metal atom bonded on COF and E_{MCOF} and E_M are energy of metal atom decorated COF and isolated metal atom (Sc and Y), respectively. To explore the interaction between metal (Sc and Y) atom and COF, the density of states, charge density difference plot and Bader charge analysis (BCA)

were analyzed. The H₂ molecule storage capacity (H_{sc}) has been computed by using below formula:

$$H_{SC} = \frac{nM_{H_2}}{M_{MCOF} + nM_{H_2}} \times 100, \quad (3)$$

where, M_{H_2} and M_{MCOF} are the mass of H₂ molecule and MCOF, respectively.

To study the H₂ desorption, the Van't Hoff desorption temperature (T_D) of H₂ molecules was computed by the equation:

$$T_D = \frac{E_{ads}}{K_B} \left(\frac{\Delta S}{R} - \ln p \right), \quad (4)$$

where, R , K_B , ΔS and p represent the gas constant, Boltzmann's constant, change in entropy for H₂ molecule change from gas phase to liquid phase and equilibrium pressure, respectively.

III. RESULTS AND DISCUSSION

A. Geometry of the Pure COF and H₂ molecule Adsorption on the COF

Ground state geometry of 2D COF is shown in the Fig. 1 (Brown, gyan and white color spheres represent C, N and H atoms, respectively). It is noticed that the quinoxaline ligands are connected to benzene ligands through the nitrogen (N) atoms, resulting in a planar geometry with pore diameter of 14.4 Å which is consistent with experimentally assessed pore size (14.5 Å) [16].

The H₂ adsorption on COF is studied by optimizing the H₂ molecules with COF. The optimized ground state geometry of COF with H₂ molecule is shown in Fig. 2. It is also observed that the average interatomic distance of adsorbed H₂ molecules (l) is 0.752 Å. The distance between H₂ molecules and COF (d) is around 3.78 Å which is higher than the interaction distance reported in previous studies [3]. By using Eq. (1), the adsorption energy of H₂ molecule on COF (E_{ads}) is calculated to be -0.16 eV/H₂ and is below the suitable H₂ molecule adsorption energy of US-DE. The calculated d and E_{ads} indicate that the pristine COF is not reliable for H₂ physisorption.

B. Interaction of Metal Atoms and COF

Based on ground state geometry of isolated COF, metal (Sc and Y) atom was bonded on various positions of COF, as S1-S4 (see Fig. 1) to find the suitable binding position. As depicted in the Fig. 1, the interaction between metal atom (Sc and Y) and the COF at four various positions, above the benzene of quinoxaline (S1), above the pyrazine like ring (S2), above the benzene (S3) and inside the pore of COF, that is nearer to nitrogen atoms (S4) were analyzed. Based on the obtained ground state geometry, the binding energy (E_{ads} in eV) per metal atom on COF was computed at S1-S4 sites (Eq. 3) and are given in Table I.

TABLE I. THE COMPUTED BINDING ENERGY (E_{BE} , IN EV) OF METAL ATOM AT DIFFERENT SITES (S1-S4) OF ScCOF AND YCOF.

Position	E_{BE}	
	ScCOF	YCOF
S1	4.90	5.06
S2	3.96	4.05
S3	3.08	3.23
S4	4.96	5.18

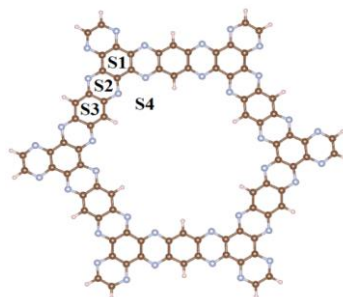


Figure 1. Optimized geometry of COF.

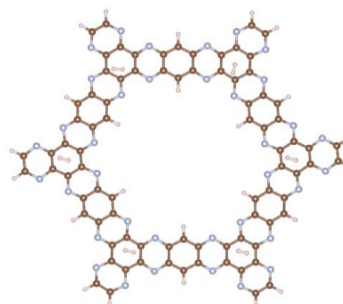


Figure 2. Optimized geometry of COF with H₂ molecules.

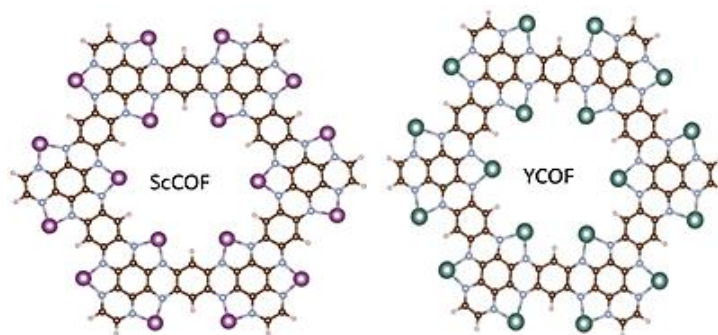


Figure 3. Ground state geometry of metal atoms bonded COFs. Green and violet spheres represent Y and Sc respectively.

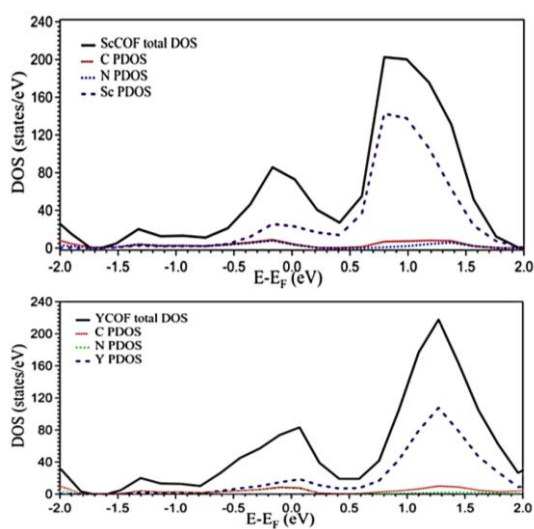


Figure 4. DOS of studied ScCOF and YCOF. The E_f of ScCOF and YCOF is -3.45 and -1.56 eV, respectively.

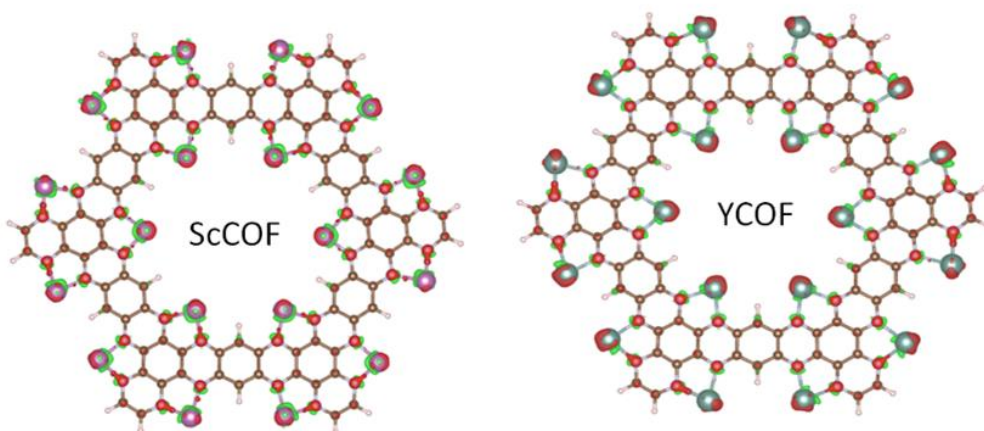


Figure 5. The charge density difference plot of MCOFs. The iso-surface value is set to 0.01 a. u.

From the tabulated E_{BE} values, it has been evident that the metal atoms, Sc and Y prefer to bond at $S4$ site with the E_{BE} of around 5 eV per metal atom. In total, the 18 metal atoms are effectively bonded at $S4$ sites of the COF and the geometry of 18 metal atoms (Sc / Y) bonded COFs (MCOFs) was optimized and is depicted in the Fig. 3, the MCOFs remain planar and the metal atoms (Sc and Y) were bonded with N atoms of COF with a average distance of 2.05 Å. In MCOFs, the C-N bond lengths are elongated by around 0.04 Å when the metal atom is decorated. The E_{BE} of 4.3 eV per Sc atom and 4.4 eV per Y atom was calculated which is more than the previously reported E_{BE} for Sc atom decoration on paracyclophane (1.43 eV) and Y atom decoration on paracyclophane (1.66 eV) [17]. The density of states (DOS) and partial DOS (PDOS) of MCOFs are depicted in the Fig. 4. It is evident that the Sc and Y metals are substantially contributing to the conduction band region of MCOFs and the absence of band-gap in MCOFs which shows the metallic property of MCOFs. To assess the charge exchange between metal atoms and COF, the Bader charge analysis and charge density difference (CDD) plot were analyzed.

From Bader charge analysis, it is evident that each metal atom of MCOFs gain ~ 1.10 Coulomb of charge from the isolated COF. The CDD plot of MCOFs is depicted in the Fig. 5. Here, it is also found that the charge gain (green region) and charge loss (red region) are in the vicinity of bonded metal atoms and N atoms present in MCOFs, respectively.

C. Adsorption of H_2 Molecules on Metal Atoms Bonded COF

Adsorption of H_2 molecules on MCOFs was analyzed by optimizing MCOFs with distinct number of H_2 molecules. The neutral geometry of 2, 4, 6 and 8 H_2 molecules adsorbed on each metal atom of MCOFs (MCOFs+n H_2 , when n= 36, 72, 108 and 144) is optimized. The average distance between MCOFs and H_2 molecules in ScCOF+36 H_2 and YCOF+36 H_2 is ~ 2.05 and 2.33 Å, respectively. The average H_2 adsorption energy per H_2 molecule calculated from Eq. (1) is -0.54 and -0.52 eV for ScCOF+36 H_2 and YCOF+36 H_2 , respectively. The calculated average distance between MCOFs and adsorbed H_2 molecule, interatomic distance (l) of H_2 molecule and adsorption energy per H_2 molecule are listed in the Table II. As given in the Table II,

for all the cases, the calculated E_{ads} falls within the H_2 adsorption energy range of -0.2 to -0.6 eV, recommended by US-DE which show the H_2 adsorption feasibility of MCOFs. When 8 H_2 molecules are adsorbed on each metal atom of ScCOF and YCOF, the metal atoms move away from planar geometry and the calculated interaction distance (d) between H_2 molecules and metal atoms is higher than 3 Å. The above findings indicate that the Sc and Y atom bonded COF can successfully adsorb 6 H_2 molecules per metal atom.

That is, a maximum of 108 H_2 molecules can be adsorbed on the studied MCOFs. In MCOFs+n H_2 , the interatomic distance (l) of H_2 molecule is increased by around 0.1, 0.05 and 0.01 Å for n=36, 72 and 108 from the optimum distance of 0.74 Å which indicates that H_2 molecules are adsorbed on studied MCOFs in their molecular form.

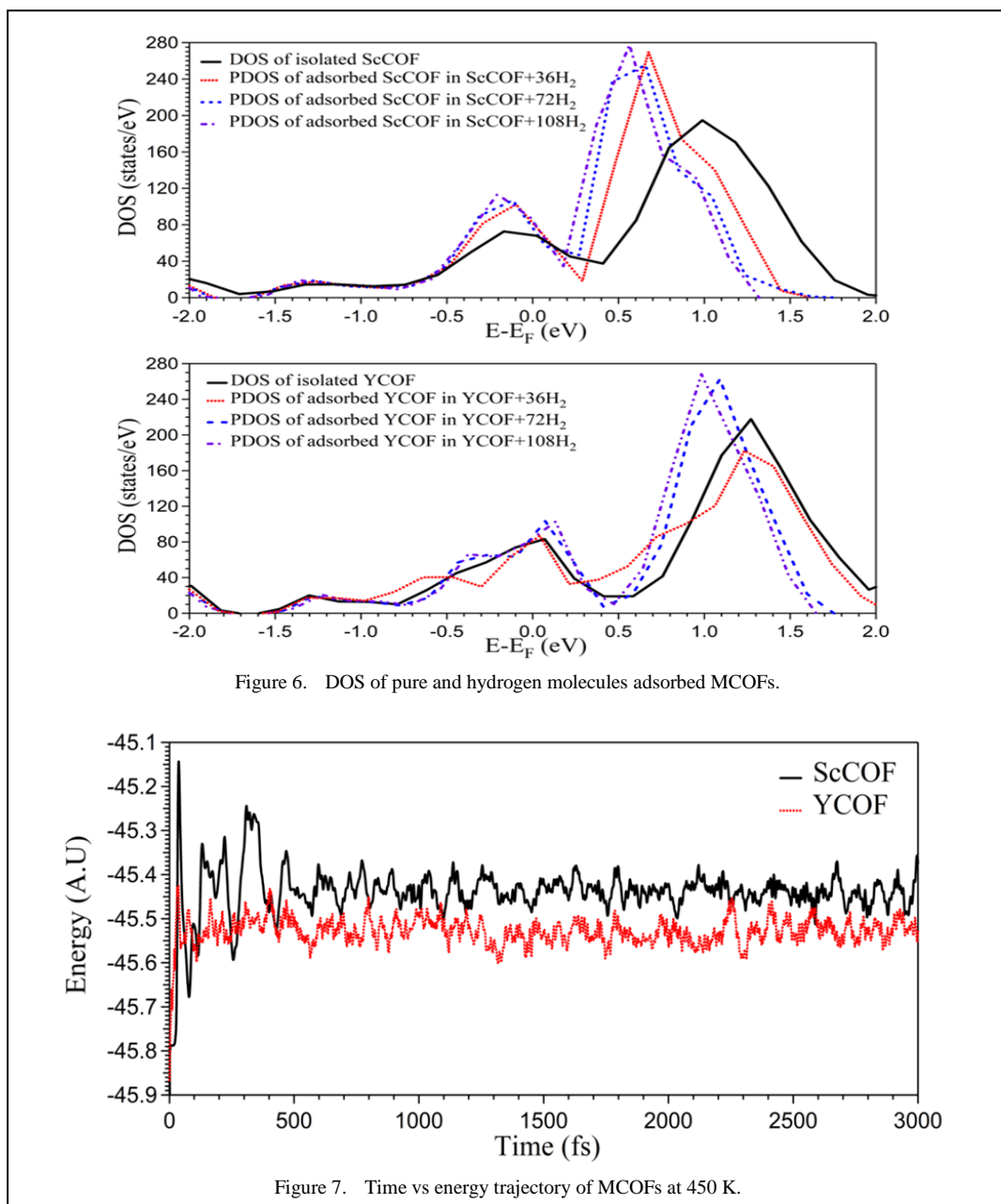
To understand the interaction between MCOFs and H_2 molecules, the DOS and Bader charge analysis were investigated. Fig. 6 shows the DOS of MCOFs before and after H_2 molecule adsorption. It is explained that the adsorption of H_2 molecules increases the DOS of MCOFs indicating the charge transfer from the H_2 molecules to MCOFs. Bader charge analysis

TABLE II. DISTANCE BETWEEN THE H_2 MOLECULE AND METAL (SC / Y) ATOM (d), AVERAGE INTERATOMIC DISTANCE OF H_2 MOLECULE (l), AVERAGE H_2 ADSORPTION ENERGY (E_{ads}) OF MCOFs WITH VARIOUS AMOUNT OF H_2 MOLECULES.

MCOF+n H_2		d (Å)	l (H-H) (Å)	E_{ads} (eV)
36 H_2	ScCOF	2.05	0.89	-0.54
	YCOF	2.33	0.85	-0.54
72 H_2	ScCOF	2.10	0.80	-0.48
	YCOF	2.34	0.80	-0.48
108 H_2	ScCOF	2.16	0.75	-0.36
	YCOF	2.35	0.78	-0.35
144 H_2	ScCOF	3.30	0.74	-0.31
	YCOF	3.31	0.75	-0.32

shows that ScCOF accepts 0.38, 0.20, and 0.13 Coulomb / H₂ of charge and YCOF accepts 0.192, 0.190, and 0.16 Coulomb / H₂ of charge from 36, 72 and 108 H₂ molecules, respectively. For reliable H₂ molecule storage, the HSM should have the desired H₂ molecule storage capacity (H_{sc} , in wt%), as suggested by US-DE. The H_{sc} of ScCOF and YCOF is 8.4 and 6.5 wt % which is sufficient to meet the target H_{sc} reported by US-DE [18]. By using Eq. (4), the

computed Van't Hoff desorption temperature is 436 and 447 K which falls in the desired span for H₂ physisorption [3]. In order to assess thermal stability of studied MCOFs, Abinitio molecular dynamics (AIMD) simulation was conducted in canonical ensemble at constant temperature and pressure (450 K and 1 atm). The AIMD simulation was conducted up to 3 pico second with 1 femto second time step. By analyzing the variation in structure and energy of the studied MCOFs, it is observed that the maximum



variation in bond distances of MCOFs is around 0.2 Å throughout the AIMD simulation period. As depicted in the Fig. 7, the energy variation of ScCOF and YCOF is negligible. The obtained AIMD simulation studies confirm the stability of Sc bonded COF and Y bonded COF at temperature of 450 K.







IV. CONCLUSIONS

In this study, the H₂ adsorption abilities of Sc and Y metal atom decorated quinoxaline and benzene connected covalent organic framework (MCOF) were studied using the density functional theory calculations. The 18 metal (Sc / Y) atoms were effectively bonded on COF with average binding energy of approximately 4.3 eV per Sc metal atom and 4.5 eV per Y metal atom. Each metal atom of MCOFs adsorbs six H₂ molecules with average H₂ adsorption energy of approximately -0.35 eV, resulting a H₂ storage capacity of 8.43 and 6.5 weight percentage for ScCOF and YCOF, respectively. The computed H₂ molecule storage capacity of MCOFs meets the require H₂ molecule storage capacity, reported by US-DE for H₂ molecule storage application. The DOS and Bader charge analysis results show the electronic interaction between H₂ molecules and MCOFs by transferring charge from H₂ molecules to MCOFs. The Van't Hoff desorption temperature of H₂ molecules present in ScCOF and YCOF is computed to be 436 and 447 K. The Abinitio molecular dynamic simulation study confirms stability of metal atom bonded COF at temperature of 450 K. These findings show that Sc and Y metal atom decorated quinoxaline and benzene-based COFs are suitable adsorbents for H₂ physisorption.

REFERENCES

- [1] Yang, J., Sudik, A., Wolverton, C., & Siegel, D. J. (2010). High capacity hydrogen storage materials: attributes for automotive applications and techniques for materials discovery. *Chemical Society Reviews*, 39(2), 656-675.
- [2] Bosu, S., & Rajamohan, N. (2024). Recent advancements in hydrogen storage-Comparative review on methods, operating conditions and challenges. *International Journal of Hydrogen Energy*, 52, 352-370.
- [3] Vasanthakannan, V. M., & Senthilkumar, K. (2024). Hydrogen storage property of the Sc decorated azatriphenylene based covalent organic framework. *Journal of Power Sources*, 604, 234505.
- [4] Mane, P., Vaidyanathan, A., & Chakraborty, B. (2022). Graphitic carbon nitride (g-C₃N₄) decorated with Yttrium as potential hydrogen storage material: Acumen from quantum simulations. *International Journal of Hydrogen Energy*, 47(99), 41898-41910.
- [5] Mahamiya, V., Shukla, A., Garg, N., & Chakraborty, B. (2022). High-capacity reversible hydrogen storage in scandium decorated holey graphyne: theoretical perspectives. *International Journal of Hydrogen Energy*, 47(12), 7870-7883.
- [6] Singh, M., Shukla, A., & Chakraborty, B. (2022). An Ab-initio study of the Y decorated 2D holey graphyne for hydrogen storage application. *Nanotechnology*, 33(40), 405406.
- [7] Shangguan, W., Zhao, H., Dai, J. Q., Cai, J., & Yan, C. (2021). First-principles study of hydrogen storage of Sc-modified semiconductor covalent organic framework-1. *ACS omega*, 6(34), 21985-21993.
- [8] Kalidindi, S. B., et al. (2012). Metal@ COFs: covalent organic frameworks as templates for Pd nanoparticles and hydrogen storage properties of Pd@ COF-102 hybrid material. *Chemistry—A European Journal*, 18(35), 10848-10856.
- [9] Mahamiya, V., Shukla, A., & Chakraborty, B. (2022). Exploring yttrium doped C24 fullerene as a high-capacity reversible hydrogen storage material: DFT investigations. *Journal of Alloys and Compounds*, 897, 162797.
- [10] Chakraborty, B., Mane, P., & Vaidyanathan, A. (2022). Hydrogen storage in scandium decorated triazine based g-C₃N₄: insights from DFT simulations. *International Journal of Hydrogen Energy*, 47(99), 41878-41890.
- [11] Yang, H., et al. (2022). Intramolecular hydroxyl nucleophilic attack pathway by a polymeric water oxidation catalyst with single cobalt sites. *Nature Catalysis*, 5(5), 414-429.
- [12] Blochl, P. E. (1994). Projector augmented-wave method. *Physical Review-Section B-Condensed Matter*, 50(24), 17953-17979.
- [13] Perdew, J. P., Burke, K., & Ernzerhof, M. (1996). Generalized gradient approximation made simple. *Physical review letters*, 77(18), 3865.
- [14] Grimme, S., Antony, J., Ehrlich, S., & Krieg, H. (2010). A consistent and accurate ab initio parametrization of density functional dispersion correction (DFT-D) for the 94 elements H-Pu. *The Journal of chemical physics*, 132(15).
- [15] Gao, P., Liu, Z., & Zhang, F. (2022). Computational evaluation of Li-doped g-C₂N monolayer as advanced hydrogen storage media. *International Journal of Hydrogen Energy*, 47(6), 3625-3632.
- [16] Wang, L., et al. (2017). Photocatalytic oxygen evolution from low-bandgap conjugated microporous polymer nanosheets: a combined first-principles calculation and experimental study. *Nanoscale*, 9(12), 4090-4096.
- [17] Sahoo, R. K., Kour, P., & Sahu, S. (2022). Reversible hydrogen storage capacity of Sc and Y functionalized [1, 1] paracyclophane: Insights from density functional study. *International Journal of Hydrogen Energy*, 47(69), 29881-29895.
- [18] Hu, S., Yong, Y., Zhao, Z., Gao, R., Zhou, Q., & Kuang, Y. (2021). C7N6 monolayer as high capacity and reversible hydrogen storage media: A DFT study. *International Journal of Hydrogen Energy*, 46(42), 21994-22003.

Valorizing the Invasive Macrophyte *Eichhornia crassipes* as a Potential Bioenergy Feedstock: Preliminary Assessment from Thermochemical Characterization

Maxwell de Arandas Pimentel¹, Fernando Mateus de Oliveira Santos²,
Gabriela Aurora Alexandre de Vasconcellos³, Jhonatas Wagner Barbosa de Costa Gouveia⁴,
José Luiz Francisco Alves⁵, Silvia Layara Floriani Andersen⁶

^{1,2,3,4,5,6}Federal University of Paraíba, Laboratory of Materials and Environmental Chemistry, João Pessoa – PB, Brazil

¹maxwell.pimentel@estudante.cear.ufpb.br, ⁶silvia@cear.ufpb.br

Abstract—The explosion in demand for energy resources since the Industrial Revolution has led us to seek more renewable energy sources. Although the evolution of renewable energies in the energy matrix represents significant advances, non-renewable energies are still more predominant. Biomass, particularly water hyacinth (*Eichhornia crassipes*), offers an alternative from the Amazon Basin. This aquatic plant grows at an astonishing rate, but its overabundance can cause disturbances in the ecological balance. Knowledge about the fundamental physicochemical characteristics of water hyacinth is essential for its potential as a renewable biomass towards relevant management strategies in line with the UN Sustainable Development Goals (SDGs), as provided in this work. With a volatile matter content of 67 wt.%, 37.5 wt.% carbon, a calorific value of 17.2 MJ/kg, and low sulfur content, water hyacinth shows potential as a raw material for thermochemical biomass conversion processes into value-added products. Experiments were conducted using a thermogravimetric analyzer in an inert atmosphere at four heating rates (5, 10, 20, and 30 °C.min⁻¹) to obtain the pyrolysis behavior of water hyacinth. The thermal degradation showed three stages of mass loss: (1) less than 7.1 ± 1.1 wt.% from 50 to 200 °C due to water evaporation and organic decomposition; (2) 48.1 ± 1.5 wt.% from 200 to 400 °C due to the decomposition of

hemicellulose, cellulose, and lignin; and (3) 12.3 ± 0.6 wt.% above 400 °C, mainly due to lignin decomposition and biochar formation.

Keywords - biomass, water hyacinth, bioenergy, bioproducts

I. INTRODUCTION

This increasing demand due to technological development and population growth over the years has caused severe environmental impacts by aggravating climate change. To overcome these challenges, renewable energy sources are well-known solutions to reduce Greenhouse Gases and mitigate environmental destruction [1-3].

The significant growth of renewable energy - still a relatively small part of total used fossil fuel as energy sources in many developing nations across the globe for recent few decades in most developed countries on up started - In this context, it is worth noting the significant shift that will be needed to finance technologies using renewable energy (solar radiation, biomass, geothermal, wind) that play an important role in decarbonization and sustainable development [4].

It is biomass one of the most important sustainable resources and it has a relevant impact



on carbon neutrality as an efficient conversion process. It also decreases greenhouse gas emissions and promotes environmental sustainability through the utilization of renewable energy sources and the recycling of organic waste [5].

Aquatic phytoresources have been widely explored for bioenergy via a number of promising conversion methods like pyrolysis, gasification, liquefaction, fermentation or anaerobic digestion and enzymatic hydrolysis. At least 60% of the conversion from macrophytes. However, these processes should be developed in a cost-effective manner [6-8].

Biomass is essentially organic material produced from plants, animals and microorganisms that is created either directly or indirectly via living organisms. Biomass stores solar energy as chemical energy through photosynthesis, making it one of the most potent sources available for fulfilling global energy demands. Biomass is a bioenergy stored as energy in form of heat and gas for future use through combustion or repeated vegetation process, being usable in heat, electricity, cooking gas and transportation fuels as well. Mostly made of carbon, hydrogen, oxygen and nitrogen it also has traces of chlorine and sulfur [9,10].

One of biomass raw materials that can be renewed is Water hyacinth (*Eichhornia crassipes*). Indigenous to Brazil, in the Amazon Basin. As it is beautiful, the plant was disseminated as an ornamental across various regions of the globe since 1850s. By the late 1960s, there was proof that water hyacinth had already established internationally through tropical and subtropical ecosystems [11].

The water hyacinth is a floating aquatic plant with flexible stems, erect leaves, lilac flowers, and submerged roots, recognized for its effective nutrient absorption from water. Recognized as an invasive aquatic species, water hyacinth demonstrates an exceptionally high growth rate, with the potential to reach $220 \text{ kg ha}^{-1} \text{ d}^{-1}$. The uncontrolled spread in freshwater ecosystems disturbs the ecological balance by reducing oxygen content and solar radiation access. Such situations are not appropriate for the native fauna and leads to problems like bad water quality for the fish, hindered waterways, challenges in extracting any water and higher chances of disease transmission [5,10-14].

However, this is the reason why the uncontrolled expansion of water hyacinth causes environmental problems. However, other research related to these plants indicates some advantageous characteristics that attract interest, provided they are applied under correct control. Water hyacinth can be used in phytoremediation and contribute to the treatment of wastewater. In addition, water hyacinth and its bioproducts have the potential to be used as adsorbents for the treatment of textile effluents and phosphate removal. It is also considered an attractive raw material for biofuels [15].

The literature reports various studies on the conversion of water hyacinth into valuable products through pyrolysis, including energetic biochar, bio-oil, and non-condensable gases, each with several energy and material applications. The pyrolytic gases, such as H_2 , CO , CH_4 , and C_2H_2 , can be reformed to generate syngas with energy properties. The bio-oil, which contains a variety of compounds such as carboxylic acids, alcohols, esters, furans, phenols, aldehydes, and ketones, can be used in the production of liquid biofuels, contributing to the renewable energy matrix. On the other hand, the biochar, rich in carbon, has a wide range of applications, including soil remediation, functioning as a catalyst, serving as a precursor in the production of activated carbon, and being used as an adsorbent [11,14-16].

The objective of this work is to characterize water hyacinth (*Eichhornia crassipes*) and investigate its potential as a source of renewable biomass, focusing on its application as a raw material for energy bioproducts. Through a detailed analysis of its physicochemical properties and the behavior of mass loss under pyrolysis conditions, this study aims to highlight the potential of water hyacinth to sustainably contribute to the energy matrix while also helping to mitigate the environmental impacts arising from its uncontrolled growth.

Several Sustainable Development Goals (SDGs) are upheld by this initiative, such as SDG 7, which focuses on clean and affordable energy; SDG 12, which promotes the responsible utilization of renewable resources like biomass; SDG 13, which emphasizes climate action and the adoption of low-carbon technologies; and SDG 15, which addresses the management of invasive species, including water hyacinth, as well as the preservation of terrestrial ecosystems.

II. MATERIALS AND METHODS

A. Collection and Preparation

Water hyacinth biomass was collected in January 2024 from the Canhoto River in Canhotinho, Pernambuco, Brazil, where aquatic vegetation indicated eutrophication and the presence of invasive macrophytes. After collection, only the stems and leaves were retained, with roots discarded. The biomass underwent pre-drying outdoors for eight days at approximately 25 °C, followed by drying in a forced-air oven at 105 °C for 3 hours. It was then processed in a knife mill and manually sieved to achieve uniform particles smaller than 0.149 mm.

B. Physicochemical Characterization

The proximate analysis is a set of tests designed to quantify the contents of moisture (M), volatile matter (VM), ash (A), and fixed carbon (FC).

The moisture content was determined using the oven-drying method, in accordance with the ASTM E1756-08 [17]. An air-circulating oven, model MA035, at 105 °C, was used.

The Volatile Matter (VM) content was determined according to the ASTM E872-82R18 [18], while the Ash (Z) content was evaluated in accordance with the ASTM E1755-01R20 [19].

The elemental composition of the water hyacinth sample, including the mass percentages of carbon (C), hydrogen (H), nitrogen (N), and sulfur (S), was determined using an elemental analyzer model CE 1108 (Carlo Erba Instruments, Wigan, UK), following the standard procedures outlined in ASTM D3176-15 (ASTM, 2015). As shown in Eq. (1), the oxygen mass percentage was calculated by difference [8]:

$$O(\%) = 100 - C - H - N - S - Z. \quad (1)$$

To determine the higher heating value (HHV) of the biomass, an IKA C200 calorimeter was used, following the ASTM D5865M-19 [20]. The lower heating value (LHV) can be calculated from the value obtained for the HHV and the mass content of hydrogen, using Eq. (2) [21].

$$LHV(MJ/kg) = HHV - 0.2183 \times H. \quad (2)$$

The bulk density (BD), also known as bulk specific weight, of water hyacinth was determined following the ASTM E873-82 [22].

Thermogravimetric analyses were conducted using the SDT650 thermogravimetric analyzer (TA Instruments). The experiments were carried out under an inert nitrogen (N₂) atmosphere with 99.99% purity, at a constant flow rate of 100 mL.min⁻¹ and with a sample mass of approximately 10 mg. The temperature range used for the analyses varied from ambient temperature to 1000 °C, with heating rates of 5, 10, 20, and 30 °C.min⁻¹.

III. RESULTS AND DISCUSSION

A. Physicalchemical Characterizations

Table I highlights the physicochemical properties of water hyacinth.

When comparing the values of volatile matter and fixed carbon from Table I with the results presented by [5] for the same species, a notable similarity emerges. The authors reported a higher volatile matter content of 70.5 wt.%, along with a lower fixed carbon content of 13.7 wt.%.

According to [8], the significant result for the volatile matter in this biomass suggests that the pyrolysis process of water hyacinth can yield a high amount of condensable gases (bio-oil) and non-condensable gases.

TABLE I. PHYSICOCHEMICAL CHARACTERIZATION OF WATER HYACINTH.

Sample: Water Hyacinth (<i>Eichhornia crassipes</i>)	
Properties	Values
<i>Proximate Analysis</i>	
	Mass percentage (%)
Moisture ^a (M)	16.5
Ash ^b (Z)	18.9 ± 0.2
Volatile Matter ^b (VM)	67.0 ± 0.4
Fixed Carbon ^b (FC)	14.1 ± 0.2
<i>Elemental Analysis</i>	
	Mass percentage (%)
Carbon ^b (C)	37.5
Hydrogen ^b (H)	3.2
Nitrogen ^b (N)	4.9
Sulfur ^b (S)	0.3
Oxygen ^b (O)	35.2
<i>Heating value</i>	
	(MJ.kg ⁻¹)
Higher heating value (HHV)	17.2 ± 0.1
Lower heating value (LHV)	16.1
<i>Bulk density (BD)</i>	
	(kg.m ³)
	145.3 ± 4.9

Legend: (a) Air dried basis; (b) dry basis.

In the proximate analysis, [23] found a moisture content of 13.6 wt.%, a value close to the 16.5 wt.% obtained in this study. Regarding ash content, the cited study reported 15.1 wt.% while this work found 18.9 wt.%, indicating a good agreement between the data.

The proximate analysis of sugarcane bagasse conducted by [24] revealed a volatile matter content of 76.5 wt.% and fixed carbon content of 16.8 wt.%, results comparable to those observed in studies on water hyacinth.

Another biomass that exhibits values similar to those found in the analysis of water hyacinth is the wood from the species *Ficus nitida*, which has a fixed carbon content of approximately 16.9 wt.%, volatile matter of 68.8 wt.%, and ash content of 14.4 wt.%, as reported by [25]. Additionally, rice straw, according to the analysis by [26], also shows comparable results, with 65.2 wt.% volatile matter, 16.6 wt.% fixed carbon, and 12.6 wt.% ash. Several researchers emphasize that biomass with high volatile matter content and low ash content is particularly suitable for the pyrolytic conversion process [27,28].

The elemental analysis of water hyacinth showed carbon as the main component, with 37.5 wt.% by, followed by oxygen (39.8 wt.%), nitrogen (4.5 wt.%), hydrogen (3.2 wt.%), and sulfur (0.3 wt.%). The levels of carbon, oxygen, and hydrogen are comparable to other lignocellulosic biomasses used for energy purposes. However, the nitrogen content is higher than that found in other biomasses, which range from 0.14 wt.% to 1.8 wt.% [29,30] potentially requiring additional methods to treat NO_x emissions during the thermochemical process. The low sulfur content indicates great potential for clean bioenergy production, without the need for extra treatment for sulfur oxides [30]. Thus, the elemental composition of water hyacinth reinforces its potential as a sustainable alternative for bioenergy production.

When comparing the ash content of water hyacinth, which is 18.9 wt.%, with other lignocellulosic biomasses, as shown in studies by [31], it is noted that this value is similar to or lower than several analyzed residues, such as eucalyptus bark (19.0 wt.%), mint stems (18.2 wt.%), moringa oleifera leaves (21.5 wt.%), and bamboo cane residues (39.6 wt.%).

Ash, as an inorganic residue, increases transportation, handling, and processing costs,

TABLE II. COMPARATIVE RESULTS OF ELEMENTAL ANALYSIS OF WATER HYACINTH.

Sample: Water Hyacinth (<i>Eichhornia crassipes</i>)				
C(%)	H(%)	N(%)	O(%)	Reference
39.9	5.3	3.5	35.2	[32]
40.0	5.3	1.2	34.5	[33]
37.9	5.2	2.5	25.5	[34]
37.5	4.8	3.2	35.1	Authors

influencing dust emissions, ash management, and combustion technology selection. High ash content lowers the heating value, promotes slag formation, reduces heat transfer efficiency, and raises maintenance frequency and costs for equipment [31].

The results presented in Table I, related to the elemental analysis, are consistent with the values reported in the literature. This compatibility is also evident in Table II, which presents data from studies related to the elemental analysis of water hyacinth.

Some biomass types show similar chemical compositions to water hyacinth. For example, in the studies by [26] on rice straw, the following values were recorded for the commonly analyzed chemical elements: carbon (38.6 wt.%), hydrogen (4.2 wt.%), nitrogen (1.1 wt.%), and sulfur (0.6 wt.%).

When compared to other biomass sources, this property of water hyacinth stands out, making it an attractive option for use as a biofuel in potential applications in thermochemical processes. The higher heating value of water hyacinth, as identified in this study (17.2 MJ.kg⁻¹), is comparable to or even exceeds that of various biomass sources described by [31], such as lemon peel (17.2 MJ.kg⁻¹), rice husk (15.9 MJ.kg⁻¹), tomato waste (14.2 MJ.kg⁻¹), pomegranate peel (15.2 MJ.kg⁻¹), and eucalyptus bark (16.2 MJ.kg⁻¹).

Bulk density is a crucial factor for logistical planning in the handling and transportation of biomass, as higher values typically lead to lower storage and handling costs [16]. Water hyacinth, with a bulk density of 145.3 kg.m⁻³, is comparable to *Gmelina arborea* wood (151.5 kg.m⁻³) [35] and surpasses sugarcane bagasse (119.1 kg.m⁻³) [35] and rice husk (129.0 kg.m⁻³) [36]. The use of this biomass in the bioenergy sector can be optimized through pelleting or briquetting processes [37].

B. Thermogravimetric Analysis

Thermogravimetric analysis is crucial for evaluating biomass mass loss during pyrolysis.

Energy product yields vary with temperature: lower temperatures favor bio-oil and biochar production, while higher temperatures increase pyrolytic gas production. Identifying the optimal temperature range is key, as the diverse biomass composition, including cellulose, hemicellulose, lignin, and extractives, decomposes at different temperatures, influencing pyrolysis efficiency [14].

Fig. 1 shows the thermogravimetric curves (TG) of water hyacinth, depicting pyrolysis mass loss behavior as a function of temperature at heating rates of 5, 10, 20 and 30°C.min⁻¹.

Fig. 2 presents the corresponding first-order derivative of the mass loss curve (DTG) for each heating rate.

The pyrolysis behavior of water hyacinth indicates that an initial mass loss of less than 7,1 ± 1,1 wt.% occurs in the temperature range of 50 to 200°C. In the 50 to 150°C range, the mass loss is mainly due to the evaporation of adsorbed water and the release of hydration water from the cellular structures.

The mass loss observed between 150 and 200°C is due to the thermal decomposition of light organic extractives in water hyacinth.

Literature on the pyrolysis of invasive macrophytes provides support for this mass loss occurring in the temperature range of 50 to 200°C. [10,21].

The active pyrolysis zone, the average mass loss is 48.1 ± 1.5 wt.%, occurring between 200 and 400°C. This zone is characterized by the conversion of volatile matter into condensable vapors and non-condensable gases, resulting from the devolatilization of hemicellulose, cellulose, and part of the lignin. This zone exhibits the most significant mass loss. Passive pyrolysis, beginning at 400°C and characterized by an average mass loss of 12.3 ± 0.6 wt.%, is marked by the gradual decomposition of lignin and the subsequent formation of biochar [38].

Since the experiments for each heating rate were conducted in an inert atmosphere, Table III summarizes the most relevant weight losses as a percentage for the pyrolysis of water hyacinth.

The average total mass loss of water hyacinth across the three stages is 67.5 ± 1.2 wt.%. In invasive aquatic macrophytes, stages 1 and 2 are more closely related to the decomposition of carbohydrates, such as hemicellulose and cellulose. Stage 3, in turn, is predominantly associated with the decomposition of lipids and lignin [8]. The structural differences in lignocellulosic biomass determine its decomposition order. Hemicellulose, with an amorphous and random structure, degrades most easily. Cellulose, with a crystalline structure of

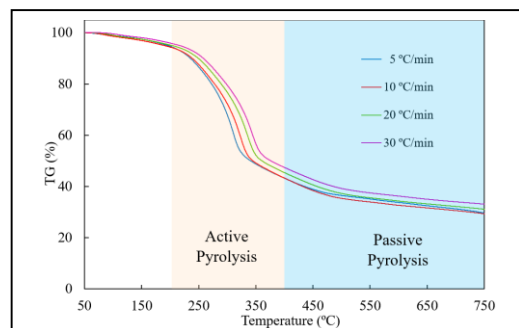


Figure 1. Thermogravimetric Curves (TG) of Water Hyacinth.

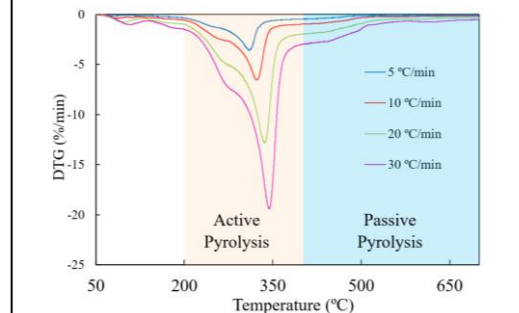


Figure 2. DTG Curves of Water Hyacinth.

TABLE III. THERMAL PYROLYSIS OF WATER HYACINTH: VARIATION OF MASS LOSS.

Sample: Water Hyacinth* (<i>Eichhornia crassipes</i>)				
Stage	Heating rate (°C.min ⁻¹)	T _i (°C)	T _f (°C)	Percent mass loss (%)
Stage 1	5	50	200	6.8
	10	50	200	8.5
	20	50	200	7.2
	30	50	200	5.8
Stage 2	5	200	400	50.3
	10	200	400	47.7
	20	200	400	47.3
	30	200	400	47.2
Stage 3	5	400	700	11.7
	10	400	700	11.9
	20	400	700	12.53
	30	400	700	13.03

Legend: (*) on a dry basis; ti: initial temperature; tf: final temperature.

glucose monomers, is more resistant. Lignin, a complex three-dimensional polymer, has the highest thermal stability [38].

In the temperature range of 200 to 350°C, the initial decomposition of light organic components, such as hemicelluloses and extractives, is observed, leading to a more pronounced reduction in mass. This trend aligns with the findings de [38]. Thermal decomposition of hemicellulose occurs between 201 and 325°C. Cellulose and part of the lignin decompose between 350 and 500°C, with cellulose mainly decomposing between 350 and 400°C, causing significant mass loss due to accelerated thermal degradation [39]. It is expected that lignin will continue to decompose over a wide temperature range, approximately from 180°C to 700°C [39]. Above 500°C, mass loss tends to slow down and stabilize, indicating the formation of carbonaceous compounds that are more resistant to thermal decomposition and the creation of pyrolytic charcoal [40]. The mass loss reduction indicates that most organic components have decomposed, and carbonaceous compounds are beginning to stabilize [33].

Devolatilization temperatures of the biomass were noted at 313°C, 324°C, 338°C, and 345°C for heating rates of 5, 10, 20, and 30°C/min, respectively. The pyrolysis solid product consists of fixed carbon and ash, with the residual mass of water hyacinth indicating the biochar yield, reflecting the proportion of fixed carbon and ash content [30]. As heating rates increased, DTG peaks shifted to higher temperatures, indicating more intense decomposition. The mass loss percentage varied with temperature, reflecting low heat transfer efficiency due to the biomass particle's thermal resistance. Volatile constituent release and their secondary reactions absorb heat in endothermic processes, hindering effective heat transfer to the particle core and reducing thermal degradation efficiency [10].

C. Challenges and Future Research

The main challenge with water hyacinth is developing effective control strategies, as methods like mechanical, chemical, and biological treatments are often costly and ineffective. However, the increasing value of its biomass has shifted focus toward sustainable use rather than eradication. A circular economy approach is needed to balance controlled reproduction for industrial applications while preventing environmental imbalances.

Harvesting methods should be tailored to local resources to ensure both economic and environmental sustainability, providing socio-economic benefits [41].

Interest is growing in optimizing biochar production from water hyacinth, primarily for use as fertilizer. Valorizing this invasive plant boosts local economies by creating jobs, supporting markets, and reframing it as a valuable resource. This approach also clears water bodies for activities like fishing, irrigation, and navigation. Biochar offers environmental benefits, including soil remediation, increased agricultural productivity, reduced dependence on mineral fertilizers, and mitigation of nitrate and phosphate pollution, gas emissions, and leaching [42,43].

Other challenges include high operational costs for industrial-scale processes, mainly due to water hyacinth's high moisture content and low material density, which require advanced drying and transportation. In addition, the plant's ability to absorb nutrients can make biochar more prone to heavy metal contamination, potentially compromising its safety for use [41].

Given the technical challenges, complementary techniques like TG-FTIR and Py-GC/MS are crucial for understanding biomass thermal degradation. TG-FTIR monitors mass loss and gas release, helping analyze degradation stages and optimize processes. Py-GC/MS detects specific volatile compounds like phenols and furans, offering molecular insights, despite its limitations with non-volatile compounds. Combining these methods enhances the understanding of biomass behavior, such as water hyacinth, and improves its conversion into bioenergy and value-added products [33].

IV. CONCLUSION

This study characterized water hyacinth by its moisture, ash, volatile matter, fixed carbon, and elemental composition. Its high volatile content makes it ideal for pyrolysis, enabling efficient biofuel conversion. Water hyacinth's superior calorific value surpasses other biomasses, emphasizing its potential for sustainable bioenergy production. Thermogravimetric analysis revealed its suitability for pyrolysis and transformation into bioproducts like biochar. Responsible reuse of water hyacinth not only supports the local economy but also mitigates the environmental impacts of its uncontrolled spread.

V. ACKNOWLEDGMENT

The authors would like to acknowledge National Council for Scientific and Technological Development - CNPq for financial support (Process: 407977/2023-6).

REFERENCES

- [1] Abi Bianasari, A., Khaled, M. S., Hoang, T. D., Reza, M. S., Bakar, M. S. A., & Azad, A. K. (2024). Influence of combined catalysts on the catalytic pyrolysis process of biomass: A systematic literature review. *Energy Conversion and Management*, 309, 118437.
- [2] Ahmad, W., Nisar, J., Anwar, F., & Muhammad, F. (2023). Future prospects of biomass waste as renewable source of energy in Pakistan: A mini review. *Bioresource Technology Reports*, 101658.
- [3] Chen, X., Zhang, H., Zhao, X. X., Gong, Q., & Chang, C. P. (2024). Do renewable energy investment and financial development mitigate climate change?. *Journal of Asian Economics*, 93, 101749.
- [4] Opoku, E. E. O., Acheampong, A. O., Dogah, K. E., & Koomson, I. (2024). Energy innovation investment and renewable energy in OECD countries. *Energy Strategy Reviews*, 54, 101462.
- [5] Mallick, D., et al. (2023). Mechanistic investigation of pyrolysis kinetics of water hyacinth for biofuel employing isoconversional method. *Sustainable Energy Technologies and Assessments*, 57, 103175.
- [6] Pal, D. B., et al. (2023). Sustainable valorization of water hyacinth waste pollutant via pyrolysis for advance microbial fuel investigation. *Chemosphere*, 314, 137602.
- [7] Ugya, A. Y., Okoh, O. O., Okoh, A. I., & Hossain, M. I. (2024). Aquatic phytoresources: An environmentally sustainable alternative biomaterial for bioenergy production. *Renewable and Sustainable Energy Reviews*, 205, 114877.
- [8] Alves, J. L. F., et al. (2019). Kinetics and thermodynamics parameters evaluation of pyrolysis of invasive aquatic macrophytes to determine their bioenergy potentials. *Biomass and Bioenergy*, 121, 28-40
- [9] Cai, J., Zhou, W., Zhu, X., Dong, Y., Zhao, S., & Tian, L. (2024). Research on the application of catalytic materials in biomass pyrolysis. *Journal of Analytical and Applied Pyrolysis*, 177, 106321.
- [10] Mishra, R. K., Singh, B., & Acharya, B. (2024). A comprehensive review on activated carbon from pyrolysis of lignocellulosic biomass: An application for energy and the environment. *Carbon Resources Conversion*, 7(4), 100228.
- [11] Djihouessi, M. B., Olokotum, M., Chabi, L. C., Mouftaou, F., & Aina, M. P. (2023). Paradigm shifts for sustainable management of water hyacinth in tropical ecosystems: A review and overview of current challenges. *Environmental Challenges*, 11, 100705.
- [12] Bronzato, G. R. F., Ziegler, S. M., Silva, R. C., Cesarino, I., & Leão, A. L. (2017). Characterization of the pre-treated biomass of *Eichhornia crassipes* (water hyacinth) for the second generation ethanol production. *Molecular Crystals and Liquid Crystals*, 655(1), 224-235.
- [13] Midhun, V. C., Jayaprasad, G., Anto, A., & Anish, R. (2023). Preparation and characterisation study of water hyacinth briquettes. *Materials Today: Proceedings*.
- [14] Pal, D. B., Singh, R. K., Gautam, S., Sharma, T., & Kundu, P. (2023). Sustainable valorization of water hyacinth waste pollutant via pyrolysis for advance microbial fuel investigation. *Chemosphere*, 314, 137602.
- [15] Allam, F., Elnouby, M., El-Khatib, K. M., El-Badan, D. E., & Sabry, S. A. (2020). Water hyacinth (*Eichhornia crassipes*) biochar as an alternative cathode electrocatalyst in an air-cathode single chamber microbial fuel cell. *International Journal of Hydrogen Energy*, 45(10), 5911-5927.
- [16] Rahman, M. A. (2018). Pyrolysis of water hyacinth in a fixed bed reactor: Parametric effects on product distribution, characterization and syngas evolutionary behavior. *Waste Management*, 80, 310-318.
- [17] ASTM E1756-08, *Standard Test Method for Determination of Total Solids in Biomass*. West Conshohocken, PA, 2015.
- [18] ASTM E872 - R18, *Standard Test Method for Volatile Matter in the Analysis of Particulate Wood Fuels*. West Conshohocken, PA, 2020.
- [19] ASTM E1755-01R20, *Standard Test Method for Ash in Biomass*. West Conshohocken, PA, 2020.
- [20] ASTM D5865M-19, *Standard Test Method for Gross Calorific Value of Coal and Coke*. West Conshohocken, PA, 2019.
- [21] Alves, J. L., et al. (2020). Lignocellulosic residues from the Brazilian juice processing industry as novel sustainable sources for bioenergy production: preliminary assessment using physicochemical characteristics. *Journal of the Brazilian Chemical Society*, 31, 1939-1948.
- [22] ASTM E873-82, *Standard Test Method for Bulk Density of Densified Particulate Biomass Fuels*. West Conshohocken, PA, 2019.
- [23] Liu, Z., Hu, Y., Wang, J., Meng, J., Zhang, Y., & Chen, R. (2023). Study on the combustion characteristics and kinetics of water hyacinth co-combustion with anthracite. *Chemical Engineering Research and Design*, 200, 637-645.
- [24] Ramirez, J. A., & Rainey, T. J. (2019). Comparative techno-economic analysis of biofuel production through gasification, thermal liquefaction, and pyrolysis of sugarcane bagasse. *Journal of Cleaner Production*, 229, 513-527.
- [25] Tabal, A., Barakat, A., Aboulkas, A., & El Harfi, K. (2021). Pyrolysis of ficus nitida wood: Determination of kinetic and thermodynamic parameters. *Fuel*, 283, 119253.
- [26] Pan, Z., Li, X., Fu, L., Li, Q., & Li, X. (2023). Environmental sustainability by a comprehensive environmental and energy comparison analysis in a wood chip and rice straw biomass-fueled multi-generation energy system. *Process Safety and Environmental Protection*, 177, 868-879.
- [27] Mumbach, G. D., et al. (2022). Investigation on prospective bioenergy from pyrolysis of butia seed waste using TGA-FTIR: Assessment of kinetic triplet,

- thermodynamic parameters, and evolved volatiles. *Renewable Energy*, *191*, 238-250.
- [28] Alves, J. L. F., et al. (2022). Prospection of catole coconut (*Syagrus cearensis*) as a new bioenergy feedstock: Insights from physicochemical characterization, pyrolysis kinetics, and thermodynamic parameters. *Renewable Energy*, *181*, 207-218.
- [29] Mumbach, G. D., et al. (2024). Unlocking the potential of pequi (*Caryocar brasiliense*) residues for bioenergy and renewable chemicals: Multicomponent kinetic modeling, thermodynamic parameter estimation, and characterization of volatile products through TGA and Py-GC/MS experiments. *Industrial Crops and Products*, *209*, 117928.
- [30] García, R., Pizarro, C., Lavín, A. G., & Bueno, J. L. (2014). Spanish biofuels heating value estimation. Part II: Proximate analysis data. *Fuel*, *117* (Part B), 1139-1147.
- [31] Parikh, J., Channiwal, S. A., & Ghosal, G. K. (2005). A correlation for calculating HHV from proximate analysis of solid fuels. *Fuel*, *84*(5), 487-494.
- [32] Huang, L., et al. (2016). Thermodynamics and kinetics parameters of co-combustion between sewage sludge and water hyacinth in CO₂/O₂ atmosphere as biomass to solid biofuel. *Bioresource Technology*, *218*, 631-642.
- [33] Huang, H., Liu, J., Liu, H., Evrendilek, F., & Buyukada, M. (2020). Pyrolysis of water hyacinth biomass parts: Bioenergy, gas emissions, and by-products using TG-FTIR and Py-GC/MS analyses. *Energy Conversion and Management*, *207*, 112552.
- [34] Gao, J., et al. (2023). In-situ catalytic bio-oil production from hydrothermal liquefaction of Cu-impregnated water hyacinth: Screening of reaction parameters. *Journal of the Energy Institute*, *109*, 101308.
- [35] Kumar, M., Upadhyay, S. N., & Mishra, P. K. (2019). A comparative study of thermochemical characteristics of lignocellulosic biomasses. *Bioresource Technology Reports*, *8*, 100186.
- [36] Abdullah, M. Z., Husain, Z., & Pong, S. L. Y. (2003). Analysis of cold dow fluidization test results for various biomass fuels. *Biomass and Bioenergy*, *24*, 487-494.
- [37] Almeida, M. C. P. dos S., et al. (2024). Valorization of wood residues from vegetation suppression during wind energy plant implementation and its potential for renewable phenolic compounds through flash pyrolysis: A case study in northeast Brazil's semi-arid region. *Forests*, *15*(4), 621.
- [38] de Paiva, E. M., et al. (2024). Pyrolysis of cashew nutshell residues for bioenergy and renewable chemicals: Kinetics, thermodynamics, and volatile products. *Journal of Analytical and Applied Pyrolysis*, *177*, 106303.
- [39] Hu, Z., Ma, X., & Li, L. (2015). Optimal conditions for the catalytic and non-catalytic pyrolysis of water hyacinth. *Energy Conversion and Management*, *94*, 337-344.
- [40] Harun, M. Y., Dayang Radiah, A. B., Zainal Abidin, Z., & Yunus, R. (2011). Effect of physical pretreatment on dilute acid hydrolysis of water hyacinth (*Eichhornia crassipes*). *Bioresource Technology*, *102*(8), 5193-5199.
- [41] Irewale, A. T., Dimkpa, C. O., Elemike, E. E., & Oguzie, E. E. (2024). Water hyacinth: Prospects for biochar-based, nano-enabled biofertilizer development. *Heliyon*, *10*(17), e36966.
- [42] Akter, A., Nadim, Md. K. A., Mitu, M., Reza, Md. S., Alim, S. M. A., & Islam, Md. M. (2023). Water hyacinth: Potential applications for environmental sustainability and socio-economic development. *Journal of Agroforestry and Environment*, *16*(1), 31-39.
- [43] Maulidyna, A., et al. (2021). Review: Economic impacts of the invasive species water hyacinth (*Eichhornia crassipes*): Case study of Rawapening Lake, Central Java, Indonesia. *International Journal of Bonorowo Wetlands*, *11*(1).

Attack Evaluation of Cyber Security Analysis in Cyber-physical Power Systems: A Review Concept

Erdem Koca¹, Musa Terkes², Alpaslan Demirci³

^{1,2,3}Electrical Engineering Department of Yıldız Technical University, Istanbul, Türkiye

¹kocaa.erdem@gmail.com, ²musa.terkes@yildiz.edu.tr, ³ademirci@yildiz.edu.tr

Abstract—After the technological advances, the volume of the digital data pool has fallen into a hazardous game due to cyber and physical attacks, expanding the scope of attacks and raising security concerns. In addition, cyber attackers are using new techniques to manipulate security systems and automate attacks, making cyber security more valuable than ever. It is essential to meticulously address hardware, software, communication, and physical-layer vulnerabilities, identify the main causes of attacks, and detail the operational evolution of attack types. Especially in complex and functionally active cyber-physical power systems (CPPS), safe and reliable operation must be guaranteed with timely detection and defense actions depending on the extent of the attack. This review explains the key terms of cyber security analysis in CPPSs and provides an in-depth overview of the process and aftermath of threats based on attack types. It discusses traditional and next-generation cyber and physical attacks and vividly illustrates the importance of security through real events resulting in cyber vulnerabilities, making the topic more relatable. The study meticulously evaluates the individual and social damages of various cyber-attack practices. It concludes that reinforcing the cyber security of digitalized energy systems is essential for national security and economic stability.

Keywords - cyber security, cyber-attack, physical attack, cyber-physical power systems, malware

I. INTRODUCTION

Cyber-physical power systems (CPPS) are unique technological infrastructures that manage and control energy generation, transmission, and distribution, integrating traditional energy systems with digital control systems designed to increase efficiency, improve autonomic energy management, and maximize system reliability. They transform the energy landscape of the modern world by combining advanced information processing technology and automation. It manages physical energy infrastructure such as power plants, transmission lines, and distribution networks through information processing, data analytics, and automation processes in cyberspace. It performs many functions to guarantee efficiency, reliability, and sustainability in the physical infrastructure. For instance, it can optimize energy flow by analyzing data collected in real time or proactively detect and manage potential outages and energy system maintenance. Thanks to its proactive behavior, the situation is controlled via early changes instead of waiting for adverse action. It can also offer solutions to carbon concerns by serving to develop renewable energy potential via data-driven management strategies. However, for this to happen, more is needed to use a single system or component in CPPS with the desired accuracy, efficiency, and ergonomics. Simultaneous synchronization and communication of multiple components is required. These include sensors continuously monitoring physical parameters and actuators



performing physical actions based on the received data. Broadband communication networks, including wired or wireless technologies that guarantee reliable and sustainable data flow and enable remote monitoring and control, form the communication framework of CPPS. In this direction, a schematic diagram of CPPS is shown in Fig. 1 [1].

One of the control, remote monitoring, and data acquisition technologies often used in system infrastructure is supervisory control and data acquisition (SCADA). The human-machine interface (HMI) enables operators to control and monitor equipment in the field, while the graphical user interface provides information on the real-time status of the facility. Alarm and notification systems alert operators in case of abnormal or malfunctioning situations, guaranteeing a fast and effective intervention. This functional process occurs as programmable logic controllers (PLC) and remote terminal units (RTU) process and evaluate data collected from sensors in the field to SCADA. PLCs, which can be expanded with different input/output

modules, send commands to actuators based on the data being processed. Often used in geographically distributed systems, RTUs are designed to operate in extreme environmental conditions (e.g., water and wastewater management) and are used to collect data. Ethernet and fiber optics are used for communication infrastructure in wired options, while radio frequency and satellite communication are often preferred in wireless alternatives. Especially in the energy sector, SCADA systems focus on increasing efficiency, reducing costs, and securing energy systems. The general structure of SCADA is shown in Fig. 2 [2]. Integrating SCADA systems with CPPS is one of the most critical aspects of the digital transformation in the energy sector. CPPS can use machine learning and artificial intelligence to optimize production processes, guaranteeing higher efficiency and adaptability. In this context, SCADA provides real-time data flow to control and manage processes. The integrated system enables faster fault condition detection and automatic response mechanisms in power generation and distribution operations.

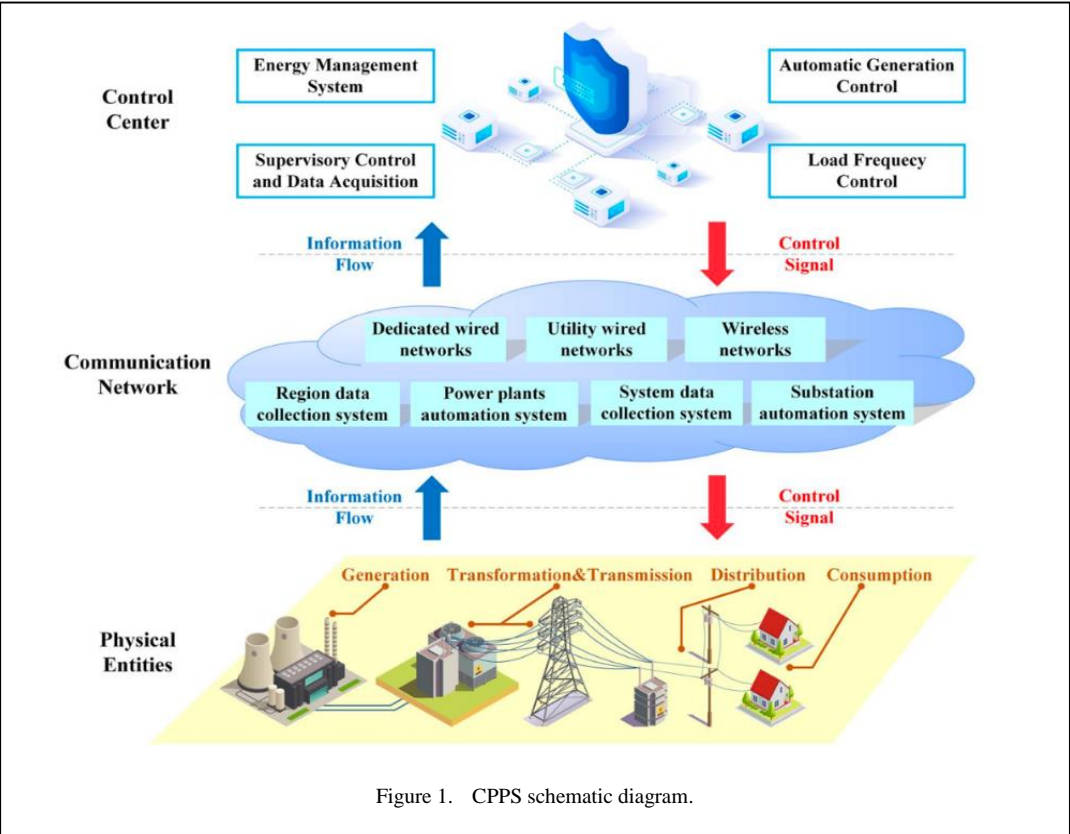


Figure 1. CPPS schematic diagram.

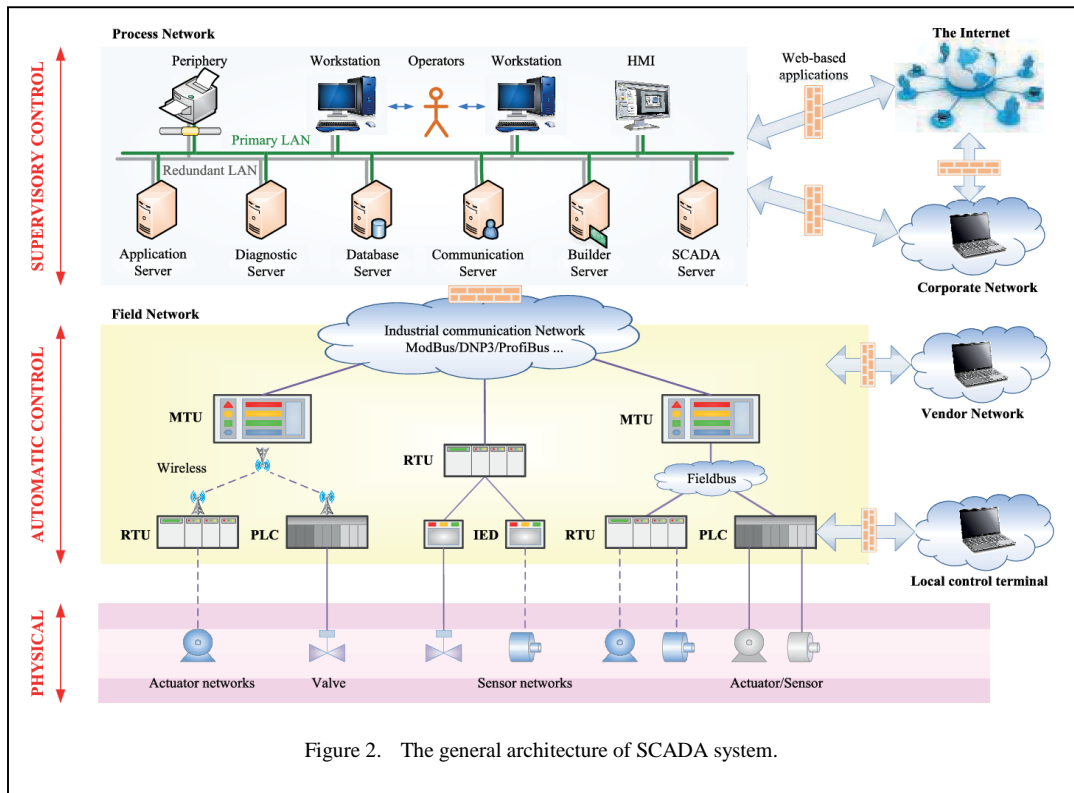


Figure 2. The general architecture of SCADA system.

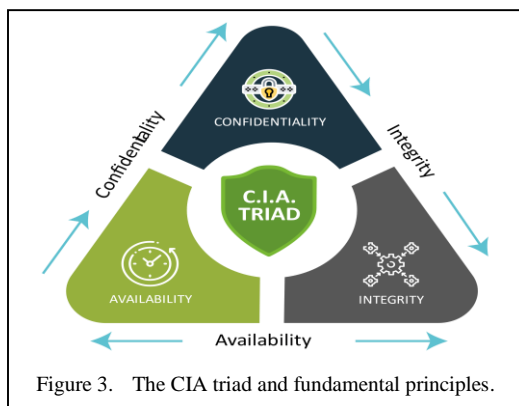
A comprehensive review of the vulnerability of CPPSs to cyber-attacks across cyber-attack types is more valuable than ever due to its complexity and critical functionality. Minor vulnerabilities, especially between layers, can profoundly impact the entire system infrastructure and cause irreversible failures and unsustainable services. To develop cyber-attack defense mechanisms and detection methods, it is essential to conduct attack analysis and know the types of attacks well. This review starts from the basic cyber security terminology for the reliable, sustainable, and social welfare of society. It discusses the types of attacks that threaten security and are at the center of the attention of attackers and their functioning process. In addition, real-life examples of cyber-attacks emphasize the importance of the potential effects of attack types. However, this review focuses only on the attack side, as the attack defense mechanism and detection methods need to be broadly addressed. Section I details the development of CPPS and its potential functional uses today, while Section II discusses the types of cyber and physical attacks, starting with cybersecurity-related terminology. Section III

highlights the inspiration for the review and draws inferences for cyber and physical attacks.

II. CYBER SECURITY ANALYSIS IN CYBER-PHYSICAL POWER SYSTEMS

A. Fundamental Terms in Cyber Security

Understanding cybersecurity terminology is essential to determining the severity and scale of a cyber-attack and evaluating the threats affecting data. The first thing that comes to mind is the CIA triangle (see Fig. 3), an idea derived from the terms Confidentiality, Integrity, and Availability, which provides a common framework for cybersecurity analysis [3]. Confidentiality, which means that information is accessible only by authorized persons, aims to minimize the risks of unauthorized persons illegally obtaining, stealing, disclosing, or using the information. Integrity means that information is accurate, complete, and unaltered. Availability is represented by making information available to authorized persons when and where it is needed. As a result, the CIA triad describes the basic principles of information security and aims to protect the organization's information assets.



Violating any of the three principles results in data loss and eliminates the functionality of the policy chain. Fig. 3 illustrates the relationship between the CIA triad and its principles [4].

A threat is a phenomenon that can damage a system or compromise data. Threats can be software, such as computer viruses, spyware, malicious bots, human error, and environmental factors, such as physical damage or natural disasters. Another concept is vulnerabilities. Vulnerabilities are gaps where an attacker can damage a system, and software errors, outdated infrastructure, weak encryption, or misconfigured networks are indicators of vulnerability. Risk is the combination of the likelihood that a threat will exploit a vulnerability and the possible consequences of that exploitation. Especially in cybersecurity, risk assessment can effectively determine which security measures to prioritize. If the necessary precautions are not taken for risks, attack threats that exploit vulnerabilities will inevitably damage the system. Various threats include distributed denial of service (DDoS) attacks, phishing, and ransomware. Analysis of attacks provides information on how to reinforce defense mechanisms and develop event response plans. Accordingly, defense mechanisms have security controls that can counter threats and address vulnerabilities. Firewalls, antivirus software, encryption, and access control systems are some of such security procedures.

B. Next Generation Cyber Attacks Against Traditional Threats

Traditional threats and next-generation cyber-attacks differ significantly in terms of both impact and prevention methods. While traditional threats are more straightforward and focused on a single vector, next-generation

attacks are characterized by complexity and multiple attack vectors. Traditional threats rely on manual interventions, making them easier to detect and prevent, while next-generation attacks use artificial intelligence and automation technologies to create widespread impacts.

While traditional threats target individual devices and small-scale systems, next-generation attacks can target critical infrastructure and large-scale organizations. There is also a big difference in the impact period. While traditional threats cause short-term problems, next-generation attacks can have long-term and permanent effects. Therefore, advanced security systems, zero-trust approaches, and solutions based on continuous threat intelligence are required against next-generation threats.

This distinction and analysis help organizations develop an effective security strategy against both traditional threats and next-generation attacks. Especially given the complexity of next-generation attacks, proactive and automated approaches are critical to ensure the sustainability of security.

C. Types of Attacks on Cyber-physical Power Systems

Attackers acting for data theft or manipulation may sometimes be unsuccessful in a similar scenario. The attacker, who tries alternative methods until he succeeds, can use many techniques in the attack organization. Here, many types of attacks, from cyber to physical, are discussed.

1) Cyber attacks

a) Time synchronization attacks (TSA)

Operational control of the power system in widely distributed systems is achieved by synchronizing the operation control time in different regions. Timescale signals from GPS satellites are used for the respective purpose and to decide the power flow in transmission and distribution systems. In CPPSSs, especially in power management units (PMU), the time synchronization device communicates in plain code without a password authentication mechanism, which introduces many flaws. Using these flaws in their cyber terminals, false synchronization time is received, and fake satellite navigation messages are transmitted via time synchronization attacks in decoding. It also causes time drift in calibration data, corruption of wide-area measurement systems, and incorrect control decisions in the power regulation and

control system. With the loss of control of the system, the attack and destruction achieve their goal [5]. The spoofing of satellite signals was analyzed in [6] using security code prediction and replay attacks. Another approach in [7] tested low-cost controller-based GPS analog positioning software that broadcasts spoofed GPS signals via multiple function calls. A unified replay strategy for suppressing and spoofing GPS signals that cause significant time jumps in time synchronization is investigated in [8]. To illustrate the situations that societies face: a time data jump caused by a malfunction in a time synchronization device caused the power control center in Western China to generate power on the wrong date and several turbines in hydroelectric power plants to shut down abnormally [9]. Although the event was not caused by a cyber-attack on the time synchronization base, it proves the potential of the threat.

b) Fake data injection attacks (FDIA)

Fake data injection attacks (FDIA) maliciously manipulate measured data at sampling terminals or state estimation results at control terminals in CPPSs. This results in incorrect assessment and management of operational status and control. The damage level is vital due to the complex topology of CPPS and the low redundancy of measurement data. It can attack sampled voltage, injected power, or line power flow data, especially in SCADA systems. It can also degrade the performance of power system state estimation and load frequency control. It can cause unstable system operations in SCADA and automatic generation control systems. The general action process of FDIA is shown in Fig. 4 [1].

The type of attack concerned is broadly divided into two categories: physical and cyber-based. In the physical-based method, which targets monitoring, control, and security devices, the level of access to various equipment is discussed in [10], the most notable being access to the main processor-based mechanism by causing the RTU software to change. While the number of devices vulnerable to such attacks is limited, cyber-based attacks are typical. The cyber-based subcategory involves the attacker violating the control system or associated applications (process layers such as forecasting, economic distribution, and energy trading) [11]. Such attacker attempts targeting system operations and services can be launched via physical communication modules. This differs

from inserting malware into a computer software system or database.

c) Distributed denial of service (DDoS) attacks

Distributed denial of service (DDoS) attacks are the most common threat to critical infrastructure today and target the communication network of systems. They prevent legitimate users from accessing services by flooding them with excessive fake traffic. Botnet creation has a series of sequential functionalities such as Command and Control (C&C) servers, target identification, traffic generation, attack methods, and sustaining and terminating the attack [12]. DDoS attacks consist of internet-connected devices (bots) infected with malware (malicious software) that cyber attackers can control. The botnet's size determines the attack's effectiveness, while remote management of the devices allows the targeted attack to be launched at any time. The botnets are managed via command-and-control servers, and the attacker determines when and how to intervene on the infected devices. Once the attack is launched, the botnet network continuously sends fake requests to the target while determining the traffic generation method that will consume the most network resources. To consume the network's bandwidth, it may send large amounts of data or requests that force server processors to perform intensive processing. In real-world examples, a cyberattack targeting the electricity supply network in Ukraine in 2015 blocked access to control systems, disabled automated systems, and left around 230,000 people in the dark [13].

d) Denial of service (DoS) attacks

Denial of service (DoS) attacks are performed to close the target system, service, or network to user access. Its primary purpose is to overload the target system's resources (CPU, memory, bandwidth, etc.) and render it unserviceable. It causes the target system to collapse, slow down, or become completely unusable. Flooding, amplification, and protocol-based attacks are available [14]. Flooding attacks cause many users' datagram protocol (UDP) packets to be sent to the target system, followed by checking the packets for validity, resulting in excessive resource utilization. Similar resource consumption can also occur when an attacker sends Internet Control Message Protocol (ICMP) "ping" packets rapidly at a high rate and size. The SYN flag initiates synchronization (SYN) flood

On the other hand, a similar example happened to Saudi Aramco in 2012. The spread of a computer virus called Shamoon increased after phishing emails containing malicious links were sent to company employees. The malware turned off around 35,000 computers and caused severe problems in the company's business operations [19]. Another example occurred in 2016 against a water utility in the US. Business employees who clicked on fake emails were redirected to a phishing site, making it easier for cyber attackers to infiltrate the system with the information they received. They accessed systems that control water treatment processes and tried to change chemical dosage settings. A severe cyber-attack that would negatively affect human health has survived [20].

g) *Side-channel attacks*

Side-channel is a type of attack that extracts indirect information from the physical operation of the computer or device. It analyzes the by-products (electromagnetic emissions, power consumption, processing times, acoustic signals, etc.) the target system performs while operating, i.e., physical data. The most essential feature is that instead of stealing data directly, it uses information exfiltrated during the normal activities of the target system. Cyber attackers' main methods to obtain information are timing, power, electromagnetic and acoustic analysis. In timing analysis, secret information is obtained by measuring the time spent during the execution of the process. In the field of cryptology, the use of different key/input variations in decryption is subject to various processing times, and by analyzing the time differences, the attacker can detect a specific part or all of the cipher. An example is the Rivest-Shamir-Adleman (RSA) algorithm, widely used in cryptology. The algorithm includes different time intervals depending on the cipher size being exchanged and using modular exponentiation. If the attacker can measure the execution times accurately enough, they can guess some of the private cipher's bits. Power analysis measures the energy consumed by the device during execution. There are two types: simple and differential. Simple power analysis provides critical information by observing the power consumption during a single operation. Differential power analysis performs statistical analysis of many measurements and sophisticated information extraction [21].

Another approach is to study the electromagnetic waves emitted by the device

during the operation. Specifications for the process are obtained by focusing on high-frequency processes. Acoustic cryptanalysis is used to analyze the sounds emitted by devices during operation. The sounds produced by various keystrokes and the sounds the processor makes for a task can provide information about the command. High-sensitivity microphones can be used for these tasks, while audio recordings are analyzed to achieve the goal. To prevent side-channel attacks from being effective in CPPS, device physical security measures should be improved, electromagnetic shielding should be used, and processing times should be standardized.

h) *Man-in-the-Middle attacks (MitM)*

MitM is performed by getting between two sides to eavesdrop, redirect, or modify the communication. The attacker controls the entire data flow, but the victims think they are communicating securely. There are processing steps such as eavesdropping, data monitoring and modification, false identity, and spoofing. This cyber-attack usually impersonates the server via Address Resolution Protocol (ARP) and DNS spoofing, Secure Sockets Layer (SSL) stripping, and Wi-Fi eavesdropping. To determine which IP address devices on the network correspond to, devices send an ARP request. To fulfill this request, an ARP response containing the device's Media Access Control (MAC) address is received. In this reliable and seamless process, the ARP protocol has no mechanism to verify the responses sent. The attacker sends spoofed ARP responses to the ARP tables of one or more devices on the network. The spoofed responses associate the attacker's MAC address with IP addresses on the target system. Traffic that would have been routed to IP addresses is falsely routed to the attacker's device, which can then be manipulated (eavesdropping, modifying, or blocking). It is considered part of high-damage attacks, with a high risk of infecting ransomware. The system that converts the IP addresses of devices on the Internet into human-understandable domain names is known as DNS, and a similar cyber-attack can be carried out via this platform. The computer performs a DNS query on the web addresses visited, and the user's internet service provider will inevitably redirect to its own or another DNS server after the query. The attacker interferes with this process and generates fake DNS responses and the user is redirected to the incorrect IP address.

TABLE I. A CLASSIFICATION OF DoS ATTACKS AND A SAMPLE CODE SEQUENCE.

Class	DoS Attack Type	Sample Command
Flooding Attack	UDP flood	hping3 --udp -p 80 -i u-100 <target_IP>
	ICMP flood	ping -f <target_IP>
	SYN flood	hping3 --S -p 80 --flood <target_IP>
Amplification Attack	DNS	dig +short ANY example.com @<DNS_server_IP>
	NTP	ntpd -n -c monlist <target_IP>
Protocol Based Attack	Smurf	hping3 --icmp -a <target_IP> --spooof <edition_IP>
	Fraggle	hping3 --udp -a <target_IP> --spooof <edition_IP>

TABLE II. COMPARISON OF DoS AND DDoS ATTACKS.

Attack Type	DoS	DDoS
Specifications		
Number of resources used	Typically, a single resource	Multiple resources
Scale	Smaller-scale attacks	A more aggressive attack
Detection difficulty	Easier detection	More difficult detection
Complexity	Simpler	More complex

The attack can be performed over the same local area network (LAN) or a different DNS server. SSL stripping weakens the security of a secure HTTPS connection, reducing it to an insecure connection. Wi-Fi eavesdropping involves the unauthorized capture and listening to data transmitted over wireless networks. Due to the high threat potential in weakly encrypted and insecure Wi-Fi networks, it can easily intercept personal information, log cookies, emails, passwords, and other private data. It is considered a passive attack as the data-based network is monitored and listened to, but the traffic is not intercepted. The general process of MitM attacks is shown in Fig. 5 [22].

2) Physical attacks

While the most common threatening attacks are cyber-based, the unique physical layer attack on CPPS should be addressed. Here, the aim is to penetrate directly into the power infrastructure and damage the physical system. Electromagnetic attacks can damage electrical devices without touching them using overvoltage or electromagnetic pulses.

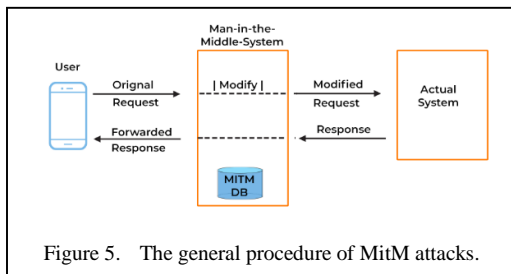


Figure 5. The general procedure of MitM attacks.

Resonance attacks (RA) are a typical example and cause abnormal frequency or control variation rates in the power system by changing the power load or contact line signal relative to the resonant source. Since every system has a resonance point, routine detection methods may not easily detect it. This distorts the state signals of weak loads or generators. The RA process is illustrated in Fig. 6 [1]. It continues to be of interest to researchers. For example, the investigation of resonance implementation possibilities via two-domain load frequency control and the irreversible effects of RAs on power system frequency control were studied in [23]. RAs effects on first-order and higher-order linear and nonlinear terms, automatic voltage regulators, and power system stabilizers in similar single- and multi-domain frequency-controlled systems are studied in [24]. It has been experimentally demonstrated that the harmful RA effect may not stay in one region but may spread to other connected areas and cause severe damage.

3) Coordinated cyber and physical attacks

Coordinated cyber-physical attacks have recently been presented due to the complex and robust infrastructure of CPPSs. Switching between cyber and physical attack types is easy with two parallel overlapping layers. A general flow of the coordinated attack plan is shown in Fig. 7 [1].

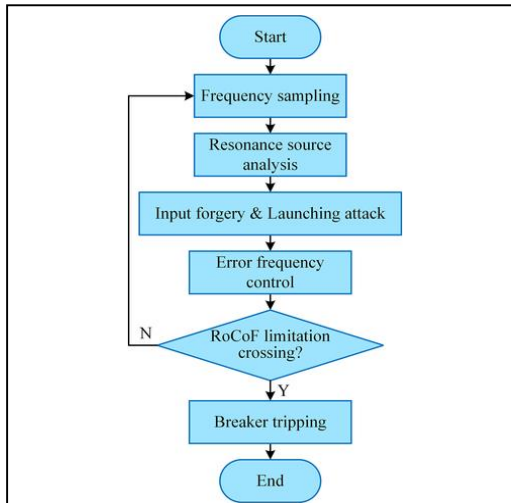


Figure 6. The general procedure of Ras.

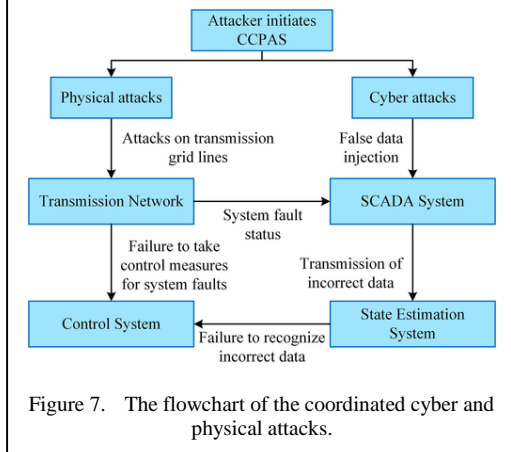


Figure 7. The flowchart of the coordinated cyber and physical attacks.

Venezuela also suffers from a holistic attack plan that facilitates the transition from a singular attack to a large-scale and potent threat. The incident in 2019 exposed the weaknesses of delaying attack detection and exploiting the window of time, proving its great offensive power and defensive challenge [25].

III. CONCLUSIONS

The changing landscape and growing data usage in power systems and CPPS are potential targets for cyber-attacks. What are the terminologies often used in cybersecurity analysis? What types of cyber threats have organizations and systems faced today, and what vulnerabilities have caused them? What are the types of cyber-attacks to which high-risk victims may be exposed? The key to addressing these questions lies in the continuous evolution of cyber-attack operational processes.

This review aims to provide a comprehensive discussion of the types of cyber-attacks, along with an evaluation of commonly used security standards and terms, their strengths and weaknesses, and the security issues in CPPSs. Defense mechanisms and detection methods in response to cyber-attacks are excluded from the review, focusing on attack analysis and types. With the support of modern communication resources and technology, integrating various physically distributed computing and control mechanisms for CPPS development can solve complex problems with improved capacity performance and promote intelligent resource allocation and energy management. However, the complex structure of power systems can face many types of cyber-attacks due to their distributed and interactive features in time-based operations and their dynamic operation characteristics. For attackers, given the most vulnerable points of the power system, fake data injection attacks are a powerful trump card that can circumvent common detection mechanisms. Due to the high coupling at the cyber and physical layers, an underestimated vulnerability in CPPSs can spread rapidly, creating large-scale power outages and profoundly affecting the sustainable economy. By further exploring attack mechanisms and sequential fault analysis and types in this way, cyber defense architecture can be reinforced, and improving the performance of strategic developments for attack detection can guarantee societal security and welfare. Future work aims to evaluate the societal and economic impact of specific types of cyber-attacks on CPPSs to understand further the critical role of these systems on society and the economy, not just limited to technical security measures.

REFERENCES

- [1] Adepu, S., & Mathur, A. (2021). Distributed attack detection in a water treatment plant: method and case study. *IEEE Transactions on Dependable and Secure Computing*, 18(1), 86–99.
- [2] Assante, M. (2016). *Confirmation of a coordinated attack on the Ukrainian power grid*. 23, 1–5. Available at: ics.sans.org/blog/2016/01/09/confirmation-of-a-coordinated-attack-on-the-ukrainian-power-grid
- [3] Ayiad, M. M., Leite, H., & Martins, H. (2021). State estimation for hybrid VSC Based HVDC/AC: Unified bad data detection integrated with gaussian mixture model. *IEEE Access*, 9, 91730–91740.
- [4] Content Team. (2021). *What is the CIA TRIAD & its importance for cybersecurity*. Web Security Store. Available at: <https://websitesecuritystore.com/blog/what-is-the-cia-triad/>
- [5] Distrack, S., & Update, M. (2017). Joint security awareness report (JSAR-12-241-01B). 3, 16–18.

- [6] Do, V. L., Fillatre, L., Nikiforov, I. V., & Willett, P. K. (2017). Feature article: security of SCADA systems against cyber-physical attacks. *IEEE Aerospace and Electronic Systems Magazine*, 32, 28–45.
- [7] Fruhlinger, J. (2020). *The CIA triad: Definition, components and examples*. CSO Online.
- [8] He, X., Liu, X., & Li, P. (2020). Coordinated false data injection attacks in AGC system and its countermeasure. *IEEE Access*, 8, 194640–194651.
- [9] Humphreys, T. E. (2013). Detection strategy for cryptographic GNSS anti-spoofing. *IEEE Transactions on Aerospace and Electronic Systems*, 49(2), 1073–1090.
- [10] Ingram, D. M. E., Schaub, P., Campbell, D. A., & Taylor, R. R. (2012). Evaluation of precision time synchronisation methods for substation applications. In *2012 IEEE International Symposium on Precision Clock Synchronization for Measurement, Control and Communication Proceedings*. (pp. 1–6).
- [11] Kim, J., & Tong, L. (2013). On topology attack of a smart grid: undetectable attacks and countermeasures. *IEEE Journal on Selected Areas in Communications*, 31(7), 1294–1305.
- [12] Kovacs, E. (2016). *Attackers Alter water treatment systems in utility hack: report*. Available at: <https://www.securityweek.com/attackers-alter-water-treatment-systems-utility-hack-report/>
- [13] Liu, C., Liang, H., & Chen, T. (2021). Network parameter coordinated false data injection attacks against power system ac state estimation. *IEEE Transactions on Smart Grid*, 12(2), 1626–1639.
- [14] Liu, K., Ma, S., Ma, A., Zhang, Q., & Xia, Y. (2021). Secure control for cyber-physical systems based on machine learning. *Acta Automatica Sinica*, 47(6), 1273–1283.
- [15] Liu, S., Hu, Z., Wang, X., & Wu, L. (2019). Stochastic Stability analysis and control of secondary frequency regulation for islanded microgrids under random denial of service attacks. *IEEE Transactions on Industrial Informatics*, 15(7), 4066–4075.
- [16] Liu, X., Li, Z., Liu, X., & Li, Z. (2016). Masking transmission line outages via false data injection attacks. *IEEE Transactions on Information Forensics and Security*, 11(7), 1592–1602.
- [17] Mahmoud, M. S., Hamdan, M. M., & Baroudi, U. A. (2019). Modeling and control of Cyber-Physical Systems subject to cyber attacks: A survey of recent advances and challenges. *Neurocomputing*, 338, 101–115.
- [18] Mohajerin Esfahani, P., Vrakopoulou, M., Margellos, K., Lygeros, J., & Andersson, G. (2010). Cyber attack in a two-area power system: Impact identification using reachability. In *Proceedings of the 2010 American Control Conference*, (pp. 962–967).
- [19] Mohanakrishnan, R. (2022). *What is a man-in-the-middle attack? Definition, detection, and prevention best practices for 2022*. Spiceworks. Available at: <https://www.spiceworks.com/it-security/data-security/articles/man-in-the-middle-attack/>
- [20] Qian, B., & others. (2020). Review on time synchronization attack in power system. *Power Syst. Technol*, 44(10), 4035–4045.
- [21] ShangGuan, X.-C., He, Y., Zhang, C.-K., Jin, L., Jiang, L., Wu, M., & Spencer, J. W. (2021). Switching system-based load frequency control for multi-area power system resilient to denial-of-service attacks. *Control Engineering Practice*, 107, 104678.
- [22] Su, L., Ye, D., & Zhao, X. (2020). Static output feedback secure control for cyber - physical systems based on multisensor scheme against replay attacks. *International Journal of Robust and Nonlinear Control*, 30(18), 8313–8326.
- [23] Tippenhauer, N. O., Pöpper, C., Rasmussen, K. B., & Capkun, S. (2011). On the requirements for successful GPS spoofing attacks. In *Proceedings of the 18th ACM Conference on Computer and Communications Security*, (pp. 75–86).
- [24] UCL Crypto Group. (n.d.). *Theoretical Models for Side-Channel Attacks*. Available at: <http://www.dice.ucl.ac.be/fstandae/tsca>
- [25] Wang, Q., Tai, W., Tang, Y., Zhu, H., Zhang, M., & Zhou, D. (2019). Coordinated defense of distributed denial of service attacks against the multi-area load frequency control services. *Energies*, 12(13), 2493.

Sustainability: A Bibliometric Review of Cassava in Flour and Starch Processing from an Environmental Perspective

Julio Cesar Sales Bezerra¹, Murilo dos Santos Oliveira², Emanuely Alves Pelogio³,
Emerson Ribeiro Machado⁴, Raphael Abrahao⁵

^{1,2}Graduate Program in Renewable Energy, Federal University of Paraiba, Joao Pessoa, Brazil

³Department of Administration, Federal Institute of Science and Tecnology, Almenara, Brazil

⁴Biolink soluções Estratégicas, Uberlândia, Brazil

⁵Department of Renewable Energy Engineering, Federal University of Paraiba, Joao Pessoa, Brazil

¹julio.bezerra@estudante.cear.ufpb.br, ²murilo.oliveira@estudante.cear.ufpb.br,

³emanuely.pelogio@ifnmg.edu.br, ⁴emersonrm.bio@gmail.com, ⁵raphael@cear.ufpb.br

Abstract—The present study aimed to use a bibliometric approach to examine the current state of research on the Life Cycle Assessment (LCA) of cassava flour/starch. Exploring an initial sample of 137 documents obtained from the Scopus database, it was observed that most addressed a variety of topics related to cassava, with an emphasis on areas such as renewable energy production, starch properties, environmental impacts, biofilm and biodegradable packaging, sustainability in starch production, and animal feed. However, only a small proportion of these documents actually dealt with the LCA of cassava. The bibliometric analysis identified a gap in the scientific knowledge related to the life cycle of cassava, especially in the context of flour/starch production. Although there is growing interest in various topics related to cassava, the lack of specific studies on the cassava life cycle highlights the need for more research in this field. The study concluded that, despite the interesting publication patterns observed in the analyzed documents, there is a significant opportunity to expand knowledge about the LCA of cassava, especially in the context of flour/starch production. It is hoped that this study will stimulate future investigations and encourage the academic community to explore more deeply the challenges and opportunities related to cassava flour/starch production, aiming for more sustainable agriculture and processing.

Keywords - root, peel, processing, LCA, environmental impact, life cycle

I. INTRODUCTION

Cassava (*Manihot esculenta* Crantz), a plant native from Brazil, is recognized for its economic importance due to its production of tuberous and starchy roots, which represent a valuable source of food for both humans and animals. Additionally, it serves as an option for the production of renewable energy, such as ethanol or ethyl alcohol [1]. Cultivated in almost all Brazilian states, cassava ranks among the top nine agricultural products in terms of cultivated area in the country and sixth in production value [2].

Cassava, a long-lived, shrubby plant, has more than 300 varieties. Its root is its most important part, used both for direct consumption and for industrial production of flour, starch, and tapioca. The cassava crop is highly adaptable, drought-resistant, and can be planted in various climatic and soil conditions throughout the year, as long as there is sufficient moisture for the plant's establishment. Its growth period ranges from 9 months to 2 years, depending on the variety [2].



The tuber represents the main by-product of this crop. However, there is a progressive increase in the use of the aerial part of the plant for animal feed, especially during periods of food resource scarcity, which significantly contributes to enriching ruminant diets with supplemental nutrients. Despite this significant potential, the full use of the aerial part remains underutilized, as only the stem is traditionally used for replanting, while the upper third of the aerial part is generally discarded in the field and later incorporated into the soil during the harvest process [3-8].

The production of cassava flour is divided into seven stages, represented in Fig. 1: first stage: planting, management, and harvesting of cassava; second stage: peeling of the roots; third stage: washing; fourth stage: grating; fifth stage: pressing; sixth stage: sieving; seventh stage: roasting. Reference [9] estimate that, generally, from every 100 kg of raw cassava, between 25 to 35 kg of minimally processed flour are produced.

The waste generated in cassava processing stands out as an important resource for adding value to the final product. These residues are produced during the production of flour and starch and differ in their composition. In general, three types of waste are generated: peels from the initial processing, fibrous by-products (produced during grinding and sieving), and starch residues (after the decantation of starch and wastewater effluents). These wastes can cause soil and water contamination [10].

However, cassava peels have been the subject of research in various fields. References [11,12] explored them as an ingredient for the production of nanofibers, aiming for biodegradable food packaging. Reference [13] conducted studies confirming the feasibility of cassava peels for biogas production through anaerobic digestion. Reference [14] studied the commercial viability of cassava pulp and wastewater for biogas and biofertilizer production. These studies highlight potential

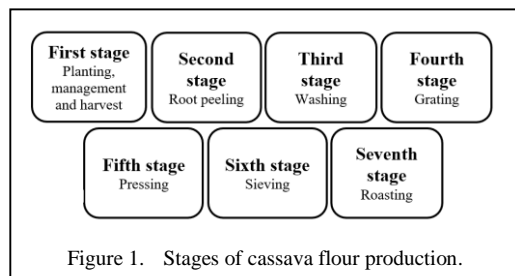


Figure 1. Stages of cassava flour production.

applications for cassava by-products, indicating promising opportunities for their use in various industrial sectors.

Considering the economic and sustainable potential in the valorization of agro-industrial waste, as mentioned by [15], the need for proper management of these resources becomes evident. The possibility of transforming these residues into value-added products not only contributes to the economy but also reduces environmental impact, promoting a more sustainable approach to agricultural waste management.

The understanding of the environmental impacts associated with cassava flour production is still incomplete. To address these impacts more comprehensively, the Life Cycle Assessment (LCA) tool can be used. This approach is widely recognized in the scientific community as an effective method to measure, assess, and compare various environmental impacts in an integrated manner. Comparative research using LCA began in the 1960s and 1970s and has undergone methodological refinements over time, experiencing remarkable growth during the early years of the 21st century [16].

LCA represents an essential tool for evaluating the environmental impacts of various products and services in a comprehensive and systematic manner. According to the United States Environmental Protection Agency [17], the life cycle of a product is defined as the set of main activities from raw material acquisition, through manufacturing, use, and maintenance, to disposal or recycling. According to [18], LCA is a methodological approach employed in the context of environmental impacts to quantitatively analyze the life cycle of products and services.

Considering that, a bibliographic survey consists of gathering previously analyzed and published works in different media, both written and electronic, such as books, scientific articles, web pages, and websites, the importance of this approach in supporting and substantiating the development of academic and scientific studies becomes evident.

The combination of qualitative and quantitative approaches allows for obtaining more comprehensive information than would be possible if obtained separately. Based on these concepts, a bibliometric study was conducted with the aim of quantifying the articles and

reviews that have addressed, over the years, the life cycle assessment of cassava in the process of flour or starch production.

II. METHODOLOGY

This research adopted a quantitative approach to the literature on the LCA of cassava during the process of transforming tubers into flour/starch, utilizing the Scopus database. Scopus was chosen due to its status as one of the largest and most comprehensive abstract and citation platforms in the world, widely recognized and utilized in the academic field. It provides access to a vast range of scientific literature across various areas of knowledge. In addition to its extensive coverage, Scopus indexes other renowned databases such as ScienceDirect, Springer, Wiley-Blackwell, Taylor & Francis, among others, making it an essential tool for research and systematic reviews, facilitating the tracking of advancements in various disciplines.

The keywords used in the research were the English equivalents for: “cassava”, “flour”, “starch”, “life cycle”, “emission”, “carbon footprint”, “LCA”, “environmental”, and “impact”. To maximize the number of publications, some synonymous words were incorporated, along with the use of Boolean operators “AND” and “OR”. An asterisk (*) was also used at the end of words to capture variations in suffixes.

According to the keywords and Boolean operators, the search string was structured as follows: ((“CASSAVA” OR “YUCCA” OR “MANIOC”) AND (“FLOUR” OR “STARCH”) AND (“LIFE CYCLE” OR “EMISSION*” OR “CARBON FOOTPRINT” OR “LCA” OR “ENVIRONMENT* IMPACT*”).

Moreover, the inclusion criteria for the research were restricted to articles and reviews that had been fully published, without limiting the publication period, in order to cover both early works and the most recent ones, dated up to December 2023 and published in the English language. The search focused on the titles, abstracts, and keywords of the publications.

Choosing English as the language for searching scientific articles is advantageous for several reasons. First, English is widely considered the universal language of science, meaning that the majority of scientific publications, especially in high-impact journals,

are available in this language. This broadens access to a greater quantity of relevant and up-to-date literature. Additionally, many international databases predominantly index English-language articles, ensuring that the most recent and influential research is easily accessible.

To enrich the analysis of keywords, Zipf's Law was employed, a statistical principle that describes the distribution of words in a text or dataset, indicating that a few words are very common while most are rare [19].

The collected data was analyzed using VOSviewer software [20], version 1.6.2, a tool widely used in scientific research, particularly in areas such as bibliometrics and information science. This software, chosen due to its open-source nature and broad acceptance in the academic community, enabled the identification of competitive patterns among keywords in the analyzed publications.

Based on the state of the art as an evaluation criterion, the analysis aimed to identify the number of academic publications over the years, the most cited works, the impact factor of the journals that published the articles, and the co-citation of keywords. All literary sources were examined and refined to identify the most academically relevant works aligned with the objectives of this research.

III. RESULTS AND DISCUSSION

The research conducted in the Scopus database on February 13, 2024, using specific terms and previously established inclusion criteria, resulted in the identification of 137 records. Of these, 126 corresponded to original articles and 11 were reviews. However, after reading the titles and abstracts of the articles, it was found that most of these publications, corresponding to 117 records, explored various study themes related to cassava but were not related to the proposed objective. Regarding the main themes of the articles identified in the database, the following was found:

- 27 articles are related to the production of renewable energy using cassava or some of its residues as a production source;
- 24 deal with studies of the physical, chemical, and functional properties of starch;

- 20 articles discuss the study of environmental impacts in cassava processing;
- 19 address the production of biofilm and biodegradable packaging produced with cassava starch;
- 19 researches are not related to any phase or process of cassava or its residues;
- 08 articles discuss sustainability in starch production;
- 07 discuss experiments in animal feed;
- 07 mention starch as a binding element in briquettes;
- 06 deal with studies related to human food.

However, although the documents obtained were relevant to the search sequence, 19 of these documents had no direct relation to cassava or its residues, that is, the direct intention was not related to the objective of studying cassava. This is why they were not incorporated into the analysis of this research. Thus, 118 papers remained, 107 articles and 11 reviews. Fig. 2 shows the temporal dynamics of the 118 articles selected for analysis.

It can be seen that scientific production on sustainability in starch production, biodegradable packaging, studies of the physical, chemical and functional properties of starch and renewable energy production has been consistent over the years, with a significant number of papers published in various years, indicating

continued interest in these areas of research. On the other hand, areas such as animal feed, human food and starch as a binding element in briquettes have a lower number of papers, suggesting lower research priority or less complexity of these topics compared to others.

The data also indicates a recent increase in interest in topics such as biofilms and biodegradable packaging, renewable energy production and studies on environmental impacts, which may reflect a growing awareness of environmental issues and a search for sustainable solutions.

Furthermore, the publication of papers since 1998 shows that environmental issues have been a constant concern over time, even if the specific focus of research has changed over the years. Currently, the most relevant investigations on the topic are concentrated in the environmental impacts group. Organizing this group based on the main topics covered in each paper allows for a clearer and more detailed view of how the studies are distributed (Fig. 3).

Cyanide contamination accounts for 10% of the total, indicating that there is a relatively low level of interest in this particular aspect. In contrast, mitigating the environmental impacts of cassava processing accounts for 15% of the research, indicating that there is relatively more interest in efforts to minimize these impacts. The use of wastewater from cassava production accounts for 25% of the research, highlighting the emphasis placed on the sustainable use of water resources. Finally, cassava LCA accounts for 50% of the studies. This indicates a greater interest in understanding the environmental

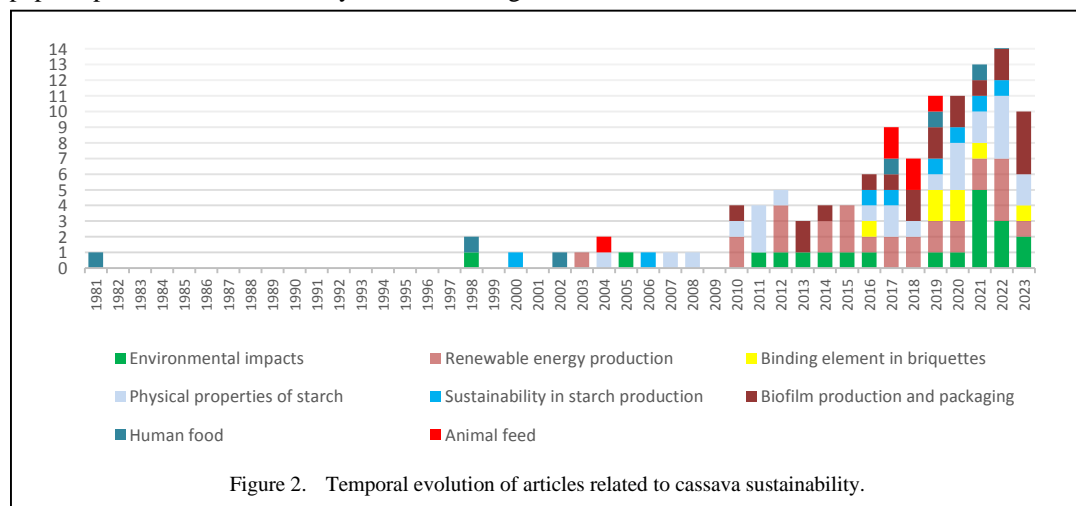
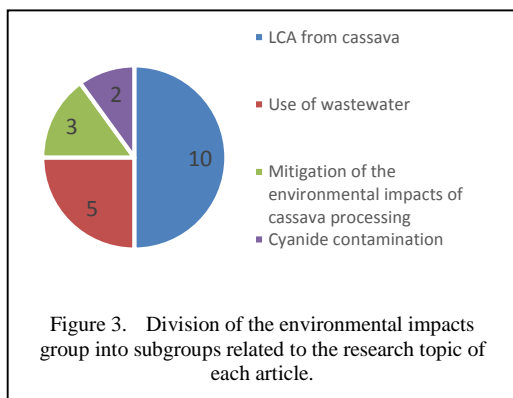


Figure 2. Temporal evolution of articles related to cassava sustainability.



effects of this agricultural product throughout its life cycle.

These data distribution demonstrates the diverse approaches and international researchers concerns about cassava environmental impacts, which are a sound basis for understanding and improving this food towards more sustainable production and processing strategies.

To ensure this bibliographic portfolio was representative, all the bibliographic references of the articles connected to LCA group were grouped together for a deeper analysis on the subject outlined in this review. Table I was

drawn up to facilitate the compilation of article citations.

Another analysis considered relevant by the scientific community in the bibliometric analysis process concerns the impact factor of journals. This is calculated based on the average number of citations that articles published in a specific journal receive during a given period. The higher a journal's impact factor, the greater its visibility and prestige within the scientific community. Therefore, having an article published in a journal with a high impact factor can mean greater visibility for the author and a greater chance for the research carried out.

In this context, during the analysis of the selected articles, it becomes relevant to identify the impact factors associated with these journals. This analysis is presented in Table II, following the same order of articles listed in Table I. The correlation between the journals and their impact factors will provide a more comprehensive understanding of the context in which these articles were published, offering additional insights into the quality and relevance of the academic contributions presented.

It can be observed that the journal with the highest number of publications on the LCA

TABLE I. ARTICLES ON SUSTAINABILITY IN CASSAVA FLOUR/STARCH PROCESSING, WITH A FOCUS ON LCA AND COUNTRIES OF ORIGIN.

	References	Title	Number of citations	Country of origin
1	[21]	Integrated Biorefinery and Life Cycle Assessment of Cassava Processing Residue–From Production to Sustainable Evaluation	1	Brazil
2	[22]	Impacts of utilization patterns of cellulosic C5 sugar from cassava straw on bioethanol production through life cycle assessment	13	China
3	[23]	Comparative sustainability assessments for integrated cassava starch wastes biorefineries	12	South Africa
4	[24]	Life cycle assessment of a biogas system for cassava processing in Brazil to close the loop in the water-waste-energy-food nexus	14	United Kingdom
5	[25]	Potential of biogas production from processing residues to reduce environmental impacts from cassava starch and crisp production-a case study from Malaysia	20	Germany
6	[26]	Development of an optimization mathematical model by applying an integrated environmental indicator for selecting alternatives in cleaner production programs	8	Vietnam
7	[27]	Biogas reduces the carbon footprint of cassava starch: a comparative assessment with fuel oil	39	Thailand
8	[28]	A comparison of energy use, water use and carbon footprint of cassava starch production in Thailand, Vietnam and Colombia	57	France
9	[29]	Environmental impacts of smallholder ethanol production from cassava feedstock for the replacement of kerosene household cooking fuel in Nigeria	7	Nigeria
10	[30]	Reduction of greenhouse gas emissions by biogas utilization in a tapioca starch factory	1	Japan

TABLE II. LIST OF JOURNALS THAT PUBLISHED ARTICLES RELATED TO CASSAVA LCA AND THEIR IMPACT FACTOR RATINGS.

References	Periodics	Impact factor
[21]	Plants	4.658
[22]	Bioresource Technology	11.889
[23]	Journal of Cleaner Production	11.072
[24]	Journal of Cleaner Production	11.072
[25]	Applied Sciences (Switzerland)	2.838
[26]	Journal of Cleaner Production	11.072
[27]	Journal of Cleaner Production	11.072
[28]	Resources, Conservation and Recycling	13.716
[29]	Energy Sources, Part A: Recovery, Utilization and Environmental Effects	2.902
[30]	Kagaku Kogaku Ronbunshu	0.338

theme was the Journal of Cleaner Production. However, the journal Resources, Conservation and Recycling, which published the article titled “A comparison of energy use, water use and carbon footprint of cassava starch production in Thailand, Vietnam, and Colombia” in 2015, has the highest impact factor among the journals analyzed. The data related to the impact factors presented in Table II were extracted from the CAPES journal list, which provides information corresponding to the year 2021.

Keyword co-occurrence is one of the key analyses within bibliometrics used to determine relationships between various research topics and how they are linked to a particular discipline. This analysis can be carried out using a versatile tool called VOSviewer, which allows you to visualize keyword co-occurrence networks. Keyword co-occurrence is basically how often two or more keywords appear together in the title, abstract and/or keyword list of a set of scientific documents. This analysis assists in identifying the primary research themes and their associations.

In VOSviewer, circles indicate keywords, and lines between nodes show the co-occurrence of keywords; together creating a network. The thickness of the edges and the distance between

nodes corresponds to how frequently co-occurrence occurs and its strength.

There are many advantages of co-occurrence analysis in VOSviewer like it finds the major topics and newly emerging themes in a specific area of research, shows correlation among different topics and disciplines. Furthermore, it enables researchers to visualize trends over time such as change in popularity of topics and allows mapping the structure of a research field including central and peripheral topics [31].

Through the VOSviewer platform, several keywords and their respective frequencies of occurrence in the publications were identified, as represented in Fig. 4.

Fig. 4 presents the keyword co-occurrence VOSviewer structure showing the main topics in cassava LCA and their relations among them. Keywords related to plants (botany), starch, and environmental impact were the most frequently occurring terms, recorded 11, 11 and 10 times respectively. From the works analyzed, it was identified that there are patterns of interest and research concentration

It can also be observed in Fig. 4 the color scheme is intended to characterize the seasonality of the articles. The lighter the color, the more recent the article; thus, the keyword environmental impact, in blue, emerges as a new trend in yellow, new tendency in academic research.

The studies assessed different aspects of sustainability along the cassava value chain, specifically focusing on production and processing. As most of these studies are focused on agro-industrial residues, the work in [21] stressed the importance of incorporating processing residues from cassava into biorefineries, pointing LCA as an important method for assessing the environmental and

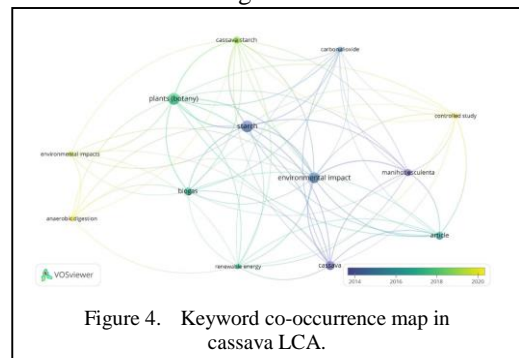


Figure 4. Keyword co-occurrence map in cassava LCA.

economic viability. That analysis can deliver fundamental information for informed decisions in the cassava processing sector by systematically considering environmental and economic facets together.

The works by [22,23] paved the way to more sustainable strategies in bioethanol production and comparative assessment of sustainability within integrated cassava starch residue biorefineries, respectively. The current studies believed in a variety of environmental and socio-economic parameters provides valuable information on planning and executing sustainable realities in this sector.

In the aspect of resource cycle closure, the studies by [24,25] studies potential for biogas production from cassava processing residues and proposes sustainable and environmentally friendly ways to make cassava processing more favorable. These studies are essential to minimize the environmental impacts of processed foods, namely starch and snacks from cassava.

The contributions of [26] provide a mathematical optimization model for the selection of alternatives in cleaner production programs based on an integrated environmental indicator. In the opposite way, [27] make a comparison between environmental impacts of cassava starch production with biogas and fuel oil for motors showing that processes using biogas show lower carbon footprints and this gas can be considered a more sustainable fueling alternative in the cassava processing sector.

Moreover, the comparison studies by [28,30] also suggest that regional differences need to be taken into account for assessing the environmental impacts of cassava starch production processes and respectively, on assessing the environmental advantages in terms of biogas as renewable energy substitute potential for cassava processing sector.

The environmental consequences of cassava to ethanol conversion were also investigated in studies such as that of [29] and other aspects, such as substitution of kerosene by ethanol in home cooking were present allowing outlining a proposal for sustainable initiatives aimed at rural and energy development.

These authors gave an overall perspective of sustainability difficulties and opportunities in cassava chain which require integrated

approaches addressing multiple environmental, economic, and social dimensions to devise more sustainable policies and practices strategically important for large number of communities across the world.

IV. CONCLUSIONS

Cassava is a native agricultural product from the Brazilian territory that stands out as a contributor to food security, income generation and sustainable development. The bibliometric analysis performed in this kind of research can shed some light on the publishing trends between high-impact academic journals within a given context. Based on their high impact factors, bioresource technology, journal of cleaner production and resources conservation and recycling were considered the main journals for these studies, highlighting that topics related to cassava attract much interest from the academic community.


Although some studies related to this are available in the literature, little specific research is conducted on the complete LCA of cassava processing from production to sustainability assessment. This indicates that the potential environmental consequences of this activity must be better understood. The way forward for research might be to refine assessment methods that assess all environmental, social and economic aspects of the entire cassava value chain.

REFERENCES

- [1] Conceição, A. J. (1981). *A mandioca*. Nobel. In M. P. Cereda (Coord.), *Agricultura: Tuberosas amiláceas Latino Americanas*, 4, (pp. 66-82). Fundação Cargill.
- [2] Embrapa. (2021). *Agroenergia*. Available at: <https://www.embrapa.br/en/agencia-de-informacao-tecnologica/tematicas/agroenergia/alcool/materias-primas/mandioca>
- [3] Moura, G. M., & Costa, N. L. (2001). Efeito da frequência e altura de poda na produtividade de raízes e parte aérea em mandioca. *Pesquisa Agropecuária Brasileira*, 36, 1053-1059.
- [4] Lima, L. C. L., Costa, M. A., & Silva, L. L. (2002). Valor nutritivo da parte aérea da mandioca (*Manihot esculenta*, Crantz) em função da densidade e altura da planta. *Magistra*, 14(2), 89-96.
- [5] Nunes Irmão, J., Silva, M. A., & Costa, A. F. (2008). Composição química do feno da parte aérea da mandioca em diferentes idades de corte. *Revista Brasileira de Saúde e Produção Animal*, 9(1), 158-169.
- [6] Ferreira, A. L., Vasconcelos, A. L. S., & Queiroz, M. A. (2009). Produção e valor nutritivo da parte aérea da mandioca, maniçoba e pornuña. *Revista Brasileira de Saúde e Produção Animal*, 10(1), 983-990.

- [7] Dantas, A. G. de M., Lopes, S. S., & Cruz, M. M. (2010). Análises bromatológicas de onze cultivares de mandioca. *Revista Caatinga*, 23(3), 130-136.
- [8] Moreira, G. L. P. (2011). *Intervalo entre podas em mandioca* (Master's thesis, Universidade Estadual do Sudoeste da Bahia). Vitória da Conquista, BA.
- [9] Cereda, M. P., & Vilpoux, O. F. (2003). *Tecnologia, usos e potencialidades de tuberosas amiláceas latino-americanas*, 3, (p. 711). Fundação Cargill.
- [10] Zhang, M., Ma, X., Wang, Z., & He, X. (2016). Biorefinery approach for cassava-based industrial wastes: Current status and opportunities. *Bioresource Technology*, 215, 50-62.
- [11] Czaikoski, A., Cunha, R. L., & Menegalli, F. C. (2020). Rheological behavior of cellulose nanofibers from cassava peel obtained by combination of chemical and physical processes. *Carbohydrate Polymers*, 248, 116744.
- [12] Leite, A. L. M. P., Zanon, C. D., & Menegalli, F. C. (2017). Isolation and characterization of cellulose nanofibers from cassava root bagasse and peelings. *Carbohydrate Polymers*, 157, 962-970.
- [13] Alrefai, A. M., Mendez, D., Patel, M. K., Benes, D. G., Riegel, A. L., & Shaikh, R. H. (2020). Impact of starch from cassava peel on biogas produced through the anaerobic digestion process. *Energies*, 13(11), 2713.
- [14] Padi, R. K., & Chimphango, A. (2020). Commercial viability of integrated waste treatment in cassava starch industries for targeted resource recoveries. *Journal of Cleaner Production*, 265, 121619.
- [15] Weligama, V. T., & Karim, M. A. (2022). A comprehensive review on the properties and functionalities of biodegradable and semibiodegradable food packaging materials. *Comprehensive Reviews in Food Science and Food Safety*, 21(1), 689-718.
- [16] Guinée, J. B., Heijungs, R., Huppes, G., Zamagni, A., Masoni, P., & Buonamici, R. (2011). Life cycle assessment: Past, present, and future. *Environmental Science & Technology*, 45(1), 90-96.
- [17] US EPA. (2006). *Life cycle assessment: Principles and practice*. National Risk Management Research Laboratory, U.S. Environmental Protection Agency.
- [18] Goedkoop, M., Oele, M., Vieira, M., & Jeroen, C. (2009). A life cycle impact assessment method which comprises harmonised category indicators at the midpoint and the endpoint level. *Potentials*, 1-44.
- [19] Guedes, V. L., & Borschiver, S. (2005). Lei de Zipf, fator de impacto e os indicadores de produção científica. *Ciência da Informação*, 34(2), 63-72.
- [20] Van Eck, N. J., & Waltman, L. (2020). *VOSviewer manual: Manual for VOSviewer version 1.6.15*. Centre for Science and Technology Studies (CWTS), Leiden University.
- [21] Andrade, L. R. S., Zhang, L., Agbor, V. B., Zhang, M., & Yuan, W. (2022). Integrated biorefinery and life cycle assessment of cassava processing residue – From production to sustainable evaluation. *Plants*, 11(24), 3577.
- [22] Lyu, H., Smith, R., & Golub, A. (2021). Impacts of utilization patterns of cellulosic C5 sugar from cassava straw on bioethanol production through life cycle assessment. *Bioresource Technology*, 323, 124586.
- [23] Padi, R. K., & Chimphango, A. (2021). Comparative sustainability assessments for integrated cassava starch wastes biorefineries. *Journal of Cleaner Production*, 290, 125171.
- [24] Lin, H., Zhang, M., Agbor, V. B., & Yuan, W. (2021). Life cycle assessment of a biogas system for cassava processing in Brazil to close the loop in the water-waste-energy-food nexus. *Journal of Cleaner Production*, 299, 126861.
- [25] Lansche, J., Smith, R., & Golub, A. (2020). Potential of biogas production from processing residues to reduce environmental impacts from cassava starch and crisp production—a case study from Malaysia. *Applied Sciences*, 10(8), 2975.
- [26] Van Tran, T., Zhang, L., Agbor, V. B., & Yuan, W. (2017). Development of an optimization mathematical model by applying an integrated environmental indicator for selecting alternatives in cleaner production programs. *Journal of Cleaner Production*, 154, 295-308.
- [27] Hansupalak, N., Smith, R., & Golub, A. (2016). Biogas reduces the carbon footprint of cassava starch: A comparative assessment with fuel oil. *Journal of Cleaner Production*, 134, 539-546.
- [28] Tran, T., Zhang, L., Agbor, V. B., & Yuan, W. (2015). A comparison of energy use, water use and carbon footprint of cassava starch production in Thailand, Vietnam and Colombia. *Resources, Conservation and Recycling*, 100, 31-40.
- [29] Ohimain, E. I. (2013). Environmental impacts of smallholder ethanol production from cassava feedstock for the replacement of kerosene household cooking fuel in Nigeria. *Energy Sources, Part A: Recovery, Utilization, and Environmental Effects*, 35(16), 1560-1565.
- [30] Kamahara, H., Hashimoto, T., Yoshida, M., & Uchiyama, S. (2012). Reduction of greenhouse gas emissions by biogas utilization in a tapioca starch factory. *Kagaku Kagaku Ronbunshu*, 38(5), 299-304.
- [31] Cobo, M. J., López - Herrera, A. G., Herrera - Viedma, E., & Herrera, F. (2011). Science mapping software tools: Review, analysis, and cooperative study among tools. *Journal of the American Society for information Science and Technology*, 62(7), 1382-1402.

Power System Stability Analysis in Presence of Renewable Energies

Nour El Yakine Kouba¹ , Amel Brik²

^{1,2}Laboratory of Electrical and Industrial Systems, University of Sciences and Technology Houari Boumediene (USTHB), Algiers, Algeria

¹nourel yakin.kouba@usthb.edu.dz, ²abrik2022@gmail.com

Abstract—This paper deals with power system stability analysis in presence of renewable energies. The main goal was assessing the impact of renewable energy sources on power system stability. This study can be used to enhance frequency and voltage regulation models to incorporate more renewable energy variability into power grid. The IEEE 39 bus have been used as test system. Three scenarios have been performed to enhance grid resilience against disturbances caused by renewable energy fluctuations. The proposed system as simulated without and with wind farm and solar PV generator integration with variable penetration factor.

Keywords - power system, stability, renewable energies, wind farm, solar PV generator

I. INTRODUCTION

Presently, system stability and control is considered as a vital aspect of managing power system efficiently and ensuring security. Power system operation and control comprise various actions such monitoring, controlling, and optimizing the generation in the aim to monitor both of voltage and frequency. Also, this system ensure the balance between the generation output from various power plants including the conventional thermal, hydroelectric, and the renewable power generation station such wind turbines, and solar PV generator to keep stable voltage and frequency system in the grid [1-3]. Conventionally, Ensuring the stability of the power grid by implementing advanced control strategies like automatic generation control (AGC), under-frequency load shedding (UFLS),

and secondary controllers. However, this task may be difficult in case of renewable energies integration. Effective and robust power system operation and control require the use of modern technologies such SCADA systems and energy management systems (EMS) to make decisions promptly and maintain grid reliability in presence of disturbances [3-6]. Nowadays, analyzing modern electric power networks in presence of renewable energies such solar PV generator and wind farm involves studying the integration of such sources into the classical grid. The insertion of a mix of green power generation sources brings many challenges such as intermittent generation, varying power output, and the need for grid stability to cope with the fluctuations caused by wind and solar variations. On the other hand, renewable sources can contribute to grid resilience by diversifying the energy mix and reducing dependence on fossil fuels. In addition, using smart technologies and artificial intelligence methods in coordination with supplementary material like energy storage systems, and FACTS devices can help to increase the integration ratio of renewable energies and improves power system stability [4-10].

In this context, this paper deals with power system stability analysis in presence of renewable energy sources including wind and solar PV generators. The rest of the paper is organized as follows. Section II presents the analytic model of the investigated IEEE 39 bus system. The obtained simulation results are presented in Section III. Finally, Section IV concludes the paper.



II. POWER SYSTEM MODEL

In this work, the IEEE 39 bus power system shown in Fig. 1 [11,12] was used as test. This system was simulated to show the integration impact of solar PV generator and wind farm on power system stability. As stated in the introduction, both of frequency and voltage profile must satisfy specific conditions for the system can remain its normal state. To maintain a perfect power balance, both of active and reactive powers need to be in balance with the changing load powers. The adopted generator model for this study is shown in Fig. 2 and Fig. 3.

In this work a typical IEEE DC1 AVR system was adopted as shown in Fig. 4. The main task of the AVR system is to keep the voltage in the system within acceptable limits. In addition, the AVR system was supported with a power system stabilizer (PSS) to modify the voltage regulation to damp the oscillations sufficiently. On the other hand, for frequency regulation there are two control loops: primary and secondary as shown in Fig. 5. The purpose of these loops is to achieve active power balance in the system by keeping the system frequency at the scheduled value [10-18].

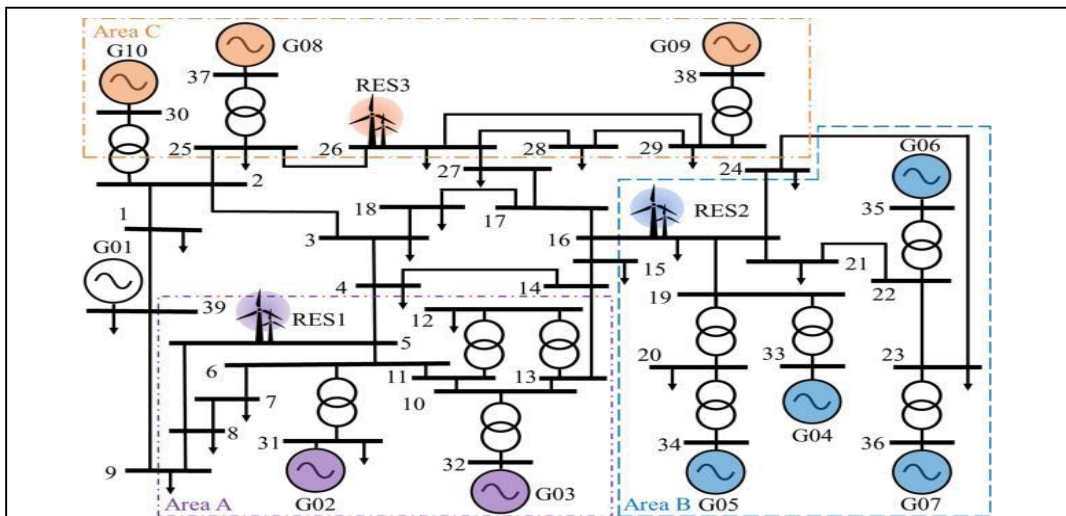


Figure 1. IEEE 39 Bus Model [16].

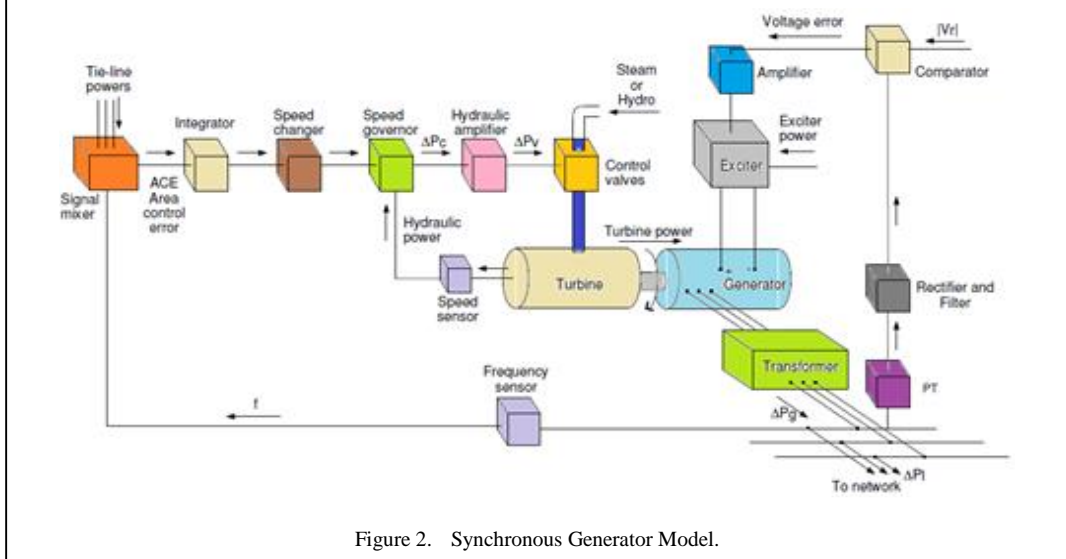


Figure 2. Synchronous Generator Model.

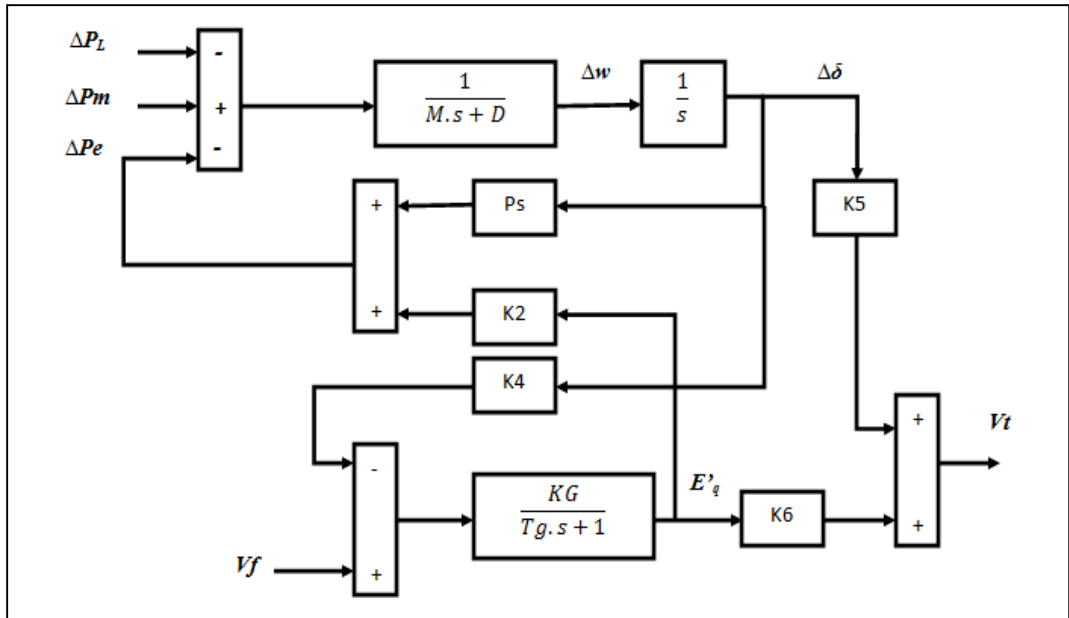


Figure 3. Dynamic Generator Model.

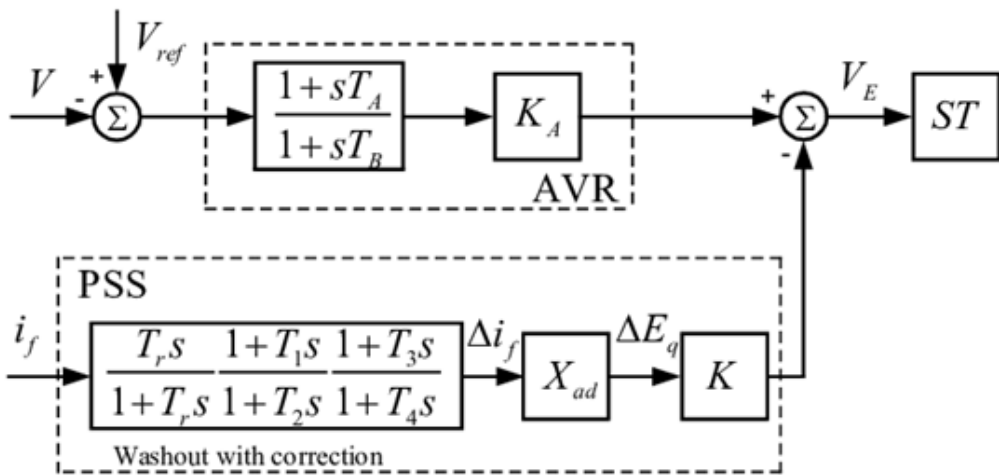


Figure 4. Voltage Controller Model.

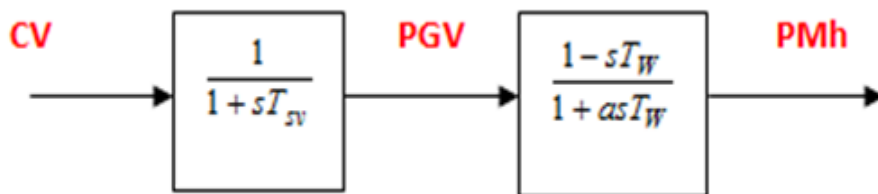


Figure 5. Frequency Regulation Model (LFC).

The mathematical model for the test system can be given by:

$$M \frac{d\Delta f}{dt} = \Delta P_m - \Delta P_e, \quad (1)$$

$$\Delta P_e = P_s \Delta \delta + K_2 E' q, \quad (2)$$

$$\Delta V_t = K_5 \Delta \delta + K_6 E' q, \quad (3)$$

$$\frac{dE' q}{dt} = \frac{1}{T_g} \cdot (KG \cdot (V_f - K_4 \Delta \delta) - E' q), \quad (4)$$

$$\frac{dP_{gv}}{dt} = \frac{1}{T_{sr}} (SC - (KG \cdot df) - P_{gv}), \quad (5)$$

$$\frac{dP_m}{dt} = \frac{1}{T_{sc}} (P_{gv} - P_m), \quad (6)$$

$$ACE = \Delta P_{Tij} + \beta_i \Delta \omega_i, \quad (7)$$

$$SC = K_p \cdot ACE + \int K_i \cdot ACE + K_d \cdot \frac{dACE}{dt}, \quad (8)$$

$$\frac{dVR}{dt} = \frac{1}{T_R} (V_t - VR), \quad (9)$$

$$V_e = V_{ref} - V_R + V_{PSS}, \quad (10)$$

$$VA = V_{A1} + V_{A2}, \quad (11)$$

$$\frac{dV_{A1}}{dt} = \frac{1}{T_B} (VA - V_{A1}), \quad (12)$$

$$\frac{dV_{A2}}{dt} = T_C \cdot V_{A1}, \quad (13)$$

$$\frac{dV_f}{dt} = \frac{1}{T_A} (K_A \cdot VA - V_f), \quad (14)$$

$$\Delta P_{Tij} = \frac{T}{S} (\Delta \omega_i - \Delta \omega_j). \quad (15)$$

III. SIMULATION RESULTS

In this part, three scenarios have been analyzed to show the impact of renewable energies integration on power system stability. In the first scenario, the IEEE 39 bus was simulated without PV generator and wind farm and the simulation results for voltage and speed variations are presented in Figs. 6 and 7. In the second scenario, a 10% penetration ratio of PV and wind power generation have been installed in the system, where the integration impact on voltage profile was presented in Figs. 8 and 9. In the third scenario, the penetration ratio have been increased up to 50% and the voltage profile was presented in Figs. 10 and 11.

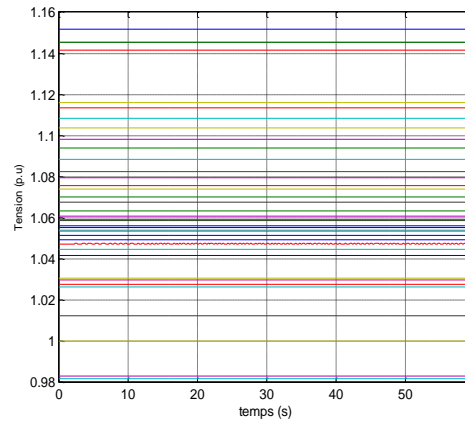


Figure 6. Voltage profile without integration.

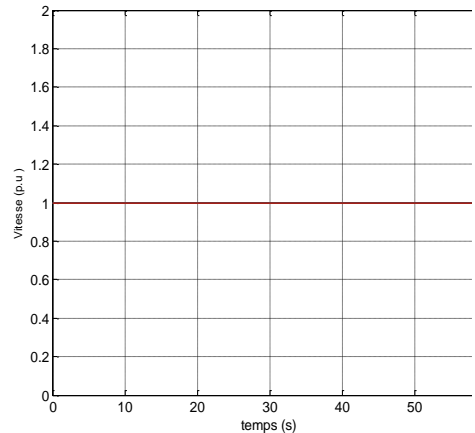


Figure 7. Speed variations without integration.

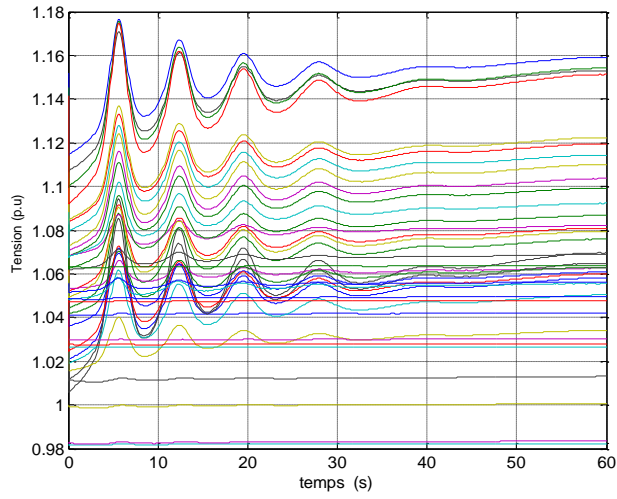


Figure 8. Voltage profile with 10% integration.

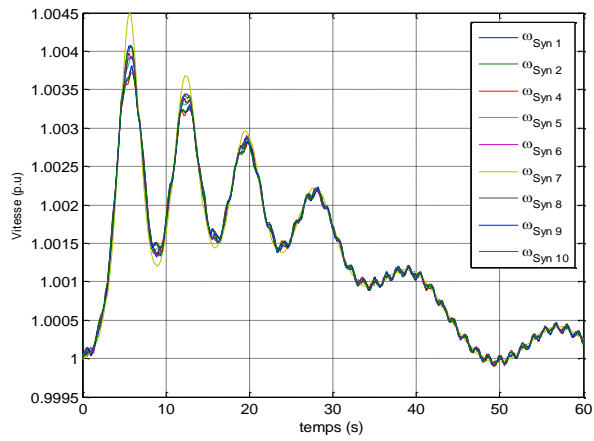


Figure 9. Speed variations with 50% integration.

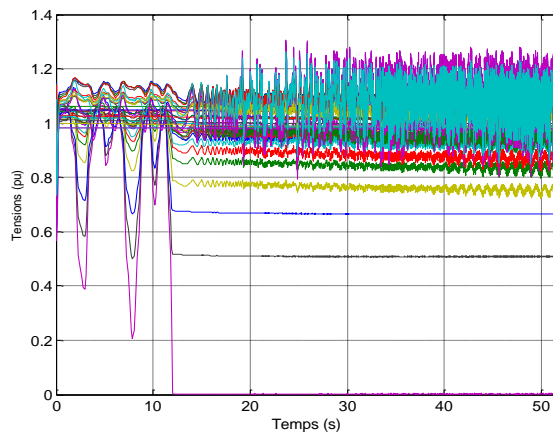


Figure 10. Voltage profile with 50% integration.

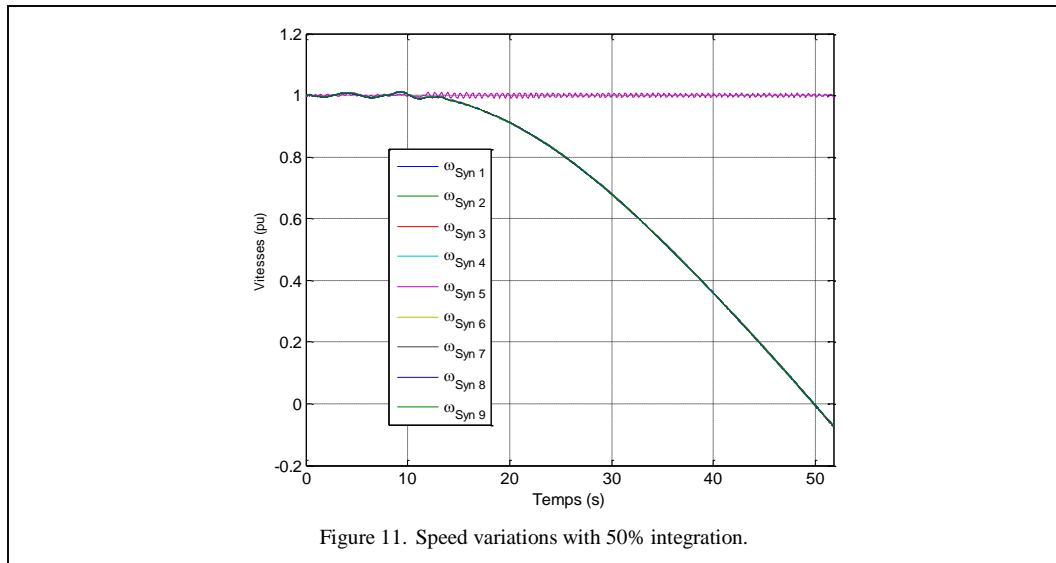


Figure 11. Speed variations with 50% integration.

It is clear from the presented results that the IEEE 39 bus system was stable before integration of PV and wind power generation, in case of 10 % penetration ratio the system stay stable, where with fort penetration of 50% the power system become instable with several oscillation that can affect system security which needs to act the auxiliary regulation action of frequency and voltage control named load frequency control (LFC) and automatic voltage regulator (AVR) devices.

IV. CONCLUSION

In this work, the integration impact of PV and wind generator on IEEE 39 bus power system stability was analyzed. The simulation was conducted in presence of various values of penetration ratio including stable and instable case studies. This work can be extended using artificial intelligent methods and nature inspired optimization algorithm with coordination of FACTS devices and energy storage system to enhance system stability. Also, various types of wind turbines and PV technologies can be integrated and tested to show the robustness of frequency and voltage regulation loops in keeping system stability during disturbances.

REFERENCES

[1] Kouba, N. E. Y., & Sadoudi, S. (2022). Optimal Energy Management of Hybrid MicroGrid Using Storage System and Fuzzy-GA Method. *Journal of Renewable Energies*, 129-141.

[2] Brik, A., Kouba, N. E. Y., & Ladjici, A. A. (2024). Power System Transient Stability Analysis

Considering Short-Circuit Faults and Renewable Energy Sources. *Engineering Proceedings*, 67(1), 42.

[3] Brik, A., Kouba, E. N., & Ladjici, A. A. (2023). Power System Stability Analysis in Presence of Renewable Energies and FACTS Devices. In *The 1st national conference on emergent technologies in electrical engineering (NCETEE'23)*. October 7-8, Setif, Algeria.

[4] Liang, K., Wang, H., Pozo, D., & Terzija, V. (2024). Power system restoration with large renewable Penetration: State-of-the-Art and future trends. *International Journal of Electrical Power & Energy Systems*, 155, 109494.

[5] Rashid, S. M. (2024). Employing advanced control, energy storage, and renewable technologies to enhance power system stability. *Energy Reports*, 11, 3202-3223.

[6] Saleem, M. I., Saha, S., Roy, T. K., & Ghosh, S. K. (2024). Assessment and management of frequency stability in low inertia renewable energy rich power grids. *IET Generation, Transmission & Distribution*, 18(7), 1372-1390.

[7] Guo, W., Qureshi, N. M. F., Jarwar, M. A., Kim, J., & Shin, D. R. (2023). AI-oriented smart power system transient stability: the rationality, applications, challenges and future opportunities. *Sustainable Energy Technologies and Assessments*, 56, 102990.

[8] Senyuk, M., Safaraliev, M., Kamalov, F., & Sulieman, H. (2023). Power system transient stability assessment based on machine learning algorithms and grid topology. *Mathematics*, 11(3), 525.

[9] Ghosh, S., Bakhshizadeh, M. K., Yang, G., Kocewiak, Ł., Pal, B. C., & Nadarajah, M. (2023). Nonlinear stability investigation of type-4 wind turbines with non-autonomous behavior based on transient damping characteristics. *IEEE Access*, 11, 76059-76070.

[10] Liaqat, M., Alsuwian, T., Amin, A. A., Adnan, M., & Zulfiqar, A. (2024). Transient stability enhancement in renewable energy integrated multi-microgrids: A comprehensive and critical analysis. *Measurement and Control*, 57(2), 187-207.

- [11] Chavan, K., Patil, G. B., & More, R. (2024, February). Transient stability analysis of IEEE test system. In *2024 IEEE International Conference for Women in Innovation, Technology & Entrepreneurship (ICWITE)* (pp. 691-695). IEEE.
- [12] Rahmouni, W., & Benasla, L. (2017, October). Transient stability analysis of the IEEE 39-bus power system using gear and block methods. In *2017 5th International Conference on Electrical Engineering-Boumerdes (ICEE-B)* (pp. 1-6). IEEE.
- [13] Kouba, N. E. L. Y., Mena, M., Hasni, M., & Boudour, M. (2017). Computational intelligence applied to power system restoration: a case study of monarch butterfly optimization algorithm. In *International Conference on Automatic control, Telecommunication and Signals* (pp. 1-6).
- [14] Shahriyari, M., Khoshkhou, H., & Guerrero, J. M. (2022). A novel fast transient stability assessment of power systems using fault-on trajectory. *IEEE Systems Journal*, *16*(3), 4334-4344.
- [15] Roy, S., & Pico, H. N. V. (2022). Transient stability and active protection of power systems with grid-forming pv power plants. *IEEE Transactions on Power Systems*, *38*(1), 897-911.
- [16] Hamilton, R. I., Papadopoulos, P. N., Bukhsh, W., & Bell, K. (2022). Identification of important locational, physical and economic dimensions in power system transient stability margin estimation. *IEEE Transactions on Sustainable Energy*, *13*(2), 1135-1146.
- [17] Aygul, K., Mohammadpourfard, M., Kesici, M., Kucuktezcan, F., & Genc, I. (2024). Benchmark of machine learning algorithms on transient stability prediction in renewable rich power grids under cyber-attacks. *Internet of Things*, *25*, 101012.
- [18] Zheng, R., Liu, Q., Jiang, Y., Chen, S., & Hu, W. (2023). Transient stable region of power systems incorporating stochasticity of variable renewable energies and system contingencies. *International Journal of Electrical Power & Energy Systems*, *144*, 108523.

A Review on Cyber Attack Detection and Defense Strategies in Cyber-physical Power Systems

Erdem Koca¹, Musa Terkes², Alpaslan Demirci³

¹Electrical Engineering Department of Yıldız Technical University, Istanbul, Türkiye

¹kocaa.erdem@gmail.com, ²musa.terkes@yildiz.edu.tr, ³ademirci@yildiz.edu.tr

Abstract—Malicious cyber-attacks on efficient modern power systems based on the Internet of Energy, which are digitized and include advanced intelligence elements, coordinating complex units such as measurement, computation, execution, and communication, cause societal risks on a small or large scale. The penetration of intelligent electronic devices, simultaneous metering technology, and information communication raise vulnerability issues. Considering the possibility of large-scale attacks due to the tight coupling between the physical and cyber layers, timely detection of cyber intrusions and robustness of defenses are critical for the reliability of advanced communication network-based cyber-physical power systems (CPPS). Accordingly, this paper provides an overview of security assessment, focusing on detecting possible cyber-attacks and defense strategies that cause instability, vulnerability, and insecurity in CPPSs. A signature, anomaly and behavior-based, hybrid, AI-scale, and state observer cyber-attack detection techniques are described, and defense fundamentals in cybersecurity, such as secure authentication, encryption, trusted access and defense technologies, and resource utilization, are discussed. Developing cyber-attack detection and defense strategies that can flexibly and dynamically respond to the unique temporal and spatial characteristics of CPPS will improve the modernization of the power grid.

Keywords - cyber security, cyber attack, cyber-physical power systems, malware, detection and defense strategies

I. INTRODUCTION

A stable and reliable power supply can be obtained using large-scale sensing measurement mechanisms, complex information communication networks, and optimizing operational processes. Recently, the traditional perception of the power system has collapsed. The scale of the cyber network has dramatically increased, and the energy internet has entered into active communication with intelligent electronic devices. Accordingly, the intersection of traditional power systems with physical equipment, information, and communication technologies, and hence cyber systems, advanced metering infrastructure, computational intelligence, and cyber-secure communication technologies form multidimensional and heterogeneous cyber-physical power systems (CPPS). Integrating control, computation, and communication functions, these structures enable smart grid technologies and the bi-directional flow of electricity and information. CPPSs improve power quality and reliability while avoiding unnecessary backup plant installation via efficient plant utilization. Enhances resilience to failures while strengthening grid capacity. Promotes predictive maintenance and self-healing responses to outages. The Internet of Things has reached this point by jointly pursuing big data, cloud computing, and networking technologies. However, it should be noted that cyber system performance will significantly impact physical power system operating characteristics.



CPPSs include most functions of the unpredictable power system network, such as generation, transmission, distribution, utilization, and sale of electricity. They are dynamic and flexible to manage real-time physical power system monitoring and control and operational decisions with embedded systems. The physical layer is more governed by physical regulations and refers to the usual power systems that operate sustainably. It is also dynamic and evaluates the physical relationship of energy flow. The cyber layer is a static infrastructure and includes information and communication services, control, and embedded systems. The comparison of cyber and physical systems is described in Table I [1]. CPPSs that assess the intersection of related systems are modeled in three subcategories: connectivity, interaction, and dependency. The discrete actions of the physical and cyber systems are evaluated in the connectivity model, while their impact on each other constitutes the interaction model. The dependency model determines the level of interdependence of both systems. A connection protocol is often used for the effectiveness of communication links between heterogeneous systems. The protocol addresses heterogeneity at three levels: functional interoperability, policy regulation, and performance assurance. Functional interoperability is the intersection rather than cyber and physical integration. Policy regulation refers to the plan changes existing operators implement for economic and operational performance. In contrast, performance assurance, it addresses defense strategies against attacks and failures, control of

sensitive parameters in the power system network, measurement accuracy, and data processing and analysis applicability. From another perspective, there are three levels of interaction in CPPS: first, second, and third. The relationship of components in the power system network, such as generators, transformers, and transmission lines, with the power system controller is evaluated at the first level. The information from the core components is transferred to the power system controller, and the control signal is calculated. Then, output feedback is provided to the core components for operational optimization of the power grid. A second interaction level occurs between the power system controller and the communication infrastructure. All functions of subsystems, such as sensors, actuators, interfaces, control, computation, and communication, are coordinated with the information and communication infrastructure. At the third level of interaction, the communication infrastructure interacts with the cyber system. The main and auxiliary system, main and communication server, two-way communication structure, computing stations, intelligent control application software, cyber-attack security, and defense mechanism are the sub-components of the cyber system. Operations such as load and condition forecasting, parameter optimization, voltage control, fluctuation analysis, data monitoring, model verification, and stability assessment are carried out with the cyberinfrastructure. Another view is that CPPS can be evaluated as component, communication and functional layers. The first layer consists of

TABLE I. COMPARING CYBER AND PHYSICAL SYSTEMS DEPENDING ON THEIR CHARACTERISTICS.

Characteristics	Physical System	Cyber System
Components	Generator, transformer, transmission line, circuit breaker, protective relay, load, etc.	Control systems, computing devices, communication networks
Nature of System	Continuous, dynamic behavior	Discrete, static behavior
Modeling	Differential-algebraic equations	Difference equations
System State	Energy flow	Information flow
Branch Model	Power grid model – energy generation, energy transmission, and energy distribution	Information flow-oriented model – data transmission, data processing, and data pool
Condition	Generation and load balance, power transmission limits	Interdependent operation balance among control, computing, and communication functions
Contingency	Physical contingency	Cyber contingency
Types of Contingencies	Line fault, generator outage, load outage, environmental effect, etc.	Cyber-attacks, communication latency, malicious control effects, etc.
Stability & Security	Power system stability & security	Networked control system stability & cyber security
Event Synchronization	Asynchronous	Synchronous

primary (generator, transformer, etc.), secondary (protection relay, sensor, actuator, etc.), and interconnected electrical devices. The secondary equipment collects operational information from the primary components. The communication architecture provides the coordination between all components of the power system network at the second level. Communication technologies such as the IEEE 802 series, network traffic, and routing components perform a functional process at this level. All operational information is stored and processed in the control center at the last level. Decision-making and defense mechanisms, control algorithms, master stations, web, communication and application servers, databases, and human-machine interfaces are the brains of centralized operations. Information and functional processes evaluate easy information exchange, coordinated interoperability, and international interface procedures, and the main station elements perform calculations.

The expansion of power system networks with increasing load demand and the growth of cyber system size has led to deploying many intelligent electronic devices (IEDs) in the network. Besides IEDs, cyber assets such as routers, Ethernet switches, and operating and business systems are also distributed in CPPS

The integration of information and communication technologies (ICTs) to perform actions such as power and information flow between cyber and physical systems has occurred over time. While the digitalized electricity grid guarantees efficient operations, it is vulnerable to cyber and other attacks due to the complex interdependence between cyber and physical systems. Stability, vulnerability, reliability, and security are its main weaknesses. Vulnerabilities, especially in cyber assets, increase the risk of external threats and attacks. Since cyber-attacks may not directly damage CPPS infrastructure, assessing cyber and physical daily actions over time is essential. Cyber system failures and attacks cause most outages in electricity grids. For example, the risk of a nuclear threat emerged in 2010 when the malicious Stuxnet worm infiltrated the SCADA system of the Bushehr Nuclear Power Plant in Iran [2]. Another example occurred in 2014 when the Dragonfly team infiltrated malicious software in US and European energy companies [3]. A cyber-attack in 2015 on the Ukrainian power system infrastructure caused widespread power outages [4]. A year later, malicious software took many computers to the Israel

power grid offline [5]. According to a report by the University of Cambridge, power grid outages in the US due to cyber-attacks caused an economic loss of at least 243 billion dollars [6]. Considering the relevant issues, it is mandatory to configure and optimize the cyber side rather than assessing the impacts on the physical power system in case of cyber threats to ensure the safe operation of CPPS.

Its complexity and critical functionality make it more valuable to comprehensively examine the detection and defense mechanisms that CPPSs will use against cyber-attacks. Considering the close interdependence of information, communication, and physical layers, even minor vulnerabilities can cause irreversible infrastructure damage and economic imbalances. In this case, it is necessary to know the techniques that can detect the presence of a cyber-attack and the defense mechanisms formed accordingly. The most critical elements of cyber security analysis, cyber-attack detection methods, and defense mechanisms are the main inspirations of this study. Two main interrelated problems and their solutions, which are at the center of attention of researchers interested in cyber security, are approached from a strategic and technological perspective. The CPPS phenomenon, its evolution, and modernity are described, and signature, anomaly and behavior-based, state observer, and AI-scale detection methods are discussed in a functional cost-benefit relationship. Innovations such as secure authentication, encryption and trusted access technologies are introduced to expand cybersecurity coverage at the strategic scale. Section I discusses the development of CPPS, its functional uses, and security threats, Section II explains cyber-attack detection techniques, and Section III presents the defense mechanism from a technological perspective. Section IV outlines the conclusions of the review and future directions for cybersecurity.

II. CYBER ATTACK DETECTION IN CYBER-PHYSICAL POWER SYSTEMS

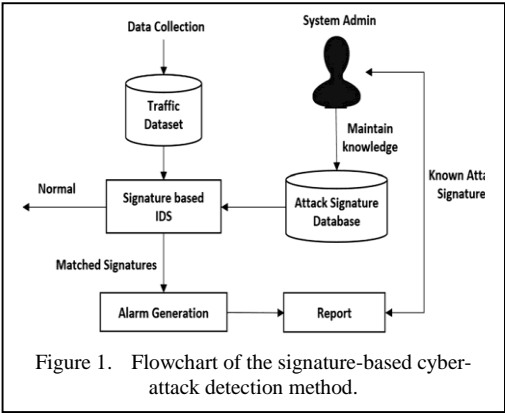
Cybersecurity attack detection requires a comprehensive effort that includes data collection and analysis, real-time monitoring and response, and intervention to ensure system security. In particular, data on network traffic, system event logs, and control commands from SCADA systems, sensors and actuators, and other control devices are collected. It is directed to the pre-processing stage to make it suitable for

analysis. Data analysis is initiated after preprocessing, such as cleaning, normalization, and noise reduction. Pattern recognition techniques are used to identify normal and abnormal behavior patterns, and detection algorithms are developed to identify abnormal activities. Data deviations in the analysis results represent potential attacks and defense strategies against attacks are implemented. Detailed reports on the attack are prepared concerning the actual event. The system's vulnerabilities are identified, and necessary updates and improvements are made. Such a plan can guarantee the reliability of the CPPS.

A. Cyber Attack Detection Methods

1) Signature-based methods

Signature-based method aims to detect anomalous activity in CPPS using known attack models and signatures. Its functional processes include storing attack signatures in a database and continuously comparing event logs of the system's network traffic with the stored signatures. Intrusions in the monitored environment that match the signatures stored in the database are considered attacks. Upon detection of a known attack, an alarm is triggered, and the type of attack is detected quickly and accurately. Since not every activity and network traffic in the monitored environment is evaluated and only known signatures in the database are searched, there is very little memory overhead. Although it analyzes the known threat payload, especially in system calls, the attacker's possible signature change in known attacks can easily bypass the defense strategy. On the other hand, it does not cause unnecessary actions in the system and avoids overloads in case of low false alarms, known as false positives. Overall, Fig. 1 shows the flowchart of the signature-based cyber-attack detection method [7].



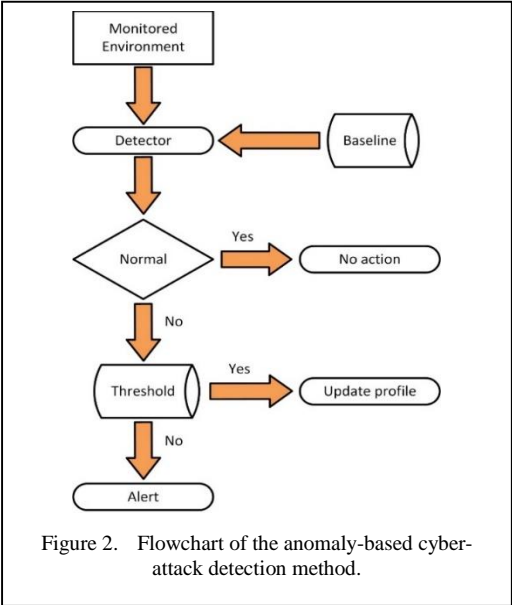
Intrusion detection systems, while easier to modify and improve than distributed signatures or rules, require regular maintenance of the information they store. In addition, the method needs to constantly update itself and have an extended signature database. Data from the traffic network is sent to the signature-based detection strategy and checked for matching with the signature profile in the database. An alarm is produced if there is a match, and the generated report is sent to the system administrator as a known cyber-attack signature. The administrator retains the information and sends the cyber-attack signature to the signature-based cyber intrusion detection method.

2) Anomaly-based methods

Anomaly-based method detects cyber-attacks by learning the expected behavior of CPPS operations and monitoring abnormal deviations. The analyzer model with detection capability identifies unknown attacks or zero-day vulnerabilities without any updates to the system. It uses data collected during task-specific operations to create operational models. It is more effective than signature-based strategies in detecting new unknown cyber-attacks because it knows how the system will work periods during normal operations thanks to patterns and is not dependent on existing signatures. It obtains the learned behavior of the monitored system by comparing the activity with a baseline profile. Profiles can be fixed or have a dynamic process. Especially in dynamic profiles, extra load is added to the system as the attack detection and security profile is updated. The cyber-attack defense action shows limited performance if the attack is spread over a long period. Since the attack will be part of the profile, a defined threshold should be used, and intrusions should be detected. Fixed profiles are more effective in detecting anomalies from normal behavior. Another aspect is related to classification: techniques based on data mining, statistics, and machine learning (ML). Statistics-based strategies are often used to detect attacks accurately. In the learning phase, statistical methods are applied to create two profiles in addition to the existing profile for intrusions whose anomaly is marked according to the base profile and the threshold settings of the monitored environment. The threshold is set based on the behavior of the monitored system. Technical anomaly monitoring in knowledge/data mining strategies is automated and increases the burden on the system [8]. It

undertakes a complex duty cycle in detecting, recognizing, and classifying anomaly conditions and generates the falsest positive and negative signals. However, the intensive use of memory resources should be considered. Situational or specification-based analysis to identify appropriate protocol anomalies is more aligned with ML techniques that work by analyzing system calls. On the other hand, developing a practicable and robust operational model is a comprehensive and challenging process, underscoring the complexity and importance of the task. However, the flexibility and power of artificial intelligence (AI) and ML can eliminate partial aspects of the drawback. This provides a flexible and powerful solution to ensure the system's security, and Fig. 2 illustrates the functional process of anomaly-based cyber intrusion detection [9]. A detector compares events observed in the cyber environment with the baseline profile. If the events match the baseline profile, no action is taken.

Otherwise, the profile is updated, provided it is within acceptable threshold ranges. Understanding the difference between the two methods is crucial for network security professionals, IT professionals, and researchers. An anomaly is detected if it is outside the threshold range, triggering the alert. Activity profiles are created based on network traffic, anomalies are detected, and a report is produced. On the contrary, the signature-based method compares the signature stored in the database with the network traffic status, applies the



security rule based on the threshold, and provides a report for the threat. The difference in their procedures is explained in Fig. 3 via the comparative process of signature-based and anomaly-based methods [10].

3) Behavior-based method

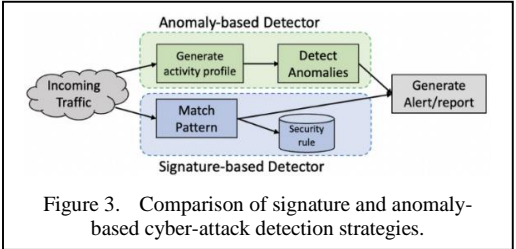
Behavior-based method monitors the expected behavior of CPPS components, detecting cyber-attacks from deviating behavior in normal operations. It generates behavioral profiles of system components using data from real-time monitoring. Because it dynamically considers the relationships and interactions between system components, detecting new cyberattacks in complex and challenging system operations is more effortless. However, it must accurately identify and update behavioral profiles, as potential errors can lead to high false positive rates. With continuous monitoring and real-time analysis, CPPS provides a flexible and dynamic solution for security.

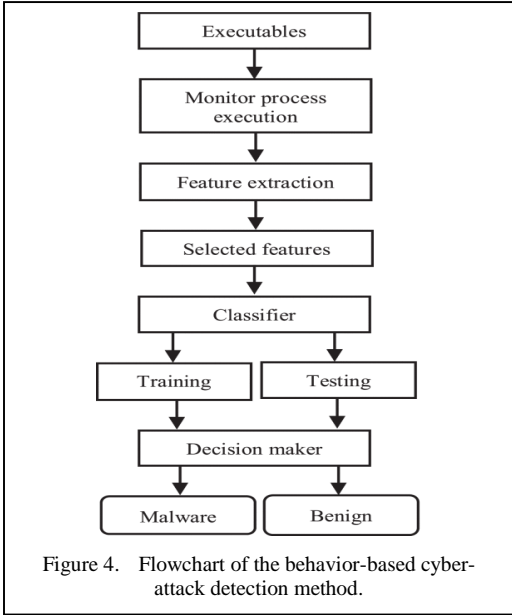
Fig. 4 shows a block diagram of behavior-based cyber-attack detection [11]. The following techniques are mostly used in behavior-based detection: automated analysis using sandboxes, monitoring system calls, process monitoring, and file changes [12], and comparing registry snapshots [13]. In this way, a dataset is created by detecting behaviors and extracting features from data mining, and specific features are selected. The selected features are classified to create training and test data, and the decision-making mechanism is trained and then tested for prediction performance.

Finally, it is determined whether the behavior in cyberspace is benign or malignant.

4) Hybrid methods

Hybrid attacks reinforce the cybersecurity infrastructure and overcome the shortcomings of individual solutions by combining the advantages of two or more defense strategies to detect known and unknown intrusions. It integrates the benefits of signature and anomaly-based detection methods while detecting a more



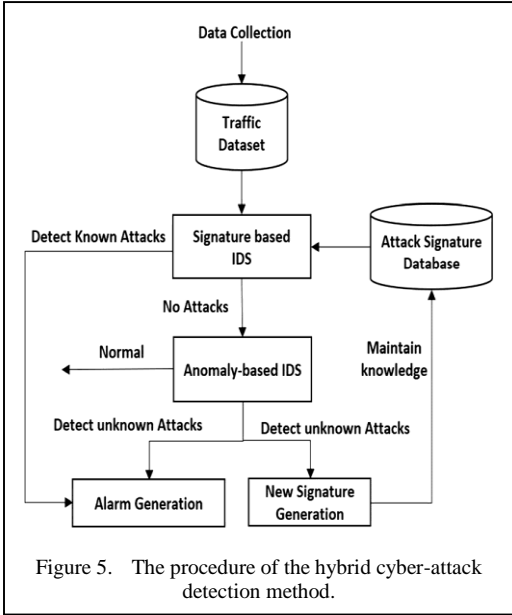


comprehensive range of attacks. It facilitates the detection of unknown attacks by learning the system's normal behavior while using updated signature models created primarily via modules to detect known attack patterns quickly and accurately. Especially for normal behavior, anomaly-based detection modules create a bidirectional approach in the known and unknown attack pool. Since signature and anomaly-based detection methods must be managed, integration and coordination issues may be encountered. However, it guarantees lower false positives and higher accuracy rates, providing a flexible, dynamic, and extended cybersecurity service for CPPSs. Responds quickly to existing threats and proactively detects new threats via real-time analysis and continuous monitoring. Fig. 5 summarizes the hybrid cyber-attack detection process [7]. The data collected from the traffic network is first directed to the signature-based cyber defense strategy. The intrusion is detected if the signature profiles in the database match the relevant situation.

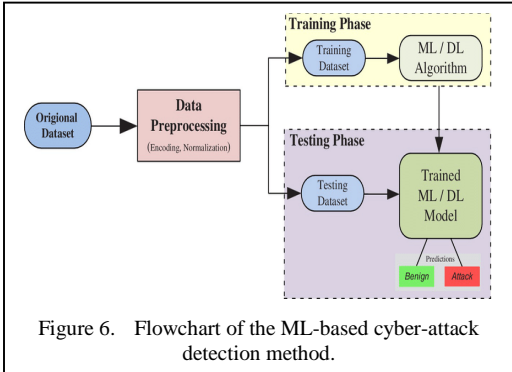
An anomaly-based defense strategy is activated if a signature-based method cannot detect a cyber threat. If a known attack is detected, an alert report is produced, while for unknown attacks, a new signature is created, and the attack signature database is updated.

5) *AI-based methods*

AI-based method is an innovative and state-of-the-art cyber-attack detection method. It detects cyberattacks by learning from large data



sets and identifying complex patterns. ML methods learn the normal operational behavior of CPPS and monitor deviation in behavior. While many techniques, such as supervised, unsupervised, and deep learning, can be applied, supervised learning distinguishes between normal and abnormal situations using pre-labeled data. In contrast, unsupervised learning generates anomaly and attack detection patterns from unlabeled data. Deep learning can perform complex and detailed analyses thanks to its multi-layered structure. Finally, it has provided accurate and precise detection with its ability to continuously monitor and analyze system data and learn new types of attacks and their development over time. Due to the need for extensive and various data sets, data processing processes can take time and effort. Training and data updating for learning requires high computational power, and regular review and optimization of the model are necessary to obtain



accurate results and reduce false positive rates in case of possible errors. Related techniques passively ensure cybersecurity, supporting CPPS reliability and promising future approaches [14]. Fig. 6 shows the ML-based cyber-attack detection flowchart [15].

There are three phases: data preprocessing, training, and testing. Data preprocessing is performed to ensure the applicability of the dataset to the algorithm and serves the purpose of coding, cleaning and normalization. The prepared data is randomly distributed into two separate classes: training and test datasets. The training data, representing 70% to 80% of the total dataset, is evaluated in the learning phase [16]. The learning times vary depending on the size of the dataset and the complexity of the proposed AI strategic model. The predictions made on the test dataset after model training according to various metrics (precision, recall, false alarm rate, true negative rate, accuracy, root mean squared error, mean absolute error, mean absolute percentage error, r^2 score, f^1 score, etc.) are briefly explained as ML techniques are discussed extensively in [15].

6) State observers

System dynamics and behavior are modeled via observers and continuously compared with real-time data. Sophisticated techniques such as Luenberger or Kalman filters are preferred as state observers to determine the current operational state and detect potential infractions.

a) Luenberger observers

It is designed to correctly estimate the actual state of CPPS in the case of linear systems. It uses designs based on modern control theory since the controlled system states can be measured. In many practical applications, measuring only a few state signals is sufficient. Theoretical applications where state vectors are known are limited, and measuring system states is costly. On the other hand, observers are used to determine state vectors. Luenberger, introduced observers and physical systems can have several delays. Especially for time-independent linear systems, one focuses on a similar point of view if the system changes without delay. Instead, in practical applications, delays occur in system states, while in fast-running systems, the time delay can be negligible. Delays are a parameter that determines the behavior of CPPS and cannot be used in delay-less system models. In single-input, single-output delayed states (SISO), and time-independent (LTI) systems, all system

states can be studied using the delayed observer model, provided the system is observable. Instead of observers, sensors can perform a similar task. However, the number of sensors to be used may increase depending on the number of states, or sensors may not be utilized for every state signal since some states cannot be measured and observers are needed. Various methods are prominent in delayed-time systems. System estimation using a state vector observer is discussed in [17]. In particular, the state space for a linear and time-independent system with a single input and additional output is given by Eq. (1).

$$\begin{cases} \dot{x}(t) = A.x(t) + B.u(t) \\ y(t) = C.x(t) \end{cases} \quad (1)$$

Here $\dot{x}(t) \in R^n$ is the state vector. $u(t)$ represents the input signal, and $y(t)$ represents the output signal. Equation (2) gives the state space model for time-delayed systems.

$$\begin{cases} \dot{x}(t) = A.x(t) + A_d.(t - \tau) + B.u(t) \\ y(t) = C.x(t) \end{cases} \quad (2)$$

Here, A_d is the delayed state system matrix, and the objective is to estimate the system states with unknown states and delay with the help of an observer. The Luenberger observer model is defined by Eq. (3) [18].

$$\dot{\hat{x}}(t) = A.\hat{x}(t) + A_d.\hat{x}(t - \tau) + L.(y - \hat{y}). \quad (3)$$

Here, $\hat{x} \in R^n$ is the state vector of the observer, and \hat{y} is the output of the observer.

$L \in R^n$ is the Luenberger coefficient vector. Similarly, the Luenberger observer for delayed-time systems can be extended to the state space expression in (4). Defining the error dynamics as in (5) is necessary to stabilize the observer and system error dynamics. Moreover, the derivative of the error dynamics for use in calculations is determined as in Eq. (6). Rearranging Eqs. (2) and (4), Eq. (7) is obtained.

$$\dot{\hat{x}}(t) = A.\hat{x}(t) + A_d.\hat{x}(t - \tau) + L.(y - \hat{y}) + B.u(t), \quad (4)$$

$$e(t) = x(t) - \hat{x}(t), \quad (5)$$

$$\dot{e}(t) = \dot{x}(t) - \dot{\hat{x}}(t), \quad (6)$$

$$\dot{e}(t) = A.x(t) + A_d.x(t - \tau) - A.\hat{x}(t) - A_d.\hat{x}(t - \tau) - LC(x - \hat{x}) \quad (7)$$

Due to the delay, the $e^{-\tau s}$ expression in the Laplace transform in Eq. (7) is expanded according to the Taylor series. The Laplace transform of the error dynamics is obtained as in Eq. (8) using the first two terms. The characteristic polynomial of the error dynamics is represented in its most general form by Eq. (10) using Eq. (9). Finally, cyber security operations can be performed by monitoring the observer and system state change using the computed Luenberger vector.

$$E(s) = [sI + A_d\tau s + LC - (A + A_d)]^{-1} e(0), \quad (8)$$

$$\det([sI + A_d\tau s + LC - (A + A_d)]^{-1}) = 0, \quad (9)$$

$$p(s) = s^n + a_n s^{n-1} + \dots + a_0. \quad (10)$$

b) Kalman filter

It is a filter that can predict cyber-attack cases in systems modeled as a state space, using prior knowledge of the model, mainly input and output information. It is an idea proposed by Rudolf, a Hungarian-American mathematician and scientist working on systems theory. It is based on observation theory around a decided point of view. Minimum variance estimation or Kalman filter is the best applicable method if stochastic or random noise is available and accounted for in the system. Like traditional estimators, the Kalman filter has a filtering property that makes it a powerful and capable tool for estimating unmeasurable system states. Comparing the model prediction to the observation and scaling the difference by a multiplier known as the Kalman gain is fed back to the model as input for subsequent predictions, and its performance is determined by adjusting the gain. Especially in a low-gain state space, the filter follows the model predictions more closely and relies only on the model predictions or a single measurement. At each time step, it estimates the unknown value with its uncertainties. When the result of the subsequent measurement is observed, these estimates are updated with a weighted average, giving more weight to estimates with lower uncertainty. The Kalman filter conditions can be fitted to the problem as in Eqs. (11) - (13).

$$\begin{cases} x_k = A.x_{k-1} + B.u_k + w_{k-1}, \\ z_k = H.x_k + v_k \end{cases}, \quad (11)$$

$$\begin{aligned} & \overbrace{\hat{x}_k^- = A.\hat{x}_{k-1}^- + B.u_k}^{\text{Prediction / Time Update}}, \\ & p_k^- = A.p_{k-1}A^T + \square \end{aligned}, \quad (12)$$

$$\begin{aligned} & \overbrace{K_k = p_k^- . H^T (H . p_k^- . H^T + R)^{-1}}^{\text{Correction / Measurement Update}} \\ & \hat{x}_k = \hat{x}_k^- + K_k (z_k - H.\hat{x}_k^-) \\ & p_k = (1 - K_k . H) . p_k^- \end{aligned}. \quad (13)$$

Analyzing these equations, the estimated value \hat{x}_k of the signal x is calculated for each k using the measured value z_k . It is suitable for situations where the accuracy of the estimated value is not sure. Here again, K_k is the Kalman gain, and \hat{x}_{k-1}^- is the previous state estimate of the signal. Each x_k value of the signal is calculated using Eq. (11) with a linear combination of its previous value x_{k-1} with the control signal (u_k , usually not used) and the preprocessing noise w_{k-1} . Any measurement value z_k is determined from the expression of the signal value and the measurement noise, while the parameters are considered Gaussian. A , B , and H represent the general notation of the matrices and take numerical values for most signals. Fixed assumptions can be made so the matrix operation is not performed based on changing values at each stage. When the system reliability increases, the arithmetic means and standard deviation of the noise functions (v_k , w_{k-1}) are estimated. While the true values are calculated with Gaussian, the Kalman filter obtains accurate estimates with suitable convergence. After the model fits the Kalman filter, the time and estimation update and the measurement adaptation and correction phases are initiated. Before the correction update, the initial raw estimation and error covariance are used. The previous state and the corresponding error covariance are estimated and used to calculate the Kalman gain in the correction phase. z_k is updated instead of the measurement; the error covariance is corrected and reassigned as input to the prediction phase.

III. CYBER DEFENSE IN CYBER-PHYSICAL POWER SYSTEMS

Increasing cyber-attacks on CPPS, dominated by multidimensional and hidden features, have drawn global attention to the cyber and physical field [19]. In addition to the time and space dimension [20], data-centric defense strategies based on data availability, integrity, and confidentiality are gaining attention [21]. Due to the increased coordinated attack types, it is mandatory to study CPPS security detection and defense methods based on the periodic evolution process of the attack event: before, during, and after.

A. Pre-cyber Attack Security Analysis and Determination of Defense Strategy

Preventing potential attacks via authentication and security encryption requires maintaining system integrity and prohibiting unauthorized access. Authenticating users or devices before they access the system will make it difficult for unauthorized persons to gain resources. Security encryption prevents unauthorized use of data and ensures the confidentiality and integrity of transmitted information.

1) Secure authentication and reliable access technologies

As each IED deals with different metering aspects and data tracking and requires “plug-and-play” access, using authentication and trusted access technologies is inevitable. Encryption is critical to ensure that any data transmitted in the system is not captured, monitored, or altered. Authentication technologies legally verify the identity of the access object, which can represent a smart device or any other equipment in the CPPS. A lightweight authentication using AI-based Markov model prediction as the first line of defense of the security mechanism is discussed in [22]. A low entropy shared password scheme is used in [23] to authorize communication devices. A blockchain-based trust reconciliation strategy for cyber terminals where there is no trust environment is discussed in [24]. Here, a multi-trust analysis mechanism is built with consortium blockchain and beta allocation, and its performance against multiple malicious attacks is verified. Data encryption encrypts plaintext data and repeats in retransmission to prevent an attacker or eavesdropper from obtaining private data. There are symmetric and asymmetric key encryption implementations, and both are widely used based

on different needs, such as data criticality and computational complexity.

2) Defense strategy and resource allocation

The development of defensive strategies, in addition to technology-based security precautions, is valuable for the early prevention of potential attacks and the optimization of defense resources. Vulnerabilities of CPPS can be detected from the attacker's point of view by evaluating the performance of defense strategies via attack analysis and simulation. The possible attack potential can be extracted, and resource allocation for subsequent security defense can be made using modeling and system extrapolation. Recently, several proposals have been made to simulate different types of attacks in the presence of noise [25]. Especially noteworthy are parameter-weighted temporal automata based on the attack tree model [26], attack graph models for quantitative analysis of network attack and inter-domain chain failures [27], and synchronous or not attack models for phasor measurement unit (PMU) measurement data [28].

After the attack analysis and the performance evaluation of the system, the allocation of defense resources and the improvement of the defense capacity are necessary based on the potential risks detected. There are also examples that do not meet this condition. For instance, a game theory-based defense resource allocation strategy based on changes in the main operating parameters in the power system is developed in [29] for false data injection attacks (FDIA), which is one of the expected attack types. However, defense resources need to be allocated appropriately in constrained resource allocation. After risk analysis based on Bayesian adaptive networks, a suitable strategy for resource allocation is proposed in [30]. If the attack scope is extended to dynamic and large-scale networks, the optimal action set should be obtained by the coevolutionary algorithm to achieve operational balance [31]. Moreover, separating attack and defense behaviors into three parts, namely, power plant, transmission, and distribution system, facilitates the development of optimal defense strategies [32]. The defense strategies and resource allocation should be distributed via the firewall and forward and backward isolation devices of the CPPS.

B. Cyber Attack Detection and Defense Technology and Strategy

1) Multi-level security line of defense approach for conventional power system and CPPS

Traditional power systems usually have three lines of defense to ensure safety against faults. The first includes fast relay protection and control strategies to guarantee stable grid operation under single-phase fault conditions. In contrast, the second line of defense provides emergency control actions such as generator and load shedding against low probability but more severe faults. The last line of defense uses frequency and voltage emergency control devices, and out-of-system-step deregulation. The relevant devices for emergency control are quickly activated in the event of multiple inevitable severe faults to prevent large-scale outages. CPPS similarly has three lines of defense. However, the first line of defense aims to strengthen communication network planning and provide efficient service routing to enhance defense resilience against expected power system construction and operation failures. The second line of defense includes network and service self-healing functions and aims to address failures quickly. The third line of defense conducts system-level improvement and repair by blocking existing terminals/channels and centralizing the management of limited communication resources. The last line of defense is activated immediately in case a severe cyber threat rapidly spreads, and grid outages are mitigated by shedding low-frequency and low-voltage loads or split of the power system. However, it is necessary to plan main and backup routing paths in the power systems communication network in case of a possible communication link failure after a cyber-attack [33]. The first line of defense is functionally realized by automatically jumping to the backup path in case of a failure in the communication network. Moreover, the synchronous digital hierarchy (SDH) ring structure, which can perform automatic rotation within 50 ms, reinforces the security procedure by providing the second line of cyber defense. The first two lines of defense may not be sufficient, as the power system sectionalization only requires calculating the power flow given the complexity of the connection between cyber and physical systems. The failure evolution and, if necessary, the interruption of one of the communication links will hinder the sustainability of many

power services. In addition, if the cyber and physical interrupting surfaces are not combined, the failure scope will expand. To address this increasing threat problem, an innovative CPPS saturation defense mechanism based on combined cyber-physical active interruptions is proposed in [34]. This way, safe and stable operations can be supported by minimizing the attack scope.

2) Cyber-attack detection and defense technology

The most valuable time for defense is gained, and the consequences of the attack are minimized if it can be accurately detected within a short period of the CPPS being attacked. CPPS can be structurally divided into power physical and information areas and is an ideal approach. Detection methods in the power physical area mainly evaluate whether electrical measurements, decision-making instructions, and sudden changes in the system's operating state obey physical laws [19]. In particular, the malicious data detection method developed in [35] considering spatial and temporal correlation in residual detection or condition constraints is an example of the relevant case. Another example is the double feed deep learning detection method, where the data obtained by the PMU is fed [36]. In addition, SCADA-based multi-step malicious data detection algorithm is another approach because of the FDIA threat [37,38]. On the other hand, on the cyberspace side, cyber-attack attempts in information technologies are usually monitored with the help of an intrusion detection system (IDS) or a security information event management system (SIEM). The addresses and network logs of cyber devices are considered by attackers and used to detect transmission traffic or communication models. Consistency detection or prior knowledge-based identification strategies may be preferred in cyber defense. For instance, researchers in [39] detected anomalous transmission events in the communication network by comparing data sent and received from sensors and actuators. Besides the proposed whale optimization algorithm and neural network-based model for intrusion detection, a method for classifying attack attempts is proposed in [40]. A novel support vector machine (SVM) based attack detection model combining smart meters and power devices is developed in [41]. The performance of an anomaly-based cyber-attack detection method based on the Gaussian mixture model and

Kalman filtering is evaluated for SCADA in [42]. A second frequency control method is proposed in [43] by realizing an intrusion detector-based design for possible denial of service (DoS) attacks on the power system frequency controller instead of SCADA. On the other hand, a distributed data-based cyber-attack detection against the FDIA threat in multi-area interconnected power systems is emphasized in [44]. Considering the large-scale electric vehicles that can be connected to such systems, a more sophisticated method is needed as the attack scope of FDIA will expand [45]. Moreover, unlike decomposing every available message, CPPS information flows must be evaluated in the mixed time-frequency domain [46]. The researchers in [46] addressed the issue via an anomaly-principled traffic spectrum clustering detection method that integrates artificial swarm optimization and SVM. It is a promising method to increase the detection speed, but only the transmission behavior characteristics of the power and communication flow are needed. Therefore, attacks and infiltrations can be accurately detected without analyzing every data packet. However, AI and ML methods for fast and accurate cyber-attack detection have recently attracted attention. Recursive neural networks and blockchain technology are integrated in [47] to defend against energy internetwork attacks and illegal operations. Another method for addressing cyber infiltration attempts is to use feature volume extraction, data preprocessing, and ML classifiers. These techniques can recognize and respond faster to complex and ever-changing cyber threats.

The main objective of CPPS defense is to ensure voltage and frequency stability and power angle balance. Cyber-attack prevention and system stability control can be integrated for operational sustainability. Especially the design of control devices is a practical approach to maintain system stability. Nowadays, two security methods in attacks against CPPS are categorized: flexible control and active defense control methods. Flexible control methods analyze the system performance and attack parameters based on a specific intrusion model. At the same time, sub-functional processes such as the Lyapunov function can be used to evaluate the resilience constraints in the attack. After the analysis, a resilience control triggering mechanism is designed to ensure the stability of the input state [48], but the relevant cyber

defense method follows a more conservative behavior. On the contrary, active defense control methods are based on the ideology of active compensation to prevent cyber-attacks and maintain the control system's performance. These defense mechanisms mainly adopt predictive control [49] and multi-channel networked strategies [50]. This way, the control system performance is guaranteed by responding to attacks quickly and efficiently. Apart from the predictive and multichannel strategy, Honeypot technology is an exciting defense technique that works on a trap set in the network defense to fool the attacker [51]. The attacker is baited via network service providers, hosts, or messages, and the attack behavior is detected to determine the attacker's means and attack strategy. This method can infer the attack intent and motivation and weaken the attack by consuming resources. Honeypot technology protects system resources and critical information by allowing attackers to focus on the traps instead of the system components.

IV. CONCLUSIONS

The scope of possible cyber threats has expanded by integrating cyberinfrastructure into smart power systems. This study highlights the development of modern CPPS infrastructure. It addresses the detection of cyber violations and defense mechanisms from a technological and strategic point of view within a systematic plan. The functional processes of innovative cyber-attack detection techniques based on signatures, anomalies, and behaviors, including state observers, are evaluated in a cost-benefit relationship. At the same time, a similar approach is maintained for modern AI-scale reliability schemes. Moreover, hybrid methods that overcome the vulnerabilities of individual techniques are discussed, and defense mechanisms on secure authentication, encryption, and access technologies are evaluated.

Future investigations of attack violations in CPPS communication networks and security protection modes are needed. Quantitative security procedures should be performed for fusion attack modeling and defense detection, especially by analyzing the probabilities of sequential failures caused by cyber-attacks. Qualitative differences between ordinary failures and intense attacks, real-time sustainable security analysis, and online auxiliary decision-making in cyber-attack defense should be emphasized. The

information and physically integrated layer of cyber defense and the prevention, emergency, and recovery aspects must be addressed at multiple spatial and temporal scales. Focus on technological advances such as blockchain and quantum computing to reinforce cybersecurity performance by considering the cyber characteristics of wireless measurement and monitoring networks and with the help of big data analytics. Blockchain and quantum computing, when integrated into CPPS cybersecurity frameworks, can offer security and performance advances beyond traditional methods. While blockchain is an immediately practical technology for data integrity and distributed security solutions, quantum computing can deliver more innovative solutions in the long term. Blockchain technology can be used to track and store data in the short term securely. Quantum computing can be used in the long term to achieve higher security standards and adopt quantum-based solutions to solve big data problems. However, a cyber security strategy that is both effective and cost-sustainable should be developed before investing in these two technologies, considering the suitability of the CPPS' current infrastructure and sectoral requirements. In conclusion, a functional analysis of cyber-attack methods and a good knowledge of applicable and up-to-date possible defense mechanisms are the most effective ways to deal with new cyber intrusions.

A different perspective is to carefully select both technical and operational metrics to assess the success of cybersecurity advances in CPPSs. To prioritize these advances in the short term, the industry should focus on critical infrastructure security, cost-effective solutions, human factors, threat intelligence, and standards compliance. These approaches can provide a practical roadmap to make CPPS systems more secure and sustainable. The industry can prioritize cybersecurity investments and improvements in the short term by optimizing the processes of Focusing on Securing Critical Infrastructure, Fast and Cost-Effective Solutions, Investing in Human Factors, Threat Intelligence-Based Strategies, and Facilitating Adaptation and Certification Processes.

Eventually, the scope of the study will be extended to analyze the cost-benefit relationships of different detection techniques and defense mechanisms in more detail. The practicability of the proposed methods will be evaluated considering not only the technical conditions but

also the economic cost-benefit relationship. Thus, the realistic applicability of the proposed methods in practical and financial aspects will be revealed.

REFERENCES

- [1] Adepu, S., & Mathur, A. (2021). Distributed attack detection in a water treatment plant: Method and case study. *IEEE Transactions on Dependable and Secure Computing*, 18(1), 86–99.
- [2] Ahmad, Z., Shahid Khan, A., Wai Shiang, C., Abdullah, J., & Ahmad, F. (2021). Network intrusion detection system: A systematic study of machine learning and deep learning approaches. *Transactions on Emerging Telecommunications Technologies*, 32(1).
- [3] Alsughayyir, B., Qamar, A. M., & Khan, R. (2019). Developing a network attack detection system using deep learning. In *2019 International Conference on Computer and Information Sciences (ICIS)*, (pp.1-5).
- [4] André, É., Lime, D., Ramparison, M., & Stoelinga, M. (2021). Parametric analyses of attack-fault trees. *Fundamenta Informaticae*, 182, 69–94.
- [5] Aslan, O., & Samet, R. (2017). Investigation of possibilities to detect malware using existing tools. In *2017 IEEE/ACS 14th International Conference on Computer Systems and Applications (AICCSA)*, (pp. 1277–1284).
- [6] Aslan, O., & Samet, R. (2020). A comprehensive review on malware detection approaches. *IEEE Access*, 8, 6249–6271.
- [7] Assante, M. (2016). *Confirmation of a coordinated attack on the ukrainian power grid*. 23, 1–5. Available at: ics.sans.org/blog/2016/01/09/confirmation-of-a-coordinated-attack-on-the-ukrainian-power-grid
- [8] Ayiad, M. M., Leite, H., & Martins, H. (2021). State estimation for hybrid VSC based HVDC/AC: Unified bad data detection integrated with gaussian mixture model. *IEEE Access*, 9, 91730–91740.
- [9] Azad, M. A., Bag, S., Perera, C., Barhamgi, M., & Hao, F. (2020). Authentic caller: Self-enforcing authentication in a next-generation network. *IEEE Transactions on Industrial Informatics*, 16(5), 3606–3615.
- [10] Bangui, H., Ge, M., & Buhnova, B. (2022). A hybrid machine learning model for intrusion detection in VANET. *Computing*, 104(3), 503–531.
- [11] Ferrag, M. A., & Maglaras, L. (2020). DeepCoin: a novel deep learning and blockchain-based energy exchange framework for smart grids. *IEEE Transactions on Engineering Management*, 67(4), 1285–1297.
- [12] Gu, Y., Yu, Z., Diao, R., & Shi, D. (2020). Doubly-fed deep learning method for bad data identification in linear state estimation. *Journal of Modern Power Systems and Clean Energy*, 8(6), 1140–1150.
- [13] Guan, S., Wang, J., Yao, H., Jiang, C., Han, Z., & Ren, Y. (2020). Colonel blotto games in network systems: models, strategies, and applications. *IEEE Transactions on Network Science and Engineering*, 7(2), 637–649.
- [14] Haghnegahdar, L., & Wang, Y. (2020). A whale optimization algorithm-trained artificial neural

- network for smart grid cyber intrusion detection. *Neural Computing and Applications*, 32(13), 9427–9441.
- [15] Head, T. M. (2015). *Business Blackout The insurance implications of a cyber attack on the US power grid Emerging Risk Report-2015 Innovation Series SOCIETY & SECURITY Lloyd's Emerging Risk Report-2015*. University of Cambridge Centre for Risk Studies. Available at: www.lloyds.com/ScenarioDesign
- [16] Hu, Z., Liu, S., Luo, W., & Wu, L. (2021). Intrusion-detector-dependent distributed economic model predictive control for load frequency regulation with PEVs under cyber attacks. *IEEE Transactions on Circuits and Systems I: Regular Papers*, 68(9), 3857–3868.
- [17] Independent Electricity System Operator. (2011). *Modernizing Ontario's Electricity System: Next Steps (2nd ed., Issue May)*. The Ontario Smart Grid Forum. Available at: <https://www.ieso.ca/>
- [18] Jan, M. A., Khan, F., Khan, R., Mastorakis, S., Menon, V. G., Alazab, M., & Watters, P. (2021). Lightweight mutual authentication and privacy-preservation scheme for intelligent wearable devices in industrial-CPS. *IEEE Transactions on Industrial Informatics*, 17(8), 5829–5839.
- [19] Jolfaei, A., & Kant, K. (2020). On the silent perturbation of state estimation in smart grid. *IEEE Transactions on Industry Applications*, 1–1.
- [20] Kamal, M., Farajollahi, M., Nazari-pouya, H., & Mohsenian-Rad, H. (2021). Cyberattacks against event-based analysis in micro-PMUs: Attack Models and Counter Measures. *IEEE Transactions on Smart Grid*, 12(2), 1577–1588.
- [21] Keshk, M., Sitnikova, E., Moustafa, N., Hu, J., & Khalil, I. (2021). An integrated framework for privacy-preserving based anomaly detection for cyber-physical systems. *IEEE Transactions on Sustainable Computing*, 6(1), 66–79.
- [22] Kushner, D. (2013). The real story of stuxnet. *IEEE Spectrum*, 50(3), 48–53.
- [23] Liu, S., Siano, P., & Wang, X. (2020). Intrusion-detector-dependent frequency regulation for microgrids under denial-of-service attacks. *IEEE Systems Journal*, 14(2), 2593–2596.
- [24] Liu, Y., Chen, Y., & Li, M. (2021). Dynamic event-based model predictive load frequency control for power systems under cyber attacks. *IEEE Transactions on Smart Grid*, 12(1), 715–725.
- [25] Mudzingwa, D., & Agrawal, R. (2012). A study of methodologies used in intrusion detection and prevention systems (IDPS). In *2012 Proceedings of IEEE Southeastcon*, (pp. 1–6).
- [26] Nejabatkhah, F., Li, Y. W., Liang, H., & Reza Ahrabi, R. (2020). Cyber-security of smart microgrids: A survey. *Energies*, 14(1), 27.
- [27] Niknami, N., Inkrott, E., & Wu, J. (2022). Towards analysis of the performance of IDSs in software-defined networks. In *2022 IEEE 19th International Conference on Mobile Ad Hoc and Smart Systems (MASS)*, 787–793.
- [28] Patel, A., Roy, S., & Baldi, S. (2021). Wide-area damping control resilience towards cyber-attacks: A dynamic loop approach. In *IEEE Transactions on Smart Grid*, 12(4), 3438–3447.
- [29] Pilz, M., Naeini, F. B., Grammont, K., Smaghe, C., Davis, M., Nebel, J.-C., Al-Fagih, L., & Pfluegel, E. (2020). Security attacks on smart grid scheduling and their defences: a game-theoretic approach. *International Journal of Information Security*, 19(4), 427–443.
- [30] Sarker, I. H., Kayes, A. S. M., Badsha, S., Alqahtani, H., Watters, P., & Ng, A. (2020). Cybersecurity data science: an overview from machine learning perspective. *Journal of Big Data*, 7(1), 41.
- [31] Shan, X. G., & Zhuang, J. (2020). A game-theoretic approach to modeling attacks and defenses of smart grids at three levels. *Reliability Engineering & System Safety*, 195, 106683.
- [32] Shi, J., Liu, S., Chen, B., & Yu, L. (2021). Distributed data-driven intrusion detection for sparse stealthy FDI attacks in smart grids. *IEEE Transactions on Circuits and Systems II: Express Briefs*, 68(3), 993–997.
- [33] Shi, L., Li, Y., & Ma, M. (2019). Latest research progress of honeypot technology. *Journal of Electronics & Information Technology*, 41(2), 498–508.
- [34] Sikorski, M., & Honig, A. (2012). *Practical malware analysis: the hands-on guide to dissecting malicious software*. no starch press.
- [35] Smith, M. D., & Pate-Cornell, M. E. (2018). Cyber risk analysis for a smart grid: how smart is smart enough? A multiarmed bandit approach to cyber security investment. *IEEE Transactions on Engineering Management*, 65(3), 434–447.
- [36] Staff, T. (2016). *Steinitz: Israel's electric authority hit by 'severe' cyber-attack*. *The Times of Israel*.
- [37] Sun, C.-C., Sebastian Cardenas, D. J., Hahn, A., & Liu, C.-C. (2021). Intrusion Detection for Cybersecurity of Smart Meters. *IEEE Transactions on Smart Grid*, 12(1), 612–622.
- [38] Symantec. (2014). *Dragonfly: Cyberespionage Attacks Against Energy Suppliers - Symantec Security Response*.
- [39] Tang, Y., Li, M., Wang, Q., & Ni, M. (2019). A review on research of cyber-attacks and defense in cyber physical power systems part two detection and protection. *Automation of Electric Power Systems*, 43(10), 1-9.
- [40] Trinh, H., & Aldeen, M. (1999). Estimation of linear functional states for time delay systems. In *1999 European Control Conference (ECC)*, (pp.3697–3702). <https://doi.org/10.23919/ECC.1999.7099905>
- [41] Tsai, C.-F., Hsu, Y.-F., Lin, C.-Y., & Lin, W.-Y. (2009). Intrusion detection by machine learning: A review. *Expert Systems with Applications*, 36(10), 11994–12000.
- [42] Wang, C., Mu, G., & Cao, Y. (2020). A method for cleaning power grid operation data based on spatiotemporal correlation constraints. *IEEE Access*, 8, 224741–224749.
- [43] Wang, Y., Gao, K., Zhao, T., & Qiu, J. (2016). Assessing the harmfulness of cascading failures across space in electric cyber-physical system based on improved attack graph. In *Proceedings of the CSEE*, 36(6), 1490–1499.
- [44] WPD-ResNeSt: Substation station level network anomaly traffic detection based on deep transfer learning. (2021). *CSEE Journal of Power and Energy*

- Systems*. <https://doi.org/10.17775/CSEEJPES.2020.02850>
- [45] Yang, T., Yan, P., & others. (2022). Research on Saturation defense method of power cyber-physical system based on active cut set. *Proceedings of the CSEE*, 42(2), 12.
- [46] Yohanandhan, R. V., Elavarasan, R. M., Manoharan, P., & Mihet-Popa, L. (2020). Cyber-physical power system (CPPS): A Review on modeling, simulation, and analysis with cyber security applications. *IEEE Access*, 8, 151019–151064.
- [47] Yu, J., Yu, L., & Yang, T. (2021). Blockchain-based trust consensus method for power internet of Things terminal. *Automation of Electric Power Systems*, 45(17), 1–10.
- [48] Yuan, H., & Xia, Y. (2018). Resilient strategy design for cyber-physical system under DoS attack over a multi-channel framework. *Information Sciences*, 454–455, 312–327.
- [49] Zhang, H., Liu, B., & Wu, H. (2021). Smart grid cyber-physical attack and defense: a review. *IEEE Access*, 9, 29641–29659.
- [50] Zhang, T., Ji, X., & Xu, W. (2022). Jamming-resilient backup nodes selection for RPL-based routing in smart grid AMI networks. *Mobile Networks and Applications*, 27(1), 329–342.
- [51] Zheng, Y., Yan, Z., Chen, K., Sun, J., Xu, Y., & Liu, Y. (2021). Vulnerability assessment of deep reinforcement learning models for power system topology optimization. *IEEE Transactions on Smart Grid*, 12(4), 3613–3623.

